Université d'Ottawa · University of Ottawa

Université d'Ottawa · University of Ottawa

FACULTÉ DES ÉTUDES SUPÉRIEURES ET POSTDOCTORALES

FACULTY OF GRADUATE AND POSTDOCTORAL STUDIES

Adrian MUNTEANU

AUTEUR DE LA THÈSE - AUTHOR OF THESIS

M. A. Sc. (Civil Engineering)

GRADE - DEGREE

Department of Civil Engineering

FACULTÉ, ÉCOLE, DÉPARTEMENT - FACULTY, SCHOOL, DEPARTMENT

TITRE DE LA THÈSE - TITLE OF THE THESIS

Scouring Around a Cylindrical Bridge Pier Under Partial Ice-covered Flow Conditions

R. Frenette

DIRECTEUR DE LA THÈSE - THESIS SUPERVISOR

R. Townsend

CO-DIRECTEUR DE LA THÈSE - THESIS CO-SUPERVISOR

EXAMINATEURS DE LA THÈSE - THESIS EXAMINERS

C. Rennie

P. Van Geel

J.-M. De Koninck, Ph.D.

LE DOYEN DE LA FACULTÉ DES ÉTUDES SUPÉRIEURES ET POSTDOCTORALES

DEAN OF THE FACULTY OF GRADUATE AND POSTDOCTORAL STUDIES

Scouring Around a Cylindrical Bridge Pier Under Partially Ice-covered Flow Condition

Adrian Munteanu

A thesis
submitted under the supervision of Dr. Richard Frenette

in a partial fulfillment of the requirements for the degree of
Master of Applied Science in Civil Engineering

Department of Civil Engineering
University of Ottawa
Ottawa-Carleton Institute of Civil Engineering
Ottawa, Ontario, Canada
K1N 6N5

June 2004

Your file Votre référence
ISBN: 0-494-01557-8
Our file Notre référence
ISBN: 0-494-01557-8

I knew the equation of my road, but the boundaries were unclear like in the mist... and sometimes I was afraid to deviate to other unknown roads. Then I met this person, who helped me define these boundaries and see the direction of my road... It was a hard process especially when we were interfering with the equations of other roads... Then I met some other people who showed me many new roads and how to analyze their equations, to predict their directions and to find their boundaries...

Now I know the boundaries of my road and even if I travel at low speed yet at least I can see its direction, but most of all I learn about many other roads and how to define new boundaries...

Spring... on the third planet from SUN

...the forth year of the new millennium

an apprentice[1]

---

[1] Part of a document that was discovered on a planet called Earth located in the far *Solar System*. It is believed that from this planet humans have started the space expansion.
Galactic Library/New City/Andromeda
Ancient Archives/document: ESS-CVG/WR-ST&SBP/#4325-2004/c3989

Acknowledgements

I would like to thank Dr. Richard Frenette for taking me on board of his research "ship", and for giving me support, guidance and precious advices during the course of this study. It has been an honor to be his apprentice.

My appreciation is also directed to Dr. Ron Townsend as my co-supervisor of this thesis, for his constant support and interest on my work.

Many thanks go out to all my colleagues, especially to Gavin Post for his assistance in laboratory work, to Troy Matsuura for sharing with me many secrets of the written English techniques, to my former colleague Sudhakar Molleti for his previous work which enable my study to have a smooth take off, and to Tarik Youssef for his valuable support.

Finally, I would like to thank my Elena for her constant encouragement and support and my son, Philippe who balanced my efforts by showing me the existence of other wonderful worlds.

ABSTRACT

Sediment transport processes represent a significant parameter in any work that involves management of water flow. Moreover, all river structures are affected and prone to various types of these processes, which are also known as the erosion/deposition phenomena. Another aspect, which has become extremely important in recent decades, is the effect of ice-cover on rivers. The presence of ice-cover in an open-channel dramatically alters many features of the flow as well as bed mobility.

This thesis reports on the first step of an ongoing study of scouring around a cylindrical bridge pier under ice-cover conditions. Previous research confirmed that sediment transport decreases in ice-covered flow compared to free-surface flow. However, most of that research was conducted in a flow depth adjustment condition, maintaining constant the energy slope for both the ice-covered and the free-surface flow. This represents a valid hypothesis when an appropriate length scale is considered (i.e. long river reaches), but numerous other phenomena must be analyzed at a much shorter length scale: i.e. river reaches that contain abutments, bridge piers, cross-section alterations, tide bends, etc. According to Zabilansky et al. (1996-2002) findings, in these cases we can confirm that for an ice-covered flow in nature it is common to adjust faster the energy slope than the flow depth, thus, leading to drastic changes in the sediment transport and scouring behaviour.

From a scouring point of view, when the flow depth has minor variations compared to the energy slope changes, the presence of an ice-cover significantly increases the flow velocities in the bottom half of the flow depth. As a result, a larger part of the flow energy is directed to the scouring process compared to the free-surface case.

The objective of this laboratory study is to determine from a sediment incipient conditions point of view the worst ice-cover configuration with respect to the free-surface flow and to uncover features of scouring around a cylindrical bridge pier for that extreme ice-cover case. In this study three ice-cover configurations are defined with respect to the presence of a bridge pier: (i) Total Ice-Cover which entirely covers the channel and completely surrounds the bridge pier, (ii) 2 Sides Partial Ice-Cover which covers two sides of the channel leaving the bridge pier in the central region of the flow in open-water , and (iii) 1 Side Partial Ice-Cover which covers only one side of the channel leaving the other side and the bridge pier in free-surface flow. First, the analysis is carried out in order to determine which case presents the extreme impact from a sediment critical condition (= incipient motion) point of view, and secondly, the same extreme case is reproduced to measure the impact on the scouring process around a cylindrical bridge pier.

Laboratory experiments are performed for all cases under clear-water conditions when the flow regime is approaching the sediment transport critical conditions and in a flow energy slope adjustment condition. The experimental results indicate the 2 Sides Partial Ice-Cover configuration as the worst-case scenario, developing in the open-water (central) region of the channel higher values for flow velocities and bed shear stresses when compared to the other ice-cover configurations and the free-surface case. In terms of scouring, the same ice-cover configuration shows up to 55% deeper scour hole around a cylindrical bridge pier compared to the free-surface case.

Table of Content

List of Symbols

General

g gravitational acceleration, [m/s^2];

ρ fluid density, [kg/m^3];

γ fluid specific weight, [N/m^3];

ν fluid kinematic viscosity, [m^2/s];

μ fluid dynamic viscosity, [kg/m s].

Hydraulics and sediment transport

B channel width, [m];

P_w wetted perimeter, [m];

S_o channel bed slope;

S flow energy slope;

h total flow depth, [m];

y local flow depth, [m];

y_o uniform flow depth, [m];

δ thickness of the laminar layer;

Fr flow Froude number;

κ von Karman constant, $\kappa = 0.4$.

B_N Nikuradse flow dimensionless parameter;

k_s bed material roughness, [mm];

u longitudinal velocity component, [cm/s];

v transversal velocity component, [cm/s];

u_* shear velocity, [m/s];

u_{*cr} critical shear velocity, [m/s];

u_*' shear velocity due to the drag effect, [m/s];

l mixing length;

τ shear stress, [N/m^2];

τ_o bed shear stress, [N/m^2];

τ_{cr}	critical bed shear stress, [N/m^2];
θ	dimensionless shear stress or Shields' parameter, $\theta = \dfrac{u_*^2}{g(s-1)D}$;
ϕ_b	bed load transport flux, $\phi_b = \phi_o(\theta - \theta_{cr})^{3/2}$;
ϕ_o	transport flux at the limit $\theta / \theta_{cr} \rightarrow \infty$;
θ'	bed surface resistance expressed in Shields' parameter (Smith & Ettema, 1995);
θ''	bed-form resistance expressed in Shields' parameter (Smith & Ettema, 1995);
f_1'	bed surface friction factor;
f_1''	bed-form friction factor;
f_1	total bed friction factor, $f_1 = f_1' + f_1''$, (notations in Smith & Ettema, 1995);
q_s	sediment transport rate, [m^3/s];
q_{sb}	bed load transport rate, [m^3/s];
q_{ss}	suspended load transport rate, [m^3/s];

Bed material

ρ_s	bed material density, [kg/m^3];
γ_s	bed material specific weight, [N/m^3];
s	relative bed material specific weight, $s = \gamma_s / \gamma$;
d_{50}	grain size for which 50 percent by weight is finer, [mm];
d_{84}	grain size for which 84 percent by weight is finer, [mm];
d_{16}	grain size for which 16 percent by weight is finer, [mm];
σ_g	geometric standard deviation;
D	grain size of a uniform material, [m];
D_*	dimensionless particle size diameter $D_* = \left(\dfrac{g(s-1)}{\nu^2}\right)^{1/3} D$;
Re_*	sediment Reynolds number.

Scouring

y_s	scour depth, [m];
y_{se}	scour depth at the equilibrium of scouring, [m];

y_{smax}	maximum scour depth, [m];
b	bridge pier diameter, [m];
K_s	bridge pier shape factor;
K_α	bridge pier angle of attack factor;
Fr_p	pier Froude number, $Fr_p = U / \sqrt{gb}$.

List of Figures

List of Tables

Chapter One
Introduction

Since the beginning of time, the sediment transport phenomenon has affected agricultural practices, river migration, fisheries, aquatic habitat, river structures and in modern times irrigation, water supplies, flood control, navigation and hydroelectric processes. In the last few years, this phenomenon also has been found to have a major impact on the transportation and subsequent effects of pollutants; toxic chemicals can be attached to, or absorbed by, sediment particles and can be transported and deposited in other areas. Therefore, controlling sediment mobility has become an important issue in water quality management.

For river structures, sediment transport represents one of the most important steps in designing safe and economical structures in streams with mobile beds. From a structural point of view, the design considerations are well defined; however, from a hydraulic point of view, the complex interaction between the flow, the structure, and the configuration of the streambed creates many problems in the design process. For example, the construction of a dam is beneficial for the communities located in the area from many aspects such as hydroelectric power, fisheries and recreation. Its construction, however, depends on many years of fieldwork as well as the incorporation of the entire basin and gathering streams in the dam reservoir. The sediment transport that naturally occurs in those streams is very important for the life of the dam, which is usually designed for decades. Miscalculations can result in the filling of the dam reservoir with sediments, which would make it useless.

1.1 Scour around bridge piers

Scouring is another important phenomenon, which occurs in tide river bents or where an obstacle is placed in the way of the flow. In the latter case, scouring may be the most dangerous occurrence of the water-structure-streambed interaction causing thousands of river structure failures. Experience has shown that scouring can progressively undermine the foundation of a structure regardless of the dimension of the water flow, but in extreme cases of unsteady flows or changes in the channel conditions, it becomes exponentially powerful, eventually leading to the failure of the structure. Despite many studies, the behaviour principles of scouring are not well established, as results of various investigations often have shown different trends. Designers are unable to predict, with sufficient confidence, the depths and the locations of scour caused by spillways, weirs, bridge piers, abutments, culverts and others hydraulic structures. Two main reasons are contributing to a lack of understanding of the scour phenomenon and to the development of accurate solutions:

(i) turbulence, which presents great complexity and variability, and
(ii) sediment transport, which is strongly dependent on the complex interactions with the turbulent flow.

An additional problem is created by the composition of the streambed, which is usually a mixture of alluvial sands, clay and weathered rocks. A sediment map of a river can display alluvium, clay banks, rock outcrops, and bars of sand and gravel; therefore, the river presents different horizontal, vertical, longitudinal, and transversal channel conditions. Bulls Bridge in the Rangitikei River (Figure 1-1), New Zealand failed in 1973 because of pier scouring.

Figure 1-1 Bridge failure due to pier scouring - Bull Bridge on Rangitikei River, New Zealand, (1973). Breusers and Raudkivi (1991)

A combination of effects led to the displacement of the location of the main stream, and increased the attack angle of the flow on the bridge pier. As a result, the local scour penetrated the superficial gravel layer exposing the bed of fine sand underneath, and completely uncovered the foundation of the pier. The economy of a river structure provides further complexity by imposing a wide variety of structural shapes and alignments; thus, the scouring process as well as sediment transport behaviour becomes a very complex phenomenon, which still needs extreme attention from engineers.

1.2 Ice conditions

An aspect which has received more attention in recent decades is the effect of ice-cover on rivers. Increasing developments in Northern regions in the last half-century have opened a new area of research: hydraulics of ice-covered flow. Previous theories related to this topic were further enhanced and developed with new findings. The presence of ice-cover in an open channel dramatically alters many features of the flow and the bed mobility: ice cover approximately doubles the wetted perimeter and thereby produces a redistribution of flow velocities and shear stresses. As a result, the water flow changes to a higher depth and/or steeper slope flow. Furthermore, changes to the roughness of the ice-cover are also expected to cause changes in the flow and sediment transport characteristics of the stream, thus, leading to changes in the bed configuration.

1.3 Study objectives

The objective of this first study is to uncover from different ice-covered channel configurations the extreme case from a sediment incipient motion point of view with respect to the free-surface configuration, and to compare the scouring and erosion/deposition processes around a cylindrical bridge pier for that case to the free-surface case.

Studies conducted by Lau and Krishnappan (1985), Wuebben (1988), Smith and Ettema (1995), Zabilansky (1996), and Ettema et al. (1999), confirm that sediment transport in ice-covered channels decreases compared to the open-water situation, if the energy slope is maintained constant and only the flow depth is adjusted. However, in the presence of an obstacle in the water flow, in the short reach upstream the obstacle the flow will adjust faster the energy slope than the flow depth, such that, for the ice-covered channel, the incipient critical conditions are much easier achieved than for the open-water channel.

In terms of scouring around bridge piers, studies performed in the same constant energy slope conditions by Bacuta and Dargahi (1986) and Olsson (2000), and filed observations made by Yankielun and Zabilansky (1998) confirm that the scouring around bridge piers under ice-cover conditions, increases compared to the free-surface scouring. Nevertheless, when the energy slope is adjusted instead of the flow depth, we predict yet a higher increase in scouring for the ice-cover case.

In order to achieve this goal, the study is divided into three parts:

Experiments: A series of flume experiments with/without ice-cover and with/without bridge pier have been conducted at the Department of Civil Engineering's Hydraulics laboratory of the University of Ottawa. Vertical velocity measurements across different cross-sections, ice-cover shear stress measurements, and scour data have been collected. The setup, the apparatus and the experimental procedure are presented in Chapter Four.

Analyses: An analysis of the existing formulation for the vertical velocity and shear stress profiles together with the scouring and the erosion/deposition processes are presented in Chapters Two and Three. All the data collected from the experiments are processed and analyzed, and the results are presented in Chapter Five.

Conclusions: Summary and conclusion of the analysis have been pointed out and organized in Chapter Six.

Chapter Two
Sediment Transport

2.1 Open channel flow

Considering flow in an open channel passing over a movable bed, the flow boundary, which takes place at the surface separating the fluid and the bed material, is subjected to the action of the shear stress generated by the flow. This shear stress varies along the entire wetted perimeter. Since the grains forming the bed possess a finite weight and have a finite friction coefficient, they cannot be moved by the flow if the magnitude of the shear stress is less than a certain finite value τ_{cr}, called critical shear stress. Therefore, the motion of the bed grains due to the drag action of the flow on the flow boundary can take place only in that part of the wetted perimeter where $\tau > \tau_{cr}$. When such a case occurs, flow transports sediment from the bed channel.

In order to better understand this phenomenon of sediment transport in open channels, scientists have studied the mechanical properties of flow. Clearly, the motion of a given bed material in a given channel depends entirely on the mechanical structure of the flow. On the other hand, experimental observations have shown that the motion of the channel bed is accompanied by certain features of its own, such as the wave deformation of the surface of the channel bottom, the diffusion of solid particles into the fluid medium, etc., which in turn can significantly impact the mechanical character of the fluid motion. As a result, the motion of the fluid and the motion of the bed material are interdependent, and thus neither of them can be studied without taking into account the mechanical properties of the other.

As a follow up, the next subsections discuss the velocity and the shear stress distribution in different flow regimes. Sediment transport theory according to these regime features, concerning the shear stress and the velocity distributions in a steady and uniform flow of a real and homogeneous fluid under either a free-surface flow or an ice-covered flow condition, are also discussed.

2.1.1 Types of flows

The flow in an open cannel can be either in laminar or turbulent regime.

Considering a flow reach of length L and cross-section A, the equilibrium of the forces acting along the x-axis, for a permanent uniform flow is given by:

$$\sum F_x = W_x - F_f = 0 \qquad (2\text{-}1)$$

where $W_x = V\rho g S$, is the component of the weight W of a fluid element;

$F_f = \bar{\tau}\, P_w\, L$, is the friction force acting along the bottom and the sides of the fluid element.

In these equations V is the volume of the fluid of the reach ($V= L*A$), $\bar{\tau}$ is the average shear stress on the solid boundaries of the reach, P_w is the wetted perimeter of the reach cross-section and S represents the energy slope. Thus, substituting in Eq.(2-1), the average shear stress on the solid boundaries of the reach can be expressed as:

$$\bar{\tau} = \rho g\, S\, A / P_w = \gamma R_h S \qquad (2\text{-}2)$$

where R_h represents the hydraulic radius. The vertical distribution of the shear stress can be determined by considering a fluid element ABCD and write again the equilibrium along the x-axis (Figure 2-1):

$$\tau(y) = \gamma S(h - y) \qquad (2\text{-}3)$$

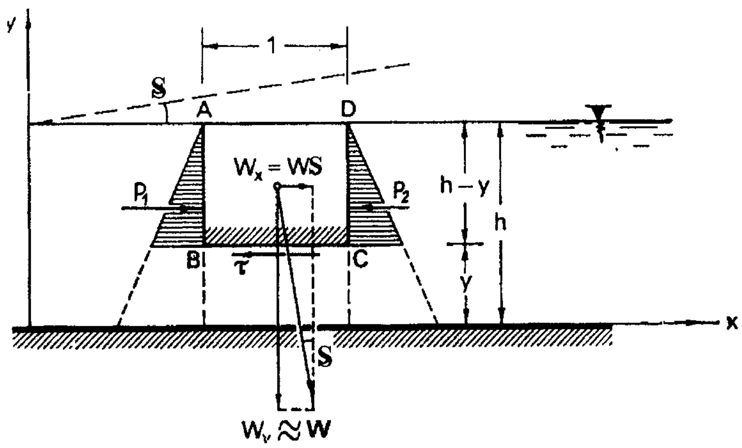

Figure 2-1 Forces acting on a unit fluid element. After Yalin (1977)

This profile is valid for large channels where the flow depth, h << B the width of the channel. The shear stress τ shows a linear variation relative to the flow depth, becoming equal to zero at the free surface and reaching its maximum value at the bed:

$$\tau_o = \gamma S h \tag{2-4}$$

The laminar regime is visualized as layers of fluid, which slide smoothly over each other without the mixing of fluid particles.

The turbulent regime is generated by instability in the flow, which creates eddies. Thus, the turbulent motion is characterized by a disorganized structure, apparently random, in which the fluid particles lose their individuality. The fluid layers and their trajectories are mixed with each other, and between them producing an intense exchange of mass and momentum.

In the case of the laminar regime, the size of the roughness has no influence on the flow as long as this size is small compared to the flow depth ($k_s <<< h$) if the laminar regime is considered to act throughout the entire flow depth. In nature, this type of regime is hardly possible. Nevertheless, in the case of the turbulent regime, a thin layer exists near the boundary where the fluid motion is still laminar.

2.1.2 Shear stress and velocity distributions

A very important feature of the turbulent regime is its unsteady character. The instantaneous velocity (u) can be expressed as the sum of the time averaged velocity ($\overline{u}$) and the instantaneous velocity fluctuation(u'): $u = \overline{u} + u'$. Using this feature, Reynolds developed the concept of the mixing process in which the turbulent flow is considered as having an averaged and a fluctuating turbulent component. Thus, the total shear stress τ corresponding to a level y of the flow depth can be expressed as the sum of laminar shear stress and turbulent shear stress:

$$\tau = \tau_l + \tau_t \tag{2-5}$$

The laminar shear stress or the viscous shear stress is due to the molecular viscosity μ, and is denoted

$$\tau_l = \mu \, \partial u / \partial y \tag{2-6}$$

where $\partial u / \partial y$ represents the velocity gradient at elevation y from the bed. In the turbulent regime, as suggested in Figure 2-2, the turbulent shear stress is caused by the passing of fluid micro-particles through the separation surface S-S of two fluid macro-particles (M_1, M_2). Analyzing the instantaneous velocity fluctuations, Prandtl proposed for the turbulent shear stress the following expression:

$$\tau_t = \rho l^2 \left(\frac{\partial u}{\partial y} \right)^2 \qquad (2\text{-}7)$$

where l is "the mixing length", and represents the average distance traveled by the fluid micro-particles involved in the mixing process.

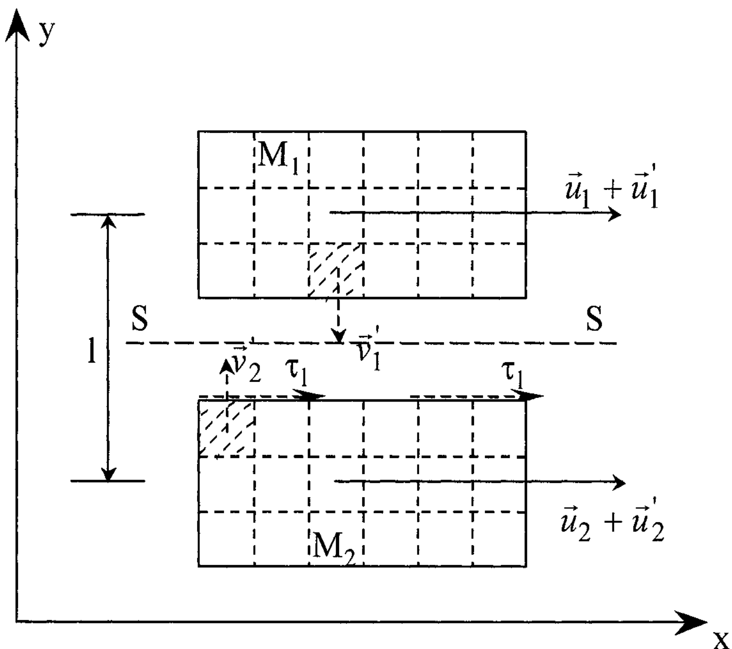

Figure 2-2 Simplified scheme of the turbulent motion. After Marian and Muste (1993)

From the Eq.(2-7), the function that governs the variation of the mixing length at the boundaries can be expressed as:

$$l = \kappa y \qquad (2\text{-}8)$$

where κ is the proportionality factor, or Von Karman constant: $\kappa = 0.4$. This factor is valid for all homogeneous fluids and for any geometry of roughness at the flow boundaries, which is sufficiently small compared to h, the depth of the flow.

For the case of the free-surface flow, Yalin (1977) suggested another function for the mixing length:

$$l = \kappa y \sqrt{(1 - y/h)} \qquad (2\text{-}9)$$

Several experiments have been conducted regarding this function. Findings show a linear variation with the flow depth (y) just in the vicinity of the bed, whereas, for larger values of y, the rate of increment slows down to its maximum value at $y=2/3h$, and progressively decreases to zero at the free surface. As shown in Figure 2-3, when approaching the free surface, l decreases at a higher rate to zero in a non-linear abrupt way. This seems to be reasonable since the free-surface cannot dampen the fluctuations as effectively as the rigid boundary (bed).

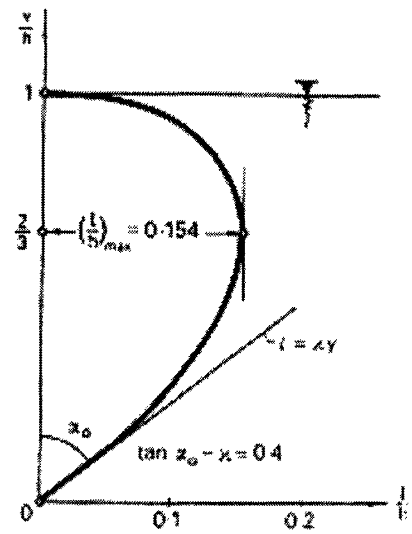

Figure 2-3 The mixing length variation with respect to the flow depth. Yalin (1977)

In Figure 2-4, Yalin (1977) clearly presents the distribution of the shear stress (laminar and turbulent) along the depth of a turbulent flow with free surface.

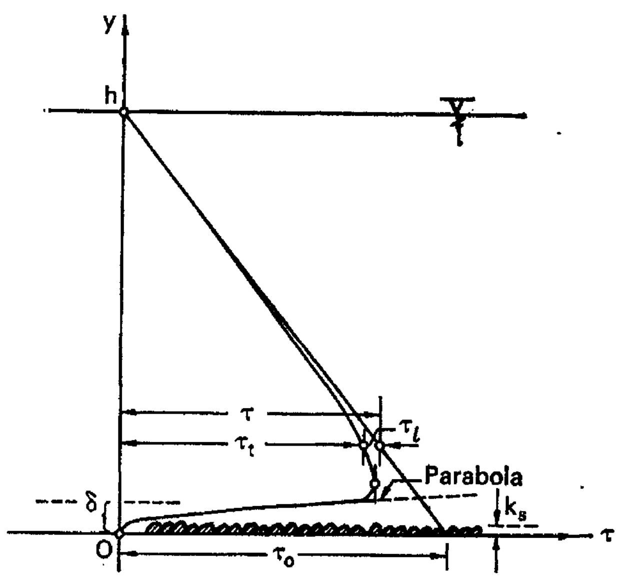

Figure 2-4 Shear stress distribution. Yalin (1977)

Summarizing the above discussion, the total shear stress τ in the turbulent flow may become:

$$\tau = \tau_l = \mu \frac{\partial u}{\partial y} \tag{2-10}$$

while τ_t =0 for any $y \in (k_s;\ \delta)$[2], which is the definition of *the laminar flow*, and

$$\tau = \tau_t = \rho l^2 \left(\frac{\partial u}{\partial y} \right)^2 \tag{2-11}$$

while τ_l =0 for any $y \in (\delta;\ h)$, which is the definition of *the fully developed turbulent flow*. In the same manner, the turbulent flow can be analyzed through velocity. Taking into account certain conditions to the bed boundary: since $y <<< h$ then $\tau \approx \tau_o$, but if $y > \delta$ then $\tau \approx \tau_t$, and Eq.(2-11) can be integrated along the flow depth; thus, the general function of velocity distribution for the turbulent regime can be expressed as:

$$\frac{u}{u_*} = \frac{1}{\kappa} \ln\left(\frac{y}{k_s} \right) + B_N \tag{2-12}$$

where u_* the shear velocity is equal to $u_* = \sqrt{\tau_o / \rho}$, and B_N is a dimensionless parameter of the flow in the vicinity of the bed. It depends on ρ, μ, u_* and k_s, and is defined by the following expressions:

$B_N = \frac{1}{\kappa} \ln\left(\frac{u_* k_s}{\nu} \right) + (const)a$, corresponding for large values of δ / k_s, or

$B_N = (const)b$, corresponding for small values of δ / k_s.

Nikuradse analyzed the variation of B_N with respect to the dimensionless parameter $\log(u_* k_s / \nu)$ and determined, for sand roughness, the following velocity distribution functions for the turbulent flow (Figure 2-5):

(i) *hydraulically smooth regime*, which is given by the condition $u_* k_s / \nu \leq 5$. For this regime the velocity distribution function becomes

$$\frac{u}{u_*} = 2.5 \ln\left(\frac{u_* y}{\nu} \right) + 5.5 \tag{2-13}$$

It is independent on the size and the nature of the roughness k_s of the bed (if k_s<<<h);

---

[2] δ is considered to be the thickness of the laminar layer of the turbulent flow

(ii) *fully developed turbulent regime* or *rough turbulent flow*, which is given by the condition $u_* k_s / \nu \geq 70$. For this regime the velocity distribution function becomes

$$\frac{u}{u_*} = 2.5 \ln\left(\frac{y}{k_s}\right) + 8.5 \tag{2-14}$$

and it is independent on the viscosity ν of the fluid;

transitional regime, which is given by the condition $5 \leq u_* k_s / \nu \leq 70$. In this regime the velocity distribution function is dependent on both viscosity and roughness, but the value of B_N cannot be given by an analytical formula. Nevertheless, the value of B_N can be estimated from the graph presented in the Figure 2-5, depending on the given values of $u_* k_s / \nu$.

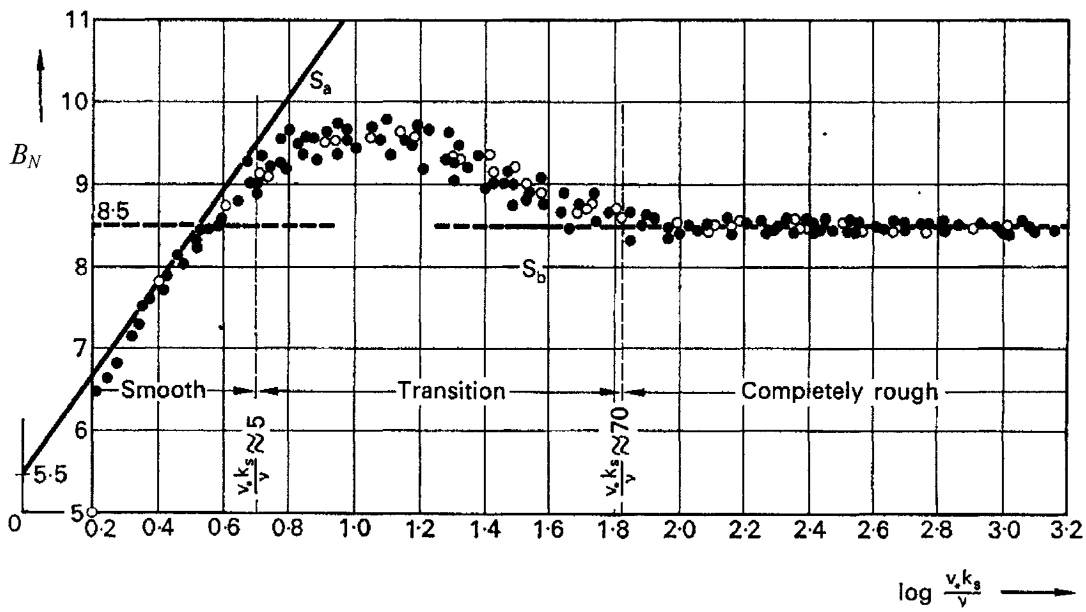

Figure 2-5 Variation of B_N with $\log(u_* k_s / \nu)$ from Nikuradse measurements. After Yalin (1977).

2.2 Sediment transport in open-water channels

Having reviewed the variation functions of shear stress and velocity for open channel flow, the analysis of the sediment transport in an open channel with a movable bed can now be considered. The following theory focuses mainly on two aspects: (i) sediment transport in an open-water channel, and (ii) sediment transport in an ice-covered channel.

2.2.1 Mechanics of sediment motion

Considering an individual grain of the mobile bed, the forces acting on it are:

F - the hydrodynamic force with its components $\mathbf{F}_x$, the dragging force tangent to the bed channel and $\mathbf{F}_y$, the lifting force normal to the bed;

W - the weight of the grain;

R = F + W - the resultant of the above forces, also called the active forces.

The passive forces comprise:

$\mathbf{F}_f$ - the friction force and

N - the normal reaction at the particle support.

Figure 2-6 (a) shows that the detachment of the grain will occur when the resultant R reaches such a position (#3) where the angle between the vector R and the direction of the normal n becomes equal to the friction angle ψ. The normal n is perpendicular to the right support of the grain, support B, represented by the line (*t,t'*) in part (b) of the figure.

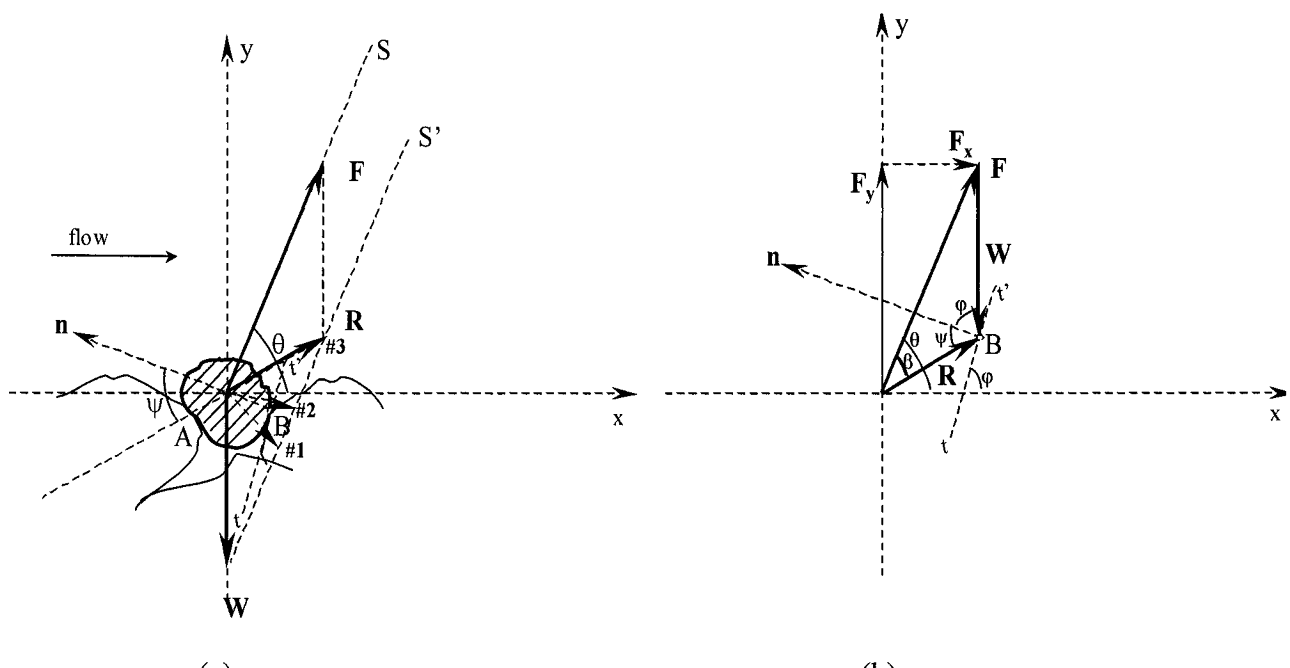

Figure 2-6 Forces acting on a grain of the bed surface. After Yalin (1977)

From the forces triangle corresponding to this stage (just before the detachment of the grain) shown in Figure 2-6 (b), the sine theorem is expressed as:

$$\frac{F}{\sin(\varphi+\psi)}=\frac{W}{\sin\beta} \tag{2-15}$$

Considering $\beta=(\pi/2)-(\varphi+\psi-\theta)$, the condition of detachment of an individual grain can be determined by:

$$\frac{F}{W}\geq\frac{\sin(\varphi+\psi)}{\cos\left[\theta-(\varphi+\psi)\right]} \tag{2-16}$$

Thus, the detachment of a grain occurs when the ratio F/W reaches a certain limit, which depends on the angles φ, ψ, and θ. The angle φ, between the direction x of the flow and the tangent at the highest downstream support B, depends entirely on the geometry of the grain and its environment. The friction angle, ψ depends on the conditions of the contact surfaces of grains. The angle θ is determined by the geometry and the grain size Reynolds number, $\mathrm{Re}_* = u_* D/\nu$. Many consider the angle θ for a large percentage of the grains forming the surface of a mobile bed to be very close to $\pi/2$ ($\theta \approx \pi/2$), and hence, the condition of detachment is expressed as $F_y/W \geq 1$, which means that the detachment of a grain is due entirely to the magnitude of the lifting force $\mathbf{F}_y$, the vertical component of the hydrodynamic force **F**.

Two main approaches have now been considered with regard to sediment transport: the shear stress τ_o, and the dynamic action of the flow, $\boldsymbol{F}$. Obviously, these two approaches are consistent, since τ_0 and **F** are interrelated: $\tau_O \propto F/D^2$, but in practice the bed shear stress is the most used concept because it gives a better computational relationship with the velocity distribution of the flow. The "mechanical" approach or the concept of the hydrodynamic force helps make the phenomenon more understandable. Therefore, the shear stress will be further used to define motion of the bed grains. Past experiments have shown that when only one grain size distribution is present, the sediment transport can be divided into three main stages. Considering q_s, the total transport rate or the specific solids discharge, q_{sb}, the bed load (rate), and q_{ss}, the suspended load (rate), these stages are:

if $\tau_o < (\tau_o)_{cr}$,	then $q_s=0$	- no sediment transport;
if $(\tau_o)_{cr} < \tau_o < (\tau_o')_{cr}$,	then $q_s=q_{sb}$	- bed load transport;
if $\tau_o > (\tau_o')_{cr}$,	then $q_s=q_{sb}+q_{ss}$	- bed load and suspended load transport.

In the bed load stage, (Figure 2-7) the grains move either by irregular jumps (saltation) or, by rolling.

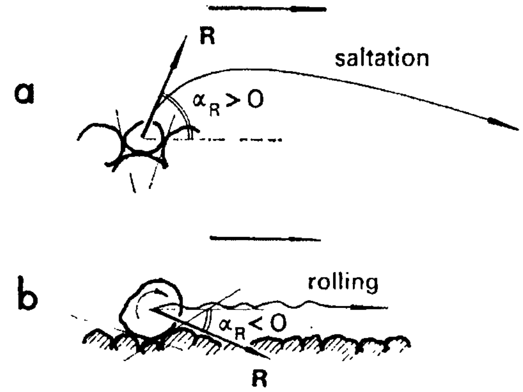

Figure 2-7 Grain incipient motion: by irregular jumps or by rolling. After Yalin (1977)

Once τ_0 begins to exceed the magnitude of $(\tau_o')_{cr}$ the amount of sediment diffusing in the fluid medium slowly becomes significant. When $\tau_o > (\tau_o')_{cr}$, the sediment transport is formed by granular material which moves in the vicinity ε of the bed $(0<y<\varepsilon)$ by jumping and rolling -bed load, and by granular material which is carried in suspension by the flow $(\varepsilon<y<h)$ –suspended load. Further discussions in this study will refer only to the bed load transport.

2.2.2 Sediment transport rates

Sediment incipient motion condition of A. Shields (1936)

Shields was the first who expressed the initiation of sediment transport:

$$\theta_{cr} = \Phi(\mathrm{Re}_*) \tag{2-17}$$

where $\mathrm{Re}_* = u_* D/\nu$ is usually called the "grain size Reynolds number", and reflects the influence of the dynamic viscosity μ ($\nu = \mu/\rho$), while $\theta = \dfrac{\tau_o}{\gamma_s D} = \dfrac{\rho u_*^2}{\gamma_s D} = \dfrac{u_*^2}{g(s-1)D}$ reflects the influence of the specific weight of grain in fluid, γ_s and characterizes the ratio **F/W**; therefore, this parameter is also known as "dimensionless shear stress". ρ is the fluid density and s the relative density of bed grains, $s=\rho_s/\rho$. In both expressions, D represents the grain size of a uniform material, or the typical grain size of a mixture.

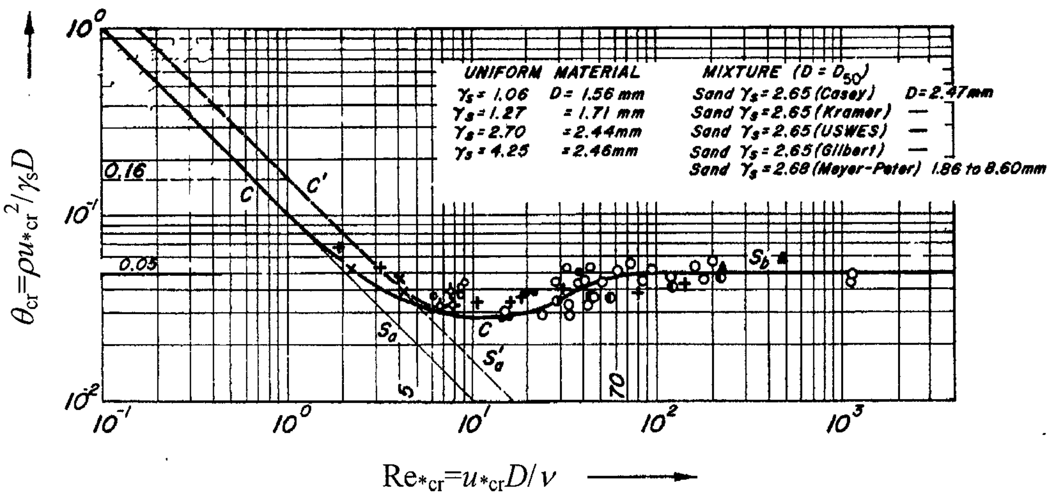

Figure 2-8 Shields curve and different experimental points that tend to follow the curve. After Yalin (1977)

Shields plotted the experimental values of θ_{cr} and Re_{*cr} (which correspond to the critical stage of the initiation of sediment transport = critical bed shear stress $(\tau_o)_{cr}$ = critical shear velocity u_{*cr}) with the intention to produce a curve, which determines the incipient motion of the bed particles (Figure 2-8).

Shields' equation for bed-load rates is expressed as:

$$q_b = \frac{10qs(\tau_o - \tau_{cr})}{(s-1)^2 D} \quad [\mathrm{m^3/m\,s}] \tag{2-18}$$

where q_b and q represent the bed-load and the fluid discharge per unit channel width, respectively.

Empirical formula of Meyer-Peter and Muller (1948)

The expression of Meyer-Peter and Muller, also called the "Swiss formulae," is the most popular formula used in practice. After a long series of experimental measurements and dimensionless analysis, they determined for the bed transport rate, q_s=q_{sb}, the following empirical relation:

$$\phi_b = \phi_o(\theta - \theta_{cr})^{3/2} \tag{2-19}$$

where ϕ_b represents the dimensionless transport flux, $\phi_b = q_s \dfrac{\rho^{1/2}}{(\gamma_s D)^{3/2}}$;

θ represents the "dimensionless shear stress," $\theta = \dfrac{u_*^2}{g(s-1)D}$, and

ϕ_o=8 represents the value of the dimensionless transport rate at the limit $\theta/\theta_{cr} \to \infty$, in which θ_{cr} corresponds to the critical stage θ_{cr} = 0.047. This equation was subjected to many experiments and calibrations within the last half-century, which help make it so popular and efficient in practice. The last calibration was made by Bennett (1995), who suggests the following values for ϕ_o

Table 2-1 Calibration values of ϕ_o, after Bennett (1995).

Nr.	Dimensionless parameter ϕ_o	Bed material characteristics
1	$\phi_o = 0.31$	ripples
2	$\phi_o = 2.3\log_{10}\theta + 4.84$	dunes
3	$\phi_o = 2.2\log_{10}\theta + 2.8$	torrential regime

Energetic formula of R.A.Bagnold(1956)

Bagnold's approach refers to the efficiency of the flow capacity to move bed particles. He defined this efficiency as $e_b = \dfrac{\text{useful work}}{\text{available energy}}$ (Figure 2-9) and by expressing each term of the ratio, he determined the relation of the dimensionless transport rate as

$$\phi_b = b_B \theta^{1/2}(\theta - \theta_{cr}) \tag{2-20}$$

where b_B =8.50 $e_b / \tan\psi_o$ is a coefficient that can be computed using Bagnold's function of the grain diameter D.

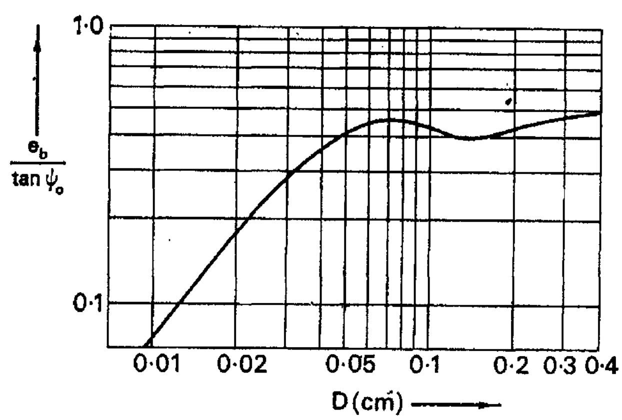

Figure 2-9 R.A. Bagnold's graph: $e_b/\tan\psi_o$ vs D

Bed load formulas of Yalin (1963) and van Rijn (1984)

Yalin and van Rijn developed a bed load transport formula based this time on the concept of the "average jump," or just the non-fluctuating characteristics. They integrated the average forces acting along the grain jump trajectory. Yalin expressed his sediment transport formula as:

$$\phi_b = 0.635 \frac{S}{\sqrt{\psi}} [1 - \frac{1}{as} \ln(1 + as)] \tag{2-21}$$

where $\phi_b = \dfrac{q_s \rho^{1/2}}{\gamma_s D^{3/2}}$ is the dimensionless transport flux, $S = \dfrac{\theta - \theta_{cr}}{\theta_{cr}} = \dfrac{u_*}{u_{*cr}} - 1$ is the dimensionless excess of the dragging force, and $a = 2.45\sqrt{\theta_{cr} / s^{0.4}}$ is the dimensionless detachment condition of the grain ($a = W / \overline{F}_y$).

Van Rijn (1984) expressed his formulae as:

$$\phi = 0.053 \frac{T^{2.1}}{D_*^{0.3}} \tag{2-22}$$

where $T = \dfrac{\theta - \theta_{cr}}{\theta_{cr}}$ represents the effective bed shear stress, or the ratio between the bed shear stress in excess and the critical shear stress and $D_* = \left(\dfrac{g(s-1)}{\nu^2} \right)^{1/3} D$, the dimensionless particle diameter expressing the physical characteristics of the grains and the fluid. It is an independent parameter with respect to the flow regime.

The above approaches and formulas represent the basics for the sediment transport theory on which most or all of the relationships developed for the motion of sediments are based on. In literature, one can find a large number of formulations and expressions, each being developed for a specific process; therefore, one must choose the right formulae for specific conditions.

2.3 Sediment transport in ice-covered channels

The large number of studies on the hydraulics of alluvial channels contains little information concerning sediment transport in ice-covered channels. This lack of information is due mainly to the high-latitude and relatively remote locations of rivers that are covered with ice on an annual basis. However, in recent decades, the growing interest in the wintertime management of reservoir-regulated rivers and in the winter environment of ice-covered rivers have led to the need to understand sediment transport in ice-covered channels and the estimation of transport rates.

The presence of ice-cover complicates the relationship between flow depth and discharge in alluvial channels during freezing periods. For two-dimensional free-surface flow, it approximately doubles the wetted perimeter, which causes dramatic increase in flow resistance. In order to make a correct comparison between open-water and ice-covered flow, the notion of equivalent flows is defined as the free-surface and ice-covered flows with identical energy slopes and identical unit discharges. Thus, for equivalent flows, one can express the ice-covered/free-surface flow depth ratio as[3]:

$$\frac{Y_c}{Y_o} = \frac{U_o}{U_c} = \left(\frac{2f_c}{f_o}\right)^{1/3} \tag{2-23}$$

where Y and U represent the flow depth and the average velocity for open-water flow and covered flow respectively. The friction factor for ice-covered flow is a composite factor, which takes into consideration the effects of both boundaries: the bed and the ice cover, such that[4]

$$f_c = 8\frac{\tau_{total}}{\rho U_c^{\,2}} = 4\frac{(\tau_1 + \tau_2)}{\rho U_c^{\,2}} \tag{2-24}$$

where τ_{total} expresses the shear stress due to the bed and the ice-cover. Since the flow resistance for ice-cover conditions is greater than for free-surface conditions, the flow depth must increase for the ice-covered flow in regards to the last two expressions.

[3] Subscript "c" for ice-covered flow, and subscript "o" for open-water or free-surface flow

[4] Subscripts "1" denote the bed and "2" the ice-cover parameters

Several studies have investigated the resistance relationship for ice-covered channels and many of the proposed models are similar in that they split the flow into upper and lower layers. This initial assumption is called the "two-layer hypothesis," and as shown in Figure 2-10, each layer is treated as an independent free-surface flow. Thus, the vertical variations of velocity and shear stress previously discussed for open-water flow are assumed valid in this case. The velocity distribution is considered to be logarithmic for both layers, reaching a common maximum value at the elevation y_V of maximum velocity. The shear stress distribution for both layers should meet and reach the minimum value (=0) at the common "free-surface" elevation, where the maximum velocity should also be located. In reality, the elevation of zero shear stress, y_τ and the elevation of maximum velocity, y_V are equal only if the roughness of both boundaries is identical. However, as Parthasarathy and Muste (1994) observed for asymmetric cases, the differences between y_V and y_τ are small, less then 5% of the flow depth. Thus, for all two-layer models of ice-covered flow, it is simply assumed that $y_V = y_\tau$.

From a sediment transport point of view, the reason for splitting an alluvial flow into these two layers is to enable the application of free-surface relationships for bed-load transport rates, bed-form existence, and bed-form geometry to the lower layer (the natural bed of the channel) in order to yield predictions for the ice-covered flow. Smith and Ettema (1995) showed that there are some inconsistencies in this concept regarding the velocity gradient, which is discontinuous at the interface between the two layers, and also in the velocity and shear stress profiles for dune-bed channels.

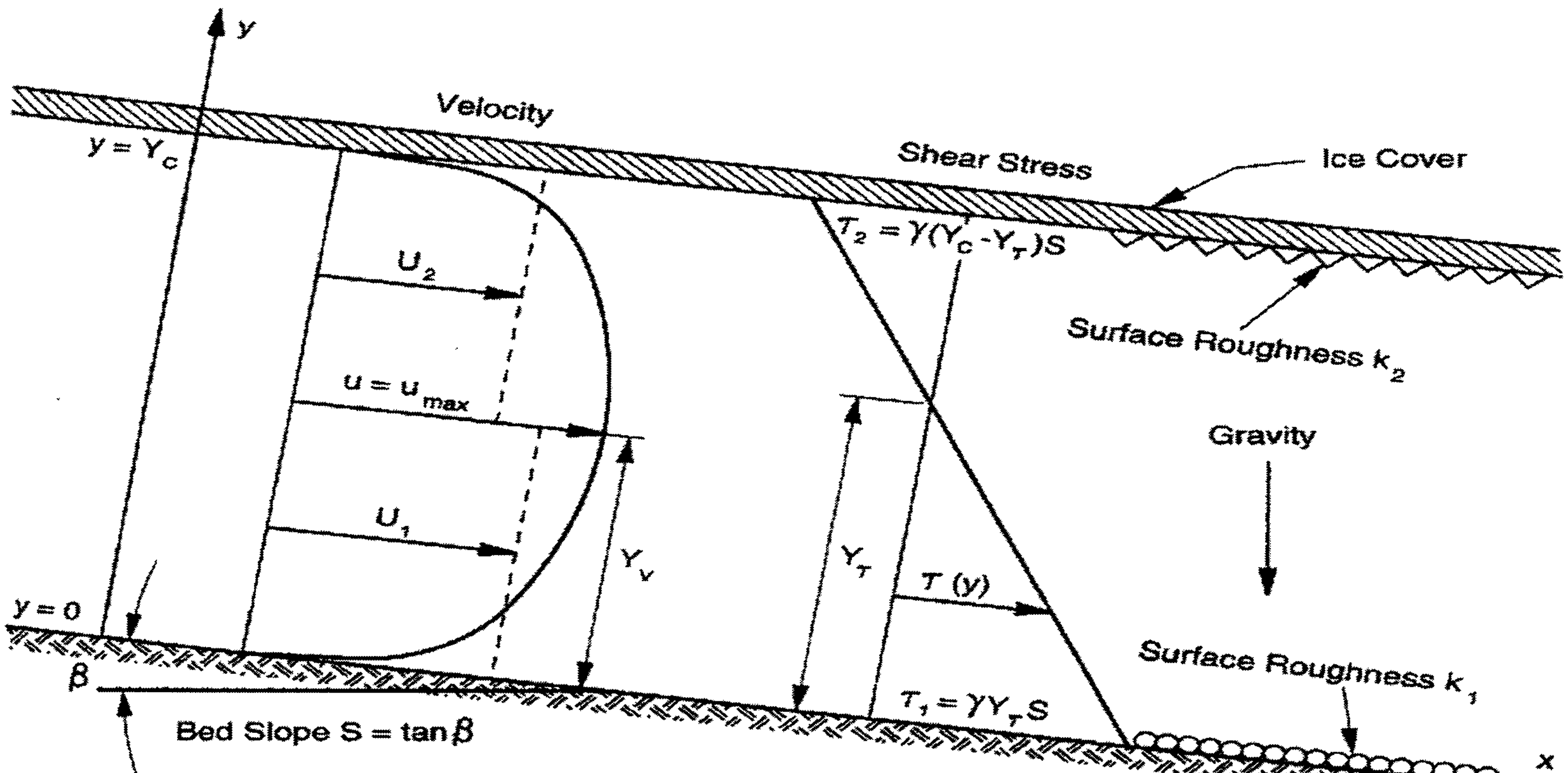

Figure 2-10 Two-layer hypothesis. After Smith and Ettema (1995)

Sayer and Song (1979)

Sayer and Song in conjunction with U.S. Geological Survey conducted an early experimental study on ice-covered alluvial flow in 1979. The main purpose of this investigation was to obtain basic information on how ice-cover affects the sediment transport characteristics of alluvial streams. Their movable bed channel consisted of 0.25mm quartz sand, and the ice-cover was simulated with plywood panels. Two types of cover roughness, smooth and rough ice, were used in their experiments which were conducted in flow depth adjustment conditions (energy slope kept constant). Their results showed 20 to 30% increase in flow depth for ice-covered flows in comparison to open-water flows for the smooth cover, and 30 to 80% increase in flow depth for the rough cover. They also observed a reduction in the total sediment discharge of approximately 80% for the smooth cover and 95% for the rough cover. In their computation, they assumed that the two-layer hypothesis was valid, and their predictions were found to coincide with their experimental data.

Lau and Krishnappan (1985)

Lau and Krishnappan investigated the effect of a floating cover on an alluvial channel using 0.15mm glass beads as sediment grains and plastic-coated plywood panels as simulated ice-cover. They observed the influence of the ice-cover for two bed slopes of 0.00059 and 0.0010 respectively, and for fluid discharge ranging from $0.0099m^3/s$ (9.9l/s) to $0.0274m^3/s$ (27.4l/s). In this study, the ice-cover produced a 9 to 23% increase in the flow depth, relative to equivalent open-water flows. The total sediment transport rates for covered flows were found to be about 1/3 of the corresponding open-water transport rate. Most of the sediment was transported in suspension, but no separate bed-load measurements were made. However, their results indicate that some of the theories for bed-load transport in open channel flows can be applied to the lower layer of the covered flow. Lau and Krishnappan used in their computation a k-ε turbulence model to estimate boundary shear stresses, stream-wise velocities, and suspended sediment concentrations.

It was determined that their predictions match well enough to the measured values, (Figure 2-11).

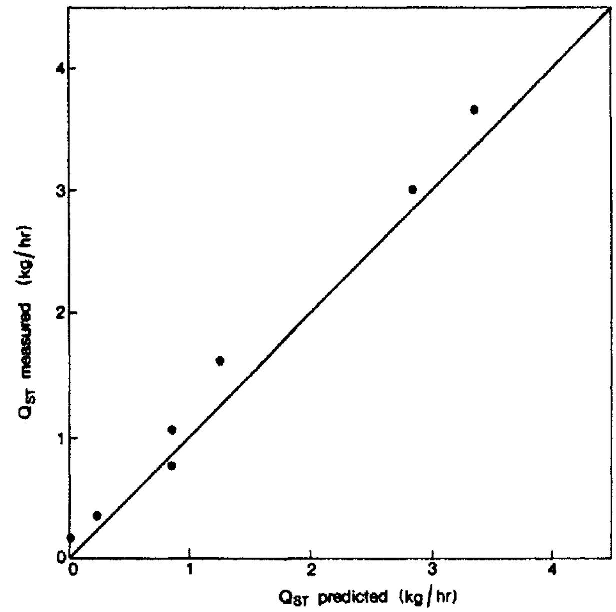

Figure 2-11 Comparison of measured and predicted transport rates for covered flows. Lau and Krishnappan (1985)

It is necessary though, to point out that their study refers to smooth ice-covered flows over rippled beds of fine sediment.

Wuebben, James (1986-1988)

Wuebben (1986) studied ice-covered alluvial flow using sand with a median size diameter of 0.45mm and Styrofoam panels to simulate ice-cover. He performed five series of open-water, smooth cover, and rough cover experiments at four discharges and found that flow depth increased, average velocity decreased, total sediment discharge decreased, and bed-form heights decreased with increasing cover roughness.

The most intriguing observation made by Wuebben was that the presence of an ice cover could provide a change in the slope of an alluvial channel. Figure 2-12 shows the findings of his experiments regarding the variation in energy slope with ice conditions, and as seen, the slope becomes steeper as the roughness of the ice-cover increases.

Another interpretation, this time made by Smith and Ettema, refers to the fact that this is a response of the laboratory-flume and not a typical response of natural channels, which adjust flow depth much faster than the slope. Even if the authors didn't mention, it is important to remind the reader that this interpretation is valid only for long reaches of natural channels. However, in the case of short reaches that contains changes in the channel geometry or an obstacle in the way of the flow, the energy slope of the ice-covered channel may adjust faster than its flow depth (Donchenko, 1975 and Zabilansky, 2002, Chapter Three).

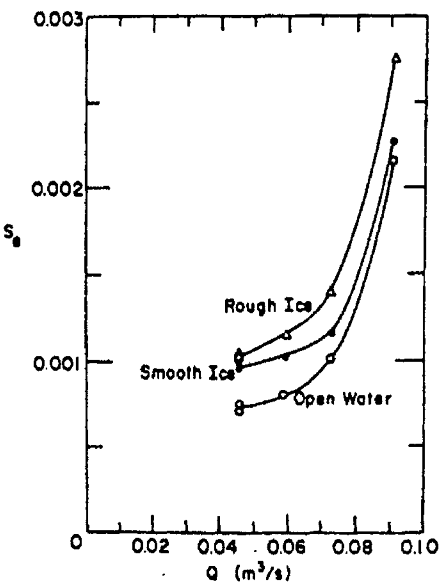

Figure 2-12 Variation in energy slope with ice conditions. Wuebben (1986)

Consequently, two years later, Wuebben investigated the two-layer hypothesis in other experiments by replicating the lower layer of the covered flow with the open-water flow, as he had suggested in his previous research. This means that first, he had run the experiments with covered flow and after the flow depth and discharge had been determined, the open-water experiments were conducted using those values. While there are still some reservations about the two-layers approach, Wuebben's findings give a practical value to this approach in the absence of another correct theoretical approach. The results show that the equilibrium slope of a system with a given discharge and flow depth agree very well for open water depths corresponding to the thickness of the lower layer of ice-covered flows. Furthermore, sediment concentrations and bed-form wavelengths appear to be relatively well correlated.

Smith and Ettema (1995)

Smith and Ettema conducted several loose-bed experiments in conjunction with ice-covered channels. Their report, which is considered one of the most elaborated research studies of ice-covered flow, examined the influences of the presence of ice-cover and its roughness on the depth, discharge, sediment transport, and bed-form geometry for alluvial channel flows.

A sediment recirculating flume of 30m long, 0.91m wide and 0.45m deep was used. The channel bed was covered with uniform coarse sand with a median size diameter d_{50}=1.28mm. The simulated ice-cover was made of plywood panels with smooth, median and rough surfaces. The loose-bed experiments were performed for a constant discharge, energy slope, and water temperature. Their conclusions were quite clear: an ice-covered flow will induce greater flow depth, smaller bulk flow velocity, smaller dune steepness, and thus smaller bed-load transport rate than the equivalent open-water flow. Interesting findings are shown in the following figures regarding the variation of bed resistance and bed friction factors with respect to the shear stress ratio $\alpha = \tau_2 / \tau_1$ of the ice-cover and the bed channel, respectively.

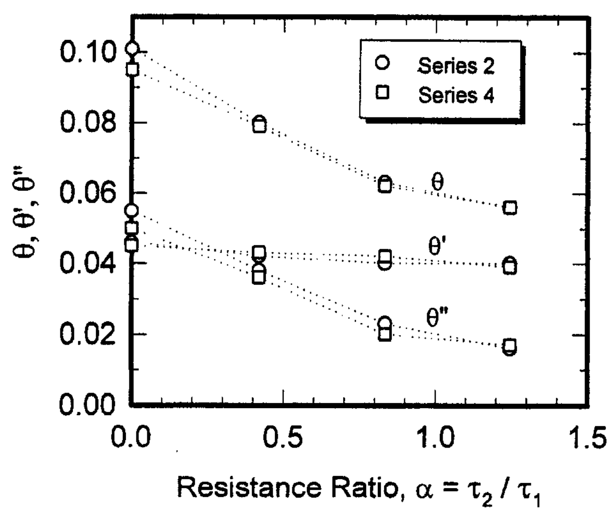

Figure 2-13 Ice-cover influence on bed shear stress, expressed in terms of the Shields parameter. Smith and Ettema (1995)

Figure 2-13 shows the variation of the total bed resistance and its components, the surface resistance θ' and the bed-form resistance θ'' with respect to the ice-cover roughness. These characteristics, which are expressed in terms of Shields' parameter, $\theta = \dfrac{\tau}{\gamma_s d_{50}}$ decrease significantly with increasing cover roughness, except for the surface resistance, which experiences only a slight decrease with increasing cover roughness. This phenomenon is due to the shear stress exerted by the re-attached flow: the presence of ice-cover and the increasing of cover roughness reduce the dune steepness → reduces the size of the flow recirculation behind the dune crest → re-attaches the flow to the bed.

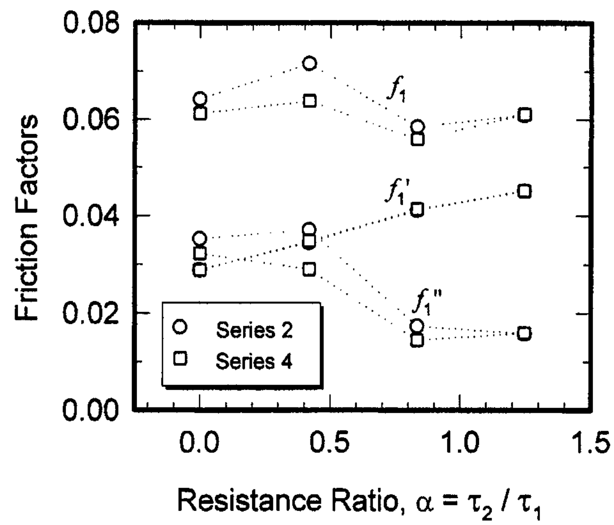

Figure 2-14 Ice-cover influence on total bed friction factor, f_1, flat bed friction factor, f_1', and bed form friction factor, f_1''. Smith and Ettema (1995)

In Figure 2-14, the total bed friction factor, f_1 is examined together with its components the surface friction factor f_1', and the bed-form friction factor f_1''. From this diagram, the effect of the changes in flow velocity has been eliminated, and thus, the results show that the surface friction factor increases with increasing cover roughness, whereas the bed-form friction factor decreases with increasing ice roughness. These observations led to the conclusion that the total bed friction factor experiences small variations with changes in ice cover roughness.

The two-layer hypothesis was questioned again because of the observation that the discrepancy between the elevations of maximum velocity and zero shear stress increases with increasing cover roughness. The elevation y_v, thus, is not an appropriate length scale for flow near the bed.

Ettema, Braileanu, and Muste (1999)

Ettema, Braileanu, and Muste conducted their experiments in the same flume that Smith and Ettema used for their study. Experiments for smooth, median and rough ice-covers were conducted. The bed material consisted of uniform fine sand of d_{50} = 0.25mm with standard geometrical deviation of σ_g = 1.4. The experiments were performed for a ripple-dune regime on the channel bed. Since this study emphasizes suspended-load transport, their conclusions are briefly noted below. The presence of a free-floating ice-cover on flow over a dune–bed channel increases the flow depth, decreases the average velocity of the flow, and decreases the total rate of sediment transport. In addition, their study confirms that bed-load transport rates under ice can be estimated using an open-water formula for the bed-load transport. A surprising result is the fact that the ratio of suspended-load rate to total sediment transport rate did not decrease with the presence of ice-cover and with an increase in cover roughness. A new formula for suspended-load rates computation was determined:

$$q_{sc} = q_{so}\left(\frac{C_{ac}}{C_{ao}}\right) = q_{so}\left(\frac{q_{bc}}{q_{bo}}\right)\left(\frac{u_{*o}'}{u_{*c}'}\right) \tag{2-25}$$

where s and b denote the suspended-load and the bed-load respectively, and u_*' is the shear velocity due to the drag effect. C_{ac}, and C_{ao} represent the reference concentrations of bed sediment moving near the bed in the ice-cover and the open-water cases, respectively.

Zabilansky, Leonard (1998-2002)

Most of the numerical and physical models used to predict sediment transport are based on laboratory tests with very little field information for validation. The effects of ice-cover or ice and debris accumulation are hardly considered in the sediment motion phenomenon.

Recently, very important studies concerning sediment transport under ice-covered flow were conducted by the US Army Cold Regions Research and Engineering Laboratory. Since their major interest is in building technology for detecting and measuring effects of ice forces, sediment erosion/deposition processes, and scouring under ice, results from their field experiments have shed light on important information about the process of sediment transport and scouring around bridge piers under ice cover-conditions.

Zabilansky (1996, 2002) conducted two studies on sediment transport on the Missouri River in Culbertson, Montana and on the Mississippi River in Andalusia, Il., and one study on scouring around bridge piers on the White River at White River Junction, Vermont (presented in subsection 3.3). In these three studies, a time-domain reflectometry (TDR) instrument was developed and patented to monitor the erosion and deposition of sediments in real time under various conditions such as ice-covers, ice and debris accumulation, and flooding.

Their objectives were to identify the parameters that trigger sediment transport and to correlate the resulting changes in the river with the different ice-cover processes: formation, growth, and break-up, and also to document the changes in the bed elevation during the winter to calibrate a numerical sediment model.

Zabilansky's findings are in agreement with previous studies showing that the presence of a free-floating ice-cover will increase the flow depth, and thus, decrease the bed and suspended-load capacity to transport sediment in comparison to open-water conditions. However, he also uncovered two very important conditions which can occur during the winter and early spring:

(i) the "free-floating" ice-cover, which refers to the cover that allows the flow depth to rise in response to any increase in discharge, and
(ii) the "confining" ice-cover, which refers to the cover that prevents the stage to adjust in response to any increase in discharge.

This last process is very common in nature and can occur over the winter as the ice thickens and becomes more rigid and strongly attached to the shoreline and channel structures. Thus, in a "confining" ice-cover situation, any increase in discharge below the break-up point of the ice-cover has to be accommodated by an increase in the mean velocity since any increase in the flow stage is prevented by the ice-cover break-up strength. At this point, a very important observation worth be mentioned: this increase in velocity is associated with an increase in the energy slope of the flow, which will also induce a higher capacity of transporting sediment compared to the open-water situation.

2.4 Conclusion

As one can see, most of the studies regarding the sediment transport in ice-covered and free-surface flow situations were conducted in a flow depth adjustment condition, maintaining constant the energy slope for both the free-surface and the ice-cover cases. This is a valid hypothesis when an appropriate length scale is considered (i.e. long river reaches). However, when a river reach contains a bridge pier, based on Zabilansky's (2002) field study, we can say that in an ice-covered channel situation the flow will adjust faster the energy slope than the flow depth. As a result, in a controlled flow depth case major changes in the sediment transport and scouring processes are predicted for the ice-covered flow compared to the free-surface flow.

Taking into consideration the shallow-water case, the average discharge and the average bed shear stress can be expressed as follow:

in the open-water case (subscript "o") where $R_h \approx h$

$$q_o = \frac{B}{n} h_o^{5/3} S_o^{1/2}, \; \tau_o = \gamma \, h_o \, S_o \tag{2-26}$$

in the total ice-cover case (subscript "i") where $R_h \approx h/2$

$$q_i = \frac{B}{n} \left(\frac{1}{2}\right)^{2/3} h_i^{5/3} S_i^{1/2}, \; \tau_i = \gamma \frac{1}{2} h_i \, S_i \tag{2-27}$$

where B is the channel width, n is Manning's roughness coefficient, considering that the ice-cover and the bed channel have identical roughness.

Analysing the variation of the flow depth and the energy slope at constant discharge (q_o=q_i), it can be shown the following:

$$\text{(i) if } S_o = S_i \Rightarrow \frac{h_i}{h_o} = 2^{2/5} \Rightarrow \frac{\tau_i}{\tau_o} = 2^{-3/5} = 0.66 \langle 1 \tag{2-28}$$

$$\text{(ii) if } h_o = h_i \Rightarrow \frac{S_i}{S_o} = 2^{4/3} \Rightarrow \frac{\tau_i}{\tau_o} = 2^{1/3} = 1.26 \rangle 1 \tag{2-29}$$

Thus in order to keep the discharge constant in both the ice-cover and the open-water cases when the energy slope does not vary, the flow will adjust the stage and the sediment transport capacity will decrease in the ice-cover case compared to open-water situation [Eq. (2-28)]. However, if the energy slope is adjusted instead of the flow depth, the sediment transport in the ice-covered case will increase compared to the free-surface flow [Eq. (2-29)]. In nature, a common situation can easily be encountered between the two limits stated above, which can be summarized as:

$$0.66 \langle \frac{\tau_i}{\tau_o} \langle 1.26 \tag{2-30}$$

Chapter Three
Scour Around Bridge Piers

3.1 Introduction

The phenomenon of scouring around bridge piers has been the focus of many studies in the past, but because of its complexity, which includes considerations such as flow conditions, sediment transport mechanisms, and occurrence periods, a universal equation or expression has not been yet developed. However, past studies are very important because they uncovered and improved knowledge about the most important parameters that govern the scouring process.

Scouring, generally speaking, is due to gradients in sediment transport caused by the presence of structures or distortions in the direction of flow. Therefore, knowledge about the sediment transport phenomenon is essential, and thus the reason for its review in the previous chapters. Before entering deeper into the analysis of the scouring process, a brief classification of scouring types are reviewed to create a better understanding on how scour can be defined:

in terms of the *Physical Process:*

(i) **General scour:** occurs as the result of natural processes independent of the presence of a structure;

(ii) **Constriction scour:** occurs if a structure causes the narrowing of flow or the reconfiguration of the channel berm or flood plain flow;

(iii) **Local scour:** occurs in river tide bents or directly from the impact of a structure on the flow. In the latter case the scour is a function of the structure type and has to be superimposed on the general and constriction scour;

in terms of the *Sediment Regime*

(i) **Clear-water scour:** referred to scouring when the bed material in the flow upstream of the scour area is at rest. Thus, in this case, the shear stress on the bed some distance away from the structure is not greater than the critical shear stress for the initiation of grain movement;

(ii) **Live-bed scour:** also referred to scour with sediment transport, and occurs when the flow induces a general movement of the bed material. The shear stress on the bed is generally greater than the critical shear stress. The equilibrium scour depths, in this case, are reached when the quantity of material removed from the scour hole by the flow equals the amount of material supplied to the scour hole from the upstream bed.

In the following subsections, the emphasis is placed on local scouring under clear water regime. In practice, designing for local scour is taken into consideration with regards to general and constriction scour, thus general considerations about the latter two types of scour are briefly discussed.

General scour

General scour occurs due to the increased capacity of a river to carry sediments during flows caused by floods or as a consequence of different man-made interventions. This type of scour represents a response to the flow regime, and would occur whether or not a structure is present in the river.

Many rivers, especially wide rivers flowing over gravel, have the tendency to develop localized channels, as shown in Figure 3-1. If a certain part of the channel coincides with the location of a bridge pier, then the two combined effects of both general and local scouring should be taken into consideration for design purposes because greater depths of scour will be produced.

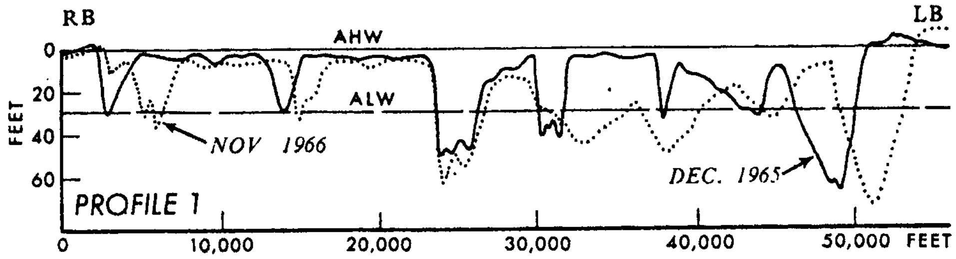

Figure 3-1 Illustration of a localized channel in a cross-section of Jamuna River, Bangladesh. Breusers and Raudkivi (1991)

Constriction scour

In order to reduce the costs associated with bridges, the cross section at a river crossing, for example, is often reduced by the encroachment of embankments on the flood plain or even on the river channel itself. When the bed of the river is mobile, the flow depth at the constriction site will increase because of the scouring. If a bridge pier is located near such an abutment, then the scouring processes associated with constriction, general and local scour will be reciprocally influenced by one another.

3.2 Local scour around bridge piers in open-water conditions

3.2.1 Mechanics of the process

The flow pattern surrounding a cylindrical pier in an open channel flow is complex. This complexity increases with the development of a scour hole. Many studies: i.e. Shen et al. (1969), Hancu (1971), Melville (1975), Melville and Raudkivi (1977), Ettema (1980), Breusers and Raudkivi (1991) etc., have been carried out in order to better understand the flow mechanisms associated with scouring around bridge piers, which lead to the formation of the scour hole. According to these studies, the flow pattern is divided into four components:

(i) bow-wave,
(ii) down-flow,
(iii) horseshoe vortex, and
(iv) cast-off vortices and wake.

Breusers and Raudkivi (1991) clearly stated that the scouring around a cylindrical bridge pier starts at the sides of the cylinder and rapidly propagates upstream around the pier until the holes meet at the centerline. The eroded material is moved downstream by the flow. Soon after scouring commences, a shallow hole, concentric with the cylinder, begins to develop around the pier, except in the wake region behind it. In this upstream region which covers about 120^{o} sector angle of the pier, the down-flow acts like a vertical jet, eroding an additional narrow groove just near the pier (Figure 3-2). The eroded material is then carried around the cylinder due to the combined action of the down-flow and the spiral movement of the horseshoe vortex. In this groove, the down-flow is turned completely in the opposite direction and the resulting upward flow is then deflected by the horseshoe vortex towards the upstream direction.

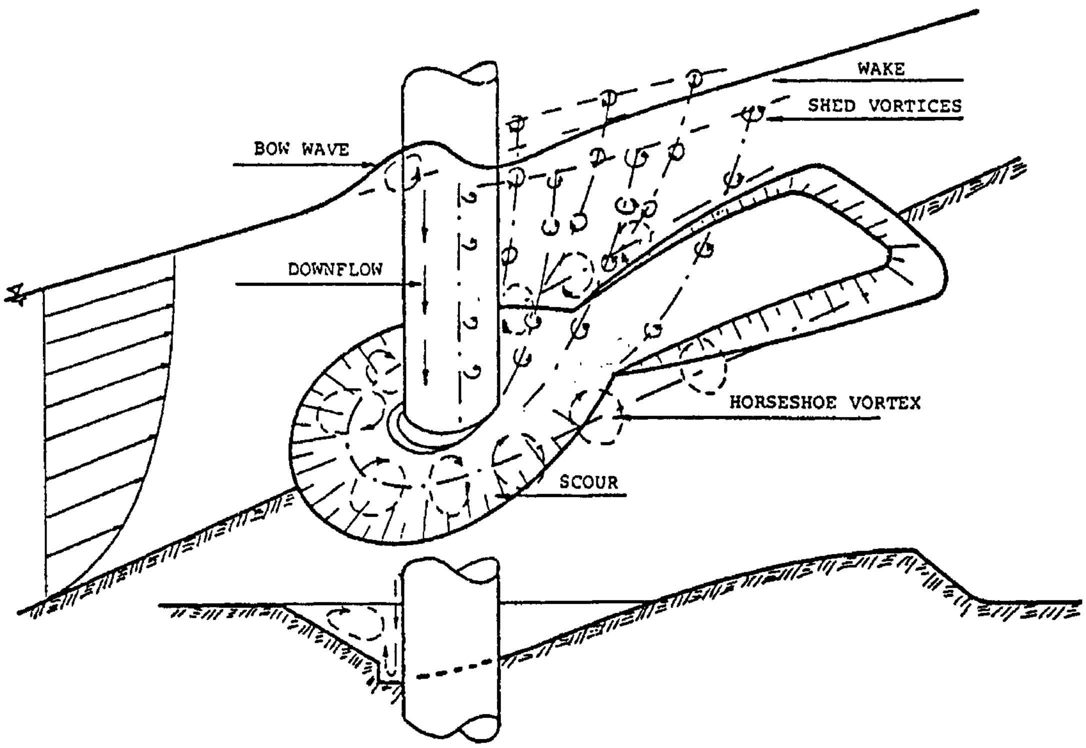

Figure 3-2 Representation of the flow pattern adjacent to a cylindrical pier. Breusers and Raudkivi (1991)

This turning point is located on the lip of the groove, a reason for which the groove is often sharp with almost vertical edges. As the process approaches equilibrium, the groove becomes shallow, and disappears completely because of the collapse of its rim. At this moment, the deflection of the down-flow throws this material up the slope of the scour hole such that some of it is pushed further by the horseshoe vortex, while the rest is directed laterally and carried away into and behind the wake region where deposition occurs as a bar. The upstream part of the scour hole develops in the shape of a slope descending towards the pier and equals the angle of repose of the bed particles under erosion conditions.

Observations have shown that the strength of the down-flow in front of the cylindrical pier reaches the maximum value just below the level of the bed when a scour hole is present. The maximum velocity of the down-flow reaches 0.8 times the average upstream flow velocity and occurs horizontally at 0.02 to 0.05 pier diameters upstream of the pier, and vertically in the scour hole at about 1 pier diameter below the bed level.

The horseshoe vortex develops as the result of separation of flow at the upstream rim of the scour hole built by the down-flow. Although this horseshoe vortex becomes very efficient in transporting sediment away from the scour hole, it represents an effect of scouring, not a cause of it. Furthermore, the horseshoe vortex expands its work downstream, passing the sides of the pier, for a few pier diameters before losing its typical behaviour and becomes part of the general turbulence.

The flow separates at the sides of the pier and as recognized from the sub-layer detachment theory, the separation surfaces enclose the wake downstream of the pier. The separation creates a region with a discontinuity in the velocity profile (with negative values), which leads to the development of cast-off vortices in the interface between the flow and the wake.

In the vertical plane, the phenomenon near the bed behind the pier becomes more complex due to the interaction of vortices in conjunction with the horseshoe vortex, which in turn will define a specific shape for the downstream scour hole. Because the pressure on the downstream face of the pier is less compared to the upstream face, these cast-off vortices act like mini-tornados that lift the material from the bed. However, because of their ability to effectively dissipate energy, the material lifted near the pier is dropped immediately downstream, where the vortex energy becomes smaller than the necessary particle lifting energy.

For a further analysis of local scour, it is important to differentiate between clear-water scour and lived-bed scour, as defined in section 3.1. Both the evolution of the scour hole with time and the relationship between scour depth and approach flow velocity depend on which type of scouring occurs.

3.2.2 Existing experimental studies

Clear-water scour occurs when bed material upstream of the scour area is at rest. In other words, the shear stress acting on the bed material is less than the critical shear stress corresponding to the incipient motion of the bed material. On the other hand, when the shear stress acting on the bed is higher than the critical value, the process is named 'live-bed' scouring. For clear-water scour, the equilibrium is reached when the combined effect of the temporal average shear stress, the weight of the bed particles, and the general turbulent agitation are in equilibrium everywhere. This means that the scour hole is deep and wide enough for the down-flow and the horseshoe vortex to move any other bed grain, but not to carry them away. In the live-bed scenario, the scour increases rapidly with time and then fluctuates around a certain value in response to the changes of certain bed characteristics including: ripples, dunes, changes in bed material, etc. The scouring equilibrium can be defined then as an average value between an average maximum and an average minimum of the scour depth.

The classical diagrams of Chabert and Engeldinger (1956) shown in Figure 3-3 clearly depicts this behaviour of the scour towards equilibrium with respect to time and shear velocity.

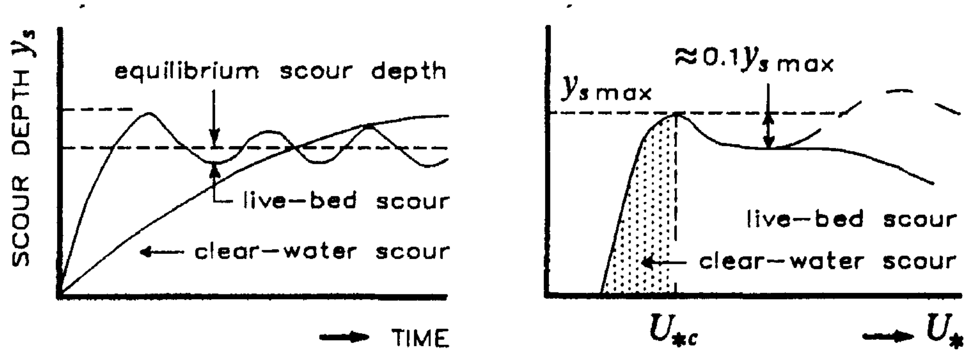

Figure 3-3 Scour depth for a given pier and sediment size, as a function of time and shear velocity. Chabert and Engeldinger (1956)

Ettema (1980) analyzed the temporal behaviour of scouring development. His findings show, as Chabert and Engeldinger observed before, that for clear-water conditions, the equilibrium depth of scour is reached asymptotically with time, whereas under live-bed conditions, the equilibrium depth of scour is more quickly attained. In this case, the scour depth begins a non-periodical oscillation movement caused by the changes in bed forms thereafter.

He also identified, for steady-state clear-water scour conditions, the following temporal steps of local scouring development around a cylindrical pier:

(i) the initial phase, or the transition from a plane bed with scour depth y_s=0 to the principal erosion phase, represents the erosion that occurs at the sides of the pier. This scouring process is weakened rapidly when the down-flow together with the horseshoe vortex becomes dominant;

(ii) the eroding phase: when the scour hole evolves rapidly in size until the entire horseshoe vortex is inside the scour hole. From this point, the horseshoe vortex and the down-flow become the dominant scouring mechanism;

(iii) the last step is a transition to a final equilibrium phase: characterized by the further deepening of the scour hole, a decreasing in the down-flow energy closer to the base of the hole, and finally, by a weakening scouring rate.

Since scour depth depends on so many variables, which describe the fluid, the bed material, the flow, and the bridge pier, many expressions and equations based on different combinations of these parameters can be found. Basically, the scour depth can be expressed as:

$$y_s = f(\nu, \rho, \rho_s, g, y_o, U, b, K) \tag{3-1}$$

where ν is the kinematic viscosity, ρ and ρ_s represent the fluid and sediment density respectively, y_0 is the uniform depth, U is the mean approaching velocity of the flow, b is the diameter of the pier, and K is a factor that includes the effect of the pier shape and pier alignment with the flow. In order to better understand the impact of these parameters, the following subsections present the influence of the sediment characteristics, the flow, and the pier (size, shape and alignment with the channel) on the scouring process.

Effect of grain size distribution

The effect of the grain size distribution integrates two aspects: (i) the sediment grading, and (ii) the grain size distribution: uniform or non-uniform bed material.

Raudkivi (1981) suggested that a second peak may exist in the scour depth diagram (Figure 3-4), depending on the bed grading. According to his findings, the results for smaller grain sizes, which induce the formation of ripples, differ from those for larger grain sizes, which do not form ripples. Thus, the lower variation curve in his diagram corresponds to fine particles for which the sediment motion and the ripple formation process occur together, commencing for shear velocities of $u_*>0.6u_{*cr}$ or $U>0.6U_{cr}$.
For coarse sediment, the scour depth decreases from the critical value or the clear-water peak value at $U\approx0.95U_{cr}$, to a minimum of about $U/U_{cr} = 1.5$ to 2, at which stage the bed is generally in its "steepest" shape (i.e. the bed-forms are at the highest temporal roughness). As the U/U_{cr} ratio increases, the scour depth increases again to a new peak value called the transition "flat bed" peak due to the absence of the bed-form drag component of energy loss. At this moment, the bed-forms are eroded to a "flat bed", and therefore a greater fraction of the flow energy is distributed into sediment transportation and scouring.

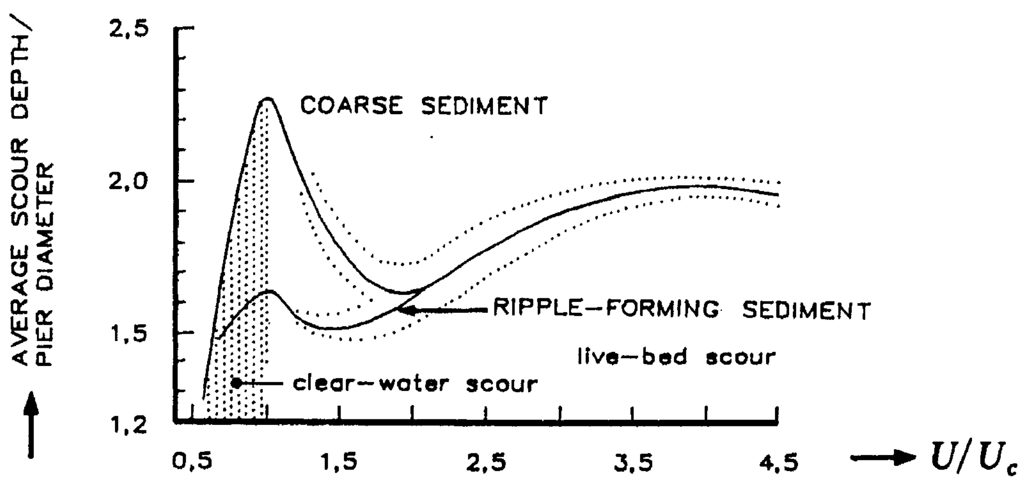

Figure 3-4 Scour depth at a cylindrical bridge pier in uniform sediment function of flow velocity. Raudkivi (1981)

For fine sediment, this second peak of scour depth is even greater than the "clear-water" peak. For higher relative velocities, the bed-forms appear again and dissipate some of the flow energy, which leads to a slight decrease in scour depth.

Ettema (1980) and Raudkivi and Ettema (1983) conducted local scouring experiments with a cylindrical pier in a 45m long x 1.5m wide x 1.2m deep flume. They performed experiments for clear-water and live-bed conditions with uniform and non-uniform sediments having a mean particle diameter d_{50} between 0.24mm and 7.80mm.

They concluded that the maximum depth of scour for uniform coarse grain, non-ripple forming bed material (d_{50} >0.7mm) is $2.1 \leq y_s/b \leq 2.3$. They also determined that grain size is not a factor. For a uniform bed material with grain size $d_{50} \leq 0.7$mm, a flat bed configuration cannot be maintained close to the critical shear stress, thus, ripples develop and the bed roughness begins to alter, inducing small amounts of sediment to move into the scour hole. This affects the boundary layer separation at the pier surface and consequently changes the strength of the horseshoe vortex. In this case, the equilibrium results show the relative scour depth $1.4 \leq y_s/b \leq 1.5$. Thus, the variation in the equilibrium of local scour is influenced only by the difference between ripple forming ($d_{50} \leq 0.7$mm) and non-ripple forming (d_{50}>0.7mm) sediments, and specific grain sizes.

The second main aspect influencing the variation of the scour depth is the bed grain size distribution, or the bed material uniformity. This degree of uniformity of the particle size distribution of sediments is described by its standard deviation σ. In practice, the most common and convenient way to measure particle size distribution is the geometric standard deviation:

$$\sigma_g = \sqrt{\frac{d_{84}}{d_{16}}} \approx \frac{d_{84}}{d_{50}} \approx \frac{d_{50}}{d_{16}} \tag{3-2}$$

Raudkivi and Ettema determined that as the standard deviation increases the rate of scouring and the final equilibrium depth decreases. The principal cause of the decrease in the equilibrium scour depth is the armoring process of the upstream layer around the perimeter of the pier. This process becomes significant when the values of the grain size standard deviation exceed 1.4 to 1.5, limits for which a bed material can be considered uniform. Their experiments were performed using fine and coarse uniform sediment ($\sigma_g \approx 1.3$) and non-uniform sediment ($\sigma_g \approx 3.5$) with $0.24\text{mm} \leq d_{50} \leq 3.8\text{mm}$. The average equilibrium scour was obtained for a cylindrical pier of 45mm diameter. This armoring process defines a new critical value for shear velocity u_{*a}, or mean velocity U_a, where the local scour depth reaches the first peak, also called the armor peak.

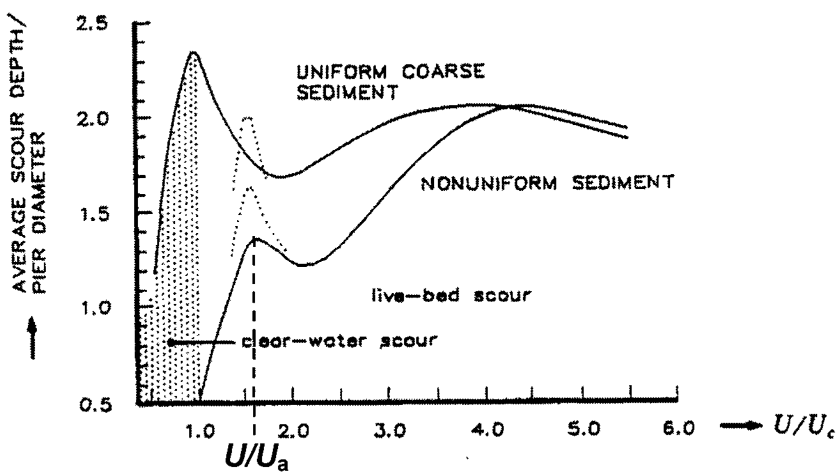

Figure 3-5 Average local equilibrium scour at cylindrical pier in uniform sediment and in non-uniform sediment. Raudkivi and Ettema (1983)

In Figure 3-5, the continuous lines in both cases plot a live-bed scouring condition, whereas the dotted lines show the scour depth evolution under a diminishing sediment transport condition. When the critical "armored" shear stress τ_{ca} is exceeded, the armor layer is eroded and sediment transport increases rapidly, leading to a decrease in local scour depth in the same manner as the transition from clear-water scour to live-bed scour. Further increases in shear stress imply further increases in the scour depth up to the "flat bed" condition. This process needs to be carefully studied in design problems because for rivers consisting of a gravel bed, field data indicate that the shear stress during flood periods seldom exceeds 2 times the critical "armored" shear stress. Pier design miscalculations must be guarded against due to the relatively quick nature of this process.

Raudkivi and Ettema also presented the variation of the scour depth with respect to the relative standard deviation for different grain size values (Figure 3-6). For grain size of d_{50} = 0.55mm at $\sigma/d_{50} \approx 0.5$ that represents a critical value for which only the armouring of the plane bed is achieved and not the armouring of the scour hole, a maximum scour depth of $y_s/b \approx 2.1$ was recorded. On the other hand, the coarser sediments reached the maximum scour depth at $y_s/b \approx 2.3$-2.4. For larger values of σ/d_{50}, the equilibrium scour depth drops off to a value between 0.3 and 0.5, regardless of the sediment size.

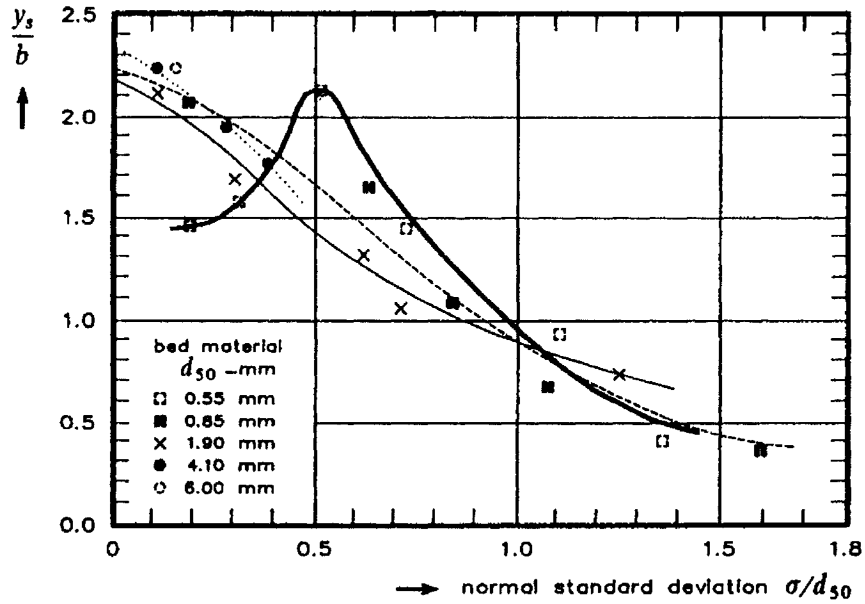

Figure 3-6 Equilibrium clear-water scour depth divided by pier diameter (y_{se}/b) as a function of sediment grading, $u_* \approx u_{*cr}$. Raudkivi and Ettema (1983)

Effect of pier size

Ettema (1980) studied the effect of pier size in the development and the equilibrium depth of local scouring. He performed experiments for six pier diameter sizes ranging from 28.5mm to 240.0mm and with sediment sizes ranging from 0.24mm to 7.80mm. The results were plotted with respect to the relative size of the pier and sediment (b/d_{50}) (Figure 3-7). Other studies conducted by Chee (1982) and Chiew (1984) presented similar variations of experimental data, but the overall observations were as follows:

(i) pier size affects the time required for the local clear-water scour to reach the final depth, whereas the sediment grading does not affect this time. This conclusion was determined by excluding the effects of the relative depth y_o/b and the relative grain size b/d_{50};

(ii) for live-bed conditions, the time taken to reach the equilibrium stage is significantly dependent on the ratio of bed shear stress to critical shear stress;

(iii) the larger the pier, the larger the scour volume and the longer the time required for the scour to develop at a given shear stress ratio.

From the temporal point of view, according to Ettema's (1980) analysis, the scour develops similarly for most values of b/d_{50}, in the initial phase. However, the development of scour for the principal erosion and equilibrium phases differs from the initial phase onward. These differences can be divided into four ranges with respect to the relative grain size b/d_{50}:

(i) $b/d_{50} \geq 130$: the sediment is fine relative to the pier diameter. In this case, both the horseshoe vortex and the down-flow directly entrain sediment from the scour hole;

(ii) $130 > b/d_{50} \geq 30$: the particle has an intermediate size in comparison to the pier diameter. The sediment is entrained from the scour hole by the down-flow but only from the groove formed around the upstream perimeter of the pier;

(iii) $30 > b/d_{50} \geq 8$: the bed material is coarse with respect to b. A greater proportion of the down-flow energy is dissipated by the bed at the base of the scour hole;

(iv) $b/d_{50} < 8$: the sediment is very coarse relative the dimension of the pier and of the down-flow velocity profile near the base of the scour hole. Therefore, the principal erosion phase of local scour does not occur. In this case, the scour is mainly due to the entrainment of bed particles by the accelerated flow at the sides of the pier and by the cast-off vortices behind the pier.

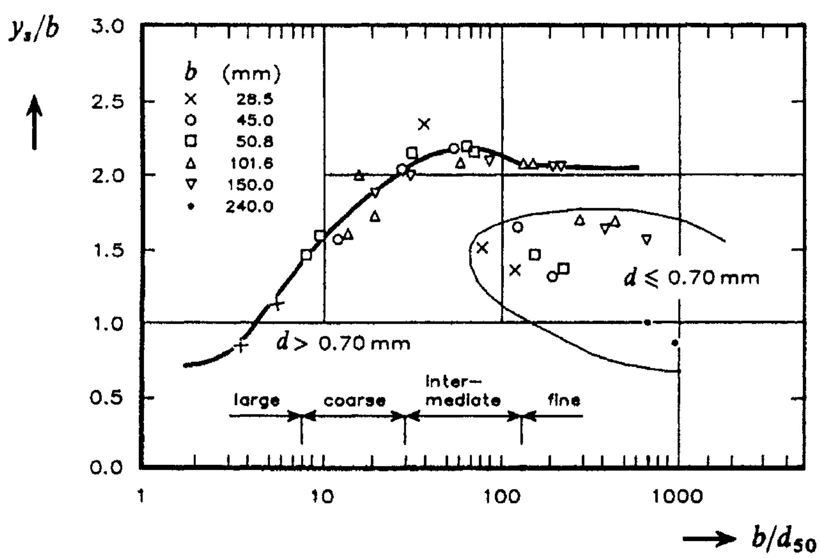

Figure 3-7 Equilibrium clear-water scour depth vs b/d_{50} at u_*/u_{*cr}= 0.90. Ettema (1980)

However, a clear difference in the features and the development of scour was observed between the two middle ranges ($b/d_{50} \geq 30$ and $b/d_{50} < 30$). Thus, for design considerations, Ettema proposed for uniform sediments of relative grain size ($b/d_{50} \geq 30$) the maximum equilibrium local scour depth in clear-water:

$$(y_{se} / \mathrm{b})_{\max} = 2.3 \tag{3-3}$$

where y_{se} represents the depth of the scour hole y_s at equilibrium stage. For uniform bed material of relative grain size (b/d_{50}<30) the maximum relative scour depth y_{se}/b can be estimated from Figure 3-7 but will not be greater than 2.3.

For non-uniform sediments, Ettema proposed the following expression for estimating the equilibrium depth of clear-water scour:

$$y_{se}(\sigma) / \mathrm{b} = \mathrm{K}_{\sigma} \frac{y_{se}}{\mathrm{b}} \tag{3-4}$$

where y_{se} is the equilibrium scour depth in uniform sediment with $\sigma_g \approx 1.0$, and K_α is a multiplying factor whose value is dependent upon whether or not the bed material is ripple-forming.

The time it takes for a scour hole to reach a certain depth, considering deep flow and a constant $u_*/_{cr} = 1.0$, was found to be a function of b^3:

$$y_s / \mathrm{b} = \mathrm{A} \ln[\frac{d_{50} \nu}{b^3} \mathrm{t}] + \mathrm{B} \tag{3-5}$$

where A and B are coefficients dependent upon the parameters u_*/u_{*cr}, y_o/b and b/d_{50}.

A very interesting case arises when experiments were performed with highly suspendable bed material such as fine sand. In this situation, the scouring is intensified by an additional effect, called the "vacuum cleaner" effect. This is caused by the cast-off vortices at the rear of the pier. Thus, the maximum scour depth may occur at the rear of the pier rather than in front of it.

Effect of the sediment regime and flow depth

The effect of the approach flow on local scouring can be expressed by the flow regime parameter u_*/u_{*cr} and by the flow depth y_o, or by the non-dimensional parameter y_o/b, the relative flow depth to the pier size.

The sediment regime influence is defined by the parameter u_*/u_{*cr}. If u_*/u_{*cr}<1, the scouring process occurs in a clear-water condition, and if u_*/u_{*cr}>1, then the scouring occurs in a live-bed condition. Chabert and Engeldinger (1956) established the influence of u_*/u_{*cr}, (Figure 3-3, right). Other researchers including Hancu (1971), Shen et al. (1969, Figure 3-8), and Ettema (1980) verified their findings.

Accordingly, the flow regime effect can be subdivided as follows:

(i) $u_*/u_{*cr} \leq 0.5$ refers to no scour condition;

(ii) $0.5 \leq u_*/u_{*cr} \leq 1.0$ refers to a clear-water scour condition. In this case, as shown in Figure 3-3, there is an almost linear increase in the scour depth with an increase in the relative shear velocity, up to the maximum depth at $u_*/u_{*cr} \approx 1.0$;

(iii) $u_*/u_{*cr} > 1.0$ refers to the live-bed condition where scouring is accompanied with continuous sediment transport.

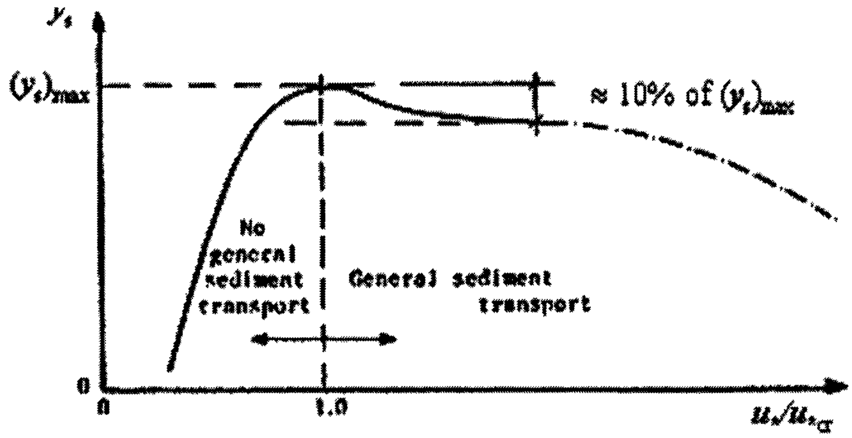

Figure 3-8 Equilibrium scour depth y_s versus u_*/u_{*cr}. After Shen et al. (1969)

A schematic presentation of the scouring process by Breusers and Raudkivi (1991) is shown in Figure 3-9. With respect to the flow depth, a pier introduces a surface roller (bow wave) at the water free-surface level and a "horseshoe vortex" at the base of the pier. These two roller motions have opposite directions of rotation. Thus, in principle, as long as they do not interfere with one another, the local scour is insensitive to flow depth. When the depth of flow decreases to a "shallow" case, the surface roller becomes the dominant motion. The "horseshoe vortex" is still maintained in the scour hole, but the bow wave interferes with the down-flow, hence, the latter becomes weaker. For shallow-water flows, the scour depth increases with depth of flow, and for greater flow depths, the scour depth is almost independent of depth.

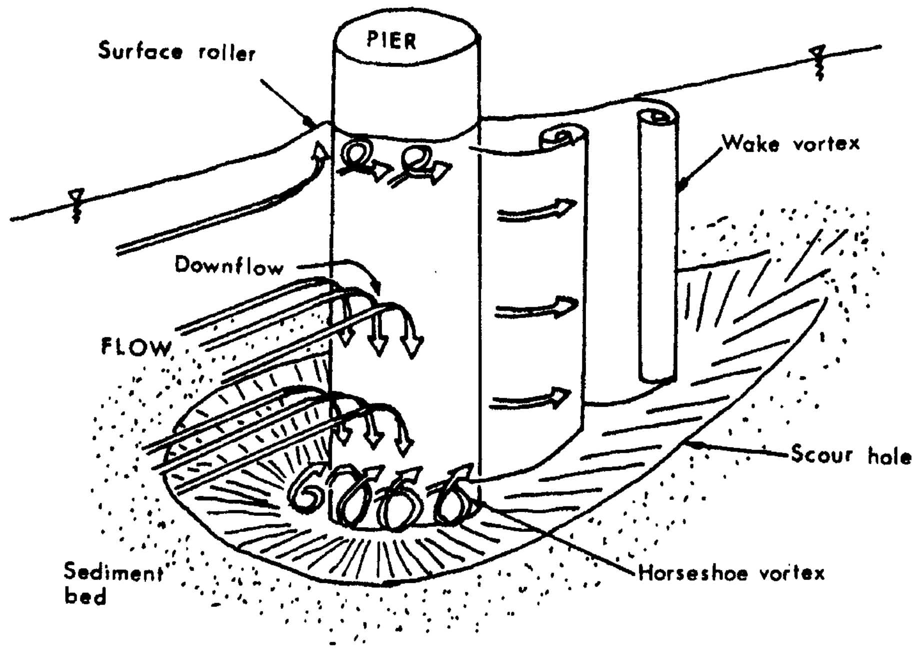

Figure 3-9 Flow structure at a cylindrical pier. Breusers and Raudkivi (1991)

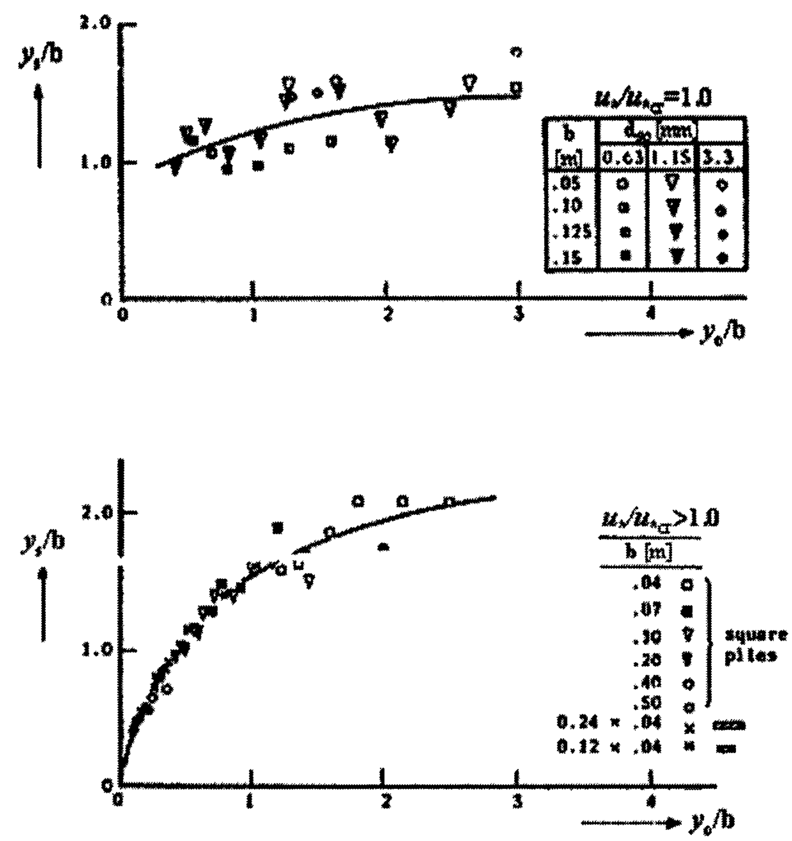

Figure 3-10 Scour depth (top- Bonasoundas 1973) and equilibrium depth (bottom- Basak 1975)

Despite numerous studies, the influence of the flow depth has not been clarified yet. However, based on research conducted by Bonasoundas (1973) and Basak (1975) (Figure 3-10), Breusers, Nicollet and Shen (1977) suggested that the effect of the flow depth, for constant values of u_*/u_{*cr}, can be neglected for values of relative flow depth $y_0/b>2$ or 3.

Ettema's (1980) extensive study conducted for shallow flows shows that the finer the sediment relative to the pier size, the smaller the range is concerning the effect of flow depth. For fine sediments, the scour depth may be insensitive to flow depth when $y_0/b>2$, while for relatively coarse sediments, this ratio may increase to $y_0/b>6$.

Effect of the pier alignment and pier shape

Many studies (Tison 1940, Laursen and Toch 1956, etc.) and field measurements have concluded that scour depth strongly depends on pier alignment to flow, for all pier shapes, except for those cylindrical in shape.

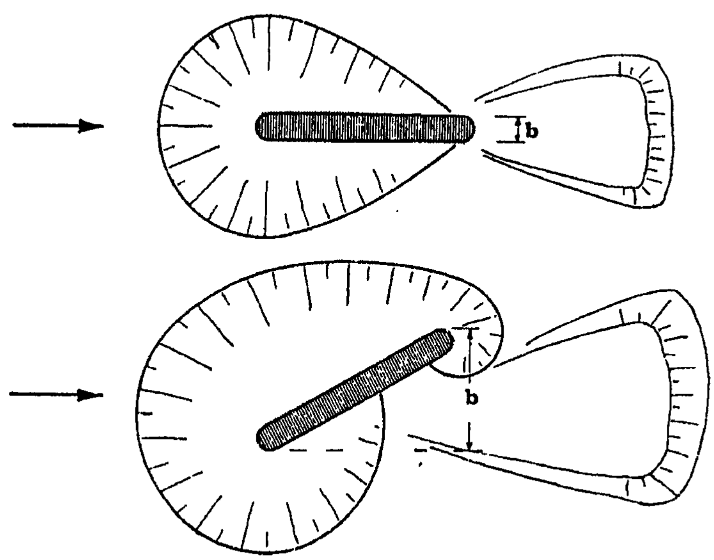

Figure 3-11 Scour shapes at a pier aligned with flow and angled with the flow direction. Breusers and Raudkivi (1991)

Many charts and diagrams were created for the computation of a multiplying factor K for the scour depth function of the angle of attack, α, and the ratio of pier width to pier length, l/b (Figure 3-12).

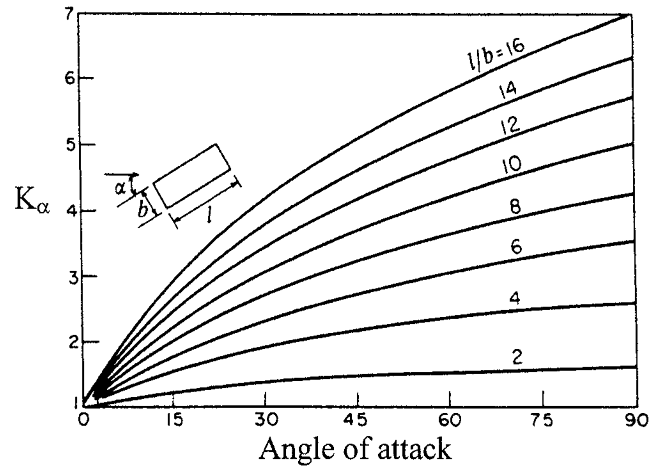

Figure 3-12 Alignment factors K_{α} for piers not aligned with flow.

Breusers and Raudkivi (1991)

As was the case for pier alignment, the shape effect is also accounted for in the same manner by a shape factor K_s, which can be found in literature through different tables. It is a function of width to overall length ratio b/l, and pier shape.

Since cylindrical piers present the best behaviour in laboratory experiments (no alignment with flow effect), most studies were conducted using piers of this shape in order to better analytically express the process of scouring.

3.3 Local scour around bridge piers under ice-covered conditions

Batuca, D. and Dargahi, B. (1986)

Batuca and Dargahi (1986) explored the influence of different parameters on clear-water scouring conditions. The experiments were performed for free-surface and ice-covered flow conditions in two concrete flumes: one with dimensions 27m x 1.97m x 1.1m and the second 22m x 0.80m x 1.2m. The bed sediment used was a ripple-forming sand with d_{50}=0.41mm and a grain size distribution of σ_g=1.88 (non-uniform sand). They used five different sized metallic cylindrical piers: 6.7cm, 10cm, 13.3cm, 16.7cm and 20cm, and two types of simulated ice-covers: plywood and aluminium. The experiments were directed to investigate the influence of mean flow velocity, relative velocity, flow depth, relative flow depth, and flow and pier Froude number ($Fr_p = U/\sqrt{gb}$).

Their findings regarding free-surface scouring supported results of previous studies (Chabert and Engeldinger (1956), Hancu (1971), etc.). However, concerning ice-cover tests, they concluded that a difference in the scour depth between free-surface and ice-covered flow increases linearly with increasing velocity, reaching almost 20% larger values for velocities greater than 0.3m/s. Similar findings were obtained when they analyzed results with respect to relative flow velocity and Froude number. They expressed the relative scour depth around a cylindrical pier as a function of three main parameters (when only one type of bed material is considered):

$$\frac{y_s}{b} = f\left(\frac{U}{U_{cr}}, \frac{y_o}{b}, Fr_p\right) \tag{3-6}$$

where Fr_p represents the pier Froude number $Fr_p = U / \sqrt{gb}$. They also produced two empirical relations for the relative scour depth of free-surface and smooth ice-covered flow. However, these relationships were validated only for clear-water condition, the bed sand characteristics mentioned above, and for $0.5 < y_s/b < 3.5$, $0.12 < Fr < 0.30$ and $0.14 < Fr_p < 0.37$.

Zabilansky and Yankielun (1996, 1998, 2000, 2002)

As was mentioned in subchapter 2.3, the US Army Cold Regions Research and Engineering Laboratory conducted important studies concerning the scouring and sediment transport processes under ice-covered flow. Yankielun and Zabilansky (1998) were the first to conduct field measurements and Yankielun eventually patented several devices for measuring ice loads and scour depths under ice, called time domain reflectometry (TDR) instruments.

A case analyzed in their studies included a bridge built in 1964 over the White River at White River Junction, Vermont. On January 1990 during an ice break-up, the bridge failed. Historically, the bridge was subjected to both higher flow rates and major impacts from thicker ice than that which was present at the time of failure. Although the ice load ultimately caused the disaster, the real factor was the cumulative effect of the scouring deteriorating the lateral support of its timber pile foundation.

The measurement technology, TDR used in their study was able to monitor the scouring progression in real time. This device, also known as an "instrumented-fish", operates based on radio transmitters. The idea was to bury many of these radios in the river bed at different depths and different locations around the bridge pier. As the scouring progressed, the instruments would be progressively exposed to the water current. As a result, the radios moving with the current trigger an "active" signal to be transmitted, showing that scouring had progressed to that depth. Once the velocity starts to decrease, and deposition begins, the radios would then again become buried and the elevation of redeposition could be detected by another signal sent by the instruments called the "stationary" signal.

Before analysing their results, it is important to remind the reader about the difference between the "free-floating" and the "confining" ice-cover which actually allows or prevents, respectively, the water stage to rise in response to an increase in discharge. Another very important observation refers to the analyzed reach of the river. The scouring process is a local process, occurring around a bridge pier or abutment. Thus it is of no use to include the bridge section of a river in a regular reach of several km in length because the entire phenomenon will be missed. Under an ice-cover condition, the problem is even worse. Zabilansky clearly shows a major difference between the upstream ice sheet of the bridge and the ice around the bridge pier. While the upstream cover can be considered "free-floating" ice, even if it is attached to the shoreline, the ice around the bridge pier is almost always a "confining" cover. Donchenko (1975) elaborated a rule of thumb to find the increase in the stage before an ice sheet starts to break-up: the stage should increase two to four times the ice-cover thickness. This can be translated, in the case of a 120m wide river with a 0.75m flow depth under a 50cm ice-cover and using the minimal rule of thumb to approach the ice break-up situation, into a 140% increase in velocity, which will drastically change the variables of scouring.

Using the TDR devices from 1992 to 1994, and obtaining real time measurements, Zabilansky and Yankielun were able to provide insight of the scouring process as well as identify some of its controlling factors. The very first major observation from these results, presented by Zabilansky (1998, 2002), showed that the presence of a solid ice-cover allowed scouring to occur at a lower discharge compared to free-surface conditions, which can actually change the main design parameter in the bridge pier design considerations.

Figure 3-13 depicts the set-up used for their experiments at the bridge site, containing the "instrumented-fish" buried at different depths in the river bed, and the so called sediment chains used as a second measuring device for the scour depth. Also presented is the sand layer with a gravel overburden, the ice sheet, and the ice collar attached to the bridge pier. In this study, the use of "stationary ice" refers to the situation when the ice sheet freezes into the vertical pier, "confining" the flow.

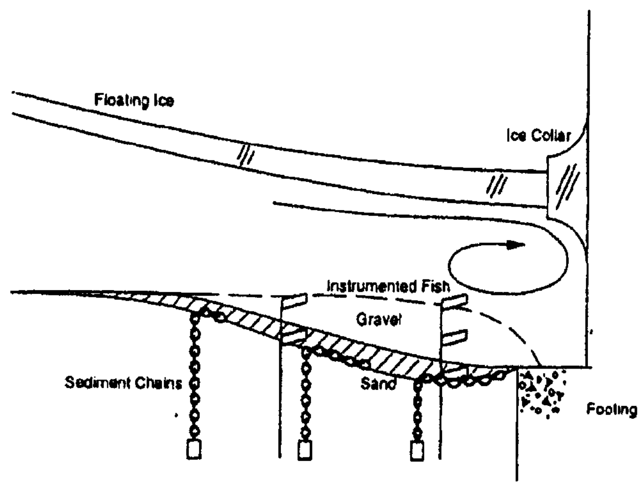

Figure 3-13 Cross-section along the projected centerline of the bridge pier. Zabilansky 1998

Zabilansky suggested two very important controlling factors of scouring under ice-cover. The first is the curvature shape underneath the ice collar, which redirects the current towards the bed. As previously mentioned in open water conditions, the incoming flow hitting the bridge pier nose will split into the surface roller (bow wave) and the down-flow (Figure 3-9). Theoretically, in the ice-cover case, the surface roller is greatly diminished due to the dampen effect of the ice-cover, and thus a large part of the energy lost in an open water situation is transferred to the down-flow energy (Figure 3-14). In nature, the curvature shape underneath the ice collar, due to the thermal conductivity of the pier combined with the water level fluctuations, will further increase the jetting action of the down-flow (Figure 3-13).

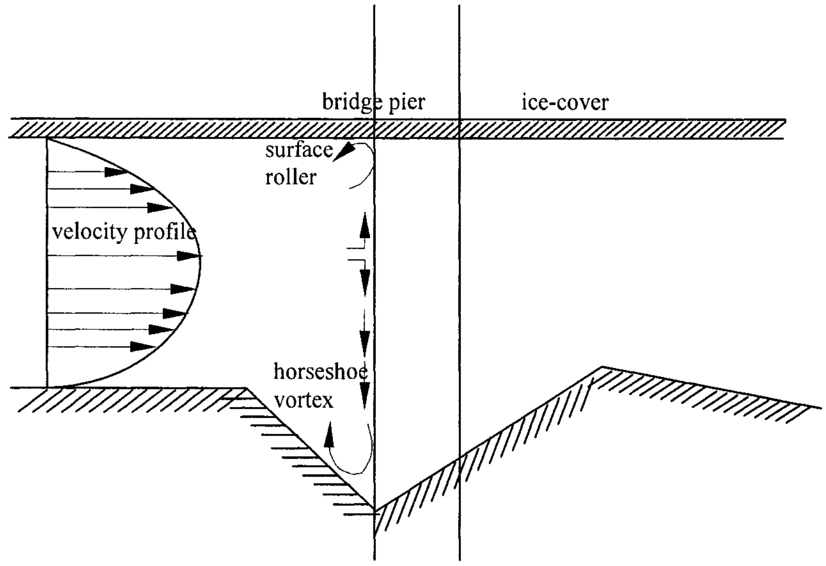

Figure 3-14 Distribution of the flow around a cylindrical bridge pier

Another factor observed during the river ice break-up process was the water pressure fluctuation, which causes sudden changes in the pore pressure in the bed soil that fluidizes the upper layers of the bed sediments. This facilitates sediment transport by the flow.

Olsson, Peter (2000)

The objective of Olsson's study was to investigate the effect of simulated ice cover on local scour depth around a cylindrical pier. His experiments were conducted in a 12m long x 0.45m width x 0.55m high laboratory flume at the Hydraulics' Laboratory of Clarkson University for different flow velocities with smooth and rough ice surfaces. The walls and the bottom of the flume were constructed using 12.7mm thick plexiglass.
The bed material consisted of uniform ripple-forming sand with d_{50} = 0.42mm and σ_g=1.29. The bridge pier was simulated by using a transparent cylindrical pipe with an external diameter of 31.8mm. The ice-cover was simulated by using Styrofoam sheets. A total of 30 experiments were performed, 20 with ice-cover and 10 in open-water.

For free-surface relative scour depths, Olsson's findings confirm the general trend when compared with Melville (1975) (Figure 3-15).

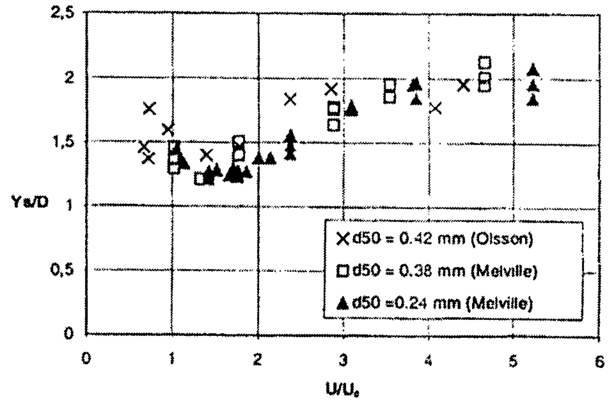

Figure 3-15 Relative scour depth agreement with Melville's tests for free surface flow. Olsson (2000)

On the other hand, the results from both clear-water conditions and live-bed conditions compared with scour at free-surface flow showed that an ice-cover may increase the local scour depth by as much as 25-35%, or in terms of pier diameters, up to 0.3-0.5b, with respect to scour depth for free surface conditions. These differences were most pronounced for relative flow velocities ranging from 1.8 to 3 (in live-bed conditions) for which the covered tests presented up to 35% larger scour depths relative to open-water situations (Figure 3-16).

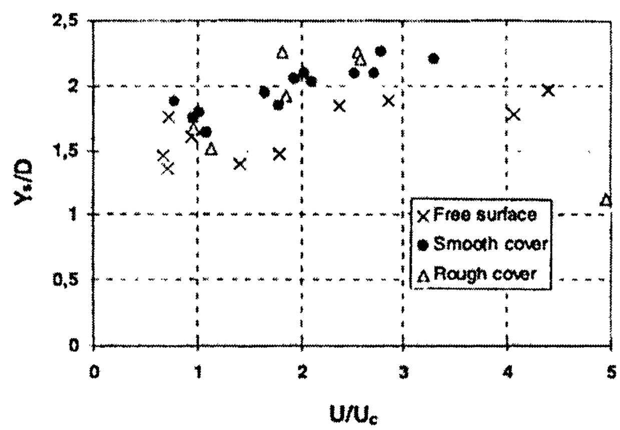

Figure 3-16 Relative scour depth vs. relative flow velocity. Olsson (2000)

The results in the clear-water case were found to be in agreement with the findings of Batuca and Dargahi (1986). The roughness of the ice-cover was found to have negligible effects on the increase in scour depth.

Chapter Four
Apparatus and Experimental Approach

In order to make a precise analysis of the scouring process around a bridge pier in an ice-covered river together with the hydraulic and the sedimentation behaviour of flow, on site measurements of velocity, shear stress, sediment transport rates, and scouring rates must be conducted. This work is very tedious, due to the remote locations of such sites and due to the conditions during the cold season. Therefore, carrying out physical modelling experiments in laboratory flumes is preferred and has a relatively high degree of confidence.

All the experiments regarding this study were conducted at the Civil Engineering Department's Hydraulics Laboratory of the University of Ottawa.

4.1 Experimental Setup

The experimental setup includes the following: concrete rectangular flume, cylindrical bridge pier, bed material, hydraulic equipment, velocity measurement system, mechanical equipment, filling/drainage sand box and pipe network, free-surface slope measurement apparatus, simulated ice covers, ice-cover shear stress measurement system, and sediment trap.

4.1.1 Laboratory flume

All experiments were performed in a 29.2m long x 1.49m width x 0.77m high rectangular flume made of concrete blocks. The bottom of the channel is also made of concrete, and together with the sidewalls was painted with black asphalt to ensure uniform water insulation along the entire length of the flume. Both sidewalls of the flume are covered with "U" steel profiles. Aluminium rails are fixed on top of these profiles, which run along the length of the flume, enabling instruments to be carried parallel to the flume. An aluminium-structure trolley is used to support and move all the equipment used for measuring the elevations of the channel bed and the free water surface, the longitudinal, transversal and vertical velocity field, and for scanning the scouring hole and the erosion/deposition features of the scouring process. Figure 4-2 depicts the layout of the entire flume.

The flume was divided into three sections along its length: Upstream false bed, Basin sand bed and Downstream false bed.

Upstream False Bed Section: This is a false bed made of metal sheets along the flume running for a length of about 9.75m covering the full width of the channel. It is supported underneath from the rigid bed of the channel by a metal-wood block structure. The false bed begins at 1.6m from the inlet pipe with a circular arc contraction shape. This contraction spans around 0.65m until it joins the elevation of the false bed at 0.254m from the bottom of the flume. This arc was designed to dampen the recirculation turbulence due to the sudden contact between the incoming water flow and the elevated false bed.

Another abrupt change occurs when the flow regime goes past the smooth surface on the upstream false bed to the rough surface in the sand basin bed area of the flume. In order to avoid this abrupt change, the upstream false bed contained a glued layer of the same sand used in the basin ensuring a unique roughness coefficient and flow regime throughout all sections of measurement. The upstream area of the channel contains four cross-sections along its length: UA, UB, UC, and UD (Upstream section A, B, C and D). Each cross-section has 9 points (1 to 9) where velocity measurements are taken. Points 1 and 9 are 0.32cm away from the sidewalls, and the remaining points are 0.18cm apart from each other. Figure 4-1 clearly describes this feature.

Basin Sand Bed Section: This is the central part of the flume located between the upstream and the downstream false beds and is filled with sand with a specific grain size distribution. It is also the region where the cylindrical bridge pier is located. The basin section is 7.32m long covering the full width of the flume. The last 0.51cm of this section is occupied by the sediment trap, which was conceived to respond to different experiment requirements (i.e. bed load rates experiments).

The basin was filled with sand and cement bricks ($16'' \times 8'' \times 2''$ and $16'' \times 8'' \times 4''$). The bottom of the section was unevenly layered with cement bricks, as shown inFigure 4-3, in order to decrease the amount of sand necessary to fill the basin. The remaining space was filled with sand such that its surface was levelled with the upstream false bed. The levelling of the sand was done with a specially designed wood screen, which could be pulled to slide along the aluminium rails of the sidewalls. The height of the upstream false bed (0.254m) was computed based on the flume dimensions, bed material size and grade distribution, flow regime, bridge pier diameter, and research information about the maximum scour depth ($2.1 \leq y_s/b \leq 2.3$, Ettema, 1980), such that the bottom layer of bricks would never be uncovered by the scouring process.

The basin has 8 cross-sections marked on the sidewall rails: BA, BB, BC, BD, BE, BF, BG, and BH (Basin section A, B etc), but with a different spacing between them as compared to measurement points in the upstream section (Figure 4-1).

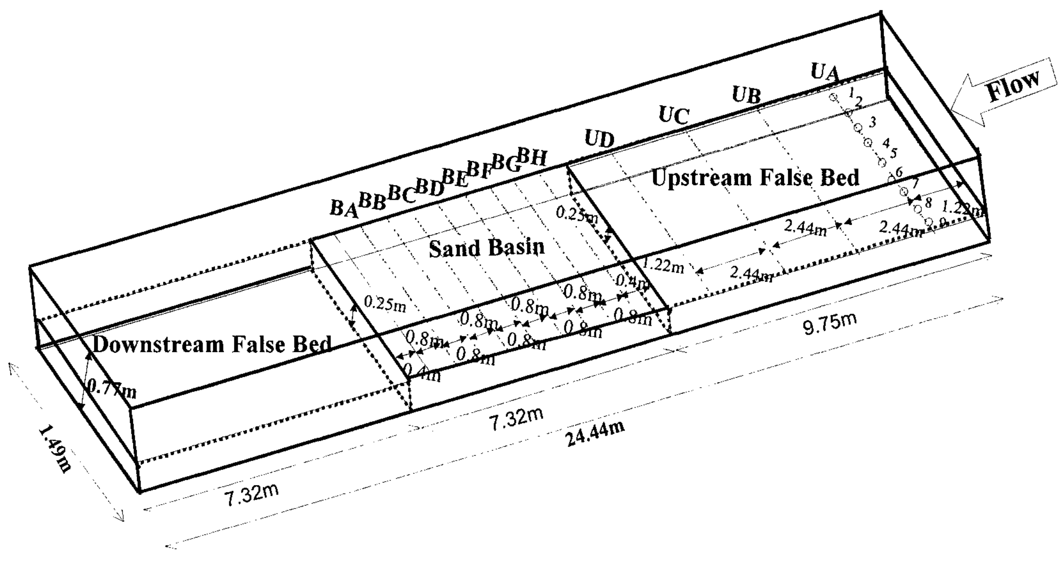

Figure 4-1 Working Sections of the Flume: Upstream False Bed (UA – UD) and Sand Basin (BA - BH)

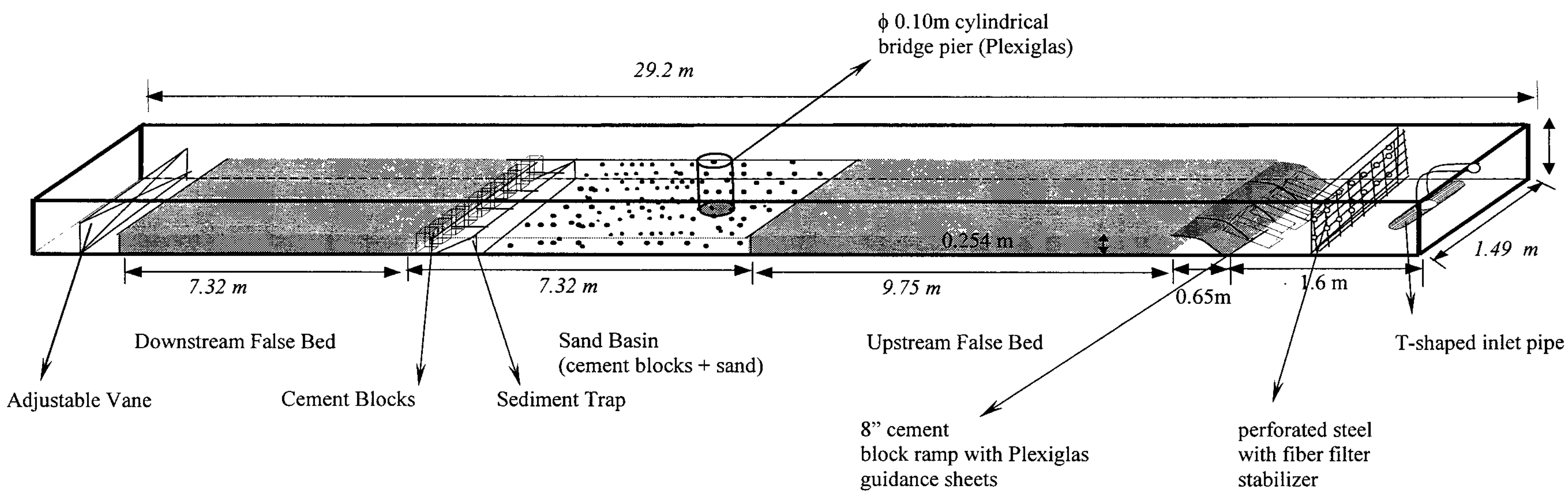

Figure 4-2 Isometric View of the Rectangular Flume

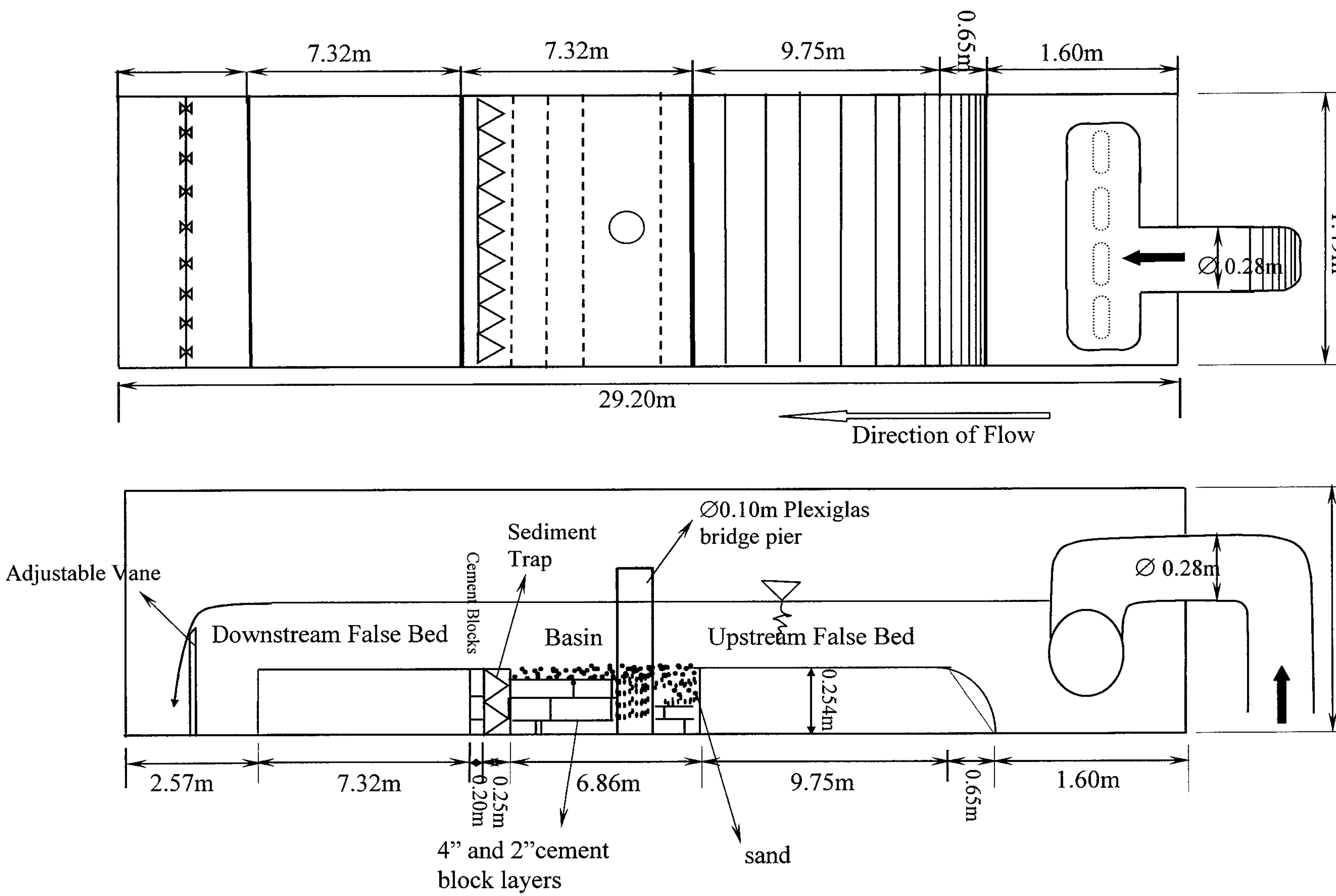

Figure 4-3 Schematic of the Rectangular Flume

Downstream False Bed Section: Another false bed consisting of metal sheets followed the basin section with dimensions 7.32m long x 1.49m width x 0.254m high. The downstream section did not include any glued sand at the surface.

4.1.2 Bridge pier

For all the experiments in this study, a 0.102m diameter Plexiglas cylinder was used as a bridge pier, and was positioned in the mid-width of the channel, 1.83m downstream from the beginning of the sand basin section. The cylinder is glued on a square acrylic sheet of 0.0125m thickness, which is bolted directly into the concrete bottom of the flume. Inside the cylinder, four measurement scales are vertically glued in the four geographic directions: North being the nose of the cylinder facing the upstream water flow, and South in the toe direction. The scouring readings around the bridge pier during the experiments were taken using a circular mirror, slide inside the Plexiglas pier (Figure 4-5).

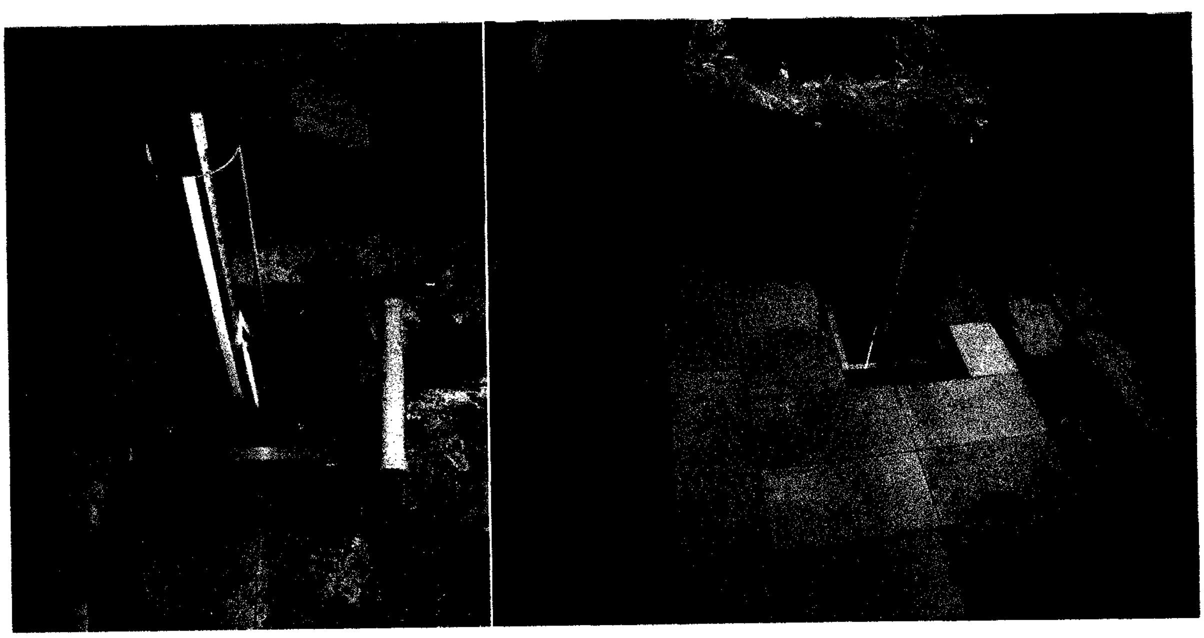

Figure 4-4 Cylindrical bridge pier

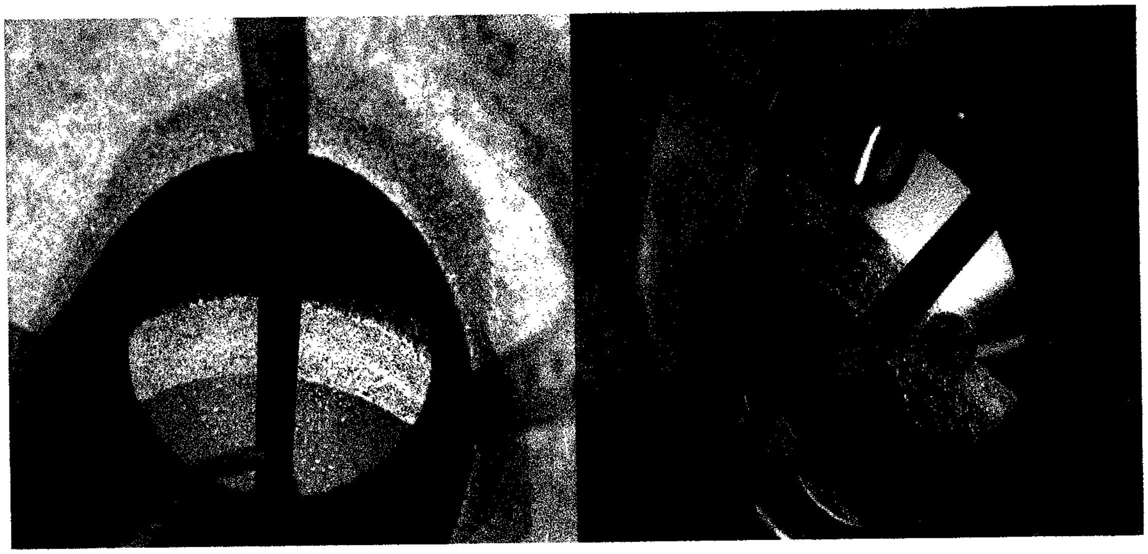

Figure 4-5 Readings of scour depths at the nose (left) and toe (right) of the bridge pier.

4.1.3 Bed material

The sand used in this study was a mixture of half original sand and half sieved sand. The original sand passed through sieve #20 (0.841mm) and was retained on sieve #30 (0.595mm). After mixing and particle size analysis, the mean particle diameter was d_{50}=0.646mm, and the particle size distribution was characterized by the geometric standard deviation $\sigma_g = 1.465$, representing a relatively uniform medium sand.
Appendix A1 shows the granulometric curve of the mixed sand and the computation of the geometric standard deviation.

4.1.4 Hydraulic equipment

Water enters the flume through a 0.28m diameter T-shaped inlet pipe, shown in Figure 4-6. It is pumped using a centrifugal pump of 870-RPM and 5000 USGM ($\approx$0.316m^3/s = 315.801/s) discharge capacity. This water is then recirculated through a large reservoir located underneath the floor of the laboratory.
Unfortunately, the T-shaped inlet pipe is not centered with respect to the channel width; thus, it has been wrapped with metal mesh and fibre filter in order to provide a more uniform spread of the turbulence due to the pipe exits across the width of the channel.

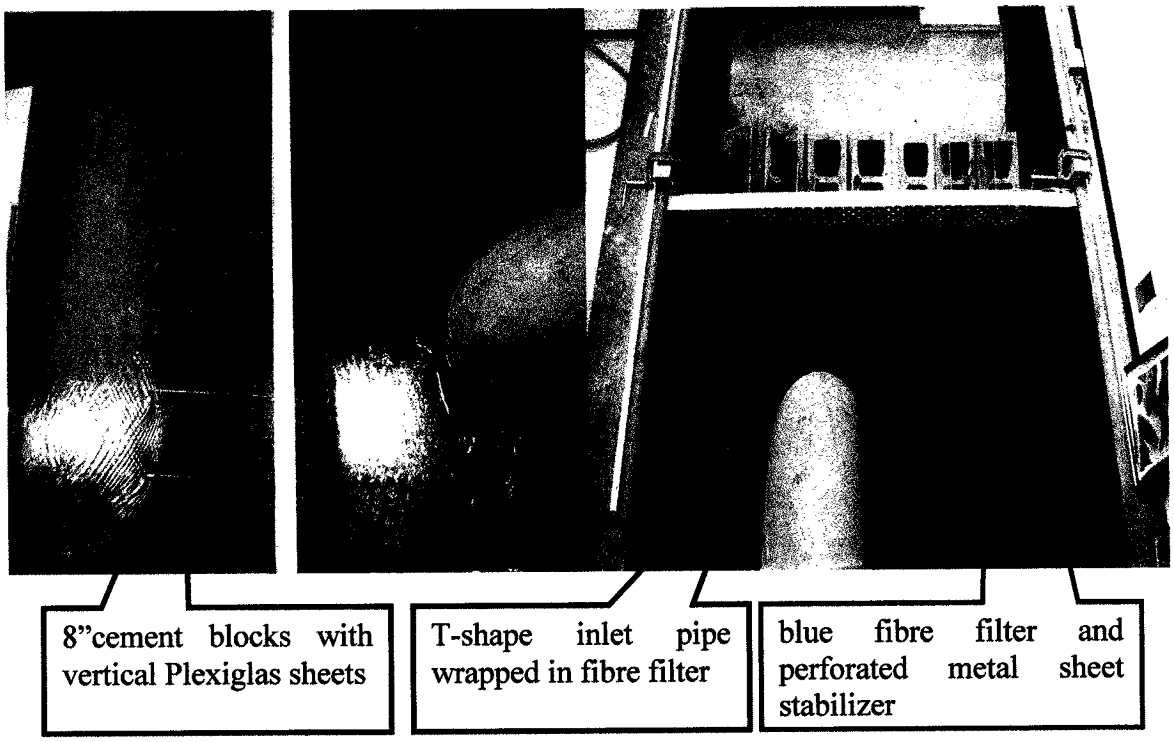

Figure 4-6 Experimental setup: inlet pipe and stabilizer

To further dampen this turbulence, two stabilizers are placed in the vicinity of the inlet pipe. The first one is a combination of fibre filter and perforated steel plate placed at 51cm from the inlet pipe. Its role is to dampen the turbulence throughout the entire flow depth of the channel section. The second stabilizer consists of a row of 8" cement blocks ($16" \times 8" \times 8"$) with vertical Plexiglas guidance sheets fixed in between each block. Its role is to increase the flow velocity in the upper layers of the flow (by increasing the bed roughness with the cement blocks) and to evenly distribute the discharge over the channel width (by using the Plexiglas guidance sheets). As a result, conditions for achieving a uniform flow were created from the beginning of the channel.

The discharge is adjusted via a butterfly-valve which has a 28cm supply guidance scale and is measured by the difference in pressure across a calibrated diaphragm plate having a 17.8cm orifice opening. The readings are taken from a mercury U type manometer, and using a polynomial calibration curve, the discharge is calculated using the expression:

$$\mathrm{Q} = a(\mathrm{R}_m - \mathrm{R}_o) + b(\mathrm{R}_m - \mathrm{R}_o)^{1/2} + c(\mathrm{R}_m - \mathrm{R}_o)^{1/4} \tag{4-1}$$

where R_m represents the manometer readings and R_o the reading at zero discharge. The parameters a, b and c are the calibration coefficients and were found to be a = -1.76957, b = 37.49139 and c = -6.29051.

At the downstream end of the flume, where the water falls back into the reservoir, there is an adjustable vane – sharp-crested weir. Its movement helps prescribe the flow depth. A second device for measuring the discharge is located in the same area. Both discharge values should agree within a reasonable error percentage range. This device consists of a glass tube that shows the elevation difference between the water free-surface and the tip of the weir. Using the method of Brater and King (1976) the discharge is calculated as follows:

$$Q = C_e L_e H_e^{3/2} \tag{4-2}$$

where L_e is the effective length of the weir $L_e = L + k_L$, with L being the actual opening of the weir and k_L being a factor which takes into account the effect of the fluid viscosity,

H_e is the effective potential energy $H_e = H + k_H$, with H being the elevation from the weir tip to the water surface and k_H the factor that introduces the effect of the surface tension, k_H=0.003ft in this study, and

C_e is a corrective factor applied to H, including the influence of head losses over the weir, the kinetic-energy correction factors, and the vena contracta shape. It can be expressed from the diagram in Figure 4-7(b), as a function of *H/P* and *L/b*, where P represents the elevation of the weir tip from the bottom of the channel.

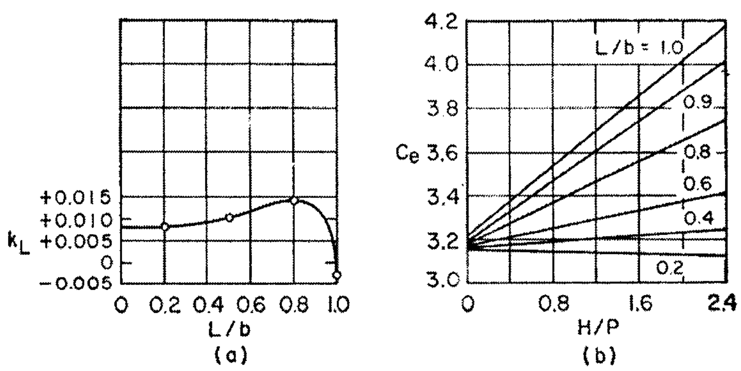

Figure 4-7 Coefficients k_L and C_e, for horizontal sharp-crested weir with end contraction. Kindsvater and Carter (1959)

The factor L_e can be approximated from the diagram in Figure 4-7(a), a function of the contraction ratio of the weir L/b, with b being the width of the channel.

For this study, a second pump of 750-RPM and 1500 USGM ($\approx 0.0948 m^3/s = 94.75 l/s$) was used to fill the flume. Its inlet, a 4" diameter PVC pipe is located at the end of the downstream part of the channel.

4.1.5 Velocity measurement system

Flow velocity was measured using an Electromagnetic Current Meter (EM) from Alec Electronics, Japan. It is an *ACM 250-D* model which consists of a 2-Axis Electromagnetic Current Sensor probe and a display unit. The sensor probe is 9mm in diameter and has a 10m signal cable connecting to the display unit as shown in Figure 4-8. Through this cable, the signals from the sensor probe are sent to the display unit shown in Figure 4-9.

The sensor probe takes two readings every second, and the display unit processes the information and outputs the moving average reading, depending on the time–constant switch settings every 1sec, 5sec, or 10sec.

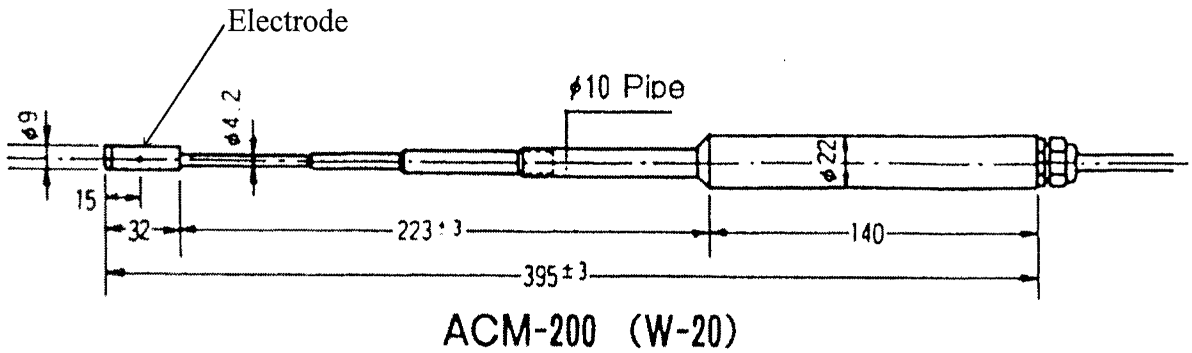

Figure 4-8 Description of the Current Sensor Probe

(ALEC Electronics operating manual)

The current probe measures velocities in the x and y-axis (transversal and longitudinal directions), as illustrated in Figure 4-10. The probe works on the principle of Faraday's law (The Electromagnetic Induction Law): when any conductive material goes through a magnetic field, an electrical current is generated in that material which is proportional to its speed and distance from the magnetic field.

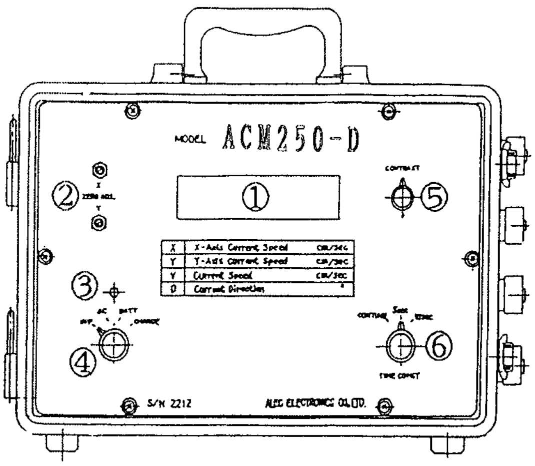

1	LCD display
2	Zero-adjustment trimmers
3	Recharge/discharge led
4	Power switch
5	LCD contrast switch
6	Time-constant set switch

Figure 4-9 Display Unit (ALEC Electronics operating manual)

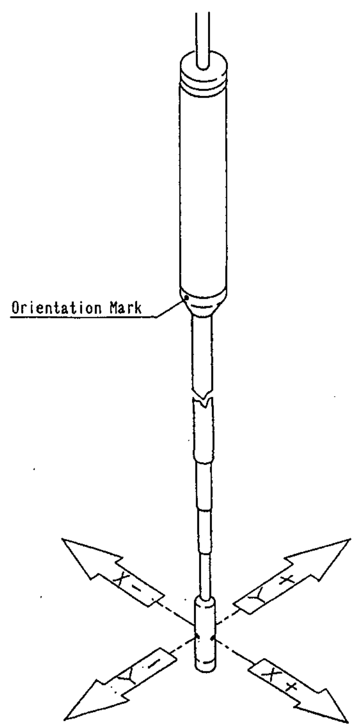

Figure 4-10 The 2-axes of the EM current sensor (ALEC Electronics operating manual)

Water, being a conductive material, produces an electrical current generated between the opposite electrodes (sensors) 2-4 and 1-3, which measure the u (x) and v (y) components of velocity. Thus, the real average flow speed U is given by $U = \sqrt{u^2 + v^2}$, and the direction of the flow with respect to the y axis is determining by computing $\tan\theta = u / v$. Figure 4-11 depicts this concept of the electromagnetic induction.

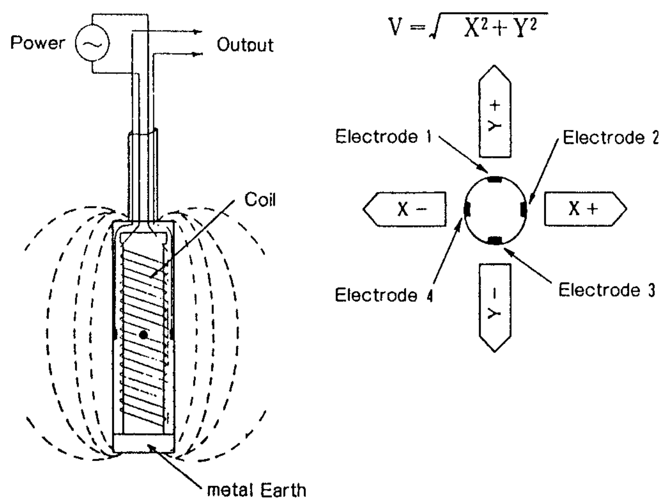

Figure 4-11 Operating principle of the EM Sensor Probe (ALEC Electronics operating manual)

This Electromagnetic current meter model has a measuring range of 0 ~ ±250cm/sec and an accuracy of 0.5cm/sec. However, the most important limitation of any EM velocity device refers to the accuracy of the velocity measurements close to the boundaries of the flow field. Once the sensor probe approaches a flow boundary, which is usually a non-conductive material (air, concrete, Plexiglas etc.) then the electrical current is interrupted, leading to errors that can easily alter the results. For laboratory tests, this is a very important aspect because the closer to the boundaries the velocity can be accurately measured, the better its vertical profile can be approximated. Thus, other flow parameters can be better analyzed. It is important to note that analyzing shallow-water flow is key to the experimental program. The EM probe used in this study was able to provide accurate measurements within 3cm of the water free-surface, which corresponded to velocity readings of up to 80-85% of the flow depth from the bottom of the channel.

This current meter also comes with a RS232C output plug which allows it to connect to a computer. Data from the sensor probe is directly transferred into the computer, and time-averaged velocity readings for a particular flow depth are easily obtained and stored into a file for later use.

4.1.6 Mechanical equipment

As previously mentioned, the aluminium rails are running along the entire length of the flume. These rails are fitted with a trolley which moves in the transversal (x) and longitudinal (y) direction along the flume. Two rack and pinion devices are installed on this trolley: one with a movable scale used for flow depth measurements, and the second with a fixed scale used to hold and position the sensor probe for velocity readings. The former device is a point gauge made of stainless steel with an accuracy of ±0.3mm. This device is also used to obtain the bed surface elevation. The difference of their readings gives the flow depth. The second device is used to support and accurately position the sensor probe within the channel. Its vertical positioning has an accuracy of ±0.5mm. Figure 4-12 shows both devices, the trolley and the complete setup of the velocity measuring device.

Another elevation reading device, a *Disto*™ *pro*^{4} *a* electronic distance measurement device from Leica Geosystems was used in the study in order to measure accurate scour hole depths as well as to measure the irregularities of the sand bed due to the erosion/deposition process. As a removable installation on the trolley, it was used to measure the sand elevations with an accuracy of ±0.8mm.

These data were used to create 2 and 3-Dimensional profiles of the scouring hole and the erosion/deposition features behind the bridge pier. This device works by utilizing the time-speed-distance equation: a laser beam is sent towards a material surface from where is reflected back. By recording the time that it takes for the beam to travel to and from the material surface, the distance is then computed by the device.

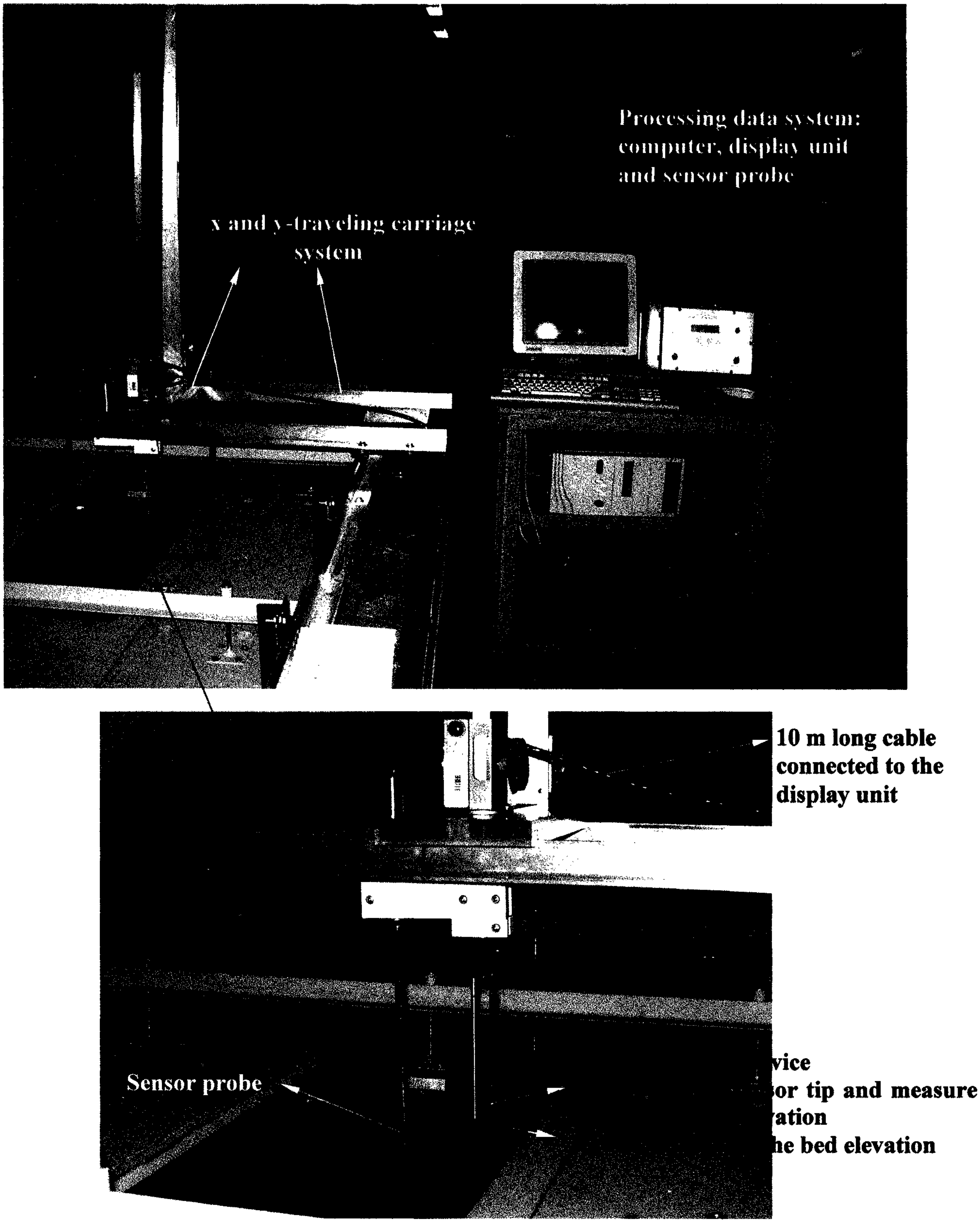

Figure 4-12 Arrangement of the measurement apparatus for bed elevation and velocity, and the data processing system

4.1.7 Filling/draining sand box and pipe network

Filling and draining the flume was a key step in the experimental procedure. Implementing a good drainage system within the flume can drastically reduce the waiting time between the dynamic measurements (velocity, scouring, and slopes) and the static measurements of the bed erosion/deposition features. This particular area of the study will have an important impact on the duration of the experimental program. Therefore, a pipe network within the flume and a sand box were designed in order to provide proper filling of and fast drainage within the flume.

The purpose of the sand box was to promote a relatively fast drainage time of the basin section. Scanning the scouring and the erosion/deposition features created during the tests were then taken shortly after flow shut down. The sand box, positioned underneath the sand on the bottom of the channel was made of a 48" x 48"x ½" plywood base covered with special fibre and painted with waterproof resin (Figure 4-13). On top, a grid of small boxes built from Plexiglas plates 2-3/8" in height covered with metal mesh, geosynthetic sand filter, and plastic mesh ensured the necessary resistance with respect to the weight of the sand above as well as prevented the looseness of the bed material. The total height of the sand box is 0.076m from the bottom of the flume. The sand box is connected through a 1-1/4" diameter pipe to an external pipe network (2" in diameter) which is attached to the outside walls of the flume. The pipe network has two direct exits leading to the laboratory reservoir, and another with the flume located further downstream near the mobile crested weir. This last connection was covered with a normal 2" diameter threaded plug such that during the tests no water was permitted to flow through the pipe network leading from the basin section. The pipe network also contained two ball-valves which ensured the double functionality of this new system: filling and draining the flume.

Once the flow is turned off, the plug from the downstream connection of the pipe network is removed, and both ball-valves are opened. The position of the weir can be maintained at the same level if necessary, which eliminates errors introduced by any potential repositioning of the weir.

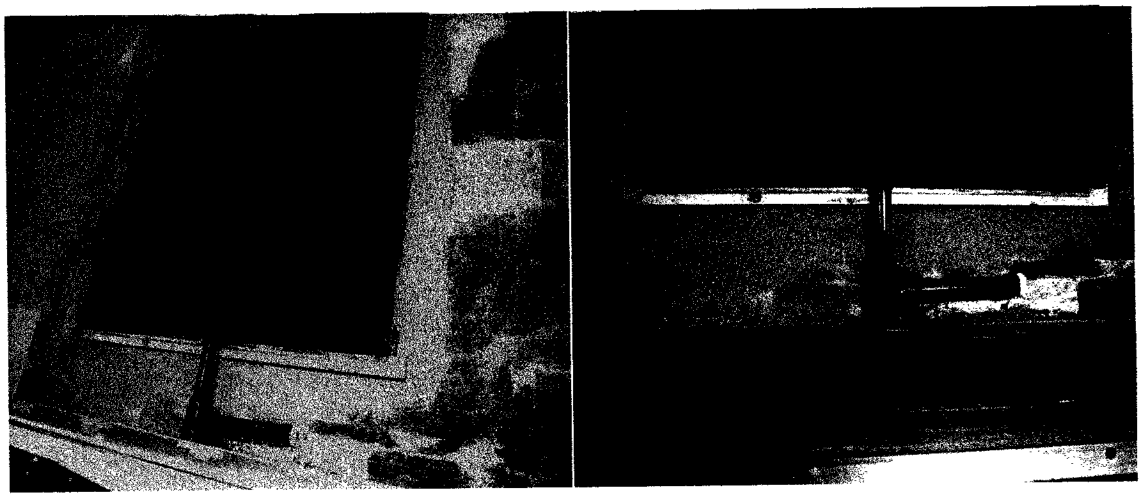

Figure 4-13 Filling/draining sand box

Another important purpose of the sand box was to provide a smooth filling of the flume without disturbing the sand bed surface. Previously the filling of the flume was performed from upstream, and every time the first small layer of water passing from the rigid surface of the upstream false bed to the surface of the sand basin created significant erosion at the separation line of the sections. This phenomenon occurs due to the fact that the sand in the basin section was not yet completely filled with water. Thus, when the first layer of water arrived in this section, the water "falls" into the sand, creating the aforementioned erosion process. If left alone, it will have a major impact on the flow regime and the sediment transport process in the basin. Therefore, it was imperative the flume to be filled not starting from the upstream direction, but from the downstream direction. Filling of the flume via this particular method was performed using the second pump described in the *Hydraulic equipment* section. Both the downstream false bed section and the sand basin section are filled at the same time through the pipe network and the sand box such that when the first layer of water arrived at the sand basin section, the sand bed was already 100% moisturized with all excess air already removed. This resulted in the elimination of any bed disturbances at the separation line between the upstream false bed section and the sand basin section.

4.1.8 Free-surface slope measurement apparatus

In open channel flow analysis, the knowledge of the free-surface slope is very important. Since significant changes in the free-surface slope were predicted to occur when making the transition from free-surface flow to ice-covered flow, a free-surface slope reading device was built. This device contains four copper tubes (1/4" diameter) positioned inside the channel. They are connected outside the flume through a transparent tubing network to four glass tubes fixed against a wall near the flume. Readings are determined by taking the difference in water levels between the glass tubes. The copper tubes were installed at the start of the upstream false bed, at the start and the end of the sand basin section, and at the end of the downstream false bed such that readings for different sections of the flume could be taken.

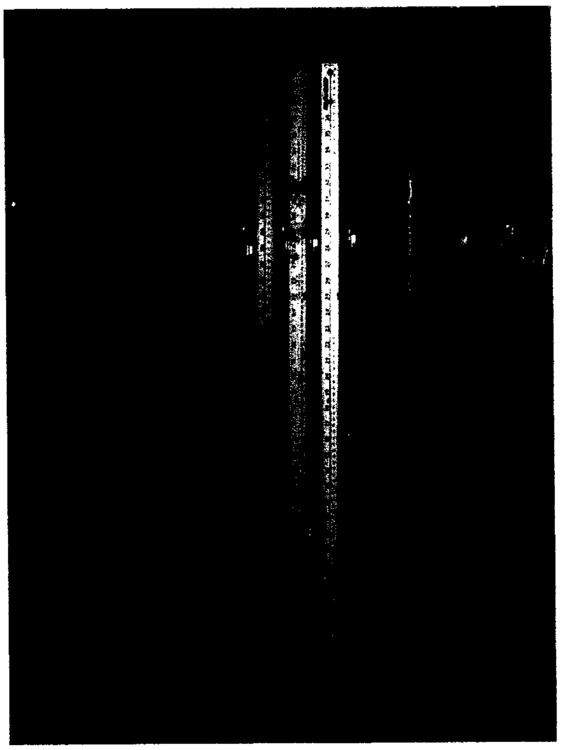

Figure 4-14 Free-surface slopes reading device

4.1.9 Simulated ice-covers

Figure 4-15 shows the simulated ice-cover panels installed on the flume. They are formed from thick plywood panels (waterproof painted) divided into 14 pieces of 2.44m long x 0.44m wide x 0.019m thick that cover the side sections of the channel and 7 pieces of 2.44m long x 0.61m wide x 0.019m thick that cover the center portion of the channel. The entire ice-cover set-up spans over 17.1m of the flume starting from the upstream false bed to the end of the sand bed basin section. The underside of these plywood panels were completely covered with 0.0254cm thick Styrofoam sheets. Thus, this study is dealing with simulating smooth ice-cover condition. In order to see the scouring and the sediment transport behaviour when these panels were in place, the centre panels, those which are located on the sand bed basin section, were fitted with large Plexiglas sheets, each 1.62m long x 0.48m wide x 0.0064m thick.

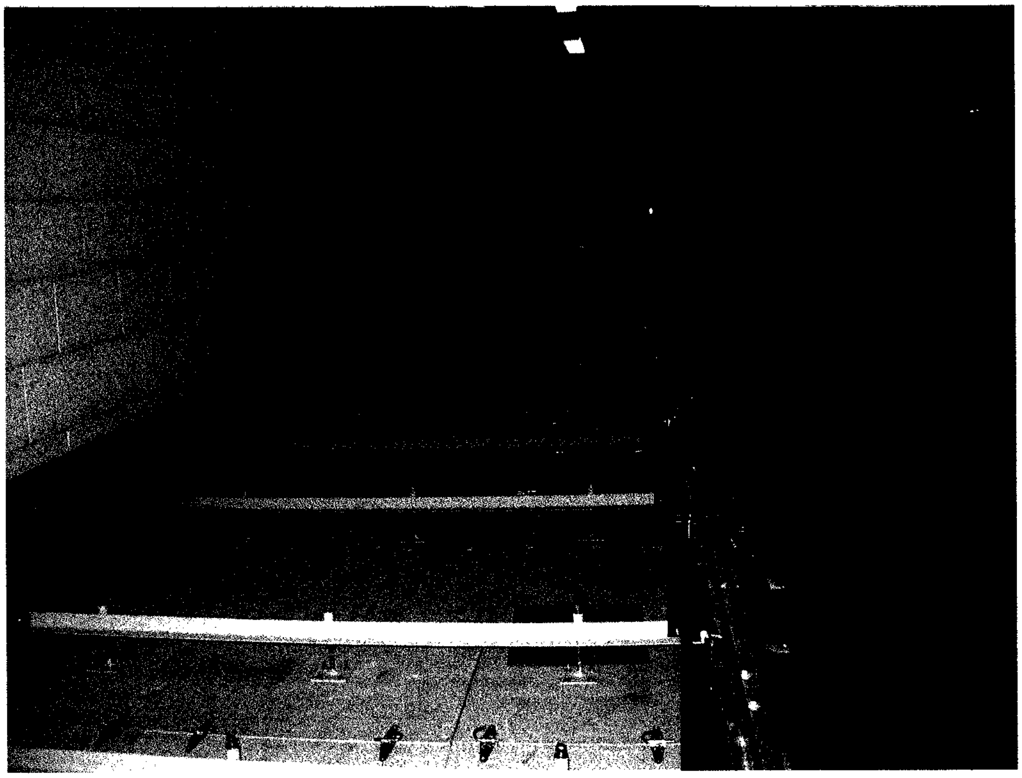

Figure 4-15 Flume covered with simulated ice cover panels

One of these panels also provides the necessary hole in order to place the bridge pier in the sand bed as well as to allow the ice-cover to float easily around the pier structure without letting water escape through the top of the panels.

The Styrofoam-plywood panels were allowed to float freely via specially designed hangers connected to the plywood, the former supported by steel frames. These frames were fixed to the steel covers of the flume sidewalls such that the panels could not move longitudinally, but can float vertically without any impediment. The transversal and longitudinal gaps between the panels were also eliminated using normal hinges and lockers in order to have a uniform, uninterrupted ice-cover configuration.

Since one of the main objectives of this study is to take velocity measurements, 3.8cm diameter holes where made along the width of each plywood panel at the same cross-sections and locations with regards to the measurements points previously defined (1 to 9). Because the diameter of the holes is of the same magnitude as the thickness of the simulated cover, alteration of the actual ice-cover roughness was suspected. Therefore, special corks were designed such that all the holes in the simulated ice were perfectly covered but one where velocity measurements were taken. In order to further minimize the effect of the holes during the velocity readings, a special cork, conceived with a hole barely greater than the probe sensor diameter was used.

Figure 4-16 and Figure 4-17 give the detailed description of these simulated panels.

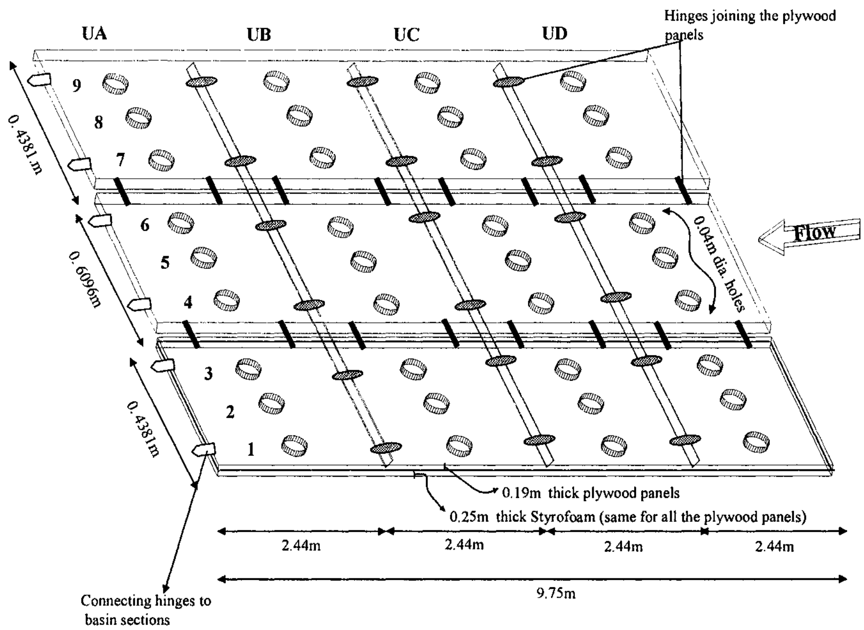

Figure 4-16 Design pattern for the upstream panels of the simulated ice-cover

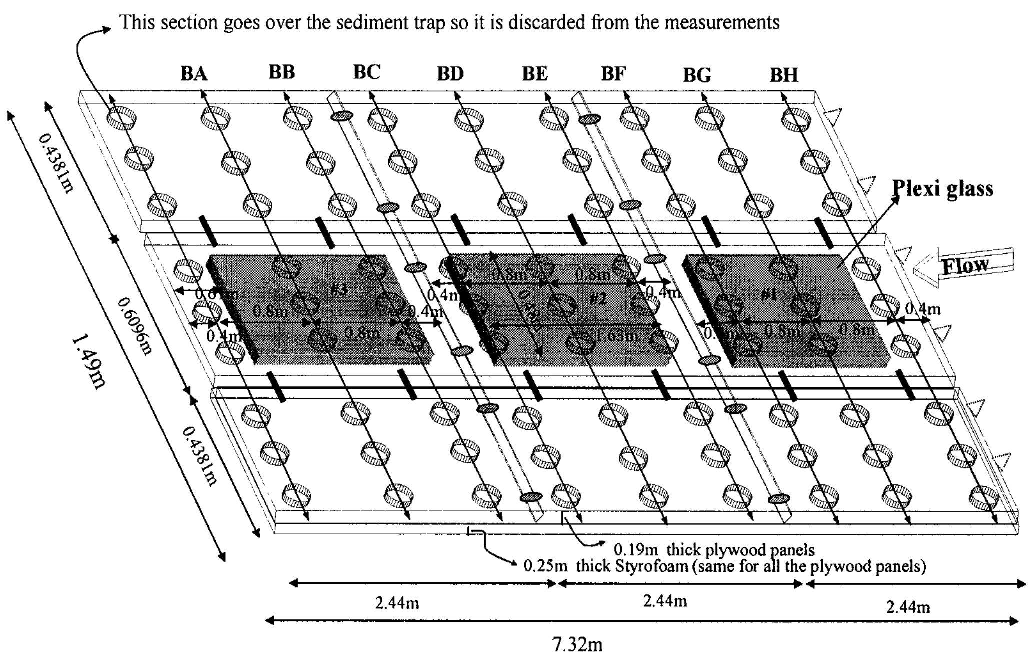

Figure 4-17 Design pattern for the sand basin panels of the simulated ice-cover

4.1.10 Ice-cover shear stress measurements device

It is important to plot the vertical and transverse velocity profiles obtained from the measurement data in order to verify different theoretical profiles (logarithmic law, power law, two-layer hypothesis, etc.), and to determine the hydraulic behavior with respect to the flow regime (deep vs. shallow water, smooth vs. turbulent flow). Measuring free-surface slopes is also important because it allows for the computation of an average value of the shear stress, which is key in any sediment transport analysis. In ice-covered flow, the average shear stress computed using energy slope readings is a rough estimation. Thus, actually measuring the bed shear stress or the ice-cover shear stress is crucial to accurately describe the sedimentation processes.

In practice, measuring the energy loss of the flow due to the friction with its boundaries is easier at the ice-cover surface than at the bed surface. The shear stress measurement device used in this study utilizes the bending moment theory. During the experiments, the upstream ice-cover is allowed to freely float vertically, while the simulated ice which covers the sand basin section is attached to the upstream ice-cover by a tie-down system.

At this junction, a series of calibrated steel coupons are placed such that when shear stress measurements are taken, they replace the previously mentioned tie-down (interconnection) system (Figure 4-18).

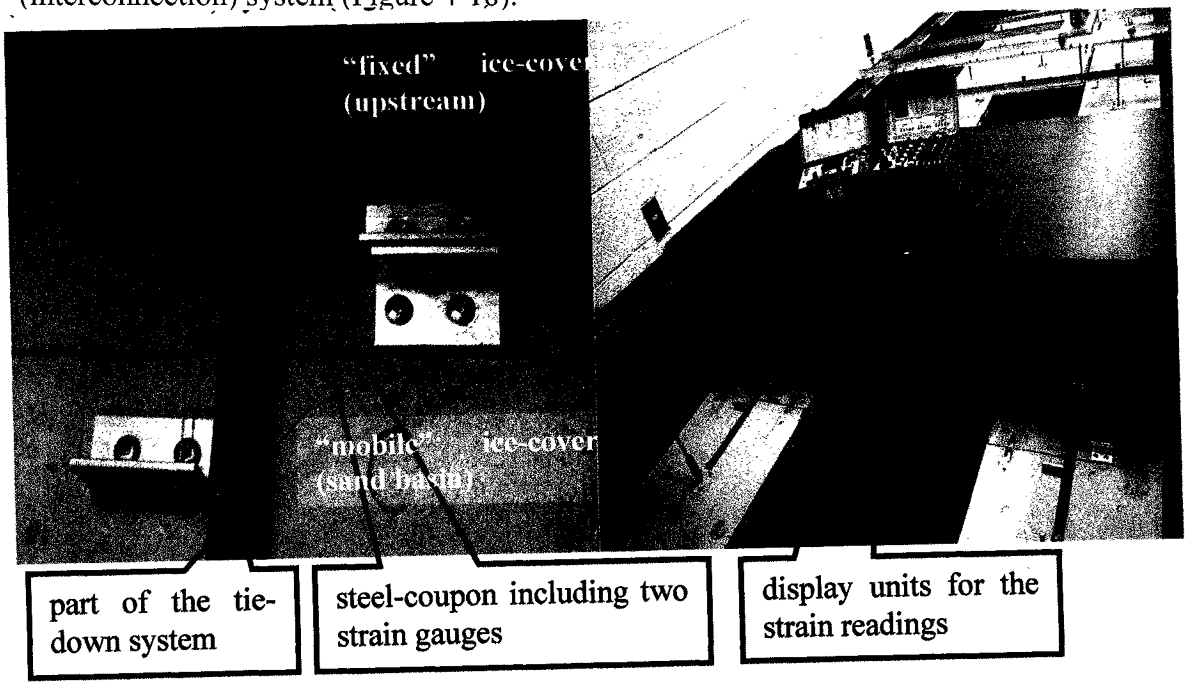

Figure 4-18 Ice-cover shear stress measurements device

Each coupon (Figure 4-19) contains two strain gauges, one on each side. The drag force of the flow underneath the ice-cover will bend the coupon, and with the help of two display units, the strain values are recorded. Knowing the geometrical dimensions of the coupons and the strain readings, the drag force of the flow can be computed. The shear stress on the ice-cover is obtained by dividing the drag force by the surface of the simulated ice-cover. Appendix A2 presents the calibration curves of the strain gauges placed on both faces of the coupon

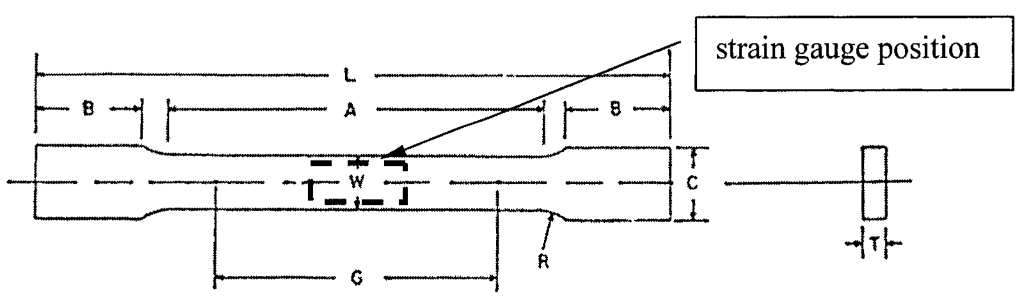

Figure 4-19 Steel coupon used for the ice-cover shear stress computation

4.2 Experimental procedure

As previously mentioned, the objective of this study is to determine for a clear-water regime as close as possible to the sediment critical condition (incipient motion), the scouring around a bridge pier under ice-cover, shallow-water and controlled flow depth conditions.

In order to make the reading easier, it worth defining now all the flume configurations that were tested during this study: (i) the free-surface flow (FS) represents the open-channel flow, (ii) the total ice-cover flow (TIC) represents the flow in a channel completely covered with simulated ice, (iii) flow with two partial ice-covers (2PIC) represents the flow in a channel opened longitudinally in the centre and covered with simulated ice on its sides, and (iv) flow with one partial ice-cover (1PIC) indicates the flow in a channel covered with ice only on one side. The experiments were divided into two parts: (i) experiments without the bridge pier in place, and (ii) experiments with the bridge pier in place. The purpose of the first part of the experiments is to determine the sediment incipient conditions for each flume configuration and through comparison to indicate the worse ice-cover case. The second part of the experiments (with a bridge pier) analyzes the scouring processes only for the extreme ice-cover configuration previously found, with respect to the free-surface configuration.

Before starting any experiment series, a one time topographical investigation of the upstream false bed and the sand bed basin section was carried out using a dummy level, the rack and pinion device, and the laser-meter device. This preliminary test was performed in order to determine the errors introduced by the trolley system, such that accurate free-surface and sand bed elevations readings could have been obtained. The free-surface slopes can be computed and verified with the readings obtained from the free-surface reading device.

Every test in this study started with a topographical survey of the upstream false bed and the sand basin section after the sand was levelled. Using the rack and pinion device with the movable scale, readings of the sand elevation were taken for every measurement point (1 to 9), on all of the aforementioned cross-sections.

From the downstream end of the channel, the second pump and the pipe network with the filling/drainage box were used to fill the entire channel. Once the water level reached the tip of the flume downstream vane, the pump was shut off and several readings were taken: (i) the level of the mercury column in the U type manometer (the first discharge device), (ii) the level in the glass tube of the second discharge device, and (iii) the level in the four glass tubes of the free-surface slope device as to determine the so-called 'zero readings'.

The first pump is then used to establish the desired flow in the channel. After a 30 minute period that allows the flow to stabilize, the readings of the manometer, the glass tube, and the slope device are again taken. The readings of the free-surface elevation are taken in all 9 measurement points for each working cross-section. Due to time constraints, the area of study was restricted to all the cross-sections of the sand basin section and cross-section UA from the upstream false bed.

The Electromagnetic sensor is installed on the second rack and pinion device and the display unit of the EM velocity device is installed on the mobile cart near the flume. The sensor probe is connected to the display unit which is itself connected to a lab PC on the same mobile cart. Once the EM probe is positioned in the designated point, the velocity measurements are taken. The time for the readings is set at 50sec, thus the probe takes 100 readings, which is automatically averaged via the PC. For each of the 9 points in each cross-section, velocity readings are taken at 5 vertical points: 0.15, 0.20, 0.50, 0.80, and 0.85 of the flow depth relative to the elevation of the levelled sand bed. After all the velocity measurements are recorded, readings of the U manometer, the glass tube, and the free-surface slope device are once more taken, and then the discharge is shut down. The ball-valves of the pipe network are turned on to begin the drainage procedure.

Different flow discharge and different heights of the adjustable vane were tested such that a shallow-water condition and incipient motion condition were coincident. Another important criteria in achieving sediment critical situation is the mechanical limitation of the hangers used to support the simulated ice-cover panels and the physical limitation of the EM sensor probe when approaching the boundaries of the flow. The hangers connecting the plywood panels to the metal frames have vertical limits such that the flow depth can create a confined flow (conduit flow) if it is too high, or the panels can be taken away by the water if is too low; on the other hand, if the flow depth is too small, the EM velocity device becomes useless as it would be too close to the boundary to take accurate velocity readings. Taking into account all these factors, the final settings for both sets of experiments are the following: the height of the movable weir was set at 0.311m from the bottom of the flume, the discharge valve opening was set at 15mm corresponding to a range of 0.042-0.045m^3/s, and the flow depth ranged between 0.13 and 0.14m.

The scouring procedure refers to the measurements taken during the run of the flow and after the flow was shut off. During the tests, readings of the scour depths around the bridge pier, as mentioned in subsection 4.1.2, were taken on the measurements scales glued inside the Plexiglas pier using a circular mirror. The geometry of the scouring process for every test performed with a bridge pier in place was recovered after the pump was shut off and water drained out from the flume. Using the laser Disto meter, readings of the bed elevation were recorded starting from 0.25m upstream the bridge pier to 3.80m downstream of it. In the area enclosing 0.25m upstream and downstream the pier edges, measurements were taken every 0.025m longitudinally and laterally. For the rest of the downstream surface, readings were taken in the same manner but every 0.05m. These measurement steps were enlarged where bed surfaces visually presented insignificant deformation from initial elevations.

Chapter Five

Results, Analysis and Discussion

5.1 Characteristics of the tests

As mentioned before (Chapter Three), the clear-water regime constitutes the worst case from a scouring point of view most of the time. Moreover, tests performed under this regime are much easier to achieve experimentally. All the tests of this study are thus under such a sediment regime. In addition, for reasons already mentioned in the Chapter Two, it was chosen to achieve the tests under controlled flow depth and varying energy slope. Indeed, the occurrence of these conditions is considered to be probable in the vicinity of bridge piers and to constitute the worst-case scenario for scouring.

Tests were also conducted under conditions as close as possible to incipient motion for the bed particles. In order to define the range of tests to be performed, an analysis was conducted with respect to flow regime, sediment motion, and bed-form occurrence. The upper limit of the flow regime corresponds to the incipient motion of the bed particles, also translated in terms of critical values of the bed shear stress, bed shear velocity, or flow velocity. The critical condition or the incipient motion is considered to be halfway between the motion of the first bed grain and the generalized movement of the bed particles (Yalin, 1977, p. 103). The lower limit of the flow regime is obtained when the shear velocity is at 80% of the critical shear velocity. Since the characteristics of the bed particles play a key role in defining sediment incipient motion, research was conducted to determine the critical values of sediment transport with respect to grain size features. Van Rijn (1984) approximates Shields' diagram by representing the critical "dimensionless shear stress" $\theta_{cr} = u_{cr*}{}^2 /[g(s-1)D]$ (Figure 5-1), with respect to the dimensionless particle diameter $D_* = \left(g(s-1)/\nu^2\right)^{1/3} D$, where D is considered to be the mean diameter d_{50}. As previously mentioned in subsection 4.1.3, the bed material used in the tests is a relatively uniform medium sand of d_{50}=0.65mm and σ_g=1.465 (see Appendix A1). Computing D_*=16.44, the Shields' parameter becomes θ_{cr}= 0.03, the bed critical shear velocity u_{*bcr}=0.018m/s, and the bed critical shear stress ($\tau_{bcr} = \rho u_{*bcr}^2$), τ_{bcr}=0.32N/m^2, corresponding to a transitional regime according to (Figure 5-1)

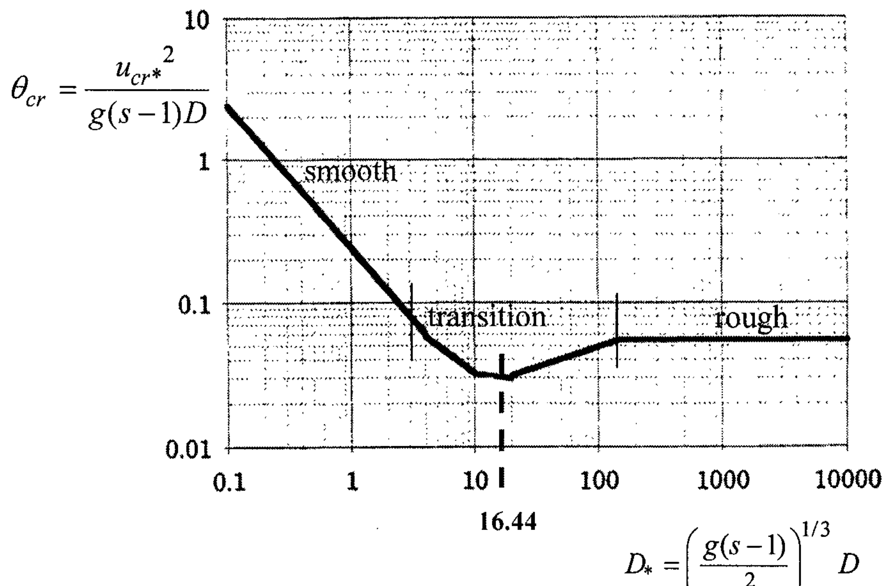

Figure 5-1 Approximation of Shields' diagram. After van Rijn (1984).

Special attention should also be directed to the possibility of having bed-forms development since it can impact on the shear stress applied on the grains. According to Bonnefille (1968, Figure 5-2) and computing the critical grain size Reynolds number ($Re_{cr*} = u_*D/\nu = 11.55$), the incipient motion condition in our tests results to lay in the region of 'flat bed'. However, as the shear velocity increases, (e.g. next to the bridge pier, see subsection 3.2.1.), the sediment motion regime is moving horizontally towards the lower dune regime (or ripples on dunes), we should impact on the shear stress applied on the grains. More discussion about this point is provided in subsection 5.3.2.

Once these sediment characteristics are computed, the following experimental strategy was adopted:

(i) since scouring is studied under ice-covered flow conditions, it is necessary to determine the incipient motion flow condition for each of the (a) total ice-covered flow (TIC), (b) two sides partial ice-covered flow (2PIC), or (c) one side partial ice-covered flow (1PIC). The tests for this step are performed without bridge pier and the results are presented in subsection 5.2.1.

(ii) for the case(s) that show(s) in (i) the lowest incipient flow conditions (the lowest discharge to achieve incipient motion) we determine the lowest possible setting of the downstream vane for which we can still achieve incipient motion, also taking into account the mechanical limitations of the EM velocity device and the simulated ice-cover system (subsections 4.1.5 and 4.1.9). This is achieved in order to obtain the highest B/h ratio possible (wide channel hypothesis). Again, this is performed without bridge pier and the results are presented in subsection 5.2.4.

(iii) determine scouring around the bridge pier for the free-surface flow and the worst ice-covered flow(s), both for the downstream vane setting determined in (ii). The results of this step are presented in subsection 5.3.

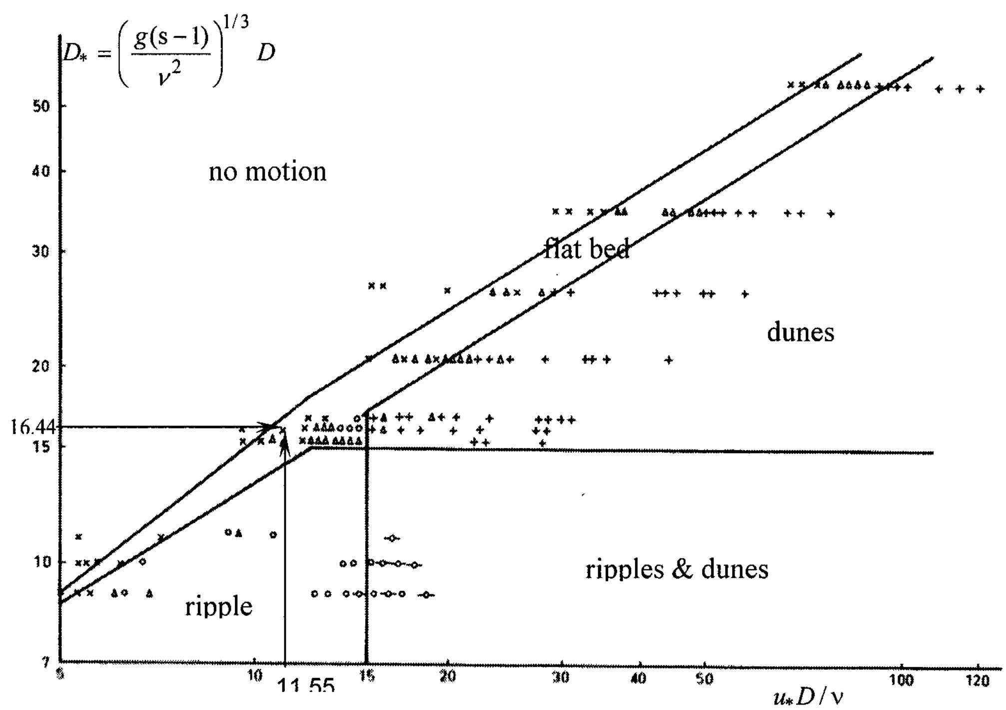

Figure 5-2 Bed-forms occurrence diagram. Bonnefille (1968)

For every experiment, velocity measurements were taken such that both vertical and lateral velocity profiles could be obtained. This allows for analyzing the flow distribution and for calibrating a numerical model called *Viscous-slip approach*, developed by Frenette and Molleti (2002) that is presented in section *Numerical Modeling*.

5.2 Tests without bridge pier

5.2.1 Sediment incipient motion under ice-covered flow conditions.

The first experiment was conducted for three ice-covered flow configurations namely TIC (total ice-cover), 2PIC (two sides partial ice-cover), 1PIC (one side partial ice-cover) and for one free-surface flow configuration, FS. The position of the downstream vane was set at 352mm from the bottom of the channel, and the discharge was slowly increased until bed particles began to move. On average, sediment movement started with a discharge of approximately 0.078m^3/s and a flow depth of about 0.209m for all tests. Velocity measurements were taken at four cross-sections in the sand basin portion of the flume: sections BH, BF, BD and BB (Figure 4-1). Table 5-1 presents some of the measured and computed parameters.

Table 5-1 Exp #1: Beginning of sediment motion in TIC, 2PIC, 1PIC and FS cases.

Configuration		TIC	2PIC	1PIC	FS
Q [m^3/s]	discharge (measured)	0.0776	0.0766	0.0776	0.0801
h [m]	flow depth (measured)	0.2090	0.2097	0.2095	0.2096
S [10^{-4}]	energy slope (measured)	3.04	2.56	1.92	1.12
P_w [m]	wetted perimeter	**3.398**	**2.786**	**2.347**	**1.909**
A [m^2]	cross-section area	0.3114	0.3124	0.3122	0.3132
R_h [m]	hydraulic radius	0.0916	0.112	0.134	0.1636
τ_T [N/m^2]	avg. boundaries shear stress	**0.2733**	**0.2817**	**0.2505**	**0.1797**
F_T [N]	avg. boundaries drag-force	6.789	5.744	4.304	2.512
u_{*T} [m/s]	avg. boundaries shear velocity	0.0165	0.0168	0.0158	0.0134

Average values of total shear stress τ_T as well as shear velocity u_{*T} and total drag force F_T were computed using the following formulas:

$$\tau_T = \gamma R_h S, u_{*T} = \sqrt{\tau_T / \rho}, F_T = \tau_T A_{domain} \tag{5-1}$$

Subscript T (total) in these computations refers to the average value of the variable computed at all friction boundaries of the flow over the sand basin section length of 7.32m: i.e. total shear stress represents the average value of shear stress considering all the friction surfaces (the channel bed, the ice-cover and the channel sidewalls). Thus, in the 2PIC case the friction surface is given by A_{domain} = wetted perimeter (channel width + 2 x flow depth + 2 x ice-cover width) x section length (7.32m). Even if these parameters are considered as indicative values only, important observations can be deduced from their analysis.

Significant changes in energy slope are recorded between different ice-covered flow configurations: for TIC sae increased values from 18 to 58% are recorded compared to 2PIC and 1PIC, respectively and up to approximately 170% higher when ice-covered flow is compared to the free-surface flow. In contrast, flow depth changes are very small. The hydraulic radius R_h also varies with changes in the geometrical dimensions of the ice-cover, which implies changes in the wetted perimeter of the flow cross-section. One important result of these tests is the evolution of the total shear stress τ_T with increasing surface coverage (Table 5-1). From FS to 2PIC we see an increase of the value of τ_T, while for TIC the value has somewhat dropped. Without claiming that the 2PIC configuration provides the absolute maximum in terms of total shear stress or even of shear stress on the bed, one can say that there can be a partial ice-cover configuration that could produce a higher shear stress (even on the bed) than the total ice-cover configuration.

In what follows, two main aspects of the measured velocities are analyzed: their vertical and lateral profiles and the corresponding vertical and lateral distribution of the discharge. And since the cylindrical bridge pier is to be installed in the middle of the flume for the scouring experiments (in line with point 5), the present analysis will focus particularly on points 4, 5 and 6 of all three (FS, TIC, 2PIC) configurations.

Velocity measurements were taken at 10 (lower), 20, 50, 80 and 85 (higher)% of the flow depth. Appendix A3 presents all the velocity profiles of this experiment. For the TIC and 2PIC cases, Figure 5-3 and Figure 5-4 depict the lateral and vertical velocity profiles based on the readings taken at every measurement point (1 to 9) at cross-section BB of the sand basin section.

The TIC configuration presents a more uniform velocity distribution, both laterally (Figure 5-3) and vertically (Figure 5-4) compared to the 2PIC configuration in which case a more disturb velocity profile is observed. For the TIC case, the maximum measured velocities are recorded at 50% of the flow depth, and for points 2 to 8, they range from 32.5 to 34.2cm/s, while for points 1 and 9, due to the vicinity of the flume sidewalls, the velocities are clearly smaller, approximately 27.5cm/s.

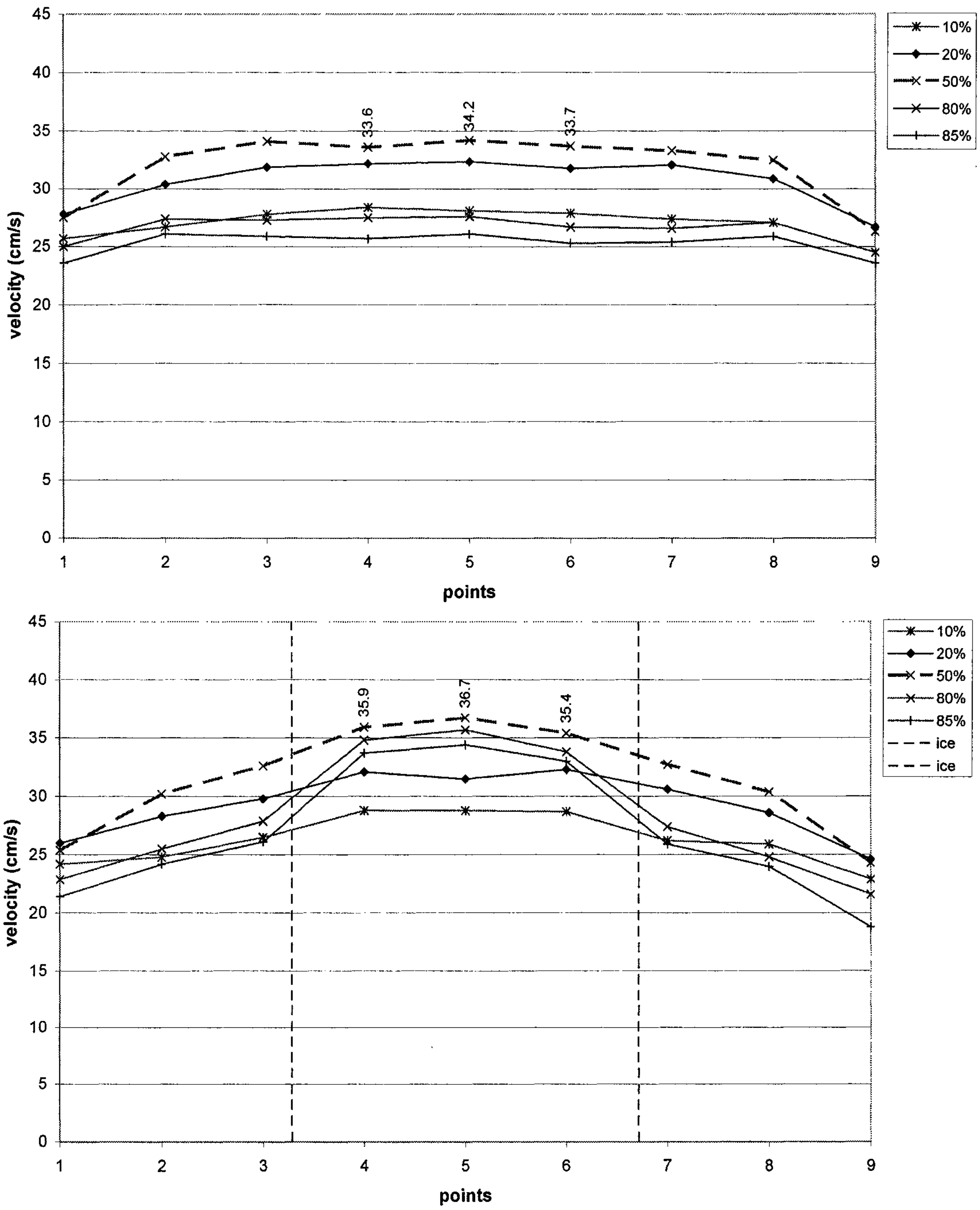

Figure 5-3 Exp#1/Lateral velocity profile at c/sBB (TIC-top and 2PIC-bottom)

By analyzing the velocities at the bed and the ice-cover boundaries the ice-cover appears to be slightly rougher then the bed channel. This observation can be explained by the additional roughness introduced by the lateral and longitudinal joints of the simulated ice-cover panels as well as the joints between the corks and the holes.

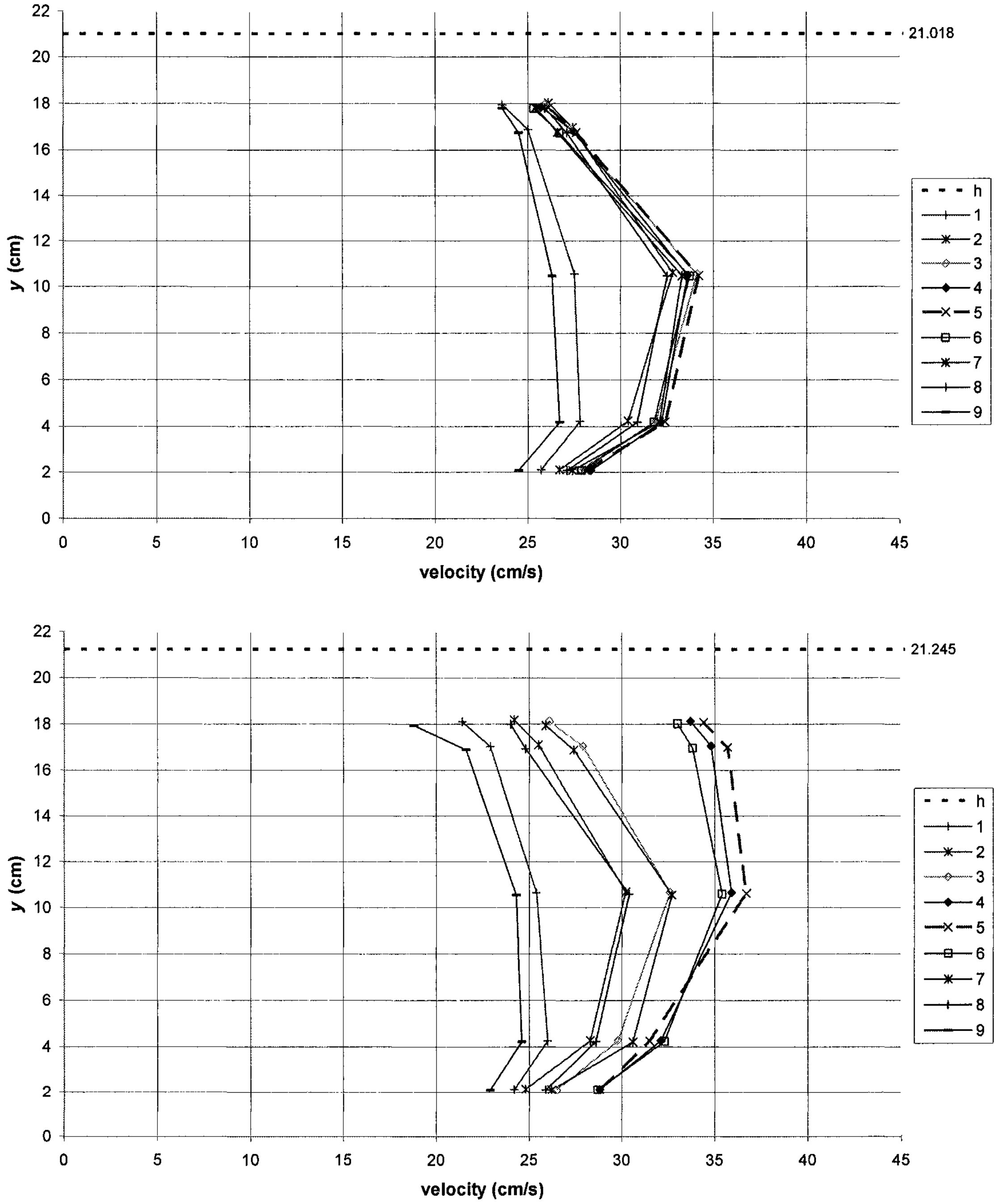

Figure 5-4 Exp#1/Vertical velocity profile at c/sBB (TIC-top and 2PIC-bottom)

Although the 2PIC configuration presents disturb velocity profiles, the symmetry between these profiles on each side of the centerline for both regions under the ice-cover (lateral pairs of points 1-9, 2-8 and 3-7) and in the open-water region (central points 4, 5 and 6) is kept. Velocity increases in magnitude from the ice-cover to the open-water zone and changes the profiles accordingly. In the open-water region, the profile is not yet fully developed due to the vicinity of the ice-covers. However, the maximum values are recorded at 50% of the flow depth, ranging from 35.4 to 36.7cm/s in the central region, and from 30.4 to 32.7cm/s in the ice-cover region. Velocity readings close to the bed boundary show small variation between 2PIC and TIC cases in the central region of the flow. In contrast, the sector between 20 and 50% of the flow depth at point 4, 5 and 6 (central region) exhibits higher values of velocities (up to 7%) for the 2PIC.

From a scouring point of view, the 2PIC configuration presents a stronger potential compared to the TIC configuration for severe scouring because of the concentration of flow (kinetic energy) that occurs in the central region, leading to stronger accelerations around any obstacle. Moreover, the downflow generated in the case of a bridge pier will increase with the kinetic energy of the incoming flow, again leading to more intense scouring.

When compared to the FS configuration, velocity profiles in the central region of both ice-covered configurations show higher values in the lower part of the flow depth ($y < 1/2h$), between 6 and 15% higher in the 2PIC case and between 6 and 12% higher in the TIC case. Thus, in the presence of an ice-cover (TIC or 2PIC), greater discharge is directed toward the lower part of the flow, thus leading to a more powerful scouring process.

For 1PIC (one side partial ice-cover) configuration, the ice-cover was located above points 7, 8 and 9. In this case, the flow is redirected toward the open-water region of the channel, which covers more than 2/3 of the channel width. Nevertheless, the highest velocities are recorded only at points 4 and 3 when compared to the FS case. Since the bridge pier was planned to be positioned along the flume centerline (point 5), this configuration was quickly abandoned as non-determining from a scouring point of view. Nevertheless, there is a need for more study of this case in order to determine the critical situation from the scouring point of view, which is suspected to strongly depend on the ice-cover dimensions with respect to the bridge pier location.

Overall, the findings of this velocity profile analysis show the 2PIC test to have the most severe potential for scouring around a bridge pier. Nonetheless, for the sake of a comparison and considering the small discrepancies between the 2PIC and TIC cases, both configurations were retained for the remaining of the tests.

5.2.2 Sediment incipient motion under ice-covered shallow water flow conditions.

Considering the results found in the previous subsection, it can be easily anticipated that shallower flow conditions will enhance the difference (velocities and discharge distributions) between both ice-cover (TIC and 2PIC) and free-surface (FS) configurations. The minimal flow depth achievable with our experimental installation is determined by the EM velocity meter limits (subsection 4.1.5) and was selected as h = 0.13m. A rough estimation of the necessary discharge to produce the same critical conditions can be computed with the help of Manning's formula and the expression of τ in rectangular cross-section (for FS case):

$$Q = \frac{1}{n} \mathrm{AR}_h^{2/3} \mathrm{S}^{1/2}, \tau = \gamma R_h \mathrm{S} \tag{5-2}$$

where $R_h \approx h$ in shallow-water condition. We thus find the following relationship between the previous flow depth h_1 and discharge Q_1 and the new ones:

$$\frac{Q_1}{Q_{new}} = \left(\frac{h_1}{h_{\mathrm{new}}} \right)^{7/6} \tag{5-3}$$

where h_{new} is the new required value of the flow depth and Q_{new} is the corresponding discharge to be computed in order to achieve incipient motion. Considering the sediment incipient motion case, from Exp#1 with h_1 = 0.209m, Q_1 = 0.078m^3/s, the new discharge is $Q_{\mathrm{new}} \approx$ 0.0448m^3/s. To reach this new set-up, the discharge was set at the new value and the vane at the downstream end of the flume was moved until the required flow depth and incipient motion were attained.. As previously mentioned in the *Experimental procedure* (subsection 4.2.) of Chapter Four, the final configuration of the flume was as follows: the height of the movable vane was reduced from 352mm to 311mm, measured from the bottom of the flume, the discharge valve opening was changed from 24mm to 15mm corresponding to a range of 0.042-0.045m^3/s, and the flow depth decreased from 0.209m to a range between 0.13 and 0.14m.

In order to get to the target flow depth h = 0.13m, intermediate experiments were performed. Exp#2, with TIC and 2PIC, was conducted for two flow conditions: flow discharge of 0.055m^3/s and 0.043m^3/s, and flow depths of 0.187m and 0.175m respectively. Velocity measurements were taken only in two cross-sections of the sand basin, sections BD and BH. Exp#3, which involved all 8 cross-sections of the sand basin, was carried out in the final configuration of the flume, with a discharge of approximately 0.044m^3/s and an average flow depth of 0.136m. This test was performed for two configurations: TIC and 2PIC. The results of these two additional experiments are in agreement with previous predictions, showing in the open-water region of the flow increasing differences in velocities between the 2PIC and the TIC cases.

Exp#4 was a rerun of Exp#3 with the addition of the free-surface configuration. The discharge was approximately 0.043m^3/s, and the average flow depth about 0.133m. Since this experiment is the most complete under the hydraulic conditions to be used for the bridge pier tests, it is presented here in more detail. In addition to velocity measurements taken in 9 cross-sections of the flume (all 8 cross-sections of the sand basin and cross-section UA in the upstream false bed), the action of the drag force of the flow on the ice-cover was also measured with the help of a force-measuring device (see subsection 4.1.10). Numerical simulations were also performed against these measurements, using the *Viscous-slip* model (Appendix A6), such that simulated velocity profiles are compared to those resulted from the experimental data and the average shear stress at the bed and the ice-cover level are computed. More details about the *Viscous-slip* approach are provided in subsection *Numerical simulation.*

5.2.3 Sediment incipient motion for free-surface flow conditions.

We also present the results of Exp#5, which was carried out with a free-surface configuration, but under free-surface incipient motion condition (as opposed to the ice-cover incipient condition used in all the other tests). This experiment was conceived in order to compare incipient conditions of 2PIC and FS configurations. The same hydraulic conditions are also used for a corresponding free-surface experiment with the bridge pier., to be presented in subsection 5.3. (*Tests with bridge pier*)

The critical conditions corresponding to the FS configuration were reached by slowly increasing the discharge until sediment motion was observed, keeping the downstream vane at the same elevation. The corresponding critical discharge is $0.06055 m^3/s$, the measured flow depth is 0.152m, and the measured energy slope is $1.923\ 10^{-4}$. Table 5-2 shows the main experimental measured and computed parameters of the four tested configurations: TIC, 2PIC and FS at ice-cover critical conditions (Exp#4), and FS at free-surface critical conditions (Exp#5). The vertical and lateral velocity profiles corresponding to these experiments are all presented in the Appendix A4 and Appendix A5.

Table 5-2 Incipient motion in shallow-water conditions for TIC, 2PIC and FS configurations[5] (Exp#4 and Exp#5)

Configuration	TIC/ Exp#4	2PIC/ Exp#4	FS/ Exp#4	FS/ Exp#5	2PIC/TIC (Exp#4)	2PIC/FS (Exp#4)	TIC/FS (Exp#4)	2PIC/FS (Exp#4/ Exp#5)	TIC/FS (Exp#4/ Exp#5)
Q [m^3/s] (measured)	0.0431	0.0429	0.0431	0.0606	0.994	0.994	1.000	0.709	0.713
h [m] (measured)	0.1332	0.1326	0.1332	0.1521	0.995	0.995	1	0.872	0.876
S [10^{-4}] (measured)	3.69	2.72	0.962	1.923	0.737	2.827	3.835	1.415	1.919
A [m^2]	0.198	0.197	0.198	0.227	0.995	0.995	1	0.872	0.876
P_w [m]	3.246	2.631	1.756	1.794	0.810	1.498	1.848	1.467	1.809
R_h [m]	0.061	0.075	0.113	0.126	1.228	0.664	0.541	0.594	0.484
τ_T [N/m^2]	0.221	0.200	0.106	0.238	0.905	1.878	2.075	0.841	0.928
F_T [N]	5.258	3.859	1.371	3.1299	0.734	2.814	3.835	1.233	1.680
u_{*T} [m/s]	0.0148	0.0141	0.0103	0.0154	0.951	1.370	1.440	0.917	0.964
F_i [N] (measured)	4.03	2.0386			0.506				
τ_i [N/m^2]	0.3694	0.3178			0.860				
u_{*i} [m/s]	0.019	0.0178			0.927				
u_{*T}/u_{*cr}	0.837	0.796	0.581	0.869				0.917	0.964
u_{*i}/u_{*cr}	1.082	1.004							

[5] subscript "i" stands for variable values measured or computed at the ice-cover boundary: i.e. F_i, τ_i and u_{*i}

5.2.4 Results and analysis

Measurements show that the TIC and the 2PIC cases present respectively an energy slope which is 3.84 and 2.83 times the energy slope of the FS case. Taking also into account the changes in the hydraulic radius introduced by the ice-covers, (τ_T) of the TIC and the 2PIC cases are respectively 2.08 and 1.89 times the total average shear stress of the FS configuration.

In the TIC case the measured drag-force of the flow on the ice-cover is approximately twice as much as in the 2PIC case, a fact that can be partially explained by the central additional cover, which represents an extra 67% in friction surface, and by the concentration of the flow in the central (open-water) region of the 2PIC case. The drag-force of the flow acting on the bed and the sidewalls of the channel F_b is estimated by subtracting the measured drag-force on the ice-cover F_i from the computed total drag-force F_T. The calculated value of F_b in the 2PIC case is 48% greater compared to the TIC case, meaning the average friction on the walls and bed is strongly increased by the redistribution of the flow. Moreover, when comparing the lateral velocity profiles of the TIC case under the ice-cover regions of the channel (lateral points 1, 2, 3 and 7, 8, 9), the readings show roughly 30% higher values compared to the 2PIC case. This implies less friction on the sidewalls and on the bed under the ice-cover (lateral) regions for the 2PIC configuration and thus a greater portion of that extra 48% in F_b is transferred mainly to the bed in the central region of the channel (points 4, 5 and 6) where the bridge pier is to be located.

As suggested from the first experiment (Exp#1), the lateral analysis of the velocity measurements shows a uniform distribution for the TIC and FS cases. In contrast, the 2PIC case presents a more disturb lateral velocity profile, although symmetrical with respect to the centerline. The explanation for this behaviour comes from the discharge redistribution: in the TIC case we suspected a vertical redistribution of the discharge compared to the FS case, while in the 2PIC configuration a more important lateral redistribution of the discharge, directed toward the central region of the channel is observed (Figure 5-5, Figure 5-6 and Figure 5-7). Therefore, considering the fact that the bridge pier is to be installed in this region, the analysis of the lateral velocity distribution and the ice-cover drag force indicates the central region of the channel as the focusing area for further analysis.

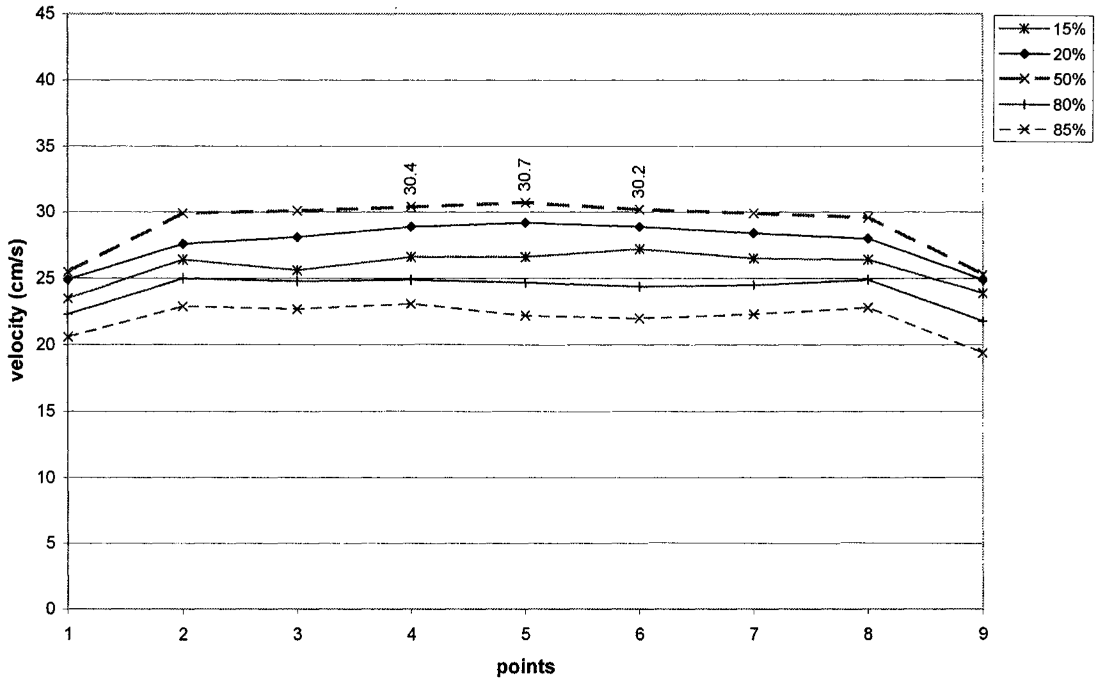

Figure 5-5 Exp#4/ Lateral velocity profile at c/s BB (TIC)

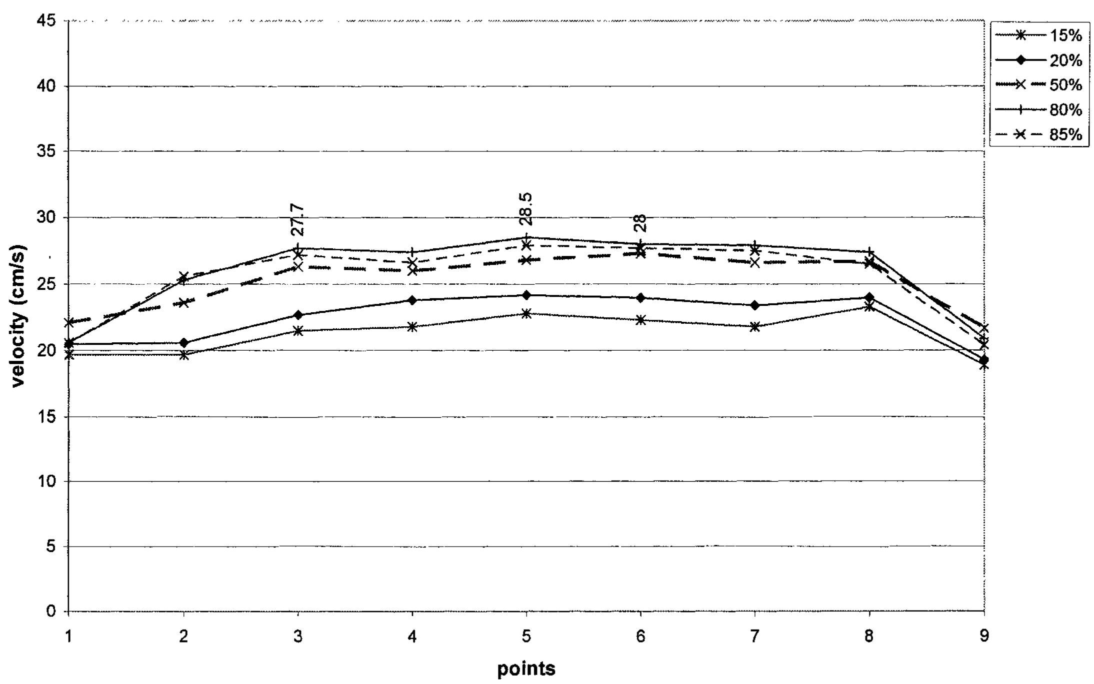

Figure 5-6 Exp#4/ Lateral velocity profile at c/s BB (FS)

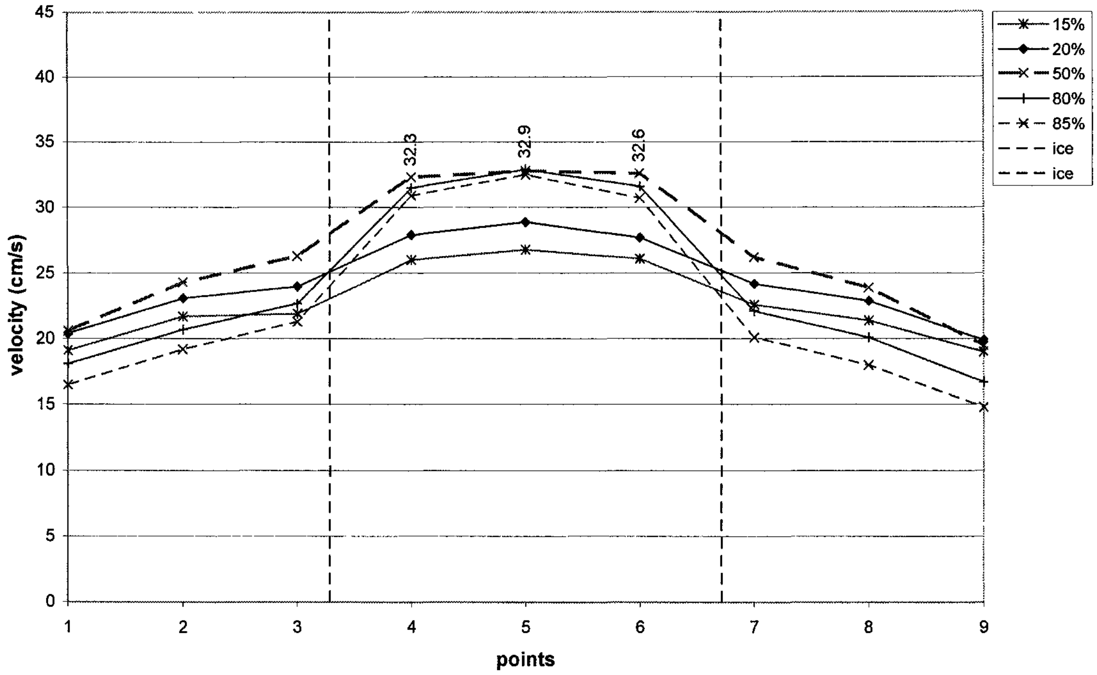

Figure 5-7 Exp#4/ Lateral velocity profile at c/s BB (2PIC)

In terms of vertical velocity distribution, analyzing the central region of the channel, Figure 5-8 depicts clearly the differences between the three studied configurations: TIC, 2PIC and FS of Exp#4.

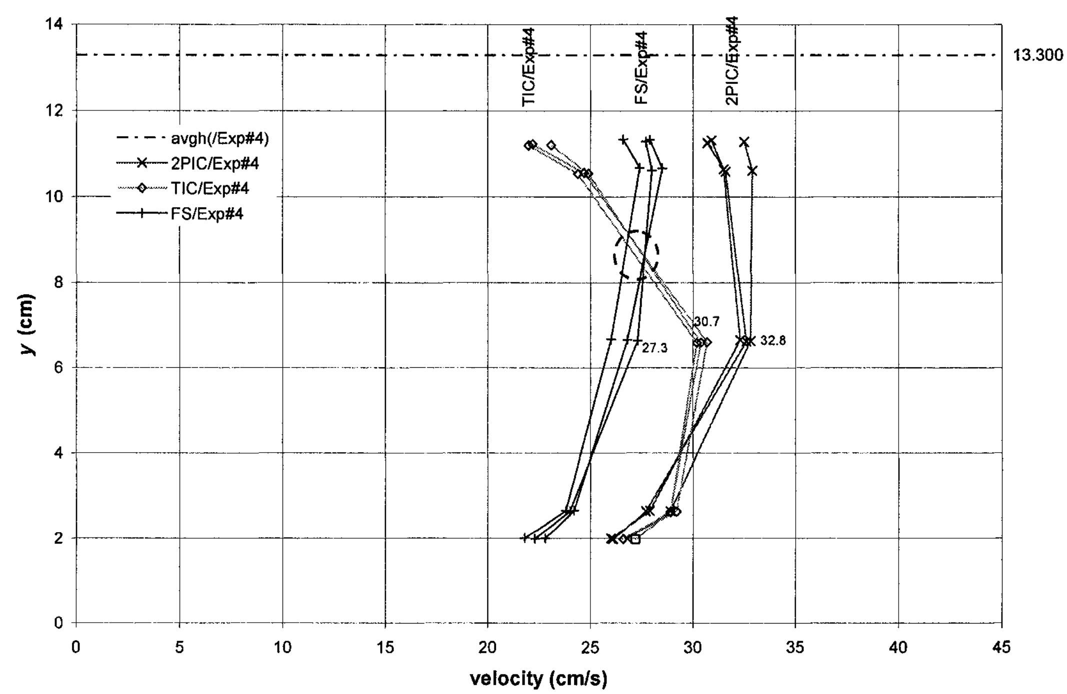

Figure 5-8 Exp#4/Vertical velocity profile at c/s BB, points 4, 5 & 6
(TIC, 2PIC & FS configurations)

For TIC, the maximum measured velocities are approximately 30.7cm/s at 50% of the flow depth. For 2PIC, at point 5, the maximum reading (32.8cm/s) is recorded at 80% of the flow depth while for the other points (4 and 6), the maximum measured values between 32.3 and 32.6cm/s are located at 50% of the depth. In the FS case, the maximum velocity is measured at 80% of the flow depth between 25.3 and 28.9cm/s.

Analyzing 2PIC vs TIC, in the lower part of the flow depth, the velocities record 6% to 8% higher values for the 2PIC case compared to the TIC case, while for the upper part of the flow ($y > 1/2h$) this difference exceeds 30% (Figure 5-8). Therefore, we suspect a higher scouring potential in the 2PIC case than in the TIC case due to a greater kinetic energy in the central region of the channel.

As for 2PIC vs FS, the 2PIC case definitely shows the highest scouring potential since in the lower and upper part of the flow the velocities are respectively 24% and 15% greater compared to the FS case (Figure 5-8).

Analyzing TIC vs. FS, the prediction of a more powerful scouring process favours the TIC case mainly because:

(i) from a vertical distribution of flow point of view, the TIC flow has higher velocities and thus higher kinetic energy than the FS case in the lower 65% of the flow depth ([illegible],Figure 5-8), resulting in a more intense downflow and horseshoe vortex for the scouring process around the bridge pier

(ii) in the free-surface case, the shallow-water conditions (shallow flow depths) takes the scouring phenomenon into the so-called "zone of flow depth influence" where bow wave creates auxiliary energy losses (subsection 3.2.2- *Effect of the flow regime and flow depth*). In a TIC condition, the bow wave influence is reduced due to damping of turbulence by the ice-cover properties (Figure 3-14), sometimes even leading (Zabilansky 2000, 2002) to an enhancement of the downflow due to the shape of the underside of the ice-cover (Figure 3-13).

In order to get similar critical conditions as the ice-covered flow, the discharge of the FS/Exp5 case had to be increased with approximately 40% compared to the discharge of the ice-covered cases, generating approximately 15% higher flow depth. Thus, due to their lower critical discharge and flow depth, the TIC and 2PIC configurations are considered more significant than the critical free-surface case. Figure 5-9 clearly shows for the FS case (Exp#5) approximately the same sediment velocity values and gradient next to the bed as in the 2PIC case, implying similar bed shear stress and incipient condition.

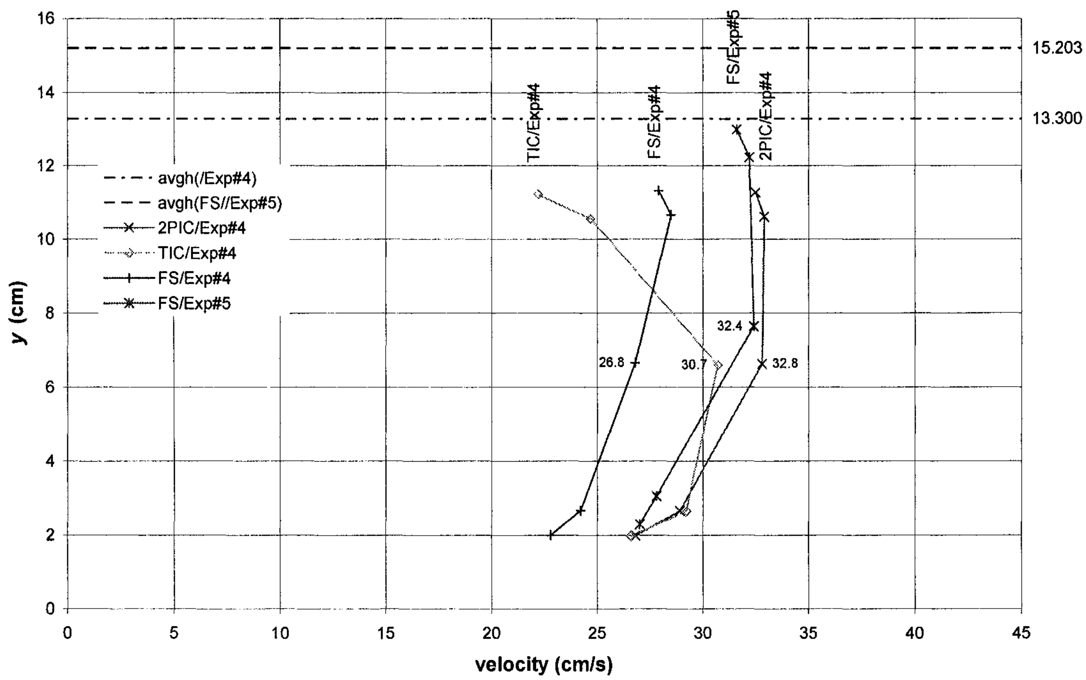

Figure 5-9 Vertical velocity profile: at c/s BB, point 5 *Exp#4* and *Exp#5*.

Numerical simulation

Considering a steady-state uniform flow of depth h, in a 2Dimensional case, the longitudinal x-momentum equation is given by:

$$\frac{\partial \tau_{xy}}{\partial y}+\frac{\partial \tau_{xz}}{\partial z}+\rho g S=0 \qquad (5\text{-}4)$$

where τ is the shear stress, ρ is the mass density, g the gravitational acceleration and S the energy slope of the flow. The coordinate system is such that x-axis is longitudinal, y-axis is vertical upward, z-axis is transversal and the origin is at the bed level.. The *Viscous-slip* approach (Frenette and Molleti, 2002) is used to define the rheology of the flow with help of a constant turbulent viscosity:

$$\tau_{xy}(y,z)=\mu_T\frac{\partial u_x(y,z)}{\partial y};\tau_{xz}(y,z)=\mu_T\frac{\partial u_x(y,z)}{\partial z} \tag{5-5}$$

where $u(y, z)$ is the cross-sectional velocity profile and μ_T is the turbulent dynamic viscosity. According to this approach, the velocities at the boundaries are not zero, but defined by a quadratic friction law such as:

$$\boldsymbol{\tau}\cdot\mathbf{n}=-\rho f u\,|u| \tag{5-6}$$

where **n** is the outward normal unity vector at the boundary, f is the boundary friction coefficient and u is the tangent velocity at $y_{\min}$ elevation from the bed channel. The viscous-slip approach defines the friction with the help of the logarithmic law-of-the-wall (ref. Eq. 2-14):

$$\frac{|u|}{u_*}=\frac{1}{\sqrt{f}}=\frac{1}{\kappa}\ln\left(\frac{(y^+)_{\min}}{k_s}\right)+B_N \tag{5-7}$$

where the shear velocity $u_*=\sqrt{|\tau|/\rho}$, the constant B_N =8.5 for turbulent rough flows, $(y^+)_{\min}=(y)_{\min}\,u_*/\nu$ represents the minimum distance from the boundary where the friction coefficient f is computed, k_s is the equivalent roughness of the boundary. In the literature, the value of $y_{\min}$ is not yet clearly defined, thus, as Frenette and Molleti (2002) proposed, a range between 0.01 and 0.04 of the flow depth is used in the numerical simulation.

In order to solve these equations, a finite-element interface called FEMLAB was used. This interface, which is a numerical layer on top of MATLAB, allows the user to analytically express the governing equations and to solve them with the choice of appropriate mesh and boundary conditions. Eq. (5-4) along with the rheological definitions in Eq. (5-5) and boundary conditions as expressed in Eqs. (5-6) and (5-7) have been implemented. The energy slope S and the solid boundary roughness k_s, (sand bed), k_i (ice-cover) and k_{sw} (channel sidewalls) are set as measured or estimated, and an automatic calibration routine enables the automatic calibration of μ_T to obtain the measured discharge Q.

Numerical simulations were performed for both TIC and 2PIC configurations of the Exp#4, at the reference cross-section BB. Appendix A6 contains all the vertical and lateral velocity and shear stress profiles of these simulations. The model also enables the calculation of shear stress on the boundaries, to be compared with the measured and computed values of laboratory experiments. Table 5-3 shows the calibrated parameters at the best match of the numerical simulation

Table 5-3 Calibrated parameters used in the numerical simulation of ice-covered flow .

Configuration		TIC	2PIC
k_s [m]	sand bed roughness	0.0007	0.00065
k_i [m]	ice-cover roughness	0.003	0.002
k_{sw} [m]	sidewalls roughness	0.00002	0.00002
ν_{Tice}	average turbulent viscosity (under ice-cover)	$6\ 10^{-5}$	$6.8\ 10^{-5}$
ν_{Tfs}	average turbulent viscosity (under open-water)		$2.04\ 10^{-4}$
y_{minice} [m]	(under ice-cover)	$3.86\ 10^{-3}$	$3.996\ 10^{-3}$
y_{minfs} [m]	(under open-water)		$2.398\ 10^{-3}$

Analyzing the vertical velocity distributions in both cases (Figure 5-10 and Figure 5-11), results show a very good correlation between the measured and the simulated values. However, in both simulations, a slight underestimation can be observed in the lower region of the flow close to the boundaries, but more evident at the bed level. This underestimation appears clearer in the 2PIC case, for the open-water region of the flow – points 4 and 5. Part of the explanation for this numerical behavior comes from the fact that the average turbulent viscosity ν_T is considered constant over the entire flow section, which probably is not the best approach, especially for the 2PIC case where open-water and ice-covered flow are combined. In this simulation case, two different values are used for ν_T, one for the regions under the ice-cover and another for the open-water region, and as the results show (Table 5-3), the ν_{Tfs} corresponding to the free-surface zone is 3 times bigger than the ν_{Tice} used for the ice-cover part of the flow. Explanation of this behavior comes from the fact that the ice-cover is a better turbulence damper than the free-surface. Moreover, the turbulence created by the inlet system of the flume is not yet completely dampen by the stabilizer system, such that remaining turbulence is still propagated further downstream.

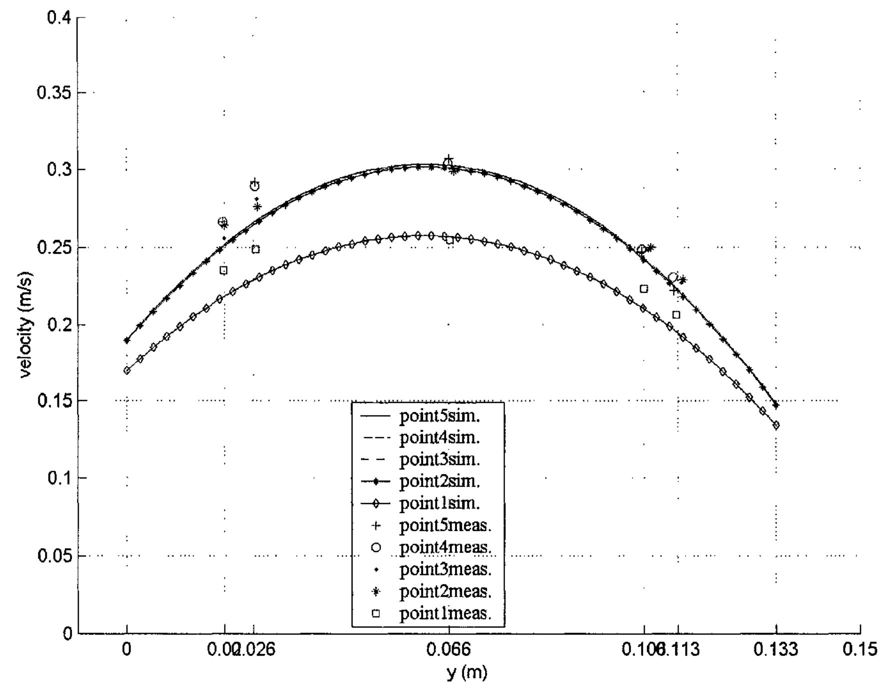

Figure 5-10 Exp#4/Vertical velocity profile at c/s BB, (measured vs simulated, TIC)

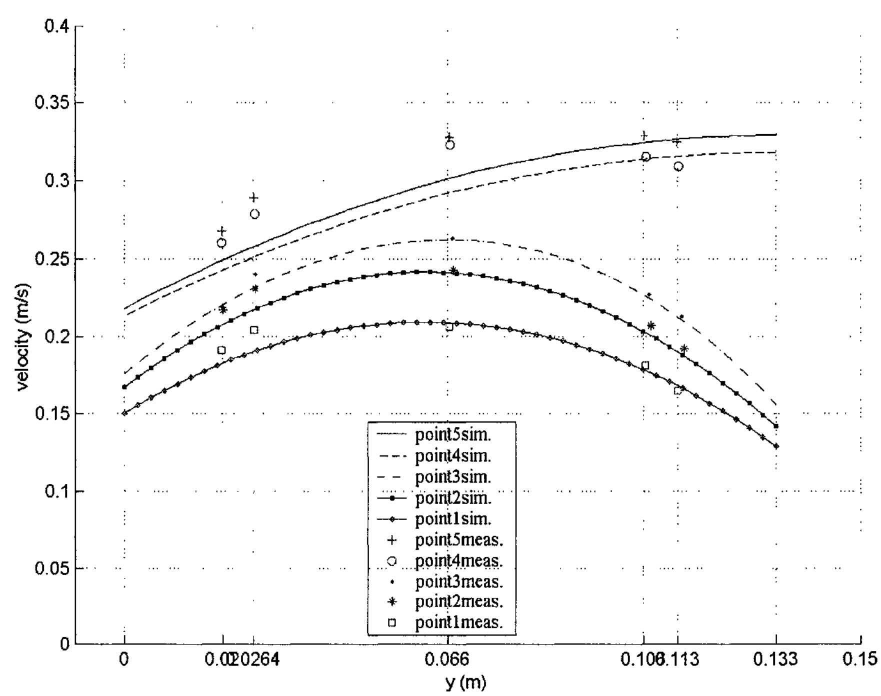

Figure 5-11 Exp#4/Vertical velocity profile at c/s BB, (measured vs simulated, 2PIC)

The same explanation is supported by the lateral velocity profiles presented in Figure 5-12 and Figure 5-13. Thus, additional work needs to be done regarding the variation function of the turbulent viscosity parameter.

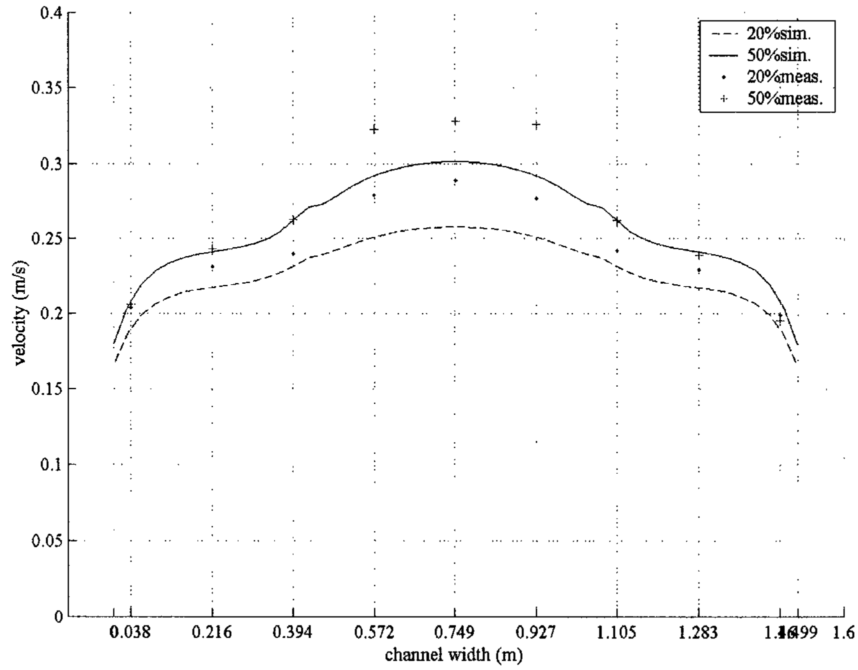

Figure 5-12 Exp#4/Lateral velocity profile at 20 and 50% of the flow depth (measured vs simulated data, c/s BB, 2PIC)

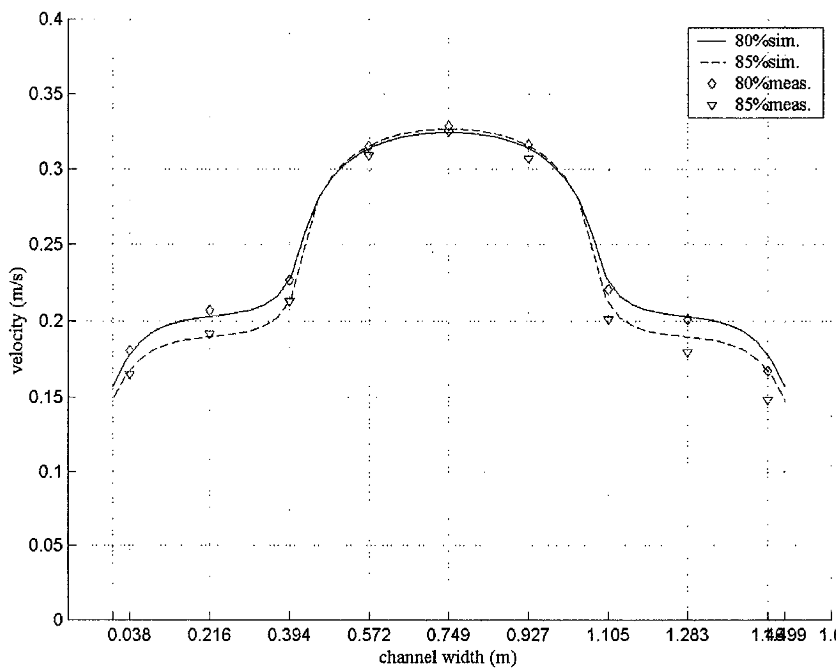

Figure 5-13 Exp#4/Lateral velocity profile at 80 and 85% of the flow depth (measured vs simulated data, c/s BB 2PIC)

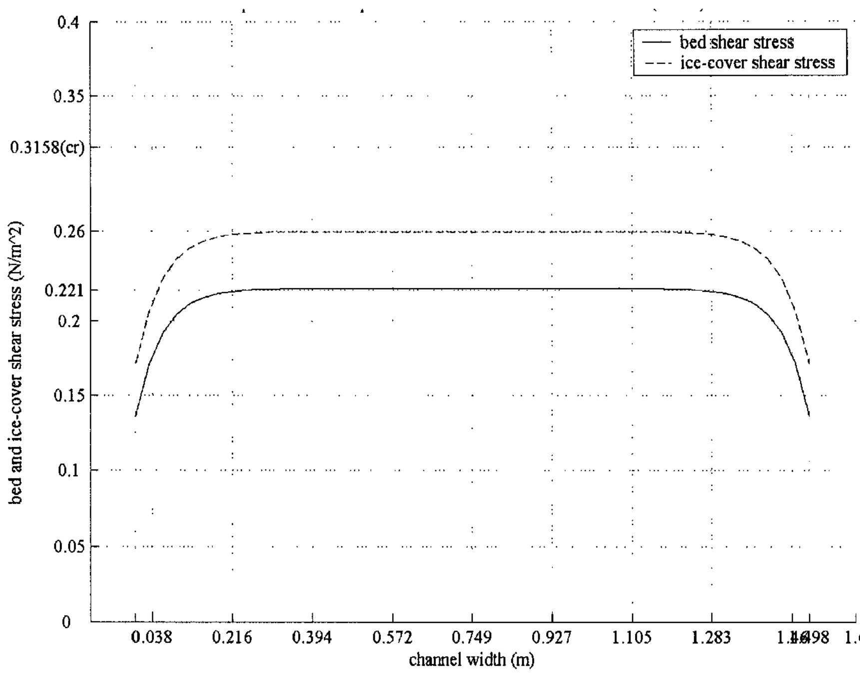

Figure 5-14 Lateral shear stress distribution at the bed and ice-cover boundaries of the flow (simulation of *Exp#4*, c-s BB, TIC)

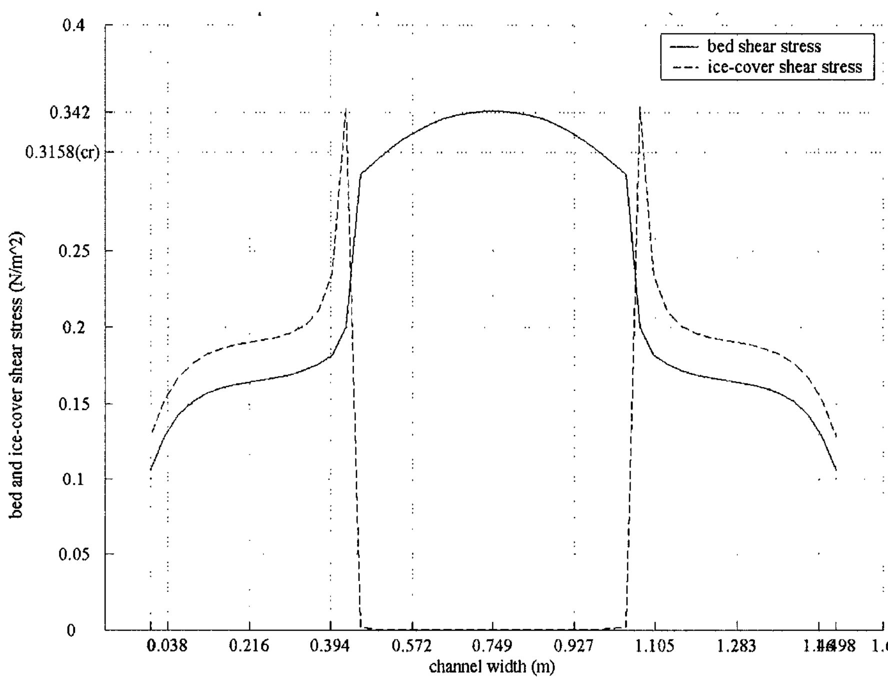

Figure 5-15 Lateral shear stress distribution at the bed and ice-cover boundaries of the flow (simulation of *Exp#4*, c-s BB, 2PIC)

In Figure 5-14 and Figure 5-15, the bed and ice-cover lateral shear stress profiles clearly present the difference between the two ice-cover configurations with respect to the worst scenario for the scouring phenomenon.

The simulated bed shear stress in the 2PIC case presents extreme high values in the central region of the flow, approximately 150% of the TIC case. The maximum value is reached in the centerline of the flow (point 5), $\tau_{bsim.5}$=0.342N/m^2, and the average value over the central region is $\tau_{bsim.fs}$=0.327N/m^2 superior even to the critical bed shear stress, τ_{bcr}=0.316N/m^2. This finding implies live-bed condition, and since observations made during the experiments show clear-water condition, it is obvious that here the numerical model produces an overestimation. Integration of the shear stress over the solid boundaries of the domain results in the drag-force/unit length acting on those boundaries. Comparison of these simulated forces to the previously computed total forces F_T divided by the length of the domain (7.32m), in both cases shows less then 1% error. But the computed forces F_T are based on the average shear stress assumption τ_T [Eq.(5-1)]. Thus, computing the drag-force on the ice-cover boundary/unit length and comparing to the corresponding measured value F_i (Table 5-2) divided by the length of the domain (7.32m), the simulated values for the TIC and the 2PIC cases are respectively 69% and 61.6% of their experimental counterparts. A major impact in these numerical overestimations of the 2PIC central region shear stress and underestimations at the ice-cover level comes from the choice of y_{min}: since the numerical model assumes a non-zero slip velocity, the values of y_{min} can easily under- or overestimate the tangent velocity u at the solid boundaries. The impact on the bed shear stress is the square of the estimated velocity [Eq.(5-6)].

Returning to the velocity profiles and estimating the velocity at the bed and ice-cover level from the experimental data, the following can be concluded:

(i) in the TIC case, the simulated velocity profile is well correlated the experimental velocities (obtained by linear interpolation of the two closest values) at the bed boundary but underestimated at the ice-cover level. The average ratio, at the ice-cover level between the simulated and the experimental velocity is $u_{sim} / u_{est} \approx 0.897$. At the bed level, the estimated bed shear stress is $\tau_{best.} \approx$ 0.221N/m^2, and the corresponding shear velocity $u_{*est.}$= 0.01486m/s; thus, the relative shear velocity is $u_{*est.}/u_{*cr.}$= 0.84, which shows the vicinity to the sediment incipient motion observed during the test.

(ii) in the 2PIC case, at the bed level, in the central region, the simulated velocities are overestimated with an average of $u_{sim} / u_{est} \approx 1.073$. The estimated average bed shear stress corresponding to the central region (points 4, 5 and 6) is $\tau_{best.456} \approx 0.284 N/m^2$, the shear velocity $u_{*est.456}$= 0.0169m/s and the relative shear velocity $u_{*est.456}/u_{*cr.}$= 0.95, which appears connected to the sediment incipient motion observed during the test.

In conclusion, from both analyzed ice-cover configurations, under controlled flow depth condition, the 2PIC case represents the extreme ice-cover configuration with respect to the scouring around a bridge pier: drastic changes occur in the velocity and shear stress distributions, resizing and redirecting their maximum values toward the central (open-water) region of the flow compared to a more uniform distribution encountered in the TIC and FS cases. As a result, the downflow receives more energy leading to a stronger scouring process. The following analysis of the scouring tests deals only with three configurations: 2PIC and FS at same ice-cover sediment incipient conditions and FS at open-water sediment incipient conditions.

From a numerical simulation point of view, the *Viscous-slip* approach produces velocity profiles in very good agreement with the experimental data for both ice-cover cases. Concerning the simulation closer to the flow boundaries, as previously mentioned, the choice of the variation function of the turbulent viscosity, ν_T and the location of the non-zero slip velocity, y_{min} from the solid boundaries has a major impact especially on the computation of the bed and ice-cover shear stresses. Thus, further investigations are necessary in order to reach better shear stress profiles in the vicinity of the flow boundaries.

5.3 Tests with bridge pier

5.3.1 Clear-water scouring tests

For all the scouring tests, the cylindrical pier was installed in the channel centerline, in the sand basin section between cross-sections BG and BF at 0.60m downstream of c/s BG and 0.12m upstream of c/s BF. In addition to the regular parameters measured in the hydraulic tests (velocity, flow depths, energy slopes, discharge, and drag-force action on the ice-cover,), readings of scour depths around the bridge pier and erosion/deposition features behind it are taken in all scouring tests. Overall, five experiments with the bridge pier in place are performed: ExpBP#1, referring to the FS configuration and ExpBP#2 to #4 all referring to the 2PIC configuration are all conducted under the ice-cover sediment incipient conditions as defined in the tests without bridge pier (Table 5-2, and Exp#4). ExpBP#5 refers to the FS test performed at the free-surface sediment incipient conditions as described in Exp#5 of the tests without pier. As previously mentioned in the First Chapter, subsection 1.3., this research represents the first step of an ongoing study, and thus, herein only the 2PIC and different FS configurations are analyzed. The following study, which will be presented by Mr. Jagadishwor Kayastha in Fall 2004, also deals with TIC and 1PIC configurations.

5.3.2 Results and Discussion

Since scouring around a bridge pier is a time-sensitive process, time considerations become important in the analysis of the hydraulics, the scouring and the deposition features. A first observation is that the flow velocities in the cross-sections upstream from the bridge pier appear to be independent of the scouring evolution. Since the experiments are performed in clear-water condition, this observation makes sense. Although the scouring does slightly propagate upstream, its influence remains rather limited and does not exceed the upstream limit of the scour hole (≈0.254m upstream the nose of the pier). Taking into consideration this first observation, the analysis was focuses on three main aspects :

(i) velocities at cross-sections upstream of the pier, in order to determine the influence of the cylindrical pier on the upstream flow (vertical and lateral distributions of velocity)

(ii) velocities at cross-sections downstream of the pier, in order to determine the influence of the cylindrical pier on the vertical and lateral distributions of velocity as well as the influence of scouring evolution on the time-variation of velocity. In the same manner, the bed and ice-cover shear stresses are analyzed.

(iii) scour depths and erosion/deposition features, in order to determine the geometrical and temporal characteristics of the scouring process.

Velocity distributions of each experiment are presented in the corresponding appendices, Appendix A7 to A12.

Considering the measured and computed parameters of the scouring tests (discharge, flow depth, energy slope, and average shear stress, shear velocity, drag-force etc), presented in Table 5-4, and comparing them to the corresponding values for the tests without a bridge pier (Table 5-2), we can conclude that both series are performed under similar hydraulic and sediment conditions upstream from the bridge pier.

Differences in discharge and flow depth when comparing analogous configurations are less than 2%. However, energy slopes in the 2PIC and FS bridge pier series show up to 29% increased values compared to the corresponding tests without a bridge pier. Since the energy slope apparatus receives the free-surface elevations from different locations of the flume, the main increasing slope is recorded in the sand basin portion, while in the upstream section the increase is less than 2%. The explanation comes from the bridge pier presence: an obstacle in the way of flow produces an important lateral redistribution of the discharge which further increases the friction forces at the ice and bed boundaries. These forces together with the additional energy loss produced by the wake of the bridge pier lead to an increase in energy slope. The energy slope values presented in Table 5-4 are computed as averages between readings taken at the beginning (S_{bs}) and at the end (S_{es}) of each test. The readings show increasing values of energy slopes with time, reaching equilibrium values with the stabilization of the scouring process. This observation is supported by the time-progression of bed roughness due to the scour hole and the formation of bed forms behind the pier.

The analysis of the drag force acting on the ice-cover illustrates minor differences between tests with and without a bridge pier. Moreover, in the case of 2PIC/ExpBP#4 when multiple readings of the drag-force are taken at different moments of the test, results show insignificant variation with time. This fact is caused by the constant ice-cover roughness, which does not change with time. Similarly to the changes in energy slope, the total average friction force F_T for the bridge-pier 2PIC tests shows 33% increased value compared to the corresponding 2PIC without bridge pier. The reasons for this are the same as for the energy slope changes (above).

Table 5-4 Experiments with bridge pier: FS and 2PIC (ExpBP#1 to #4) at ice-cover critical conditions and FS (ExpBP#5) at open-water critical conditions

Experiments with bridge pier (ExpBP#1-#5)												
Configuration	ExpBP#1 (FS)	ExpBP#2 (2PIC)	ExpBP#3 (2PIC)	ExpBP#4 (2PIC)	ExpBP#5 (FS)	#2/ #1	#3/ #1	#4/ #1	#2/ #5	#3/ #5	#4/ #5	#5/ #1
Q [m^3/s]	0.0432	0.044	0.0437	0.0439	0.0625	1.02	1.011	1.017	0.704	0.698	0.702	1.449
h [m]	0.1357	0.1362	0.1361	0.1361	0.1531	1.004	1.003	1.003	0.890	0.889	0.889	1.129
S_{bs} [10^{-4}]	0.962	3.205	2.885	3.205	1.603							
S_{es} [10^{-4}]	1.282	3.846	3.205	3.846	1.923							
S [10^{-4}]	1.122	3.5256	3.045	3.526	1.763	3.142	2.714	3.143	1.999	1.727	2	1.57
A [m^2]	0.2021	0.203	0.2028	0.2028	0.2281	1.004	1.003	1.003	0.890	0.889	0.889	1.129
P_w [m]	1.7613	2.6387	2.6384	2.6384	1.7962	1.498	1.498	1.498	1.469	1.469	1.469	1.020
R_h [m]	0.1148	0.0769	0.0769	0.0768	0.127	0.670	0.670	0.670	0.606	0.605	0.605	1.107
τ_T [N/m^2]	0.1083	0.2661	0.2416	0.2659	0.2196	2.457	2.231	2.455	1.211	1.100	1.210	2.028
F_T [N]	1.3962	5.1391	4.6666	5.1344	2.8878	3.681	3.342	3.677	1.780	1.616	1.778	2.068
u_{*T} [m/s]	0.0104	0.0163	0.0155	0.0163	0.0148	1.567	1.494	1.567	1.101	1.049	1.100	1.424
F_i [N] (measured)		2.0906	2.1208	2.0386								
τ_i [N/m^2]		0.3249	0.3303	0.31785								
u_{*i} [m/s]		0.01802	0.01817	0.01783								
u_{*T}/u_{*cr}	0.585	0.9173	0.872	0.9173	0.833	1.568	1.491	1.568	1.101	1.047	1.101	1.424
u_{*i}/u_{*cr}		1.0141	1.0225	1.0033								

where S_{bs} and S_{es} is the energy slope at the beginning and the end of test, respectively, and S is the corresponding average value.

Results form the velocity measurements at cross-sections upstream the pier (Figure 5-16) show very similar conditions when compared to the tests without a bridge pier (Figure 5-9). In details, for the 2PIC tests (ExpBP#2 to #4), in the lateral region of the flow (under the ice-cover), the maximum velocities are recorded at 50% of the flow depth between approximately 21 and 26.5cm/s. In contrast, in the central region (points 4, 5 and 6), the maximum velocities are located in the upper layers of the flow, recording values between 32.1 and 32.9cm/s. For the FS/ExpBP#1 case conducted at the ice-cover sediment incipient conditions, the readings of the maximum velocity in the same open-water region are between 27.1 and 27.7cm/s. In the other FS case (ExpBP#5), performed at free-surface sediment incipient conditions, similar locations of the maximum velocity are recorded but ranging from 32.7 to 33.4cm/s.

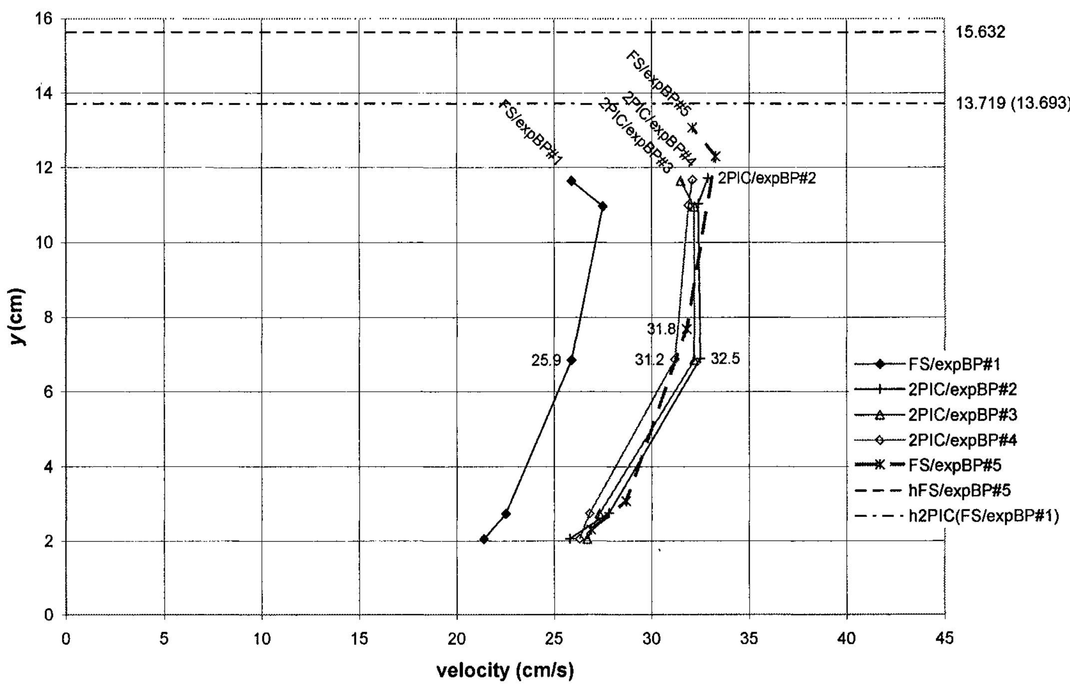

Figure 5-16 Vertical velocity profile at c/s BG, point 5, for all five scouring experiments: FS/ExpBP#1, 2PIC/ExpBP#2 to #4, and FS/ExpBP#5

The velocity differences, between the 2PIC tests and the FS case at the ice-cover critical conditions (Figure 5-16), are in the same range as for the tests without a bridge pier, namely that the 2PIC velocities record between 15% and 26% increased values compared to the FS values. For the FS/ExpBP#5 case (open-water critical conditions), as predicted in the similar test performed without a bridge pier (FS/*Exp#5*), the velocity measurements at the central region of the flow show similar characteristics as for the 2PIC case.

The lateral distributions of velocity support the above findings showing consistency and independency with respect to the scouring time-progression. Thus, it can be confirmed that the experiments performed with the bridge pier in place are presenting the same critical conditions (= sediment incipient motion) as the experiments performed without a bridge pier. In order to better visualize this analysis, lateral velocity profiles of cross-section BG are presented in the Appendix A12 (upstream bridge pier).

Cross-sections downstream of the bridge pier

Results from the readings taken in cross-sections behind the pier show the influence of the bridge pier on the vertical and lateral velocity distributions. In contrast to upstream sections, the flow behind the pier is dependent on the time-variation of the scouring and erosion/deposition processes, and the bed roughness. Appendix A13 (downstream bridge pier) contains the lateral velocity profiles of c/s BF, the first cross-section downstream the bridge pier (at 0.12m behind the pier). These lateral profiles are based on readings taken at different moments during the 2PIC tests.

The influence of the bridge pier is experienced on all cross-sections downstream of the pier. For all 2PIC tests, results show variations of velocity distribution between the lateral (under the ice-cover) and the central (open-water) regions. The following analysis is based on comparison between velocity readings taken at the downstream cross-sections and at the upstream cross-section BG (located at 6*b* upstream, where *b* is the cylindrical pier diameter). Further reference to c/s BG will be as the *upstream c/s*.

Velocity measurements in the lateral regions taken at c/s BE (9*b* downstream), show higher values ranging between 8% and 17% compared to the values of the *upstream c/s*. For convenience, Figure 5-17 depicts only points 3 and 7 for comparison. Similar percentages are also observed at c/s BD (20*b* downstream), where velocity readings taken at all the points located under the ice-cover area (1, 2, 3 and 7, 8, 9) and at different moments during the tests indicate increased values of 7.5% to 15% compared to the corresponding *upstream c/s*. Further downstream from this location, velocities in the lateral regions start to decrease and approach again the lateral velocity distribution found in the *upstream c/s* where the bridge pier has no influence.

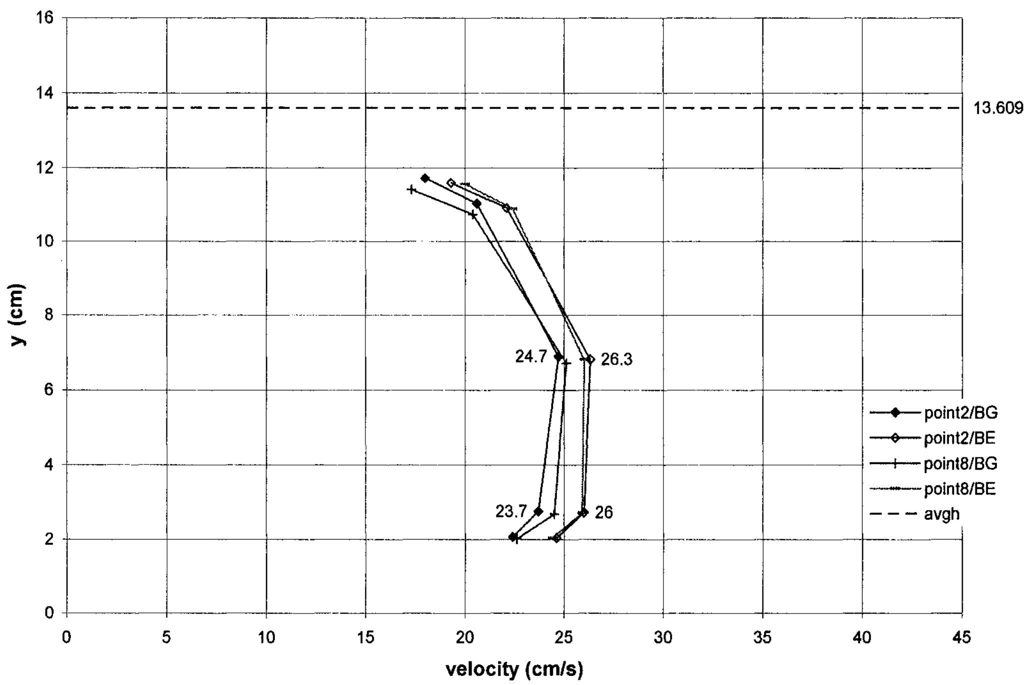

Figure 5-17 Vertical velocity profile at c/s BG and BE (ice-cover region of points 3 and 7, ExpBP#4)

This increase in velocities under the ice-cover regions recorded in all the tests is explained by a redistribution of the discharge due to the presence of the bridge pier and not to the scouring process. Moreover, this phenomenon is echoed by the formation of bed forms (dunes) . Since velocity readings start approximately 2 hours after the scouring has begun, the corresponding grain size Reynolds number, Re_* is definitely exceeding the critical value, and as presented in Figure 5-2, the conditions of sediment motion regime are shifted on the right-hand side of the diagram toward the dune formation regime. Thus, the erosion features under the ice regions are also caused by the increasing discharge and not by the scouring process around the bridge pier. However, the velocities measured under the ice-cover (lateral region) present small variations (<5%) with respect to the scouring time-evolution.

The analysis of the central (open-water) region of the channel focuses on points 4 and 6 and on point 5 (the flow centerline). At points 4 and 6, the results show at the beginning of scouring and only for the first cross-section behind the pier (BF) an abrupt increase in velocities with values between 10% and 12% compared to the corresponding *upstream c/s* values (Figure 5-18). When the tests approach the scouring equilibrium phase, the velocities just behind the bridge pier are very close to the corresponding upstream values.

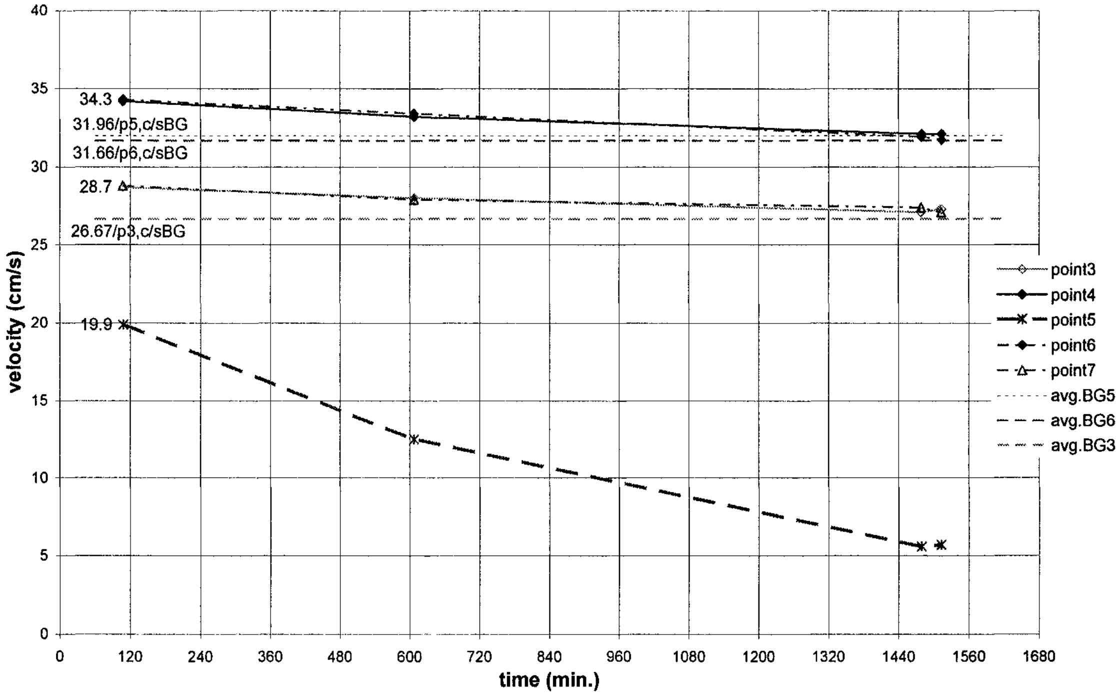

Figure 5-18 Velocity time-variation with respect to scouring evolution in c/s BF at 50% of the flow depth (2PIC tests)

As previously mentioned in subsection 3.2.1.(page32), the scouring around a cylindrical bridge pier starts at the sides of the cylinder and quickly propagates upstream around the pier. Indeed, the high values of the velocity measured at points 4 and 6 (Figure 5-18) support this description of the process. Moreover, since the velocities are taken at 1.2*b* downstream, it can easily be assumed that velocities at the bridge pier sides causing the beginning of the scouring process are even higher.

Velocity measurements taken at c/s BE (9*b* downstream) present a small decrease of approximately 4% compared to the *upstream c/s* (Figure 5-19). Further downstream, the velocities continue to slowly increase longitudinally and show little variation with time and scouring progression. Readings taken in the last cross-section BA, located at $40b$ downstream the pier show velocities at equilibrium reaching only 94% of the values at the beginning of the test. For all 2PIC tests, taking into consideration the velocity spatial distribution and variation with time in both the ice-cover and the open-water regions, the influence of the bridge pier covers a region that spans downstream up to a distance of approximately $50b$.

Analyzing the flow along the channel centerline (point 5), the velocities right behind the pier (c/s BF) record dramatic decreases with respect to the *upstream c/s*: values dropped to approximately 64% at the beginning of scouring and further down to 20% when approaching the scouring equilibrium (Figure 5-18). This variation is due to the high level of turbulence caused by the cast-off vortices, and to the scour depth time-progression associated with the erosion/deposition features behind the bridge pier.

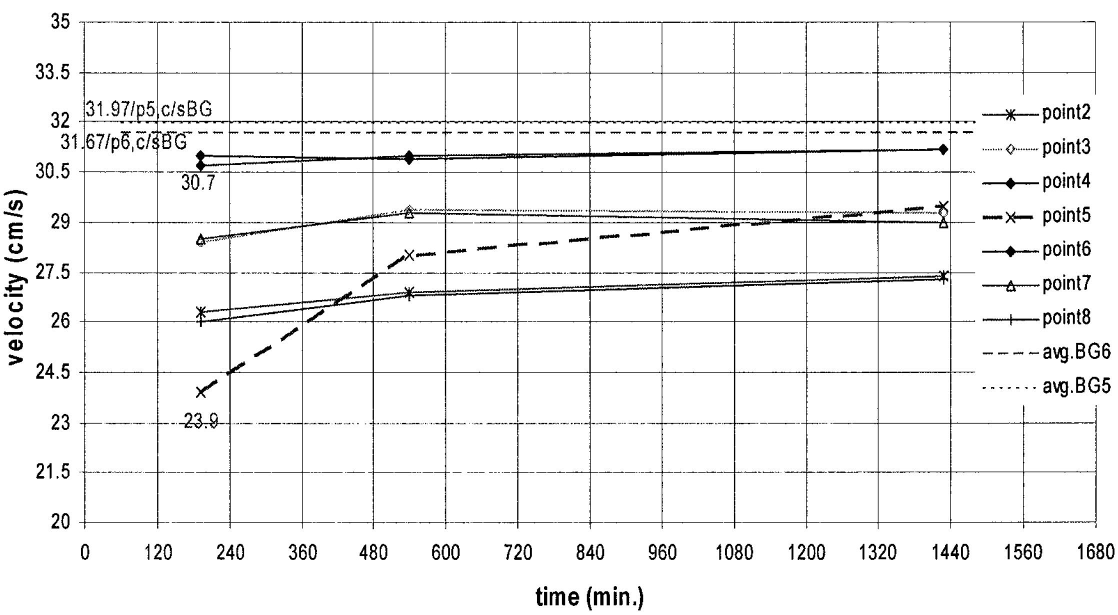

Figure 5-19 Velocity time-variation with respect to scouring evolution in c/s BE at 50% of the flow depth (2PIC tests)

Further downstream the velocities along the same centerline at the beginning of scouring registers values of 75% of the corresponding values at the *upstream c/s* (Figure 5-19). With time, in the first 9 hours of the scouring, the velocity shows increased value (up to 88%), but the highest rates of change are all observed in c/s BE. After that, approaching the equilibrium phase, the velocity rate of increase becomes similar to the rate observed at points 4 and 6. The explanation for the time-evolution of point 5 is not trivial. But we suspect that the flow around the bridge pier towards the equilibrium of the scouring process is not as diverted sideways as in the beginning when the bed is still almost flat. One reason for that could be related to the evolution of the horseshoe vortex which sinks into the scouring hole with time, thus interfering less with the surrounding flow.

For the FS tests, the same behavior is recorded, although the velocities are slightly inferior to 2PIC, down to 90% in the upper part of the flow ($y > 1/2h$).

Scour depths and erosion/deposition features

The third aspect of the analysis is dealing with comparison of the scouring process between the three different configurations mentioned earlier: 2PIC, FS at ice-cover sediment incipient conditions and FS at free-surface sediment incipient conditions. Patterns of the scour around the bridge pier, erosion/deposition behind it and bed sediment transport features under the ice-cover region are presented in the Appendix A14 (scour depths time-variation), A15 (scour depth profile along the channel centerline) A16 and A17 (scouring profile 2Dimensional and 3Dimensional).

Analyzing the scour depths around the bridge pier and the erosion/deposition features behind it (Figure 5-20), the results present a considerably stronger activity in the 2PIC case than in the FSExpBP#1 case (at same ice-cover critical conditions). As previously explained, the scouring process is acting in the central (open-water) region of the flow where the scour hole and the bar-shape deposition behind the pier are developed. The first observations refer to the maximum scour depth, which is recorded at the bridge pier nose in all five tests. The scour hole presents a conic shape, disrupted at the pier toe by a small amount of deposited sand, and elongated further behind the pier. The bed material from the scour hole is deposited downstream the pier only in the central (open-water) region of the flow in a bar-shape distribution. This feature is explained by the velocity behaviour at points 4 and 6, which presents the highest value and the smallest variation with time (Figure 5-18).

Figure 5-20 Scour depths and erosion/deposition features behind the cylindrical pier: ExpBP#3 (2PIC-left) and ExpBP#1 (FS-right)

All the other erosion features (bed-forms) in the lateral regions (under the ice-cover) result partially from the redirection of the flow discharge due to the presence of the bridge pier and partially it is suspected to be influenced by the turbulence created by the separation of the flow at the bridge pier sides (Figure 5-20). These features behind the pier appear very similar in the cases of 2PIC (ExpBP#2 to #4) and FS (ExpBP#5), but considerably different when compared to the FS/ExpBP#1 (Figure 5-21, and Appendix A16 and A17).

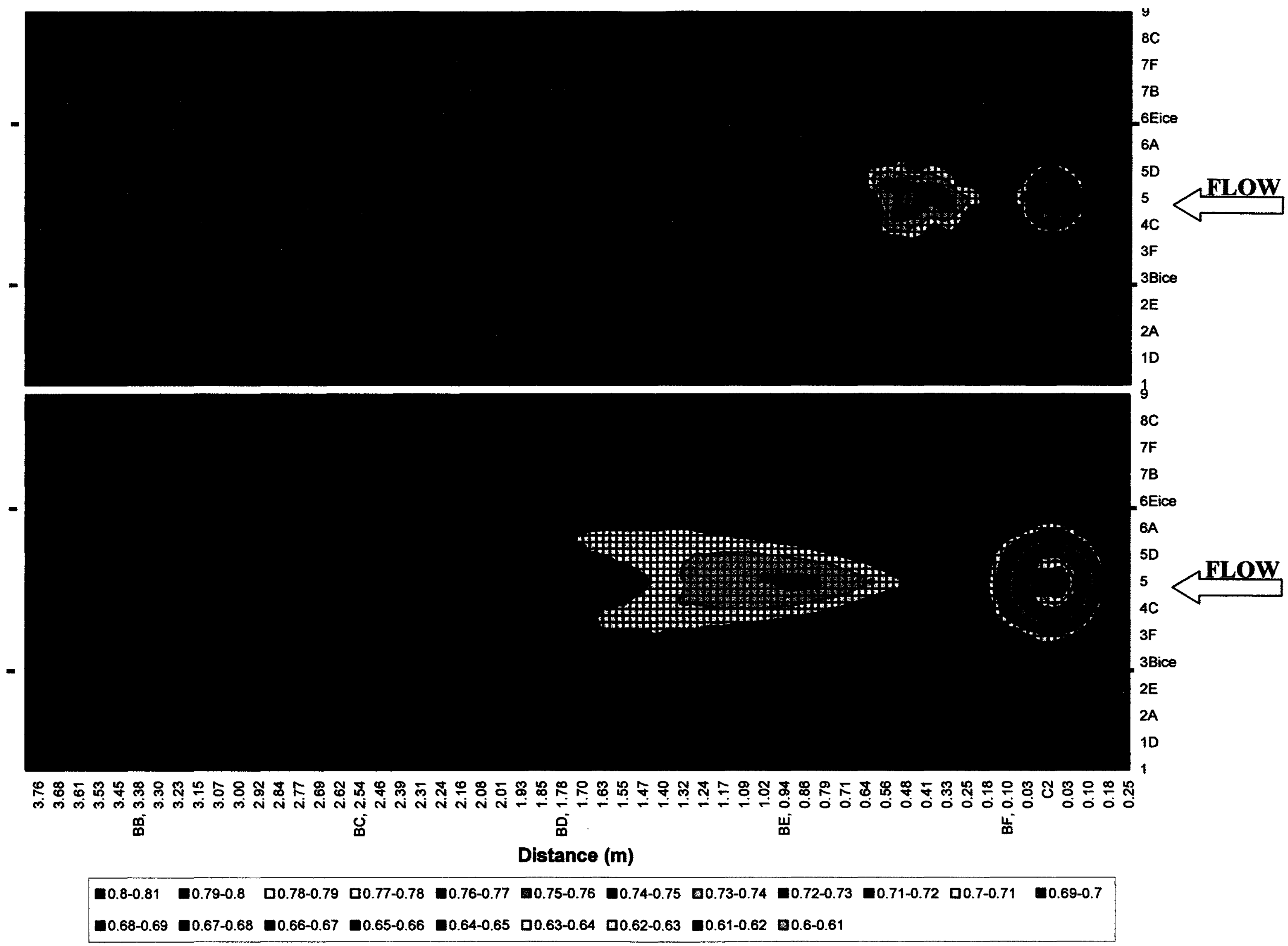

Figure 5-21 2D representation of the scour around the bridge and erosion/deposition features behind it (top – FSExp#1 and bottom – 2PICExp#3)

As predicted in the analysis of the tests without the bridge pier, for 2PIC configurations, the scour hole around the bridge pier resulted in a deeper and wider shape compared to the FS case under the same ice-cover sediment incipient conditions. Values in the 2PIC test show between 51% and 55% deeper and up to 75% wider scour hole around the bridge pier compared to the FS case (Figure 5-22 and Appendix A15).

Figure 5-22 Scour depths and erosion/deposition features at channel centerline. 2PIC (ExpBP#3) vs FS (ExpBP#1)

The scour hole for the FS/ExpBP#5 presents 5% to 8% increase in depth and approximately 11% increase in width compared to the 2PIC tests. This result supports the previous assumption of a more severe scouring process in this FS case because the open-water sediment incipient conditions are obtained by a discharge increase of 40% compared to the discharge of all other tests. Thus, in the FS/*ExpBP#5*, the discharge and the flow depth at the bridge pier cross-section are higher, which imply higher energy for the downflow and the horseshoe vortex involved in the scouring process (Figure 3-8). However, for a given discharge, the 2PIC configuration has the most dramatic impact on the scouring around a bridge pier. Appendix A15 presents the bed elevation along the channel centerline for all five experiments: comparison between the 2PIC experiments, the 2PIC and the FS cases and the FS configurations at different critical conditions.

Time-evolution analysis of scour depths is based only on readings of bed elevation around the bridge pier. The results show approximately 43% increase in the scouring rate of the 2PIC configuration compared to the FS case (FSExpBP#1) at the same ice-cover sediment incipient conditions (Figure 5-23). When compared to the other FS case (FSExpBP#5), the scouring rate presents less than 2% difference.

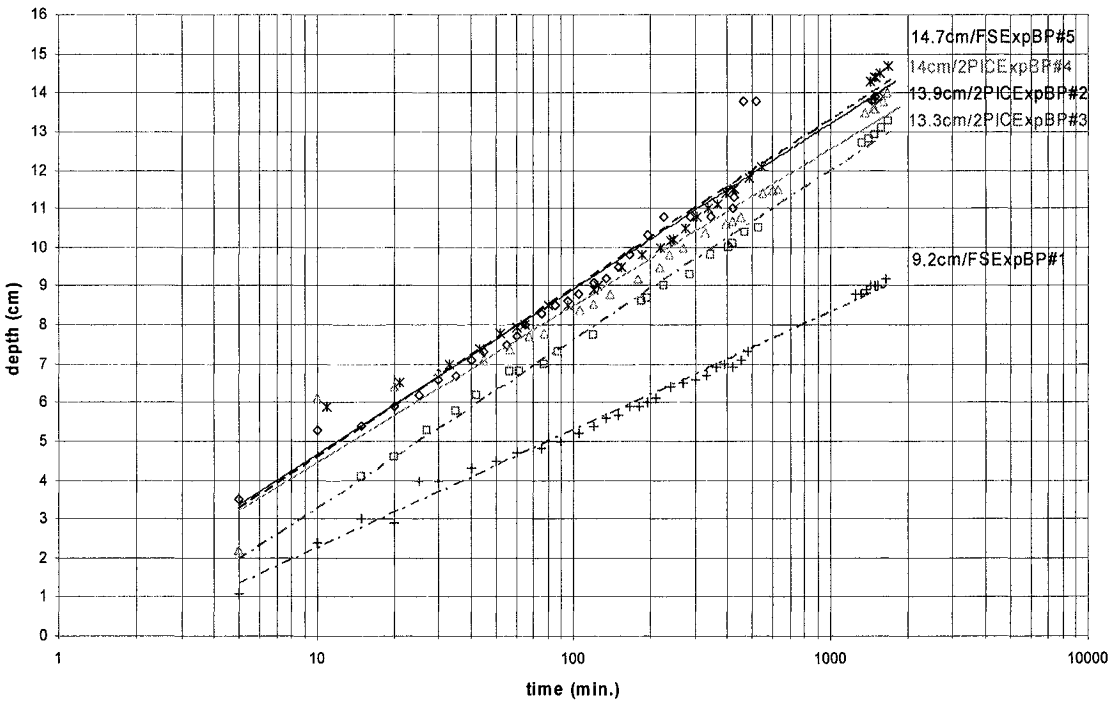

Figure 5-23 Scour depth time-evolution at the bridge pier nose (FS/ExpBP#1, 2PIC/ExpBP#2 to #4 and FS/ExpBP#5)

Measurements of the geometrical characteristics of the erosion/deposition process behind the bridge pier show a 2PIC disturbed bed region 4 times as long as the FS/ExpBP#1 case. Moreover, calculations show the sand volume scoured in the 2PIC case to be 2.8 to 3 times the volume of the FS case from the upstream part and the sides of the pier, and the deposited volume behind the pier to be approximately 2.3 to 2.7 times the FS case. However, the height of the deposition bar in the FS/ExpBP#1 case is recorded approximately 20% elevated than the 2PIC case. This particularity is explained by the fact that in the FS case, the flow behind the pier is more easily directed toward the sides of the channel leaving the central region in a low velocity flow, thus enhancing the deposition process immediately behind the pier. The absence of the ice-cover induces high velocities in the upper layers of the flow maintaining for a longer distance the high discharge on the sides of the channel. As a result, following the deposition process, the flow takes a longer distance to reestablish to a more uniform distribution compared to the 2PIC case, for which case the ice-cover tends to rapidly redirect the flow back to the open-water region once the deposition process ends.

When 2PIC experiments are compared to the FS test performed at open-water critical conditions (ExpBP#5), the erosion/deposition process shows similar evolution. In addition, investigation of the erosion features developed along the sides of the bar-shape deposition behind the pier reports that the zone of influence for the FS (Fs incipient condition) is 150% of the equivalent zone in the 2PIC case. This finding supports the earlier explanation about the fact that in the FS cases, the flow takes a longer distance to reestablish back to a more uniform distribution after its separation at the bridge pier location compared to the 2PIC configuration. Quantitatively speaking, computations on the central region of the flume record sand volume scoured around the pier and deposited downstream in this FS case up to 2.5% larger values compared to the 2PIC configuration.

Chapter Six
Summary, Conclusions, and Future Research

6.1 Summary

In the literature, most studies conducted on sediment motion under ice-covered flow found decreasing sediment transport compared to the open-water situation. However, most of these studies were conducted under a flow depth adjustment conditions, the energy slope being kept constant from one flow configuration to another. This approach appears reasonable in a long length-scale situation (uniform flow condition), i.e. long river reach, but for scouring around a bridge pier as well as other similar phenomena (abutments, narrowing cross-sections or tide river bends) the uniform flow condition is no longer valid. Thus, shorter length-scale analysis is required. In this case, as field observations have shown (Zabilansky 2002), it is common in nature for the ice-covered flow to adjust faster the energy slope than the flow depth. As a result, drastic changes occur in the flow regime and the scouring processes.

This study represents the first of a multi step research of an ongoing effort to determine the impact of different ice-covered flow configurations on the scouring processes around a cylindrical bridge pier. Three ice-cover configurations are analyzed during this study: (i) the total ice-cover (TIC), which covers the entire width of the channel and surrounds completely the bridge pier, (ii) the 2 sides partial ice-cover (2PIC), which covers the sides of the channel leaving the central part and the bridge pier in open-water flow, and (iii) the 1 side partial ice-cover (1PIC), which covers only one side of the waterway leaving the other side and the bridge pier in open-water.

The objective of this study is to determine the worst ice-cover case from a sediment incipient motion point of view considering a flow energy adjustment condition, and to determine for that case the scouring around a cylindrical bridge pier with respect to the free-surface case. The scouring process is studied under clear-water regime since it represents the worst scouring condition, which causes the maximum scour depths.

The report starts with a literature review of previous studies conducted on sediment transport under ice-cover conditions and of previous work done on scouring around bridge piers under free-surface and ice-cover conditions. As a follow up, the experimental setup is developed in order to perform tests according to the objective of the study and to the findings from the literature review. Based on the experimental results, an analysis is conducted over two aspects: velocity and shear stress distributions, and scouring and erosion deposition processes around the cylindrical bridge pier. A numerical simulation of the experimental velocity field is also integrated in the analysis.

6.2 Conclusions

The tests of this study are divided into two categories: (i) tests without the bridge pier in place, and (ii) tests with the bridge pier in place. The first category of experiments determined the 2PIC configuration as the worst-case scenario for the critical conditions of sediment transport (= incipient motion conditions). The results show a clear uniform distribution of the flow in the cases of TIC and FS, in contrast to the 2PIC case, which presents a more, disturbed flow. In the central part of the channel, the velocities measured in the 2PIC test are up to 8% higher in the lower part of the flow ($y < h/2$) and up to 30% higher in the upper part ($y > h/2$) when compared to the TIC configuration. Compared to the FS case, the flow velocities in the 2PIC test were up to 20% higher in the lower part of the flow and up to 15% higher in the upper part. This increase in velocities located in the central (open-water) region of the channel is translated as an increase in energy for the scouring process. These tests lead us to believe that the 2PIC configuration has the highest potential for scouring around a bridge pier. For that reason, this test was chosen for the following series of experiments.

The second category of experiments compared the scouring parameters (scour depths around the pier and erosion/deposition features behind it), only between the 2PIC and the FS cases. The other ice-cover configurations, TIC and 1PIC will be tested and the results presented in the next phase of this study, to be published by Jagadiswor Kayastha later this Fall 2004 . In terms of scour depths around the bridge pier, the results show a 51 to

55% deeper and up to 75% wider scour hole in the 2PIC case compared to the FS case at the same ice-cover sediment incipient conditions. Moreover, the erosion/deposition features behind the bridge pier are spread in the 2PIC case over a distance 4 times longer than in the FS case. Comparing the case of FS under open-water sediment incipient conditions (*ExpBP#5*) with the 2PIC case, the erosion/deposition features are found to be very similar in both configurations. However, the scour depths in this FS case show 5 to 8% increase and the scour hole presents approximately 11% wider circumference. It is worth mentioning that this FS case generated these slight differences by receiving approximately 40% higher discharge and 15% increase in flow depth. Therefore, from a scouring design point of view, the 2PIC configuration in the clear-water situation should be considered the most critical configuration since it generates the most dramatic scouring around a cylindrical bridge pier for the lowest flow regime conditions.

From a computational point of view, the tests without a bridge pier were also numerically simulated using the *Viscous-slip* approach model of Frenette and Molleti (2002). Although the results show very good correlations in terms of velocity profile, the shear stress distributions at the bed and ice-cover boundaries present over- and underestimations between 31 and 38% with respect to estimated values based on the laboratory measurements. These errors could come from different reasons, such as the distribution of the turbulent viscosity, ν_T , the choice of the wall friction law, or even the uncertainty related to the measurement of the energy slope.

Generally speaking, the results of this first phase show the directions for the next phases of the study. Determining the 2PIC configuration to be the leading case and providing valuable data in both hydraulic and scouring domains, will make the analysis of the next cases, TIC and 1PIC easier to put into perspective.

6.3 Future research

Results obtained from the present research generate additional questions to be addressed in future works. The following suggestions for the future direction of research on this topic cover mainly three aspects: (i) theoretical, (ii) numerical and (iii) technical.

(i) this study was conducted using only one kind of uniform sand material, one size bridge pier diameter, one size and roughness of the simulated ice-cover panels. Future studies should consider the following test strategy: for one size distribution of uniform bed material or non-uniform material, the tests should be performed using different ice-cover roughness and geometrical dimensions (in particular for 2PIC and 1PIC cases), different bridge pier diameters. Ideally, with a proper sediment feeding device, it would be interesting to perform some tests under live-bed scouring regime. Finally, the impact a non-uniform bed sediment granulometry, in particular on the armoring effect, would also be interesting to investigate.

(ii) with the help of the powerful computers available today, the ultimate goal of this research is to provide a numerical model able to simulate the natural phenomena as close as possible. The numerical approach used in this study shows promising results, although more work is required on the boundary conditions. Improvement of the friction law should be a priority. With a better numerical tool at hand, and using the results obtained in this research for calibration, a better predictive tool for flow under ice cover could be made available.

(iii) the large flume of the Hydraulic Laboratory of the University of Ottawa evolved with the progression of this study. It is worth mentioning the evolution of the stabilizer system at the flume inlet, the pipe network and the filling/draining system in the sand basin section of the flume, the free-surface slope apparatus, the ice-cover drag force apparatus and the simulated ice-cover. The flow velocities were measured with an electromagnetic velocimeter, which showed severe limitations close to the flow boundaries, restricting our capacity to analyze the velocity profiles. Thus, future research should consider a non-intrusive instrument for velocity measurements such as a Laser or an Acoustic Doppler Velocimeter. If an intrusive instrument is still going to be used, it is important to make the holes trough the simulated ice-cover as small as possible in order not to interfere with the actual ice-cover roughness.

Chapter Seven

References

Basak, V., (1975) *Scour at Square Piers (Devlet su isteri genel mudulugu)*. Report 583, Ankara, Turkey

Batuca, D. and B. Dargahi, (1986) "Some Experimental Results on Local Scour Around Cylindrical Piers for Open and Covered Flow" *Proceedings of The Third International Symposium on River Sedimentation*, The University of Mississippi, vol. III, 1095-1104.

Bonasoundas, M., (1973) "Non-Stationary Hydromorphological Phenomena and modeling of Scour Processes" *Proceedings of the 16th Congress of the International Association of Hydraulic Research,* Sao Paolo, Brazil, vol.2, pp. 9-16.

Bonnefille, R., (1968) *Bulletin du Centre de Recherches et d'Essais de Chatou, n^{o}11, 6p;* These de Doctorat, Universite de Grenoble, Grenoble, France.

Brater, E.F., and H.W., King, (1976) *Handbook of Hydraulics, sixth edition.* McGraw-Hill Book Company.

Breusers, H.N.C. and A.J., Raukivi, (1991) *Scouring: IAHR Hydraulic Structures Design Manual 2.* A.A. Balkema, Rotterdam, The Netherlands.

Breusers, H.N.C., G. Nicollet, and H.W., Shen (1977) "Local Scour around Cylindrical Piers" *Journal of Hydraulic Research,* vol. 15, 211-252.

Chabert, J. and P., Engeldinger, (1956) *Etude des Affouilements autour des Piliers des Ponts.* Laboratoire National d'Hydraulique, Chatou, France.

Chee, R.K.W., (1982) *Live-bed Scour at Bridge Piers*. School of Engineering, Report No. 290. The University of Auckland, Auckland, New Zealand.

Chiew, Y.M., (1984) *Local Scour at Bridge Piers*. School of Engineering, Report No. 335. The University of Auckland, Auckland, New Zealand.

Donchenko, R.V., (1975) *Conditions for Ice Jam Formation in Tailwaters* U.S. Army Cold Regions Research and Engineering Laboratory, Draft Translation 669

Ettema, R. (1980) *Scour at Bridge Piers*. School of Engineering Report No. 216, The University of Auckland, Auckland, New Zealand.

Ettema, R., F. Braileanu and M. Muste, (1999) *Flume Experiments on Flow and Sediment Transport in Ice-Covered Channels*. IIHR Technical Report no.404, Iowa Institute of Hydraulic Research, The University of Iowa, Iowa City.

Frenette, R. and S.,Molleti, (2002) "Viscous-slip Approach to Simulate Vertical Velocity Profile for Flow under Ice-Cover" *Ice in the Environment: Proceedings: 16th IAHR International Symposium on Ice*, Dunedin, New Zealand.

Hancu, S. (1971) "Sur le Calcul des Affouillements Locaux dans la Zone des Piles de Pont" *Proceedings: 14th Congress of the International Association of Hydraulic Research*, Paris, France, vol. 3, pp.299-306.

Kindsvater, C.E., and R.W., Carter, (1959) "Discharge Characteristics of Rectangular Thin-plate Weirs" *Trans.ASCE,* vol.124, pp. 772-822.

Laursen, E.M., and A., Toch, (1956) *Scour Around Bridge Piers and Abutments* Iowa Highway Research Board, Bulletin No.4, 60 pp.

Lau, L.Y. and B.G., Krishnappan, (1985) "Sediment Transport under Ice-Cover" *Journal of Hydraulic Engineering*, vol.111, no.6.

Larras, J., (1972) *Hydraulique et Granulats*. Editions Eyrolles, Paris, France.

Marian, L. and M., Muste, (1993) *Hidraulica si Masini Hidraulice. Vol.I.* Institutul Politehnic Cluj-Napoca, Cluj-Napoca, Romania.

Melville, B.W., (1975) *Local Scour at Bridge Sites*. School of Engineering Report No.117, University of Auckland, Auckland, New Zeeland.

Melville, B.W., and A.J., Raudkivi, (1977) "Flow Characteristics in Local Scour at Bridge Piers" *Journal of Hydraulic Research*, vol. 15 (4), 373-380.

Olsson, P., (2000) *Influence of Ice-Cover on Local Scour at Circular Bridge Piers.* Master Thesis, Water Resources Engineering, Lulea University of Technology, Lulea, Sweden.

Parthasarathy, R.N., and M.V., Muste (1994) "Velocity Measurements in Asymmetric Turbulent Flows" *Journal of Hydraulic Engineering, ASCE,* vol. 120 (9), 1000-1020.

Raudkivi, A.J., and R., Ettema (1983) "Clear-water Scour at Cylindrical Piers" *Journal of Hydraulic Engineering, ASCE*, vol. 109 (3), 338-350.

Raudkivi, A.J., (1981) *Grundlagen des Sedimenttransports* Sonderforschungsbereich 79, Univ. Hannover, Hannover, Deuchland.

van Rijn, L.C., (1984) "Sediment Transport. Part I: Bed Load Transport" *Journal of Hydraulic Engineering, ASCE,* vol. 110(10), 1431-1456.

Sayer, W.W., and G.B., Song (1979) *Effects of Ice Covers on Alluvial Channel Flow and Sediment Transport. Processes*. Report no. 218, Iowa Institute of Hydraulic Research, The University of Iowa, Iowa City.

Shen, H.W., V.R., Schneider, and S., Karaki, (1969) "Local Scour Around Bridge Piers" *Journal of the Hydraulic Division, ASCE*, vol. 95, HY6, 1919-1940.

Smith, B.T. and R. Ettema, (1995) *Ice-Cover Influence on Flow and Bedload Transport in Dune-bed Channels*. IIHR Technical Report no.374, Iowa Institute of Hydraulic Research, The University of Iowa, Iowa City.

Tison, L.J., (1940) *Erosion Autour de Piles de Pont en Riviere*. Ann. Des Travaux Publics de Belgique, vol. 41, 813-871.

Wuebben, J.L., (1986) "A Laboratory Study of Flow in an Ice-Covered Sand Bed Channel" *Proceedings of IAHR Symposium on Ice, Iowa Instituteof Hydraulic Research,* Iowa City, Iowa, pp. 3-16.

Wuebben, J.L., (1988) "Effects of an Ice-Cover on Flow in a Movable Bed Channel" *Proceedings of The 9th International Symposium on Ice, Sapporo, Japan*, Sapporo, Japan, pp.136-147.

Yalin, M.S., (1977) *Mechanics of Sediment Transport*. Pergamon Press Ltd., Headington Hill Hall, Oxford

Yankielun, N.E. and L.J. Zabilansky, (1998) "Innovative Instrumentation Techniques for Detecting and Measuring Effects of Sediment Scour under Ice" *Water Resources Engineering 98, ASCE.*

Zabilanski, L.J., (1996) *Ice Forces and Scour Instrumentation for The White River, Vermont*. CRREL Special Report 96-6, Dept. of Army, Cold Regions Research and Engineering Laboratory, Corps of Engineers.

Zabilanski, L.J., (1998) "Scour Measurements under Ice" *Water Resources Engineering 98*, ASCE, 151-156.

Zabilanski, L.J., (2002) "Ice-Cover Effects on Bed Scour: Case Studies" *11th International Conference on Cold Regions Engineering, ASCE Anchorage*, Anchorage, Alaska.

APPENDICES

APPENDIX A1

Granulometric curve distribution of the sand bed material

Granulometric Curve of " 50% Org.+ 50% Sieved" Sand Used For the Middle Basin Sand Bed

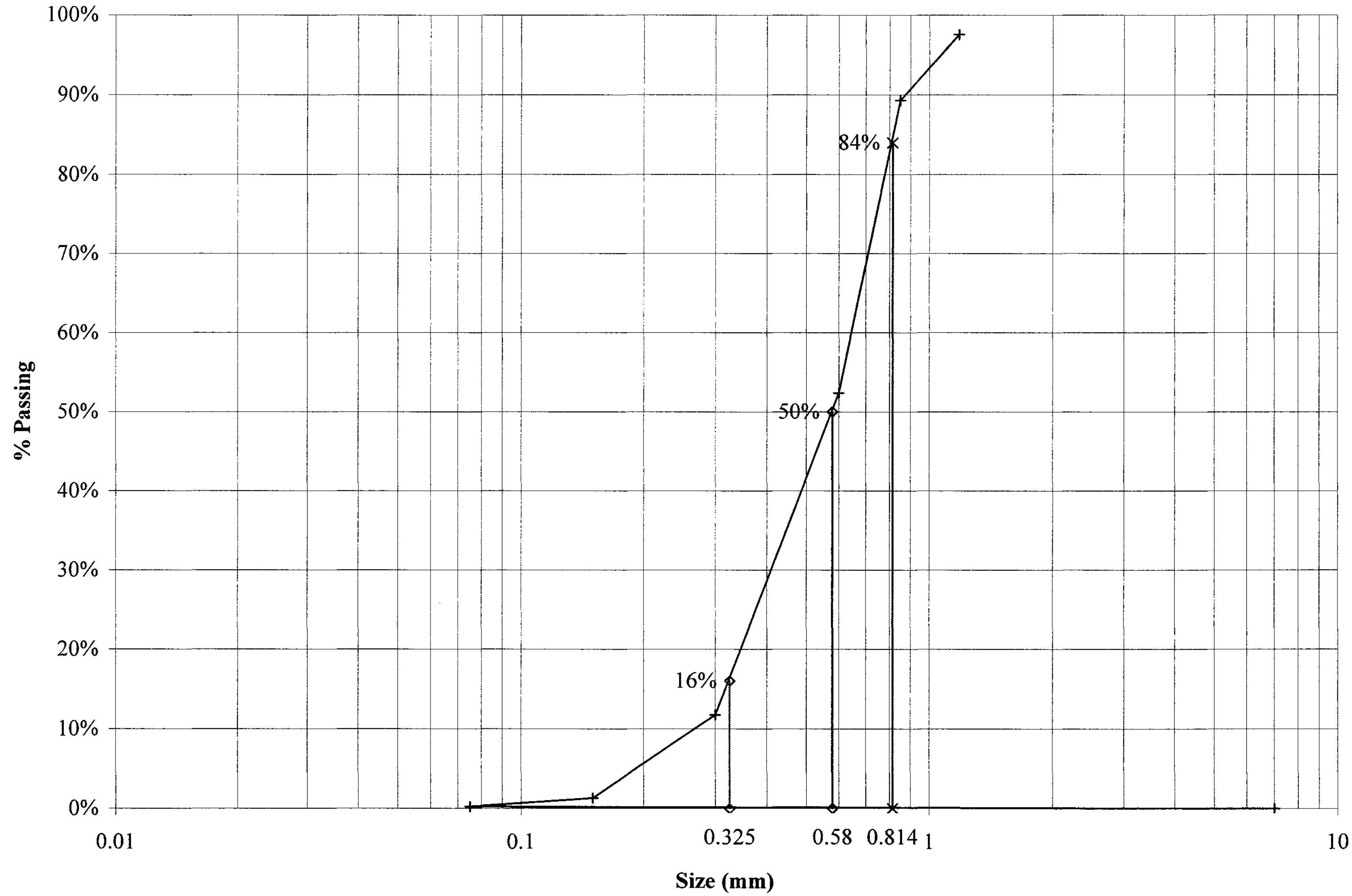

APPENDIX A2

Strain gauges calibration curves for the ice-cover shear stress measurements device

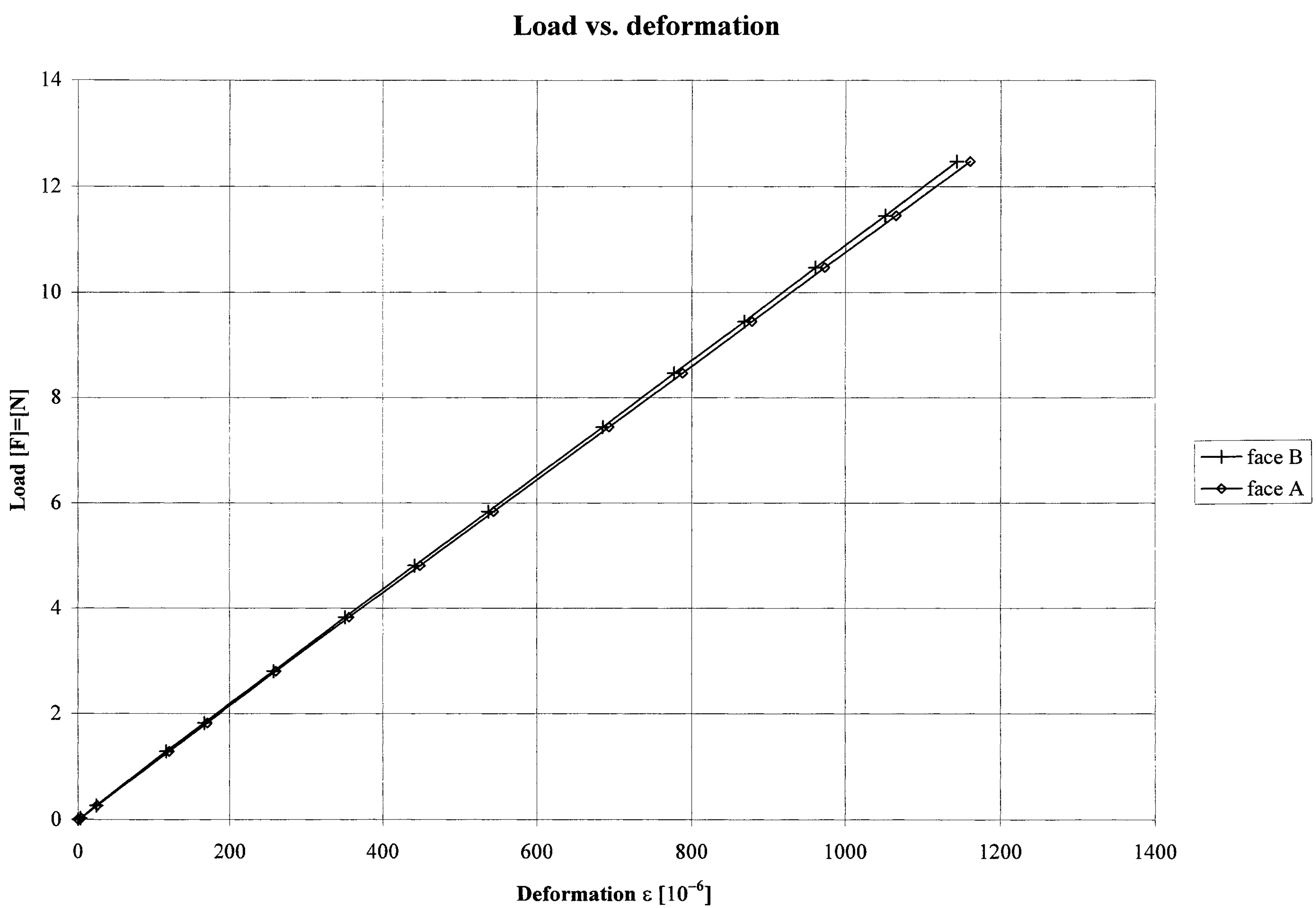

Load vs. deformation
14
12
10
8
6
4
2
0
Load [F]=[N]
0
200
400
600
800
1000
1200
1400
Deformation ε [10^-6]
face B
face A

APPENDIX A3

Exp#1

TOTAL ICE-COVER (TIC), 2SIDES PARTIAL ICE-COVER (2PIC), 1SIDE PARTIAL ICE-COVER (1PIC) and FREE-SURFACE (FS) CONFIGURATIONS at same discharge and flow depth conditions

(experiment without bridge pier)

TOTAL ICE-COVER CONFIGURATION (TIC)

Lateral velocity profiles

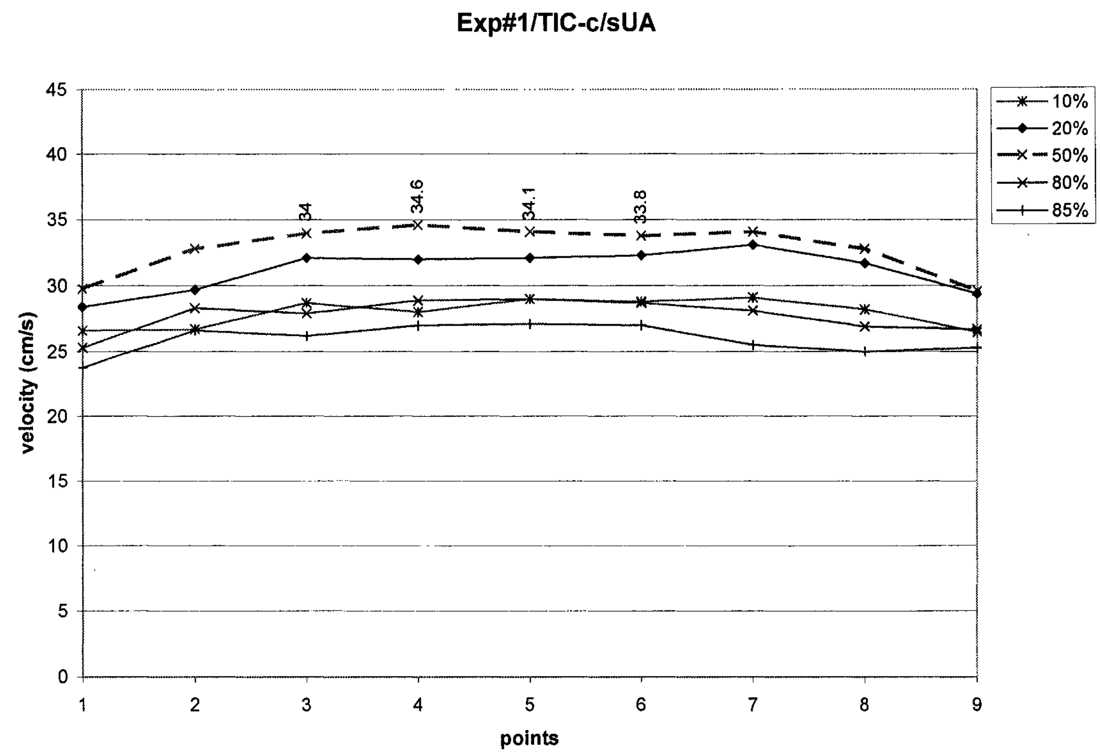

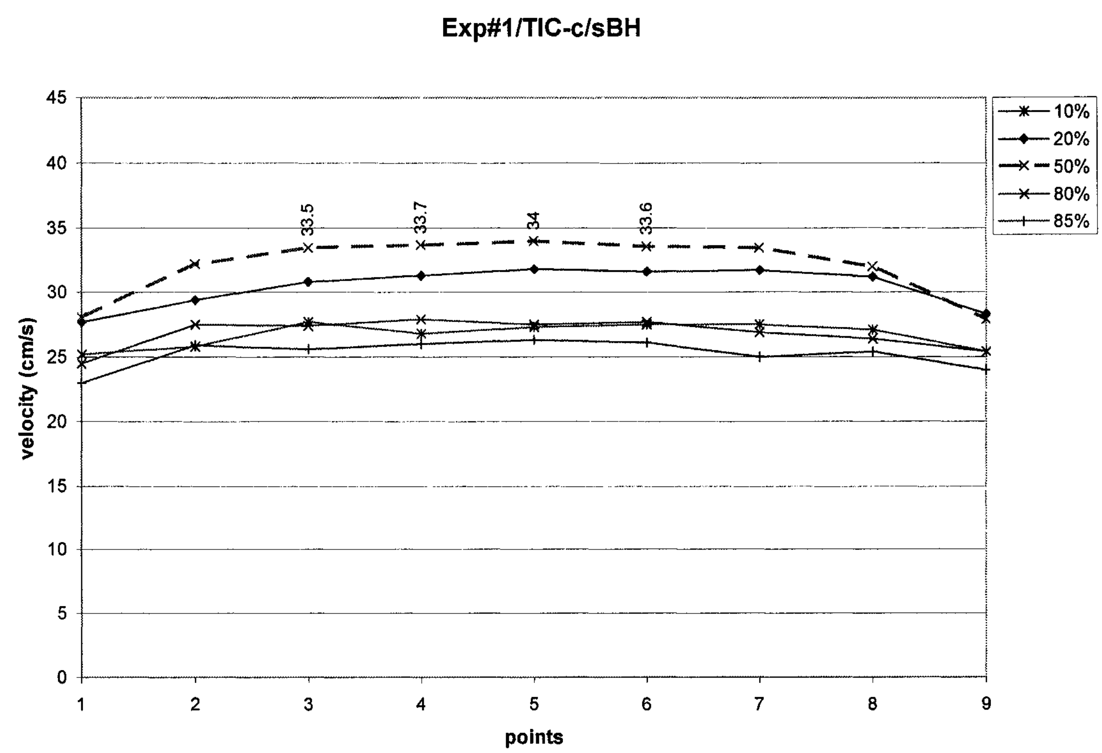

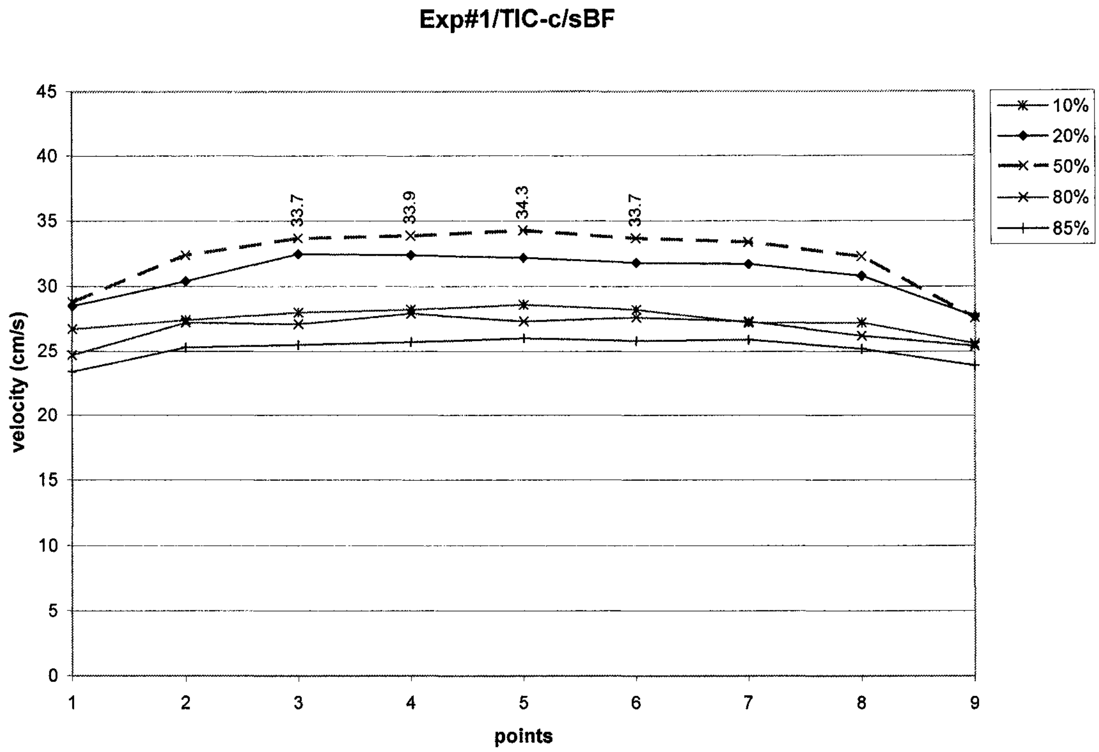

Exp#1/TIC-c/sBF
velocity (cm/s)
points
10%
20%
50%
80%
85%
33.7
33.9
34.3
33.7

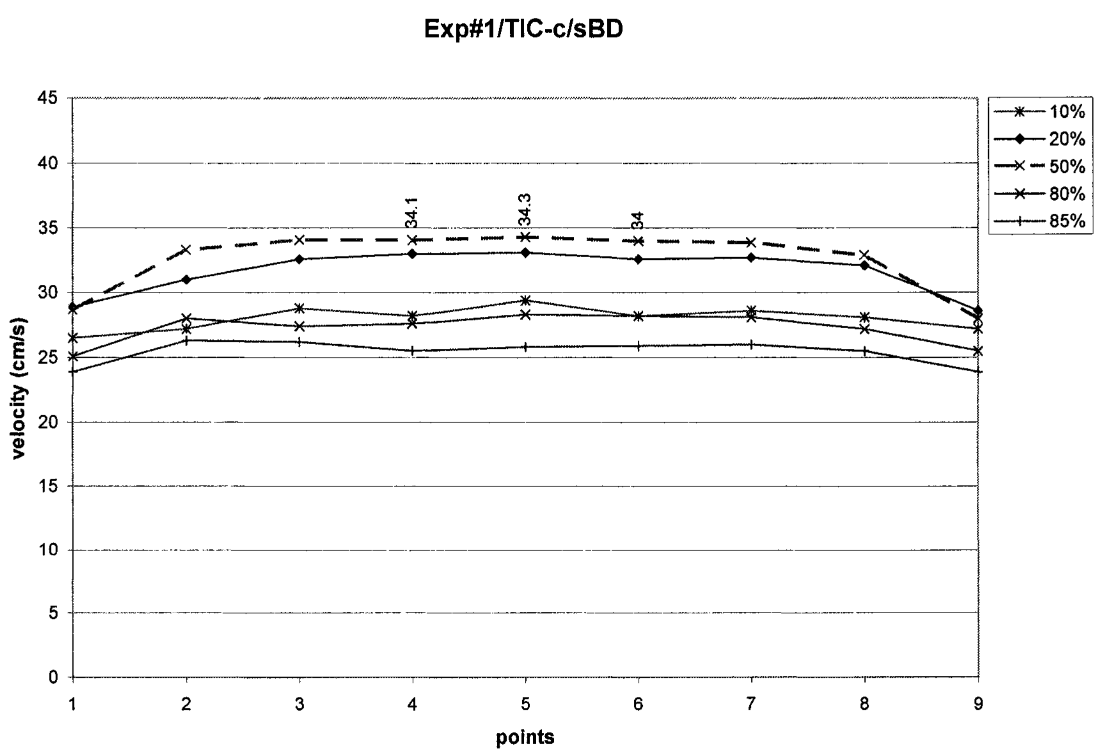

Exp#1/TIC-c/sBD
velocity (cm/s)
points
10%
20%
50%
80%
85%
34.1
34.3
34

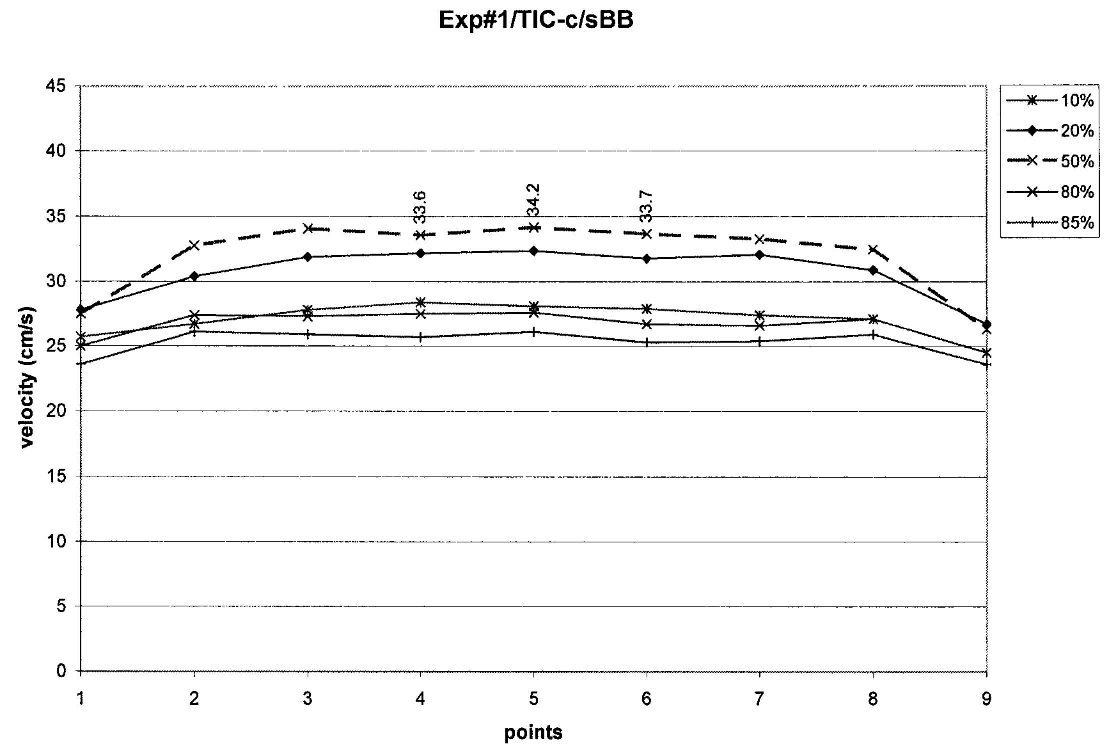

Vertical velocity profiles

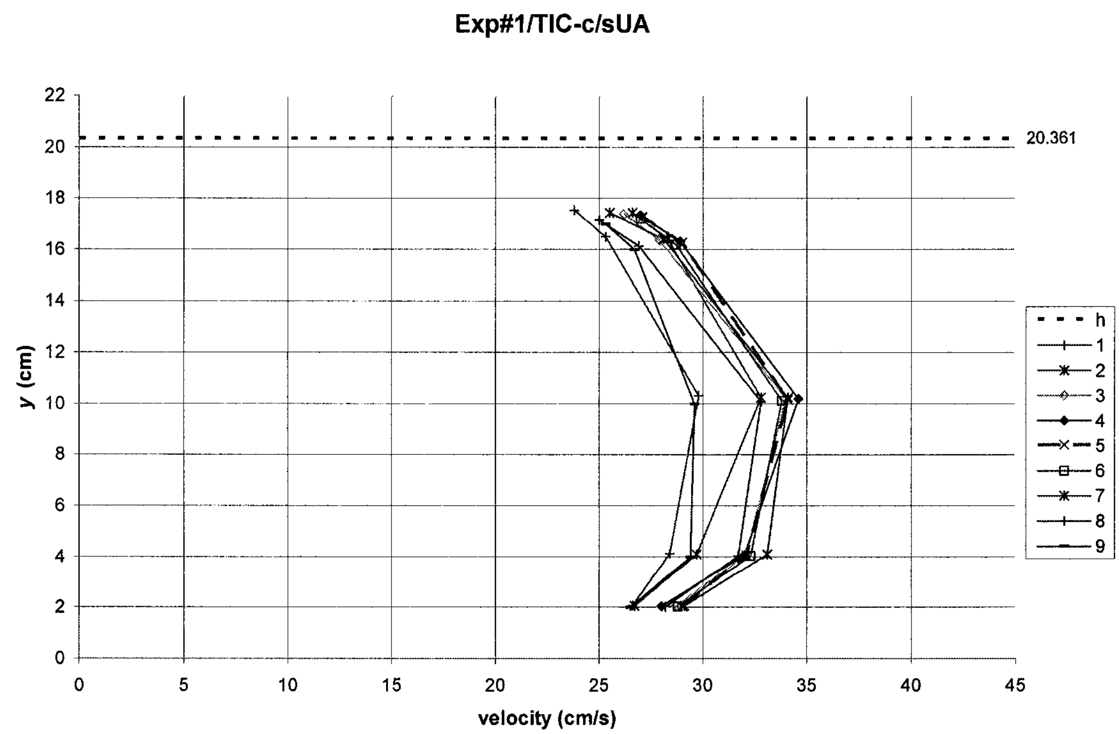

Exp#1/TIC-c/sBH

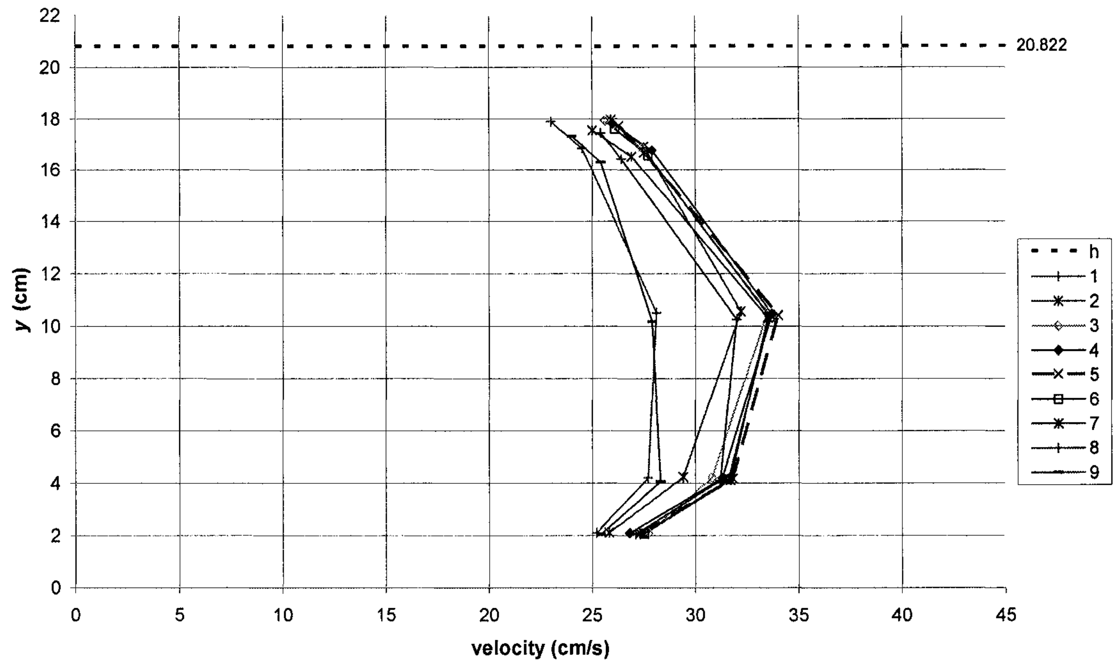

Exp#1/TIC-c/sBF

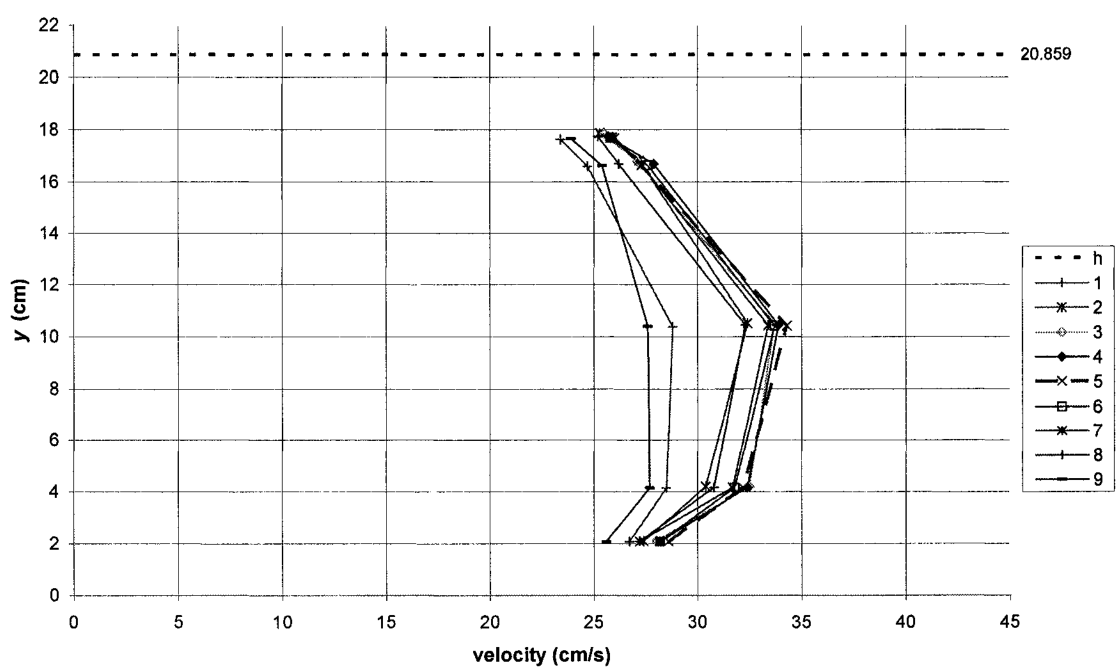

Exp#1/TIC-c/sBD

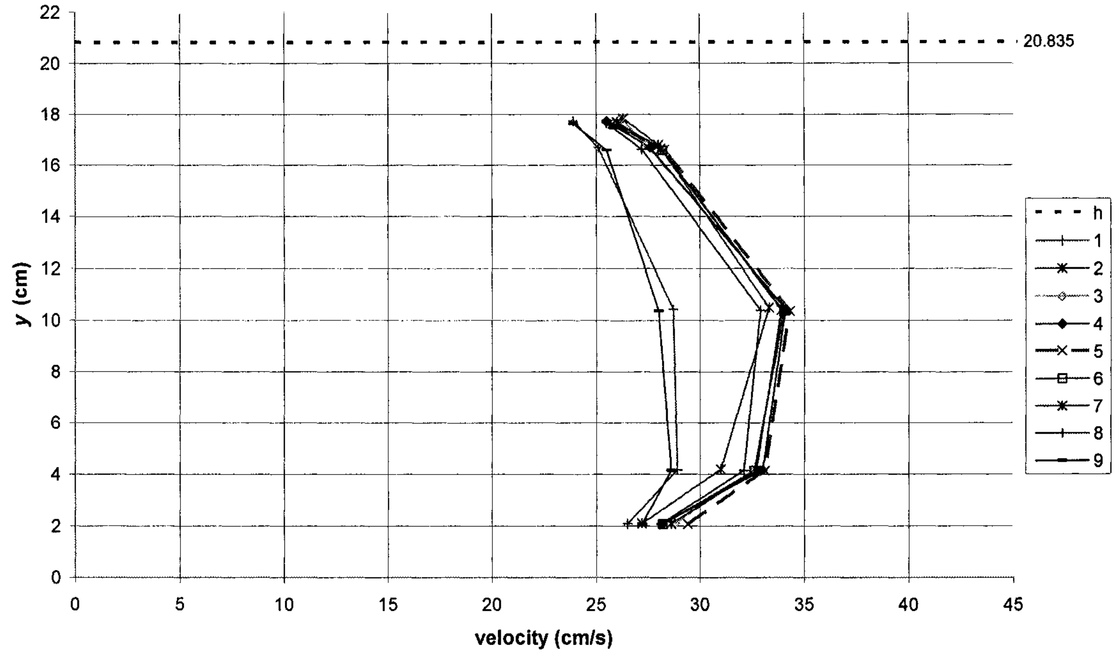

Exp#1/TIC-c/sBB

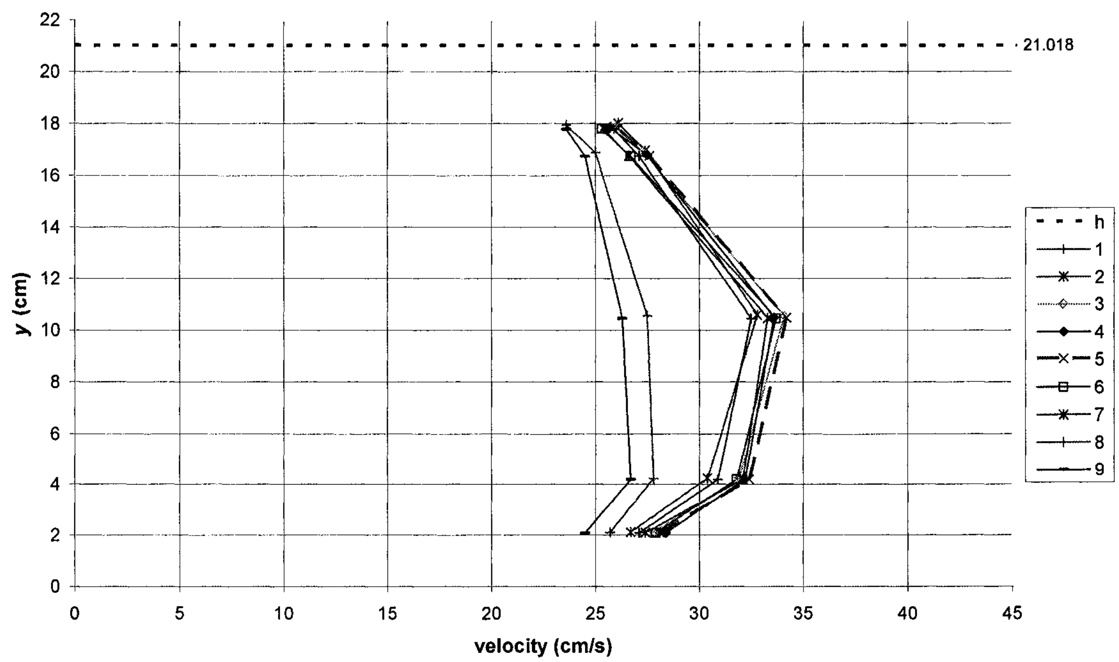

2 SIDES PARTIAL ICE-COVER CONFIGURATION (2PIC)

Lateral velocity profiles

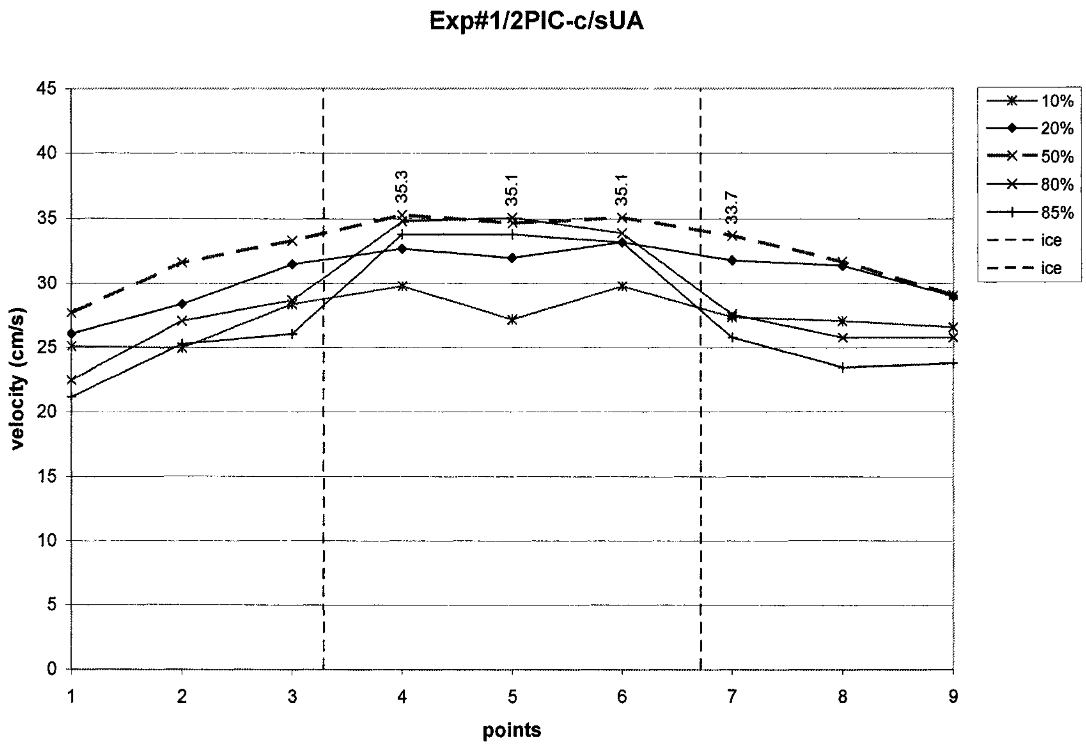

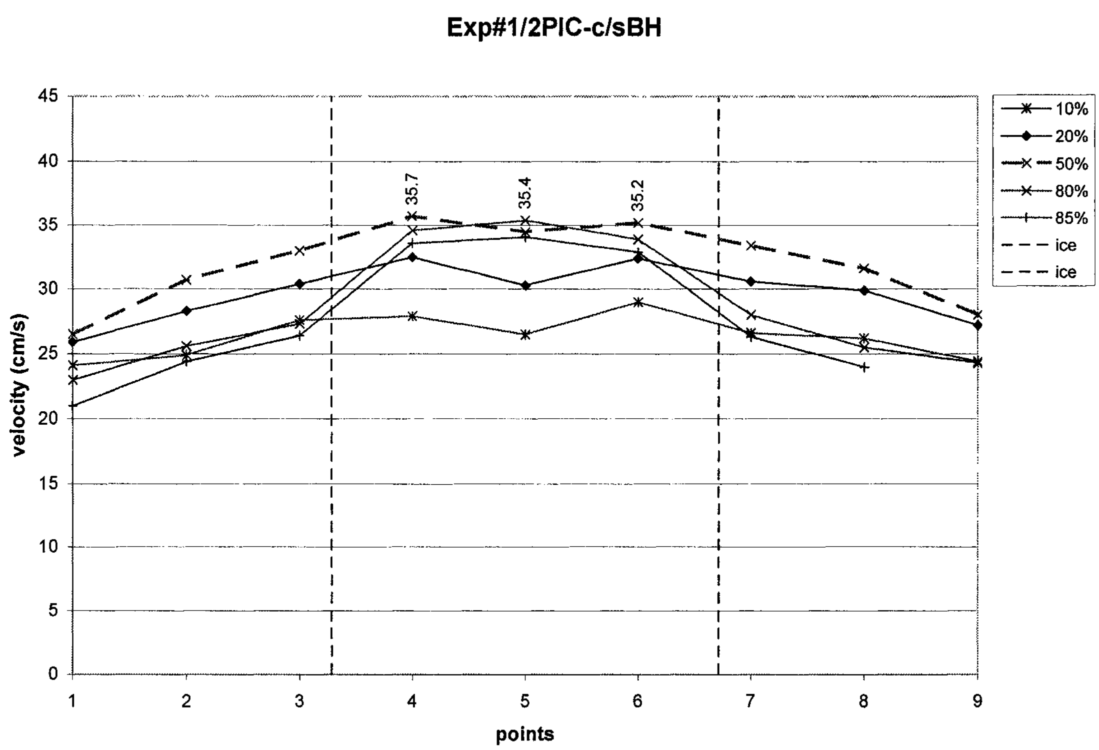

Exp#1/2PIC-c/sBF

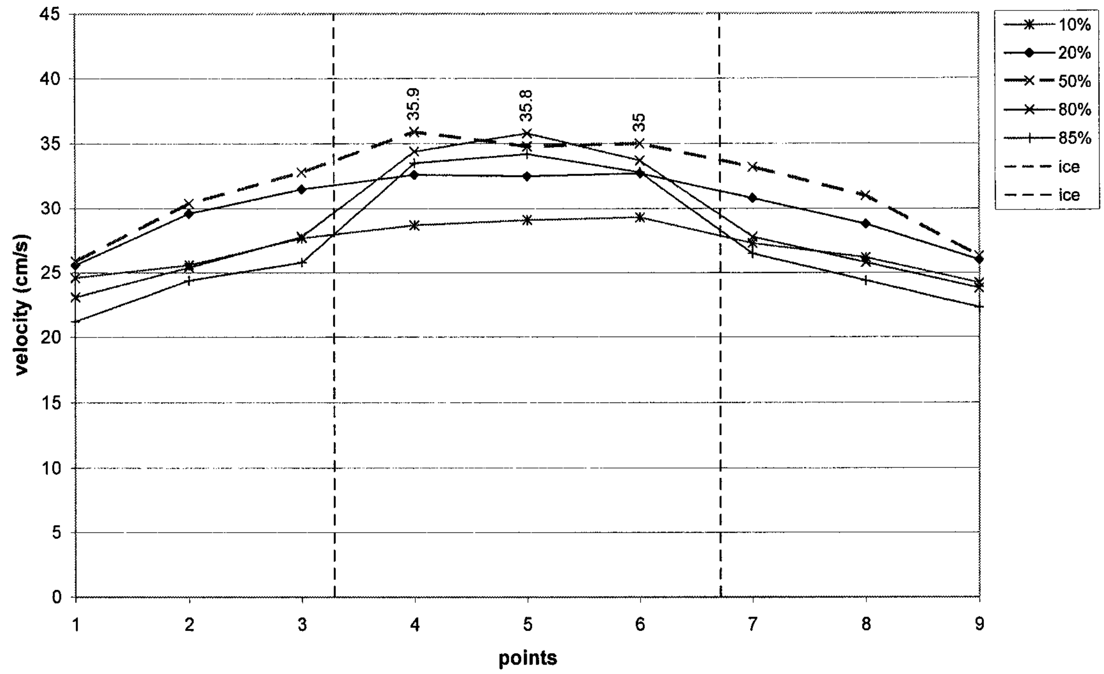

Exp#1/2PIC-c/sBD

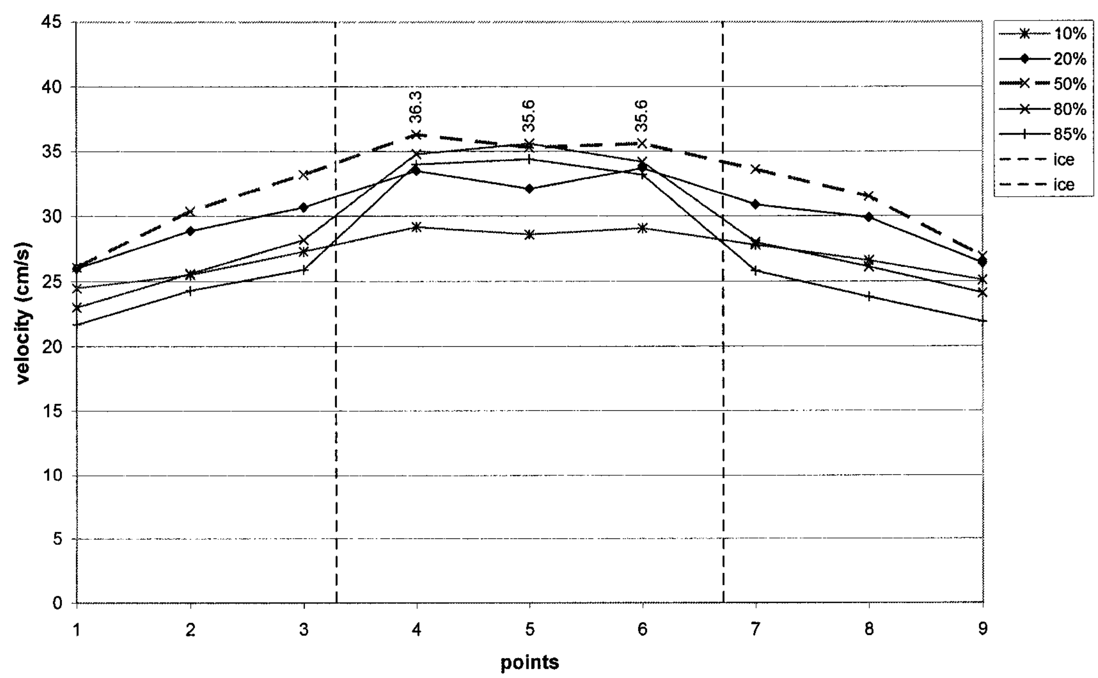

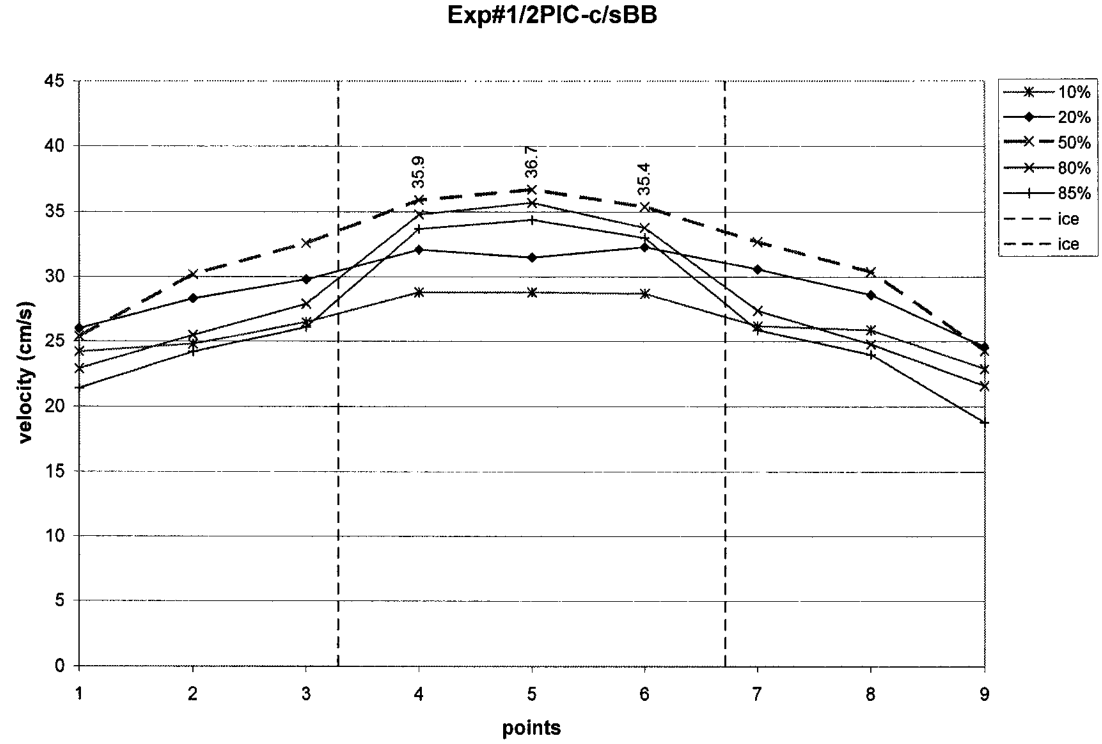

Vertical velocity profiles

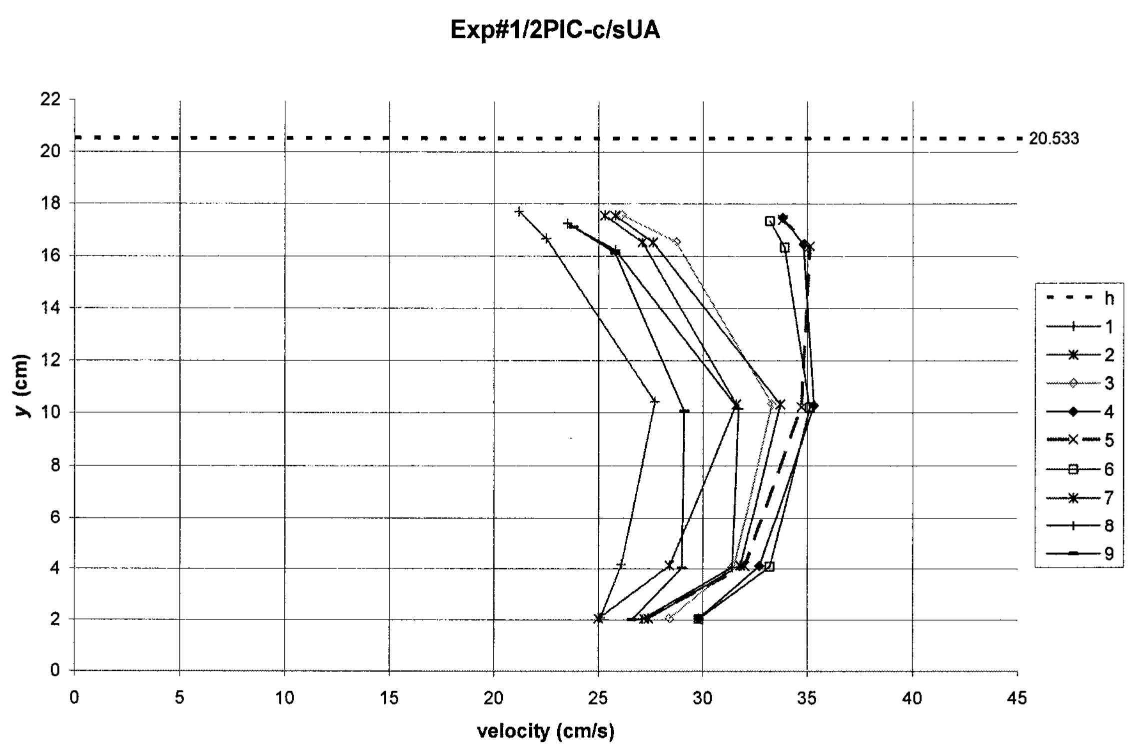

Exp#1/2PIC-c/sBH

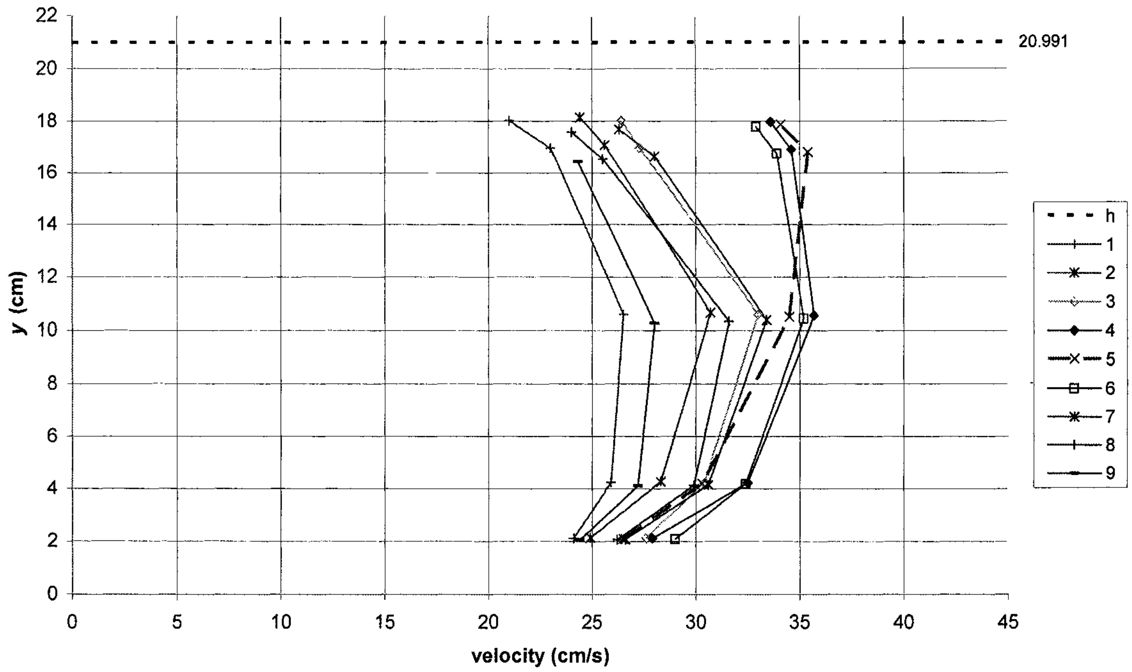

Exp#1/2PIC-c/sBF

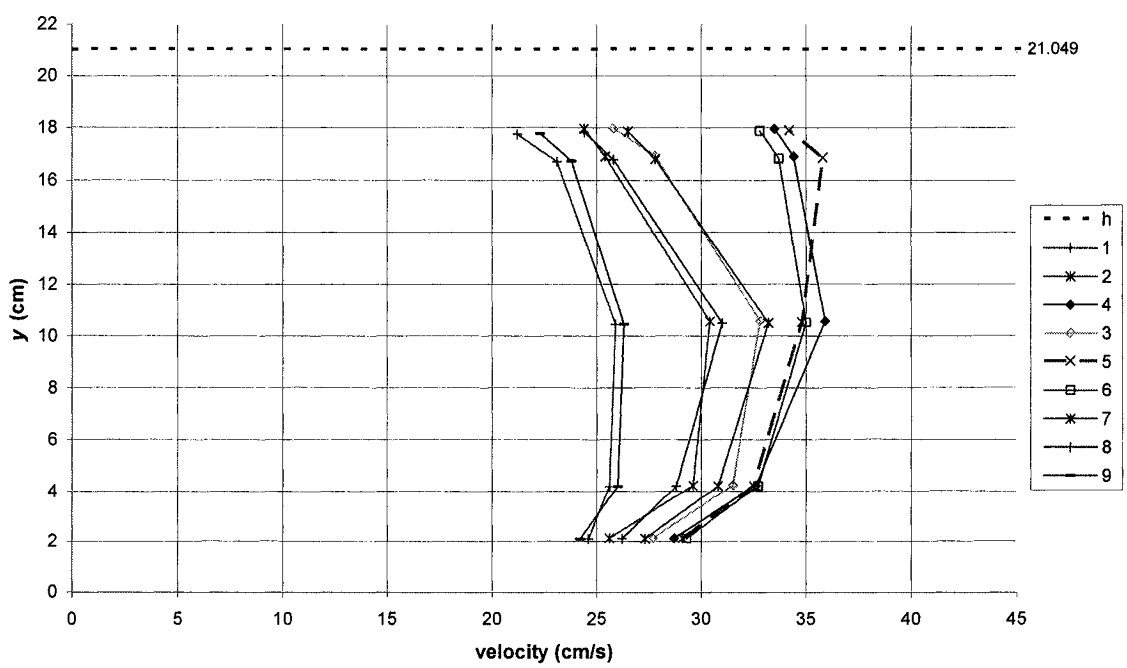

Exp#1/2PIC-c/sBD

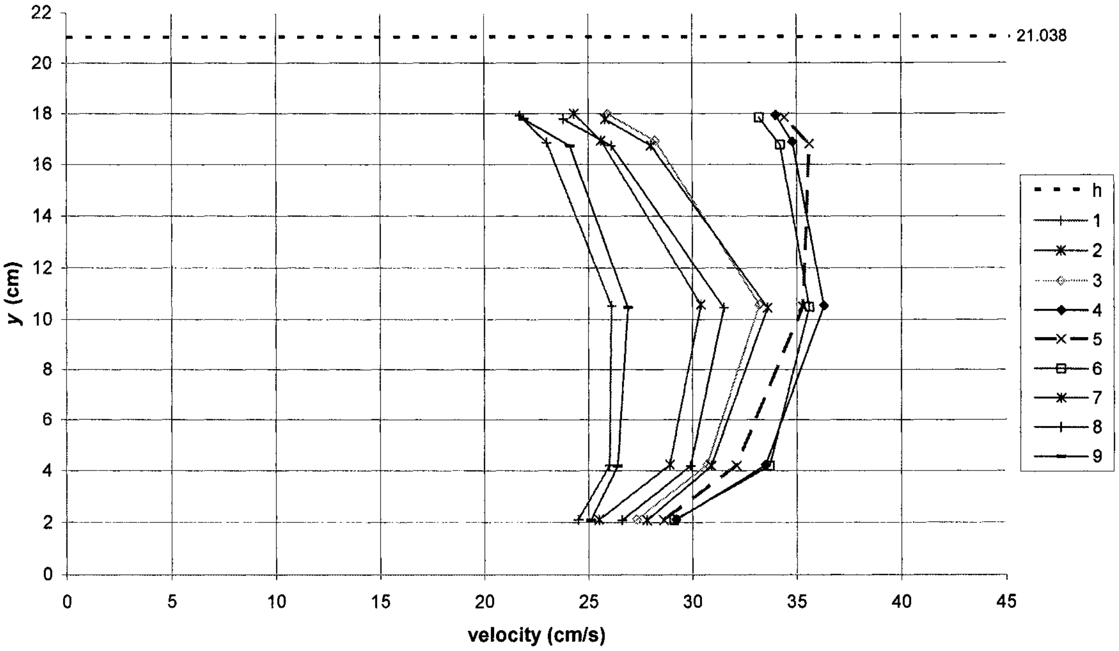

Exp#1/2PIC-c/sBB

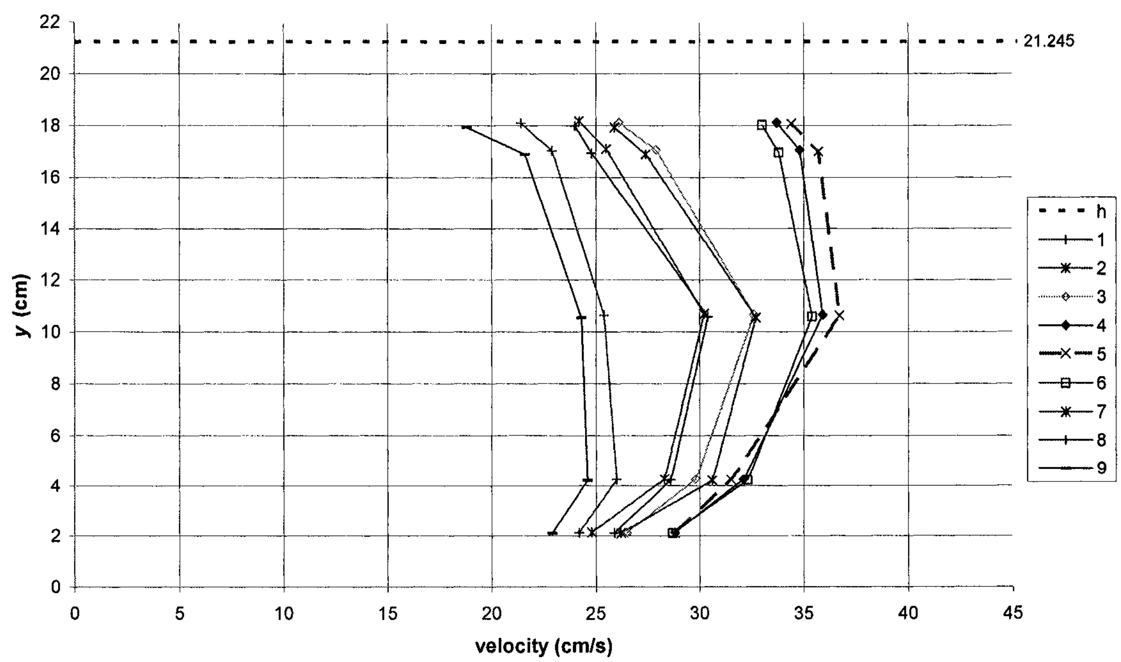

1 SIDE PARTIAL ICE-COVER CONFIGURATION (1PIC)

Lateral velocity profiles

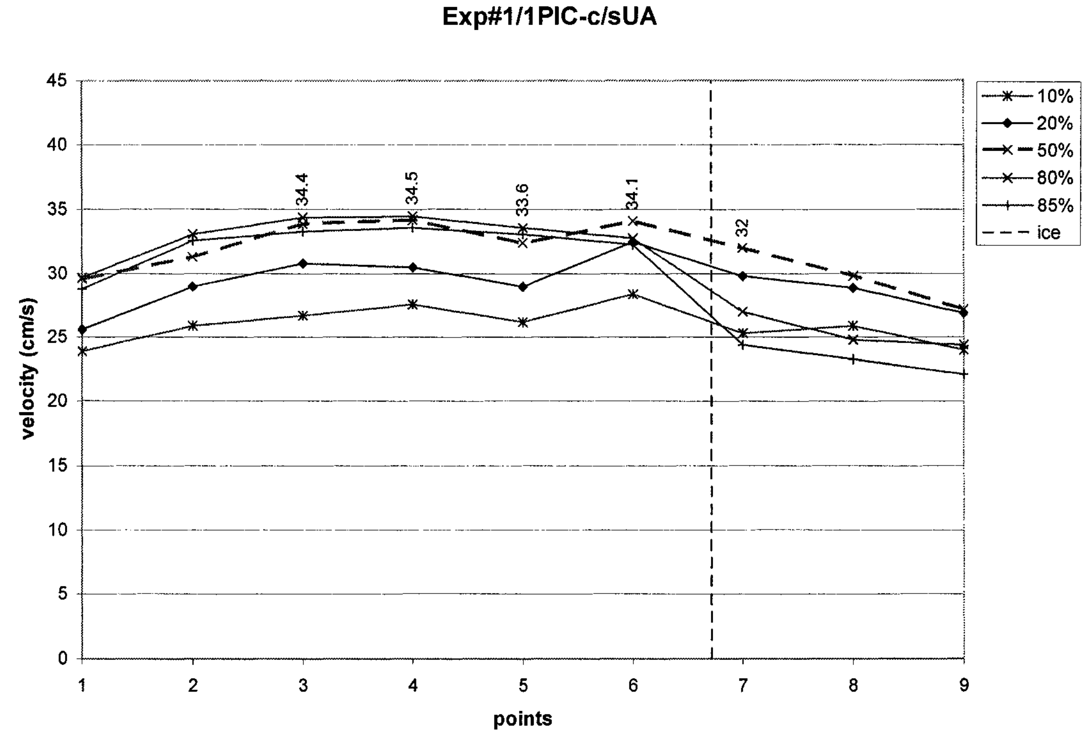

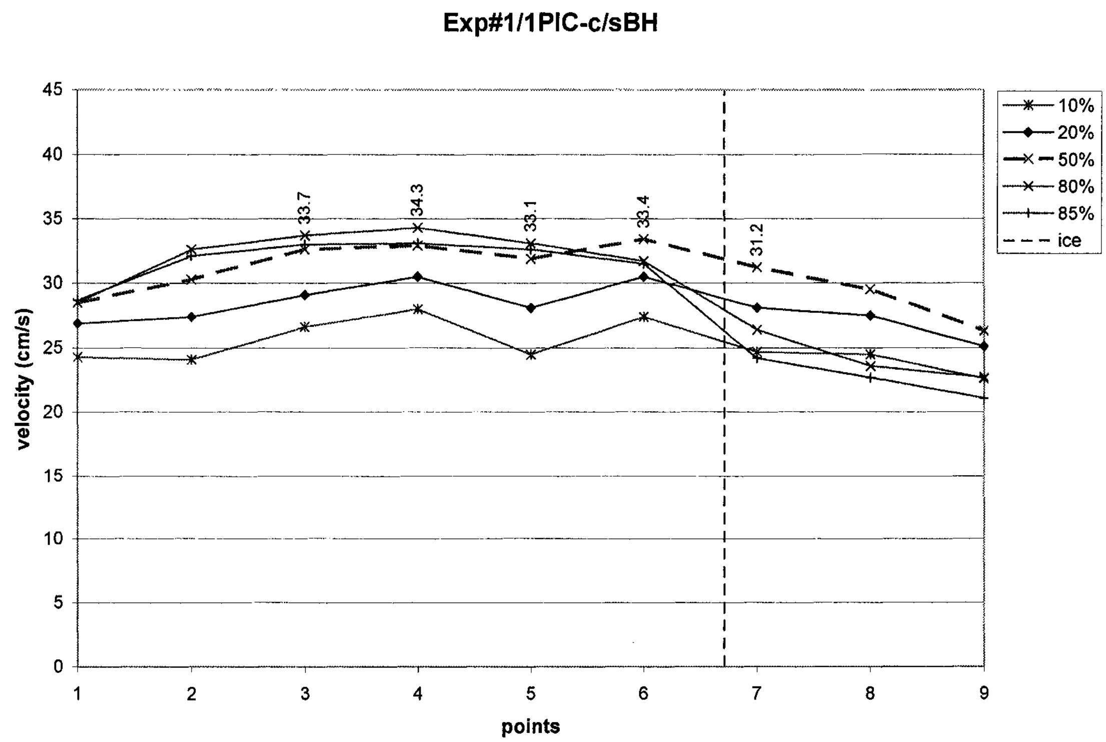

Exp#1/1PIC-c/sBF

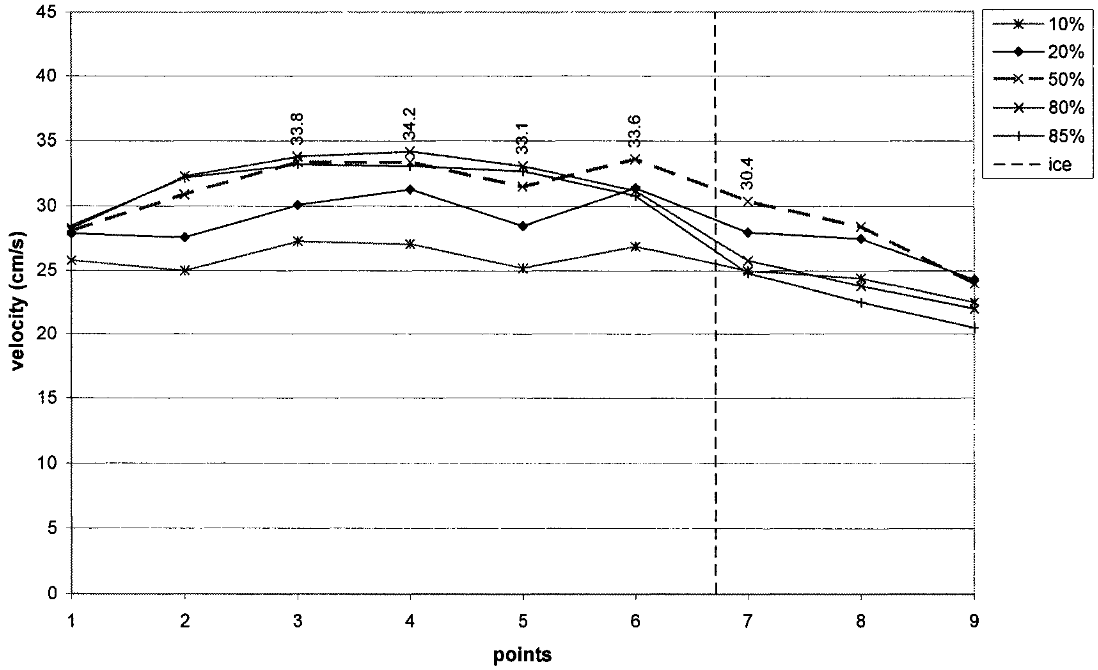

Exp#1/1PIC-c/sBD

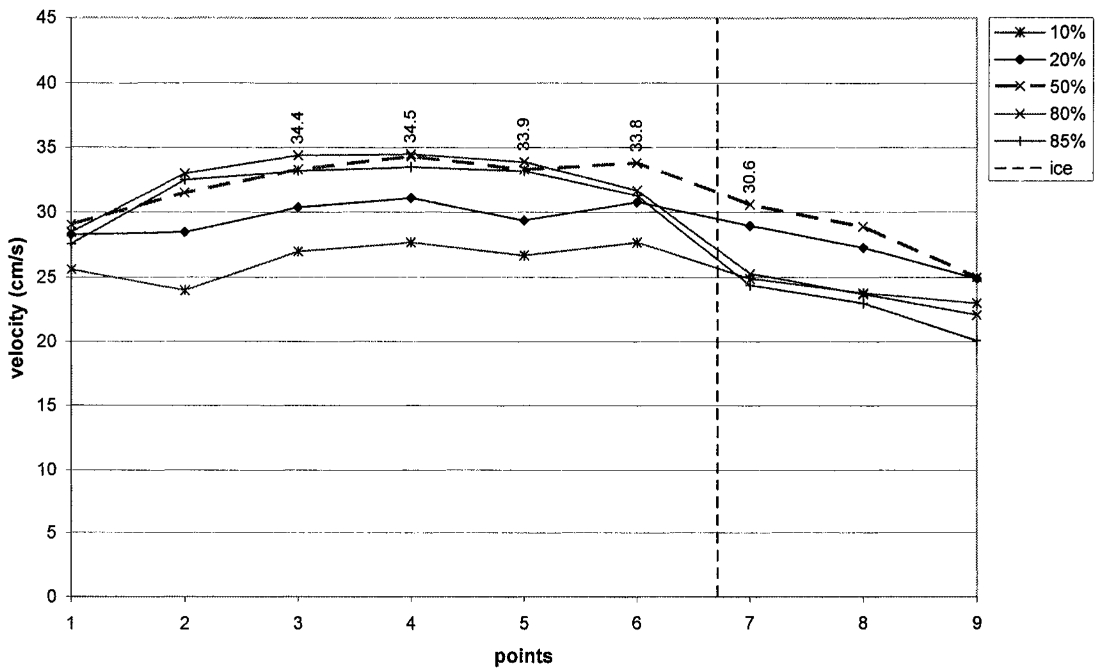

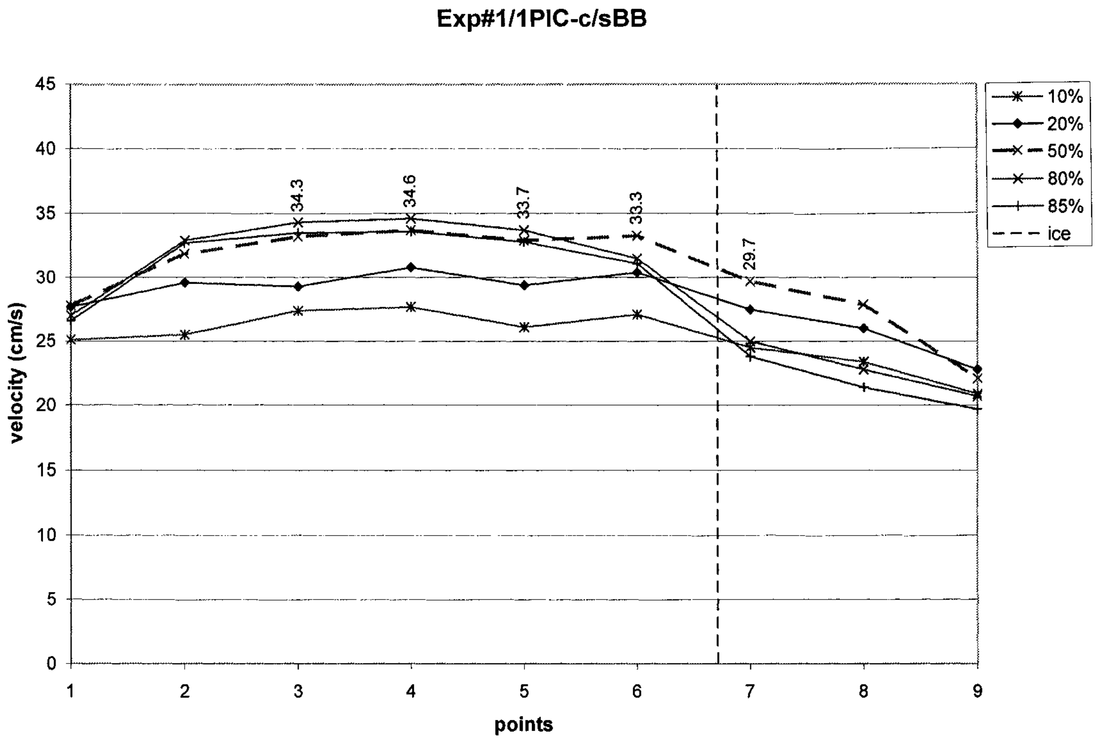

Vertical velocity profiles

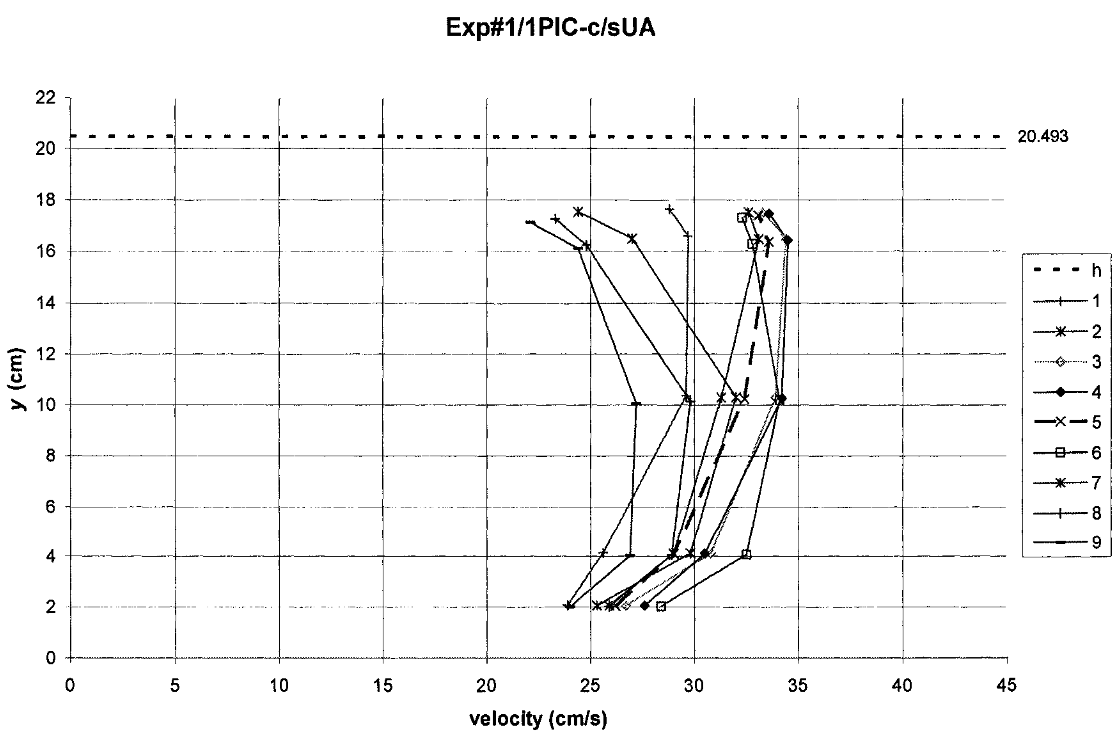

Exp#1/1PIC-c/sBH

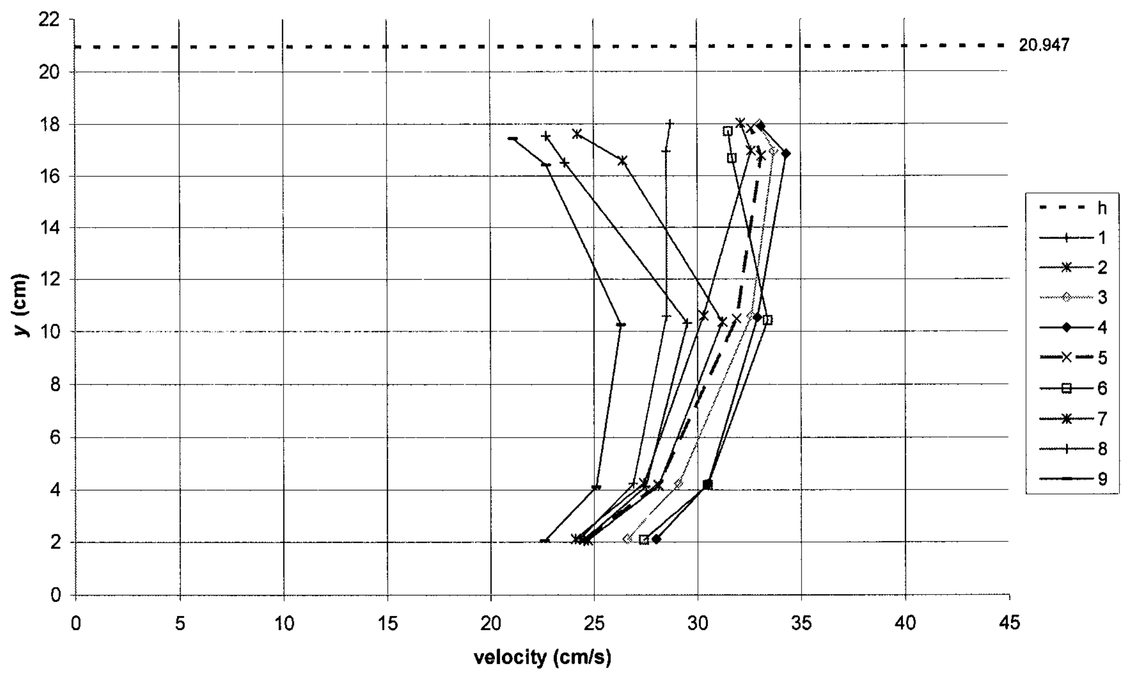

Exp#1/1PIC-c/sBF

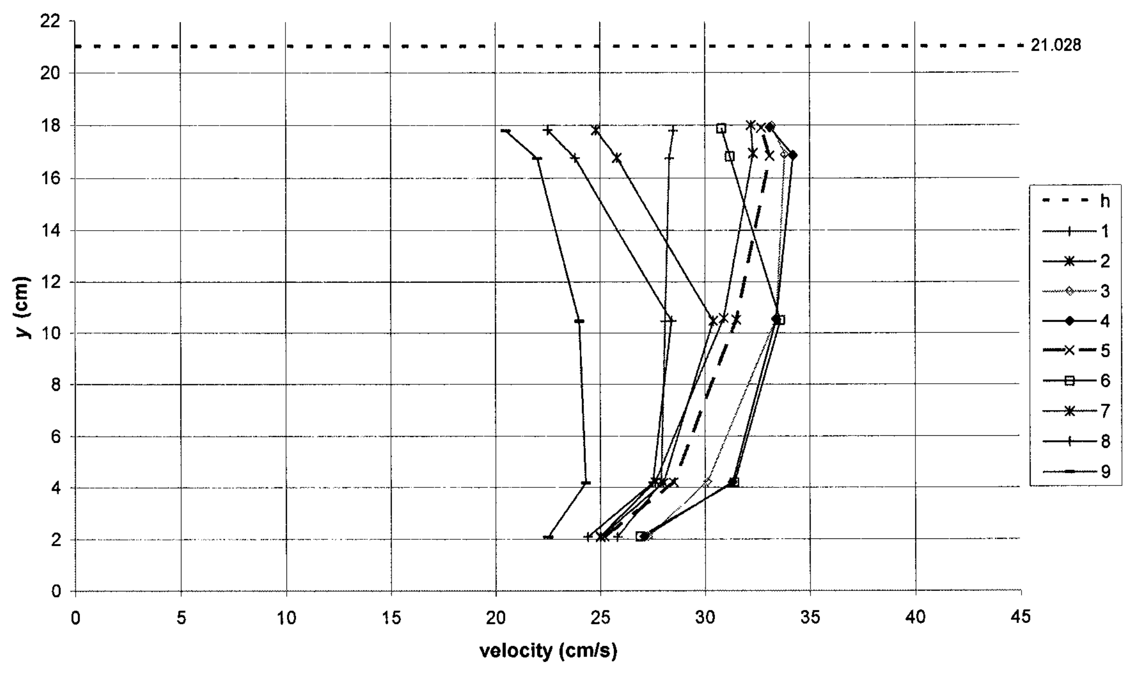

Exp#1/1PIC-c/sBD

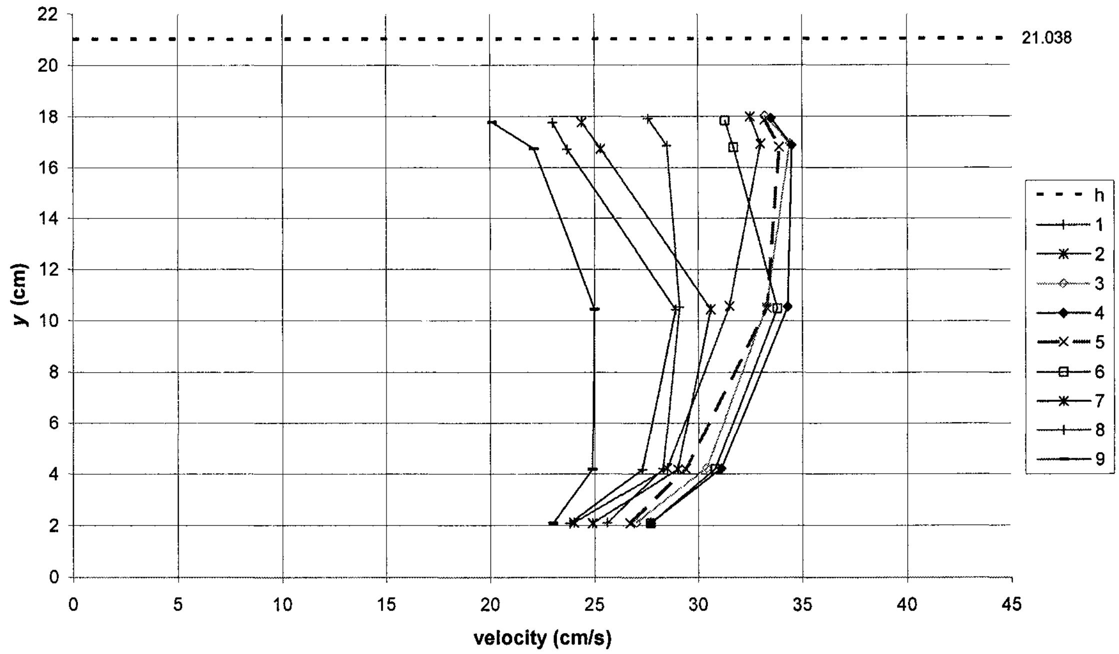

Exp#1/1PIC-c/sBB

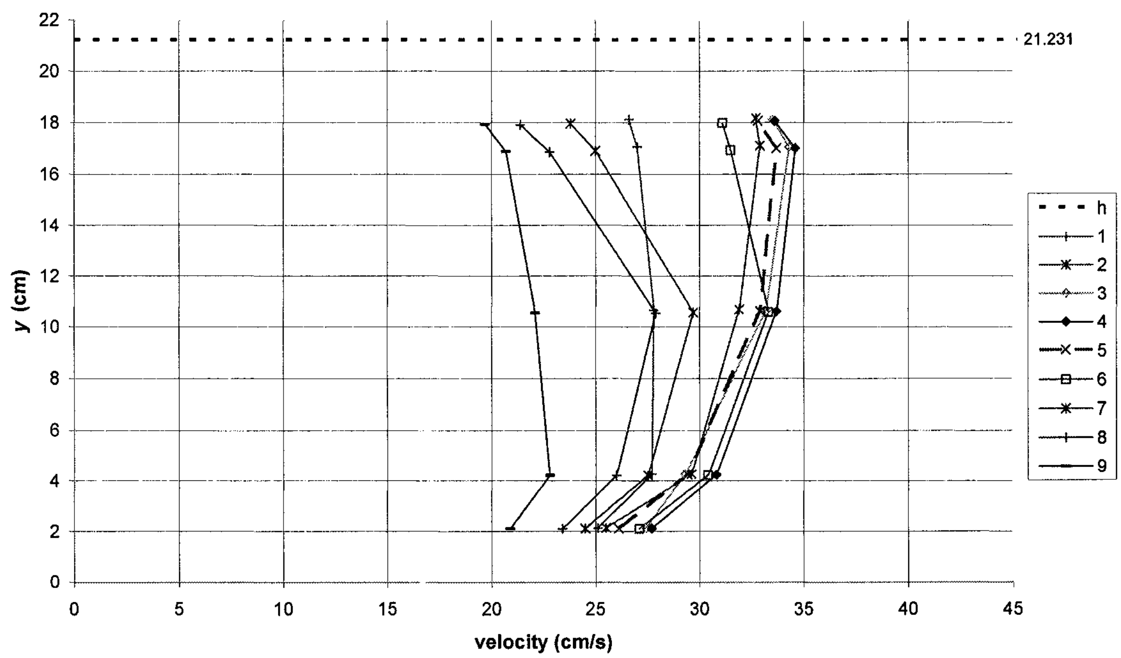

FREE-SURFACE CONFIGURATION (FS)

Lateral velocity profiles

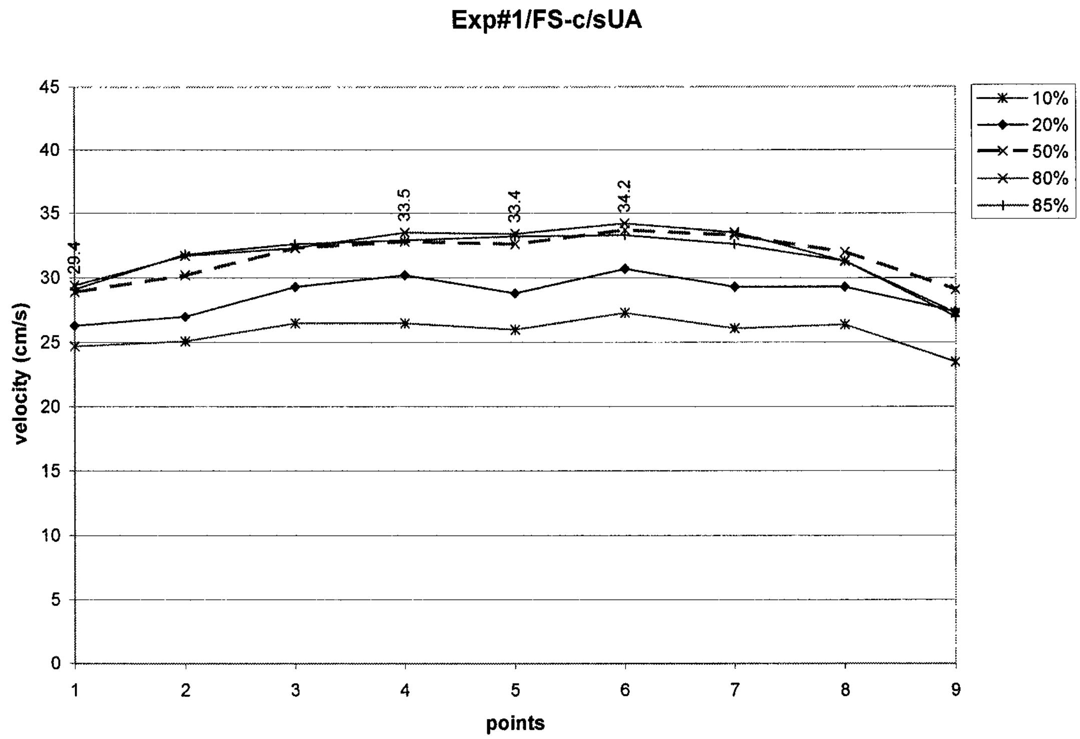

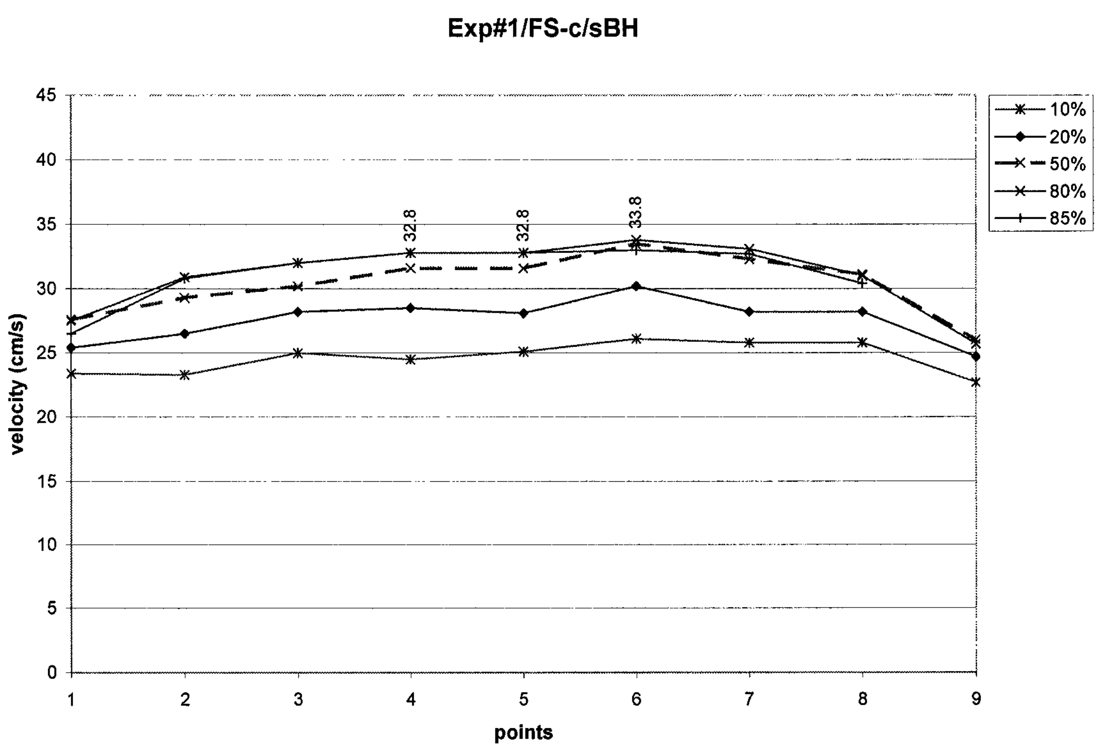

Vertical velocity profiles

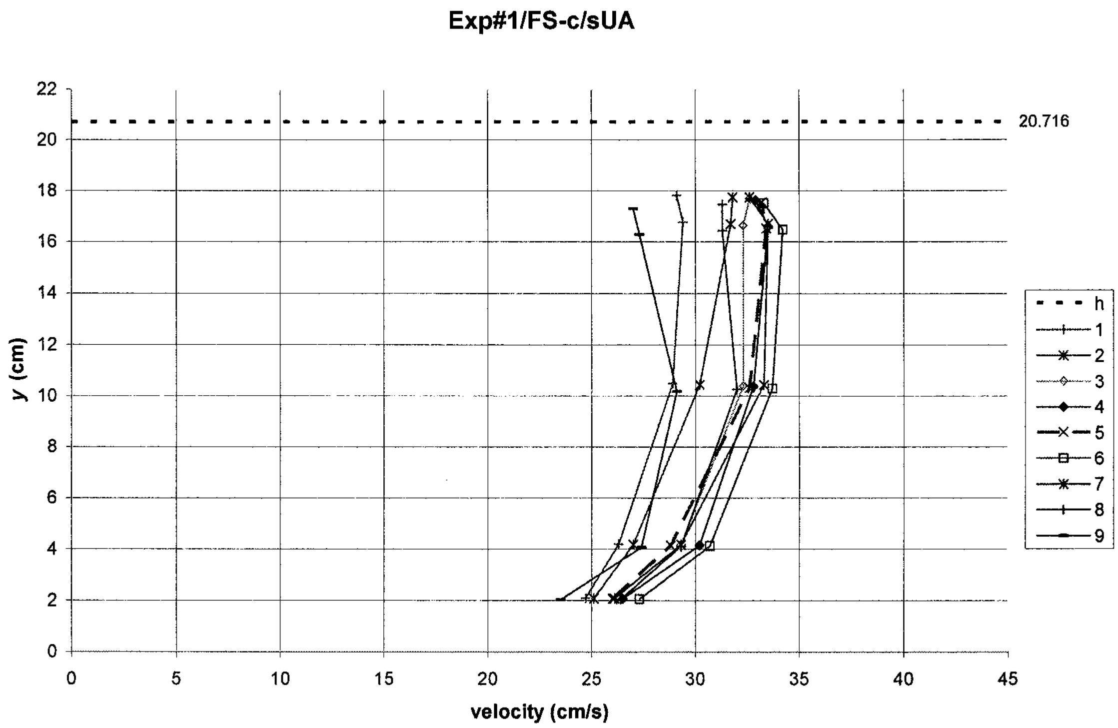

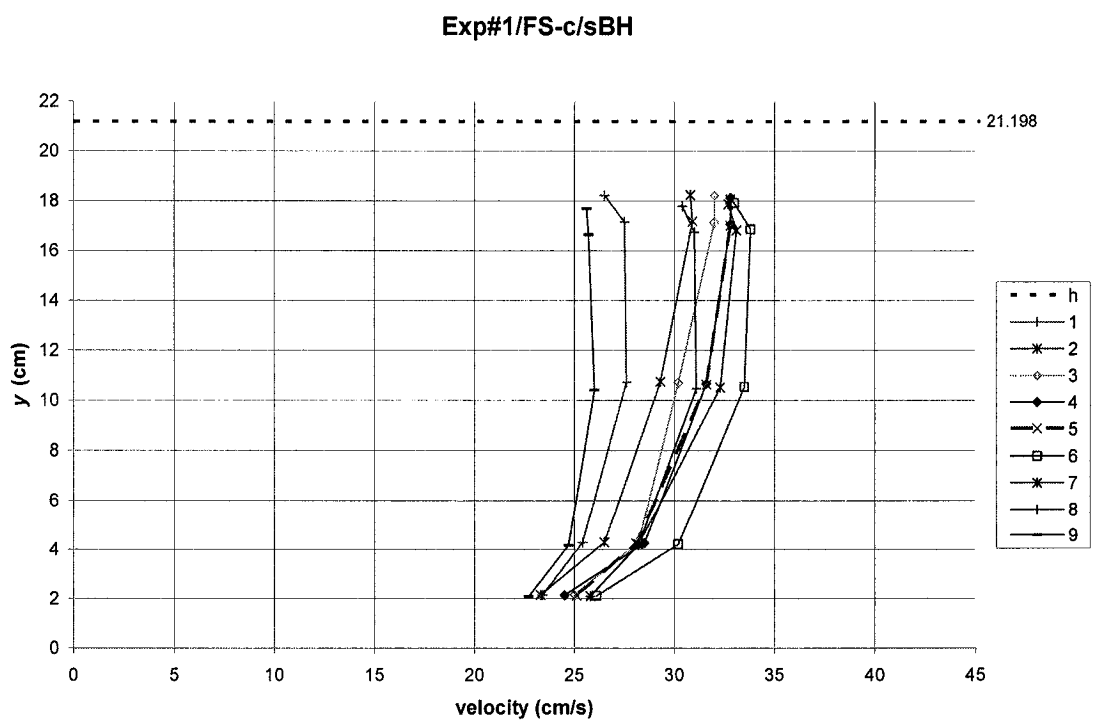

APPENDIX A4

Exp#4

TOTAL ICE-COVER (TIC), 2SIDES PARTIAL ICE-COVER (2PIC) and FREE-SURFACE (FS) CONFIGURATIONS at ice-cover critical conditions

(experiment without bridge pier)

TOTAL ICE-COVER CONFIGURATION (TIC) – Q≈0.043m^3/s

Lateral velocity profiles

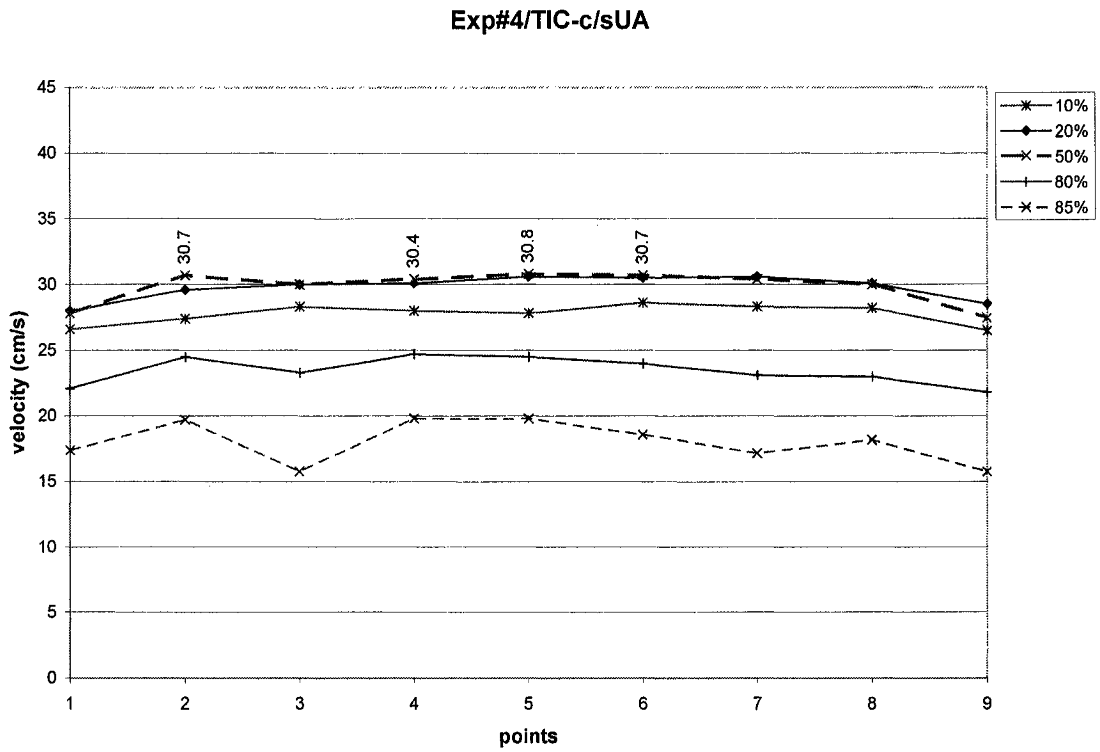

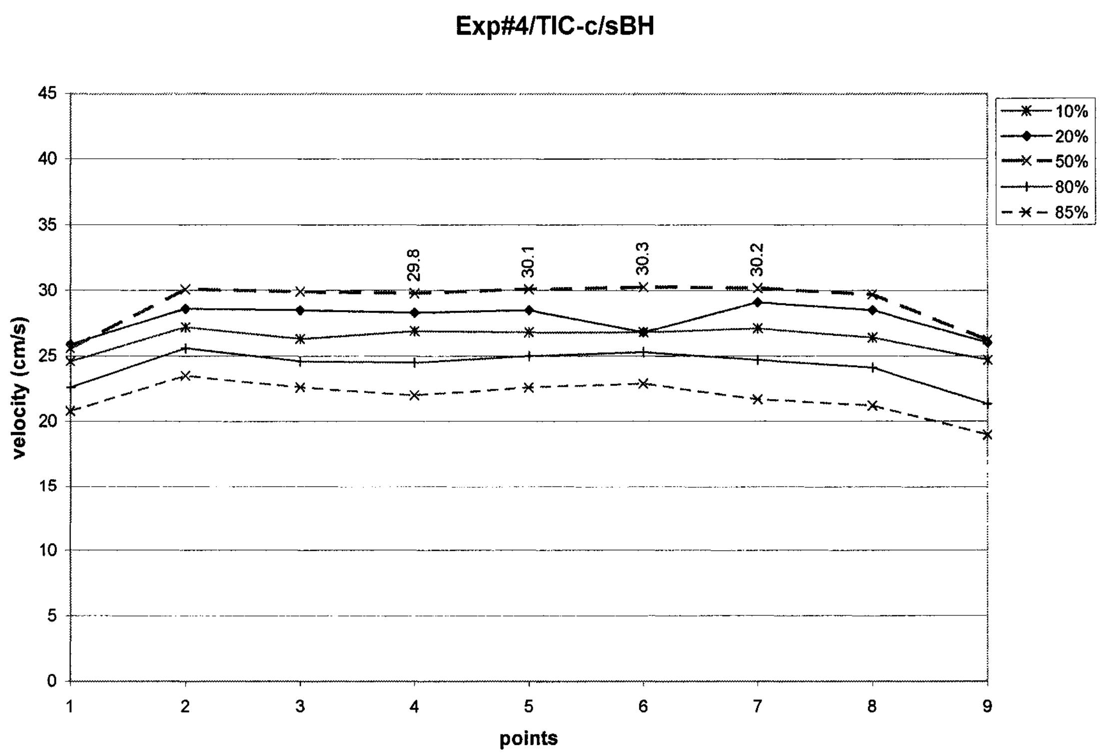

Exp#4/TIC-c/sBG

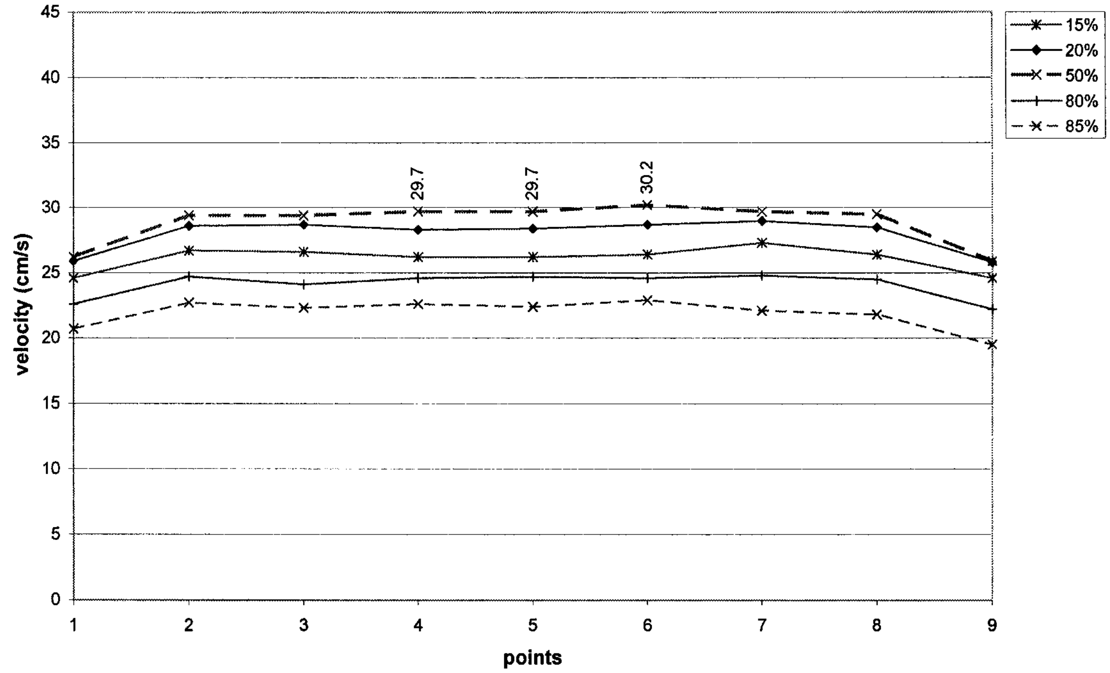

Exp#4/TIC-c/sBF

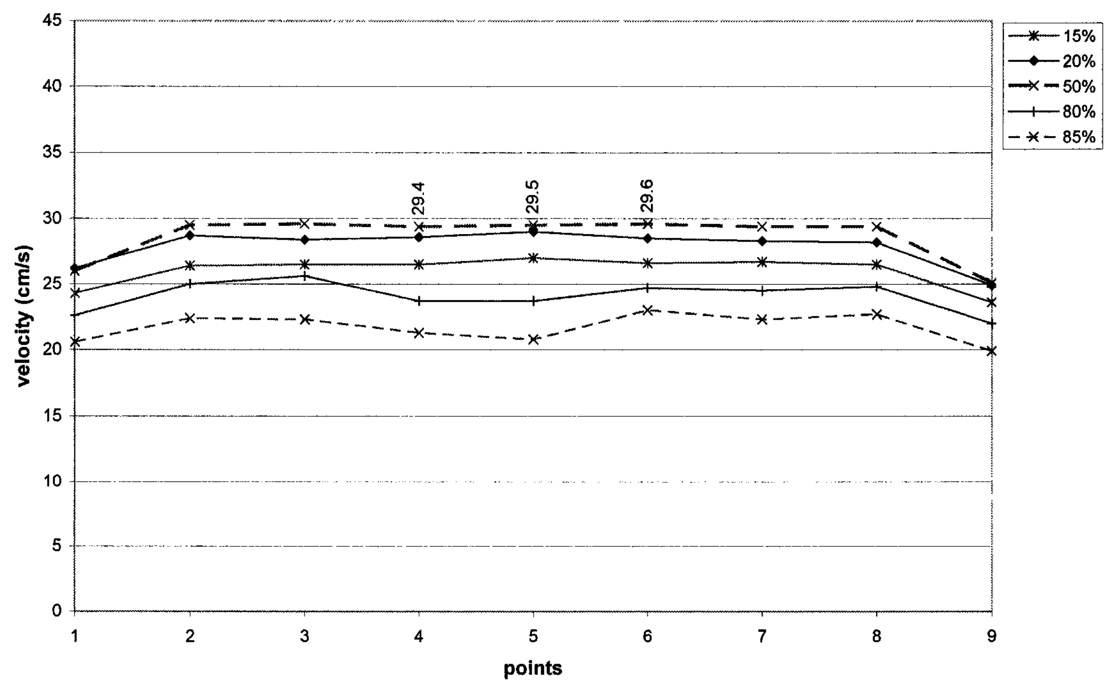

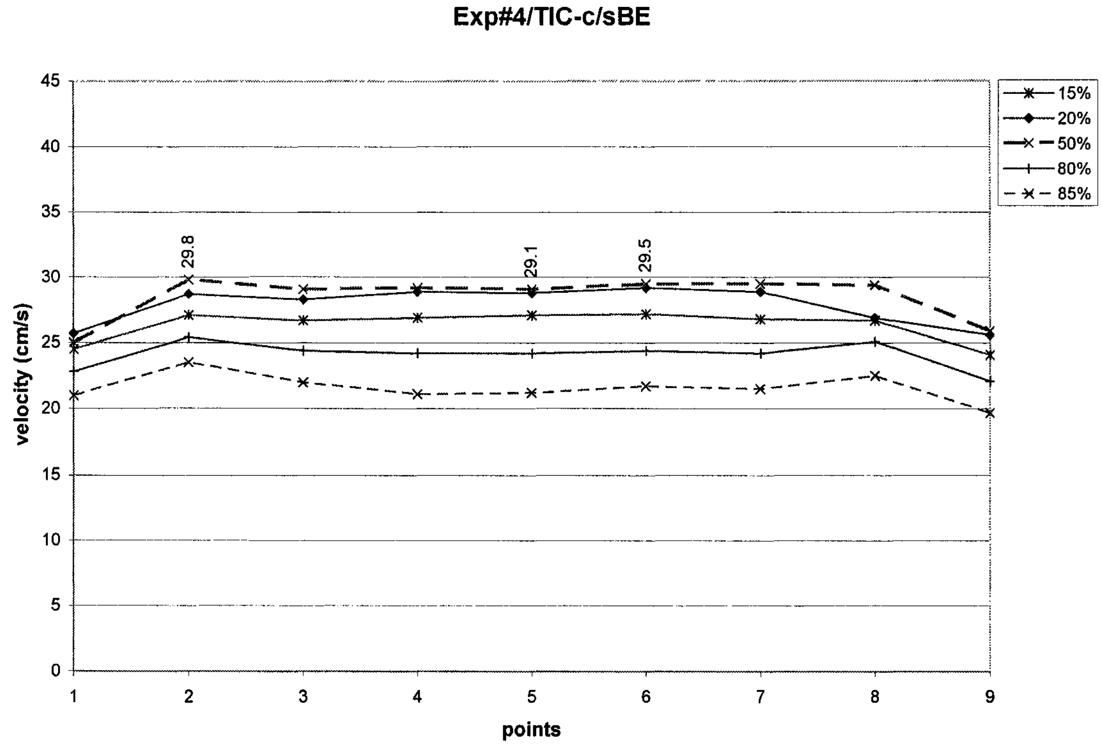
Exp#4/TIC-c/sBE
velocity (cm/s)
points
15%
20%
50%
80%
85%
29.8
29.1
29.5

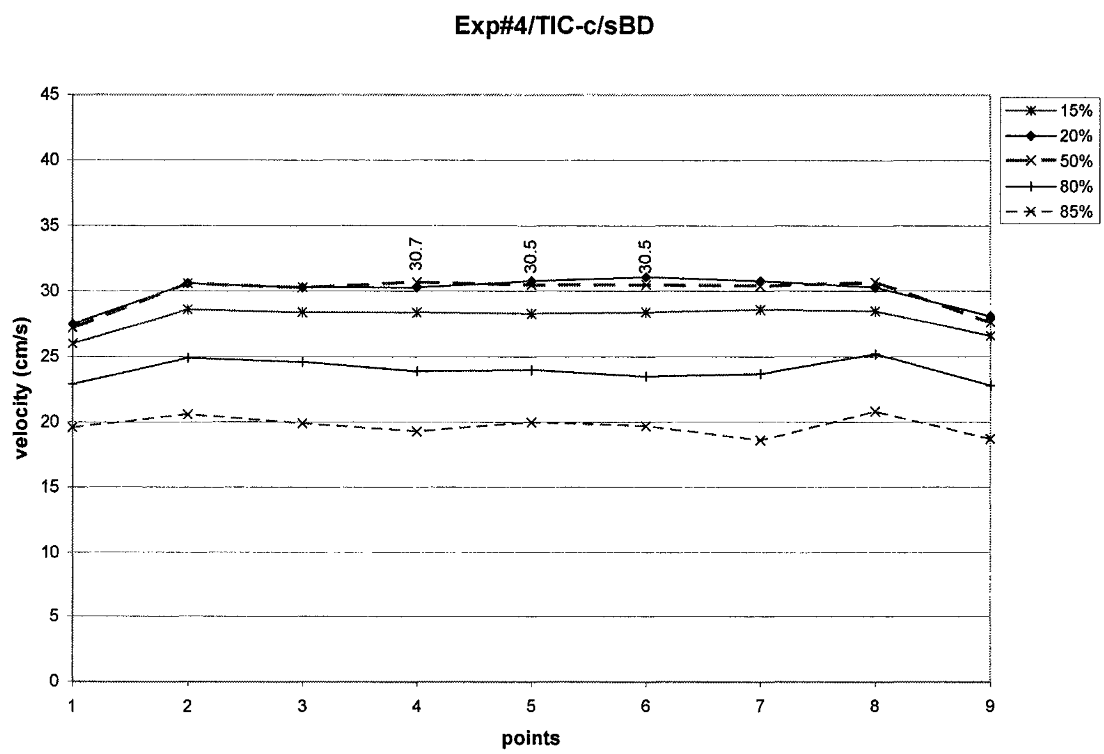
Exp#4/TIC-c/sBD
velocity (cm/s)
points
15%
20%
50%
80%
85%
30.7
30.5
30.5

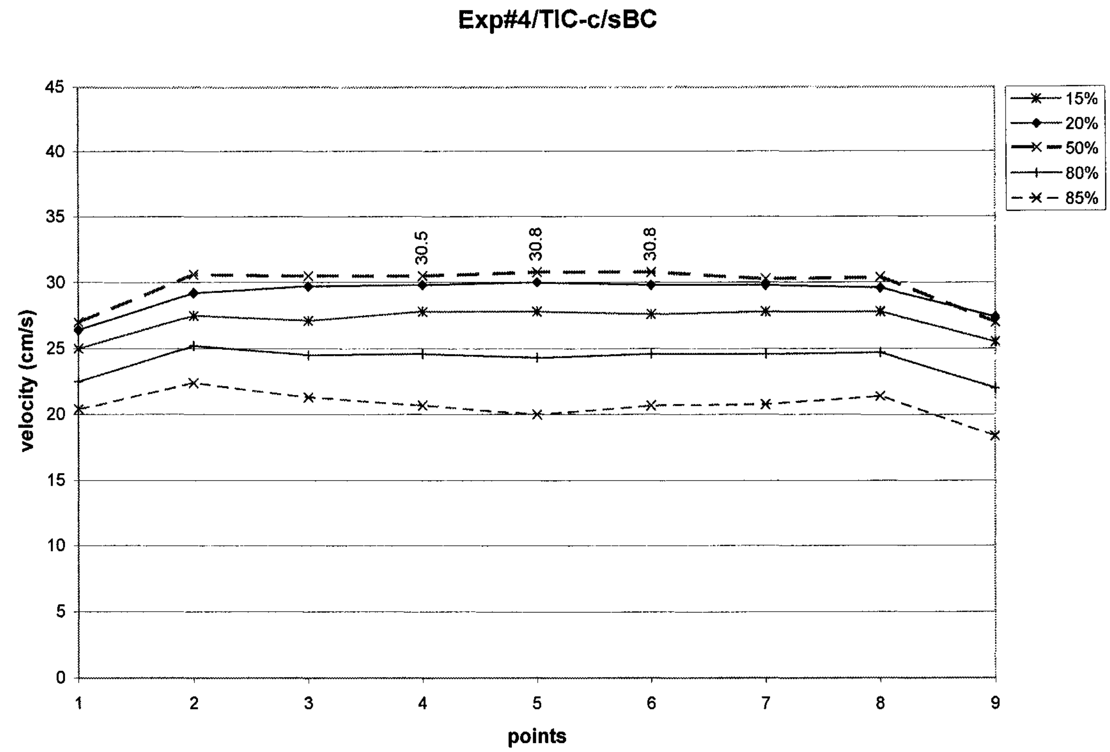
Exp#4/TIC-c/sBC
velocity (cm/s)
points
15%
20%
50%
80%
85%
30.5
30.8
30.8

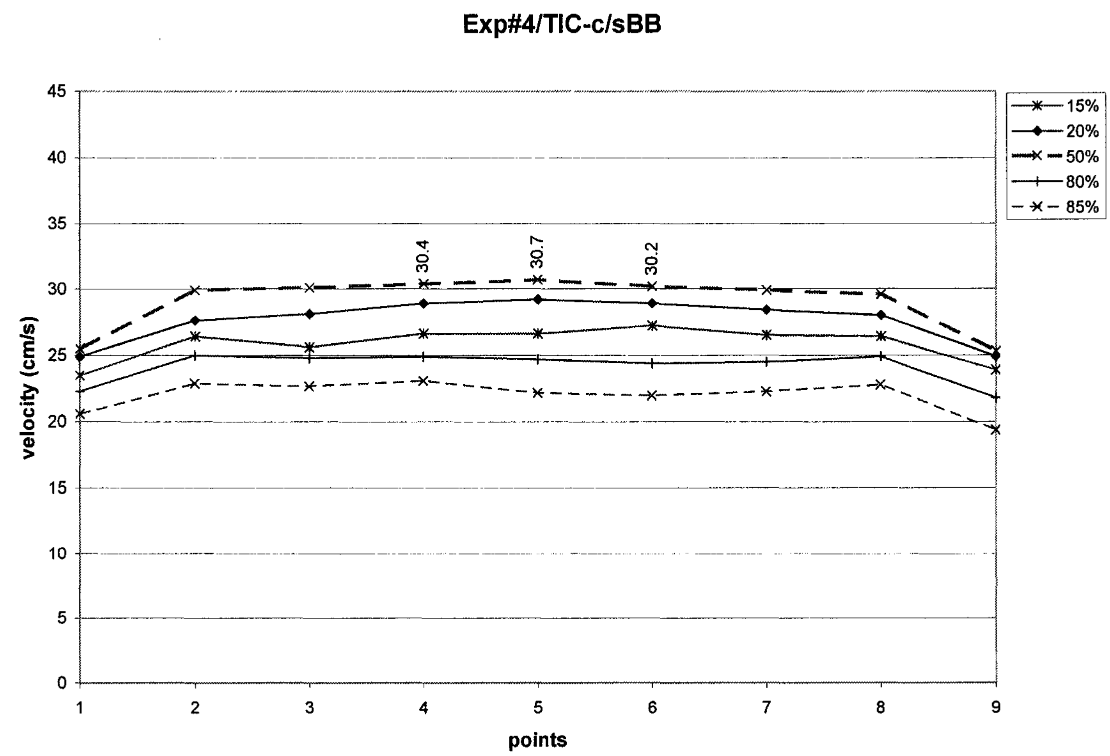
Exp#4/TIC-c/sBB
velocity (cm/s)
points
15%
20%
50%
80%
85%
30.4
30.7
30.2

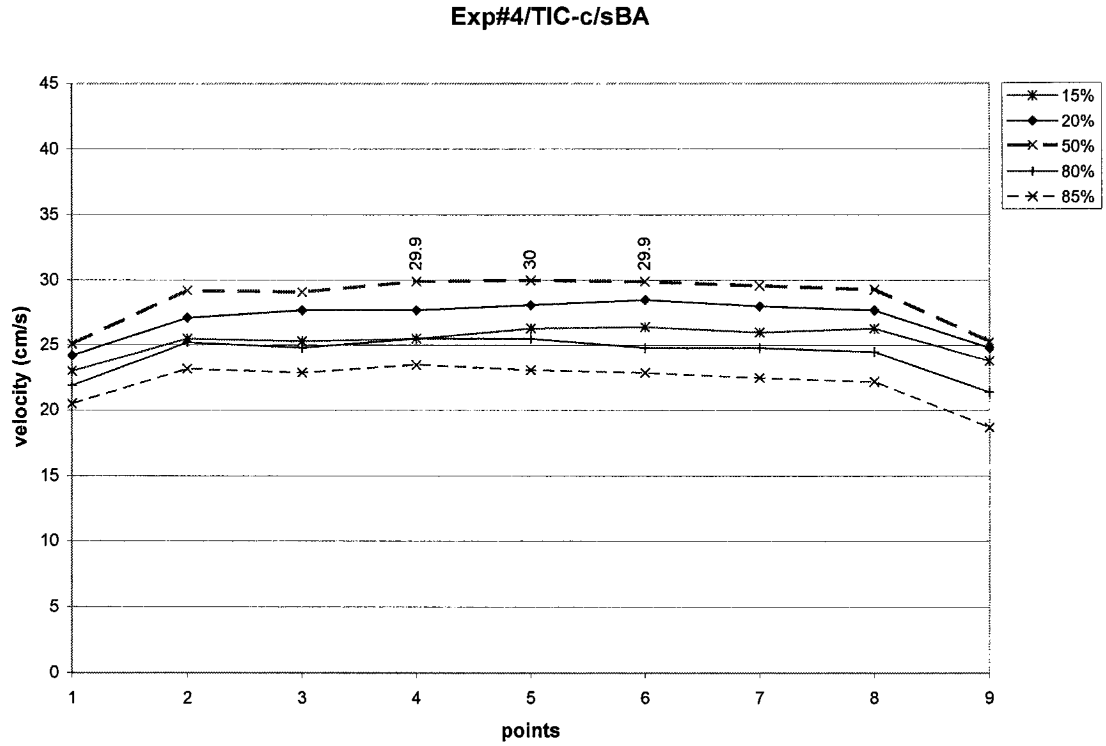

Vertical velocity profiles

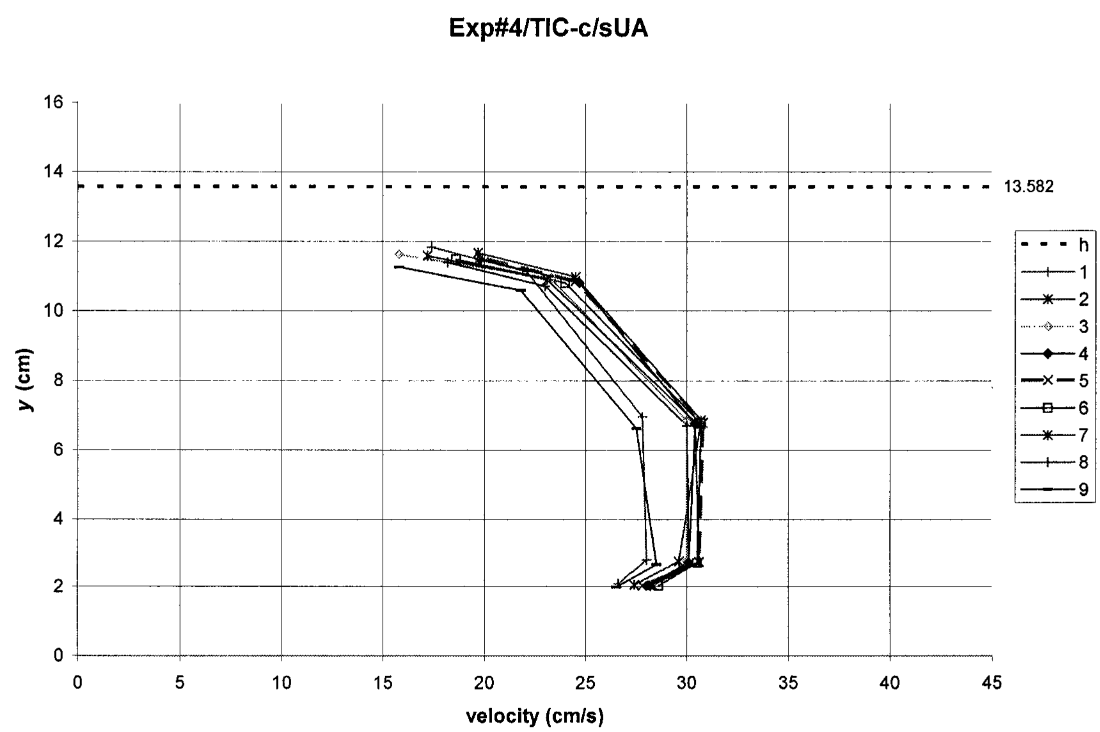

Exp#4/TIC-c/sBH

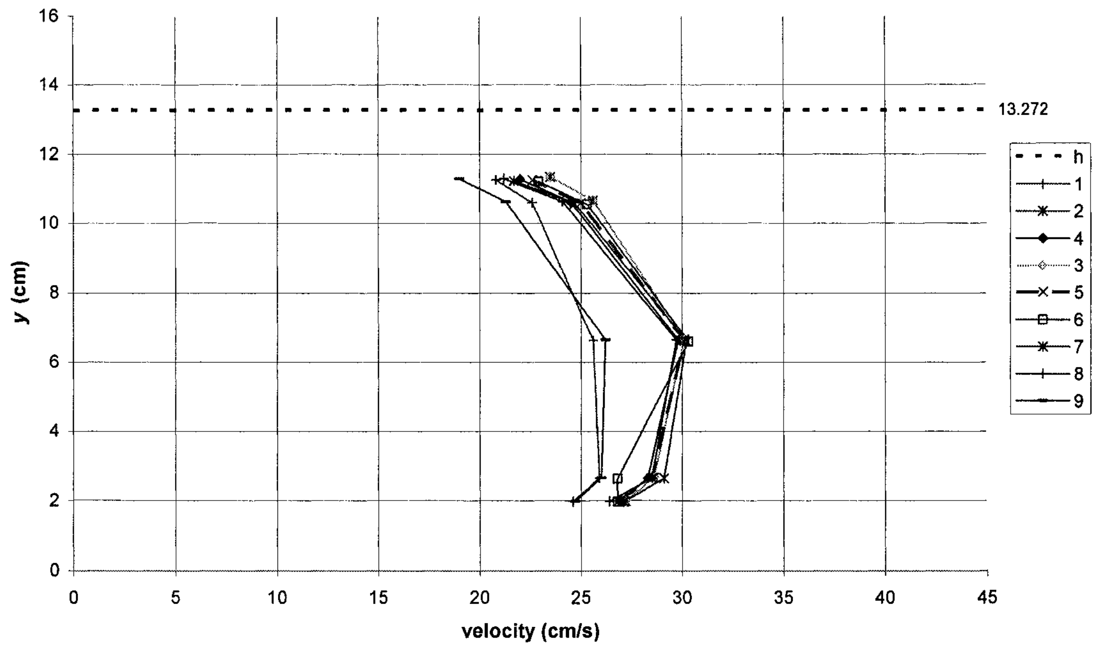

Exp#4/TIC-c/sBG

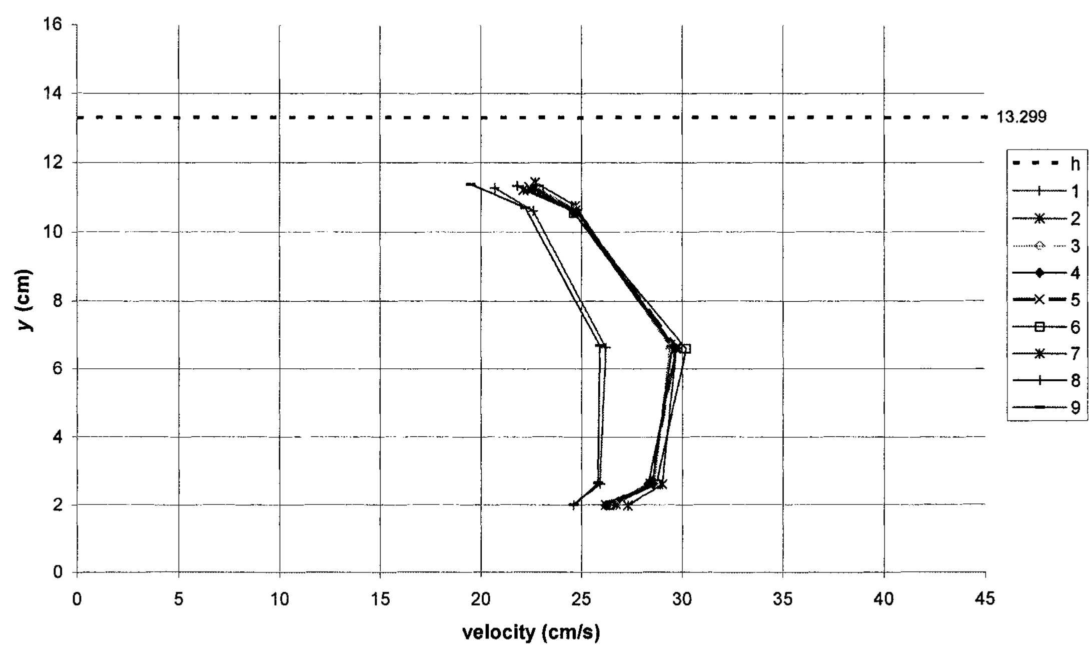

Exp#4/TIC-c/sBF

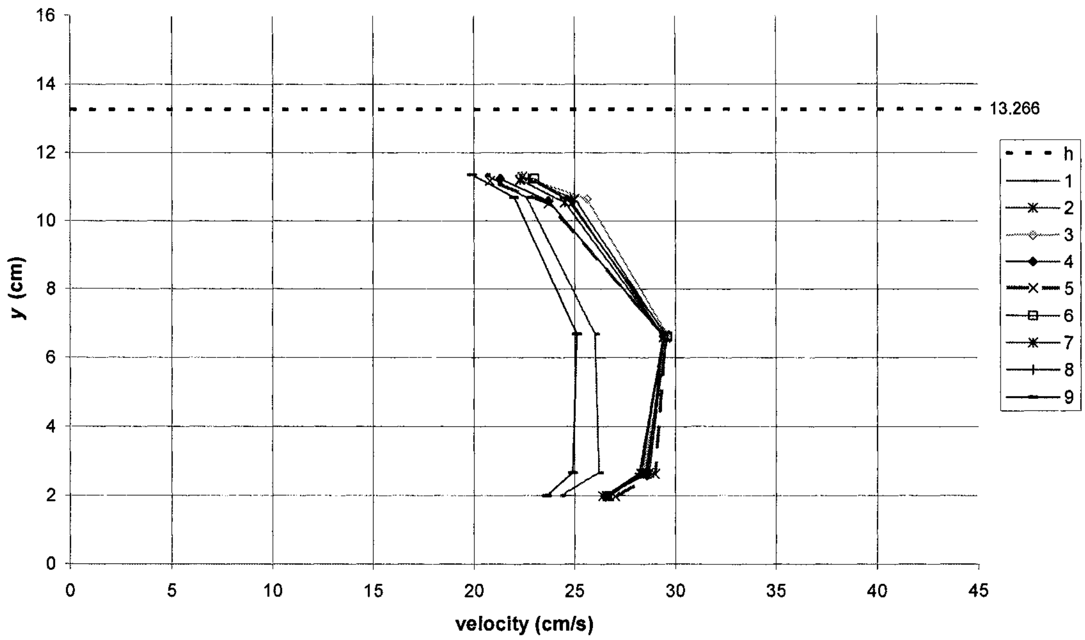

Exp#4/TIC-c/sBE

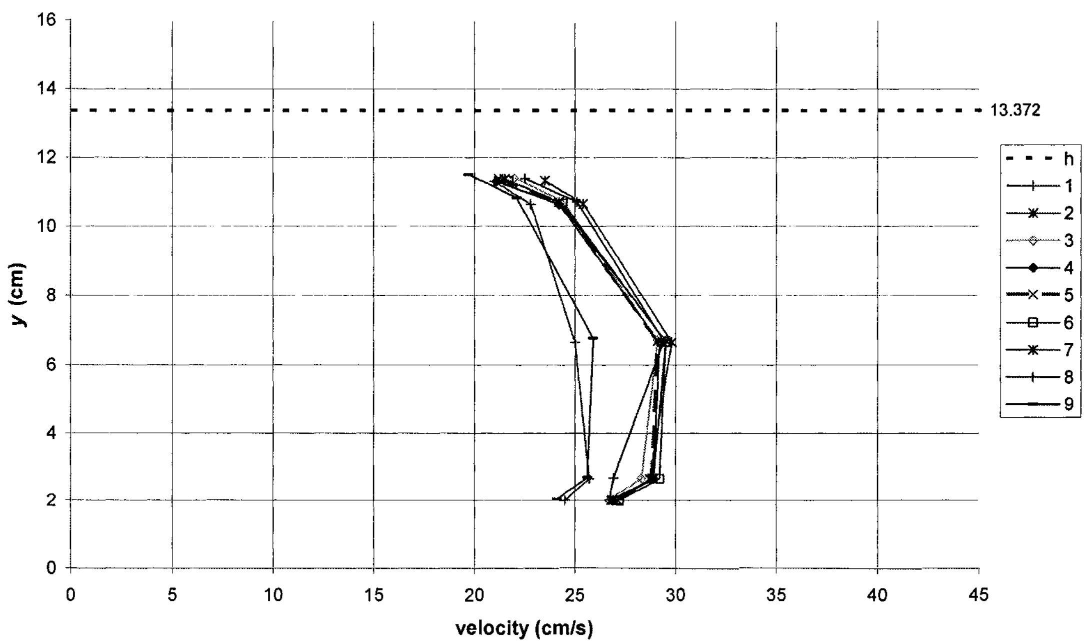

Exp#4/TIC-c/sBD

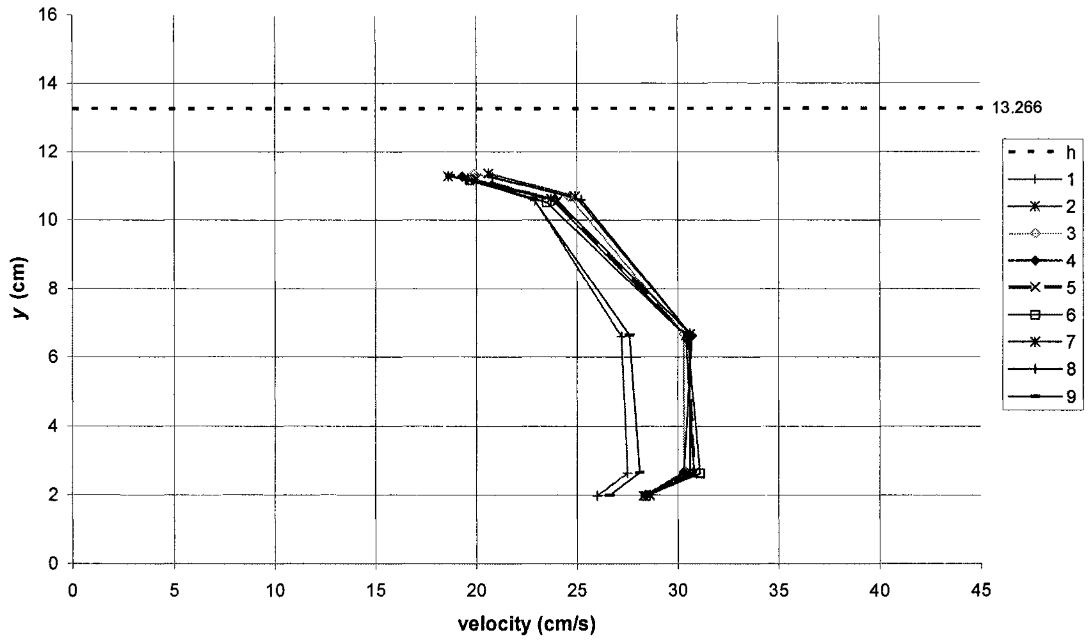

Exp#4/TIC-c/sBC

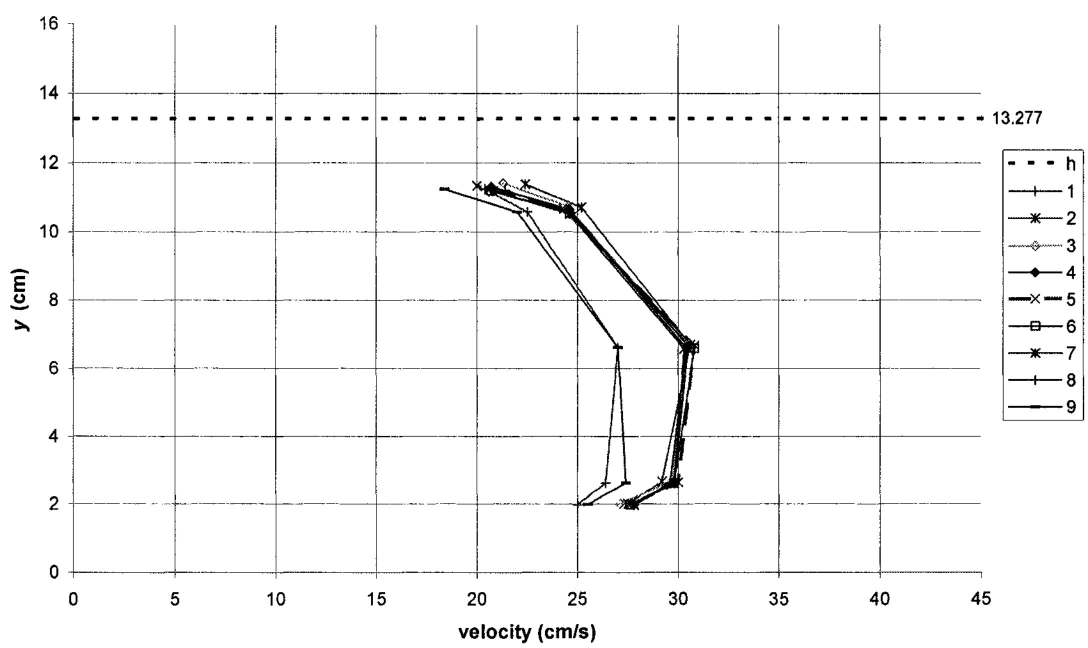

Exp#4/TIC-c/sBB

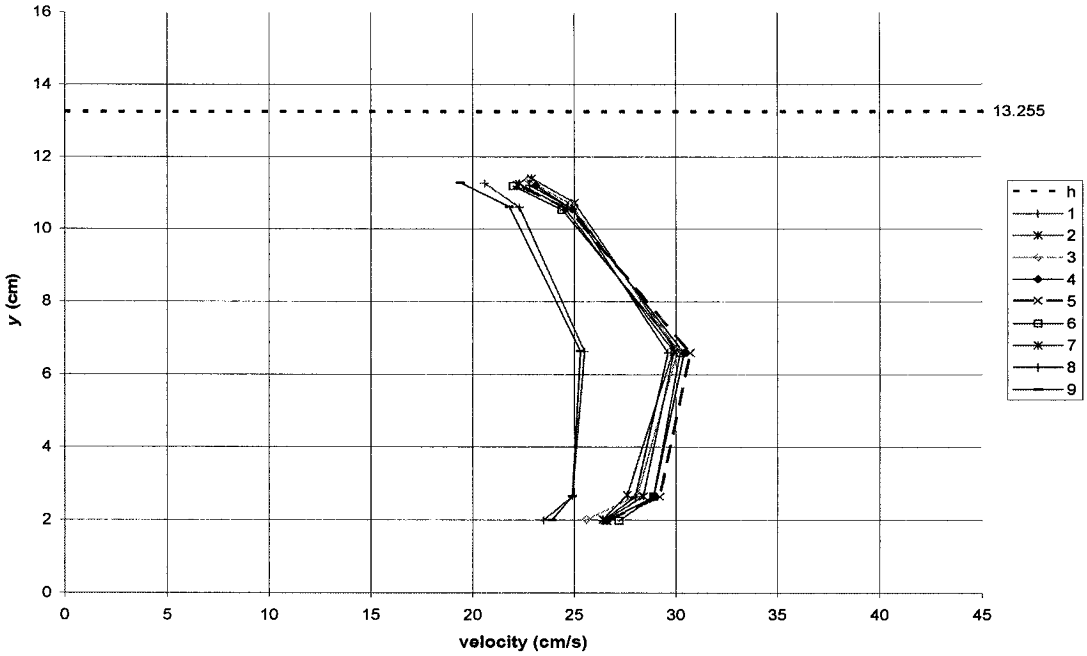

Exp#4/TIC-c/sBA

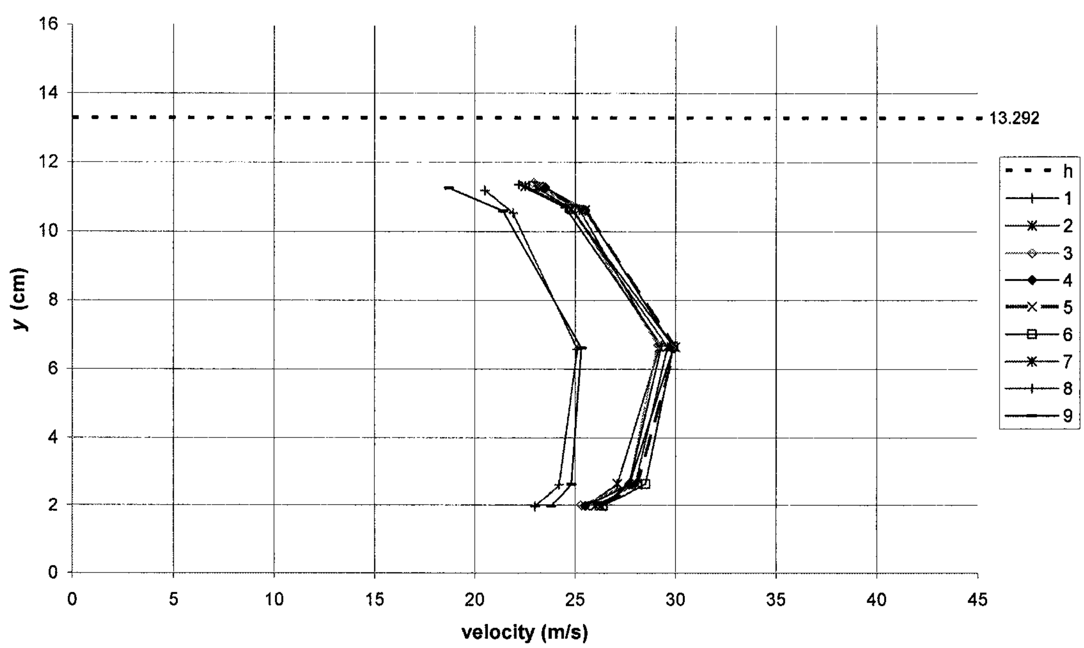

2 SIDES PARTIAL ICE-COVER CONFIGURATION (2PIC) - $Q \approx 0.043 m^3/s$

Lateral velocity profiles

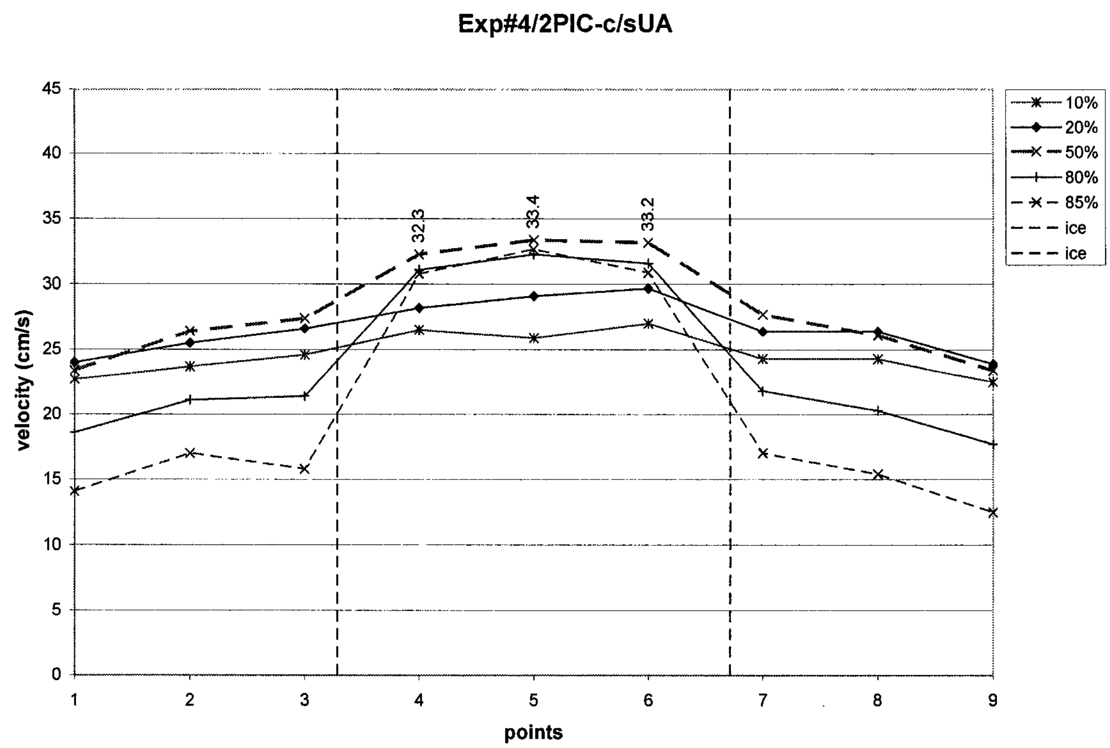

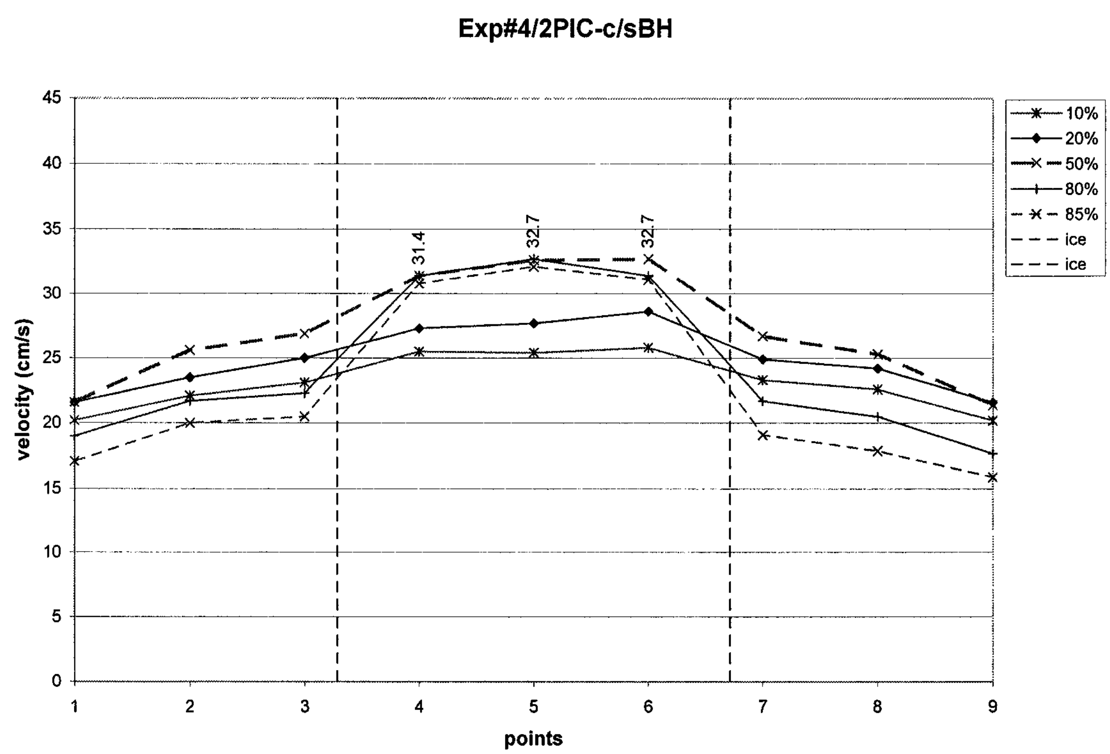

Exp#4/2PIC-c/sBG

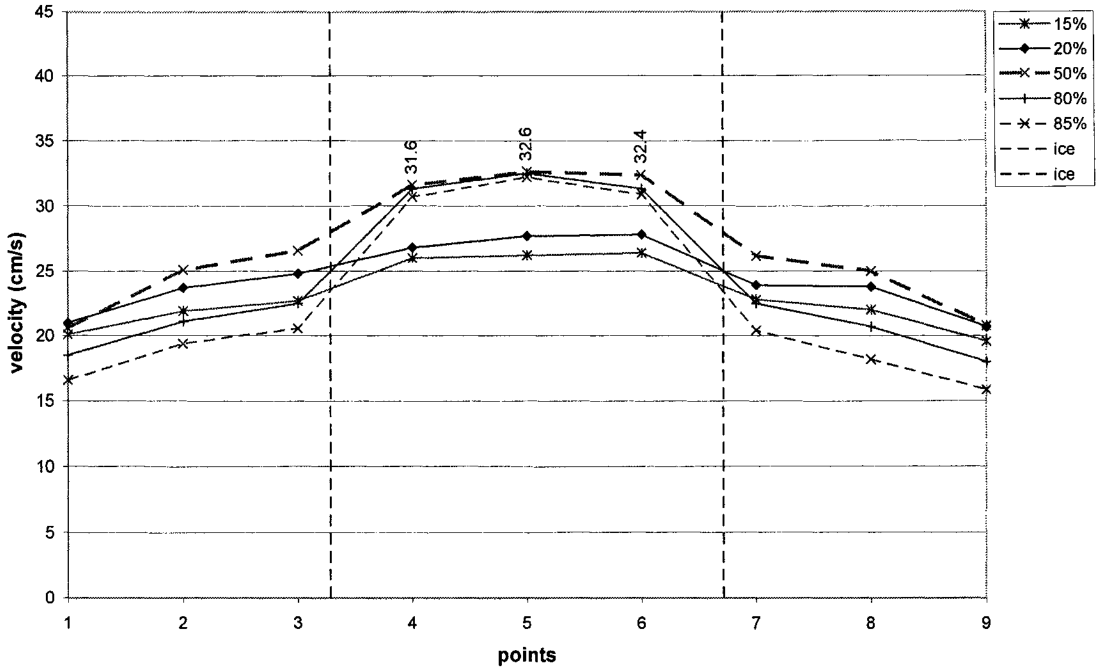

Exp#4/2PIC-c/sBF

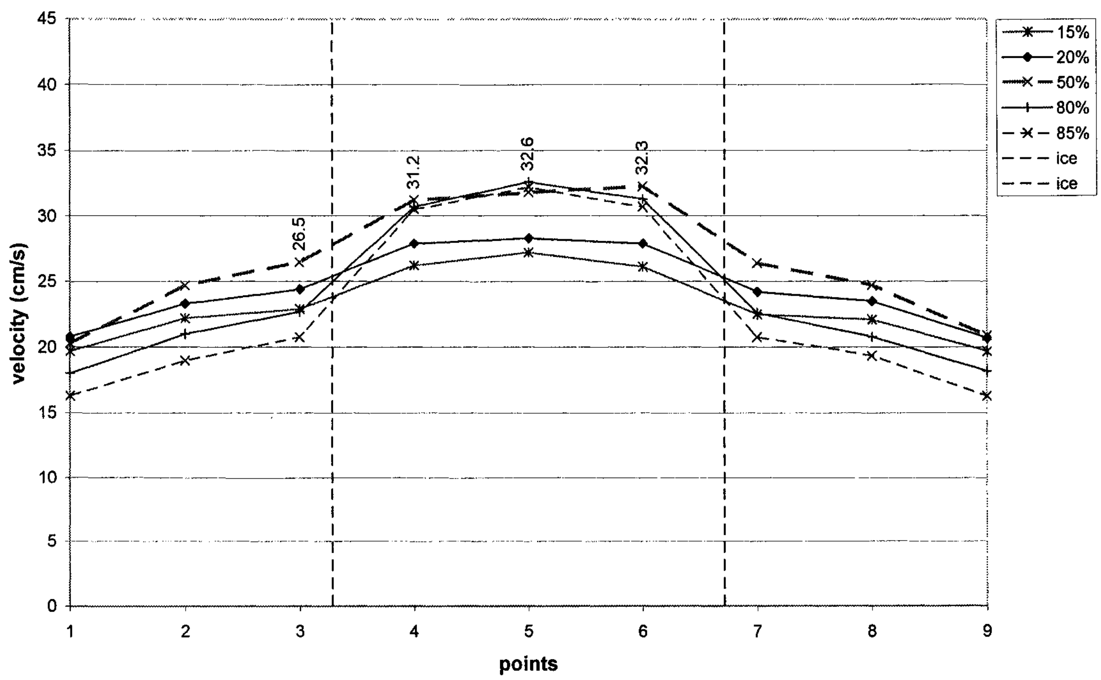

Exp#4/2PIC-c/sBE

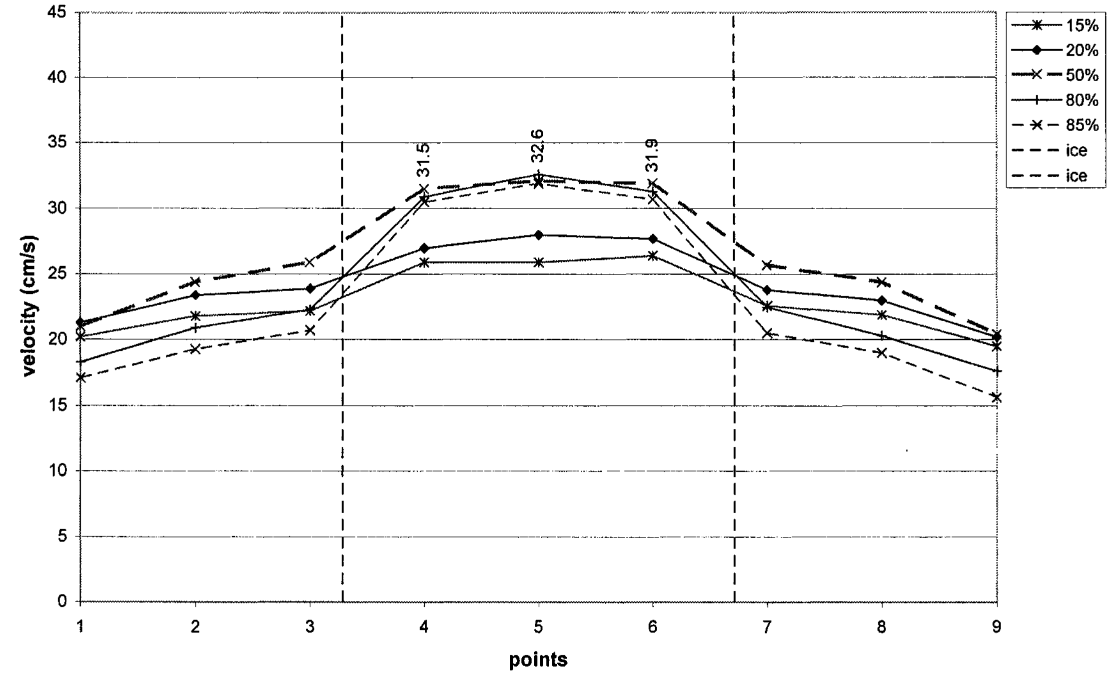

Exp#4/2PIC-c/sBD

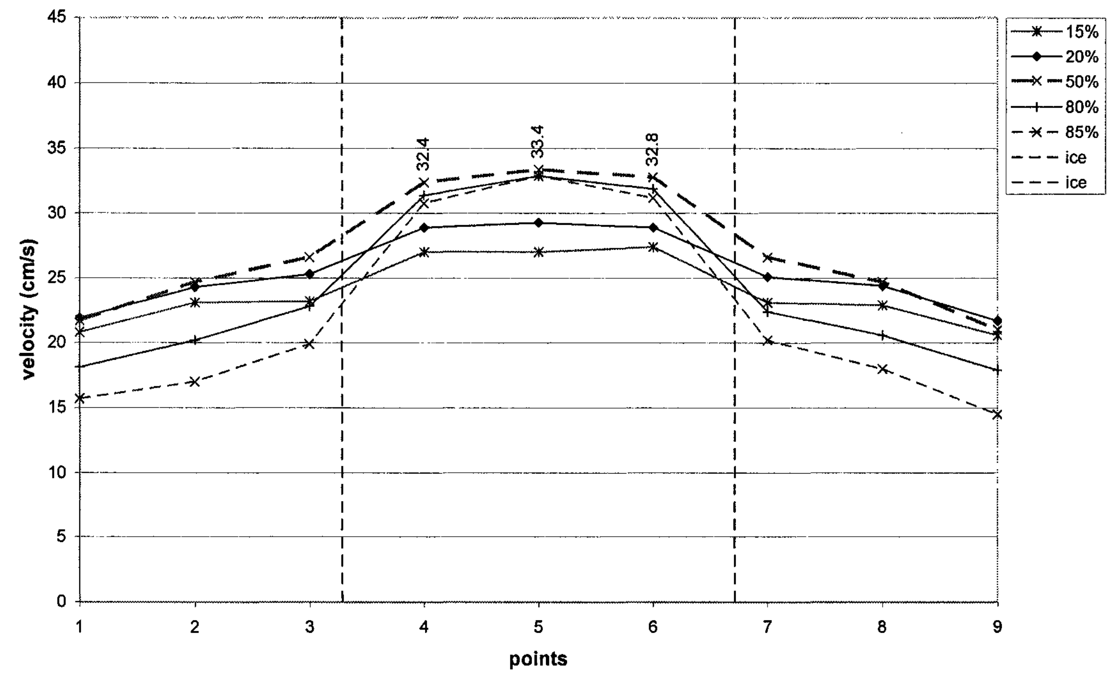

Exp#4/2PIC-c/sBC

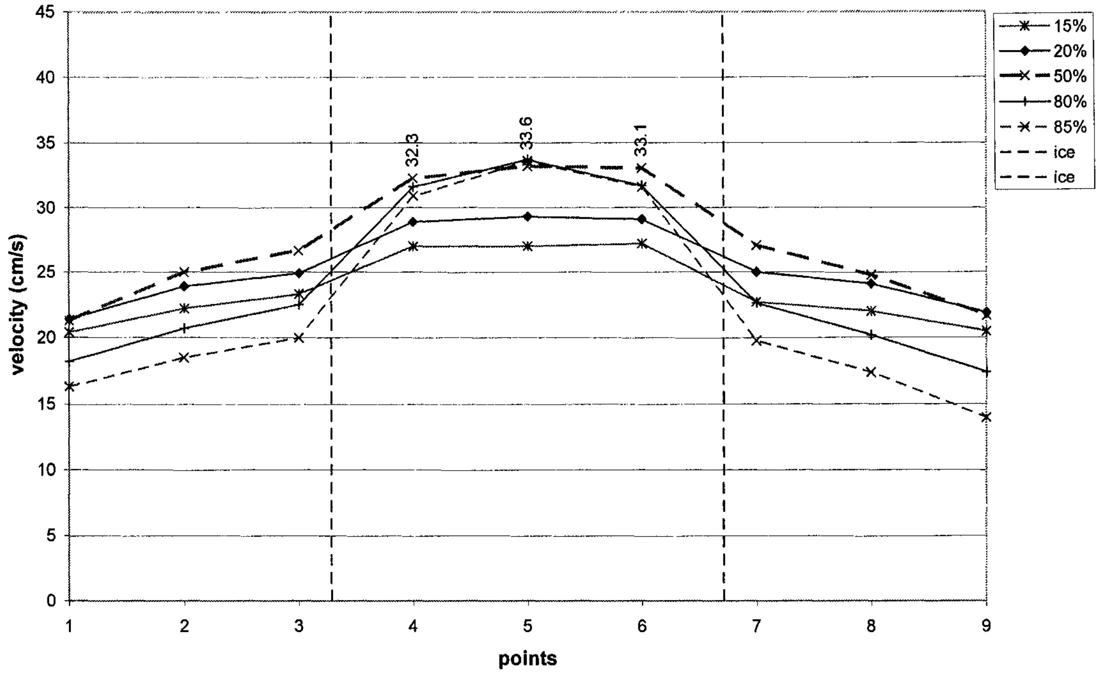

Exp#4/2PIC-c/sBB

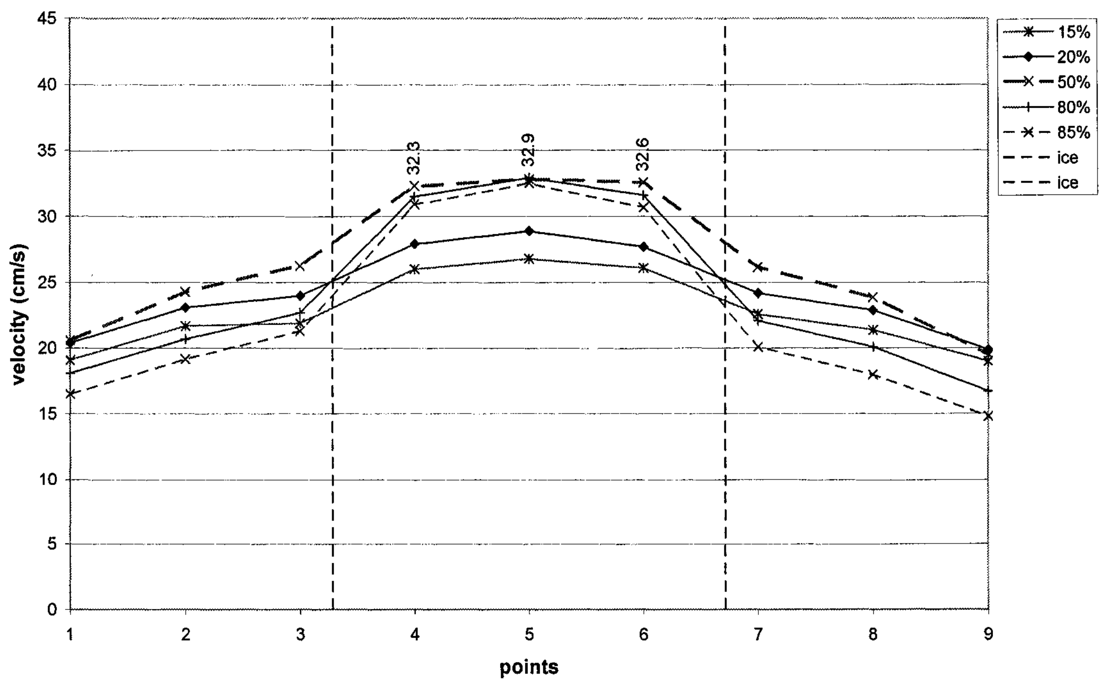

Exp#4/2PIC-c/sBA

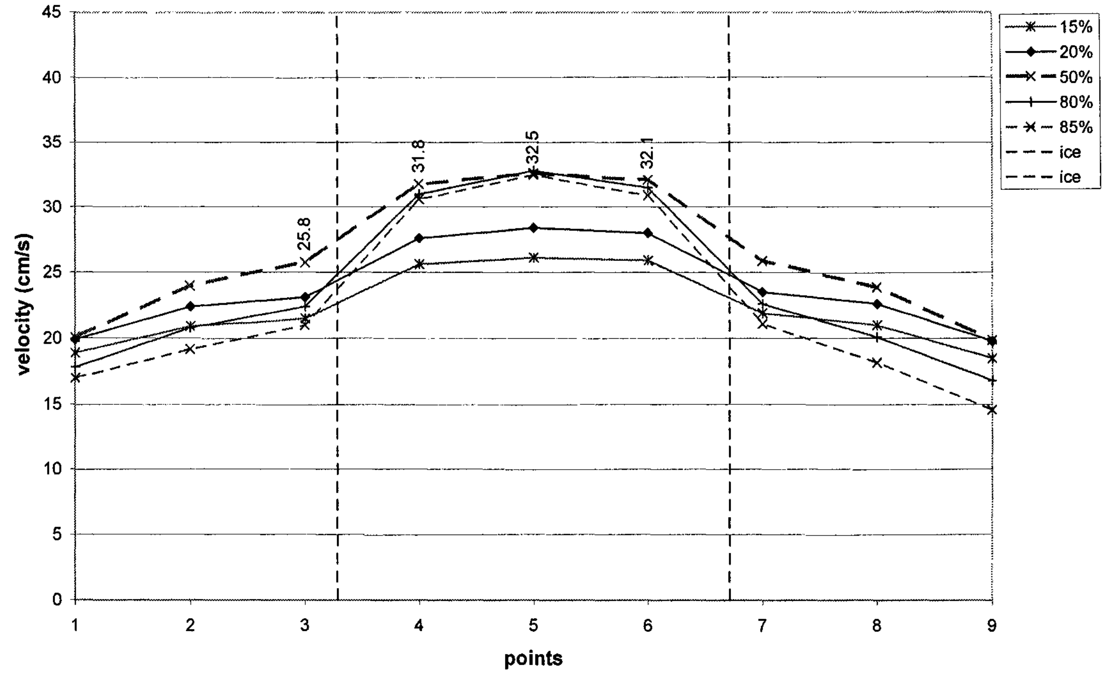

Vertical velocity profiles

Exp#4/2PIC-c/sUA

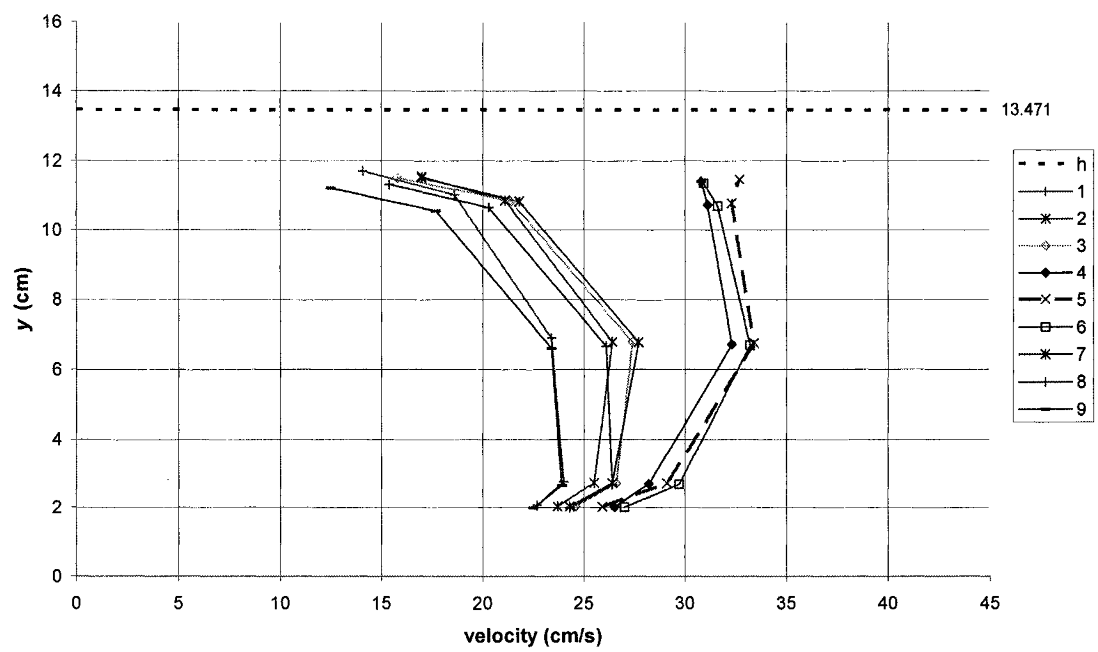

Exp#4/2PIC-c/sBH

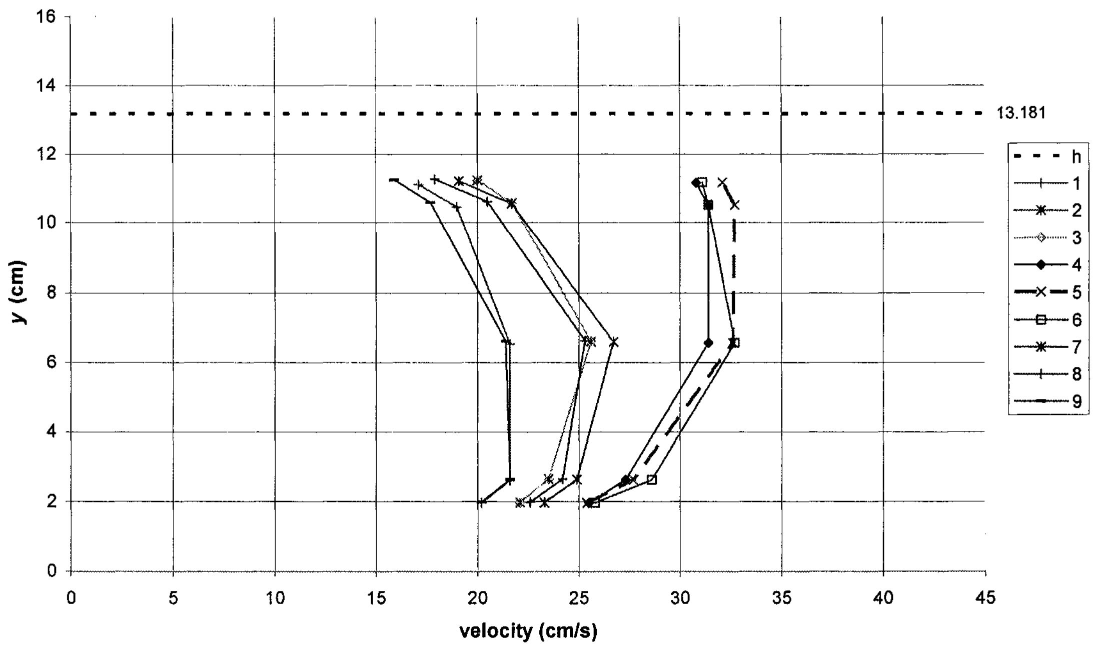

Exp#4/2PIC-c/sBG

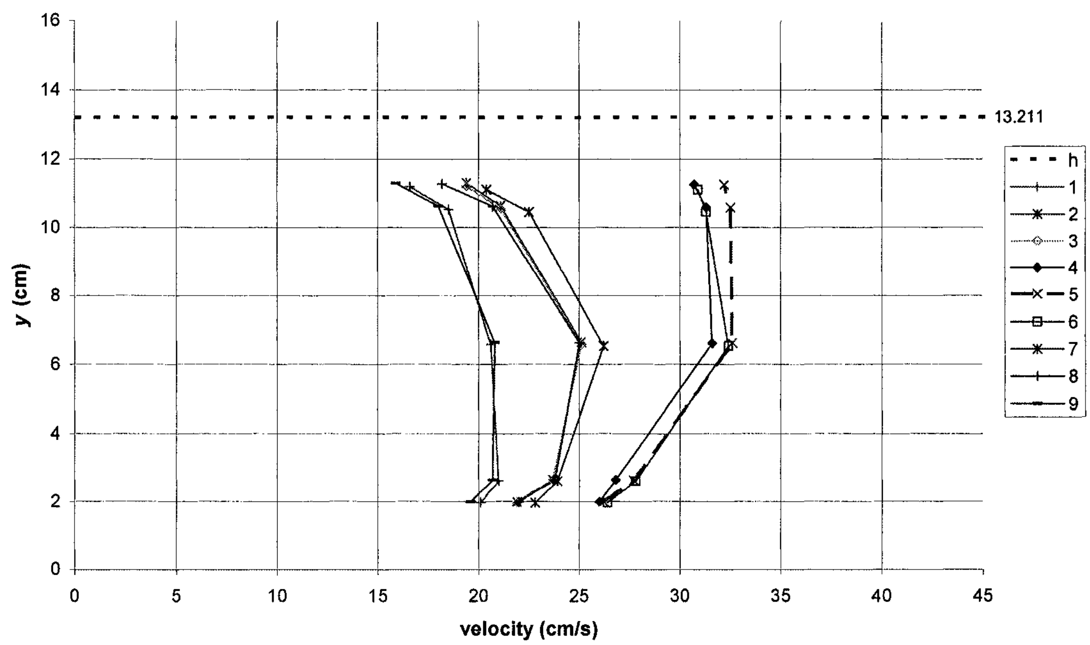

Exp#4/2PIC-c/sBF

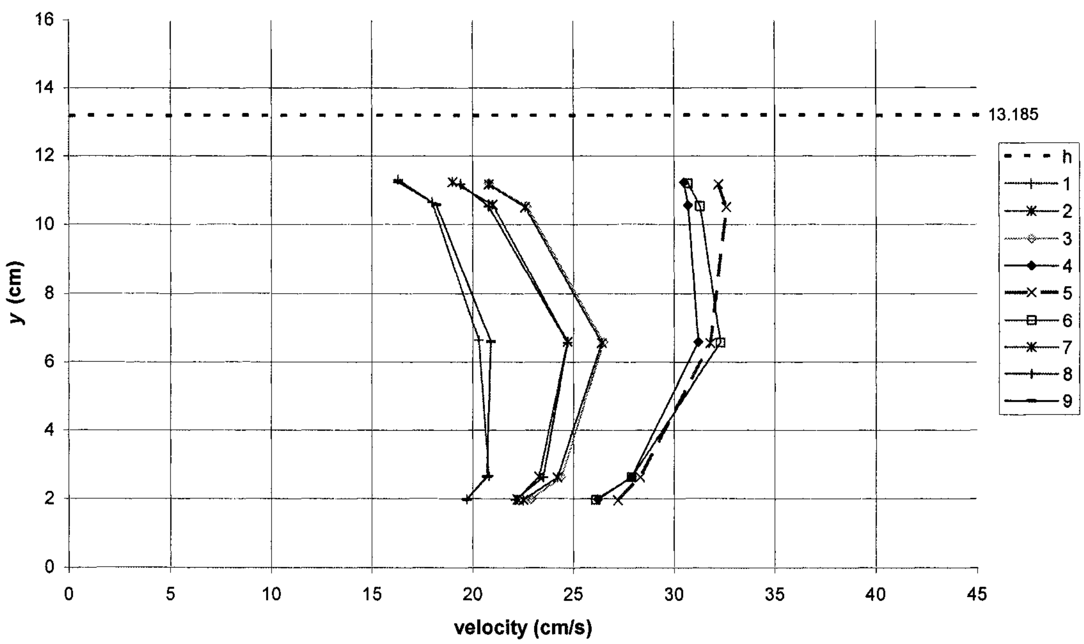

Exp#4/2PIC-c/sBE

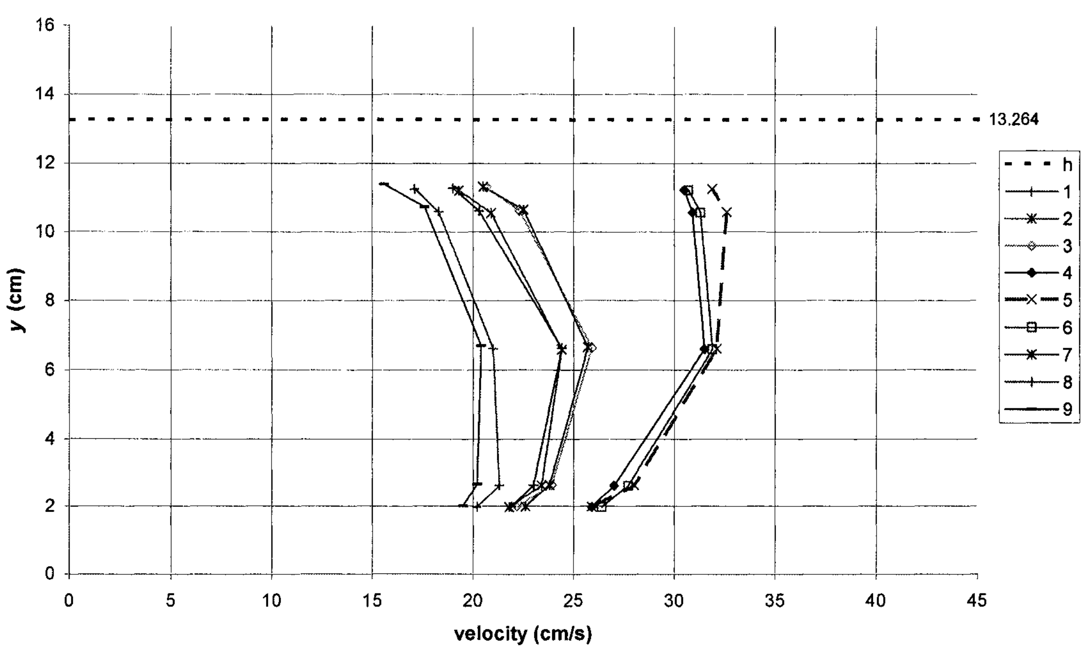

Exp#4/2PIC-c/sBD

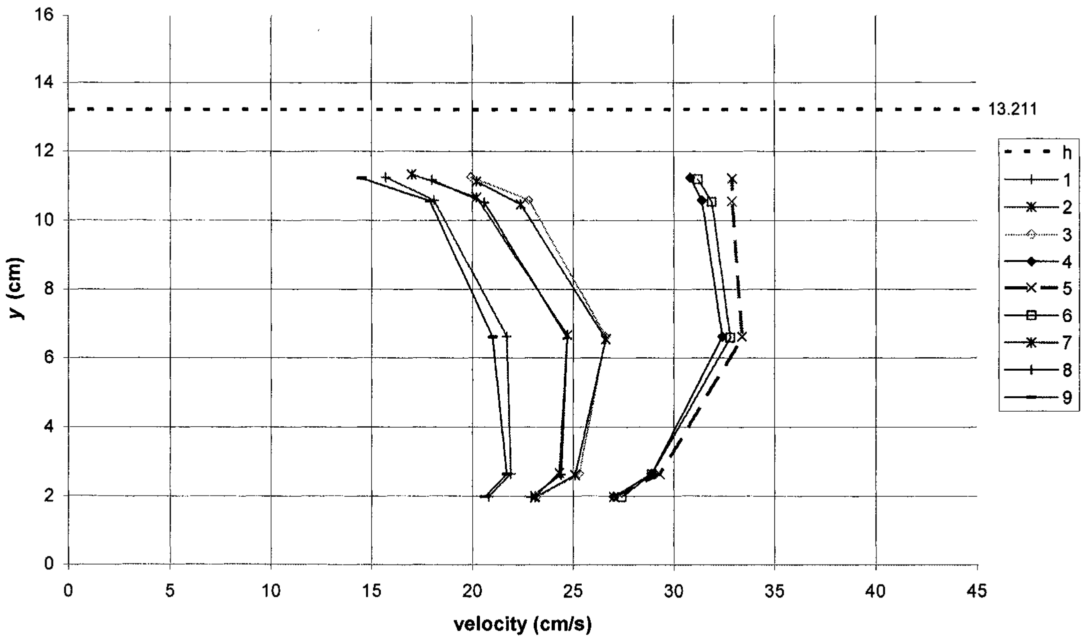

Exp#4/2PIC-c/sBC

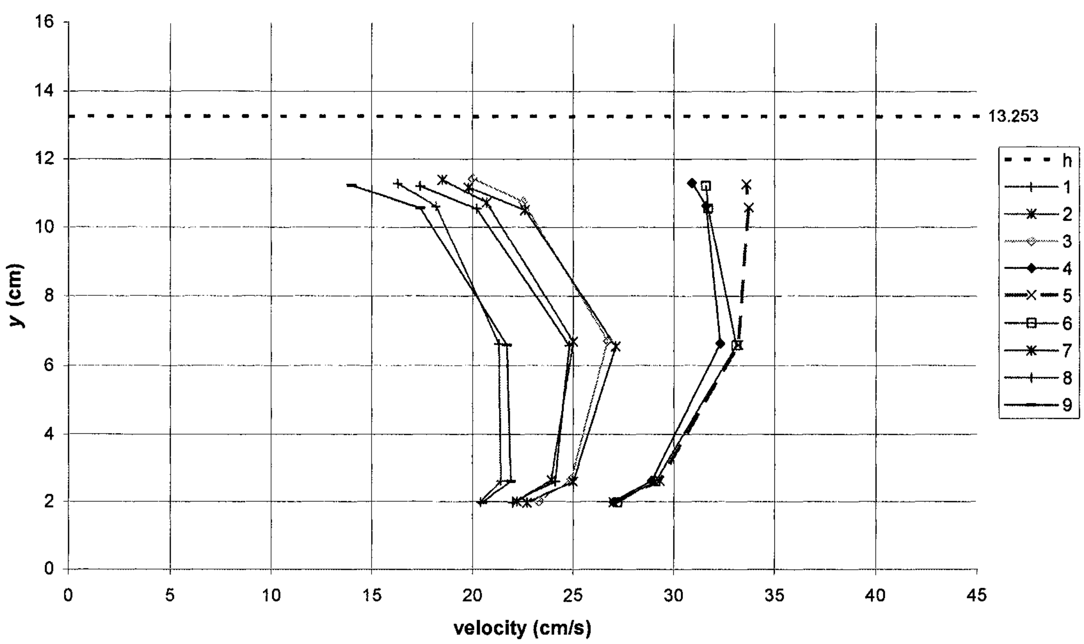

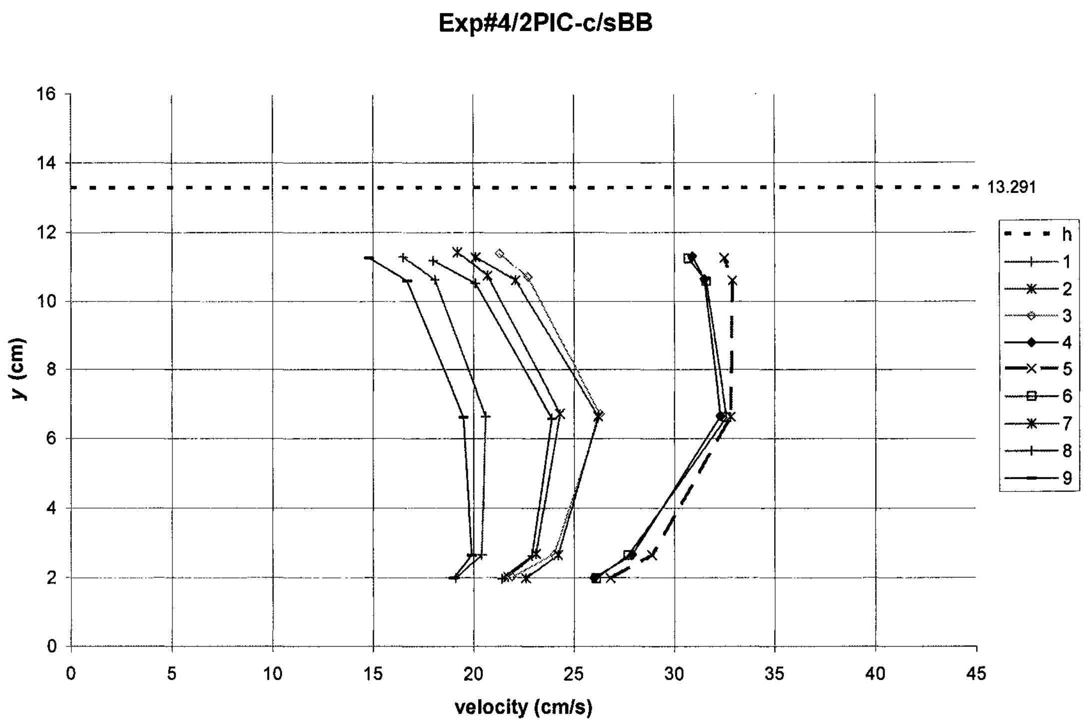
Exp#4/2PIC-c/sBB
13.291
y (cm)
velocity (cm/s)
h
1
2
3
4
5
6
7
8
9

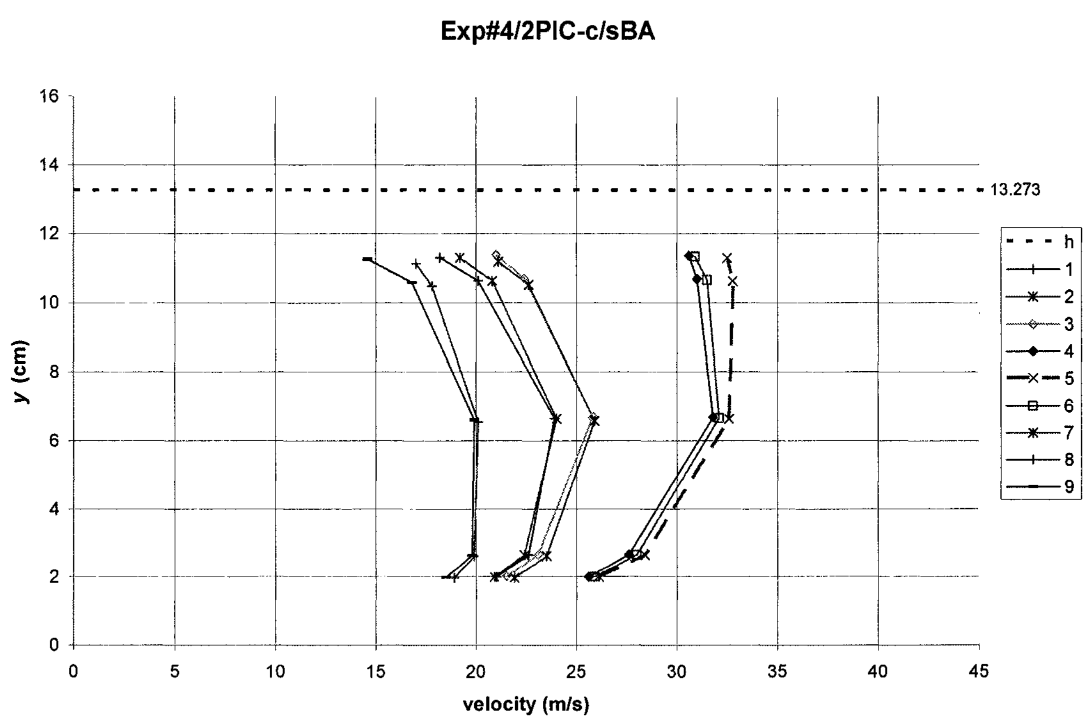
Exp#4/2PIC-c/sBA
13.273
y (cm)
velocity (m/s)
h
1
2
3
4
5
6
7
8
9

FREE-SURFACE CONFIGURATION (FS) - Q≈0.043m^3/s

Lateral velocity profiles

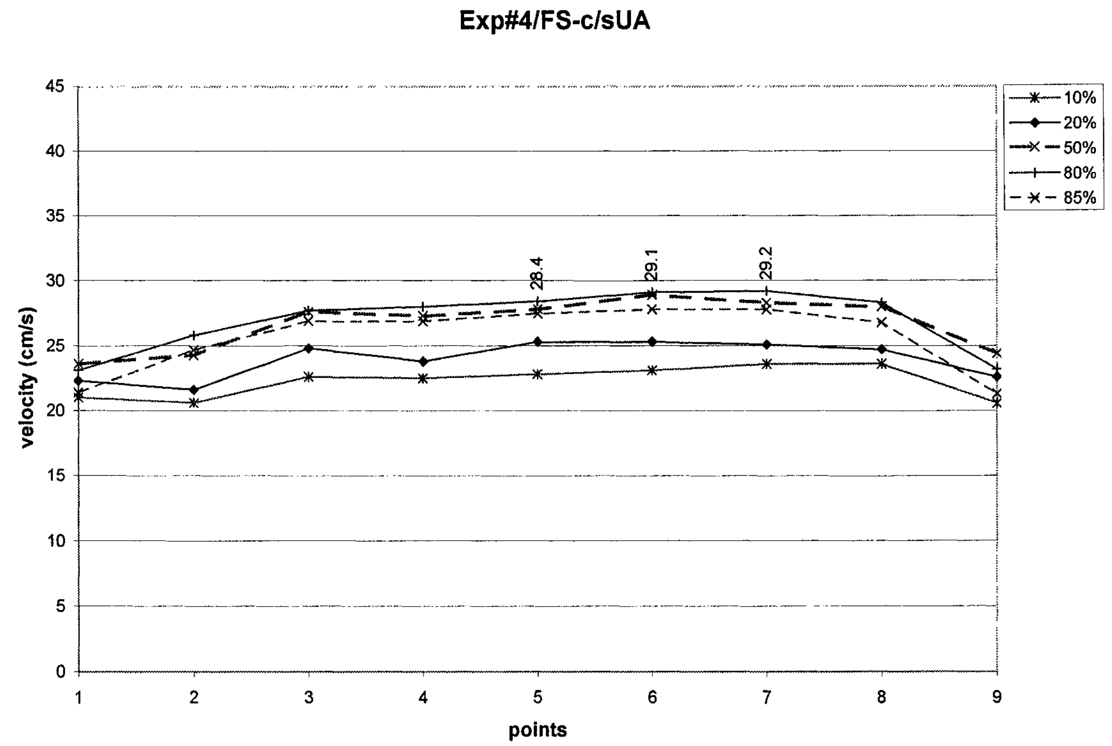

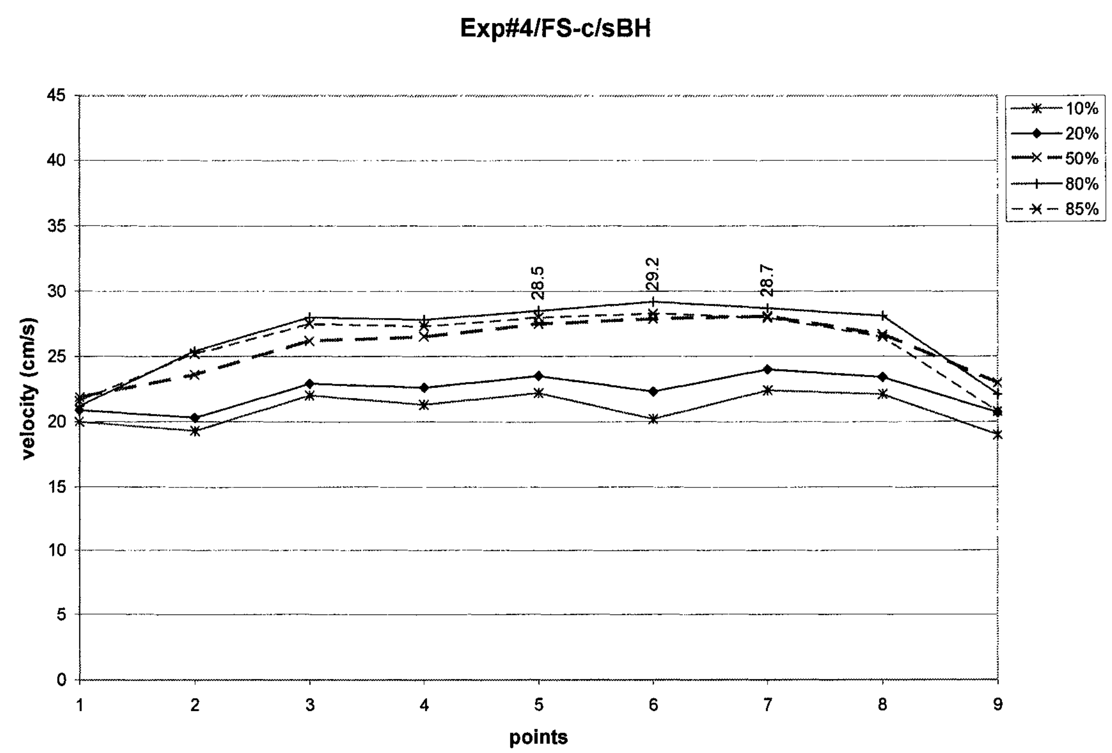

Exp#4/FS-c/sBG

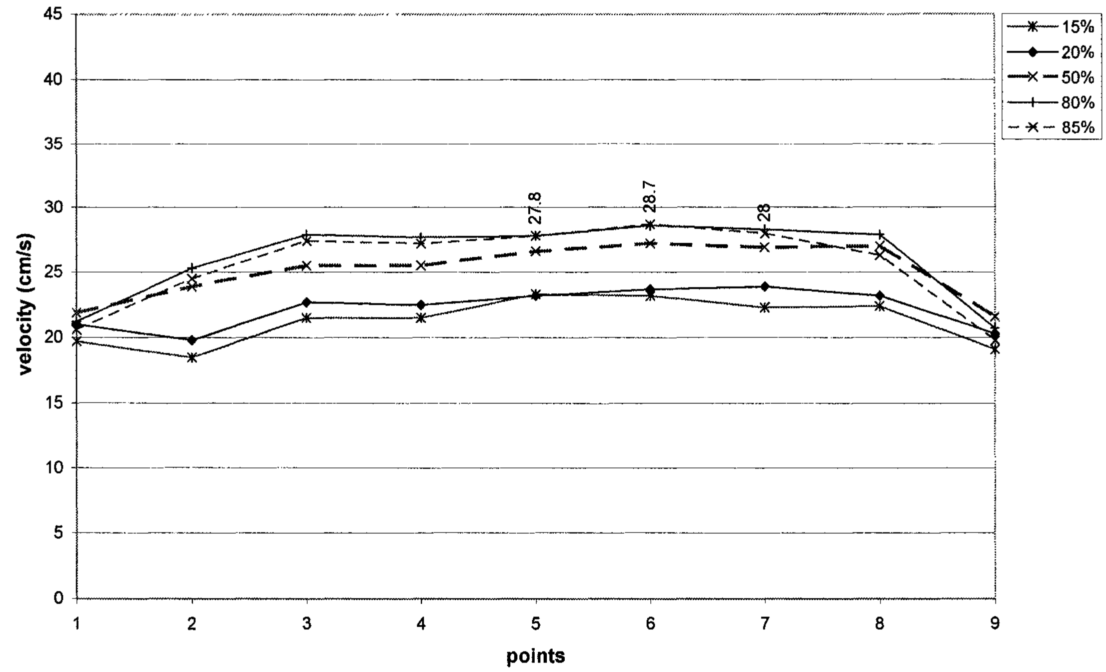

Exp#4/FS-c/sBF

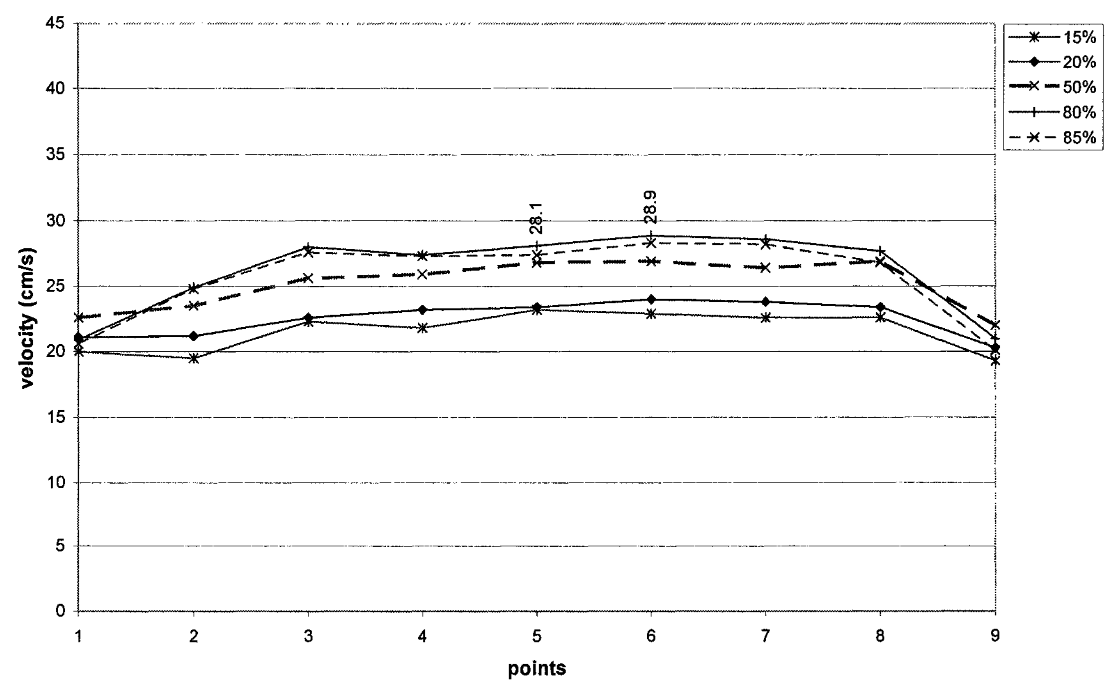

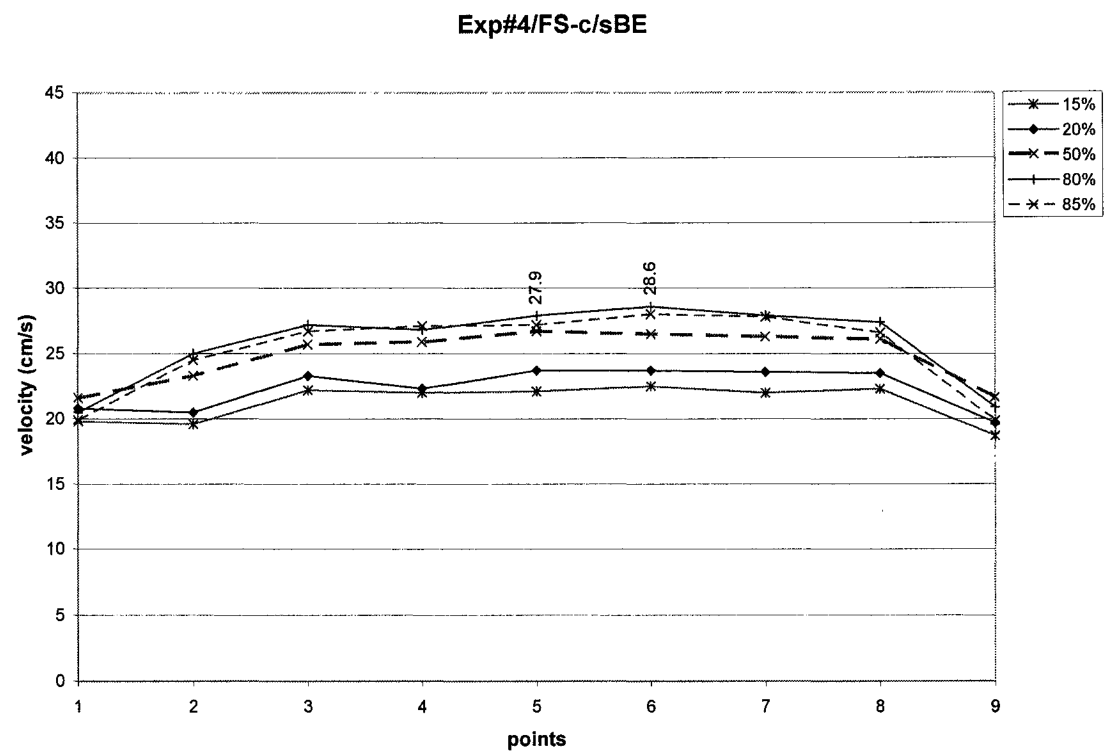
Exp#4/FS-c/sBE
velocity (cm/s)
points
15%
20%
50%
80%
85%
27.9
28.6

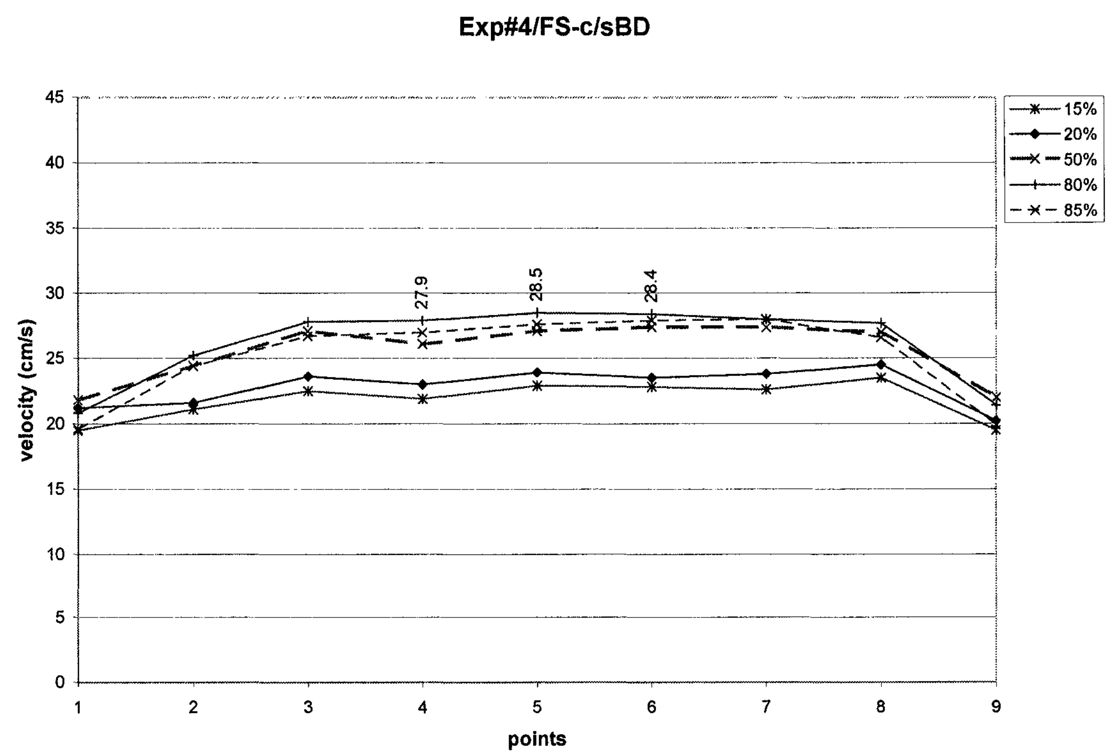
Exp#4/FS-c/sBD
velocity (cm/s)
points
15%
20%
50%
80%
85%
27.9
28.5
28.4

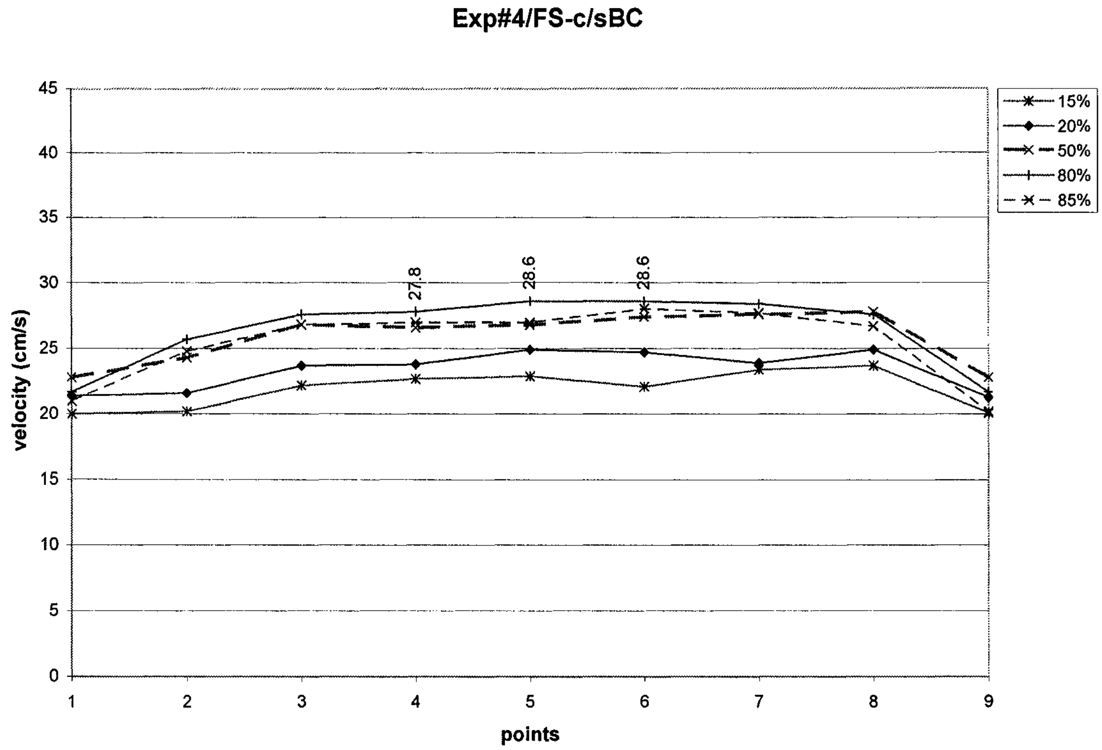
Exp#4/FS-c/sBC
velocity (cm/s)
points
15%
20%
50%
80%
85%
27.8
28.6
28.6

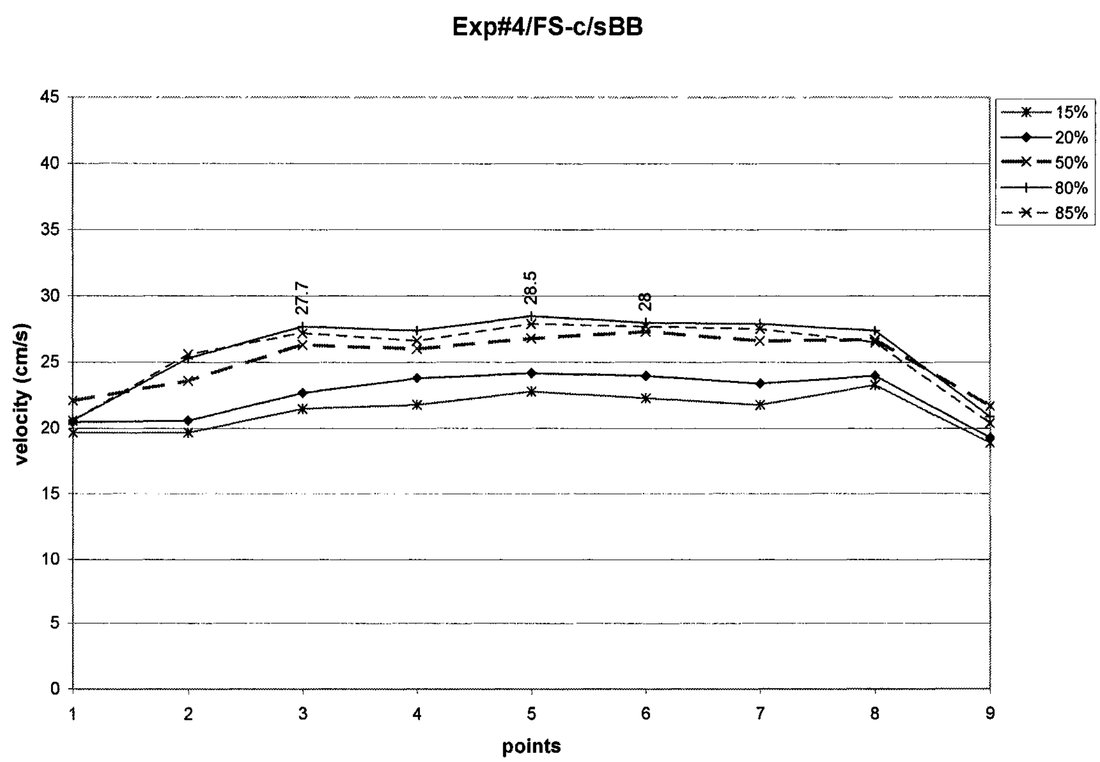
Exp#4/FS-c/sBB
velocity (cm/s)
points
15%
20%
50%
80%
85%
27.7
28.5
28

Exp#4/FS-c/sBA

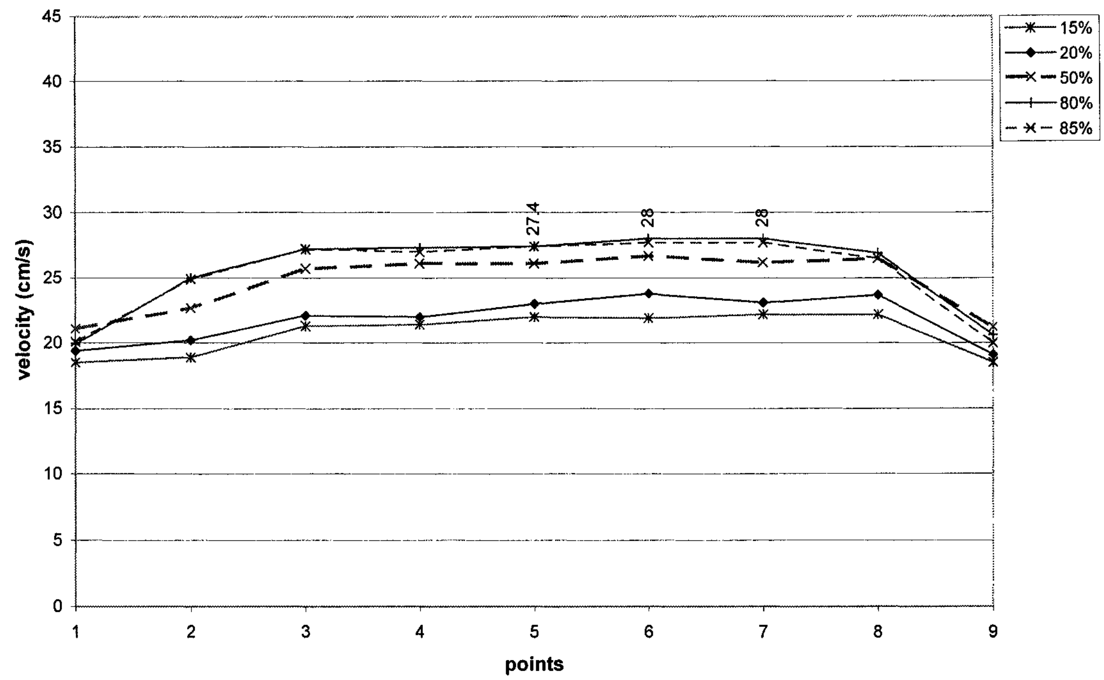

Vertical velocity profiles

Exp#4/FS-c/sUA

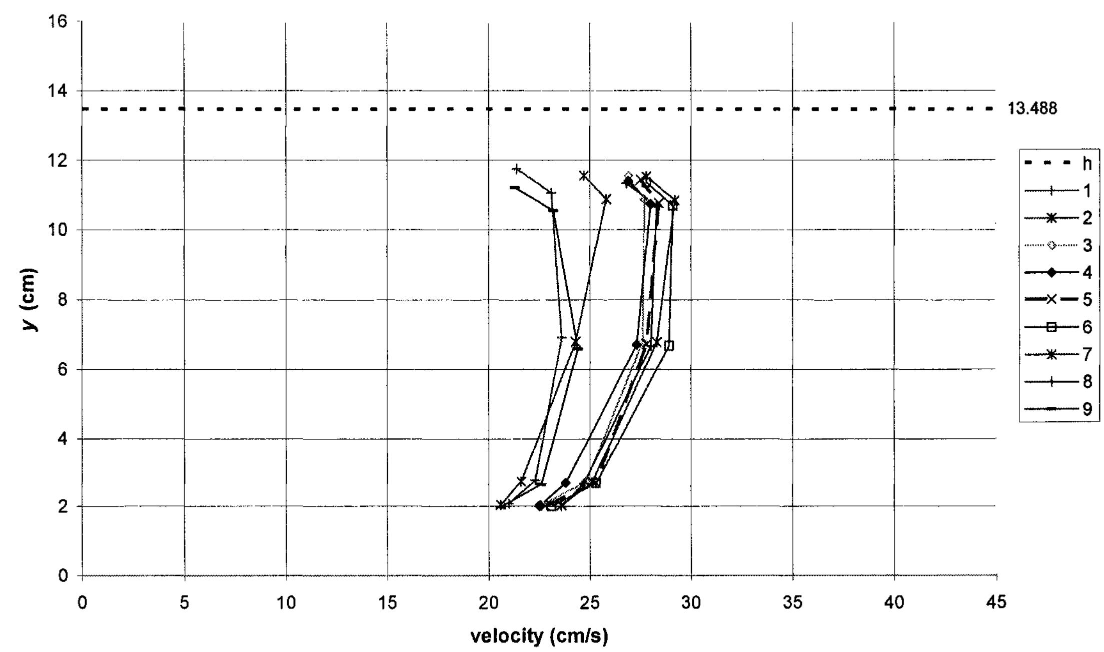

Exp#4/FS-c/sBH

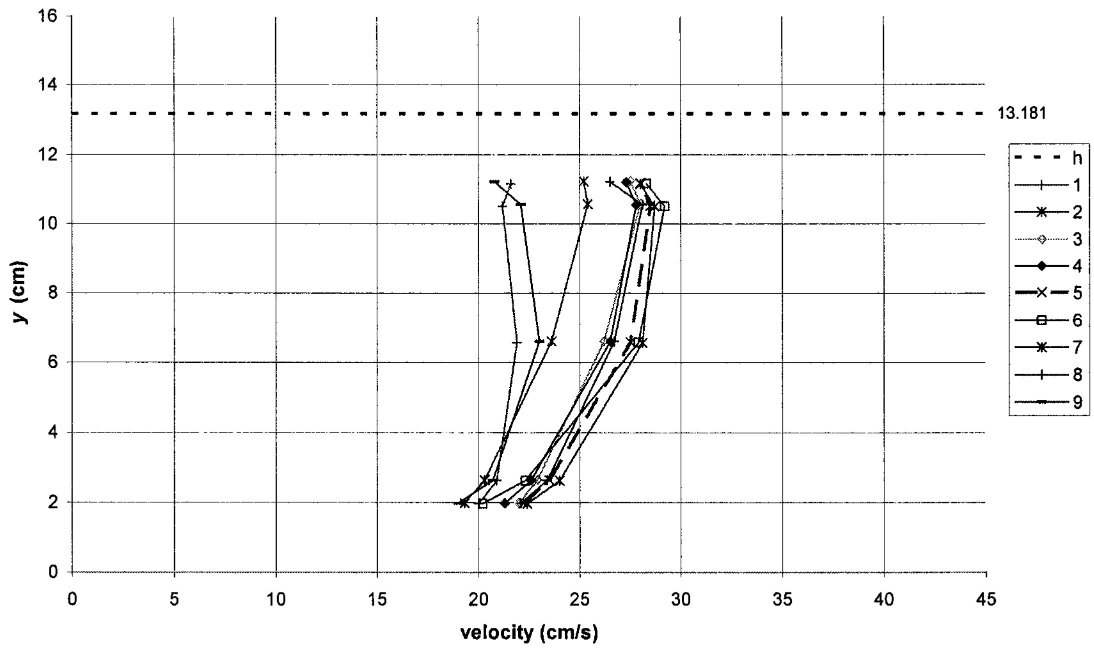

Exp#4/FS-c/sBG

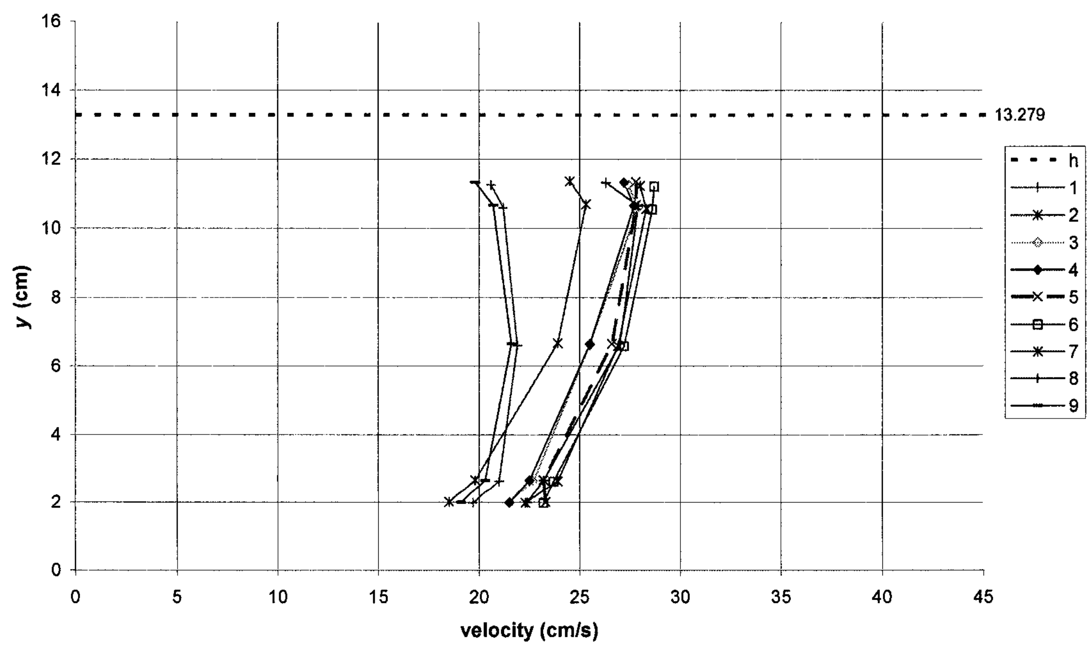

Exp#4/FS-c/sBF

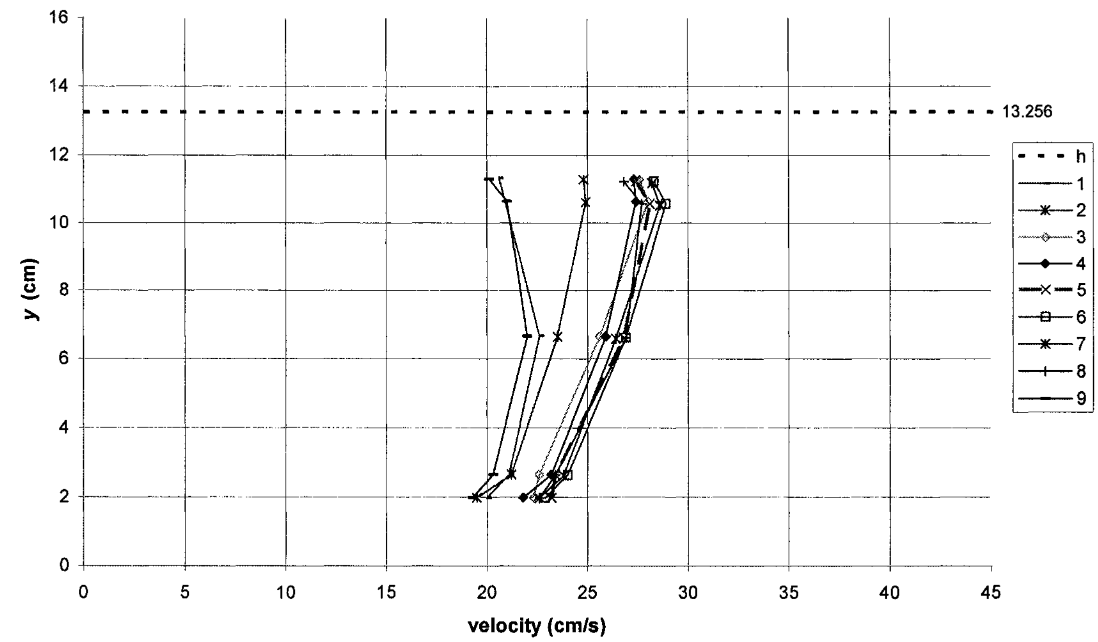

Exp#4/FS-c/sBE

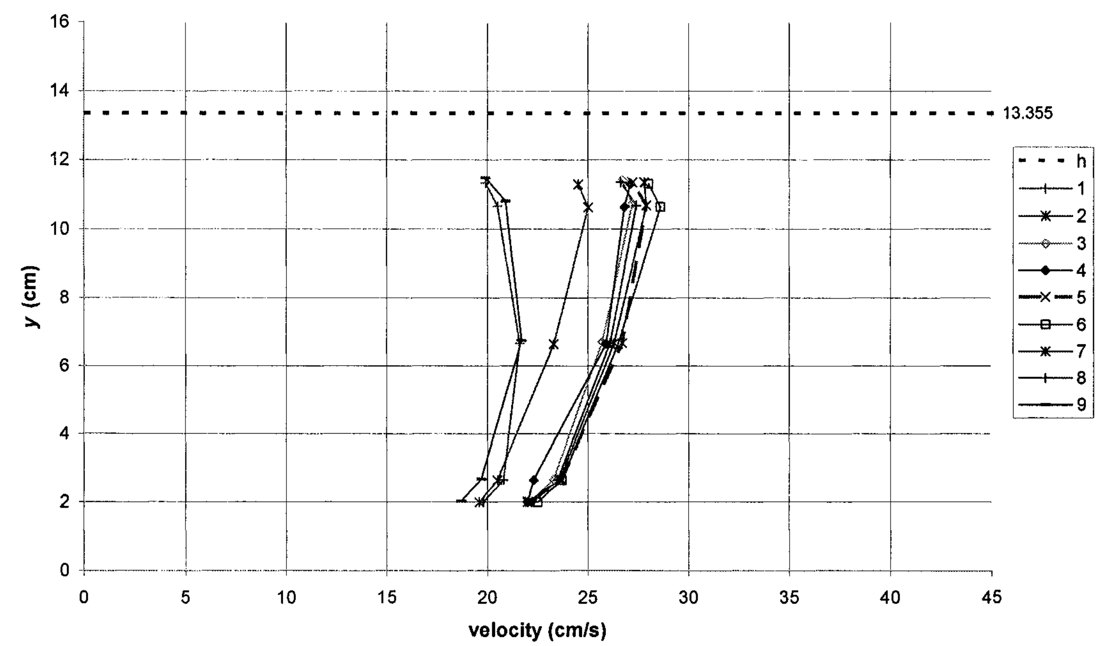

Exp#4/FS-c/sBD

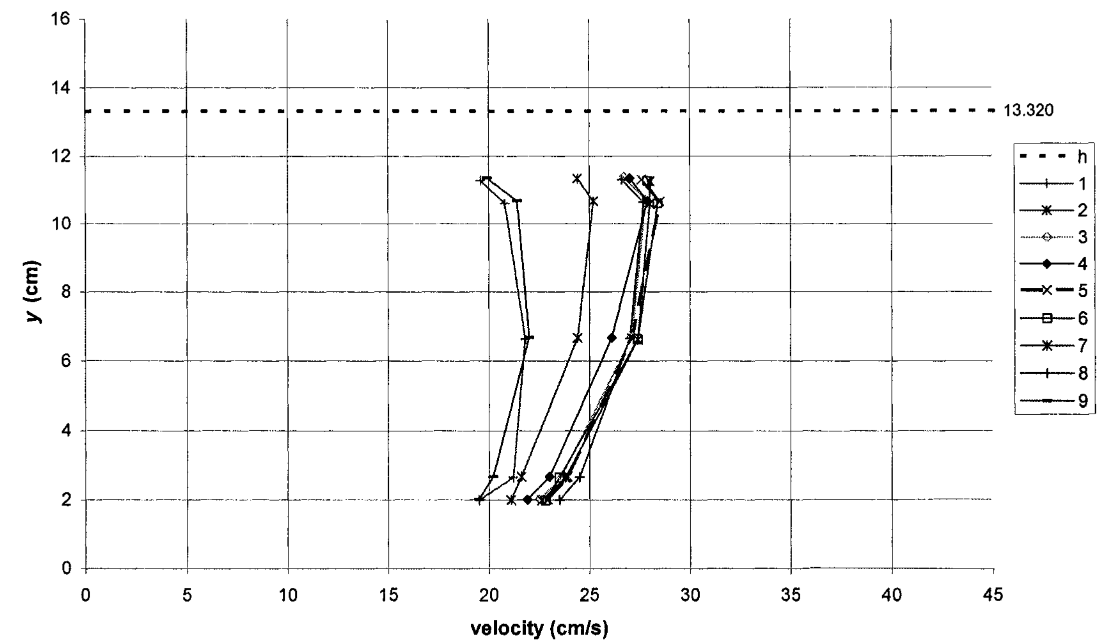

Exp#4/FS-c/sBC

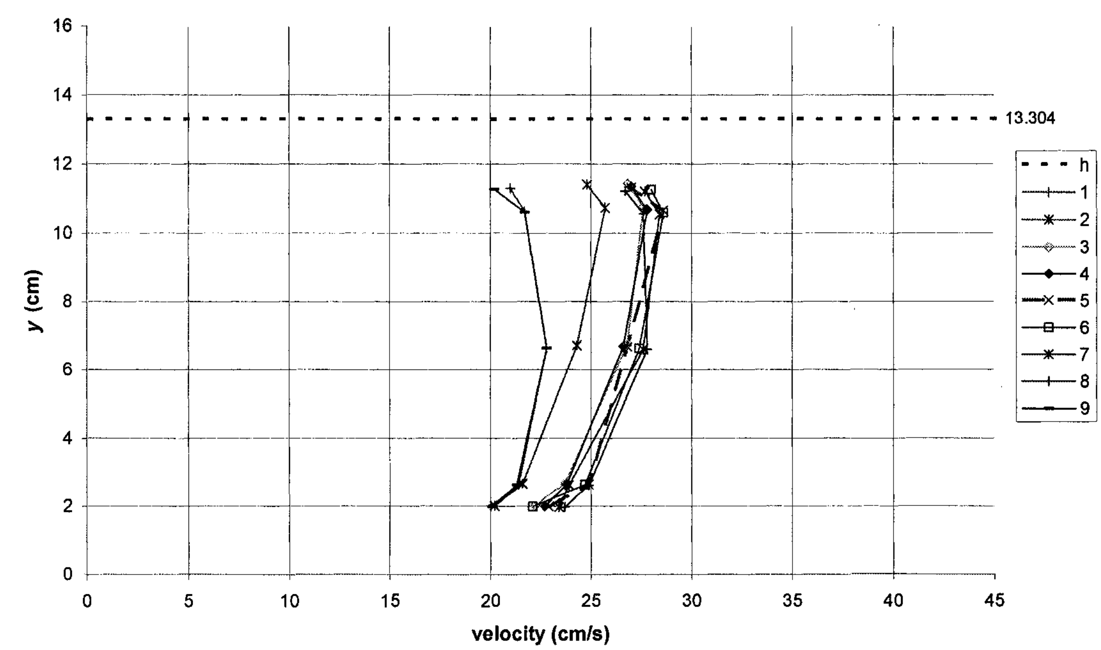

Exp#4/FS-c/sBB

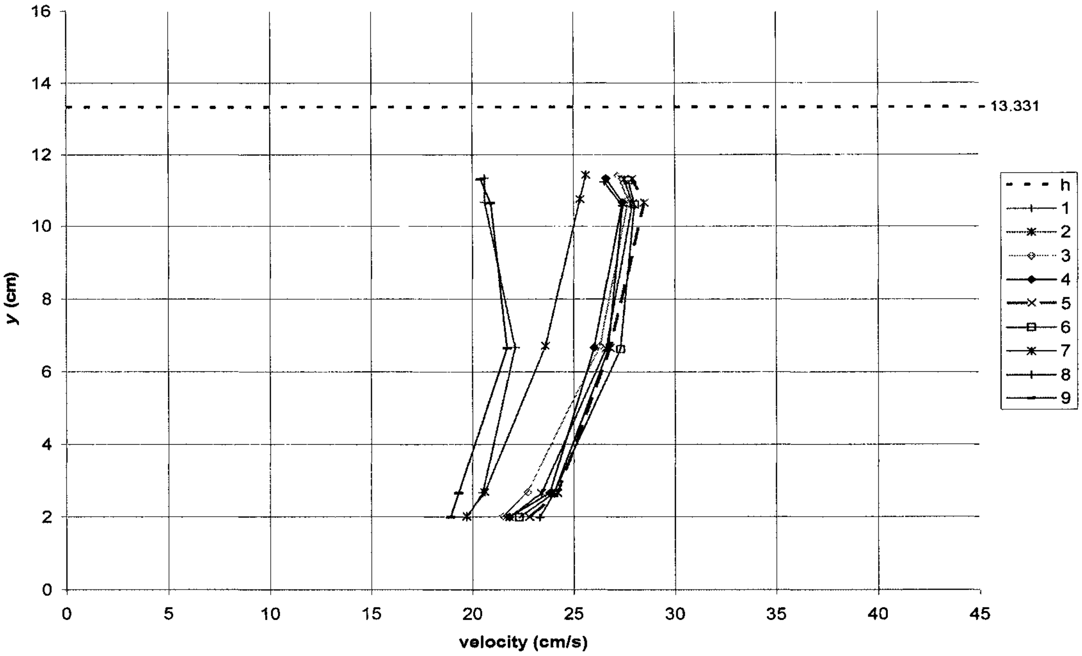

Exp#4/FS-c/sBA

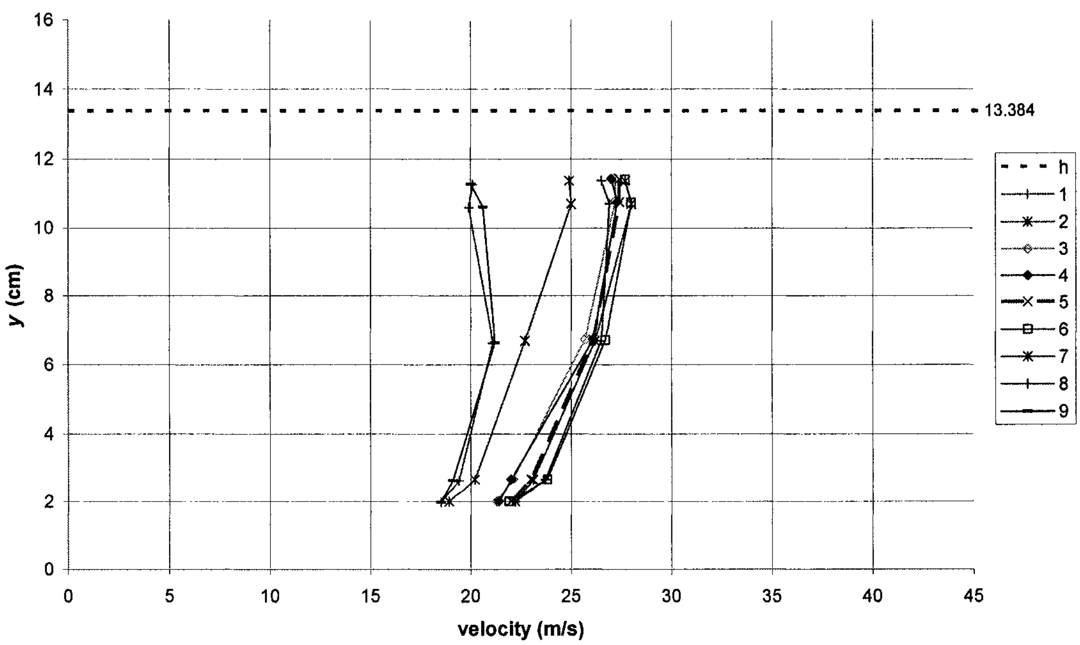

APPENDIX A5

Exp#5

FREE-SURFACE CONFIGURATION (FS) at free-surface critical conditions

(experiment without bridge pier)

FREE-SURFACE CONFIGURATION (FS) – Q≈0.0605m^3/s

Lateral velocity profiles

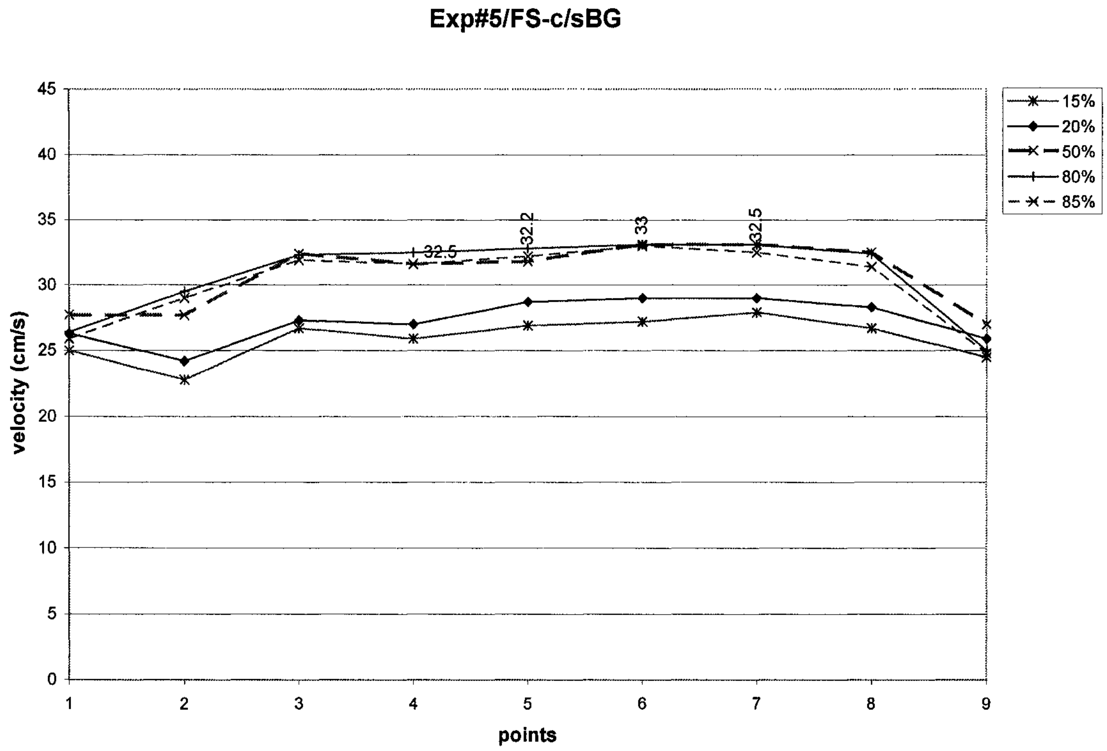

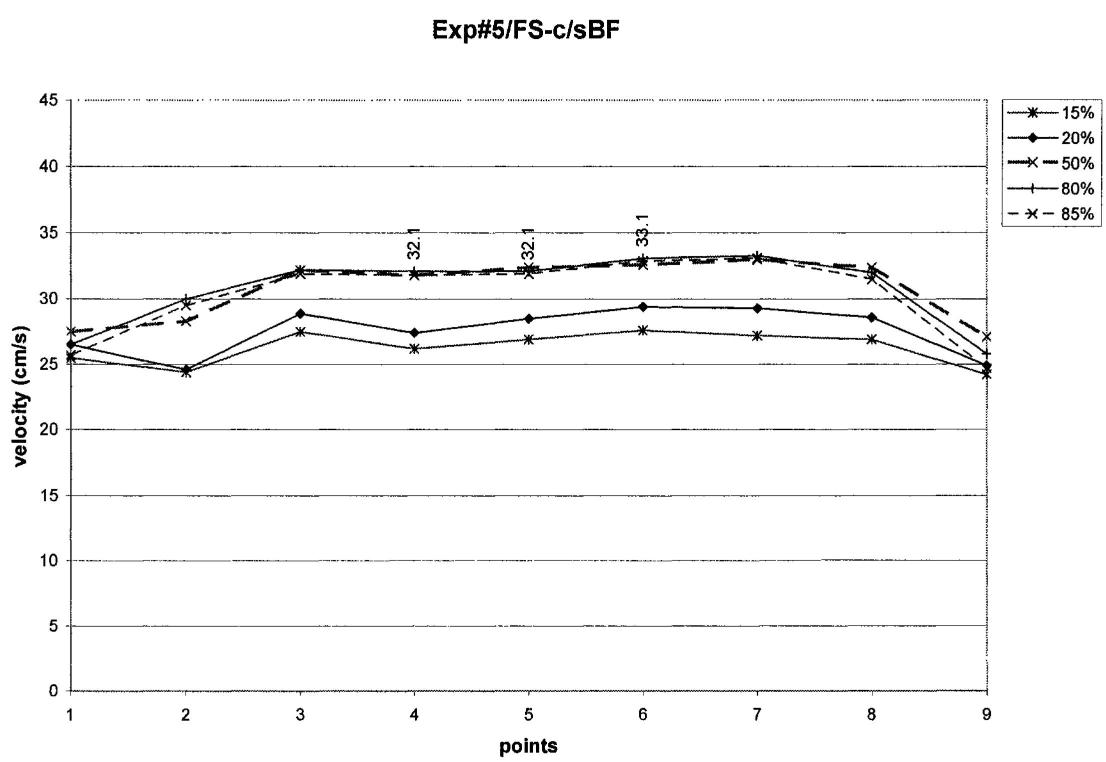

Exp#5/FS-c/sBE

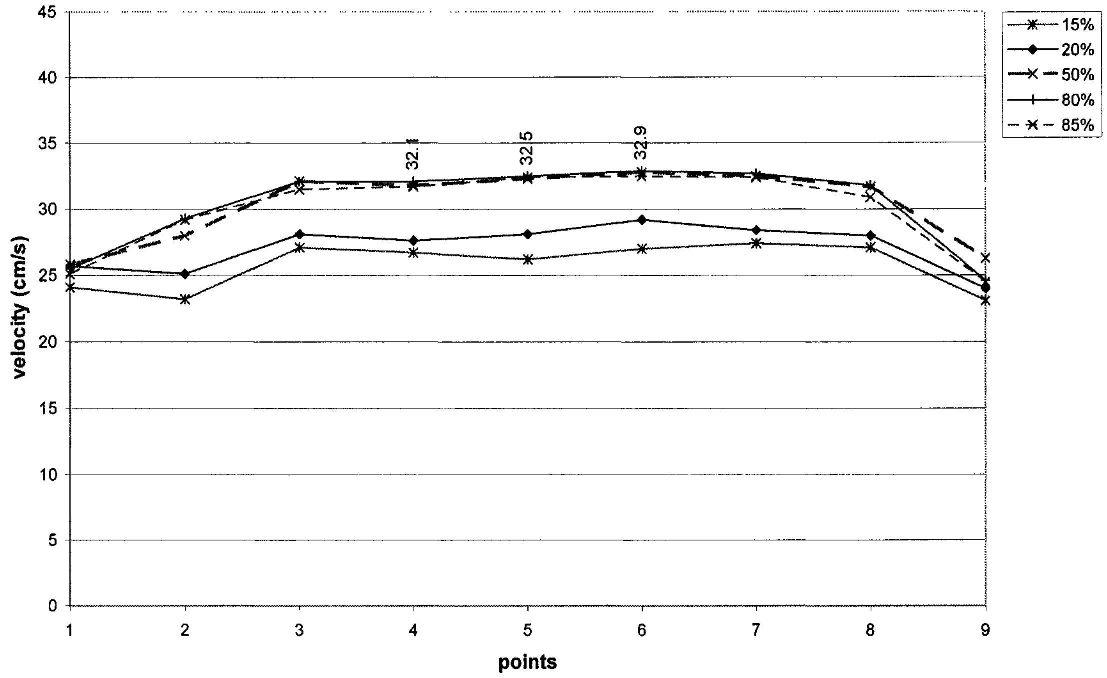

Exp#5/FS-c/sBD

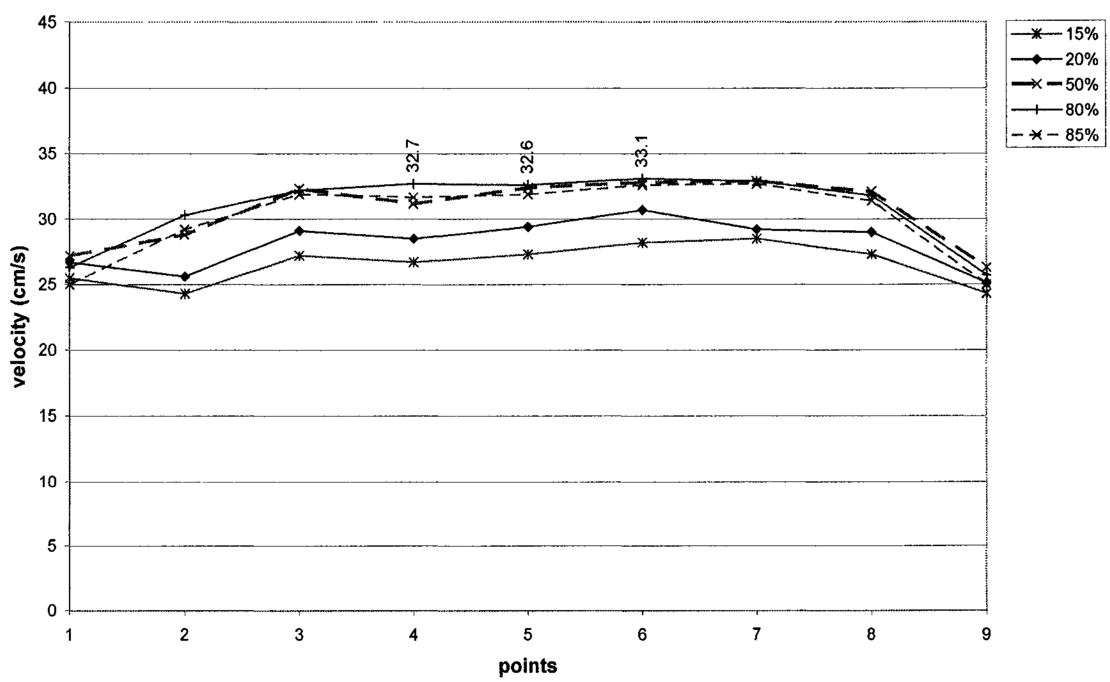

Exp#5/FS-c/sBC

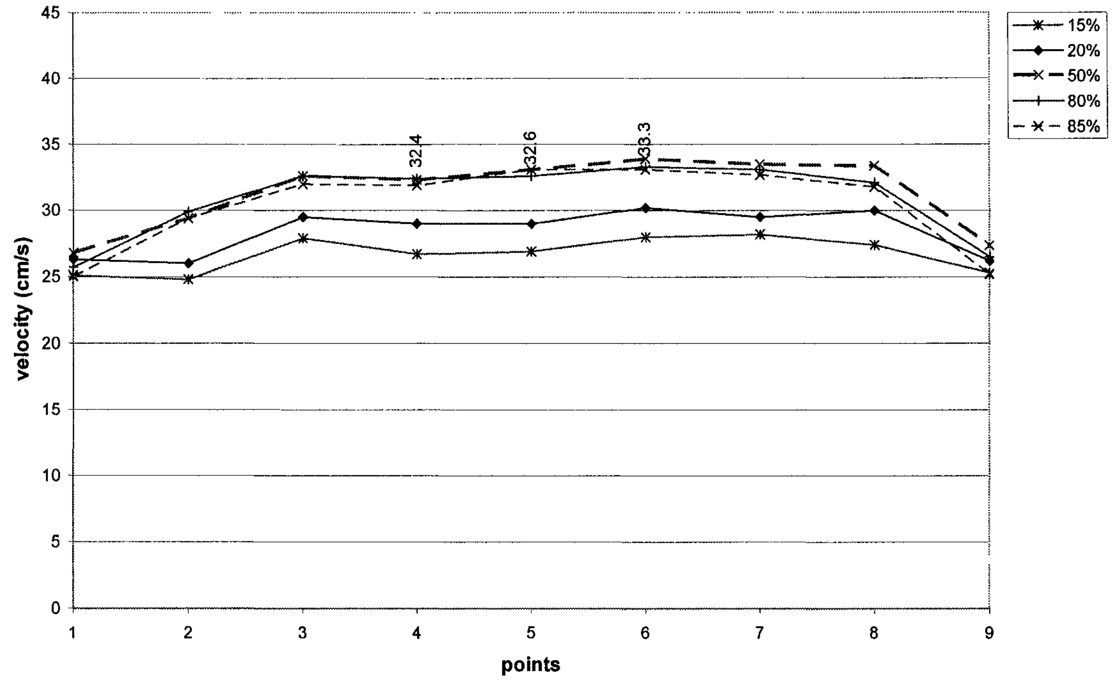

Exp#5/FS-c/sBB

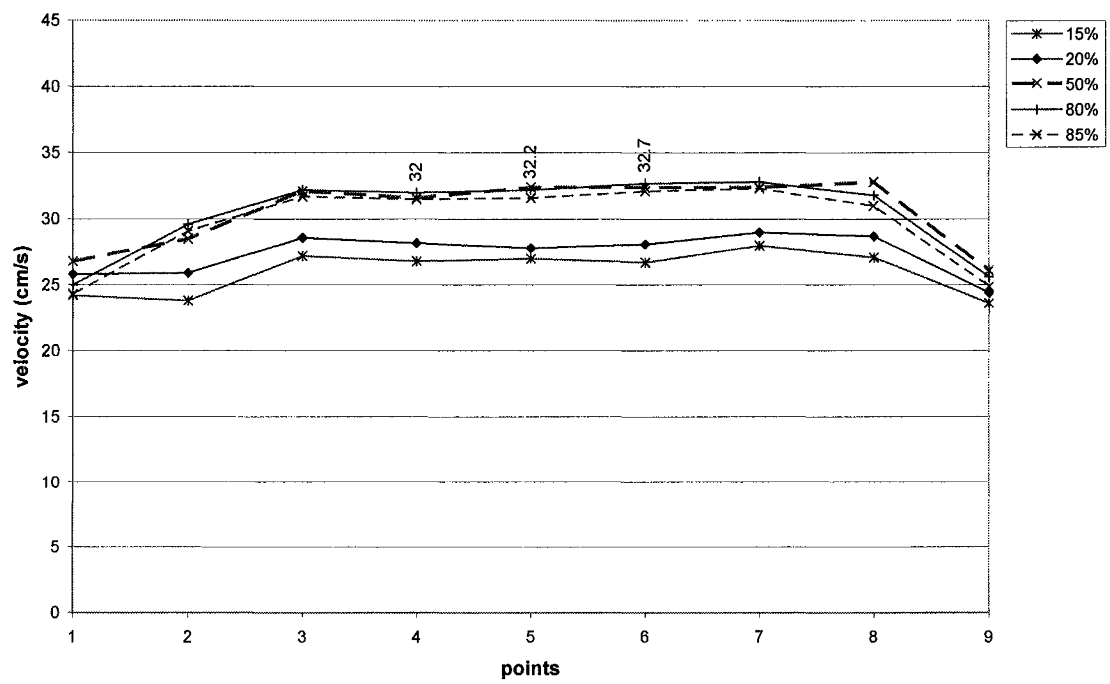

Exp#5/FS-c/sBA

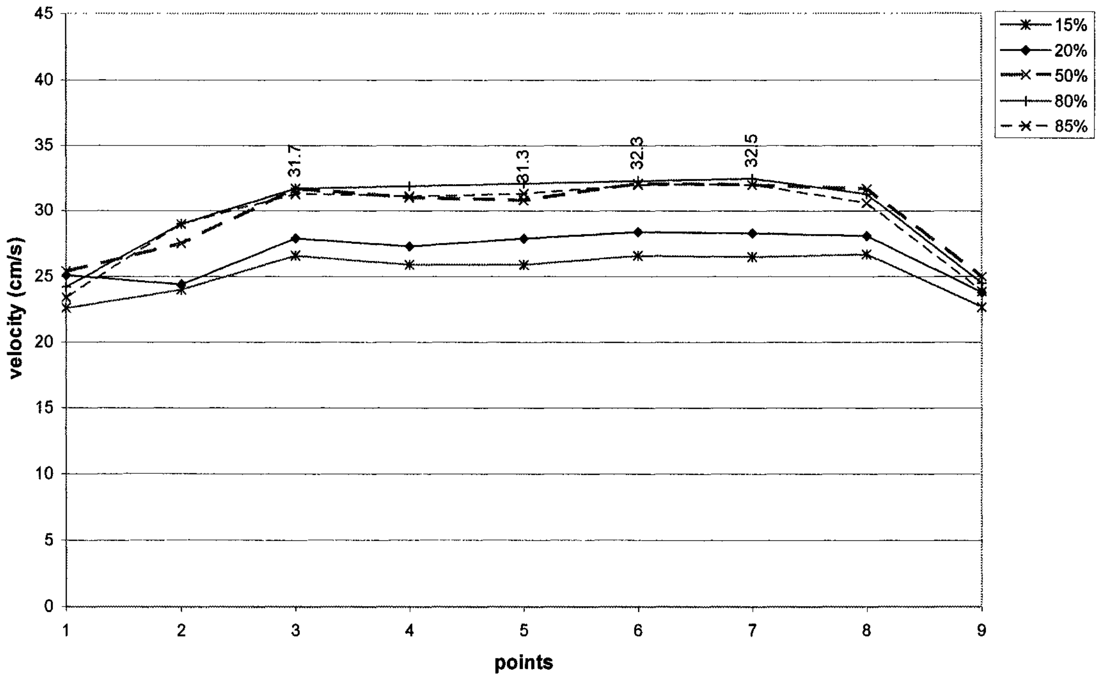

Vertical velocity profiles

Exp#5/FS-c/sBG

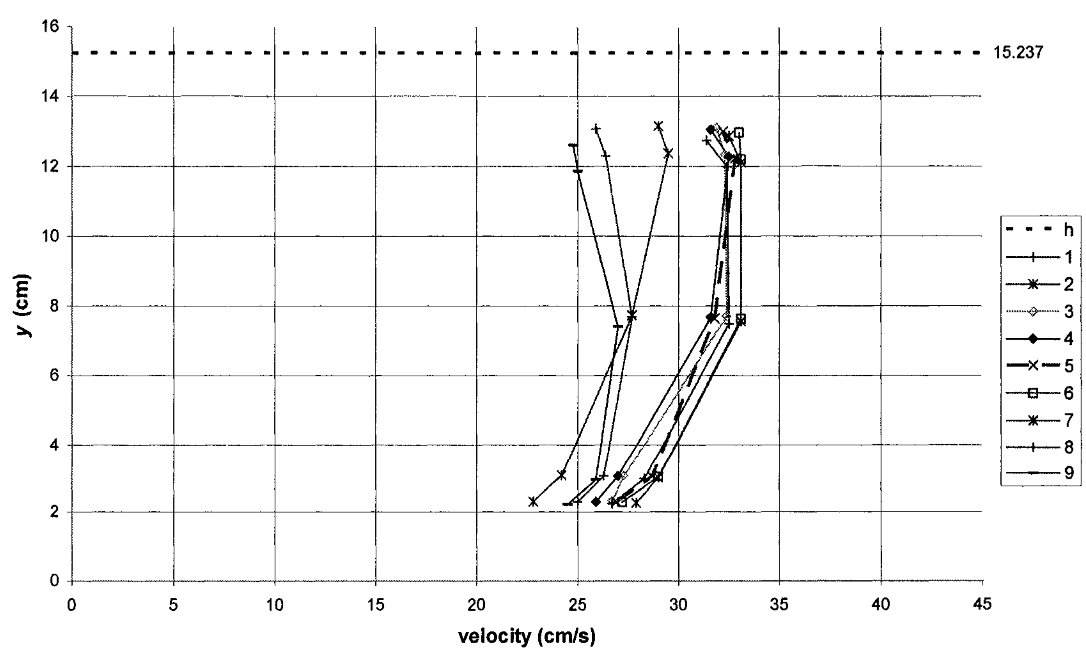

Exp#5/FS-c/sBF

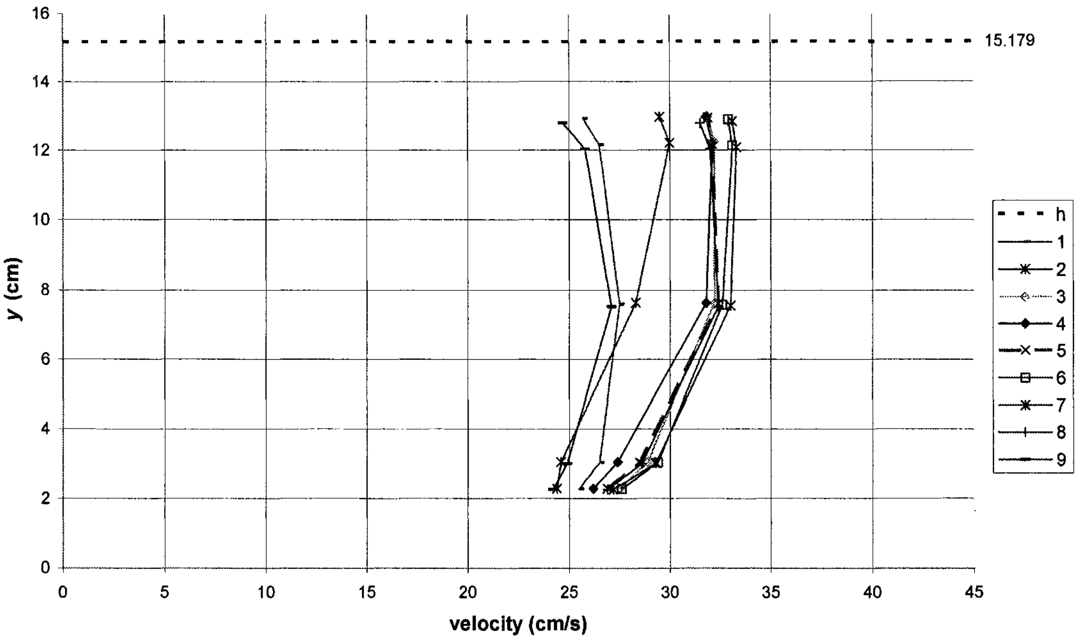

Exp#5/FS-c/sBE

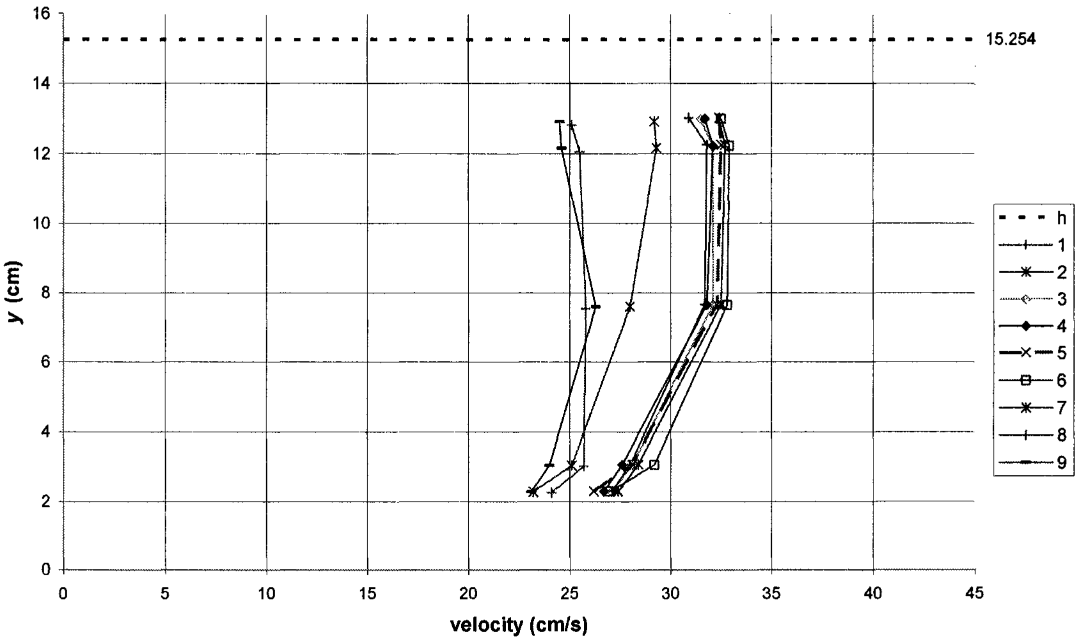

Exp#5/FS-c/sBD

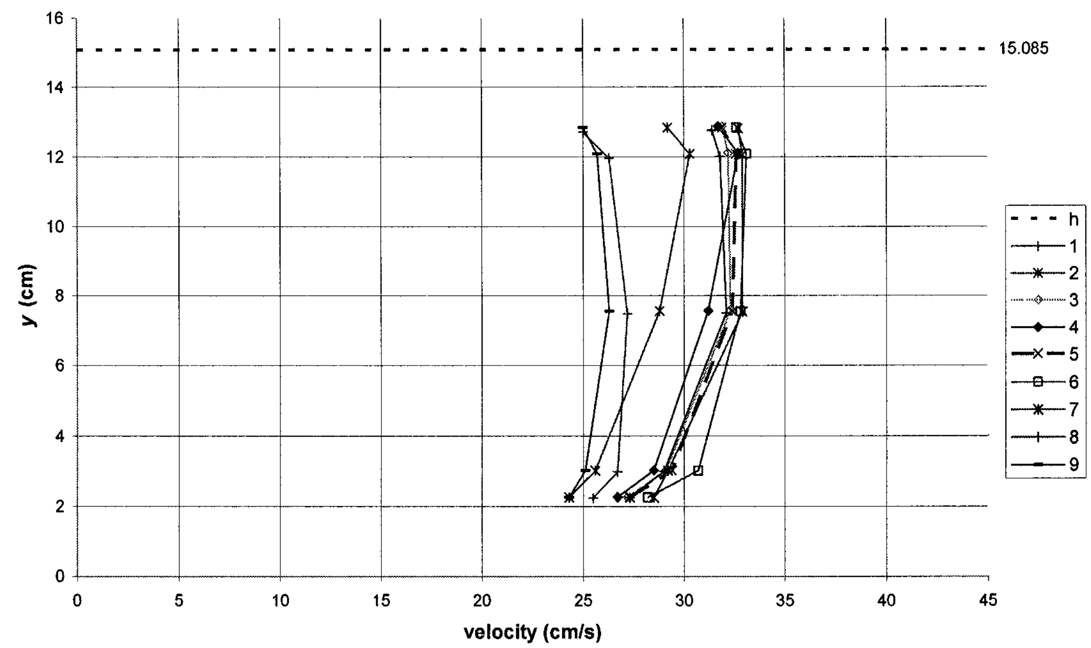

Exp#5/FS-c/sBC

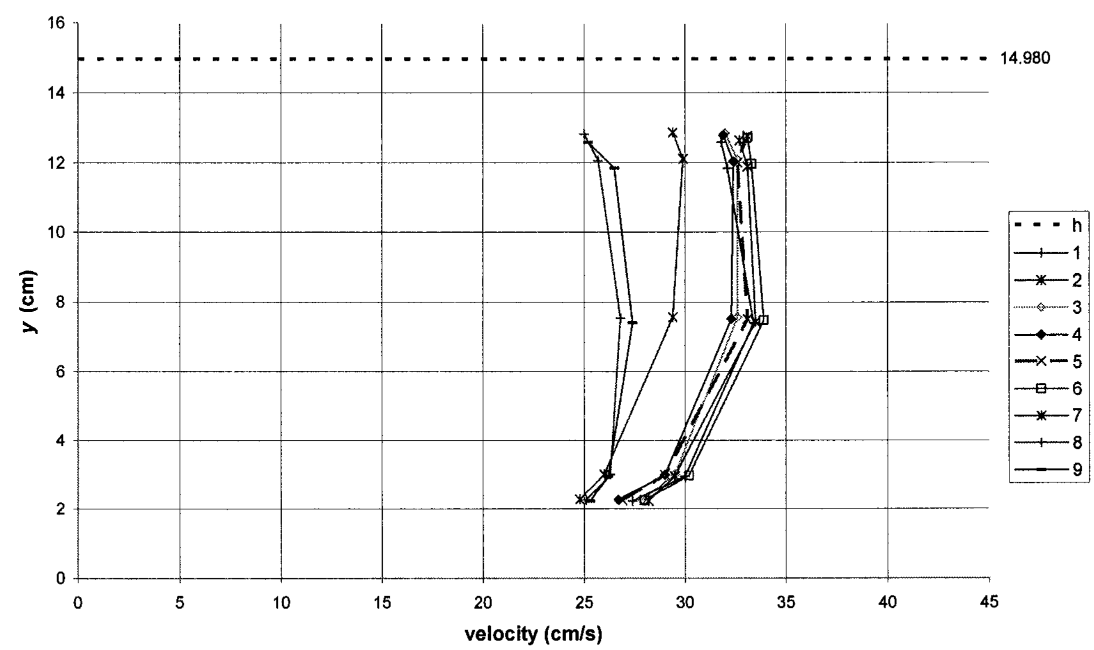

Exp#5/FS-c/sBB

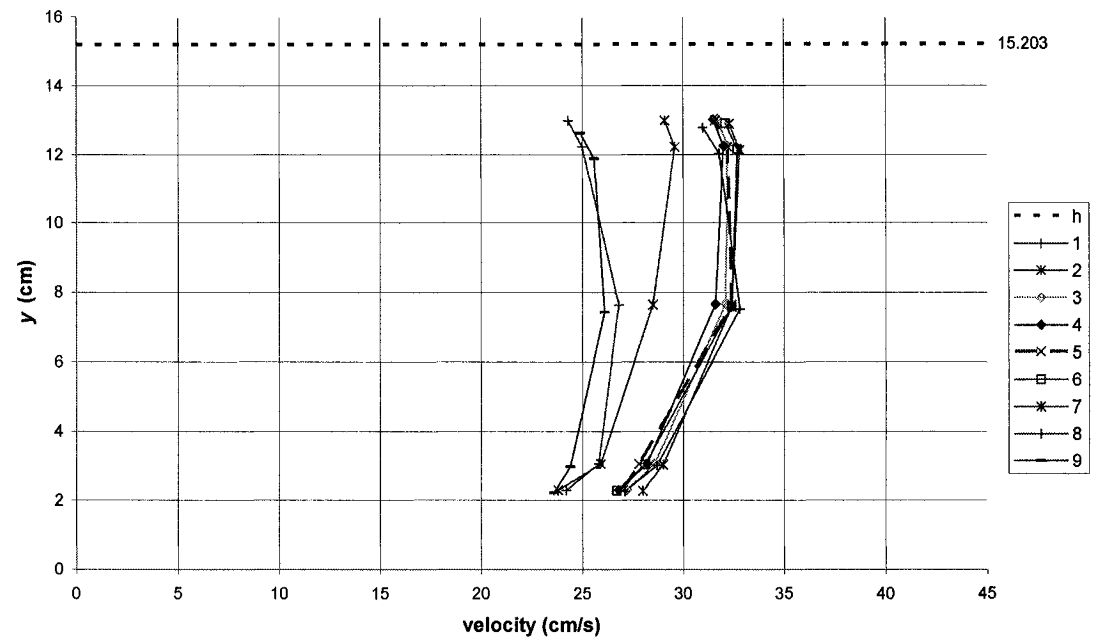

Exp#5/FS-c/sBA

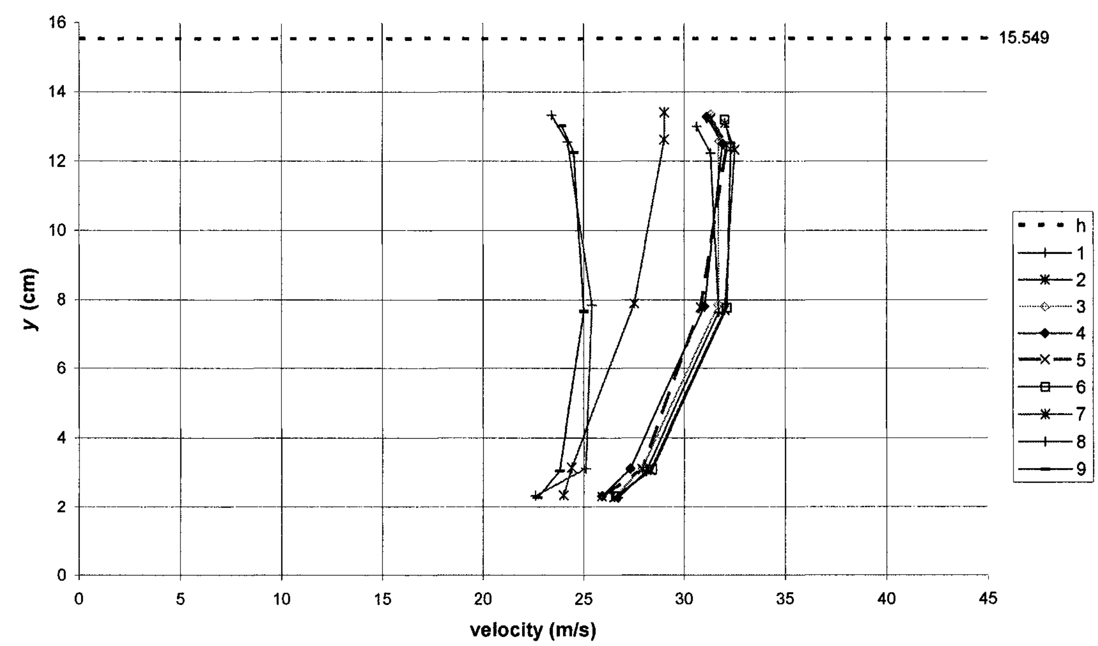

APPENDIX A6

Numerical Simulation of **Exp#4**

(TIC and 2PIC configurations)

TOTAL ICE-COVER CONFIGURATION (TIC) – simulation

Vertical velocity profile

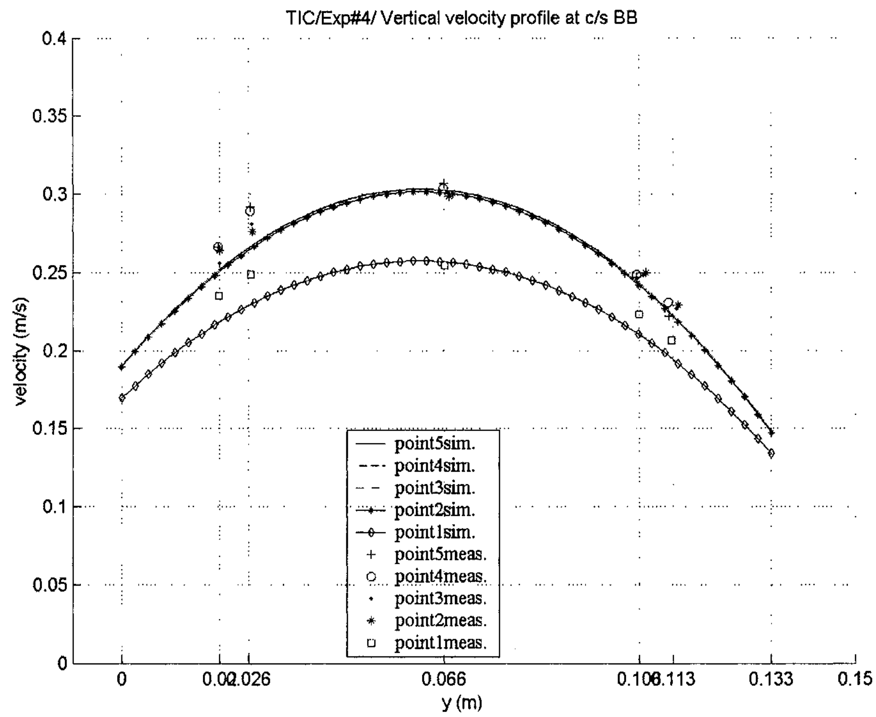

Lateral velocity profiles

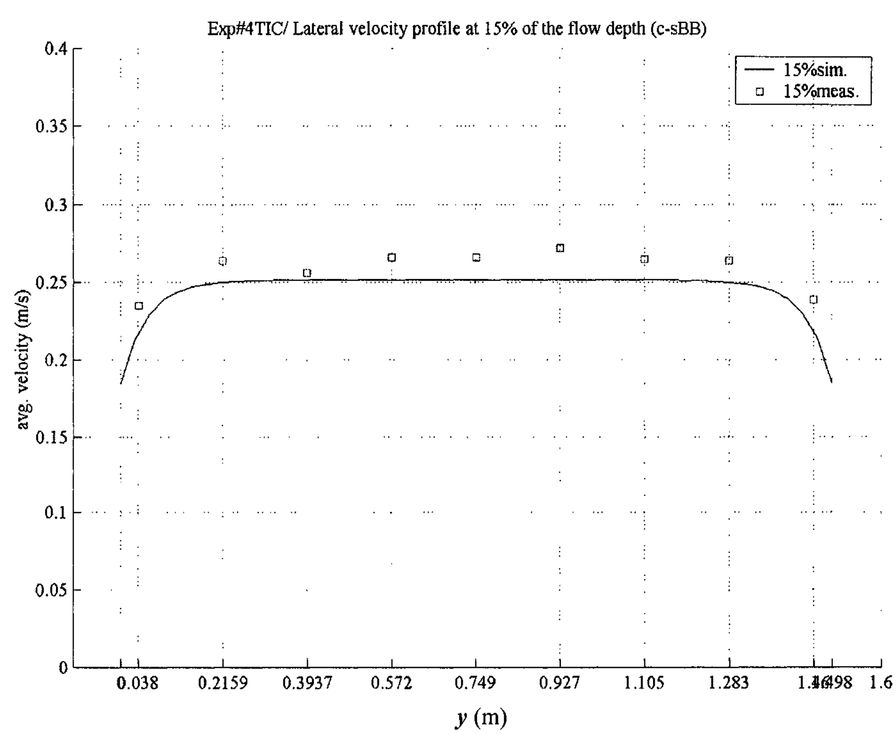

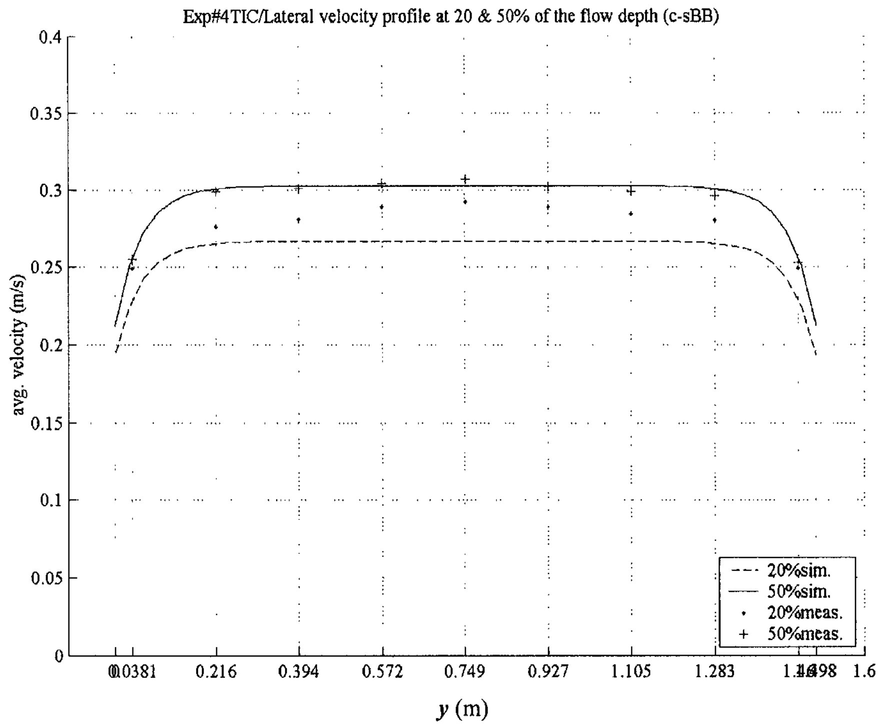
Exp#4TIC/Lateral velocity profile at 20 & 50% of the flow depth (c-sBB)
avg. velocity (m/s)
y (m)
20%sim.
50%sim.
20%meas.
50%meas.

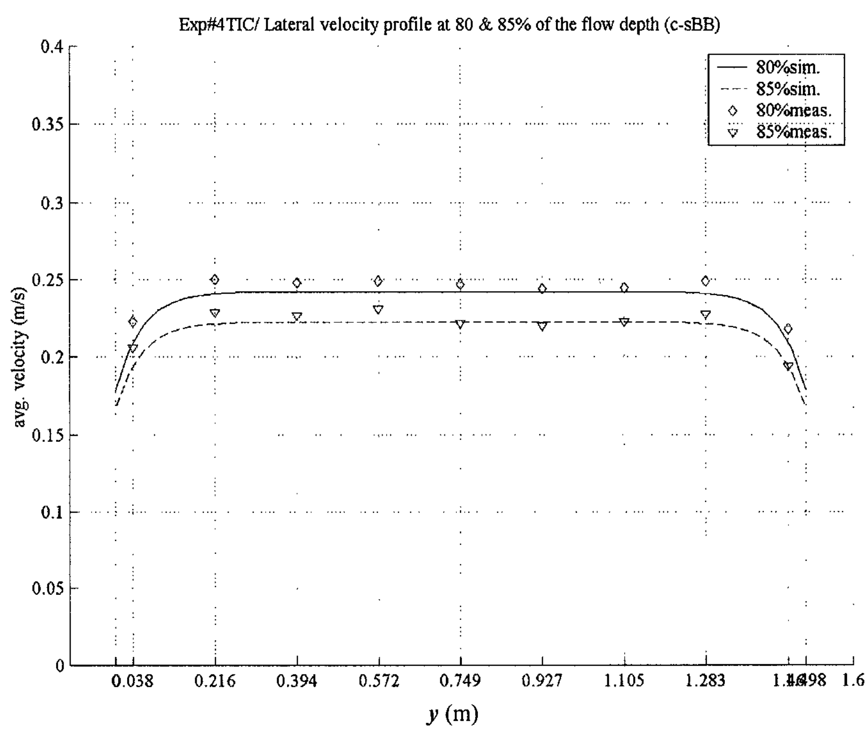
Exp#4TIC/ Lateral velocity profile at 80 & 85% of the flow depth (c-sBB)
avg. velocity (m/s)
y (m)
80%sim.
85%sim.
80%meas.
85%meas.

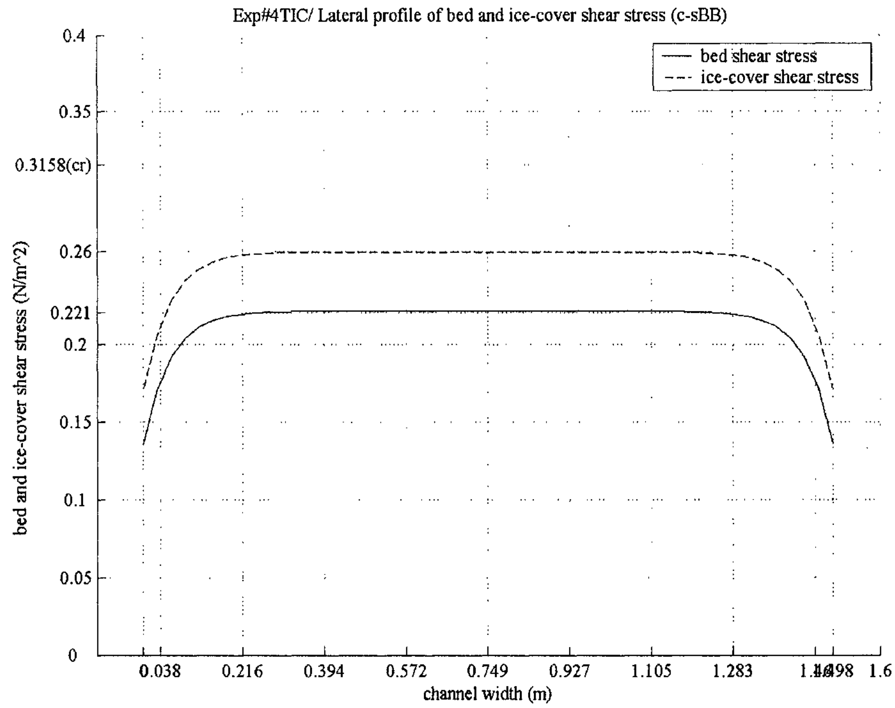

Exp#4TIC/ Lateral profile of bed and ice-cover shear stress (c-sBB)
bed shear stress
ice-cover shear stress
bed and ice-cover shear stress (N/m^2)
0.4
0.35
0.3158(cr)
0.26
0.221
0.2
0.15
0.1
0.05
0
0.038
0.216
0.394
0.572
0.749
0.927
1.105
1.283
1.6
channel width (m)

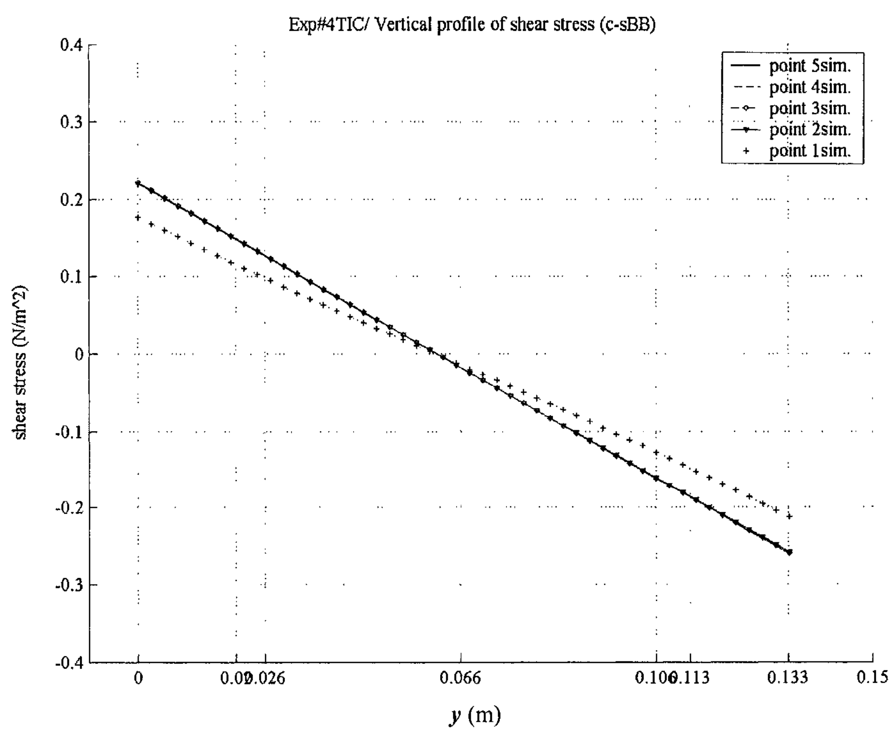

Exp#4TIC/ Vertical profile of shear stress (c-sBB)
point 5sim.
point 4sim.
point 3sim.
point 2sim.
point 1sim.
shear stress (N/m^2)
0.4
0.3
0.2
0.1
0
-0.1
-0.2
-0.3
-0.4
0
0.026
0.066
0.113
0.133
0.15
y (m)

2 SIDES PARTIAL ICE-COVER CONFIGURATION (2PIC) - simulation

Vertical velocity profile

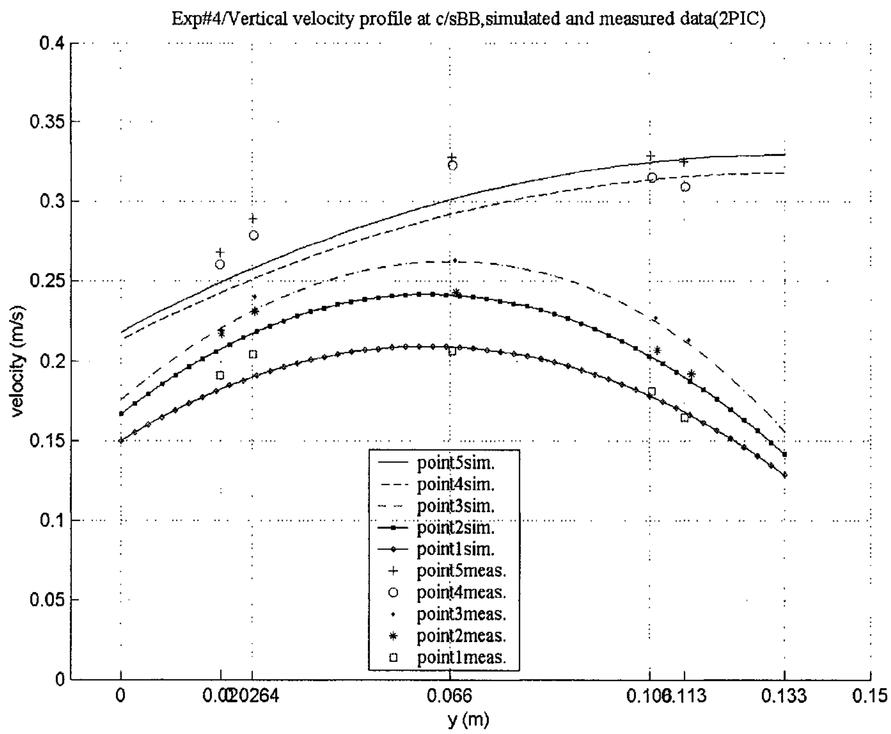

Lateral velocity profiles

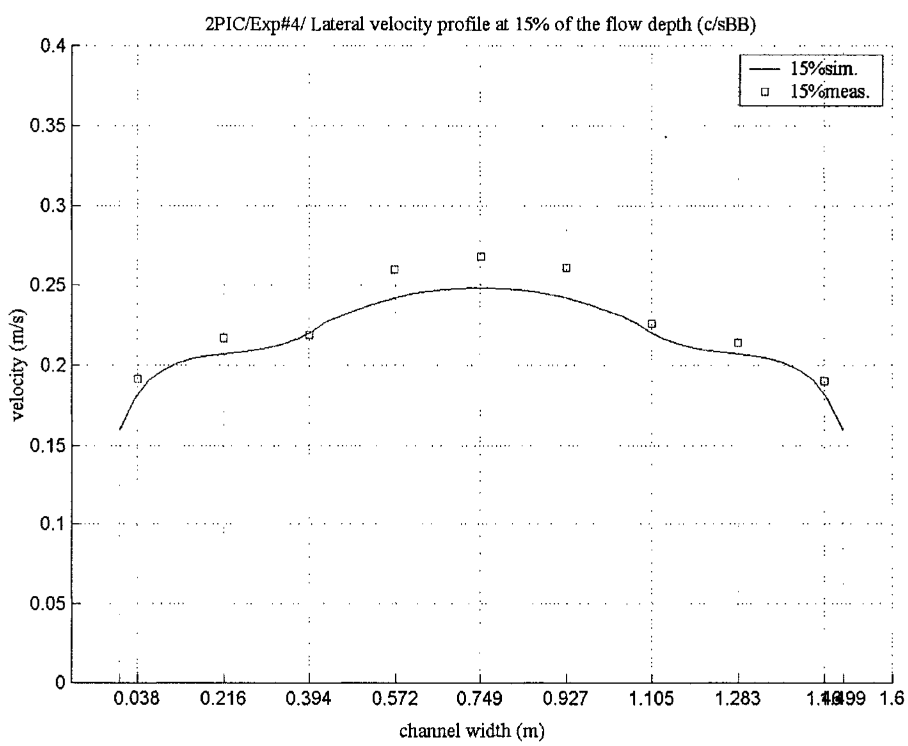

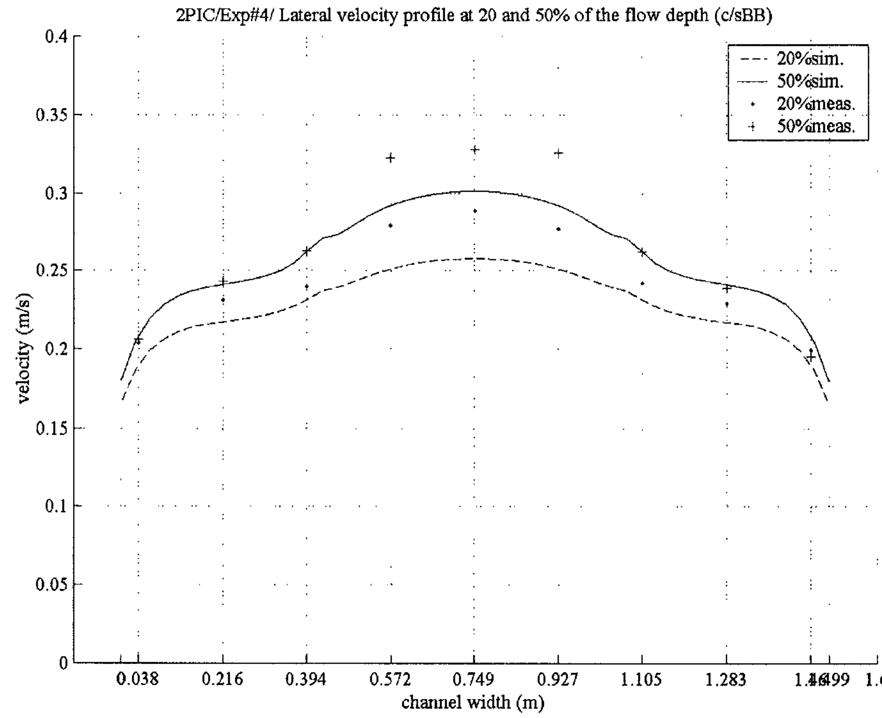

2PIC/Exp#4/ Lateral velocity profile at 20 and 50% of the flow depth (c/sBB)
20%sim.
50%sim.
20%meas.
50%meas.
velocity (m/s)
channel width (m)
0.038
0.216
0.394
0.572
0.749
0.927
1.105
1.283
1.6

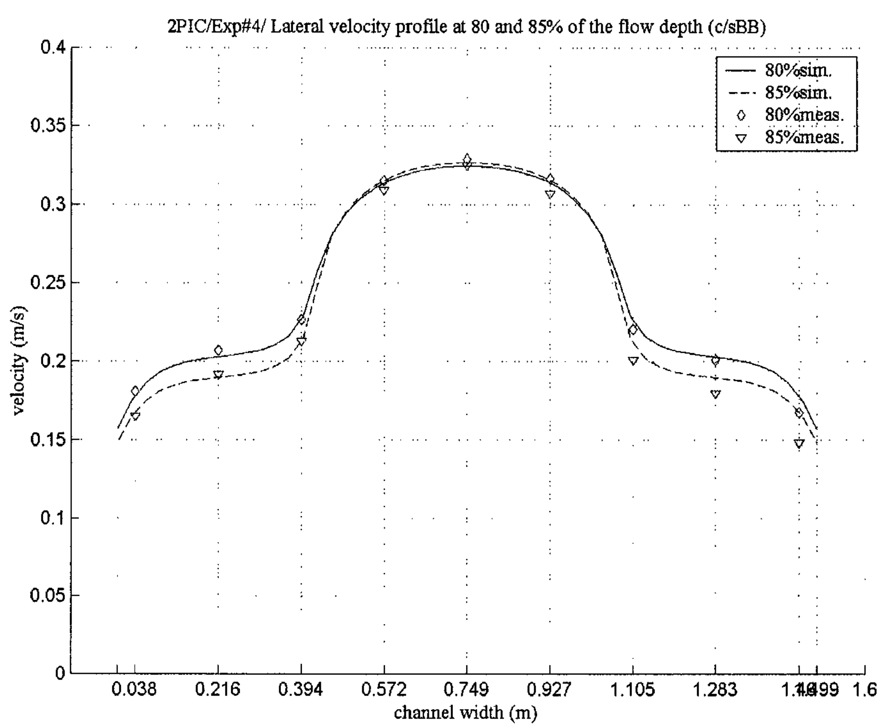

2PIC/Exp#4/ Lateral velocity profile at 80 and 85% of the flow depth (c/sBB)
80%sim.
85%sim.
80%meas.
85%meas.
velocity (m/s)
channel width (m)
0.038
0.216
0.394
0.572
0.749
0.927
1.105
1.283
1.6

Lateral and vertical shear stress profiles

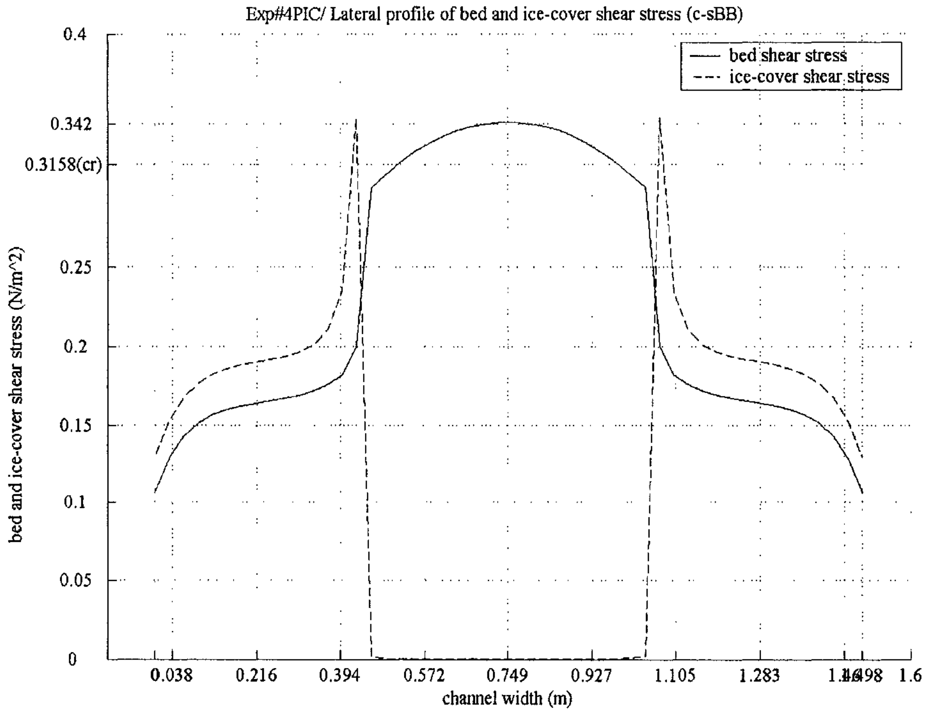

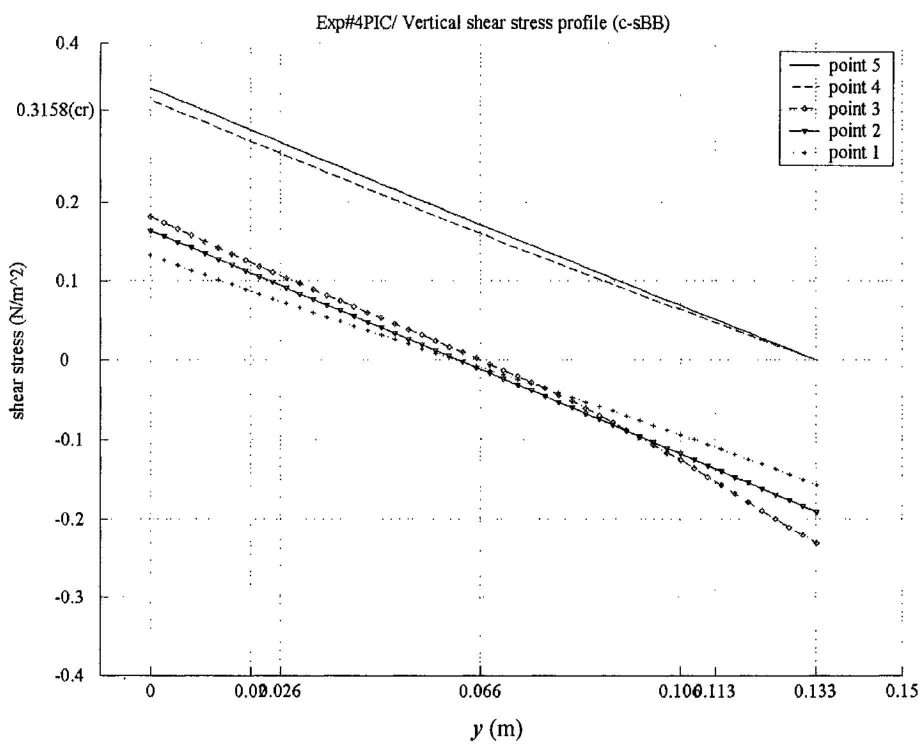

APPENDIX A7

ExpBP#1

FREE-SURFACE CONFIGURATION (FS) at ice-cover critical conditions

(experiment with bridge pier)

FREE-SURFACE CONFIGURATION (FS) – at ice-cover critical conditions

Lateral velocity profiles

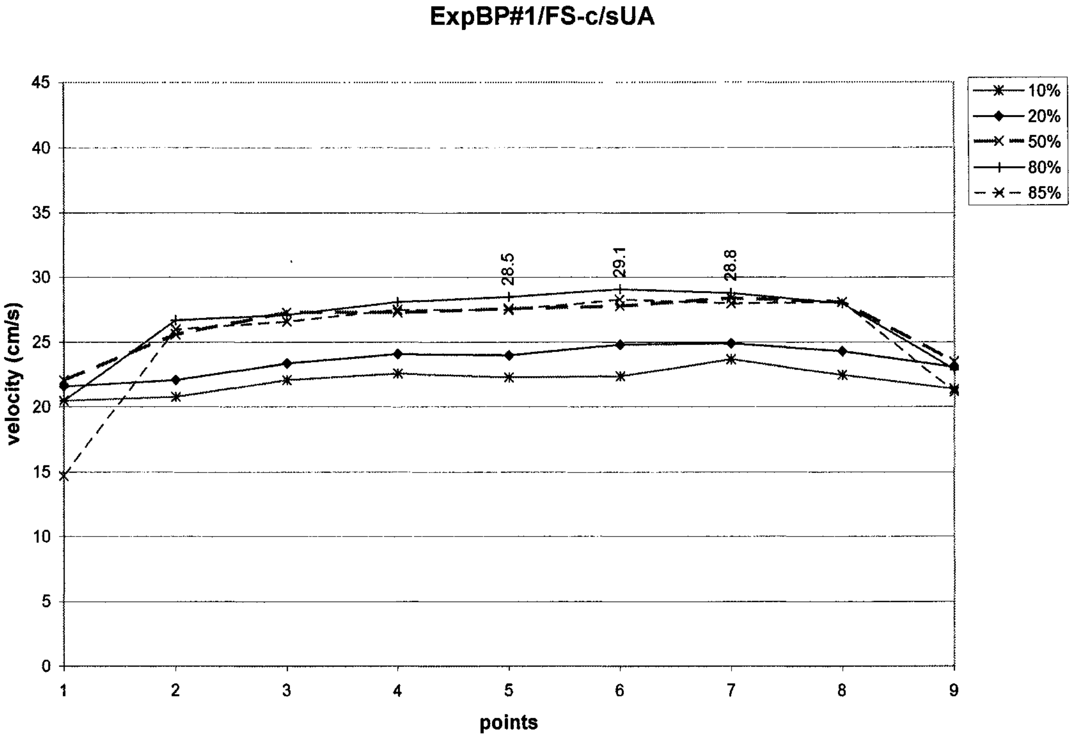

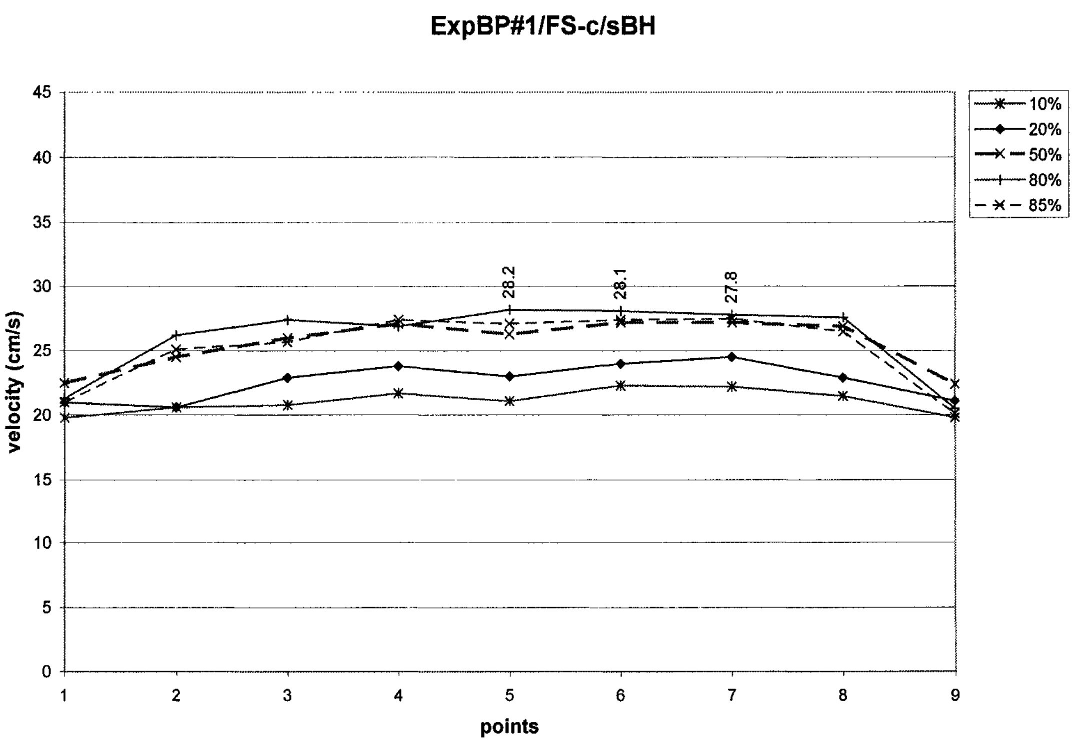

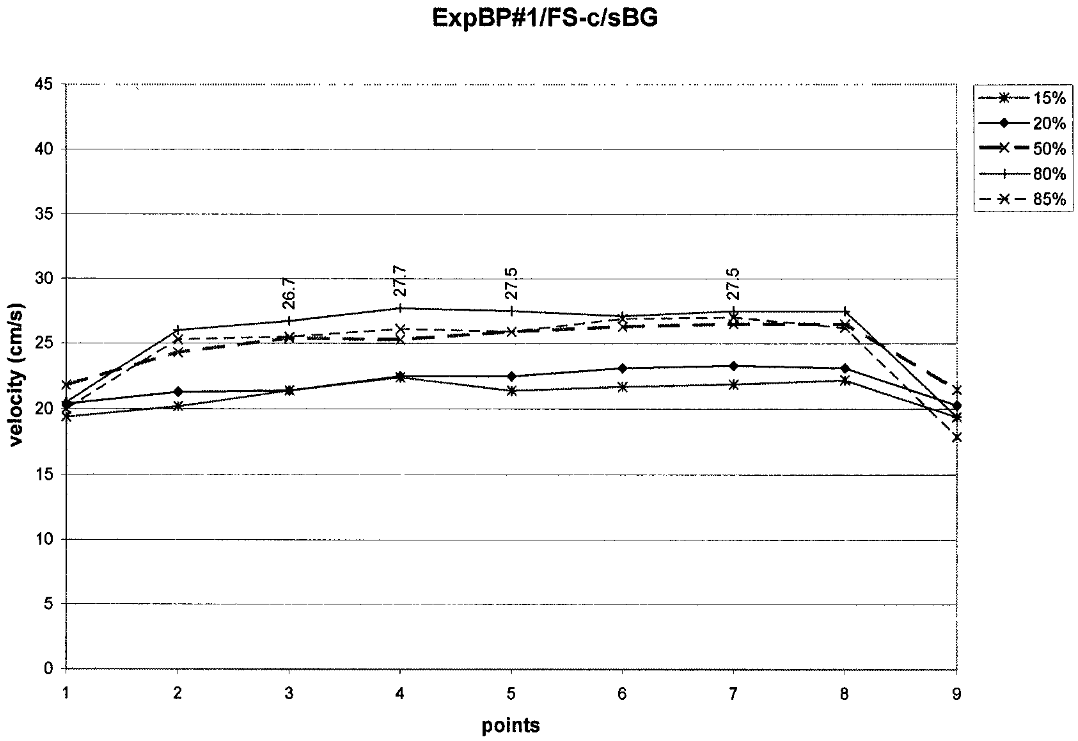
ExpBP#1/FS-c/sBG
velocity (cm/s)
points
15%
20%
50%
80%
85%
26.7
27.7
27.5
27.5

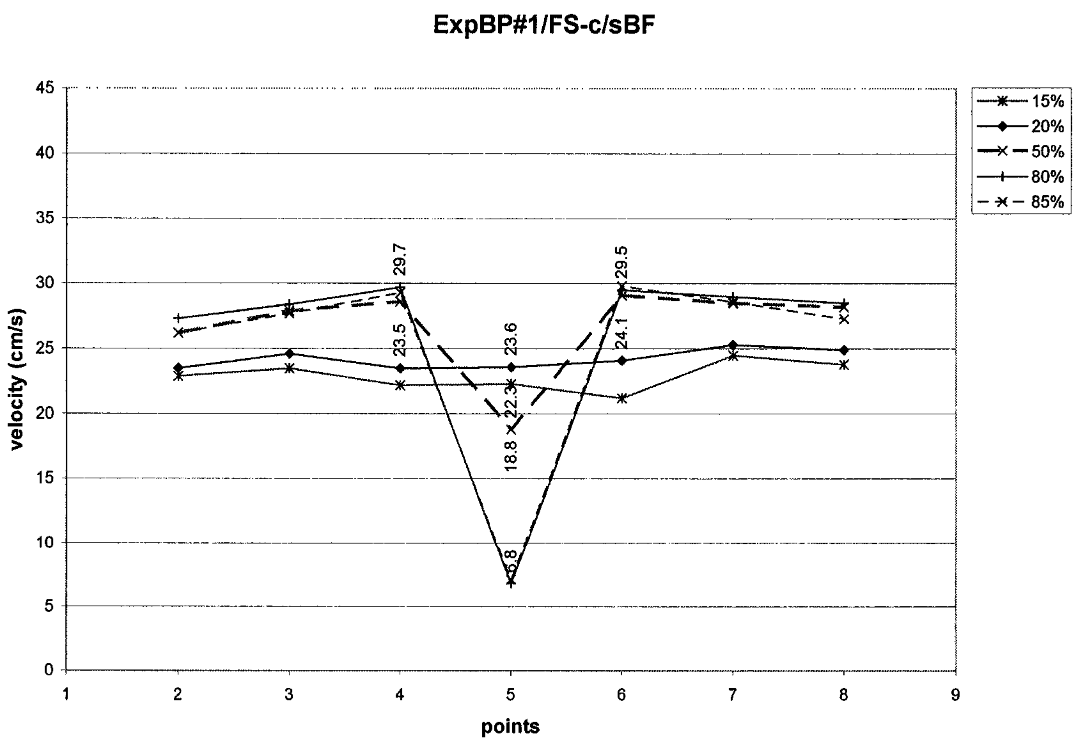
ExpBP#1/FS-c/sBF
velocity (cm/s)
points
15%
20%
50%
80%
85%
29.7
29.5
23.5
23.6
24.1
22.3
18.8
6.8

ExpBP#1/FS-c/sBE

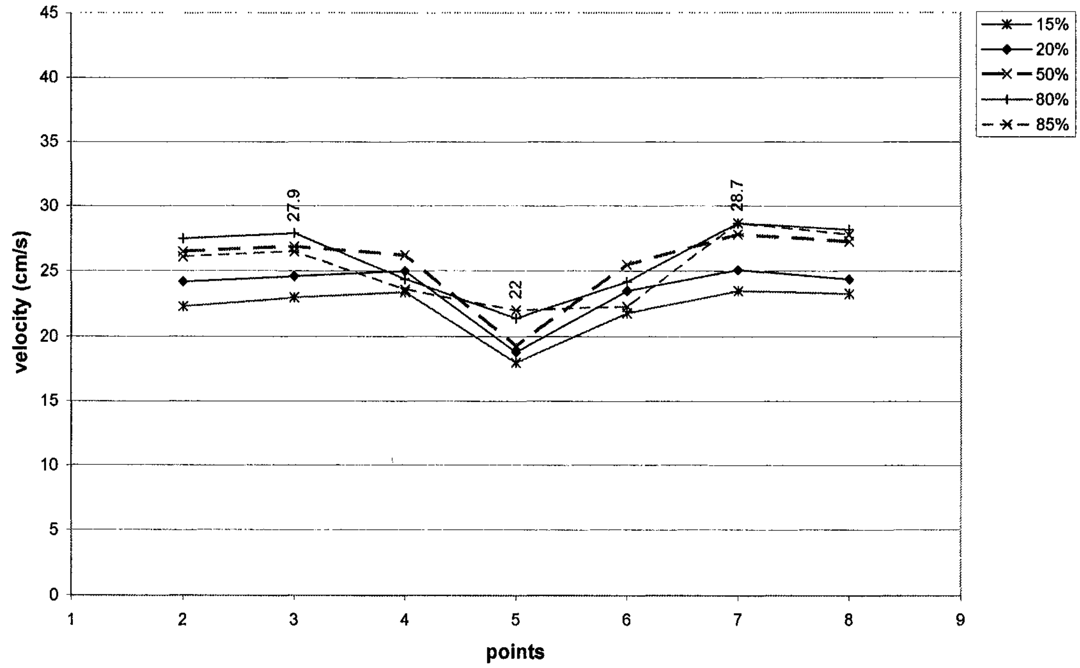

ExpBP#1/FS-c/sBD

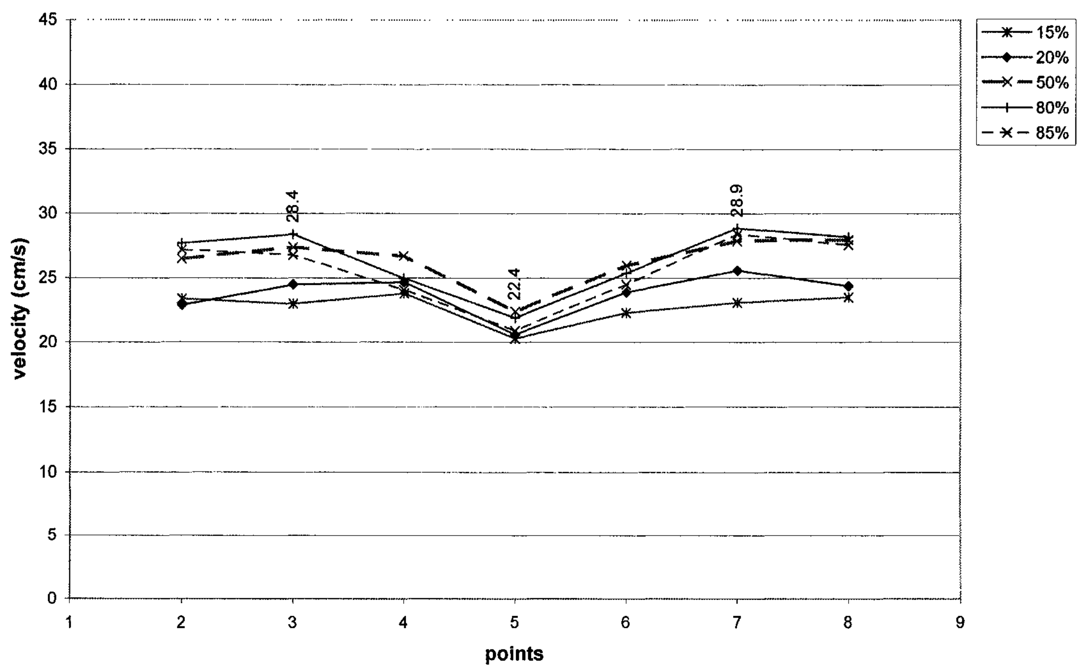

ExpBP#1/FS-c/sBC

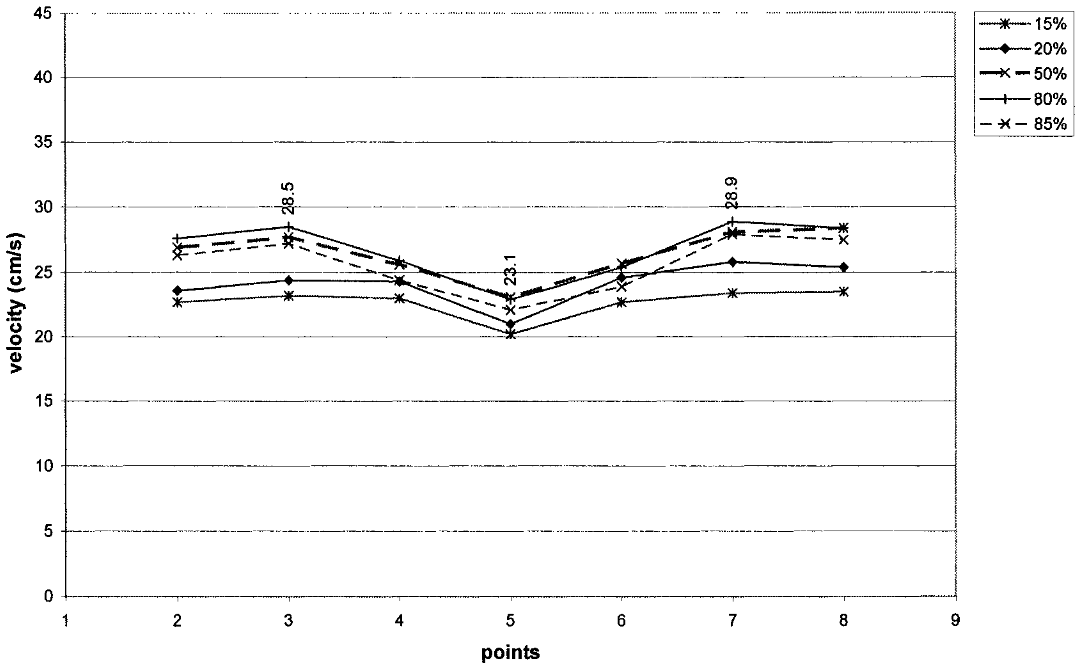

ExpBP#1/FS-c/sBB

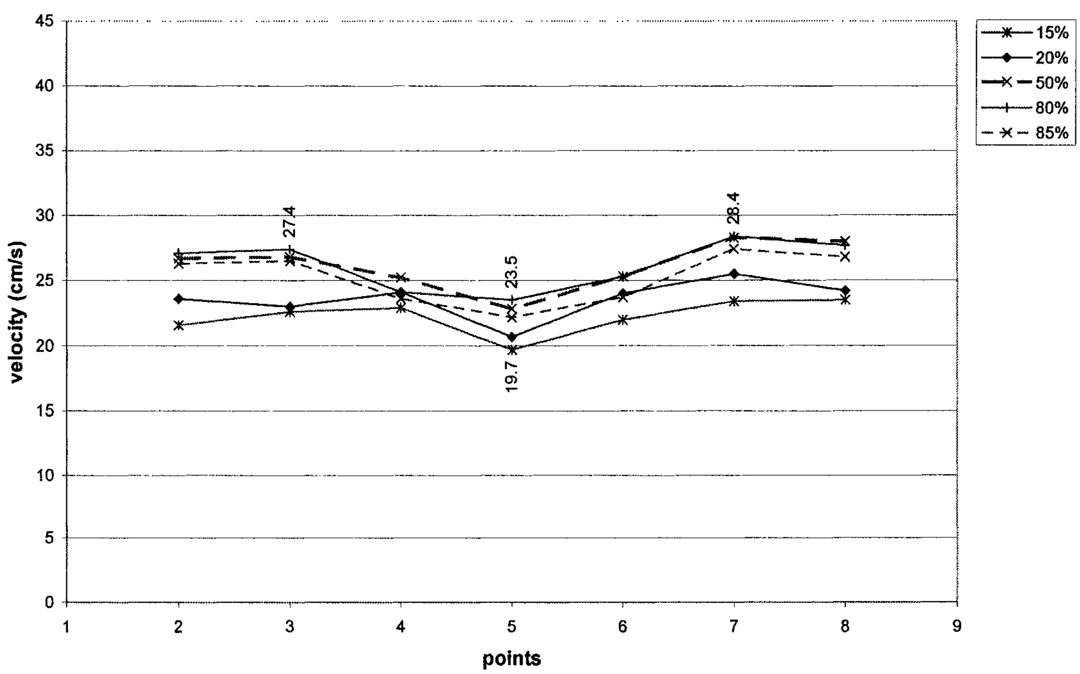

ExpBP#1/FS-c/sBA

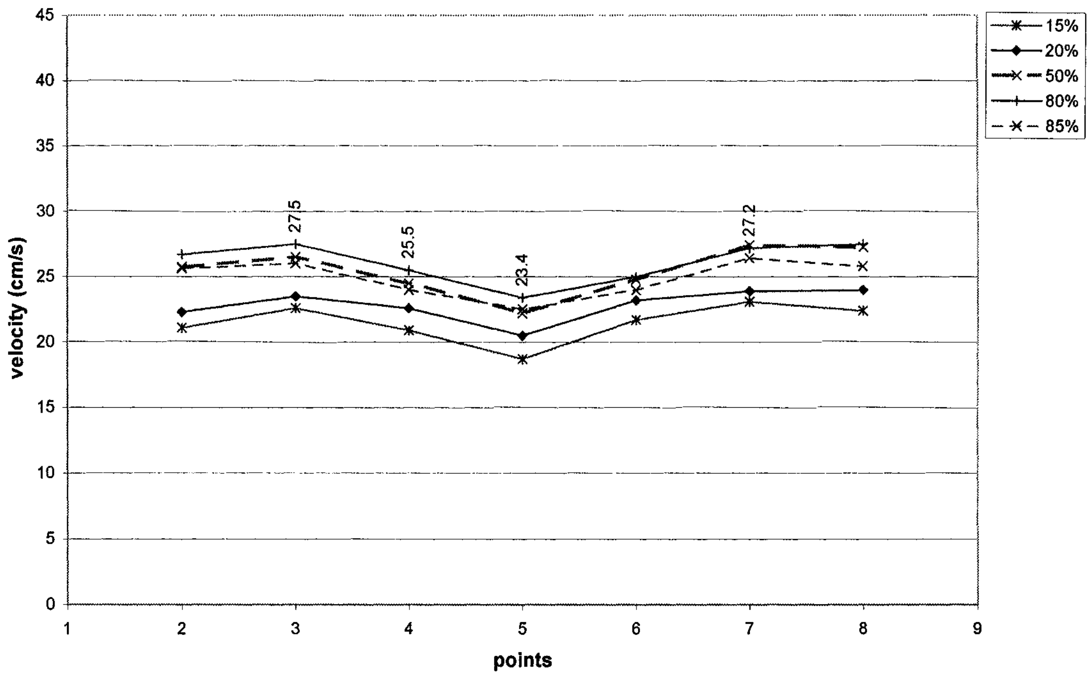

Vertical velocity profiles

ExpBP#1/FS-c/sUA

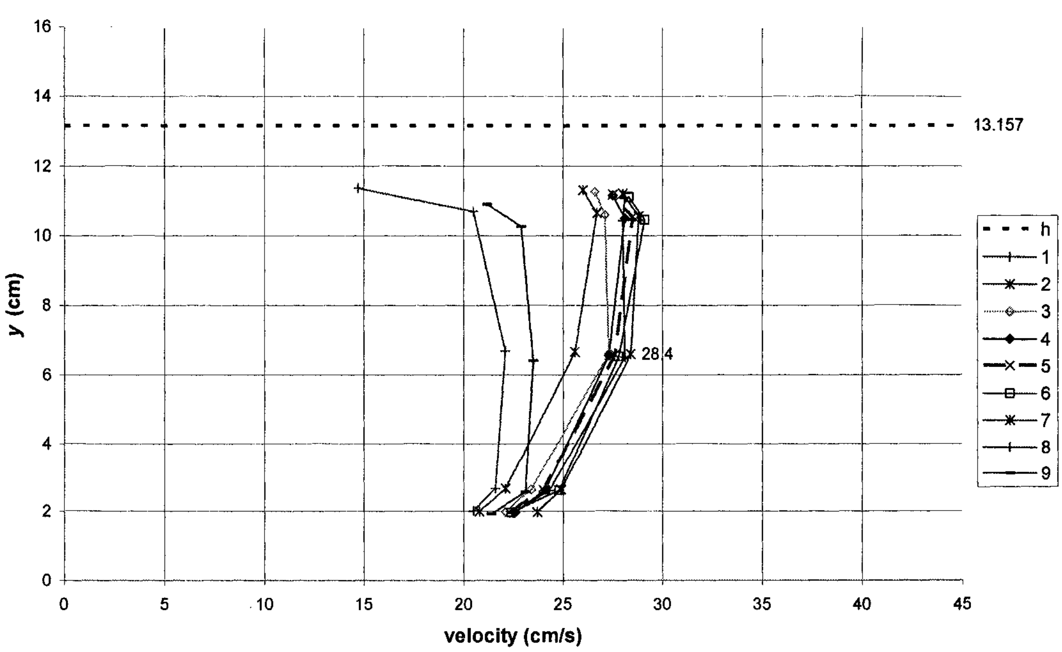

ExpBP#1/FS-c/sBH

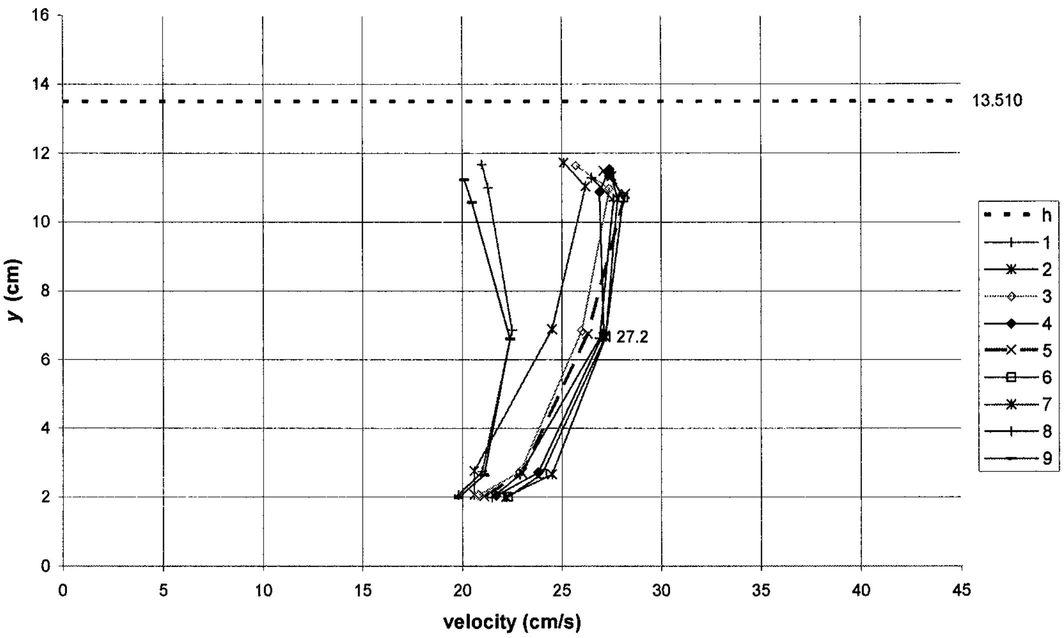

ExpBP#1/FS-c/sBG

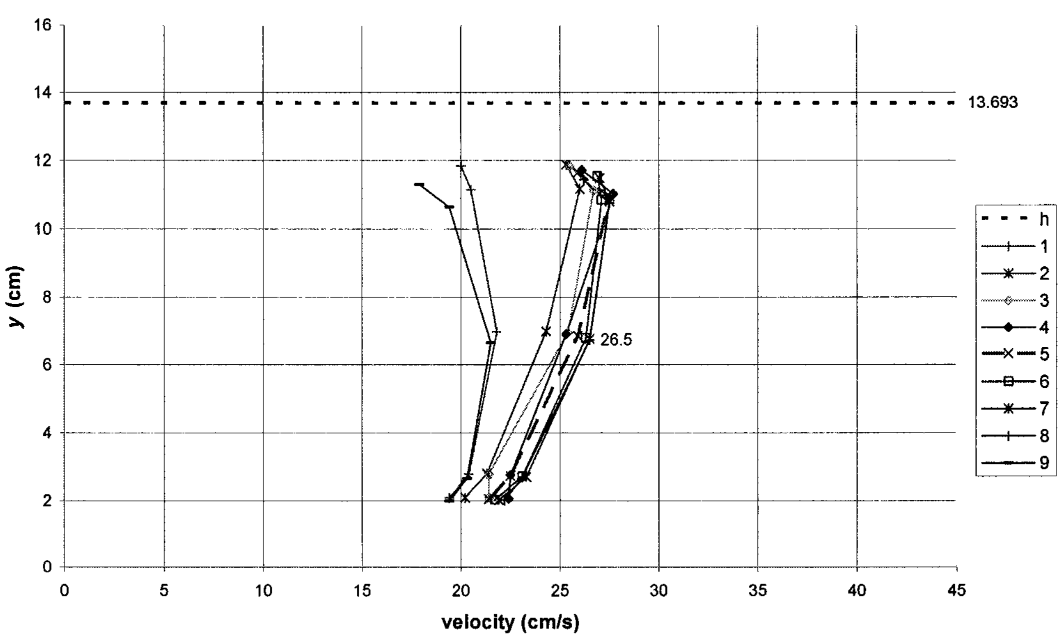

ExpBP#1/FS-c/sBF

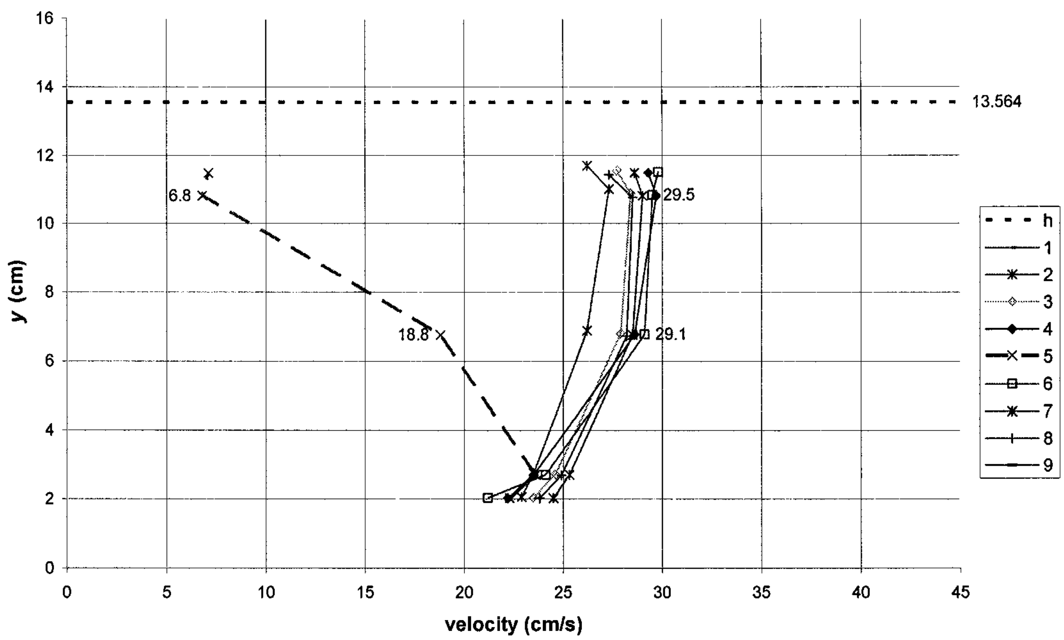

ExpBP#1/FS-c/sBE

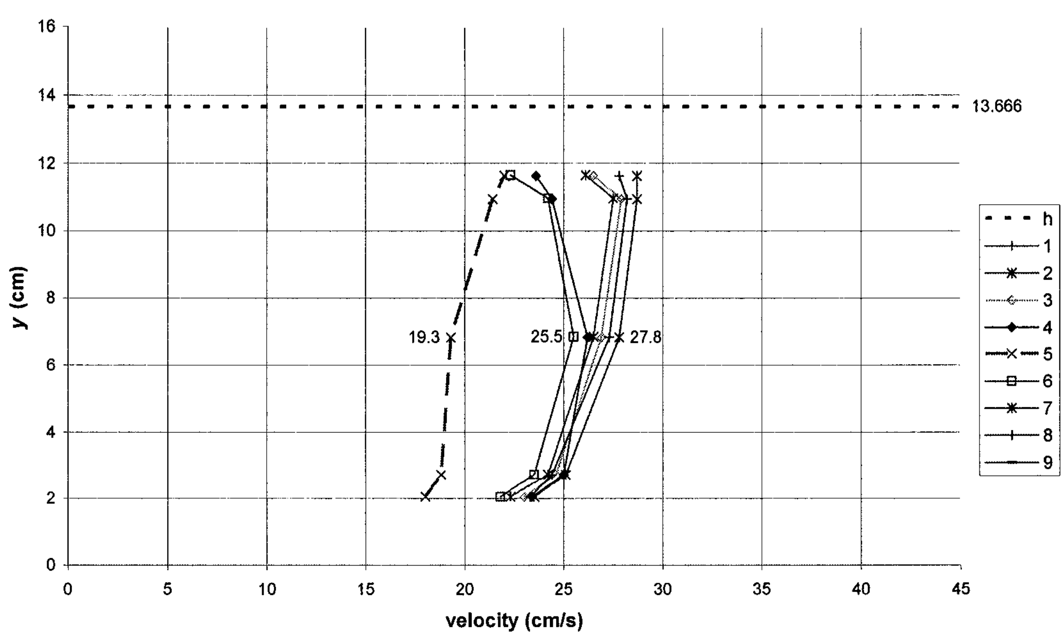

ExpBP#1/FS-c/sBD

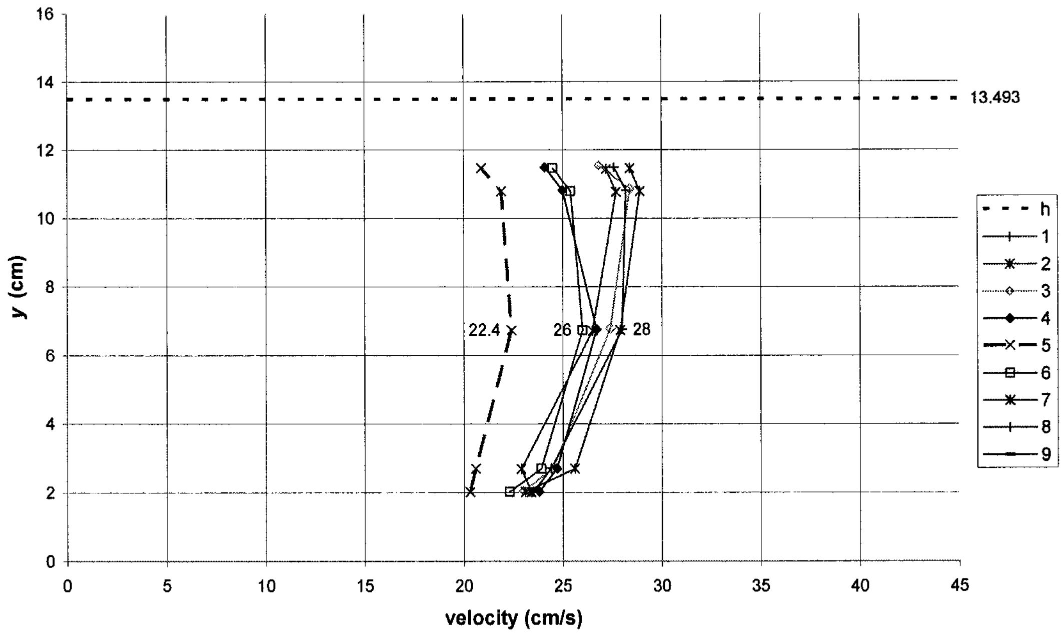

ExpBP#1/FS-c/sBC

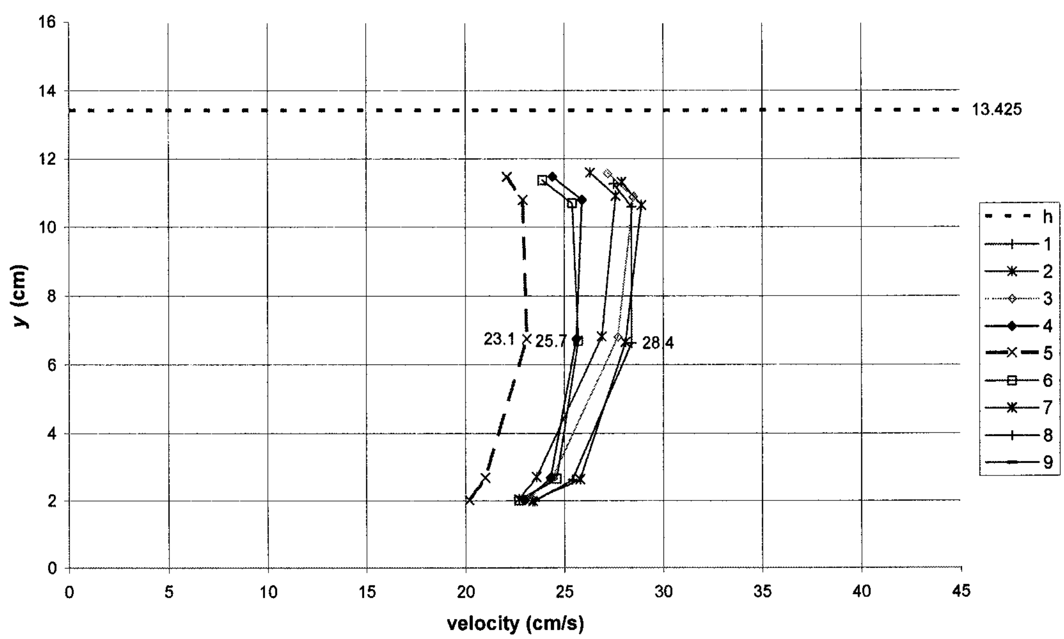

ExpBP#1/FS-c/sBB

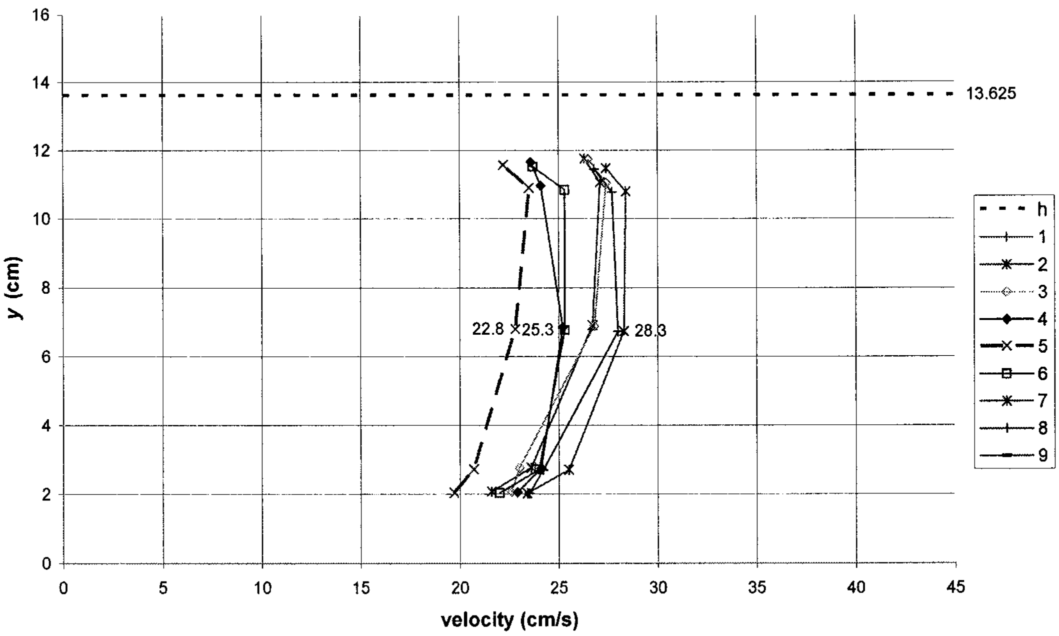

ExpBP#1/FS-c/sBA

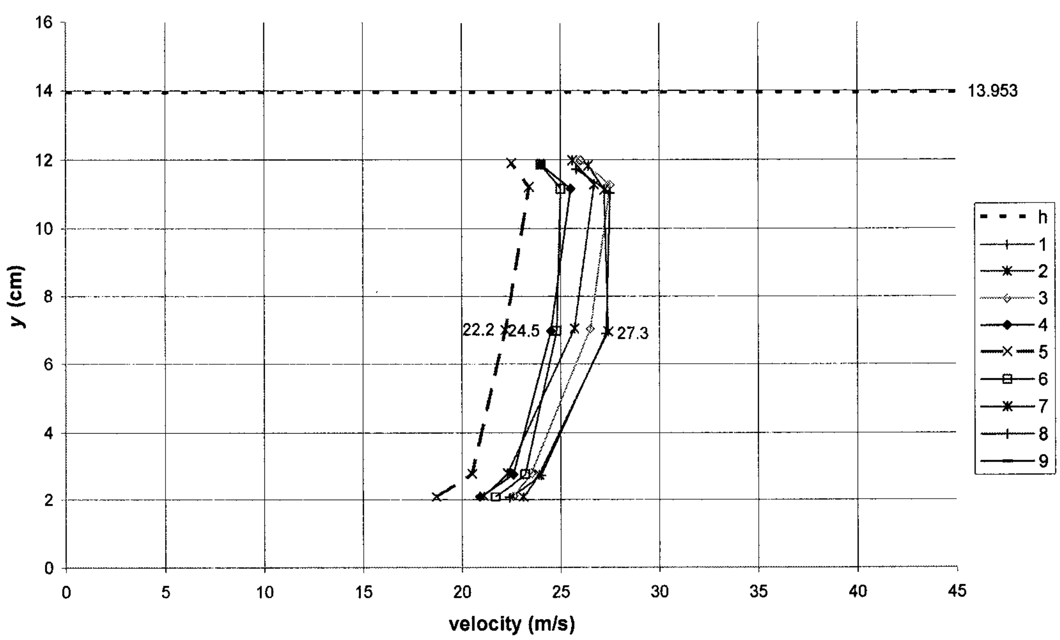

APPENDIX A8

ExpBP#2

2SIDES PARTIAL ICE-COVER CONFIGURATION (2PIC) at ice-cover critical conditions

(experiment with bridge pier)

2 SIDES PARTIAL ICE-COVER CONFIGURATION (2PIC) at ice-cover critical conditions

Lateral velocity profiles

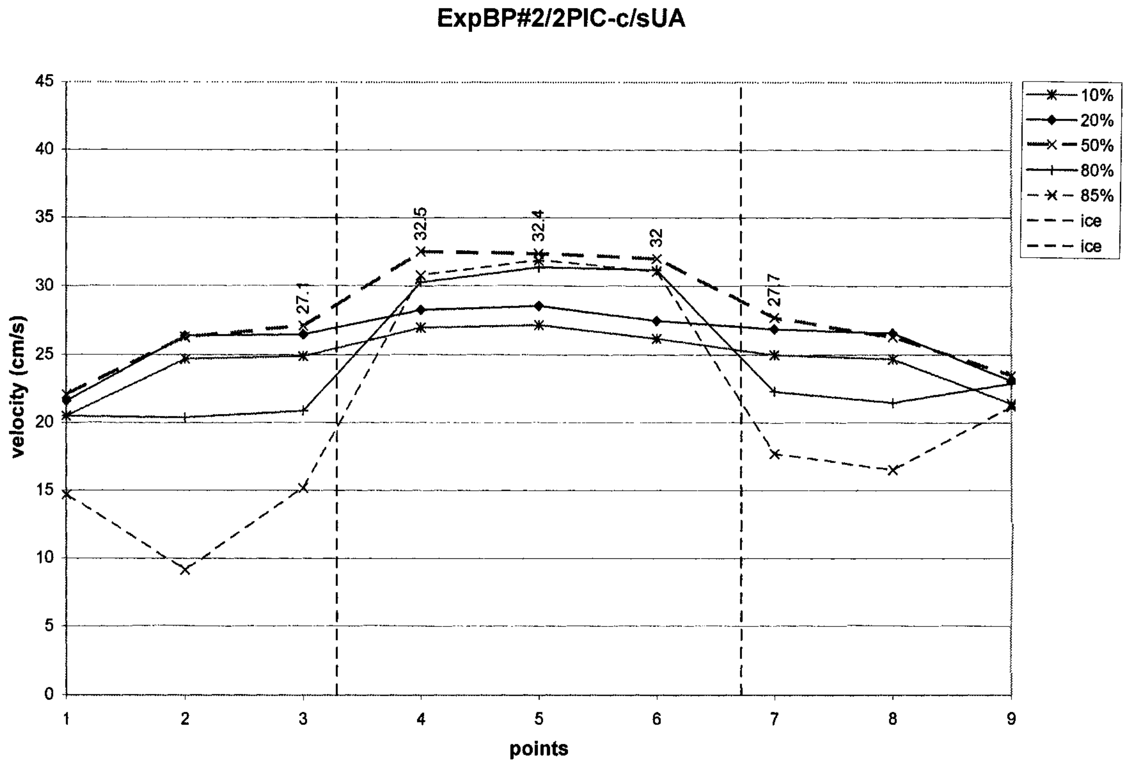

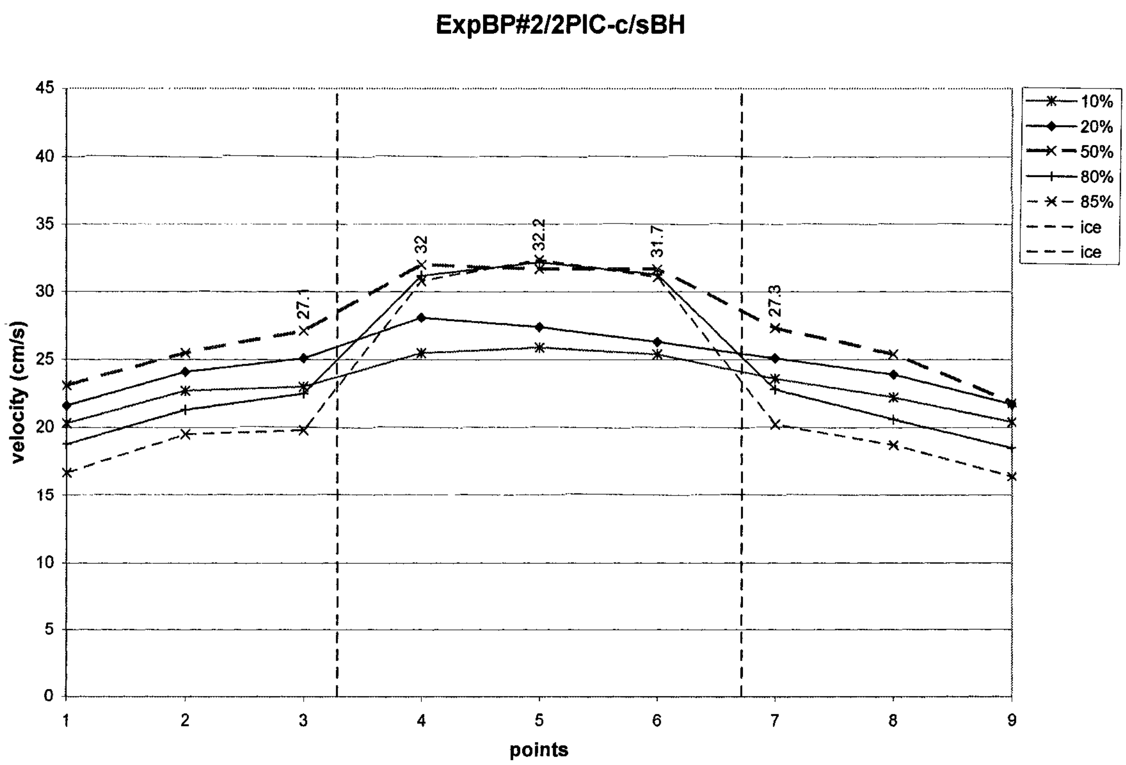

ExpBP#2/2PIC-c/sBG

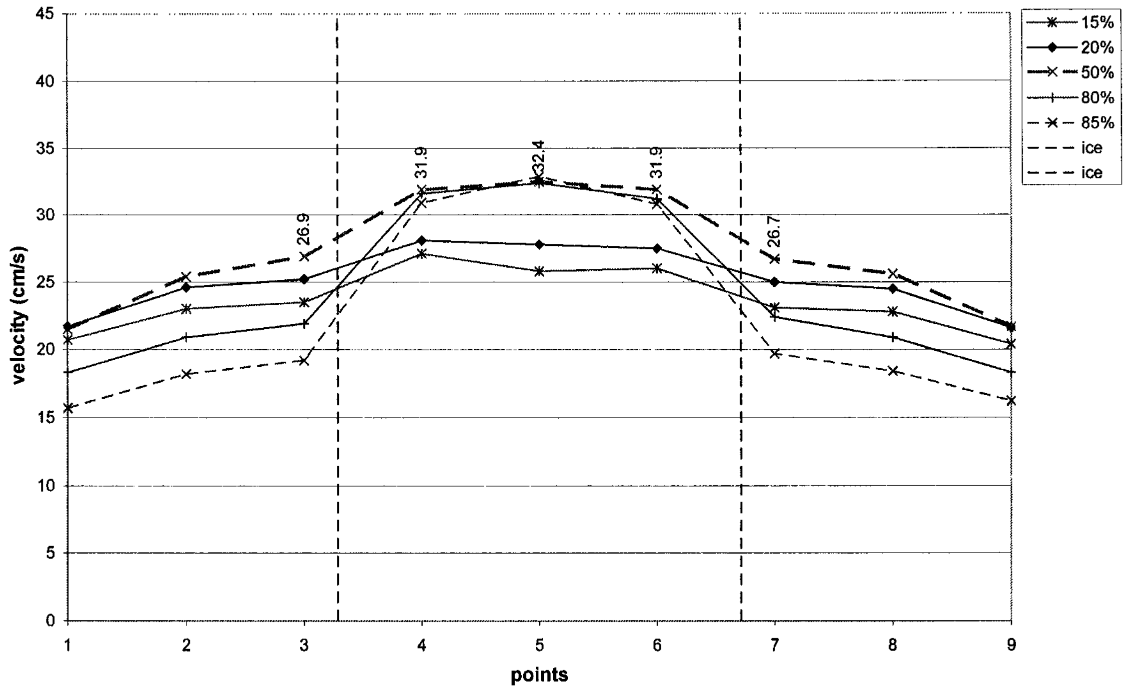

ExpBP#2/2PIC-c/sBF

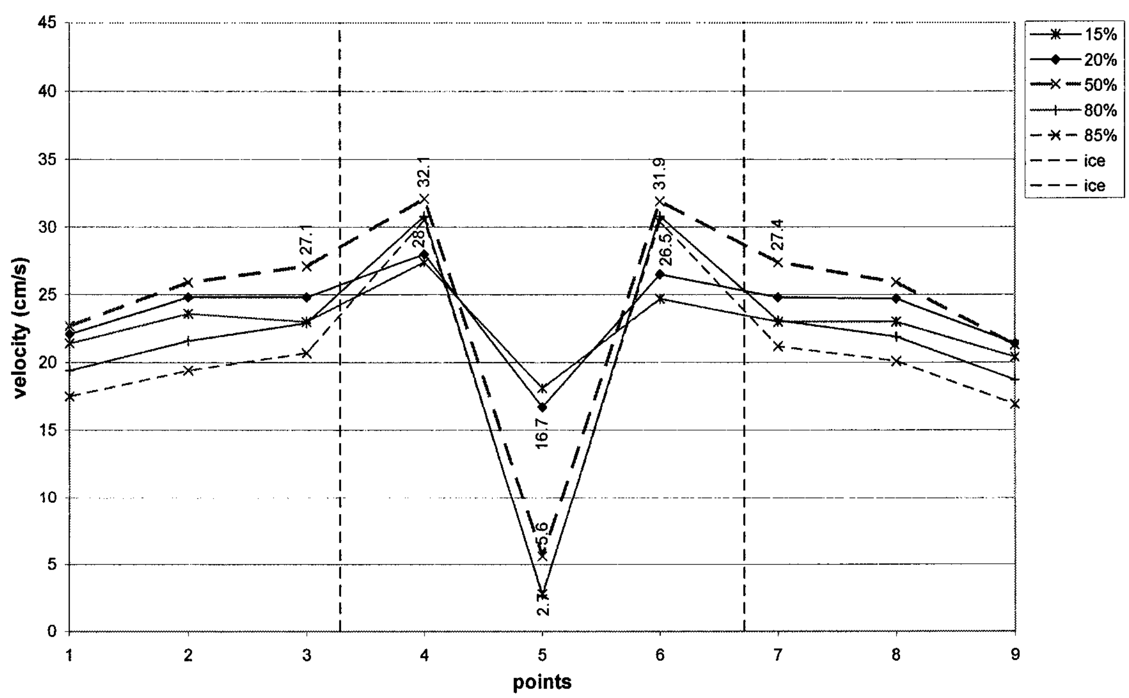

ExpBP#2/2PIC-c/sBE

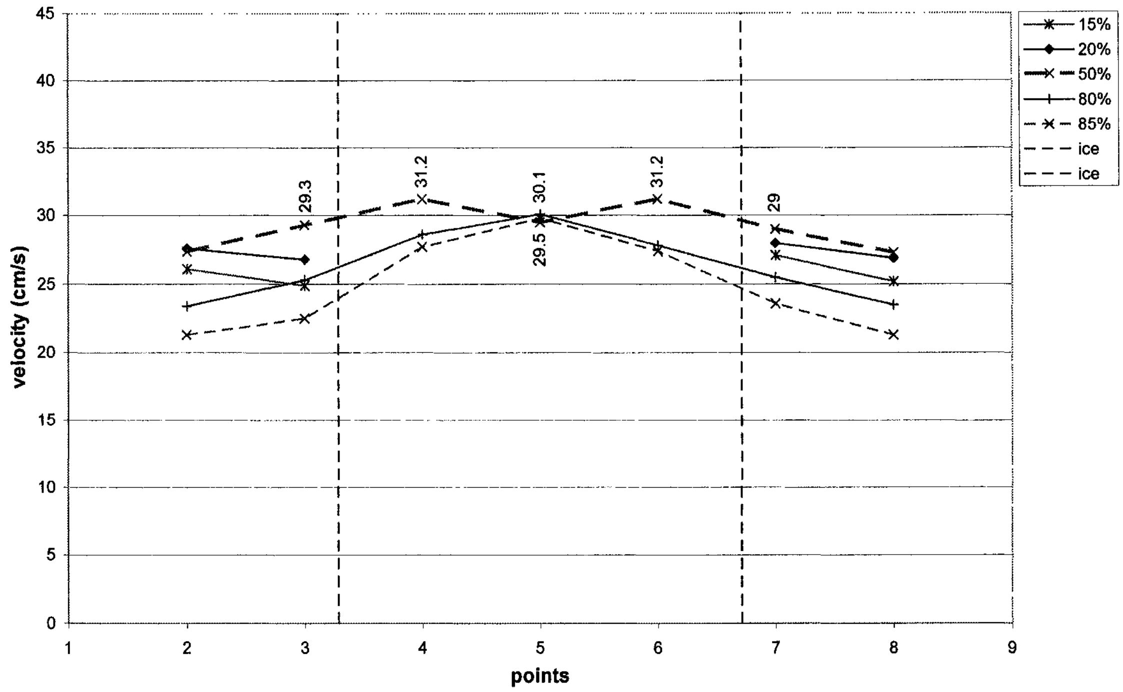

ExpBP#2/2PIC-c/sBD

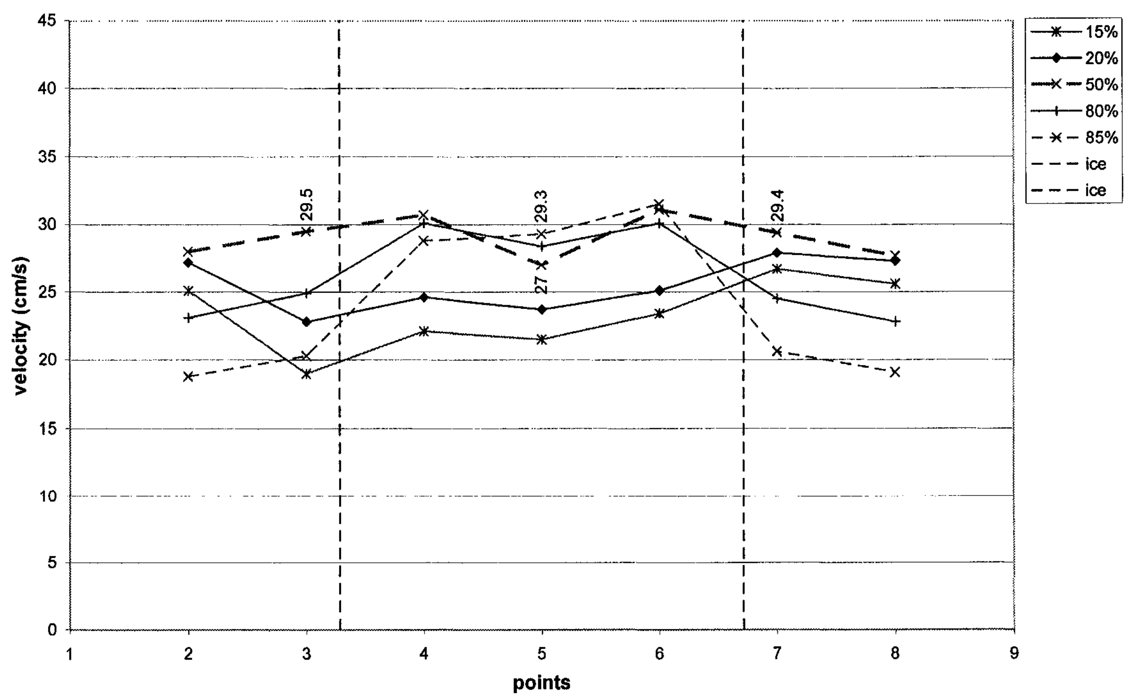

ExpBP#2/2PIC-c/sBC

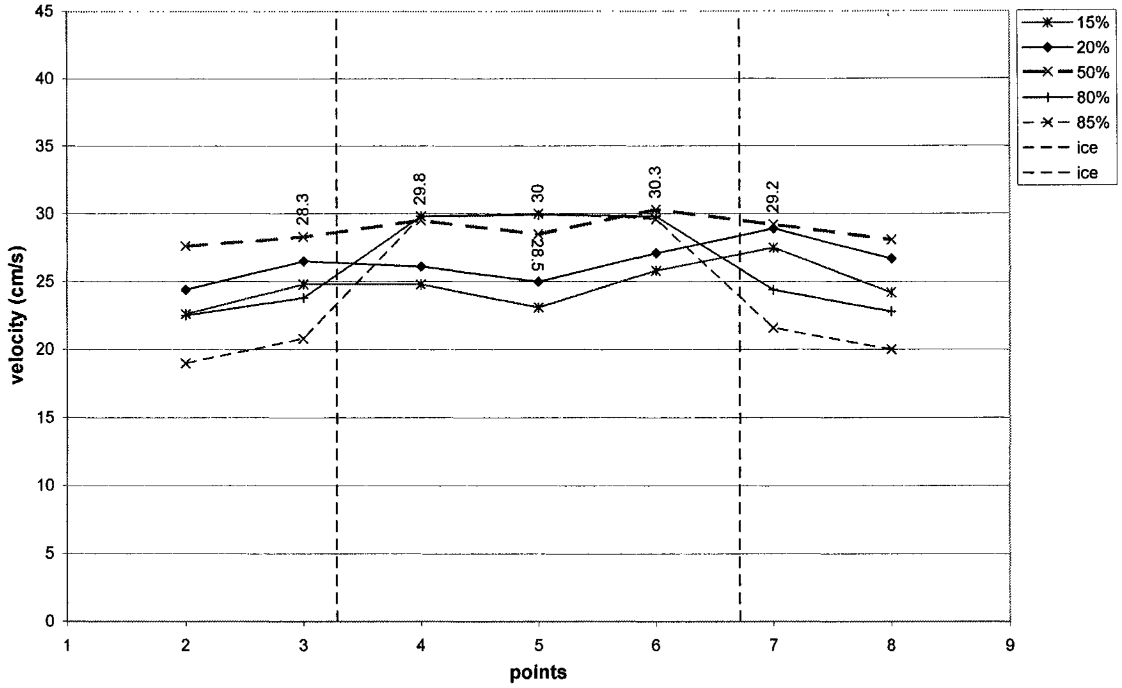

ExpBP#2/2PIC-c/sBB

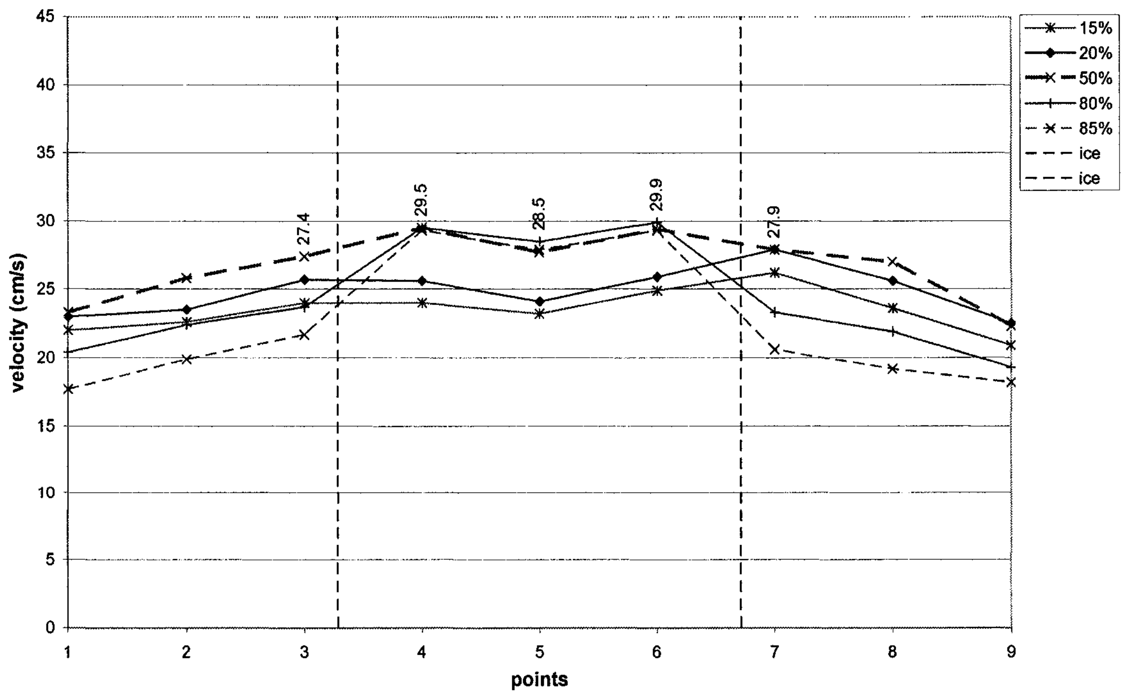

ExpBP#2/2PIC-c/sBA

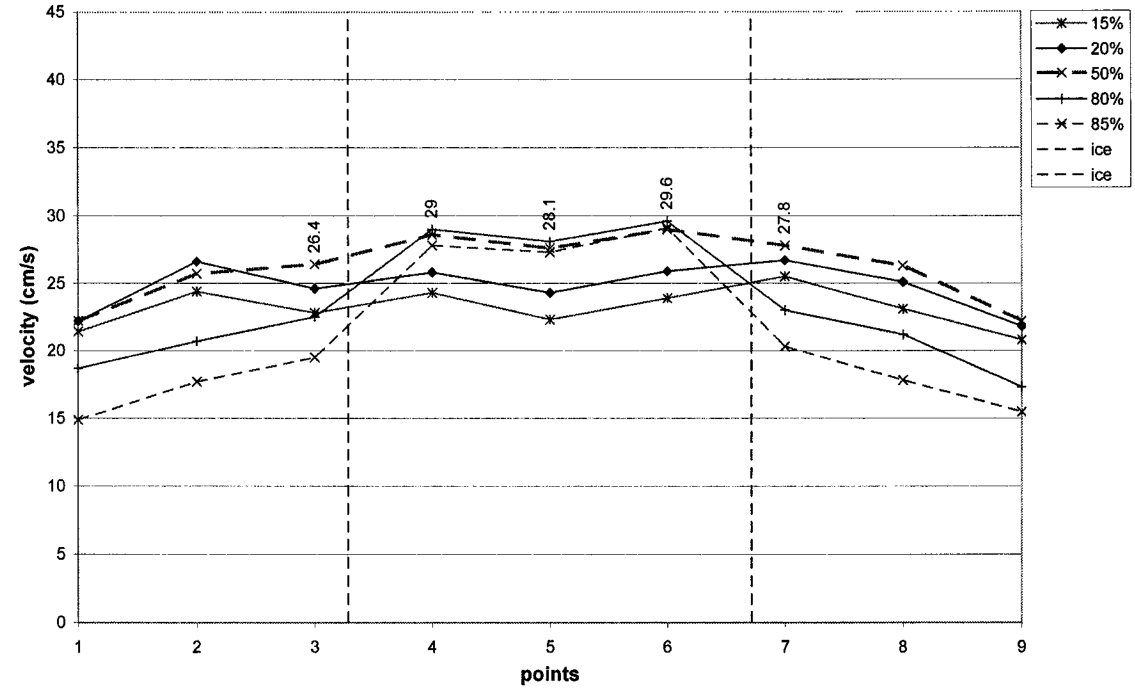

Vertical velocity profiles

ExpBP#2/2PIC-c/sUA

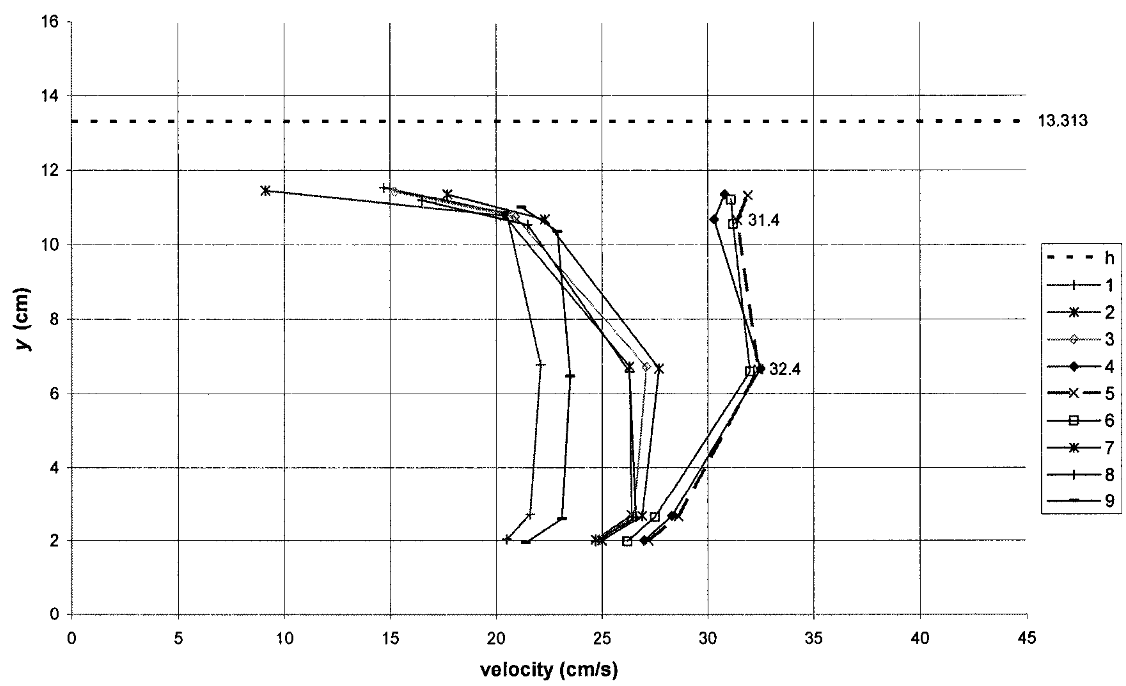

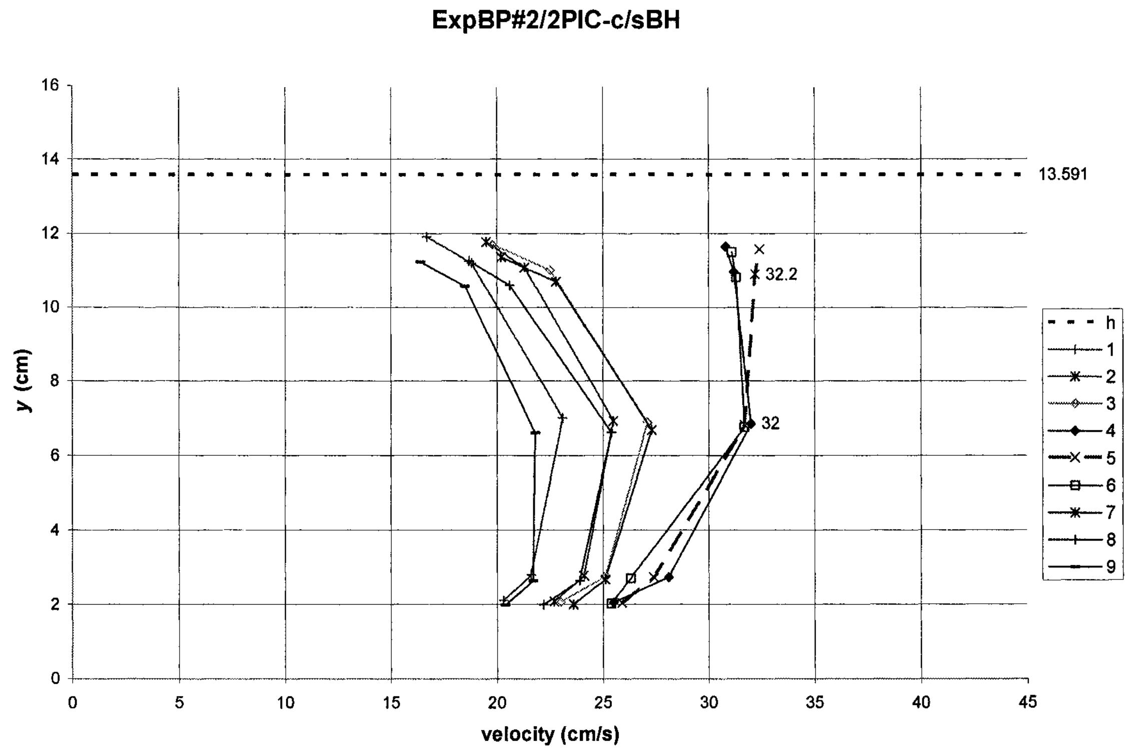
ExpBP#2/2PIC-c/sBH
13.591
32.2
32
y (cm)
velocity (cm/s)
h
1
2
3
4
5
6
7
8
9

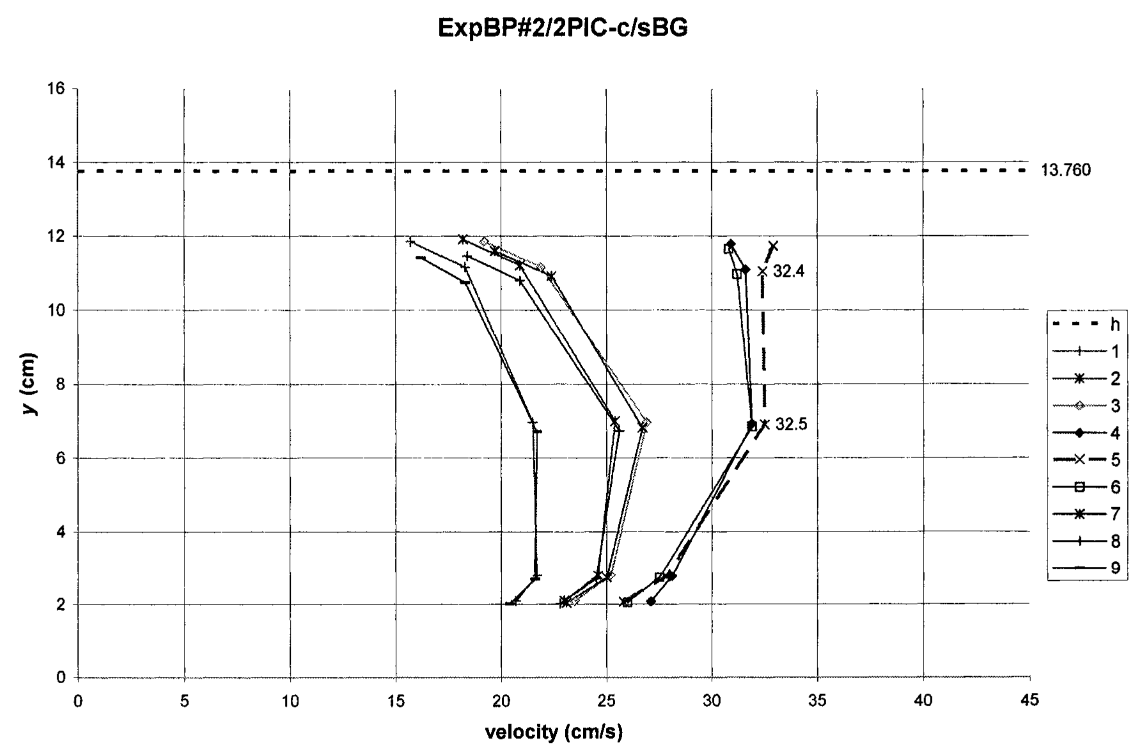
ExpBP#2/2PIC-c/sBG
13.760
32.4
32.5
y (cm)
velocity (cm/s)
h
1
2
3
4
5
6
7
8
9

ExpBP#2/2PIC-c/sBF

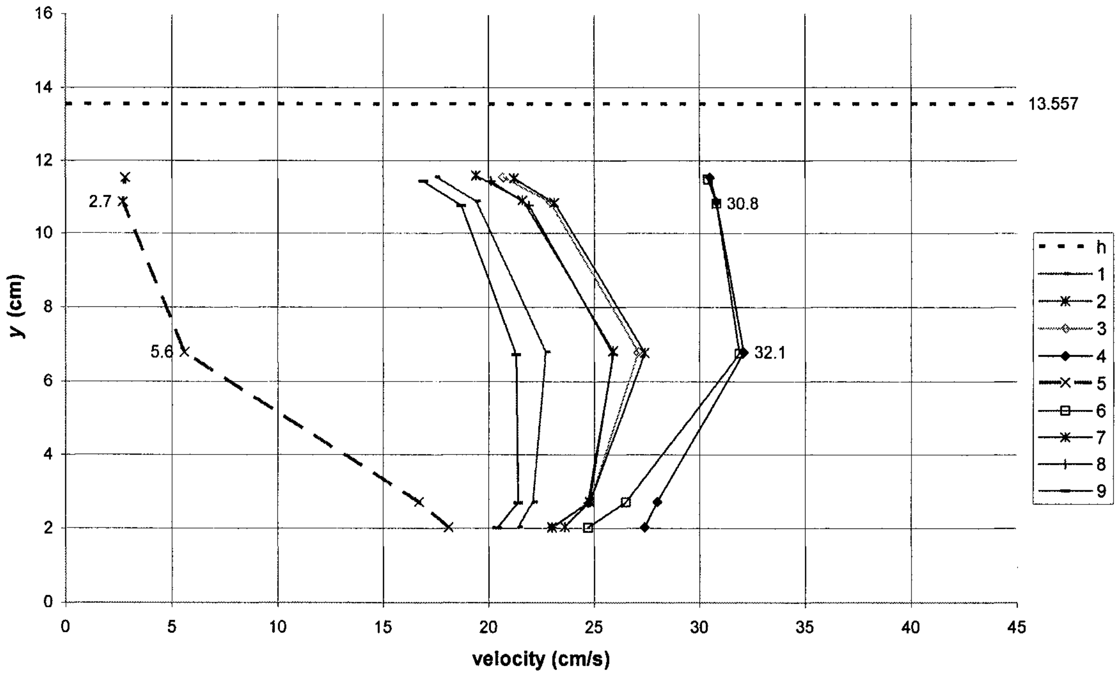

ExpBP#2/2PIC-c/sBE

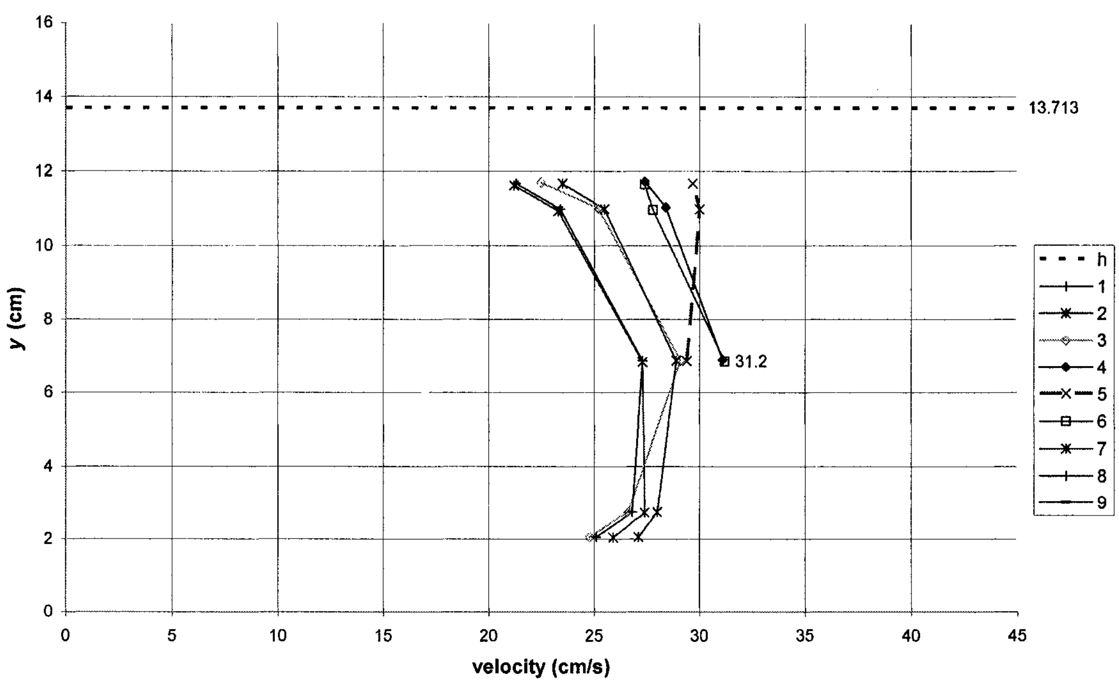

ExpBP#2/2PIC-c/sBD

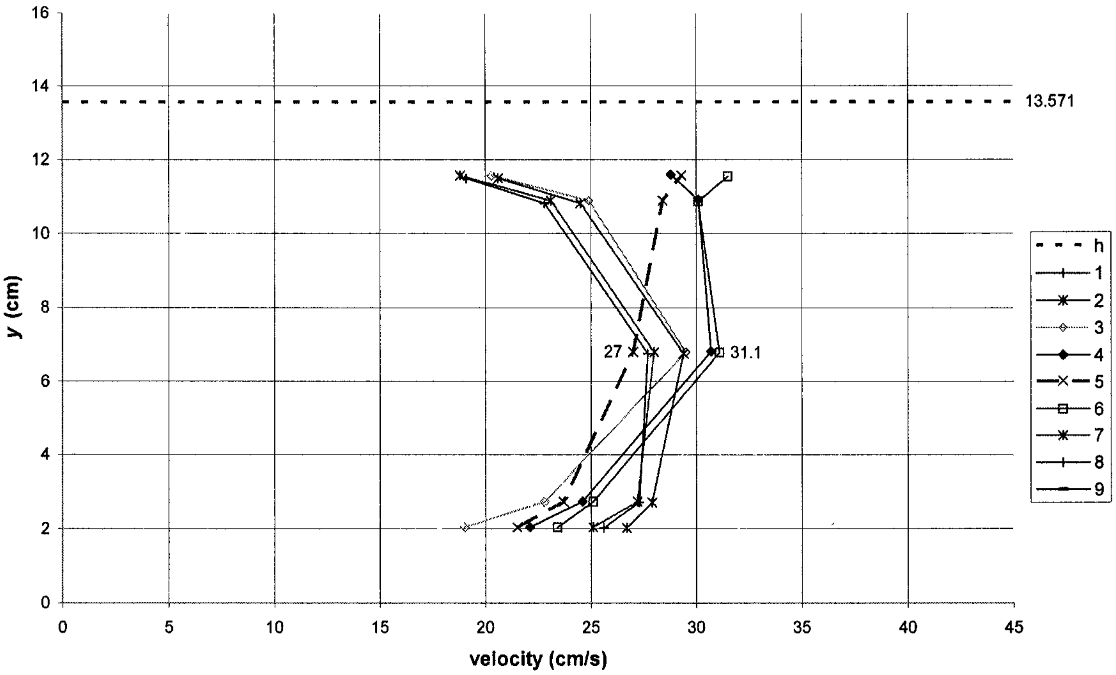

ExpBP#2/2PIC-c/sBC

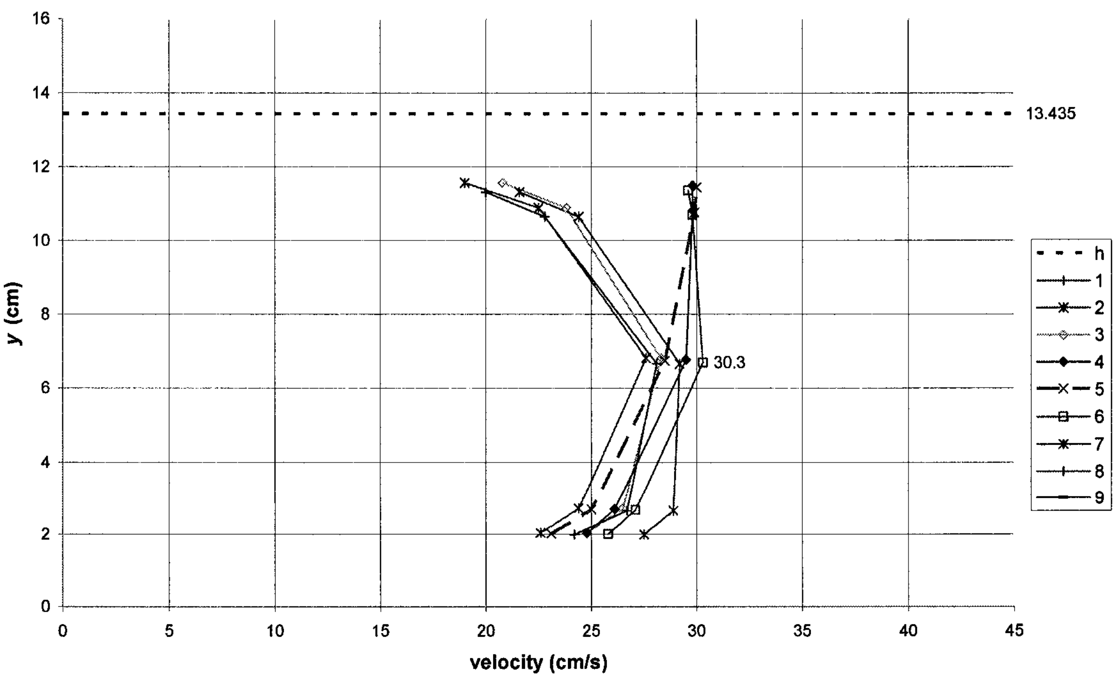

ExpBP#2/2PIC-c/sBB

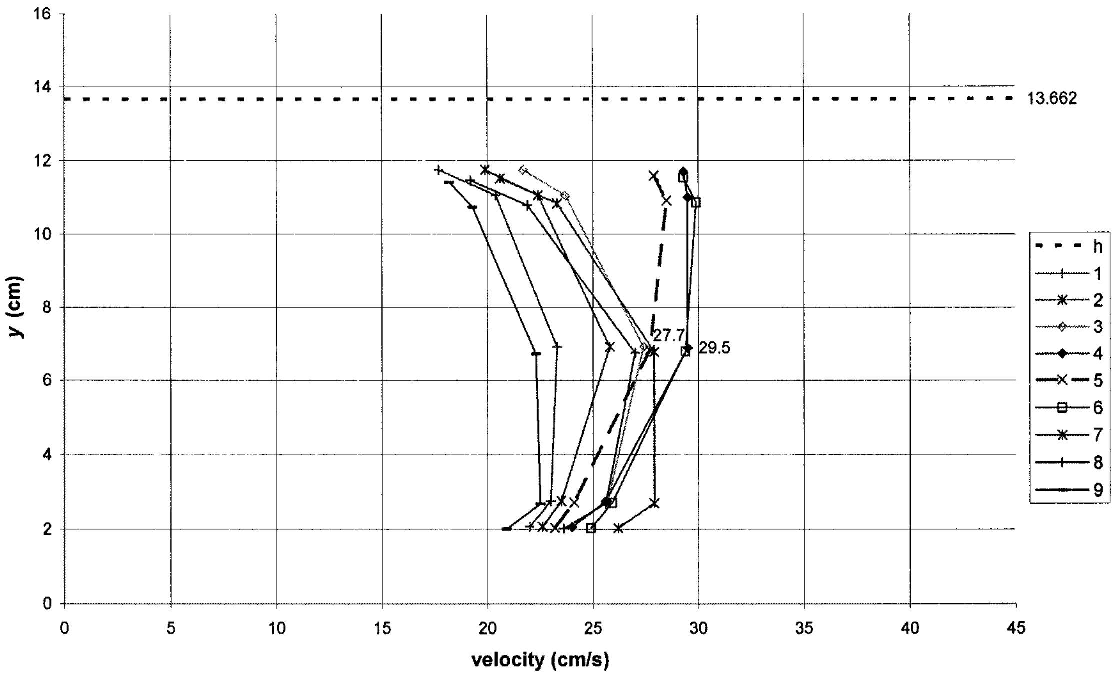

ExpBP#2/2PIC-c/sBA

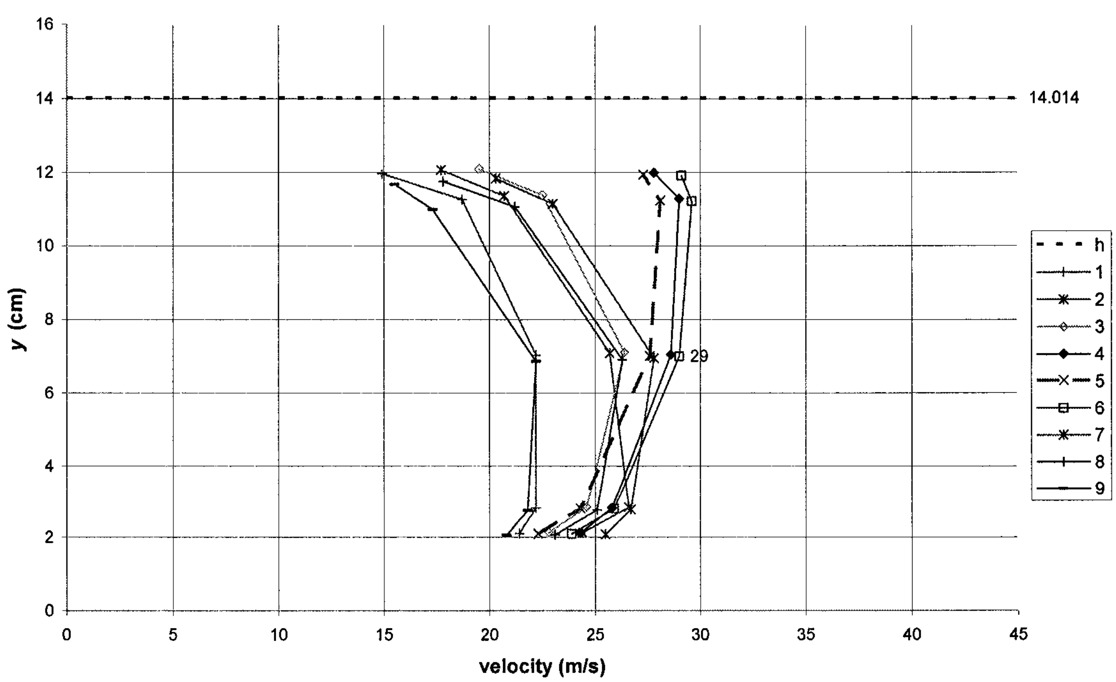

APPENDIX A9

ExpBP#3

2SIDES PARTIAL ICE-COVER CONFIGURATION (2PIC) at ice-cover critical conditions

(experiment with bridge pier)

2SIDES PARTIAL ICE-COVER CONFIGURATION (2PIC)

Lateral velocity profiles

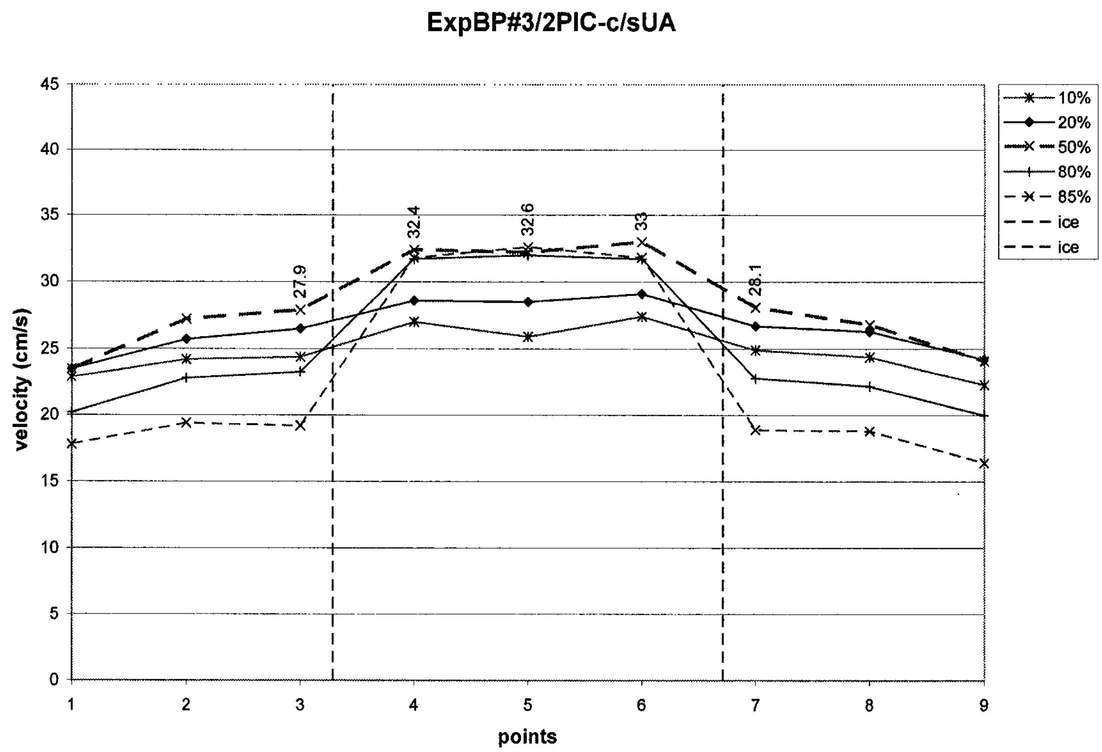

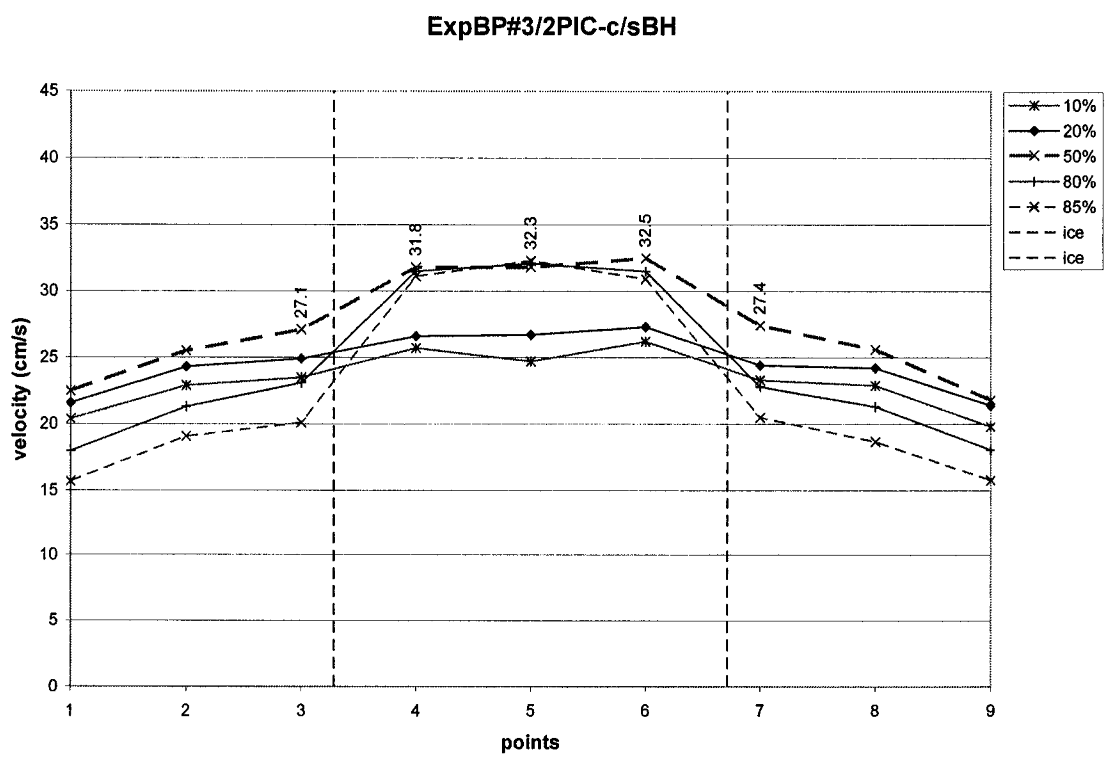

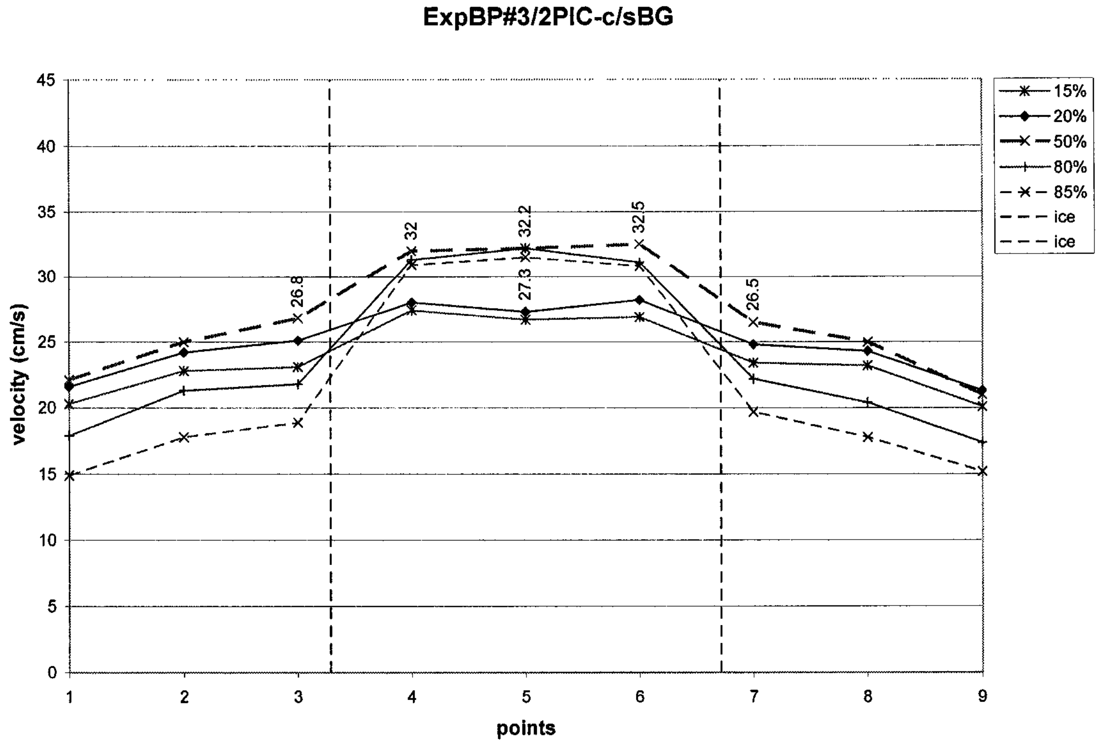

ExpBP#3/2PIC-c/sBG
velocity (cm/s)
points
15%
20%
50%
80%
85%
ice
ice
26.8
32
27.3
32.2
32.5
26.5

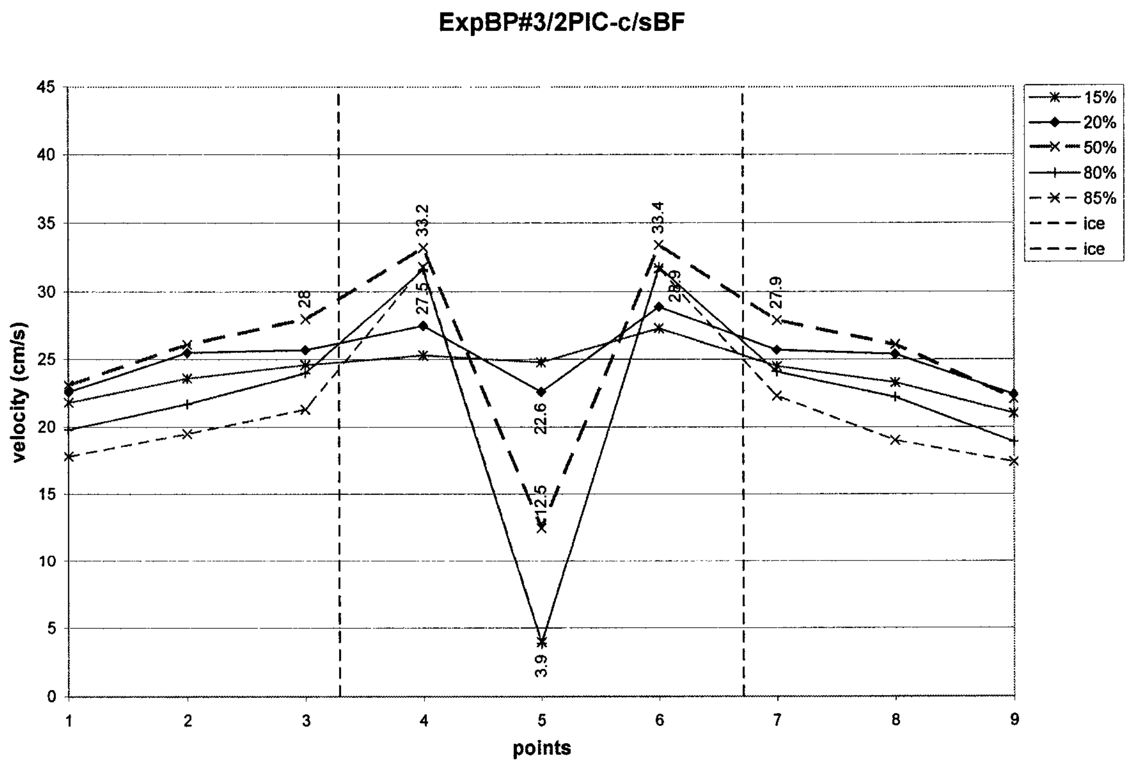

ExpBP#3/2PIC-c/sBF
velocity (cm/s)
points
15%
20%
50%
80%
85%
ice
ice
28
33.2
27.5
22.6
12.5
3.9
33.4
28.9
27.9

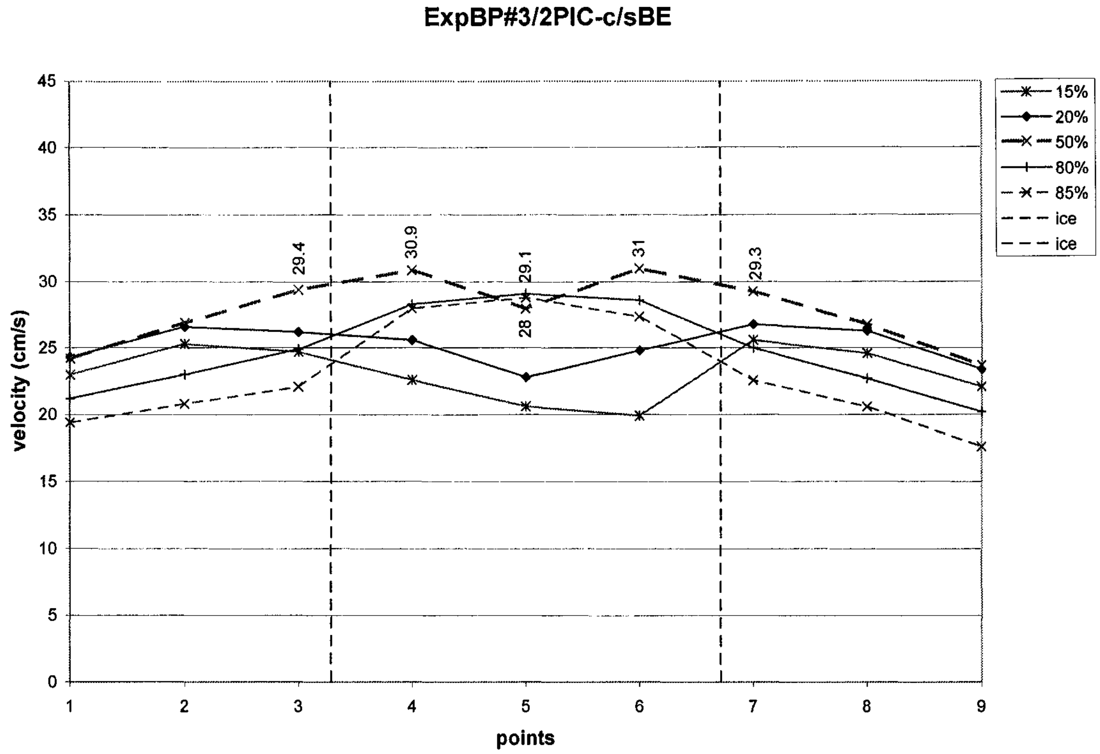

ExpBP#3/2PIC-c/sBE
velocity (cm/s)
points
15%
20%
50%
80%
85%
ice
ice
29.4
30.9
29.1
28
31
29.3

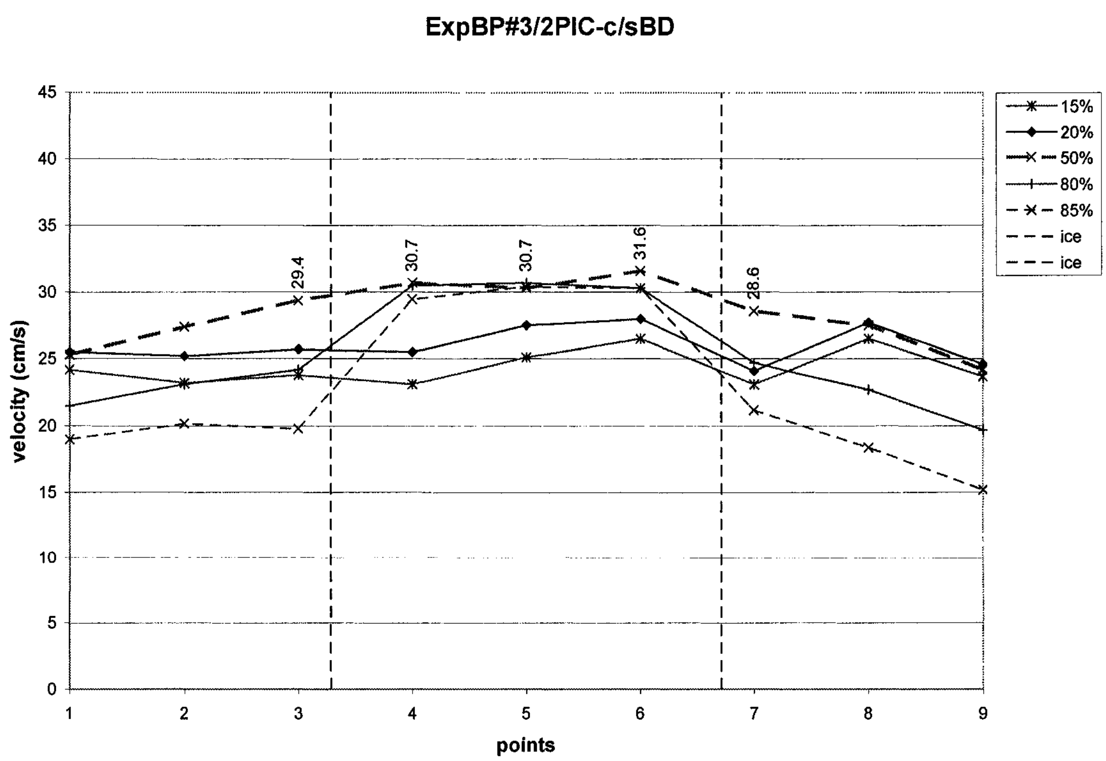

ExpBP#3/2PIC-c/sBD
velocity (cm/s)
points
15%
20%
50%
80%
85%
ice
ice
29.4
30.7
30.7
31.6
28.6

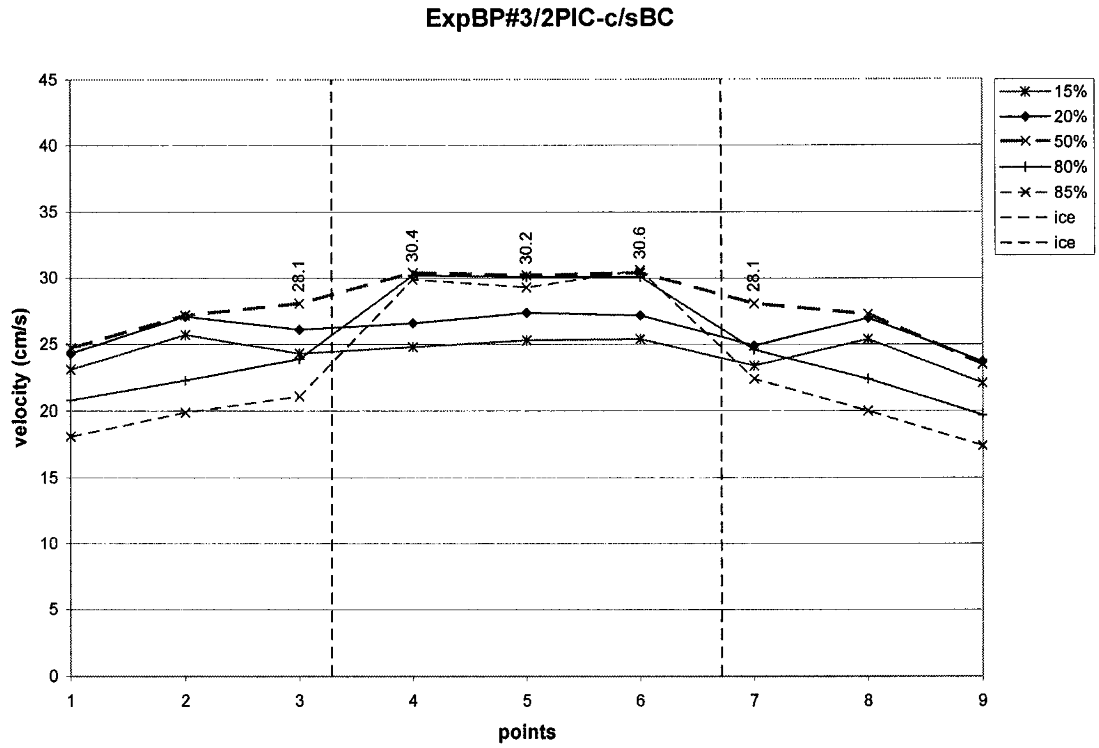
ExpBP#3/2PIC-c/sBC
velocity (cm/s)
points
15%
20%
50%
80%
85%
ice
ice
28.1
30.4
30.2
30.6
28.1

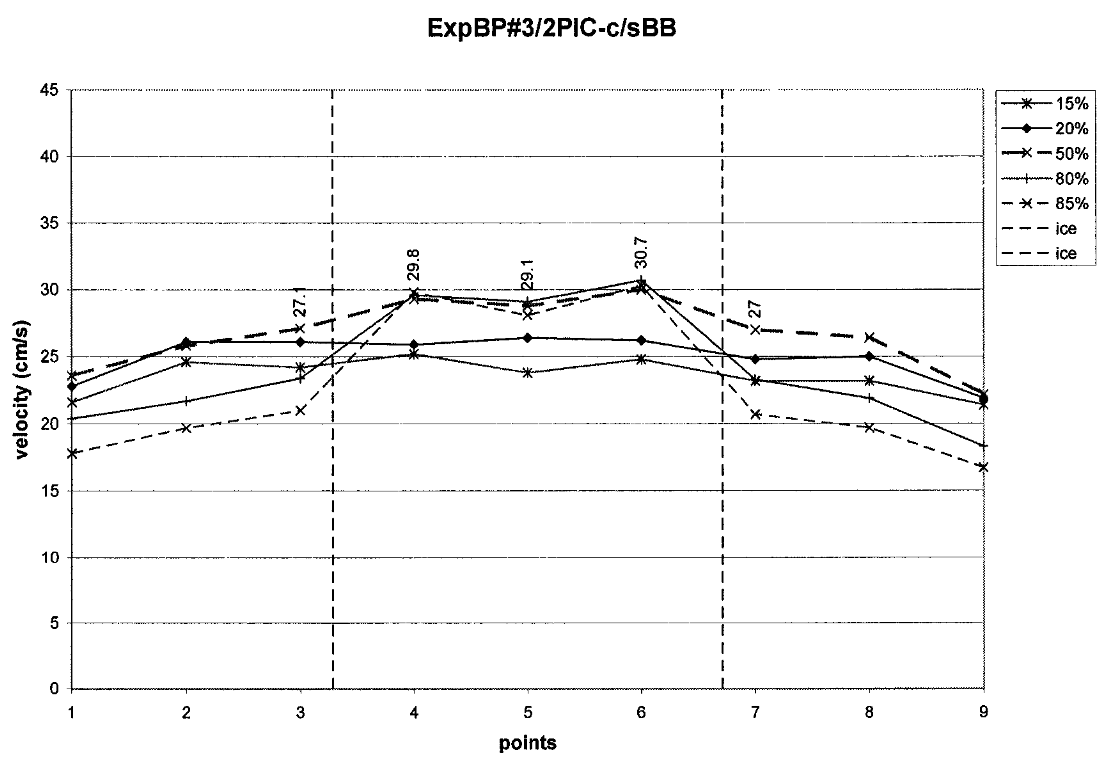
ExpBP#3/2PIC-c/sBB
velocity (cm/s)
points
15%
20%
50%
80%
85%
ice
ice
27.
29.8
29.1
30.7
27

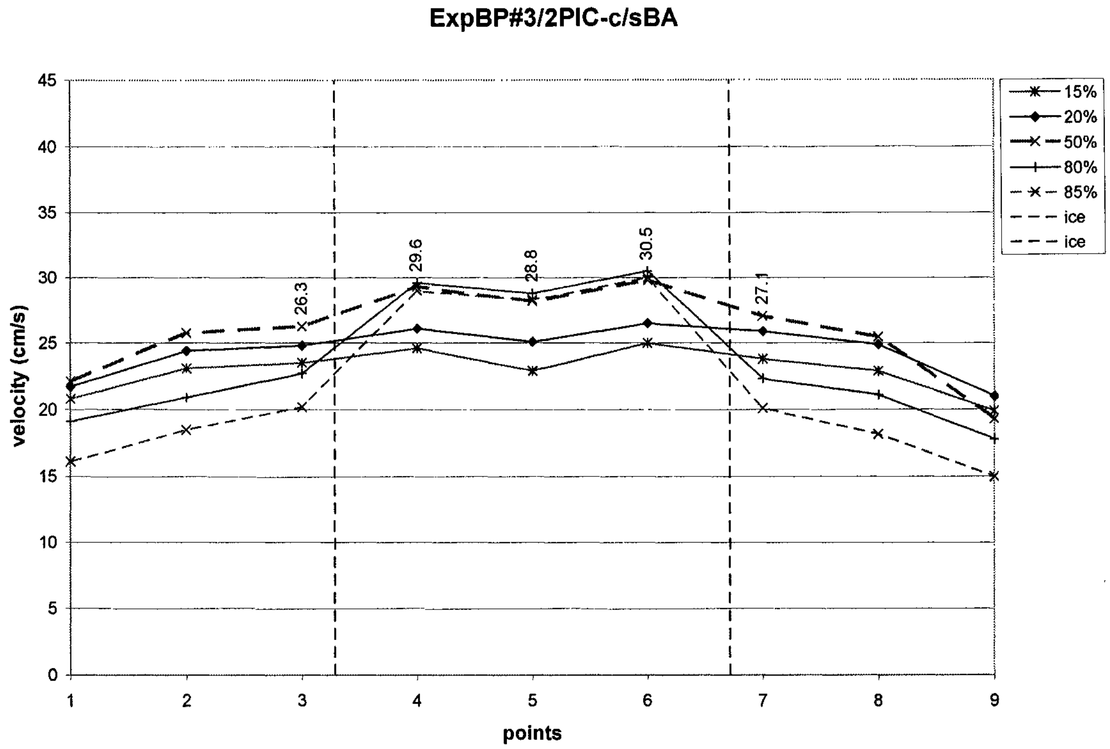

Vertical velocity profiles

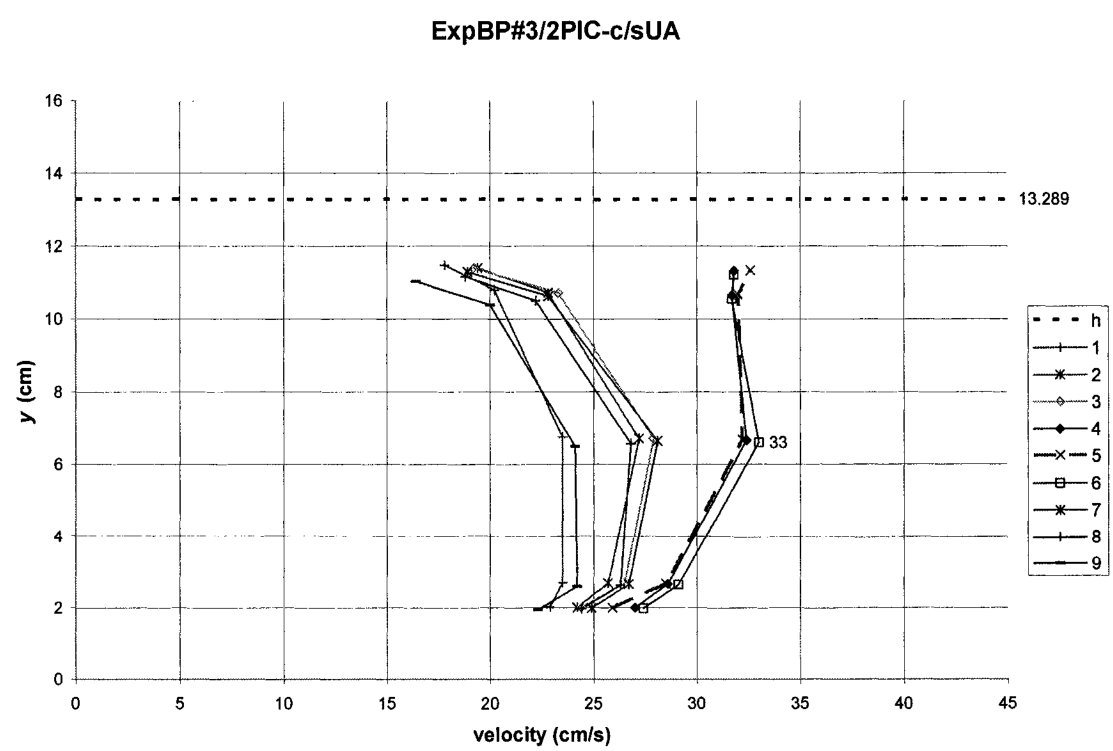

ExpBP#3/2PIC-c/sBH

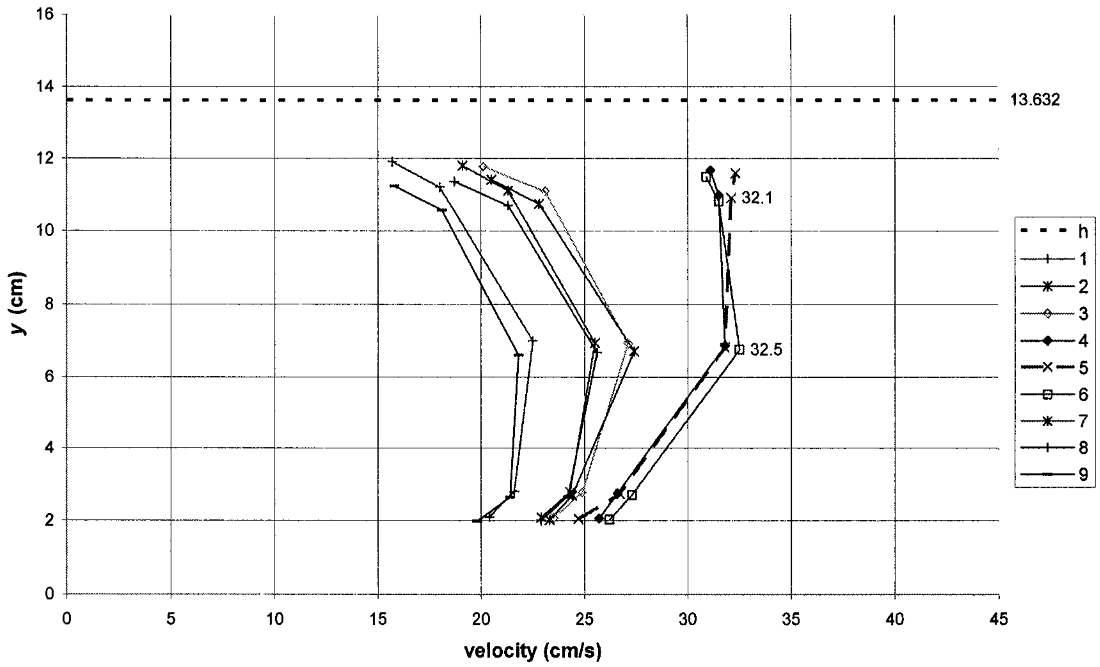

ExpBP#3/2PIC-c/sBG

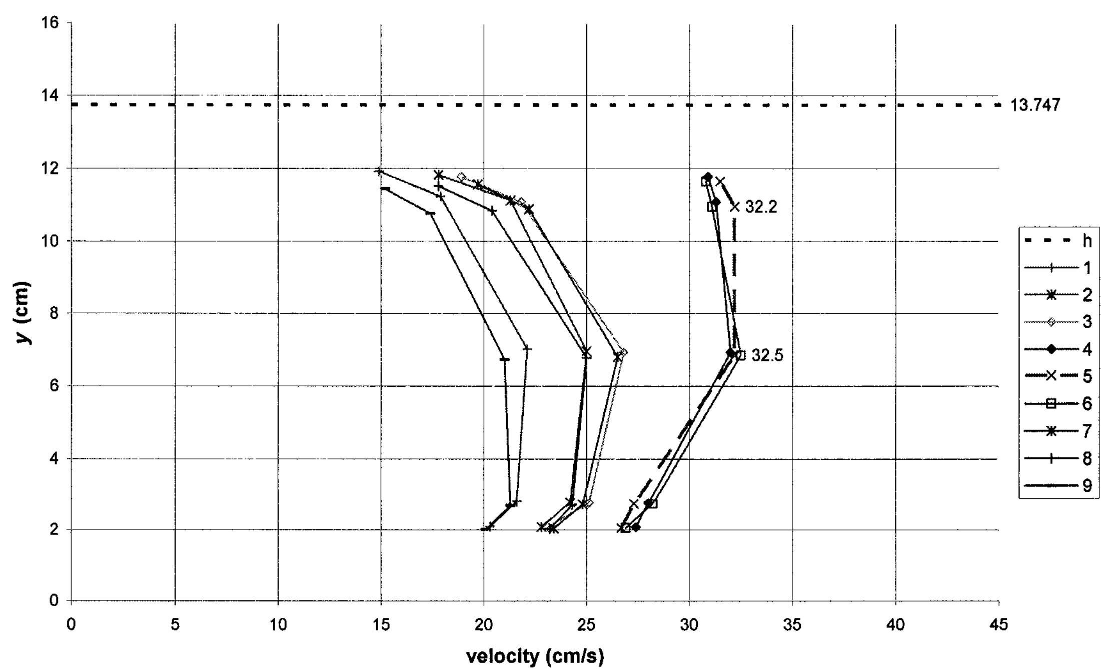

ExpBP#3/2PIC-c/sBF

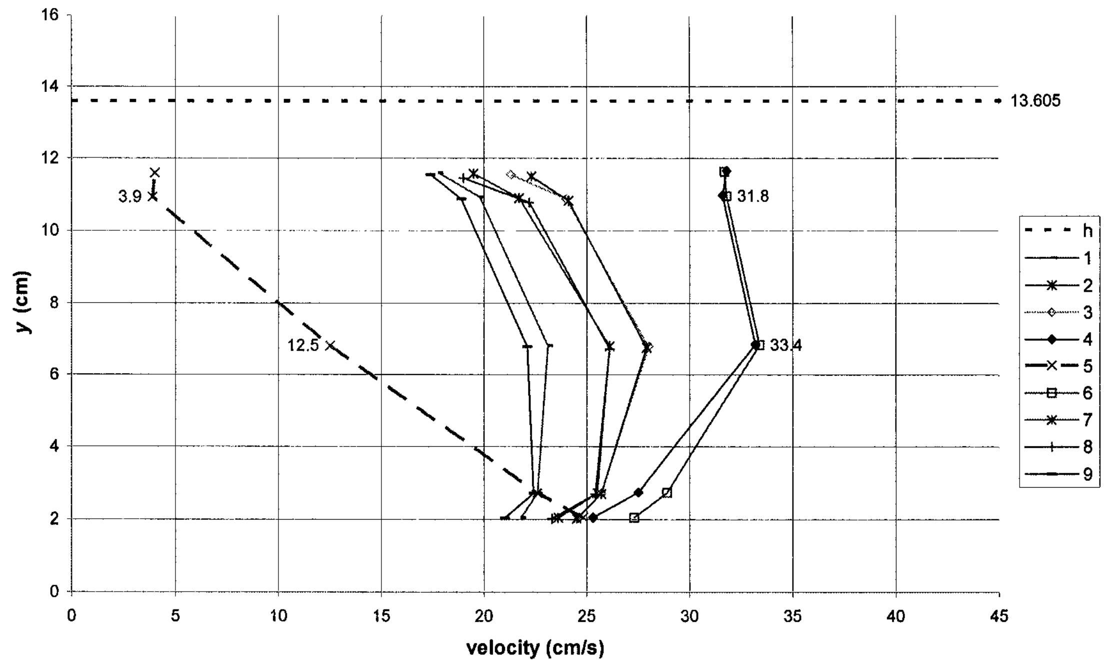

ExpBP#3/2PIC-c/sBE

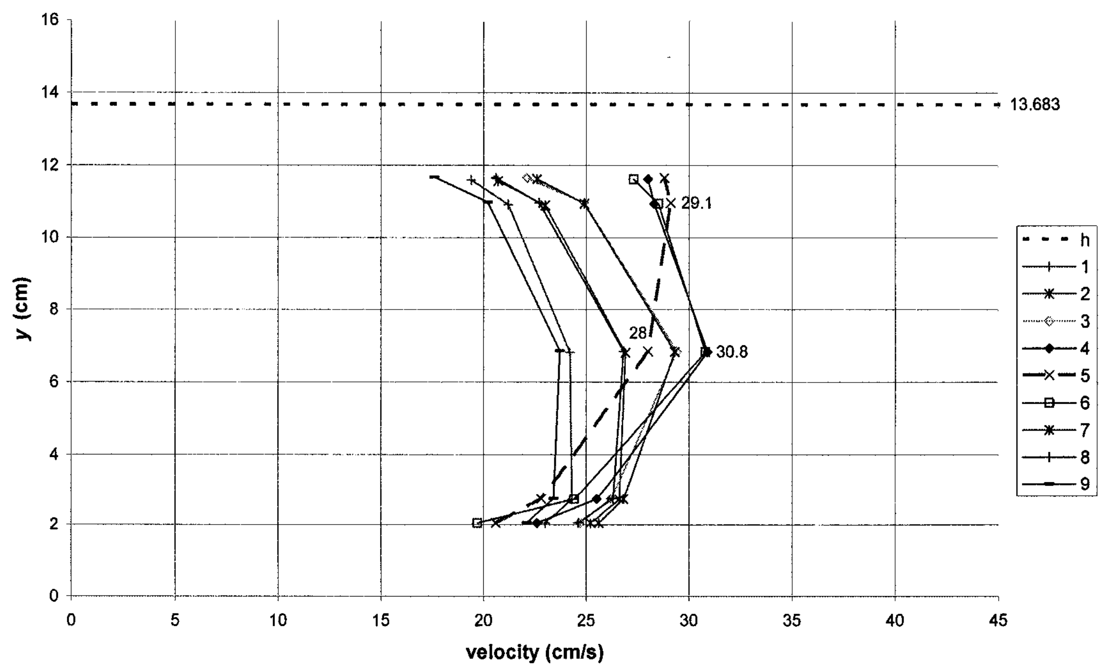

ExpBP#3/2PIC-c/sBD

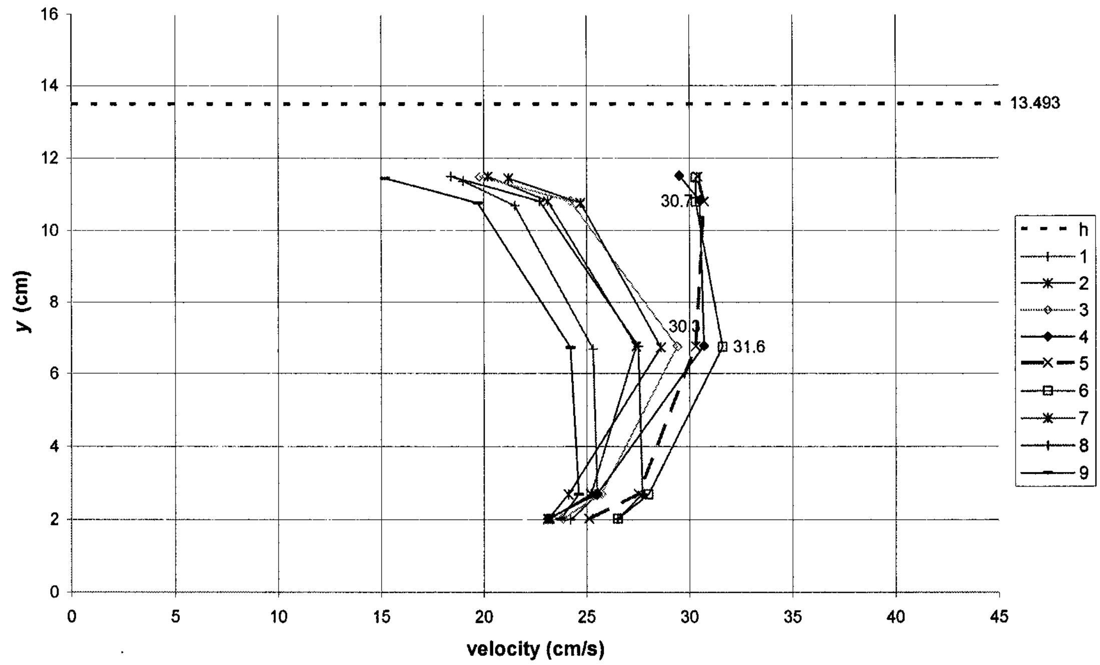

ExpBP#3/2PIC-c/sBC

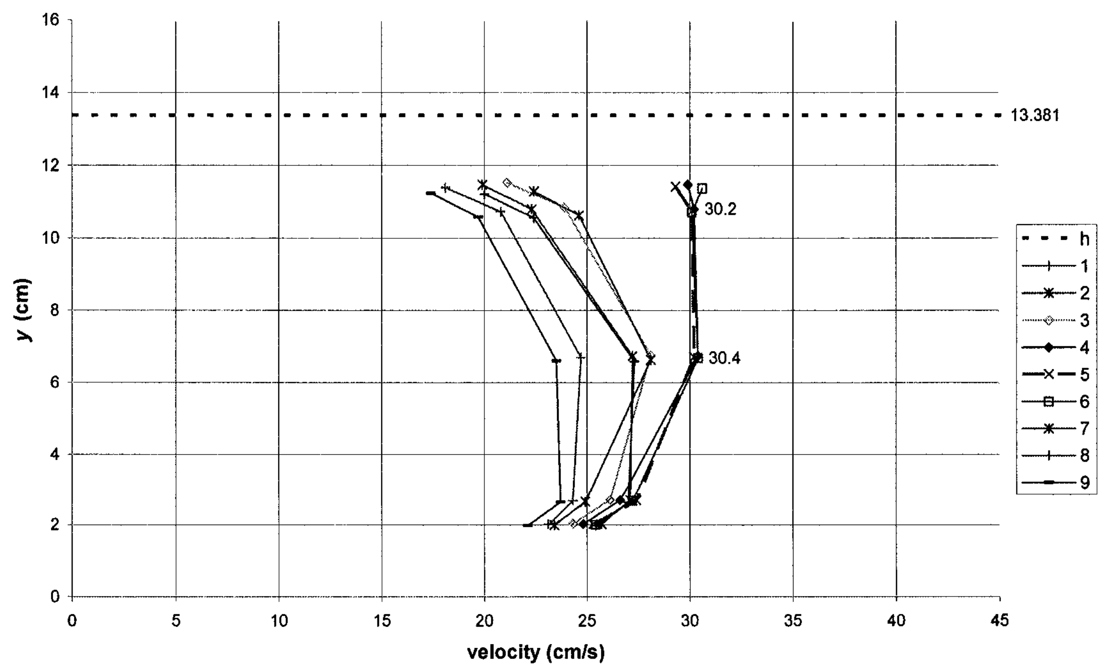

ExpBP#3/2PIC-c/sBB

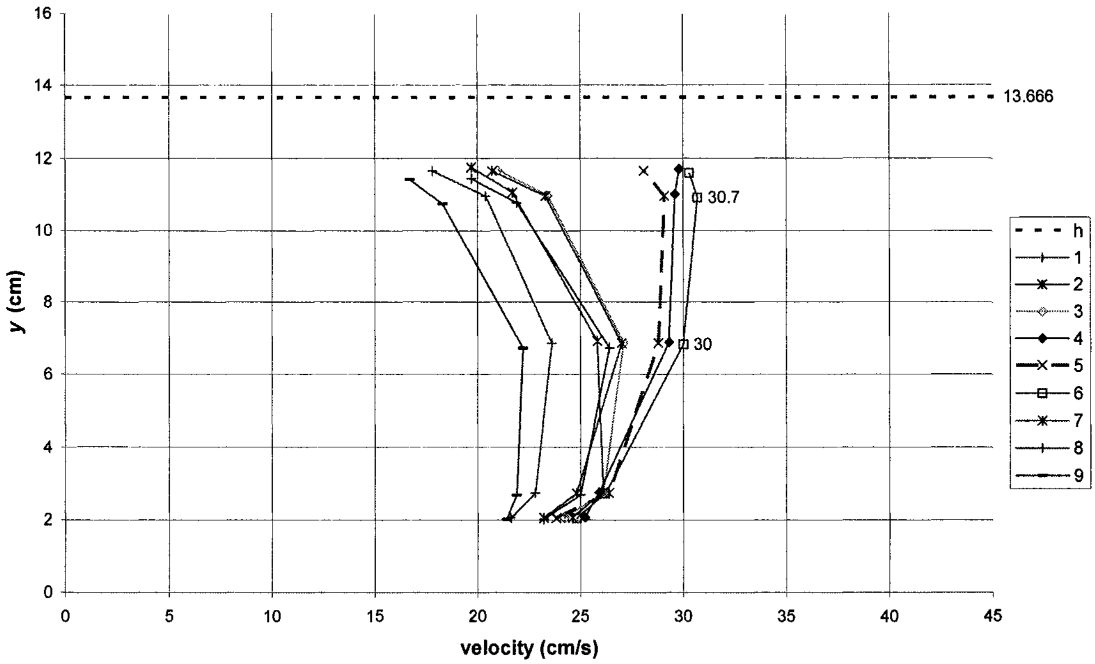

ExpBP#3/2PIC-c/sBA

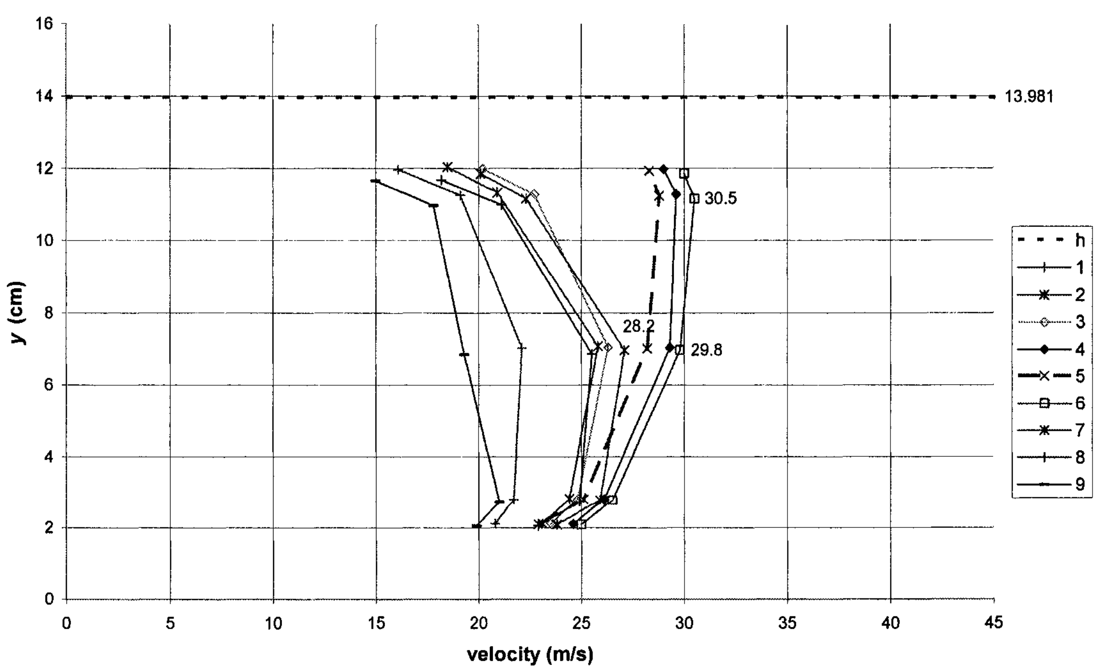

APPENDIX A10

ExpBP#4

2SIDES PARTIAL ICE-COVER CONFIGURATION (2PIC) at ice-cover critical conditions

(experiment with bridge pier)

2SIDES PARTIAL ICE-COVER CONFIGURATION (2PIC)

Lateral velocity profiles

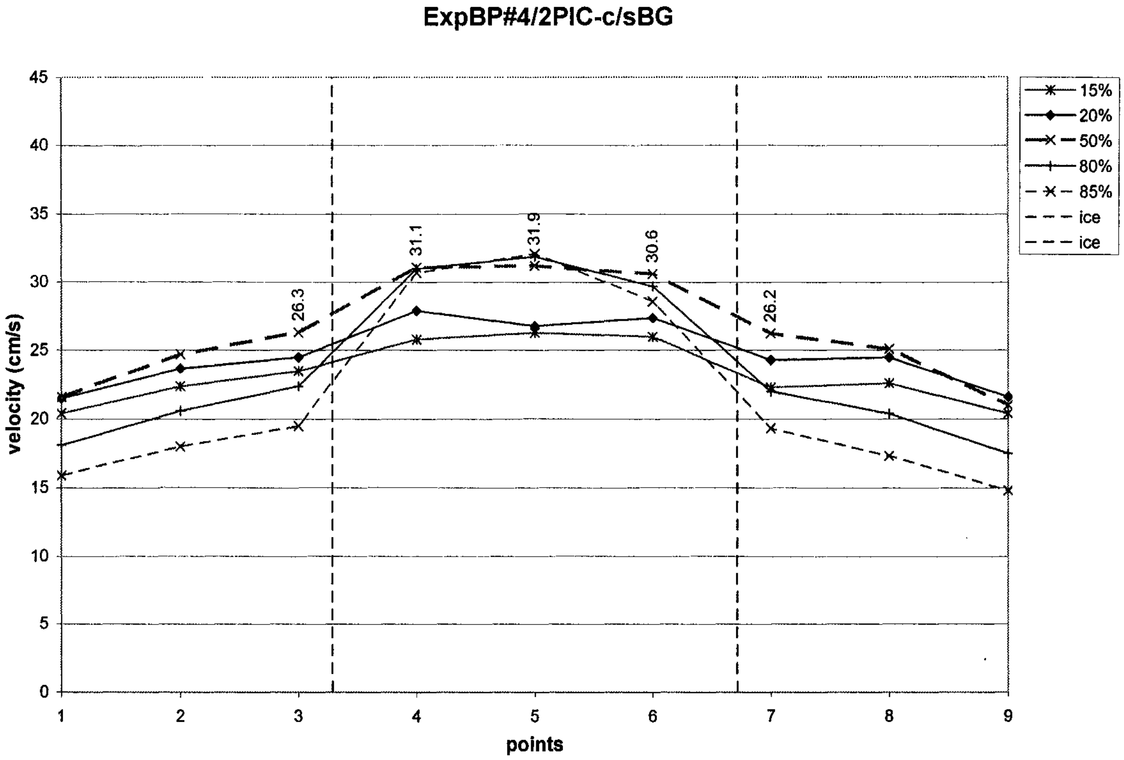

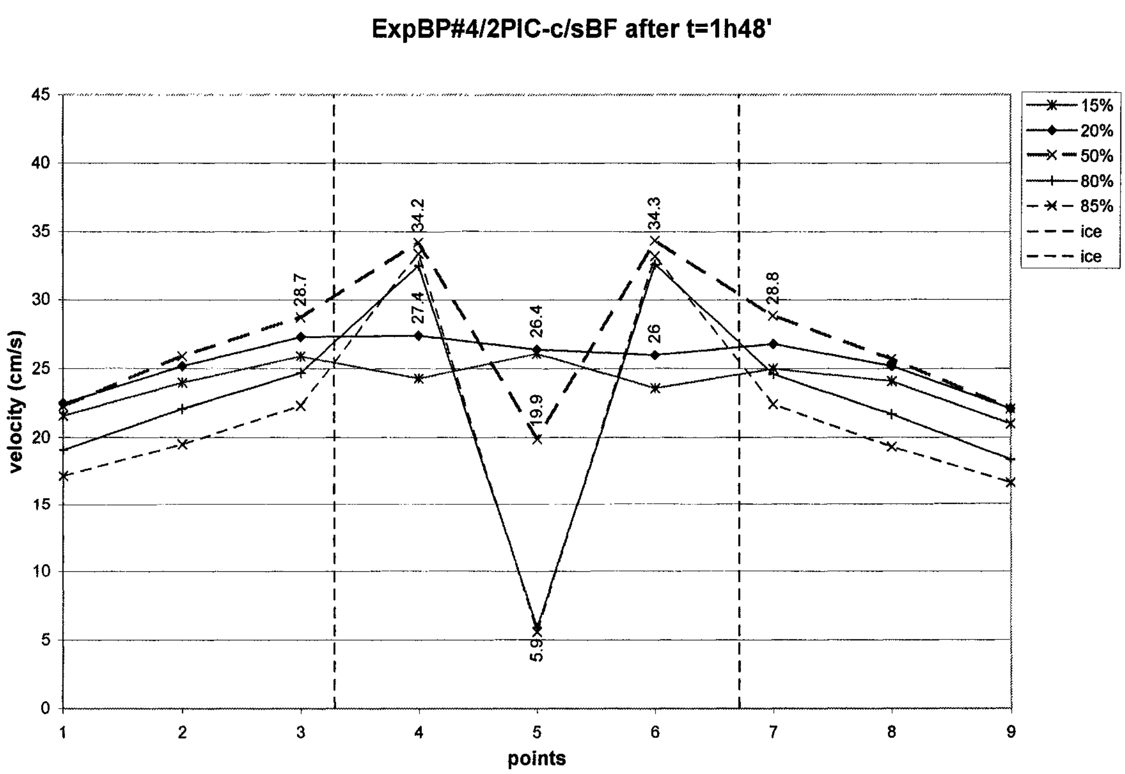

ExpBP#4/2PIC-c/sBF after t=25h

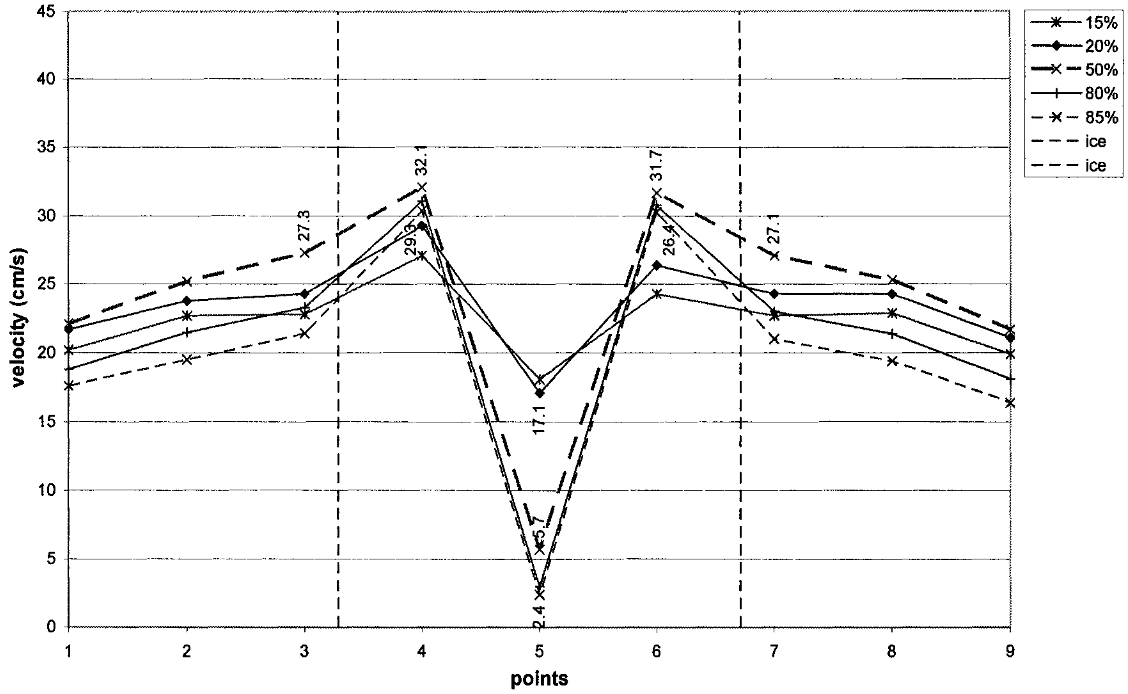

ExpBP#4/2PIC-c/sBE

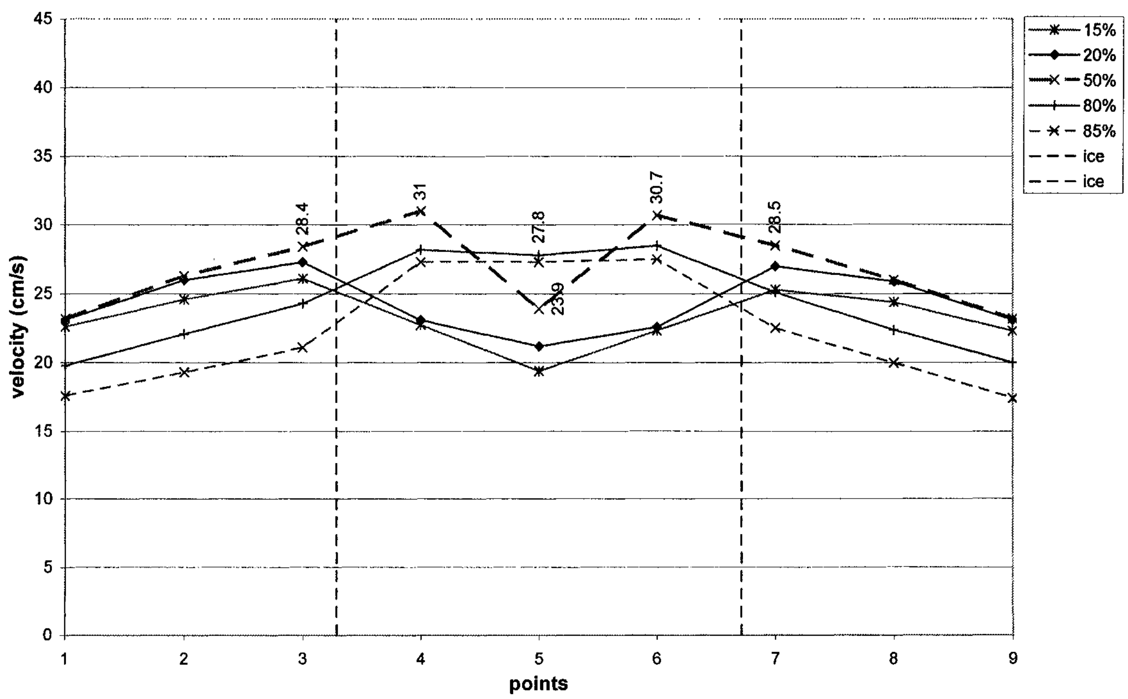

ExpBP#4/2PIC-c/sBD

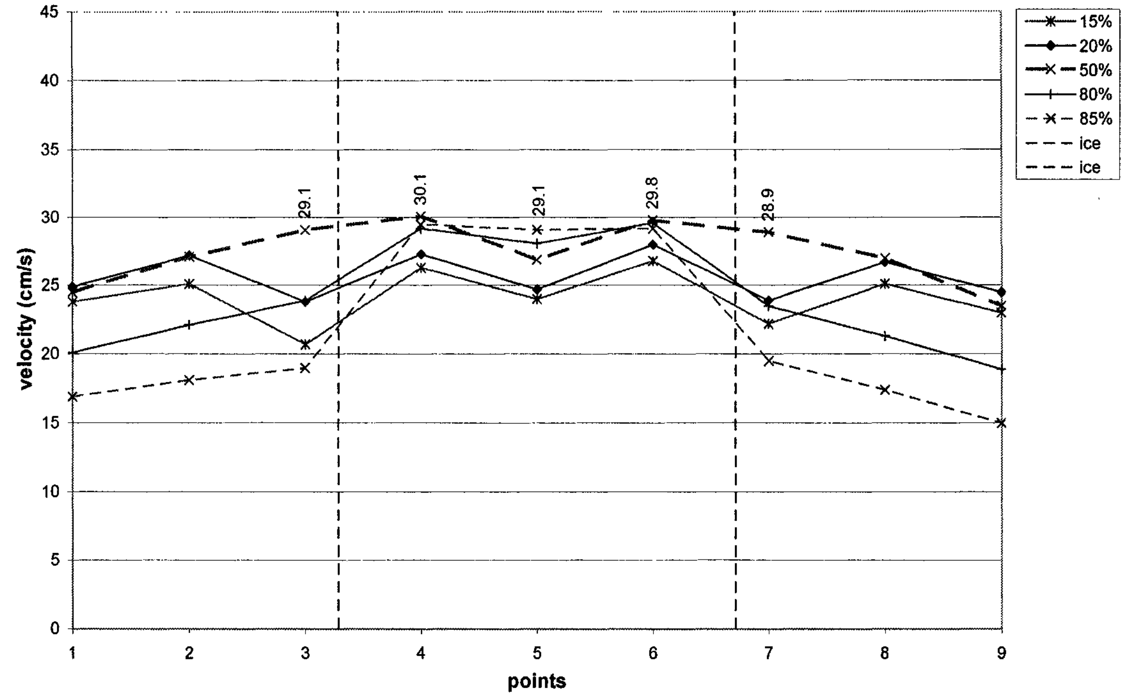

ExpBP#4/2PIC-c/sBB

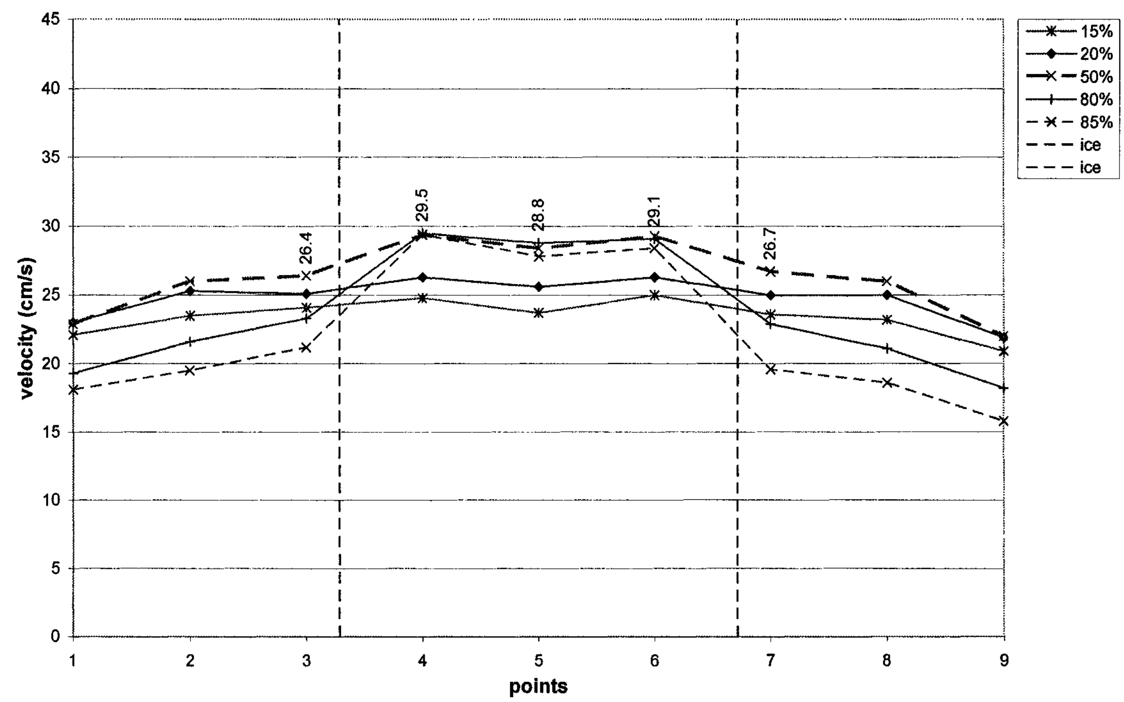

ExpBP#4/2PIC-c/sBB after t=27h

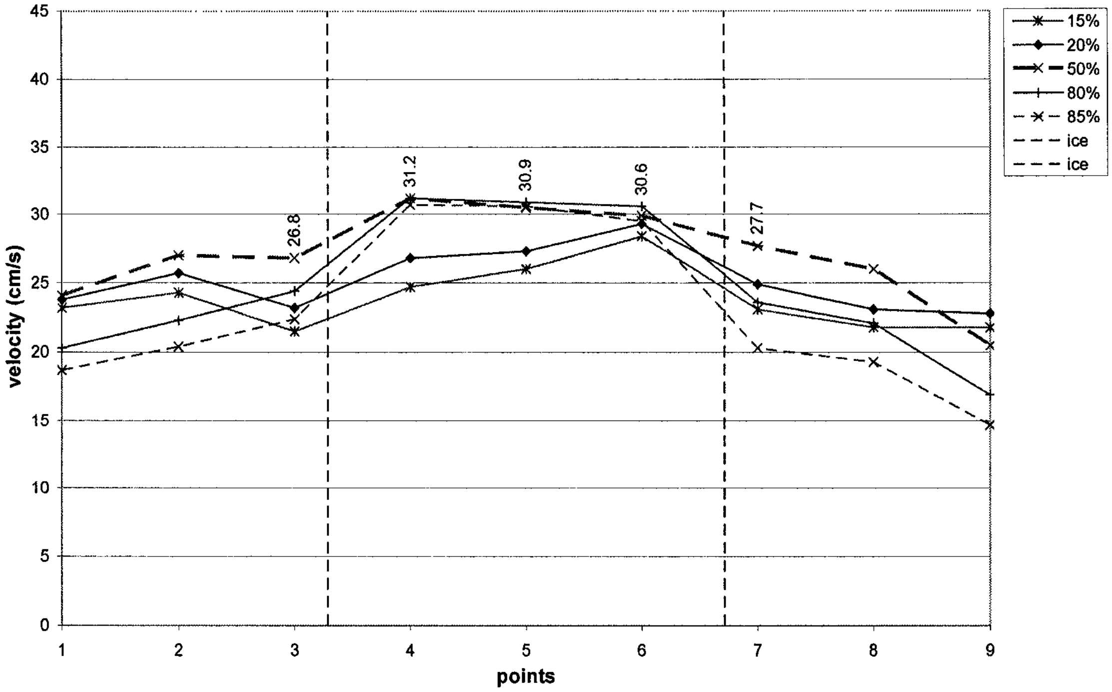

Vertical velocity profiles

ExpBP#4/2PIC-c/sBG

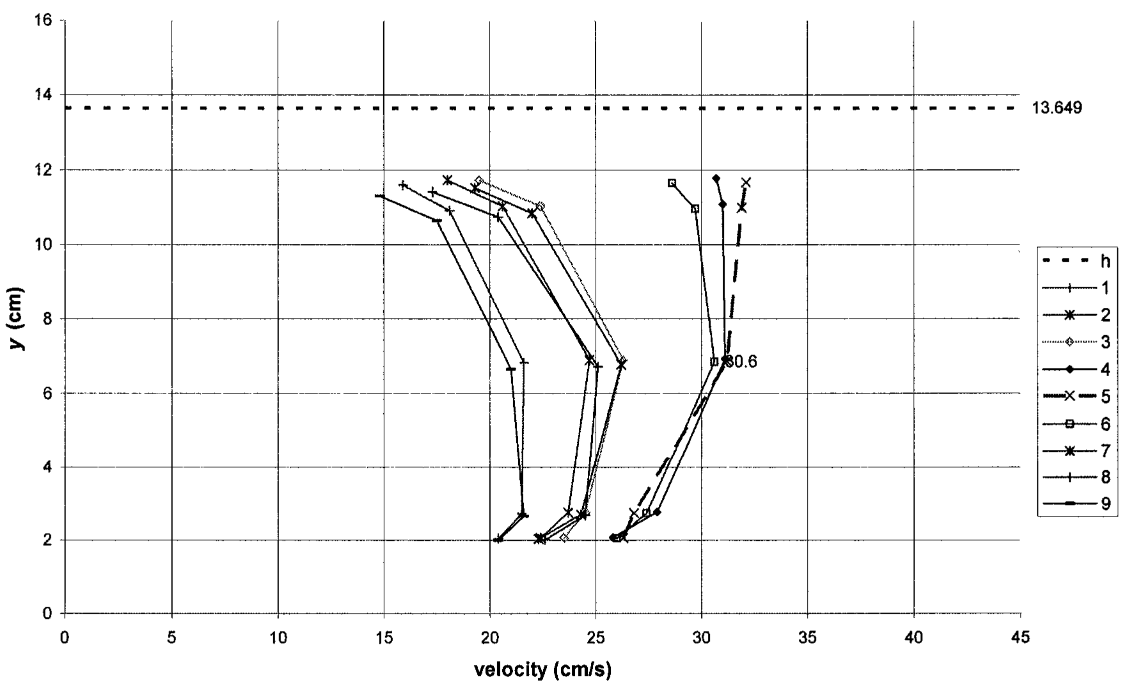

ExpBP#4/2PIC-c/sBF after t=1h48'

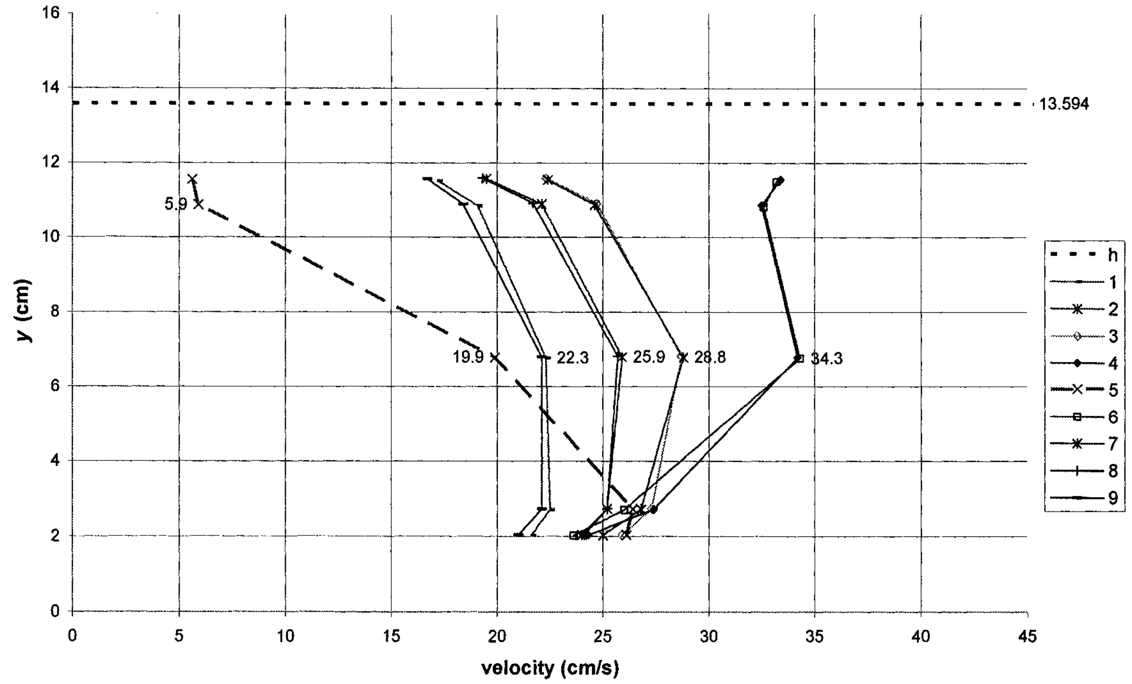

ExpBP#4/2PIC-c/sBF after t=25h

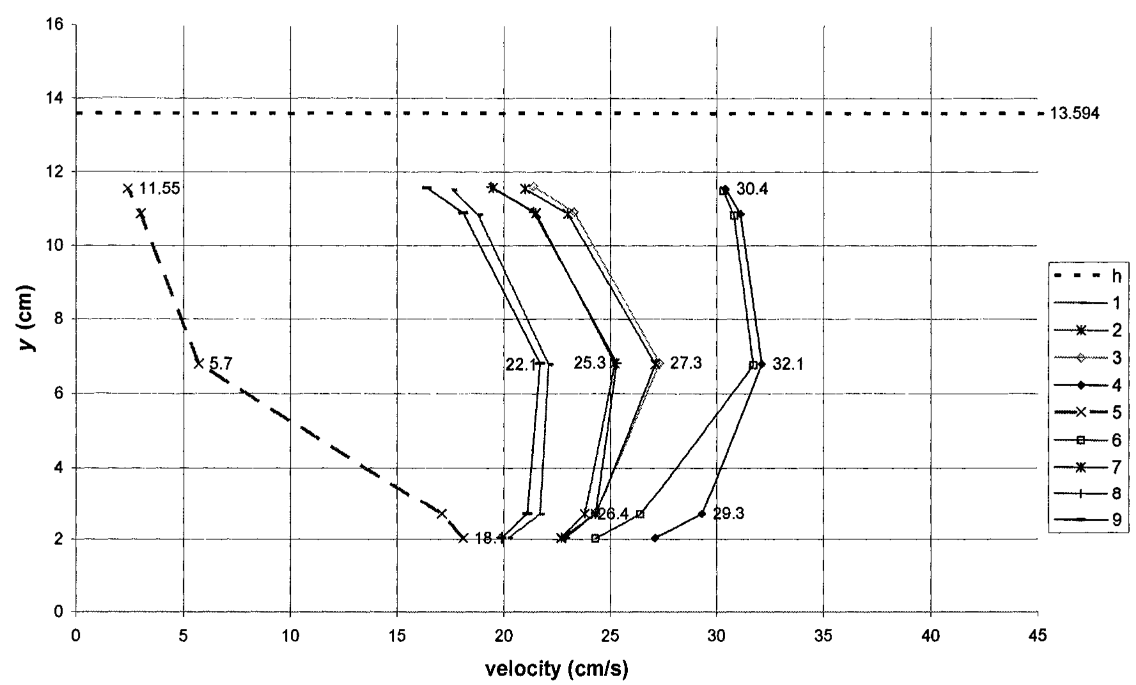

ExpBP#4/2PIC-c/sBE

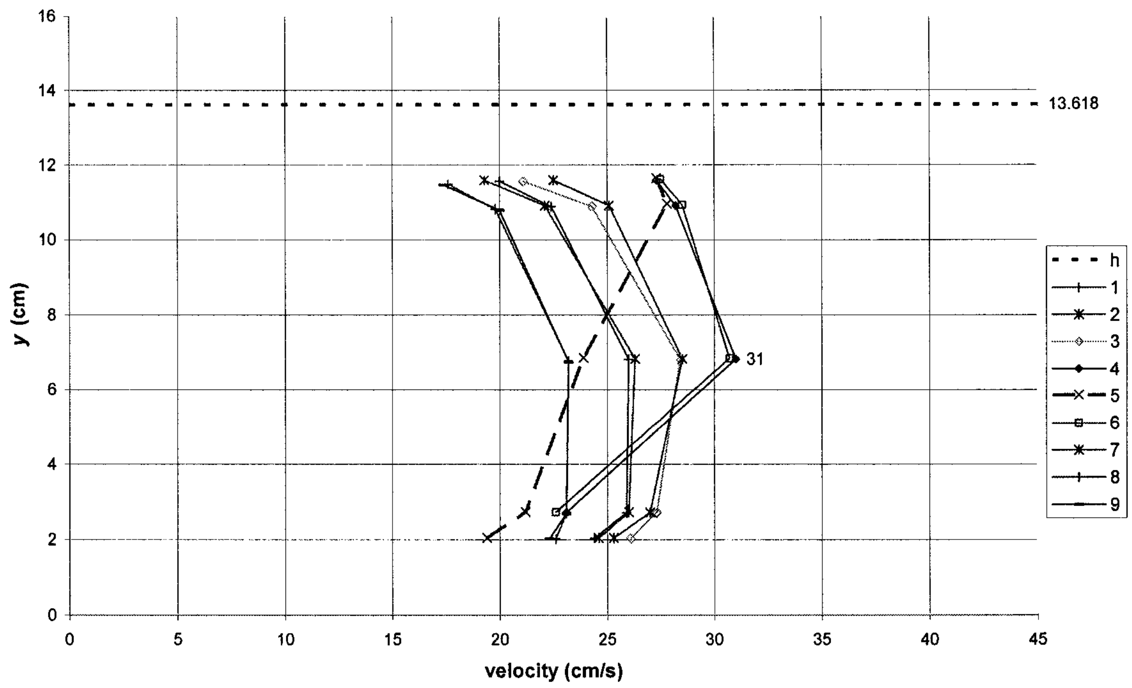

ExpBP#4/2PIC-c/sBD

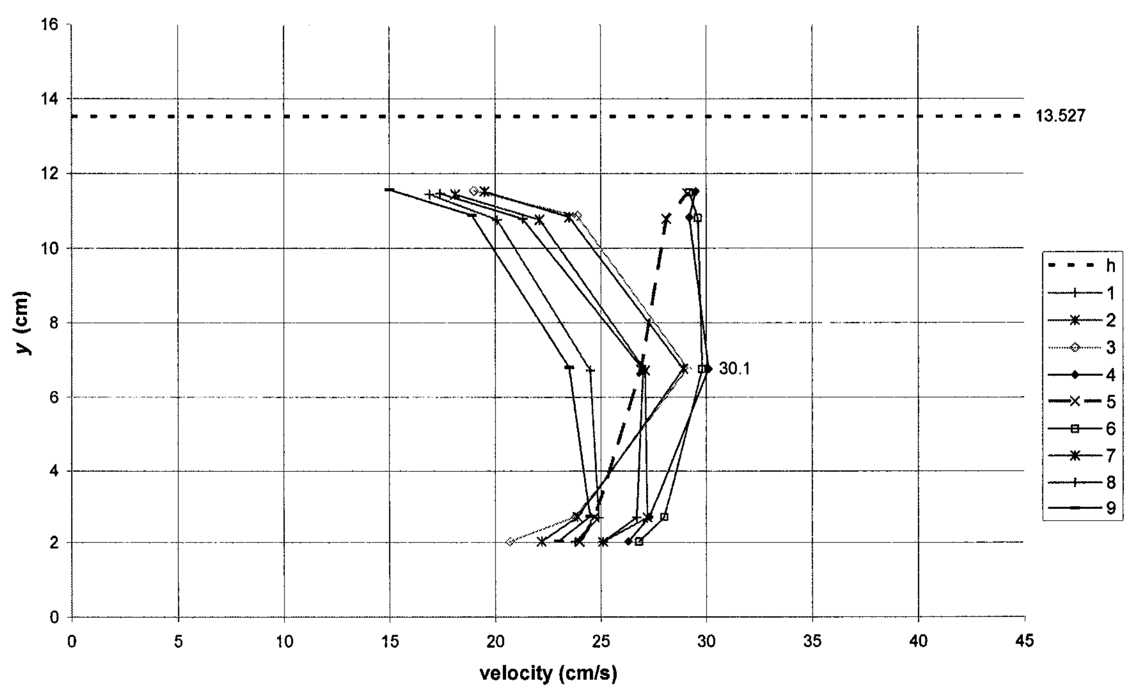

ExpBP#4/2PIC-c/sBB

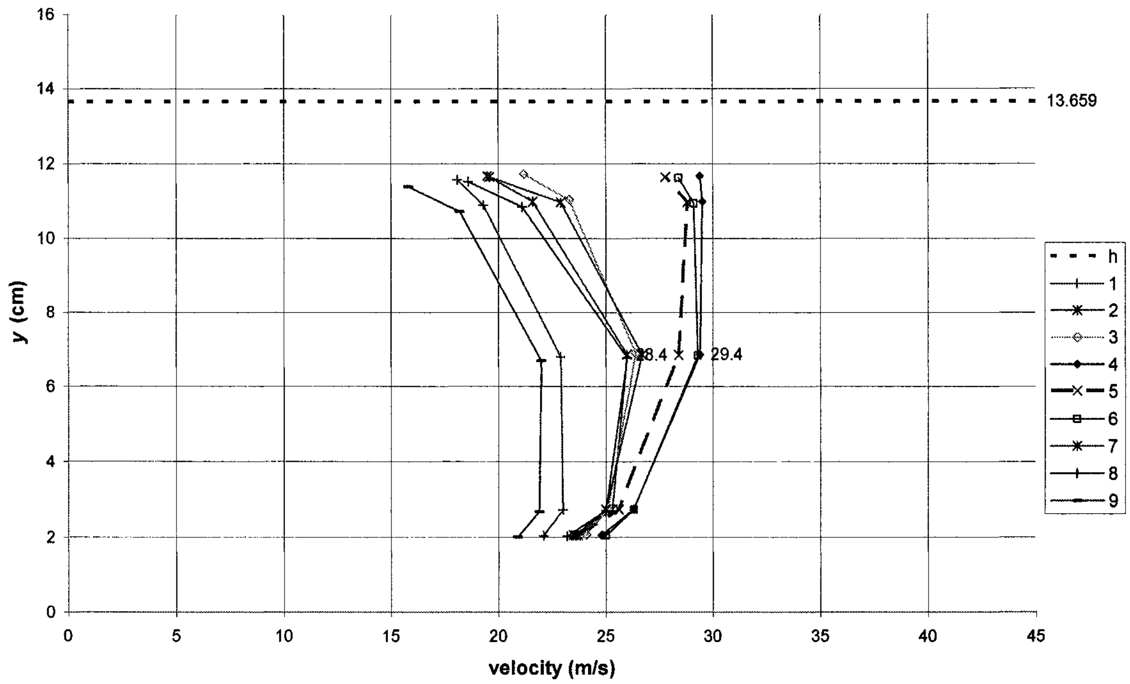

ExpBP#4/2PIC-c/sBB after t=27h

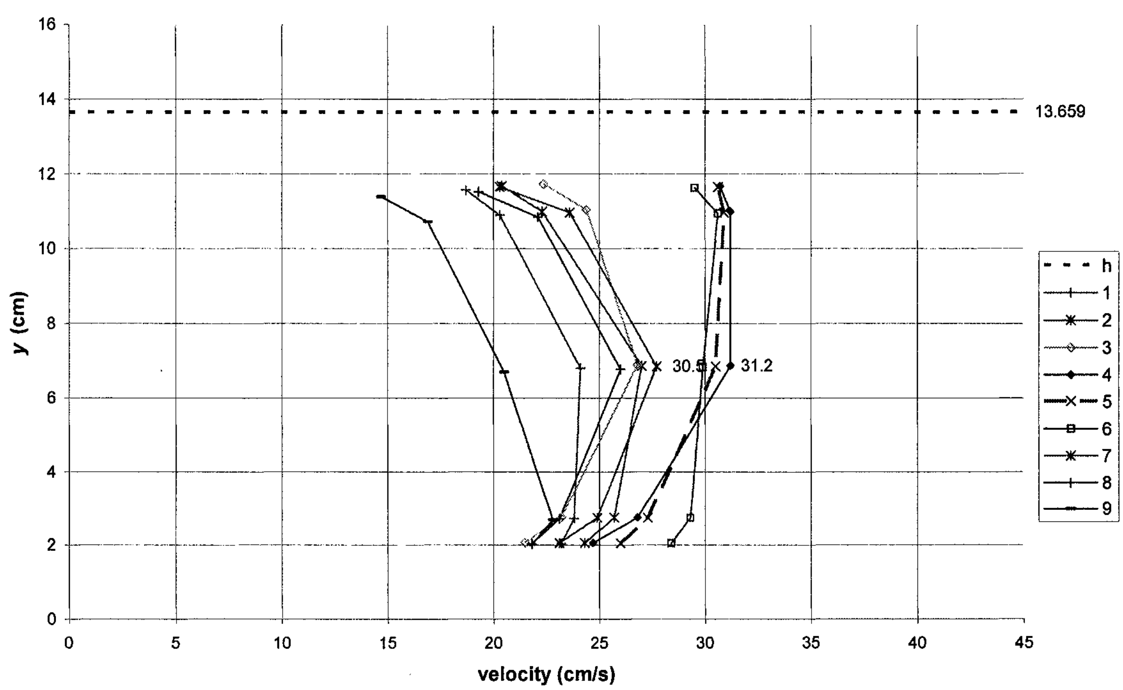

APPENDIX A11

ExpBP#5

FREE-SURFACE CONFIGURATION (FS) at free-surface critical conditions

(experiment with bridge pier)

FREE-SURFACE CONFIGURATION (FS) – at free-surface critical conditions

Lateral velocity profiles

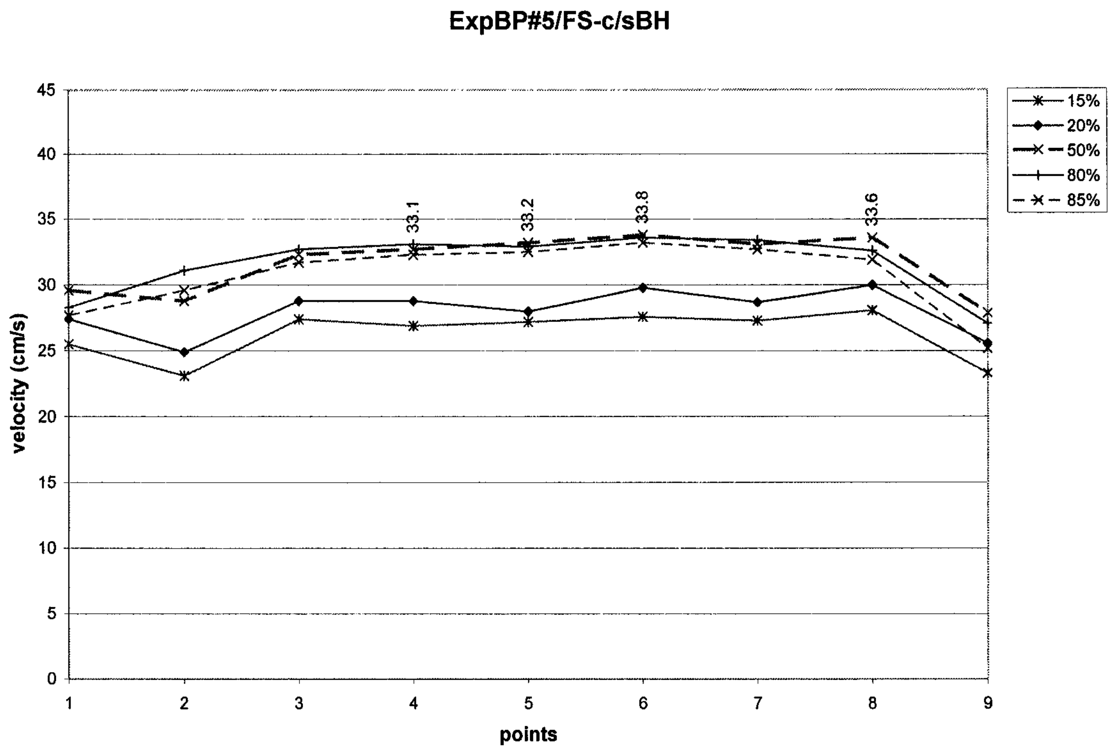

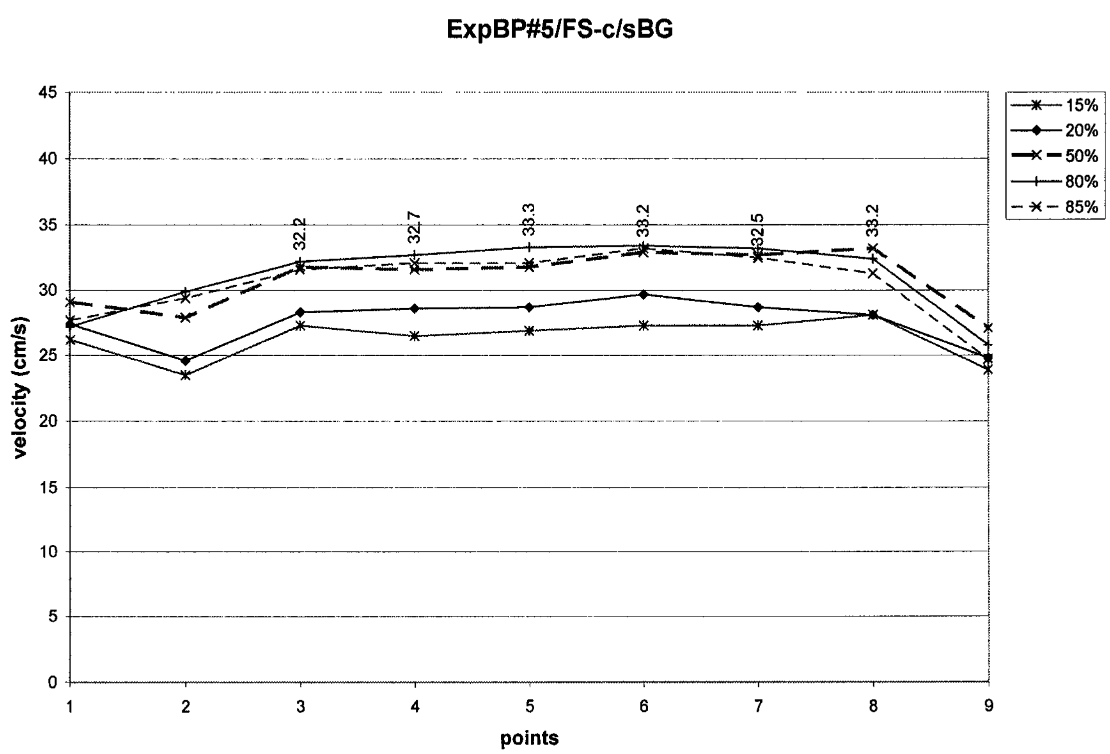

The following three velocity profiles were taken at 0.127m, 0.076m and 0.025m upstream the bridge pier nose.

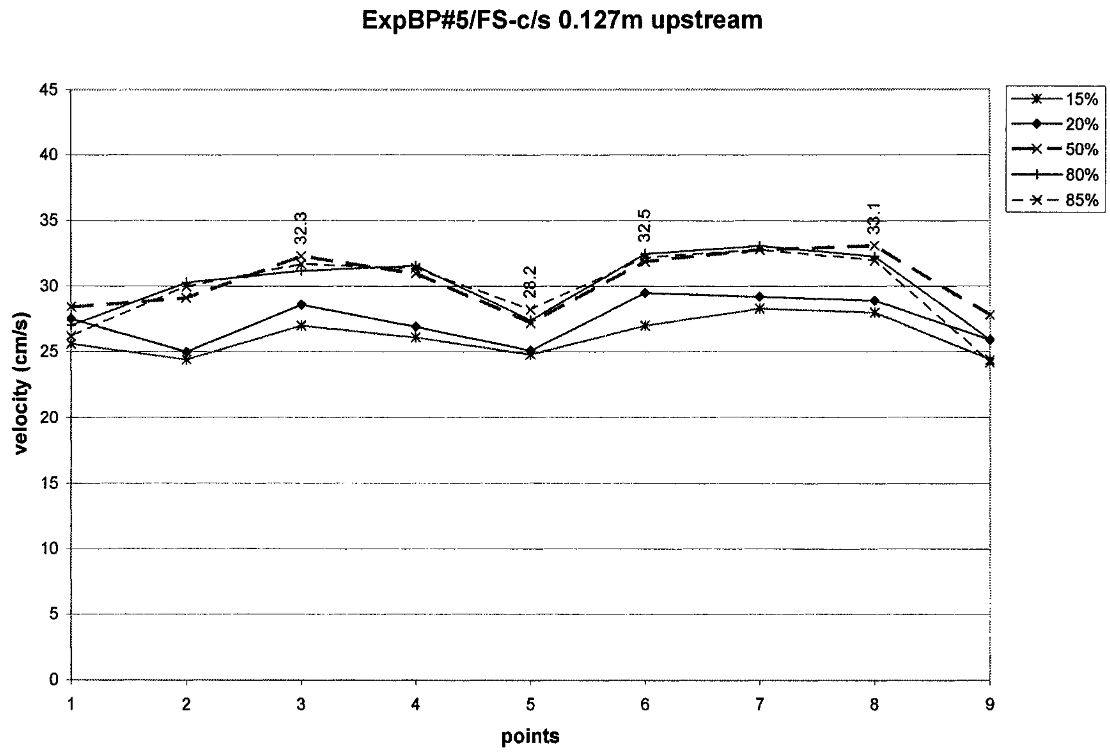

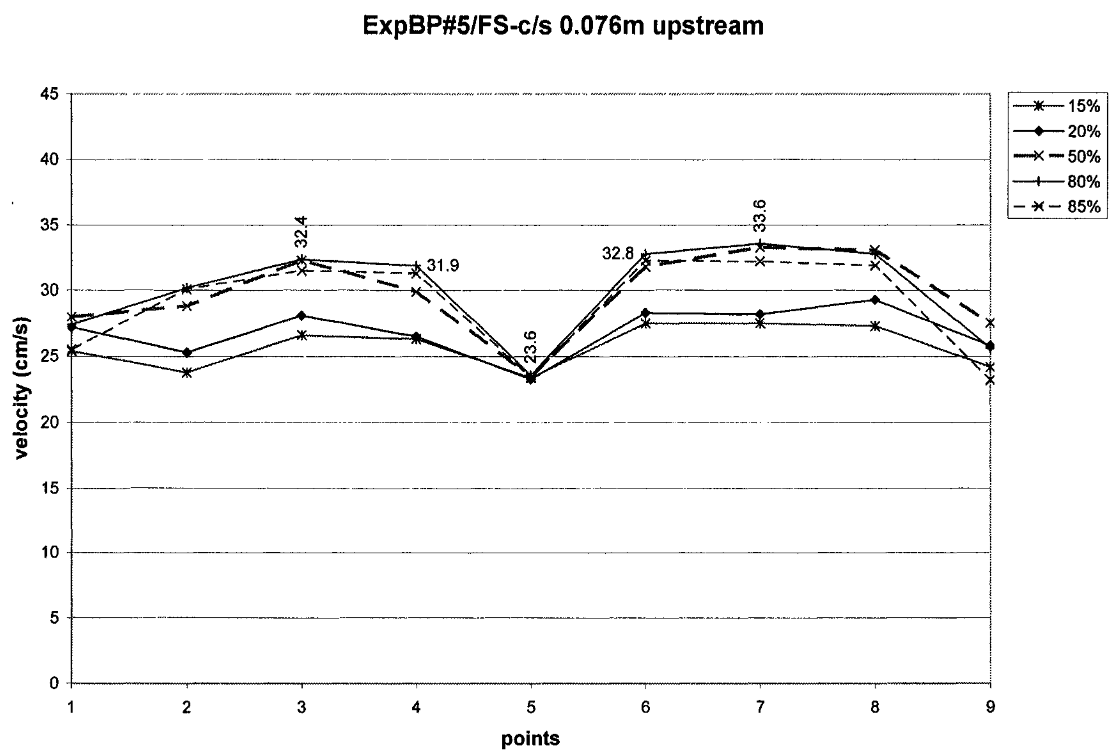

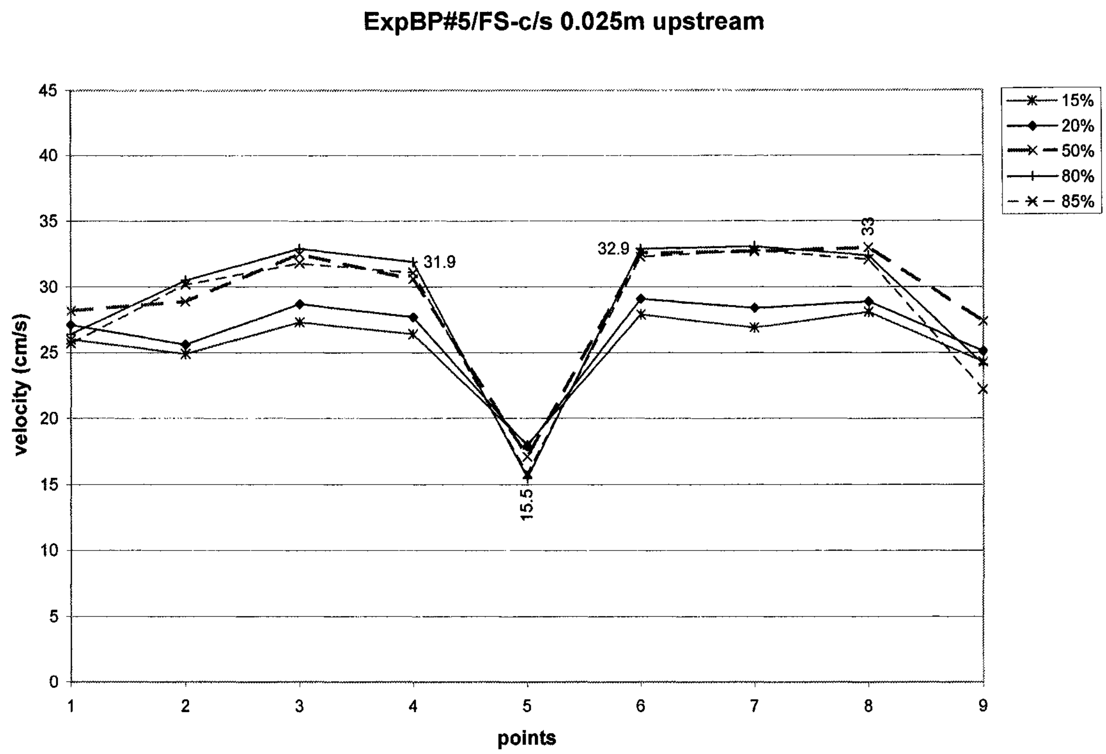

ExpBP#5/FS-c/s 0.025m upstream
15%
20%
50%
80%
85%
velocity (cm/s)
points
31.9
32.9
33
15.5

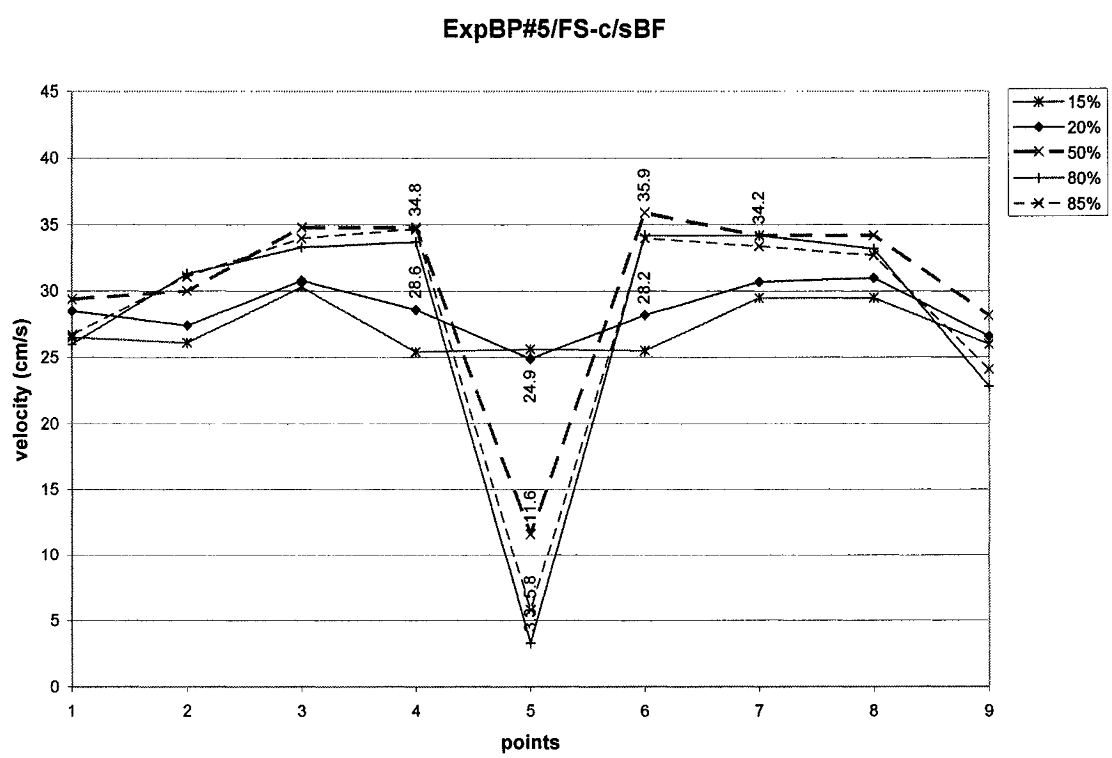

ExpBP#5/FS-c/sBF
15%
20%
50%
80%
85%
velocity (cm/s)
points
34.8
28.6
35.9
28.2
34.2
24.9
11.6
5.8

ExpBP#5/FS-c/sBE

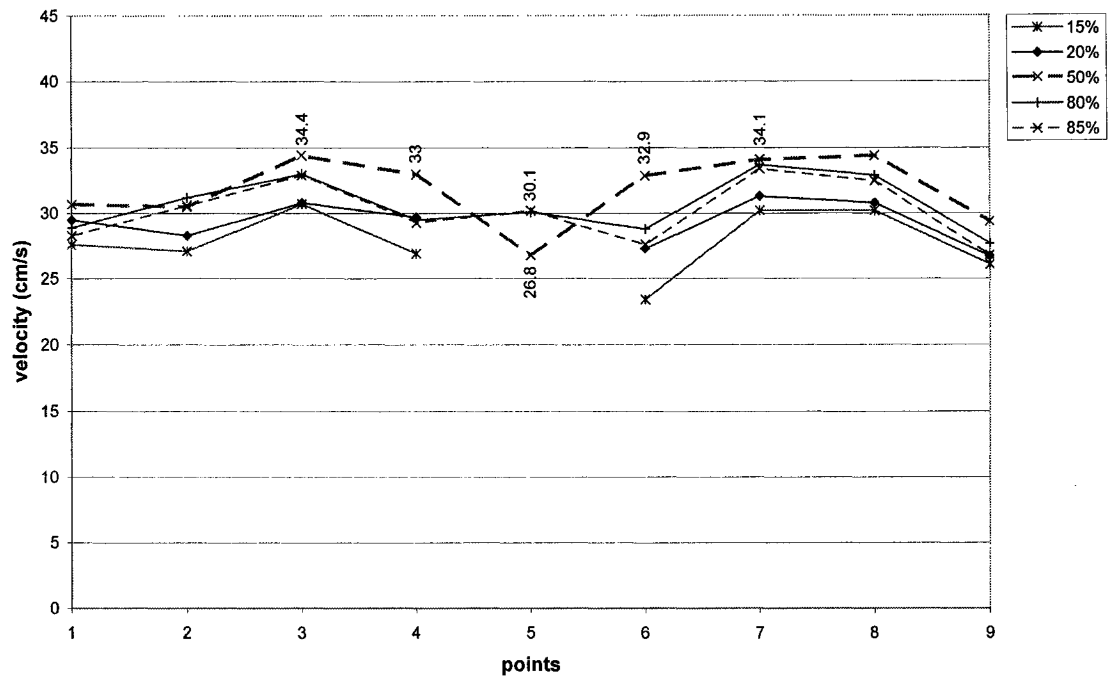

OBS: deposition behind the cylindrical pier made the recording of velocity readings for 15 and 20% of the flow depth impossible.

ExpBP#5/FS-c/sBD

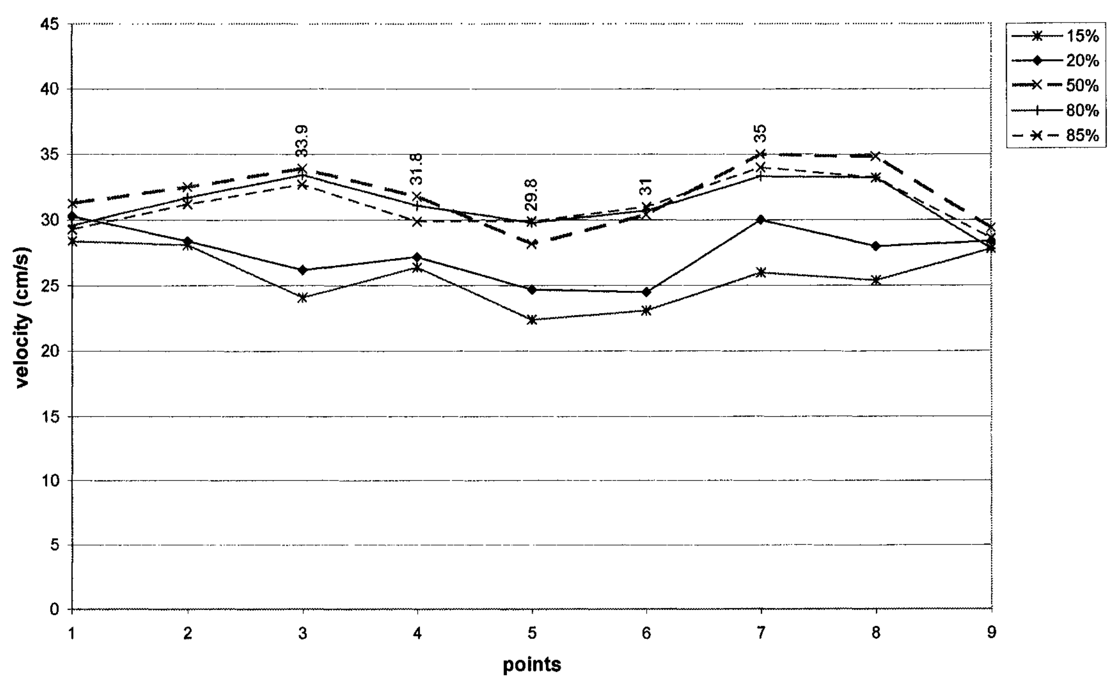

ExpBP#5/FS-c/sBC

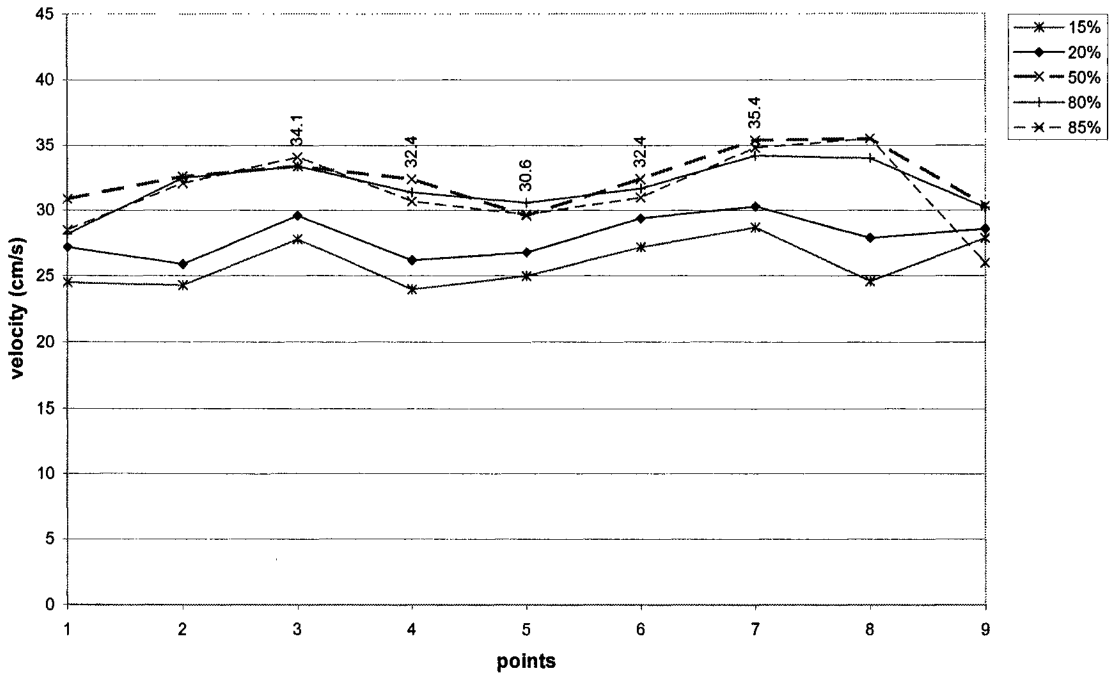

ExpBP#5/FS-c/sBB

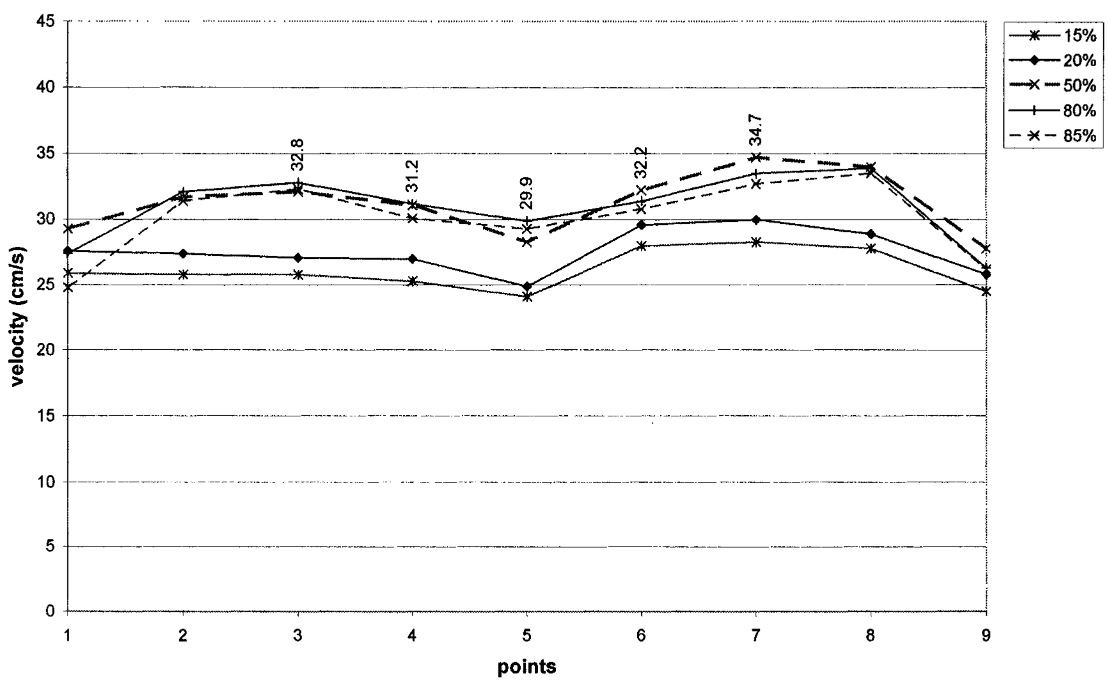

ExpBP#5/FS-c/sBA

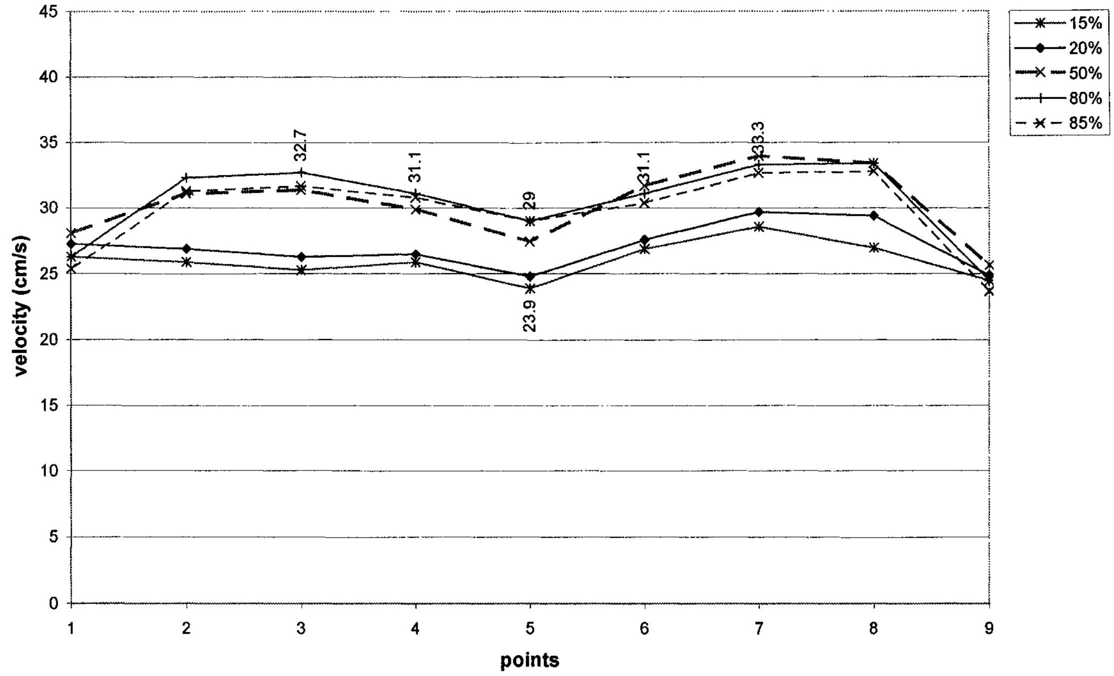

Vertical velocity profiles

ExpBP#5/FS-c/sBH

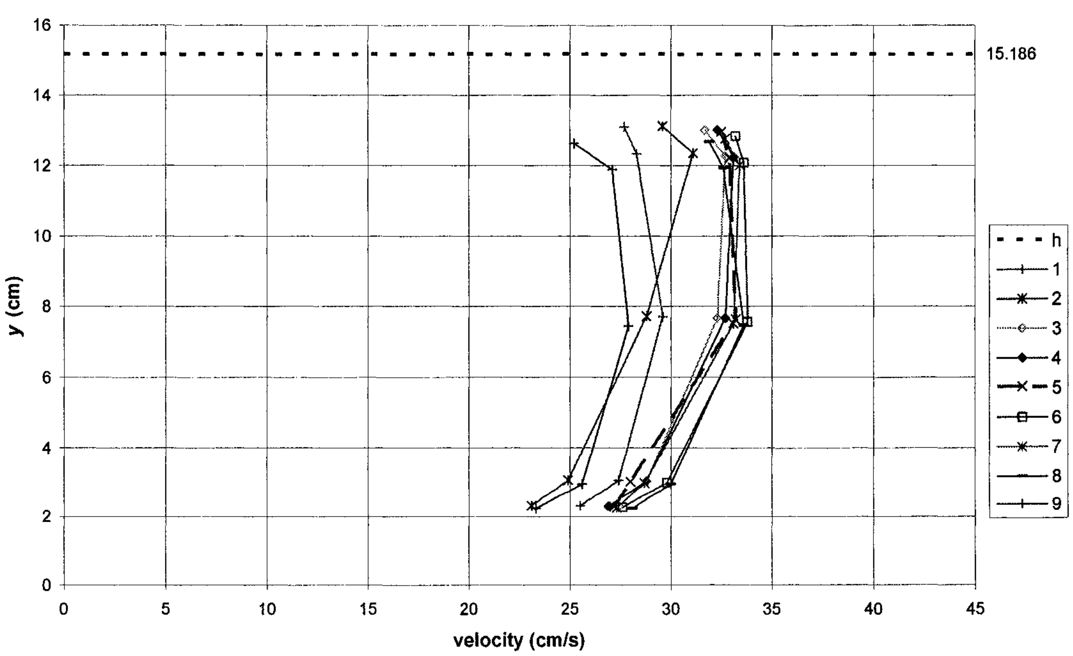

ExpBP#5/FS-c/sBG

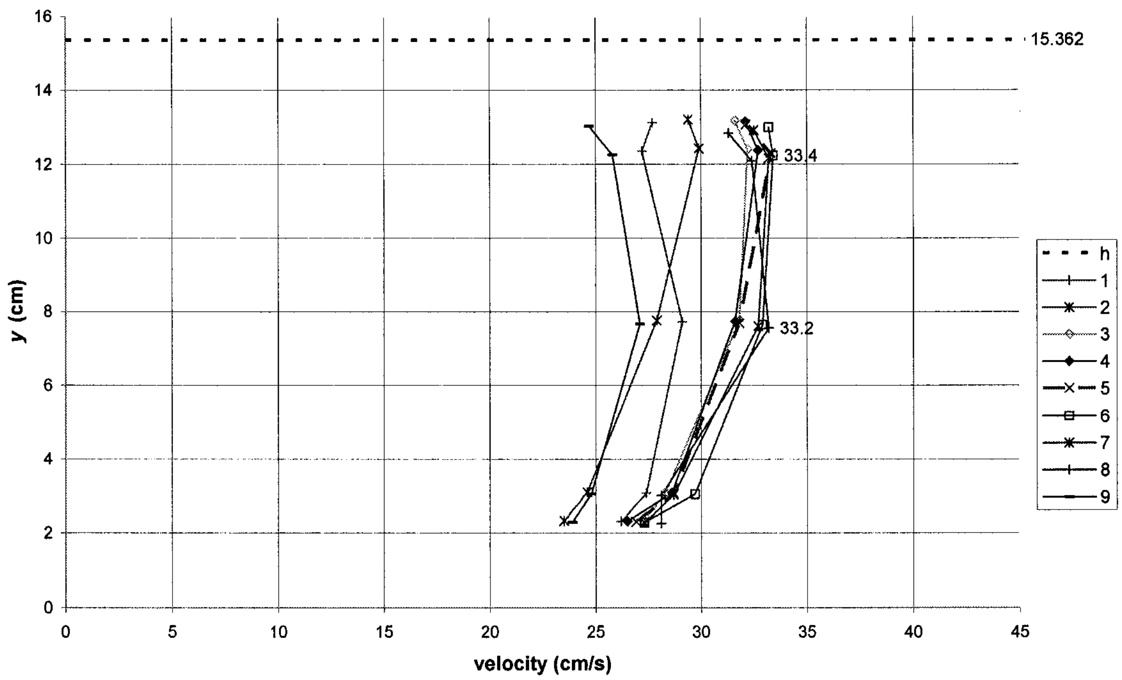

ExpBP#5/FS-c/s 0.127m upstream

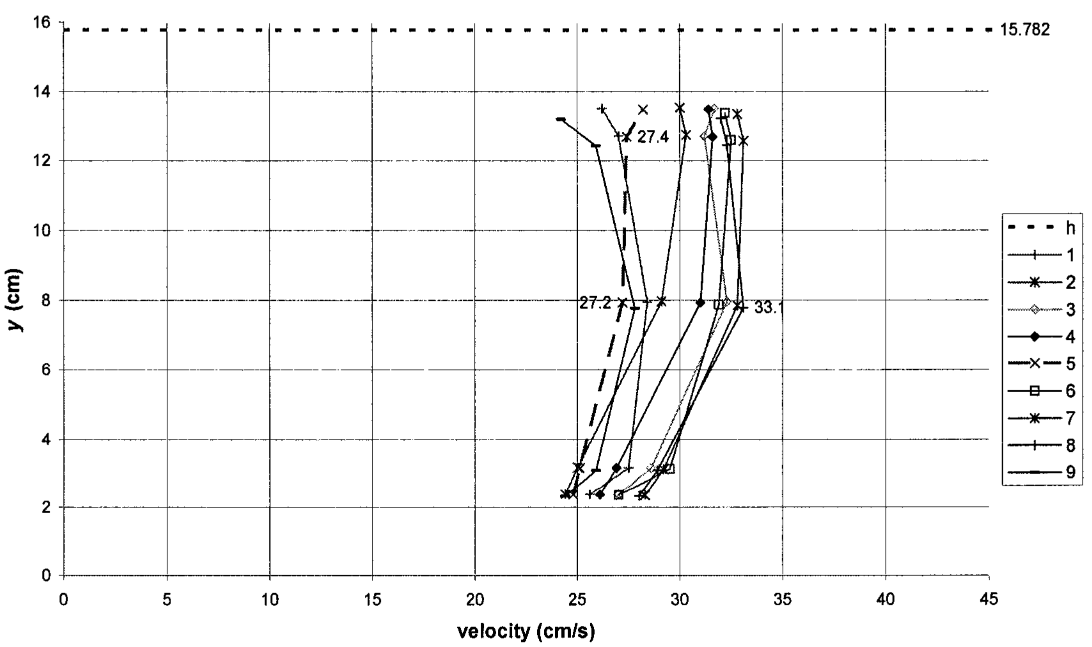

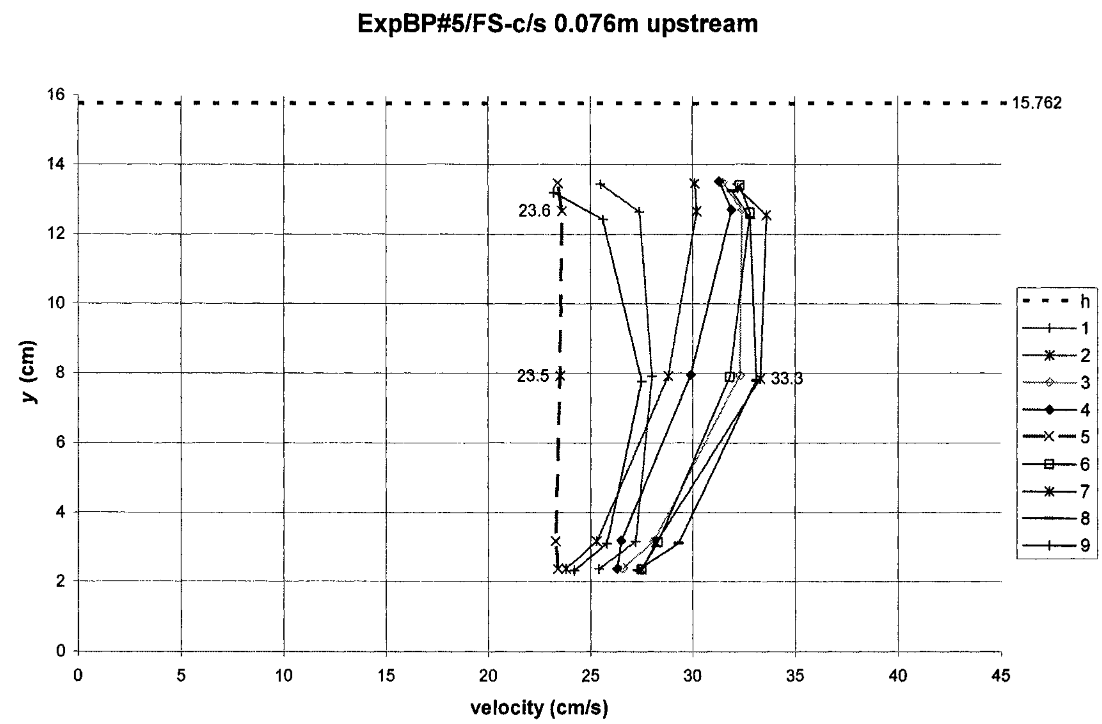

ExpBP#5/FS-c/s 0.076m upstream
15.762
23.6
23.5
33.3
y (cm)
velocity (cm/s)
h
1
2
3
4
5
6
7
8
9

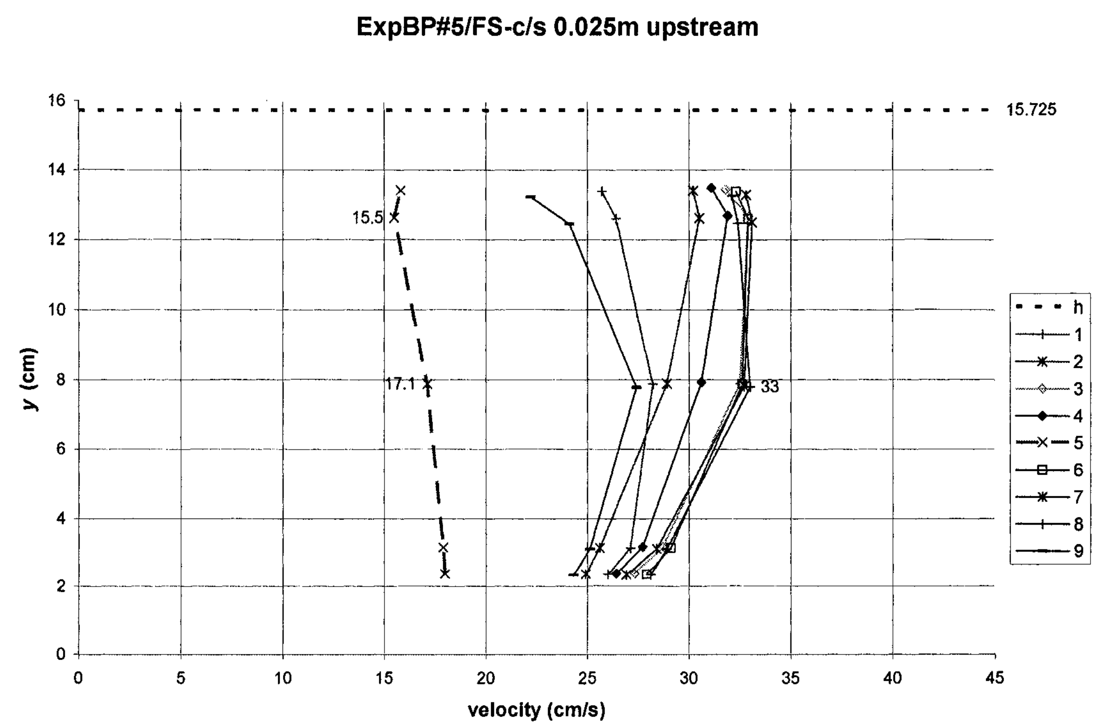

ExpBP#5/FS-c/s 0.025m upstream
15.725
15.5
17.1
33
y (cm)
velocity (cm/s)
h
1
2
3
4
5
6
7
8
9

ExpBP#5/FS-c/sBF

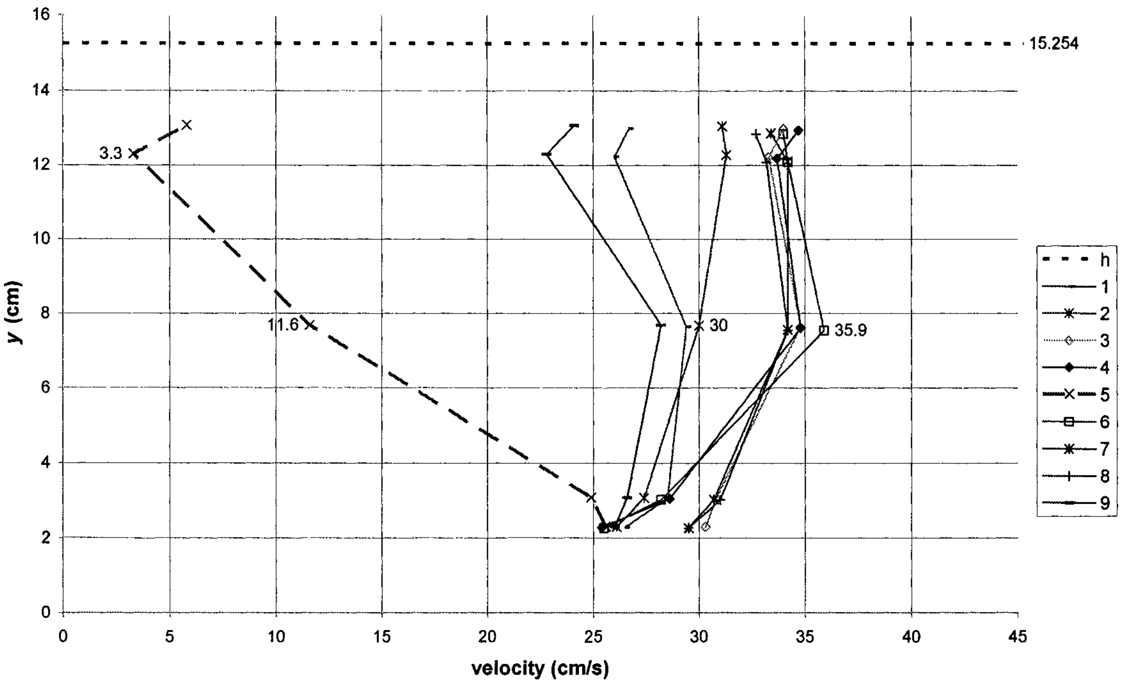

ExpBP#5/FS-c/sBE

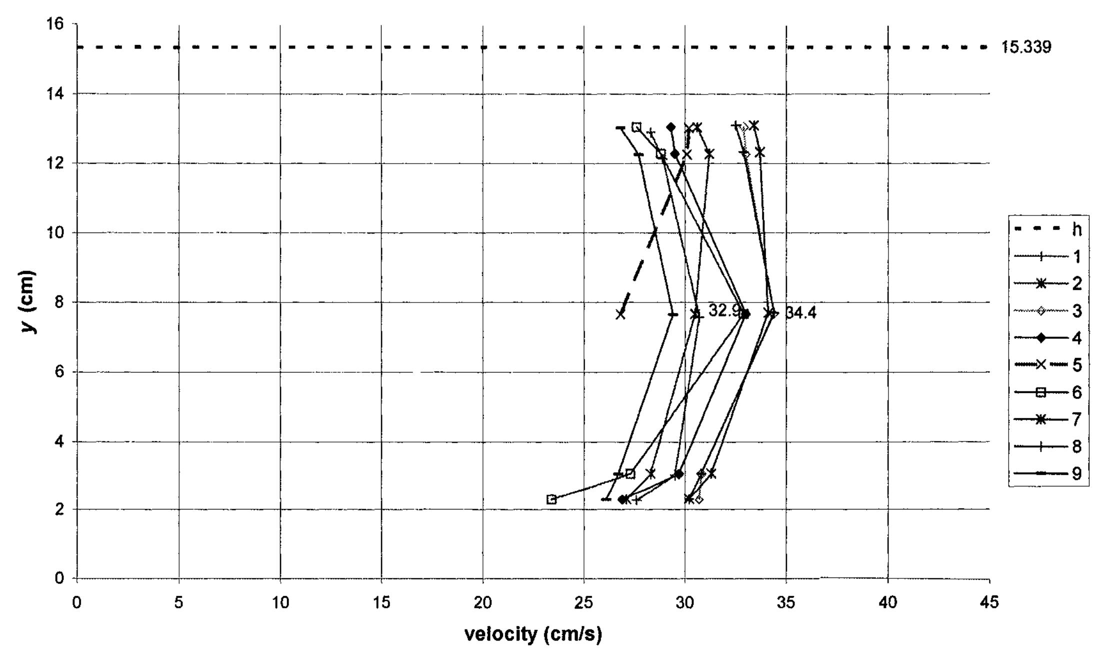

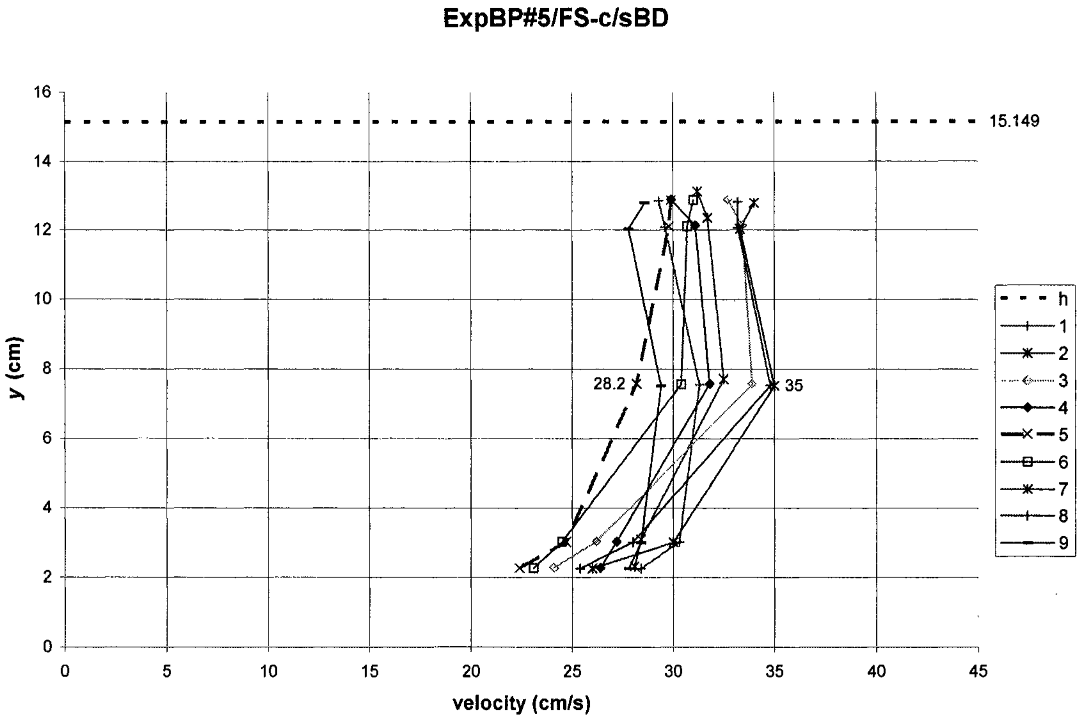
ExpBP#5/FS-c/sBD
15.149
28.2
35
h
1
2
3
4
5
6
7
8
9
y (cm)
velocity (cm/s)

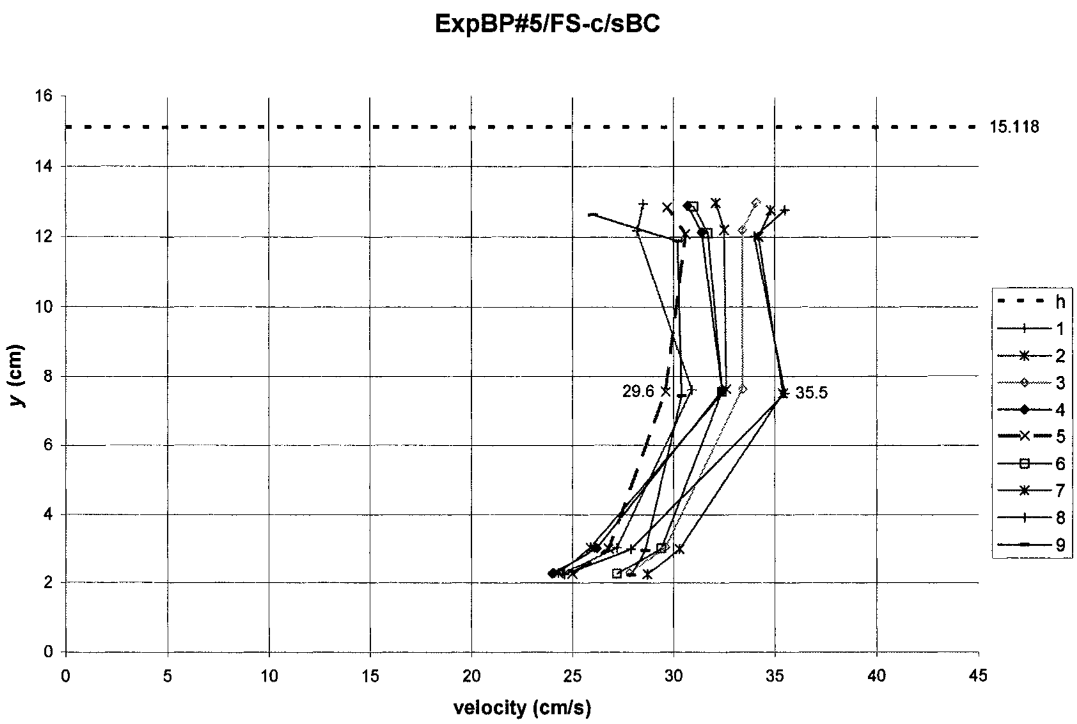
ExpBP#5/FS-c/sBC
15.118
29.6
35.5
h
1
2
3
4
5
6
7
8
9
y (cm)
velocity (cm/s)

ExpBP#5/FS-c/sBB

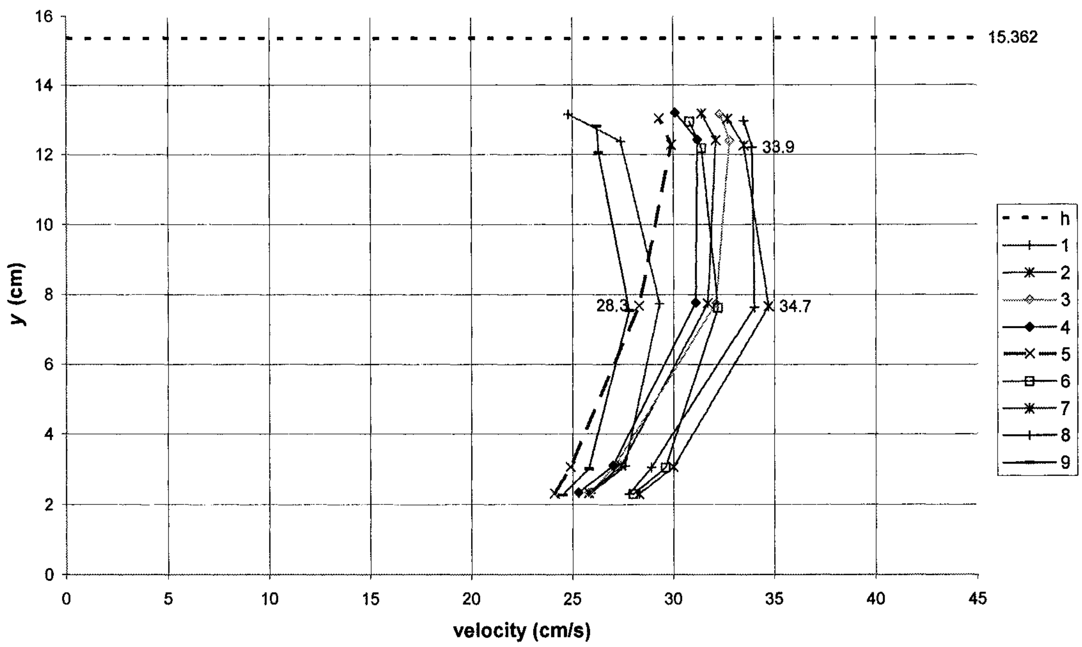

ExpBP#5/FS-c/sBA

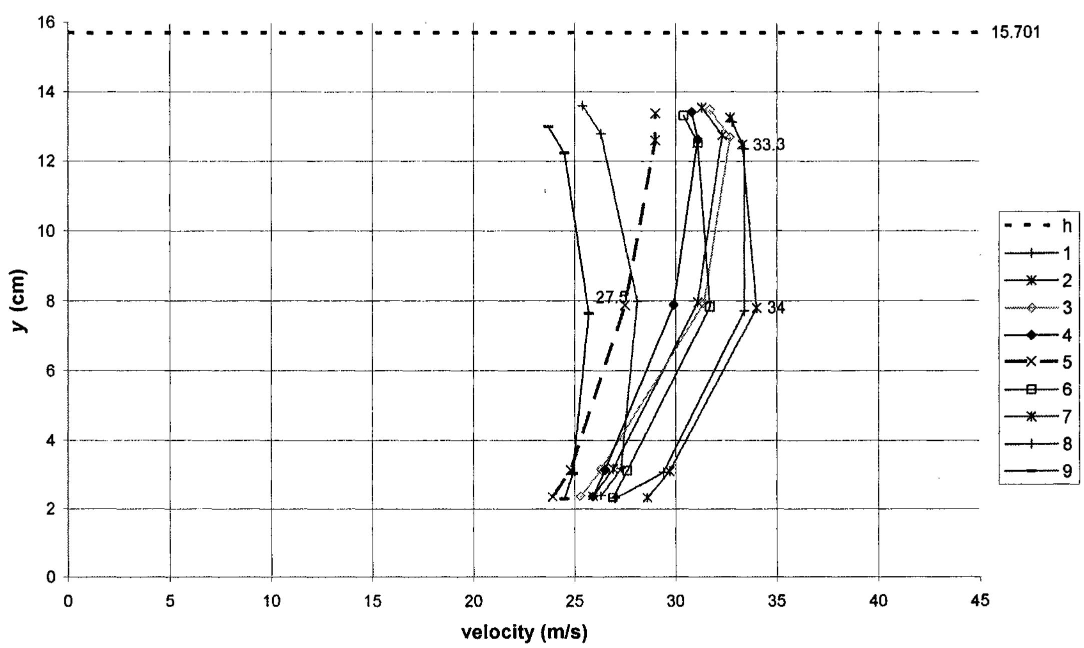

APPENDIX A12

Upstream Bridge Pier

(experiment with bridge pier)

Lateral velocity profiles of c/s BG, upstream the bridge pier based on measurements taken at different moment of the scouring process.

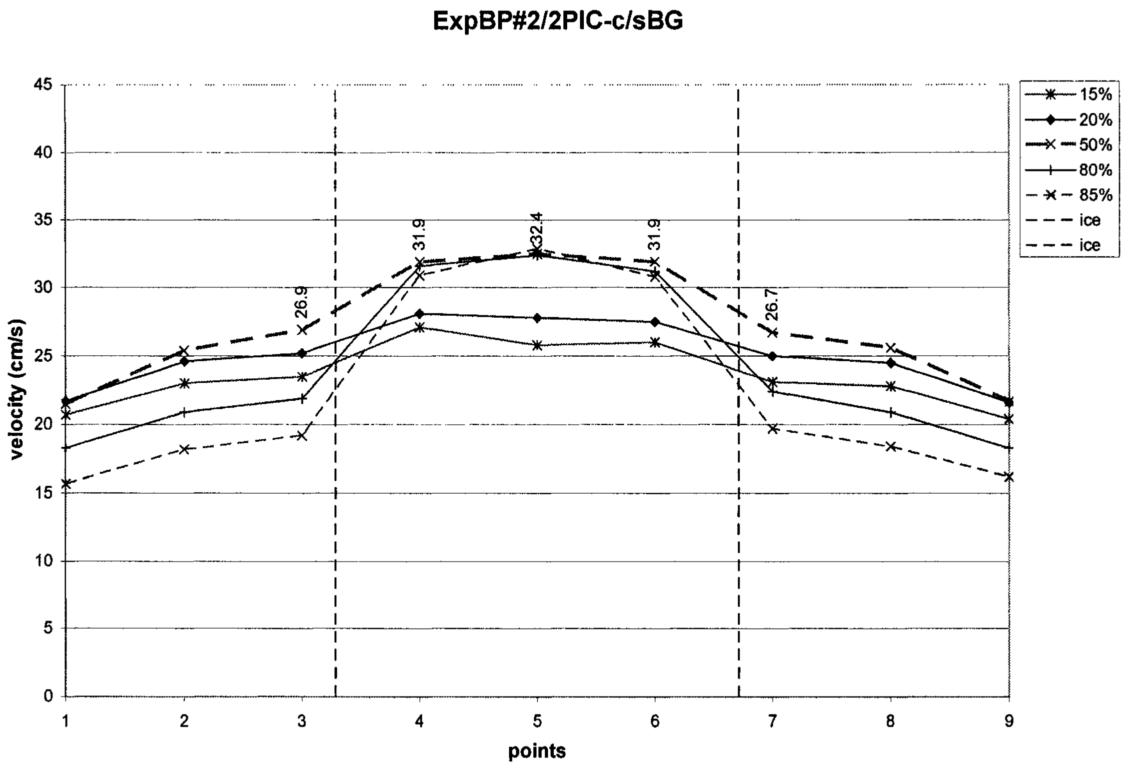

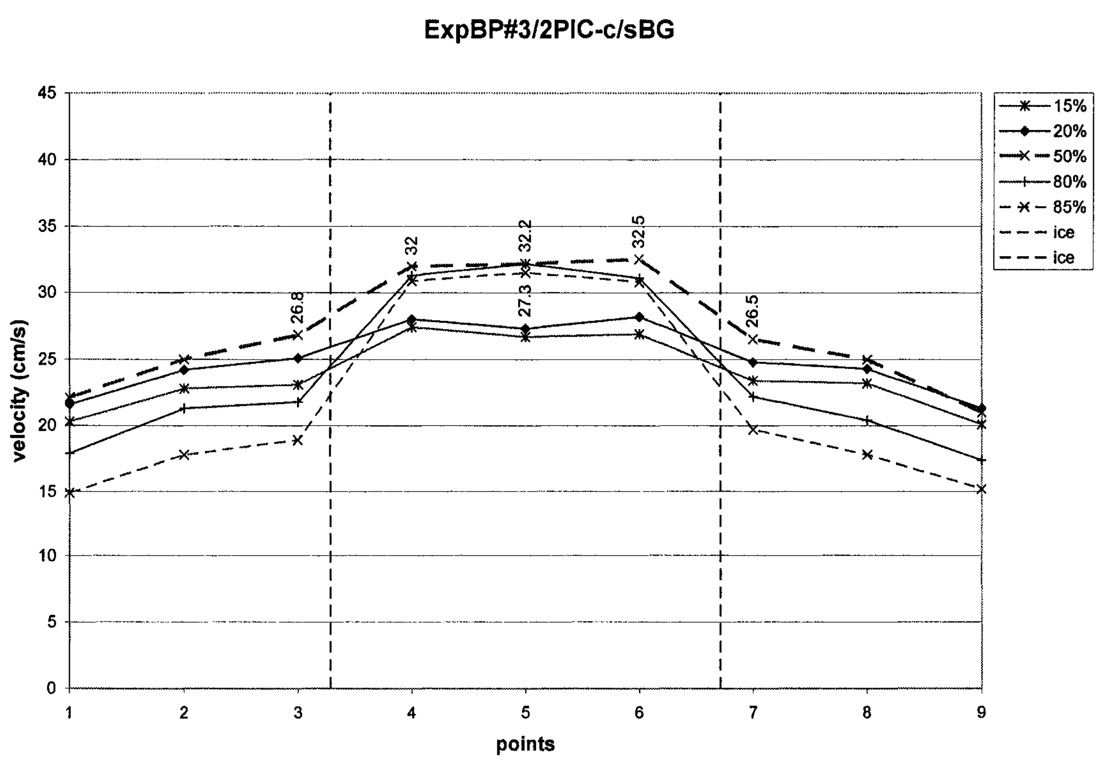

ExpBP#4/2PIC-c/sBG

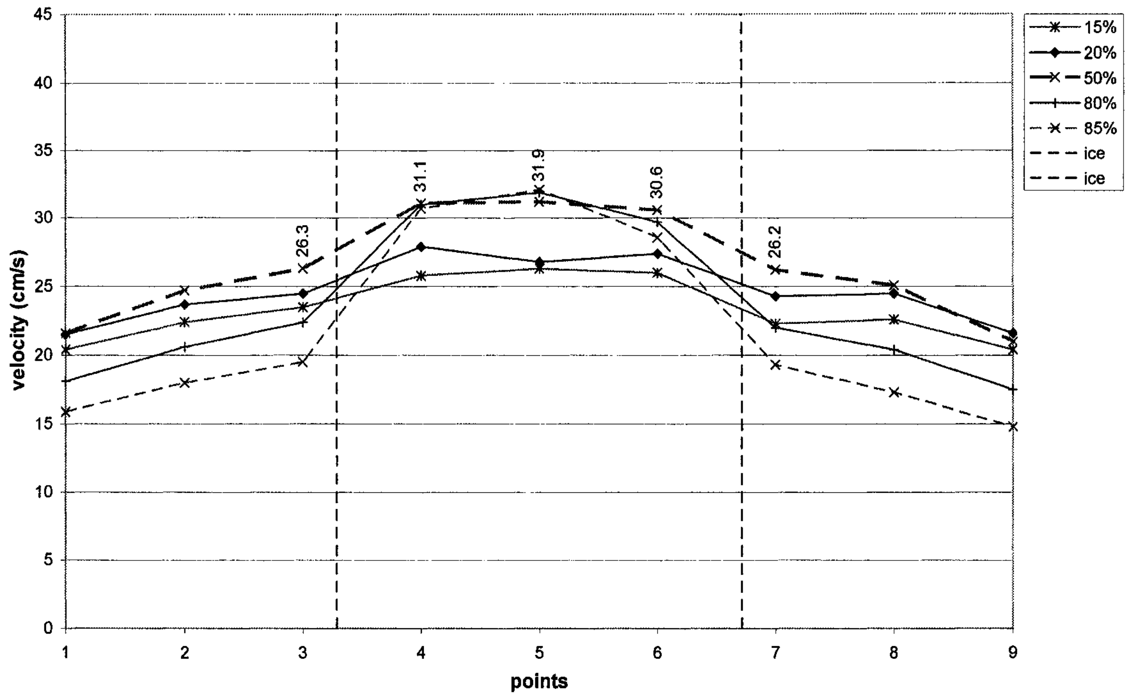

APPENDIX A13

Downstream Bridge Pier

(experiment with bridge pier)

Lateral velocity profiles at c/s BF, downstream the pier based on measurements taken at different moments of scouring process

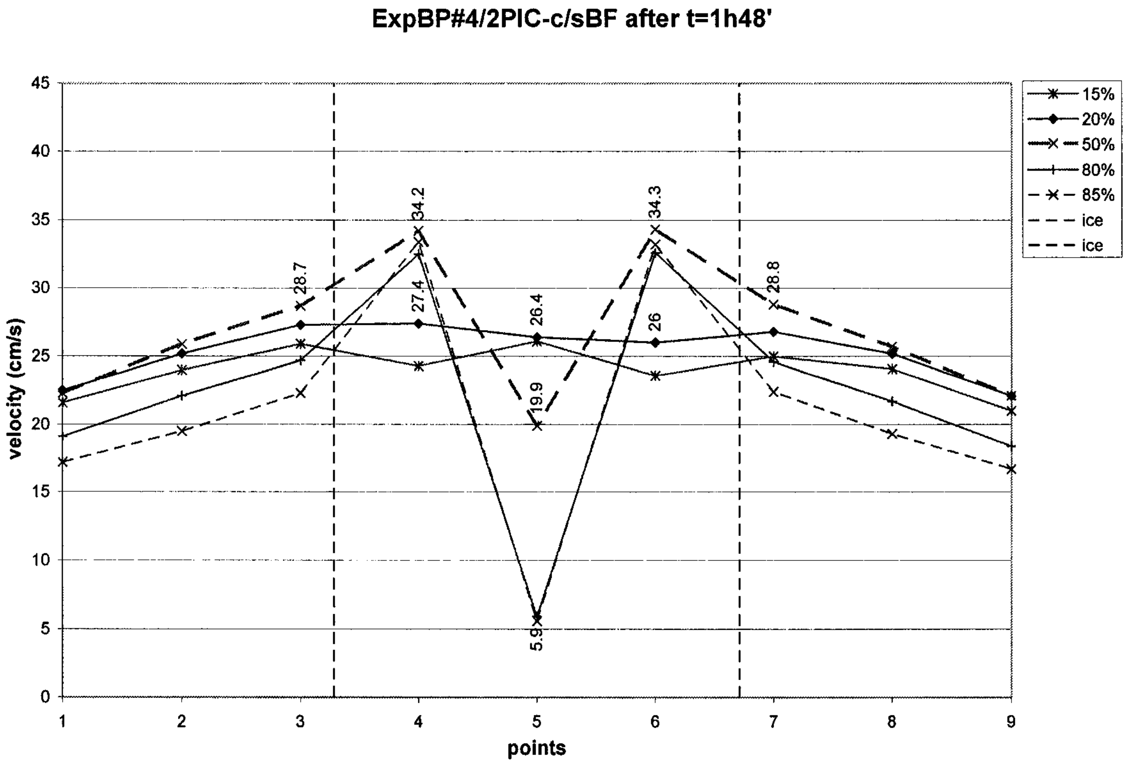

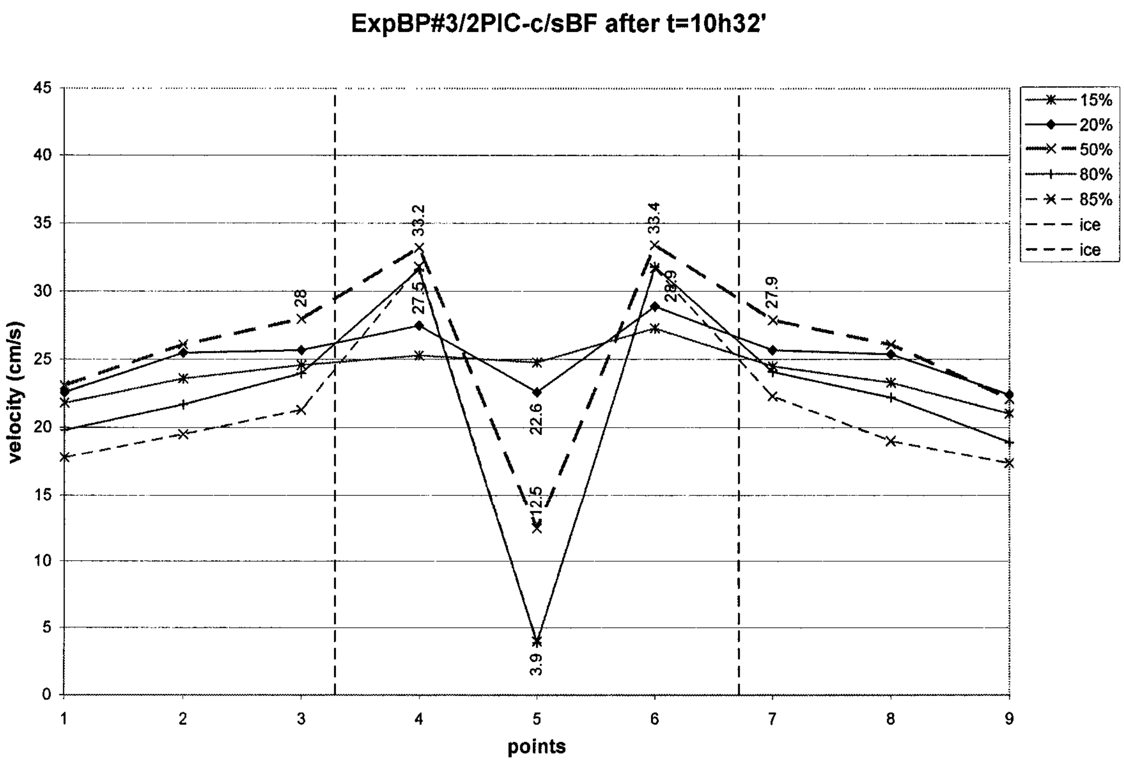

ExpBP#4/2PIC-c/sBF after t=25h

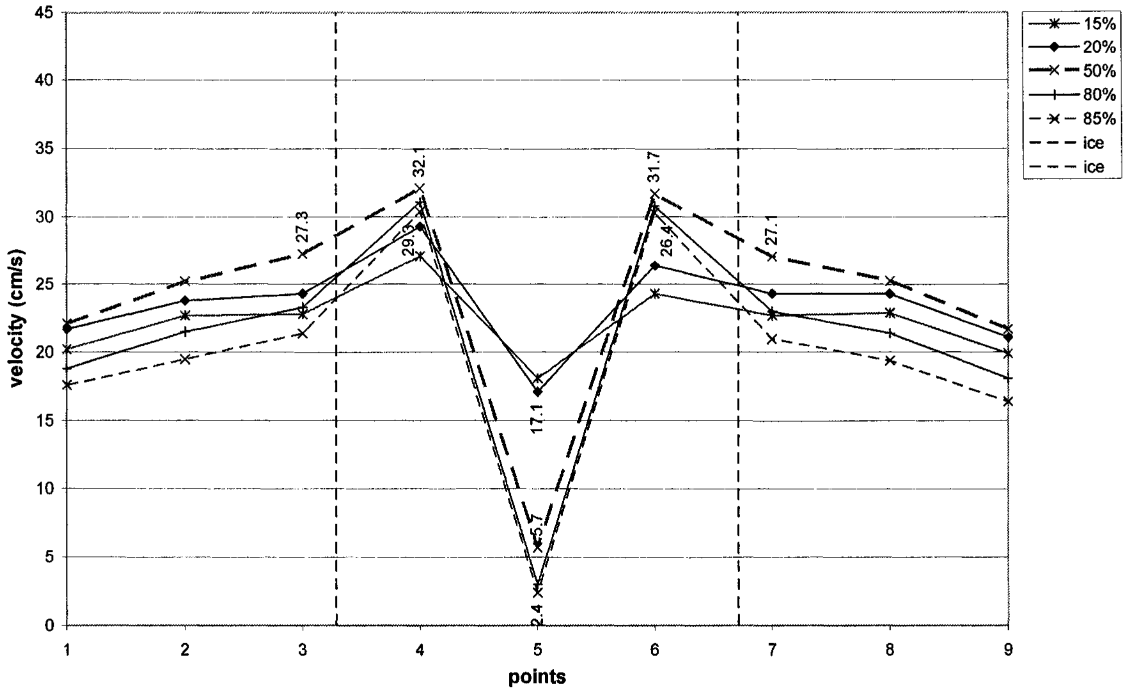

ExpBP#2/2PIC-c/sBF after t=26h

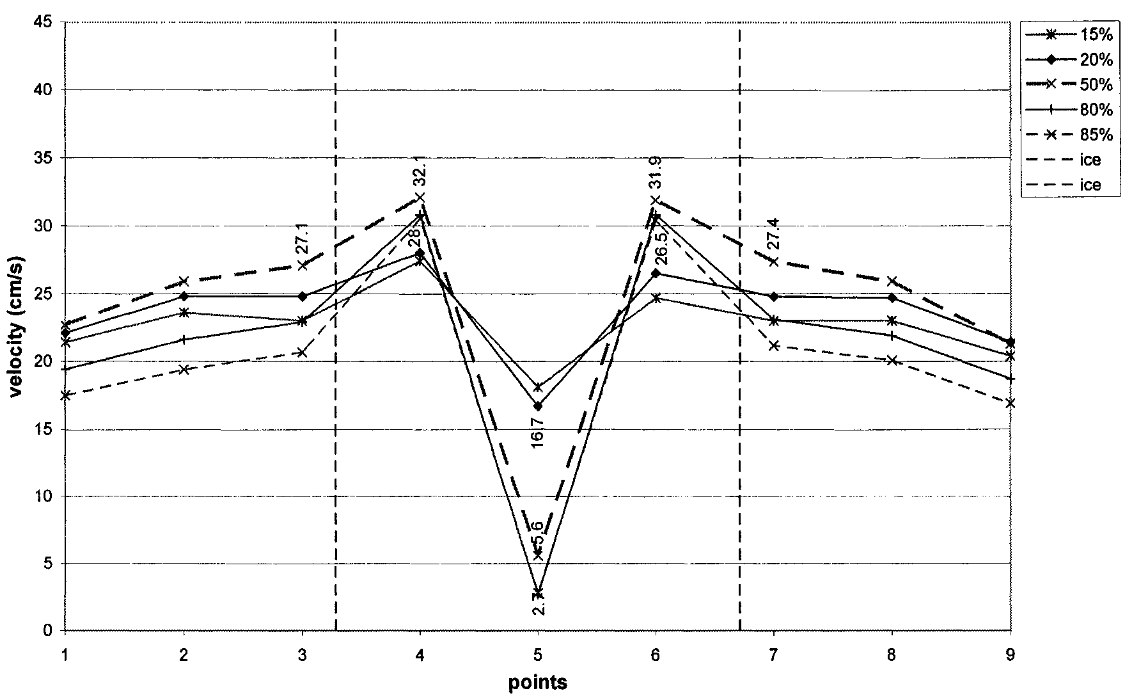

APPENDIX A14

Scour depths time-variation

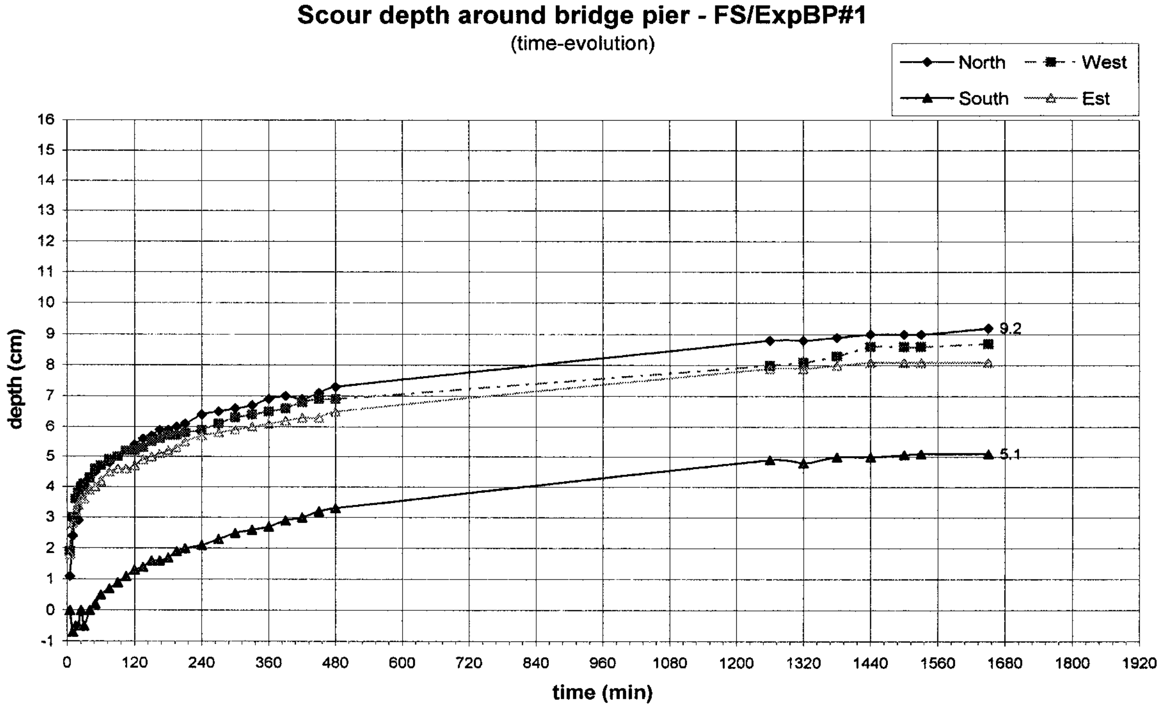

Scour depth around bridge pier - FS/ExpBP#1
(time-evolution)
North
West
South
Est
depth (cm)
time (min)
9.2
5.1

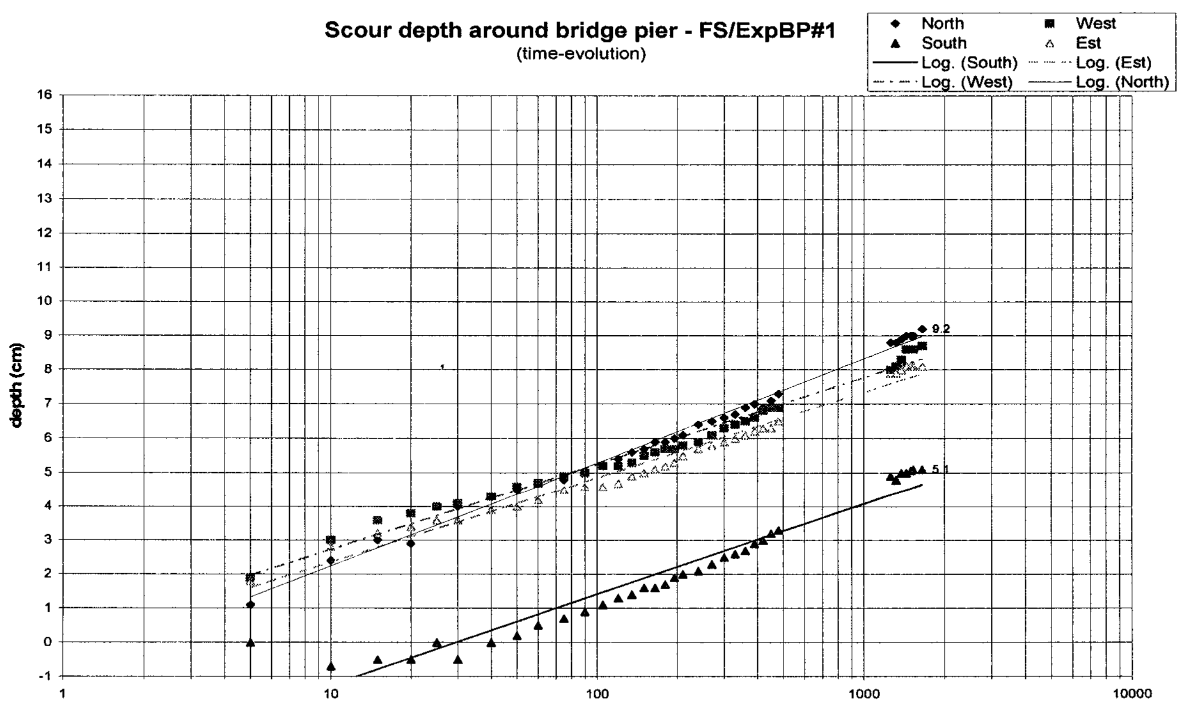

Scour depth around bridge pier - FS/ExpBP#1
(time-evolution)
North
West
South
Est
Log. (South)
Log. (Est)
Log. (West)
Log. (North)
depth (cm)
time (min)
9.2
5.1

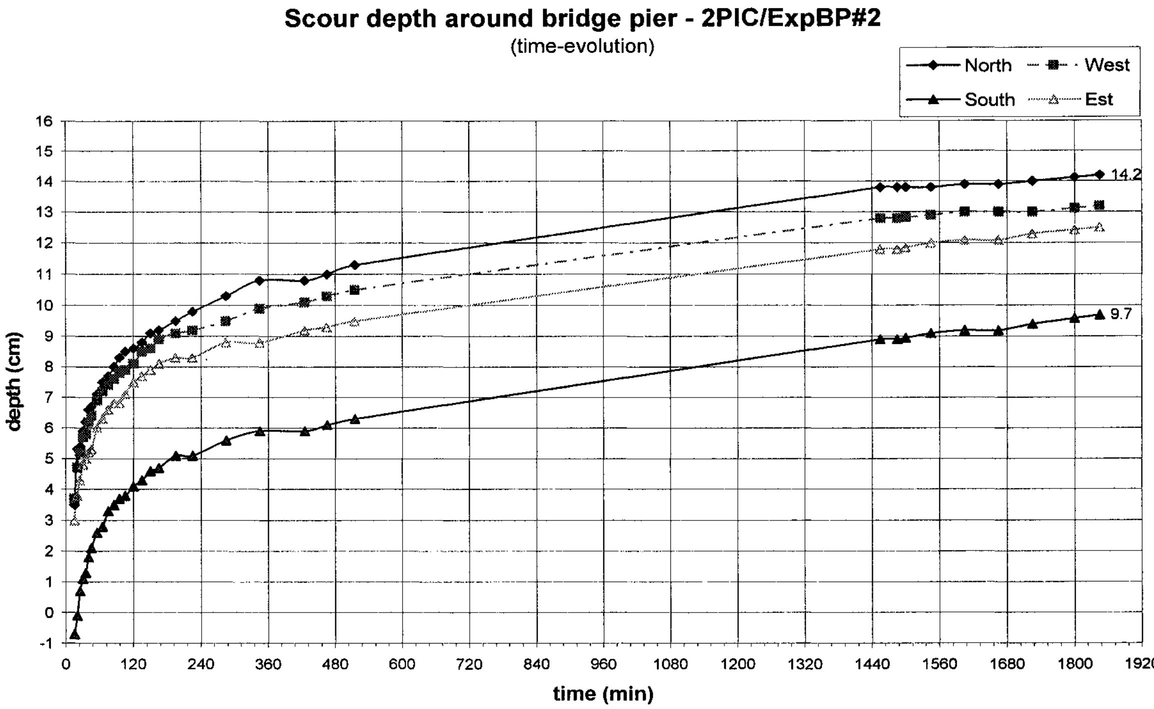
Scour depth around bridge pier - 2PIC/ExpBP#2
(time-evolution)
North
West
South
Est
depth (cm)
time (min)
14.2
9.7

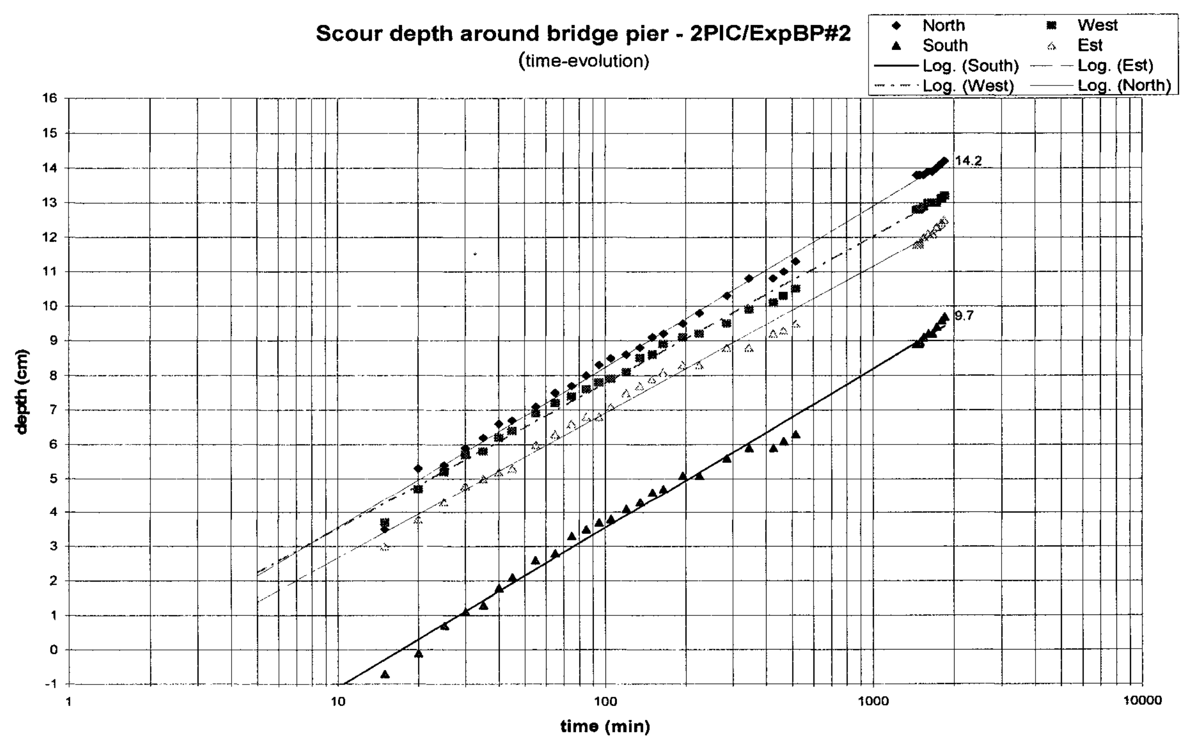
Scour depth around bridge pier - 2PIC/ExpBP#2
(time-evolution)
North
West
South
Est
Log. (South)
Log. (Est)
Log. (West)
Log. (North)
depth (cm)
time (min)
14.2
9.7

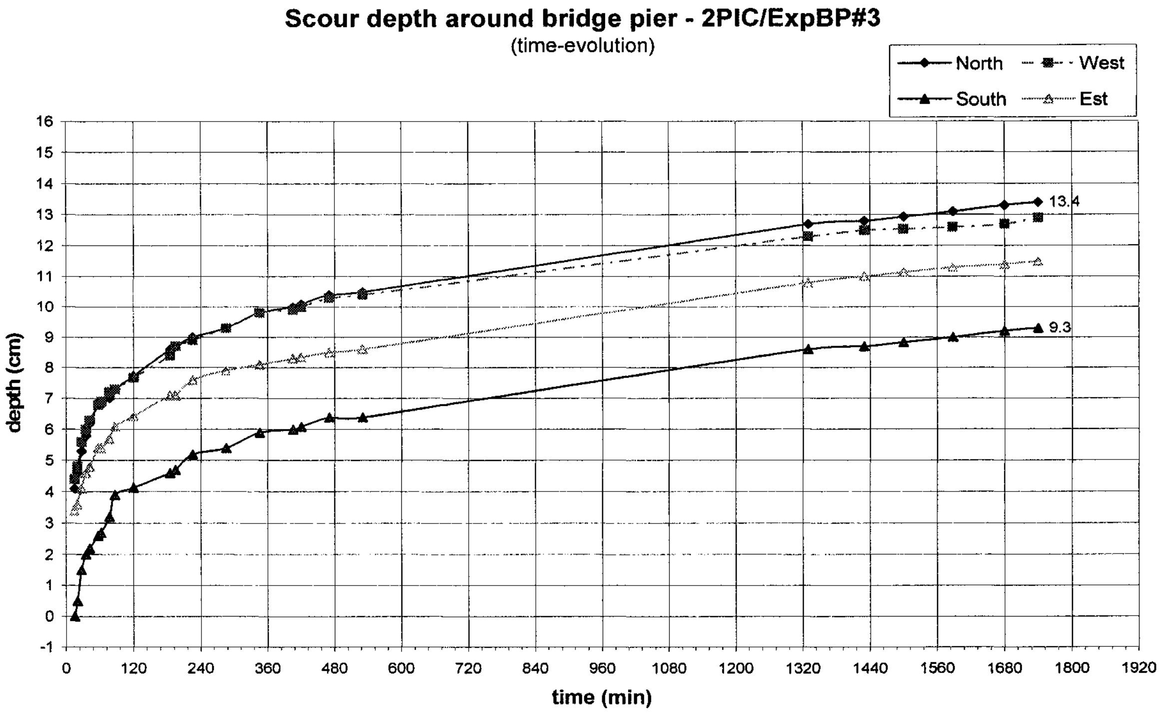

Scour depth around bridge pier - 2PIC/ExpBP#3
(time-evolution)
North
West
South
Est
depth (cm)
time (min)
13.4
9.3

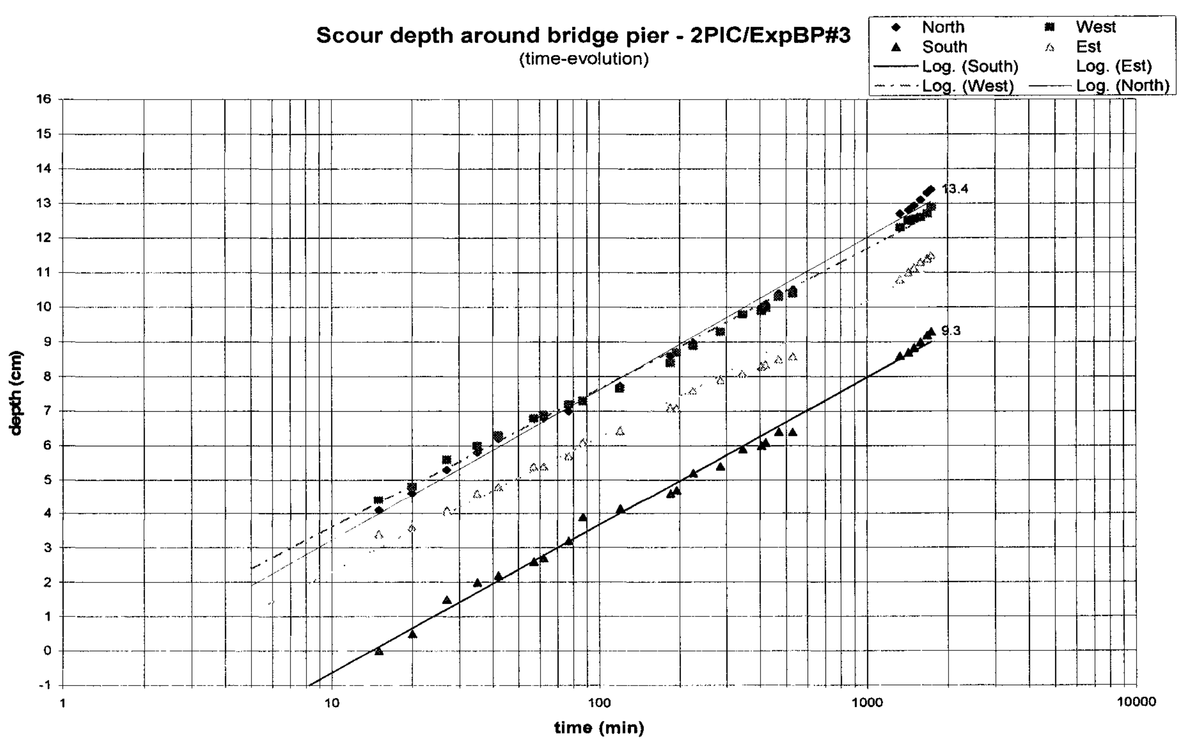

Scour depth around bridge pier - 2PIC/ExpBP#3
(time-evolution)
North
West
South
Est
Log. (South)
Log. (Est)
Log. (West)
Log. (North)
depth (cm)
time (min)
13.4
9.3

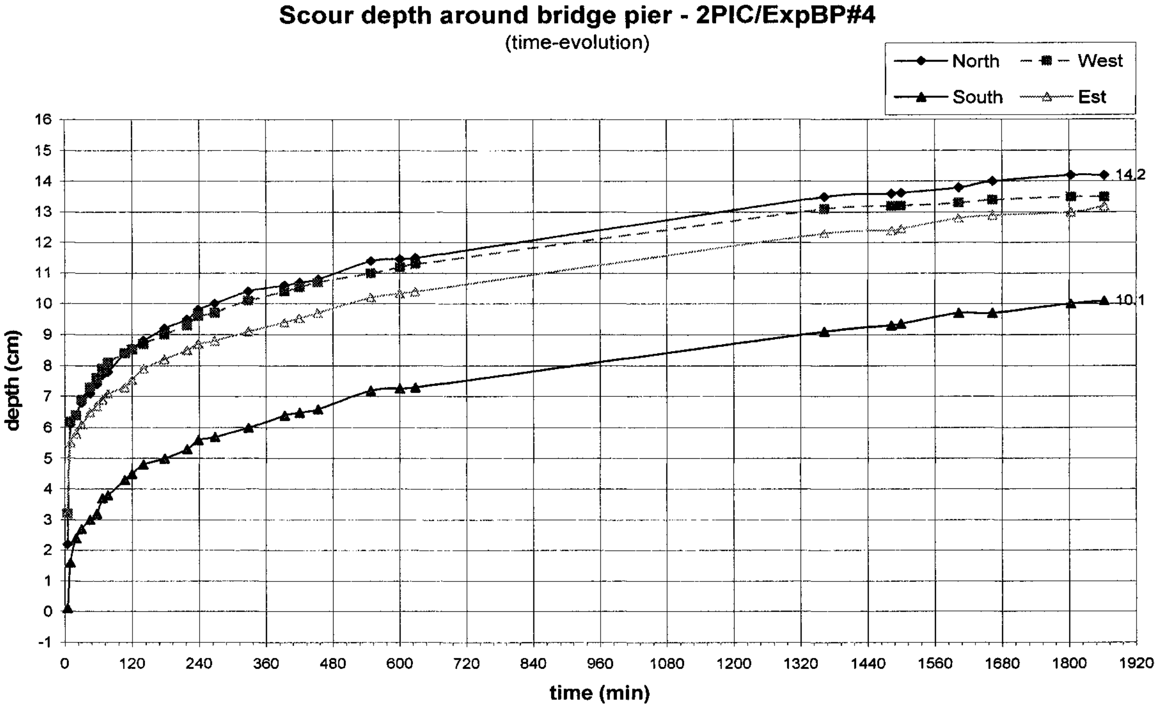
Scour depth around bridge pier - 2PIC/ExpBP#4
(time-evolution)
North
West
South
Est
depth (cm)
time (min)
14.2
10.1

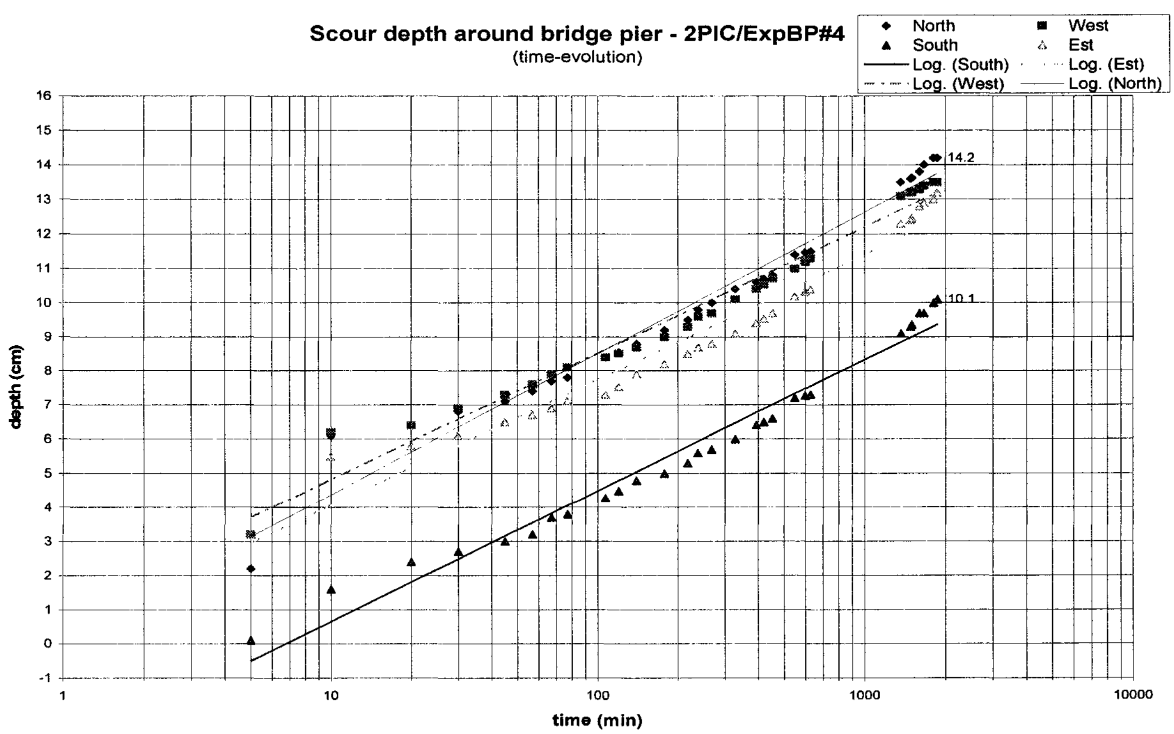
Scour depth around bridge pier - 2PIC/ExpBP#4
(time-evolution)
North
West
South
Est
Log. (South)
Log. (Est)
Log. (West)
Log. (North)
depth (cm)
time (min)
14.2
10.1

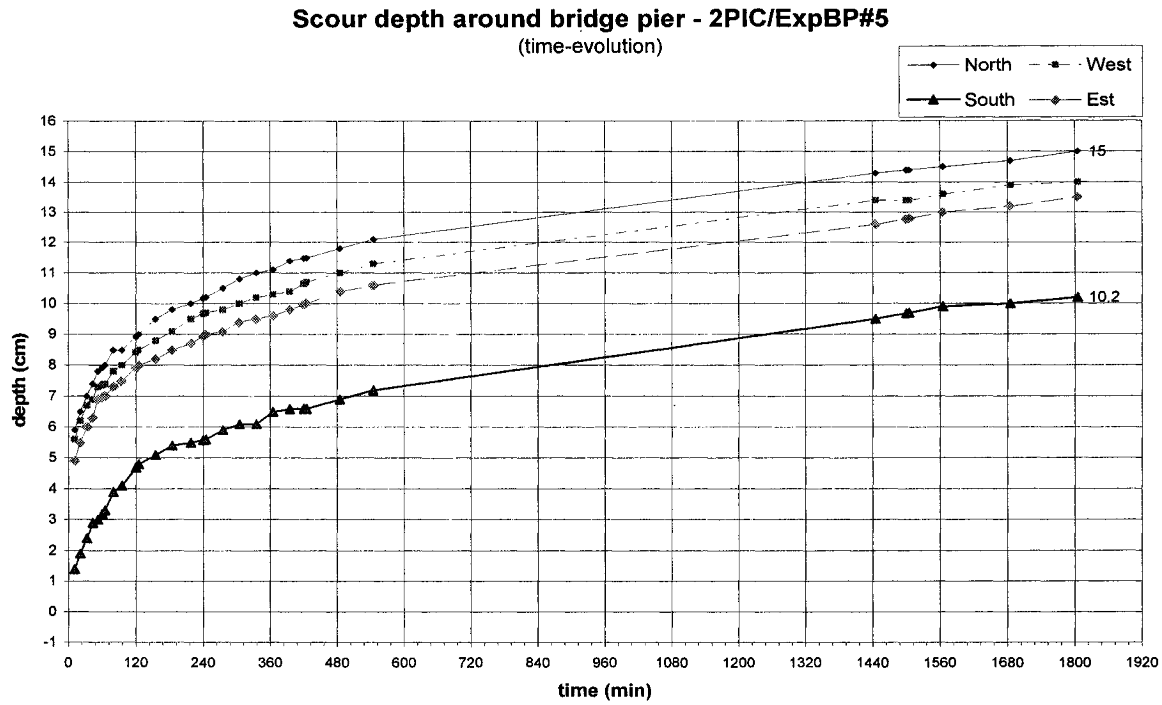
Scour depth around bridge pier - 2PIC/ExpBP#5
(time-evolution)
North
West
South
Est
depth (cm)
time (min)
15
10.2

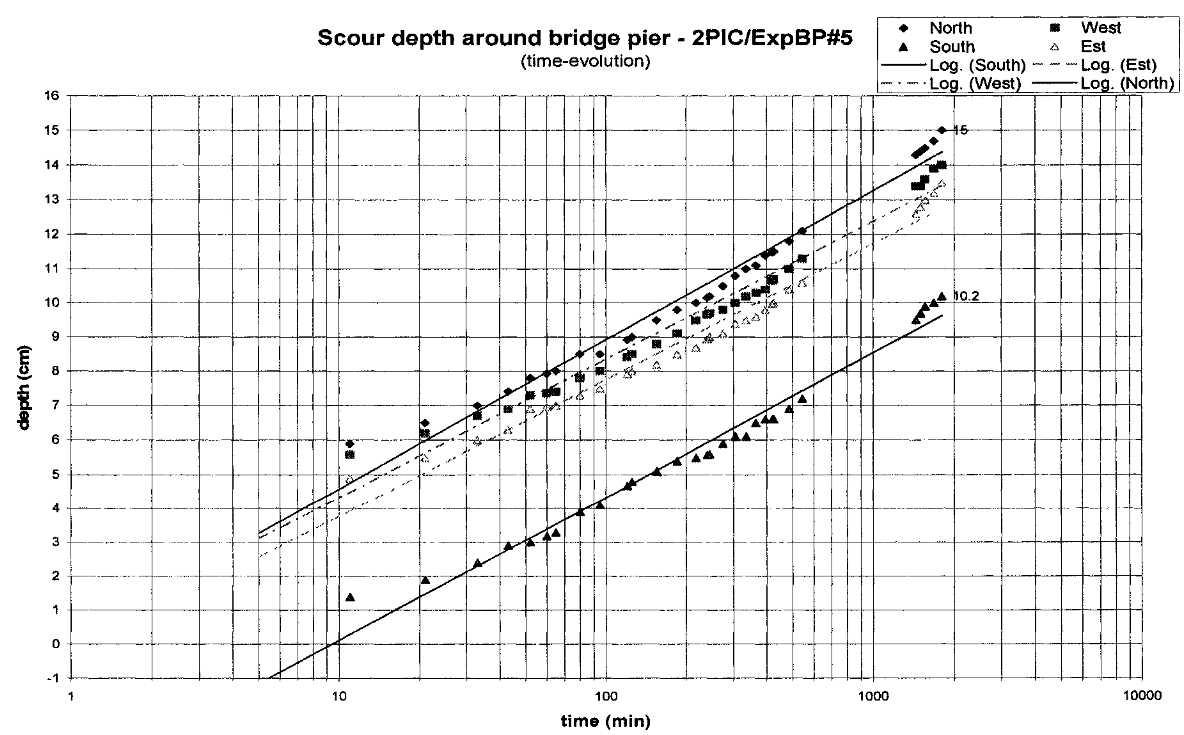
Scour depth around bridge pier - 2PIC/ExpBP#5
(time-evolution)
North
West
South
Est
Log. (South)
Log. (Est)
Log. (West)
Log. (North)
depth (cm)
time (min)
15
10.2

APPENDIX A15

Scour depths and erosion/deposition profiles

Comparison of scour depths and erosion/deposition profiles at the channel centerline (point 5)

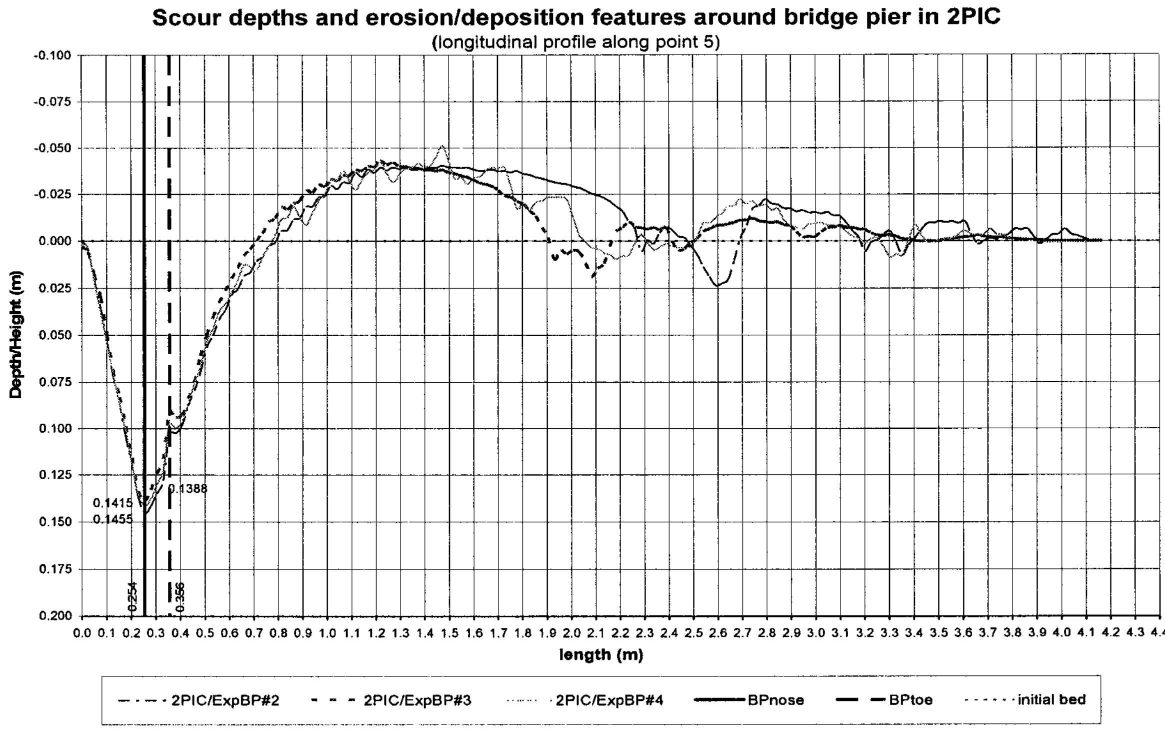

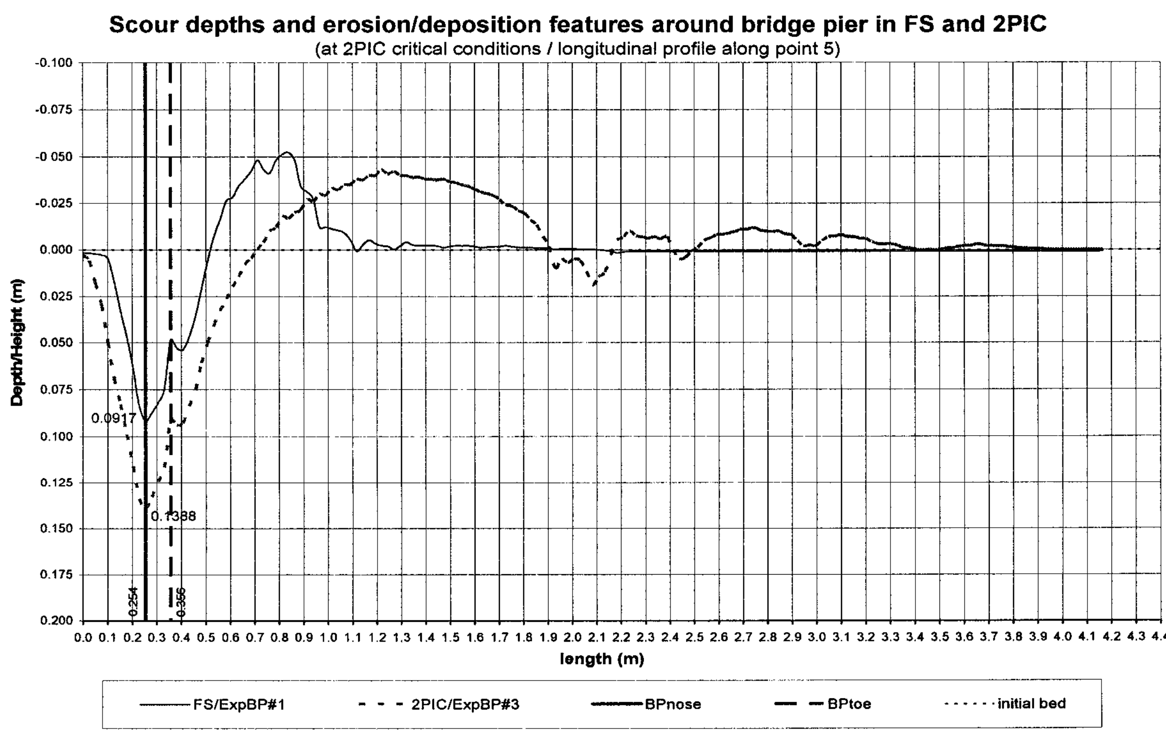

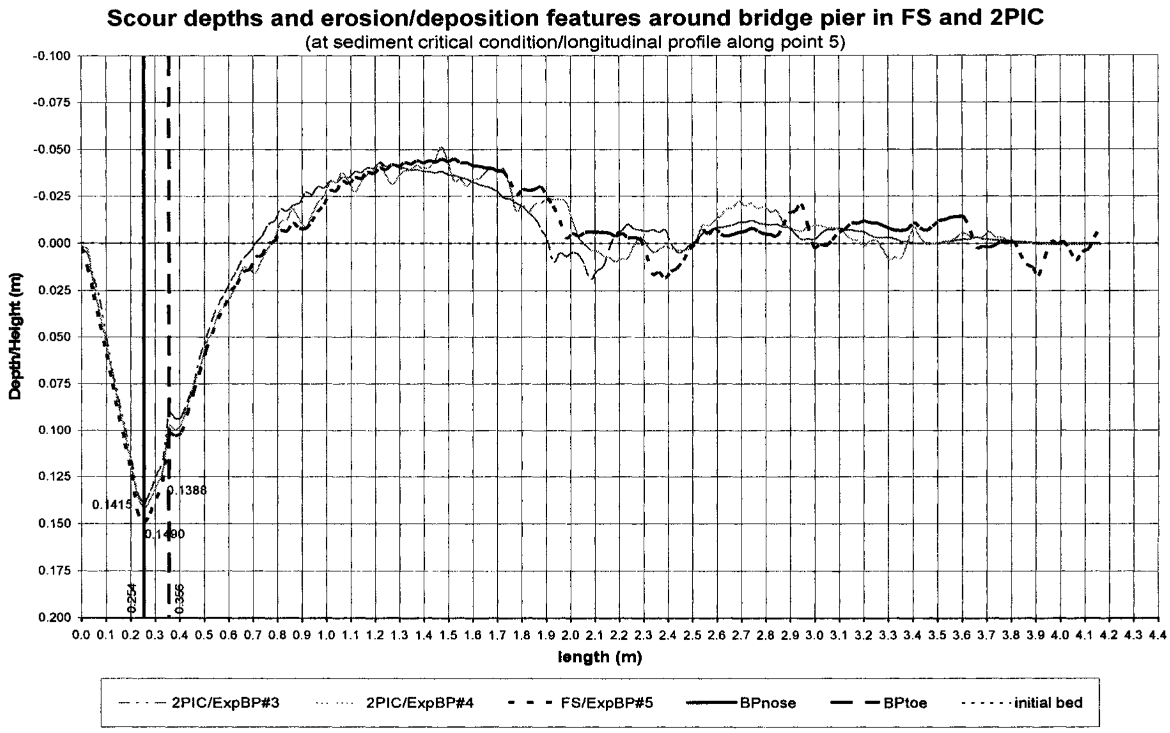

Scour depths and erosion/deposition features around bridge pier in FS and 2PIC
(at sediment critical condition/longitudinal profile along point 5)
Depth/Height (m)
length (m)
0.1415
0.1388
0.1490
0.254
0.356
2PIC/ExpBP#3
2PIC/ExpBP#4
FS/ExpBP#5
BPnose
BPtoe
initial bed

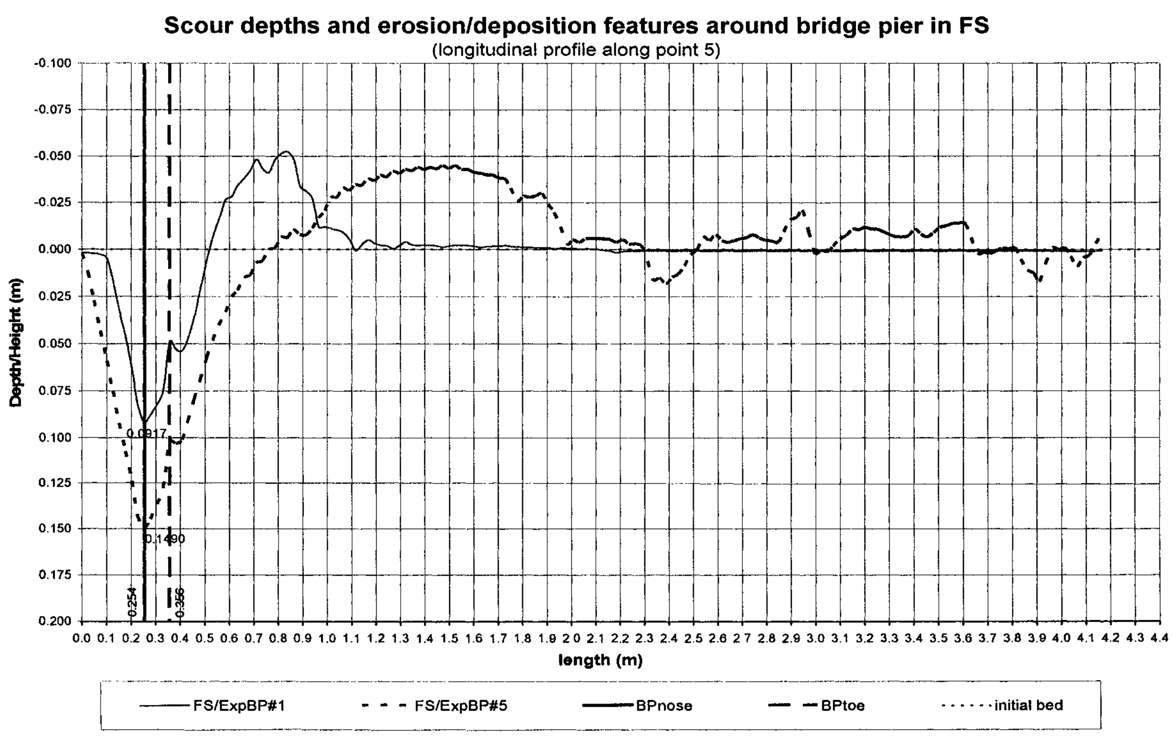

Scour depths and erosion/deposition features around bridge pier in FS
(longitudinal profile along point 5)
Depth/Height (m)
length (m)
0.0917
0.1490
0.254
0.356
FS/ExpBP#1
FS/ExpBP#5
BPnose
BPtoe
initial bed

APPENDIX A16

Scour depths and erosion/deposition profiles (2 D representation)

Scour depth around cylindrical bridge pier and erosion/deposition features downstream
(ExpBP#1/FS)

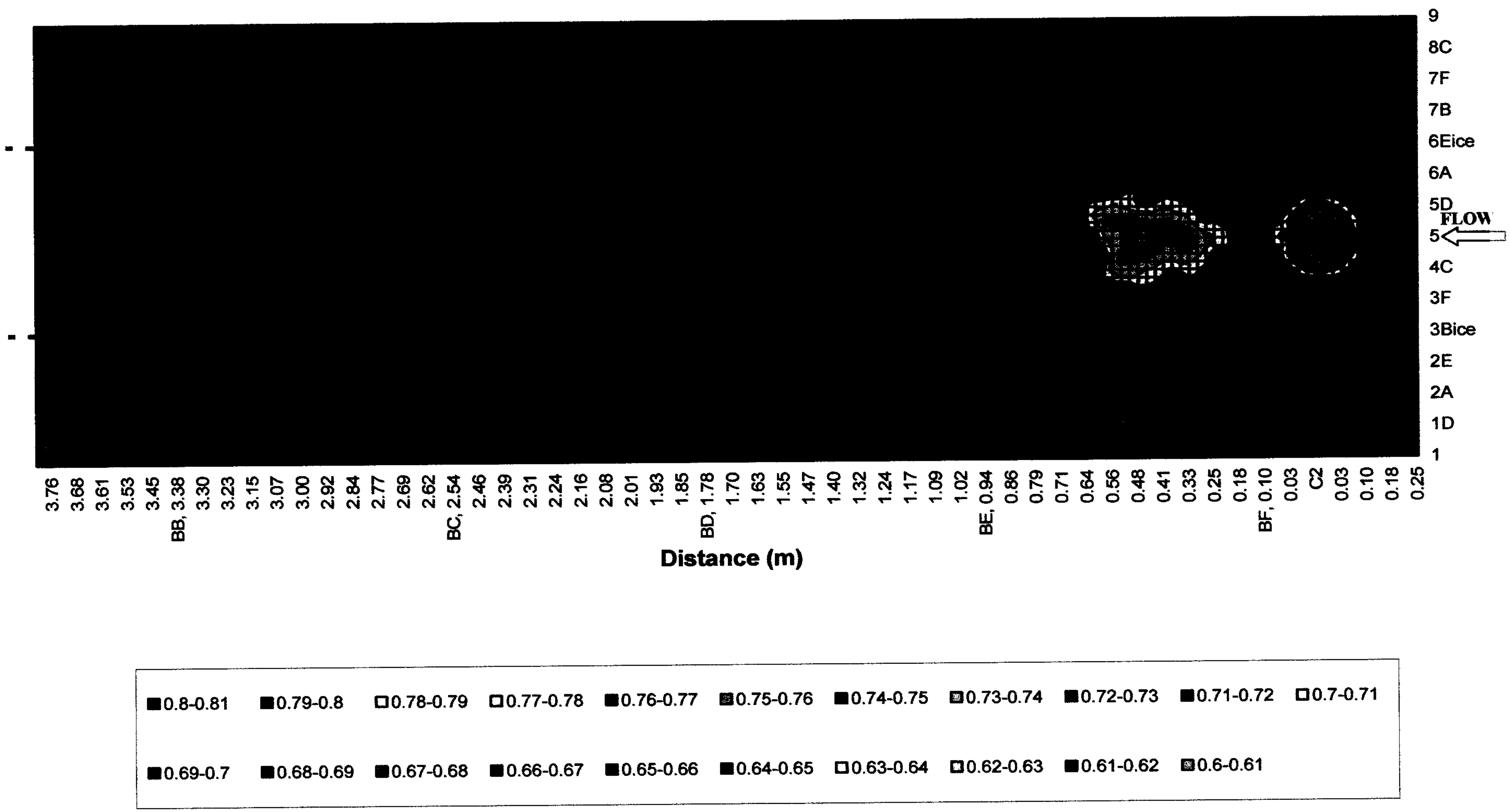

Scour depth around cylindrical bridge pier and erosion/deposition features downstream
(ExpBP#2/2PIC)

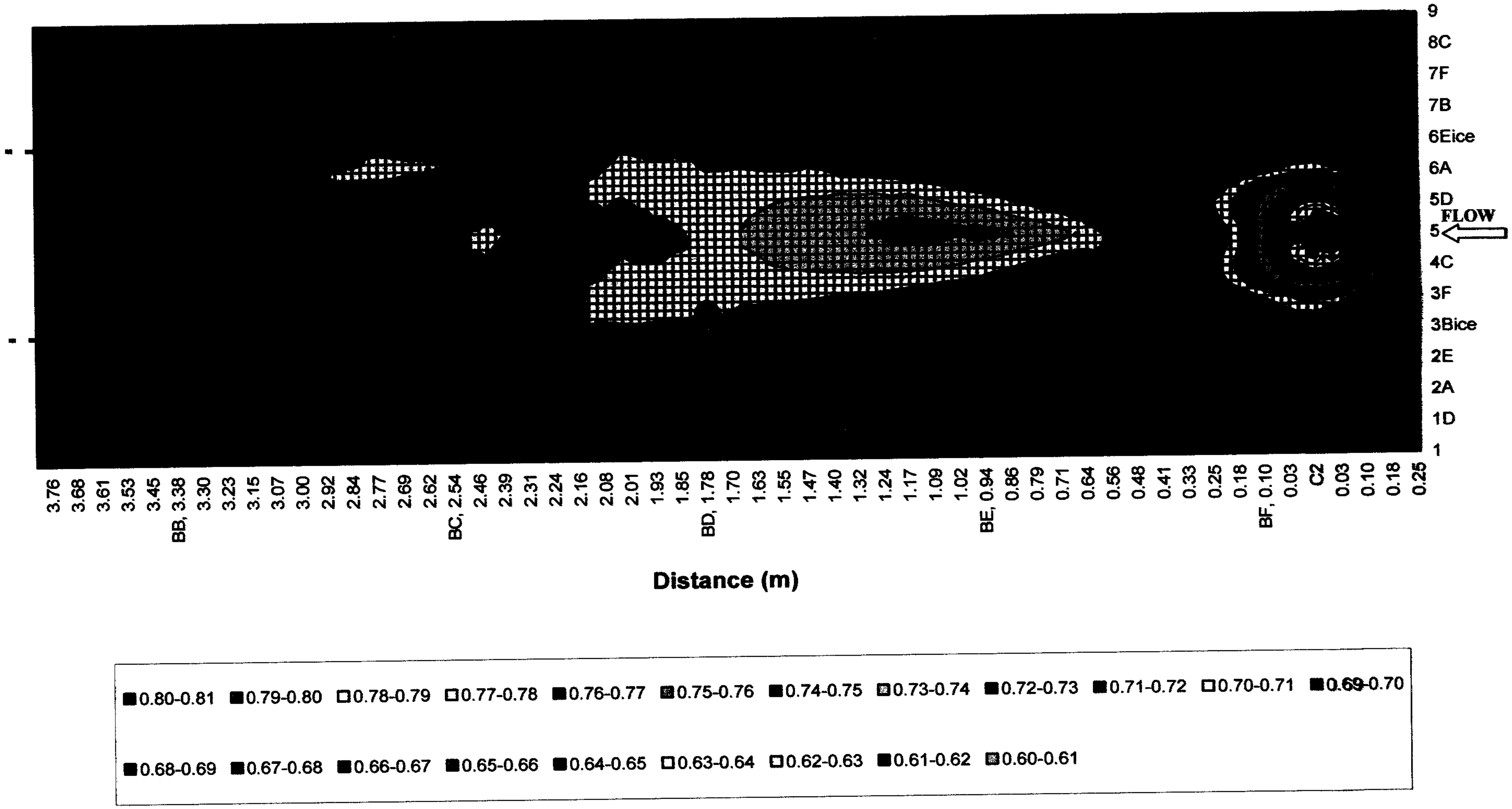

Scour depth around cylindrical bridge pier and erosion/deposition features downstream
(ExpBP#3/2PIC)

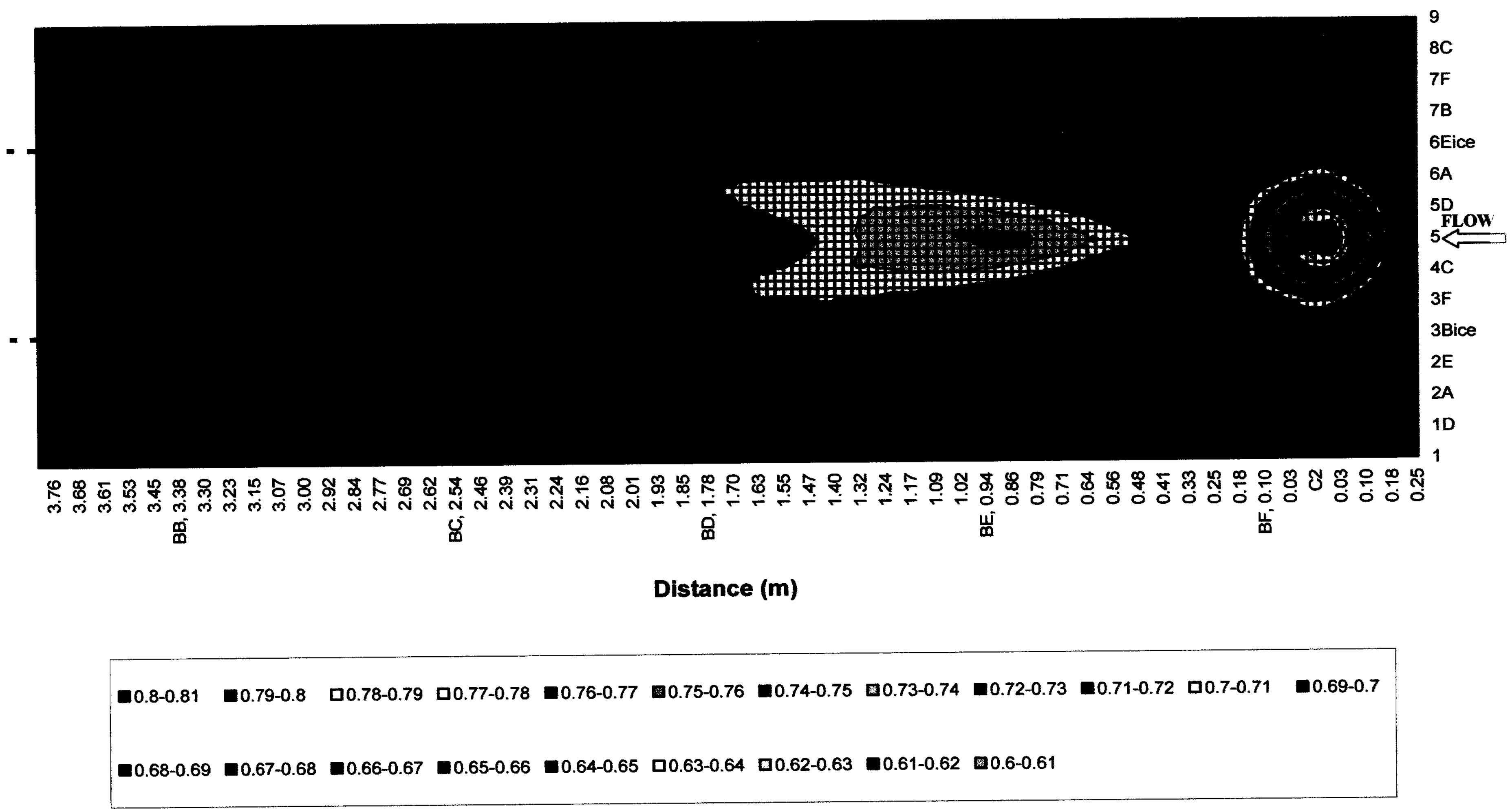

Scour depth around cylindrical bridge pier and erosion/deposition features downstream
(ExpBP#4/2PIC)

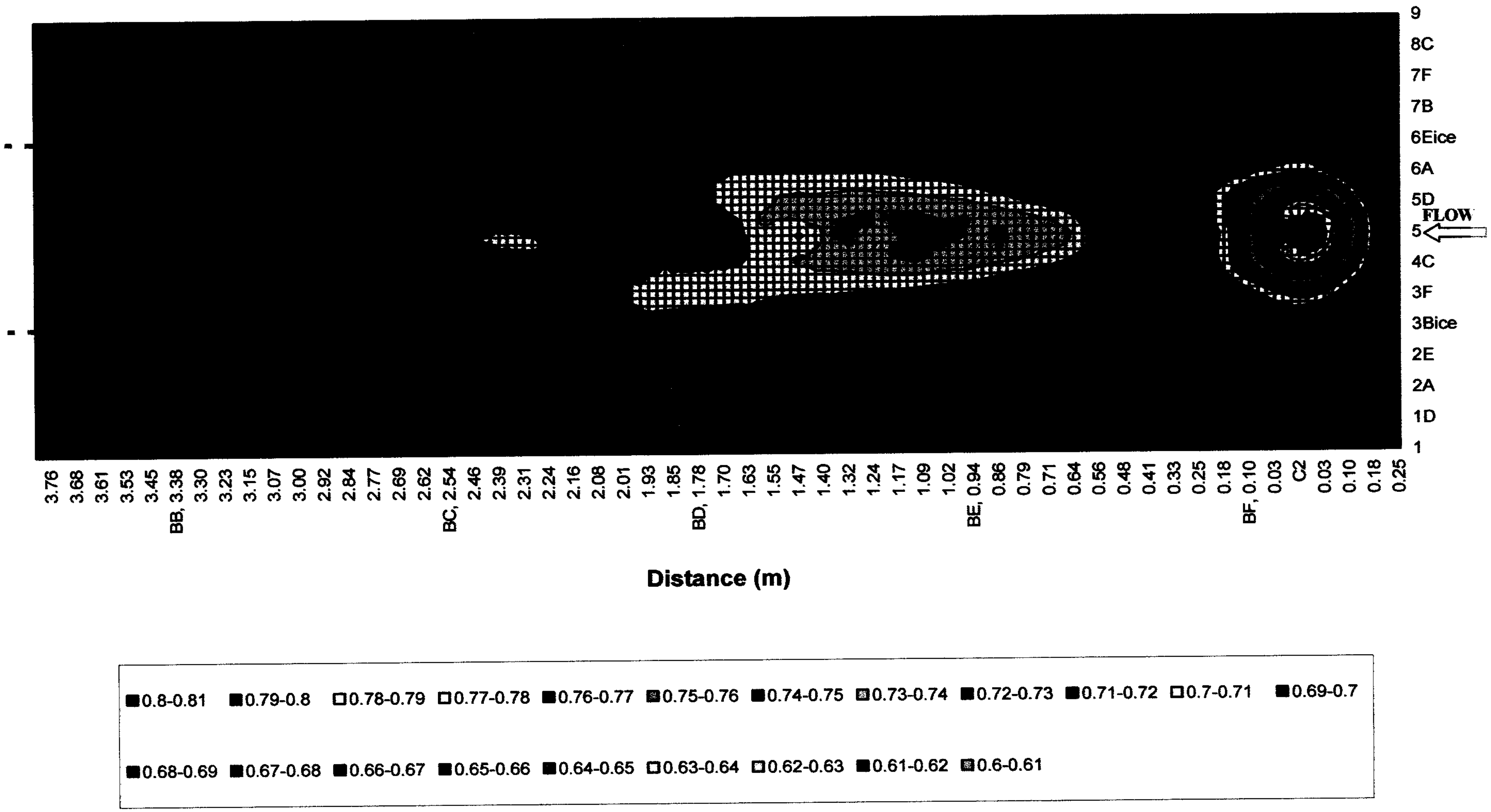

Scour depth around cylindrical bridge pier and erosion/deposition features downstream
(ExpBP#5/2PIC)

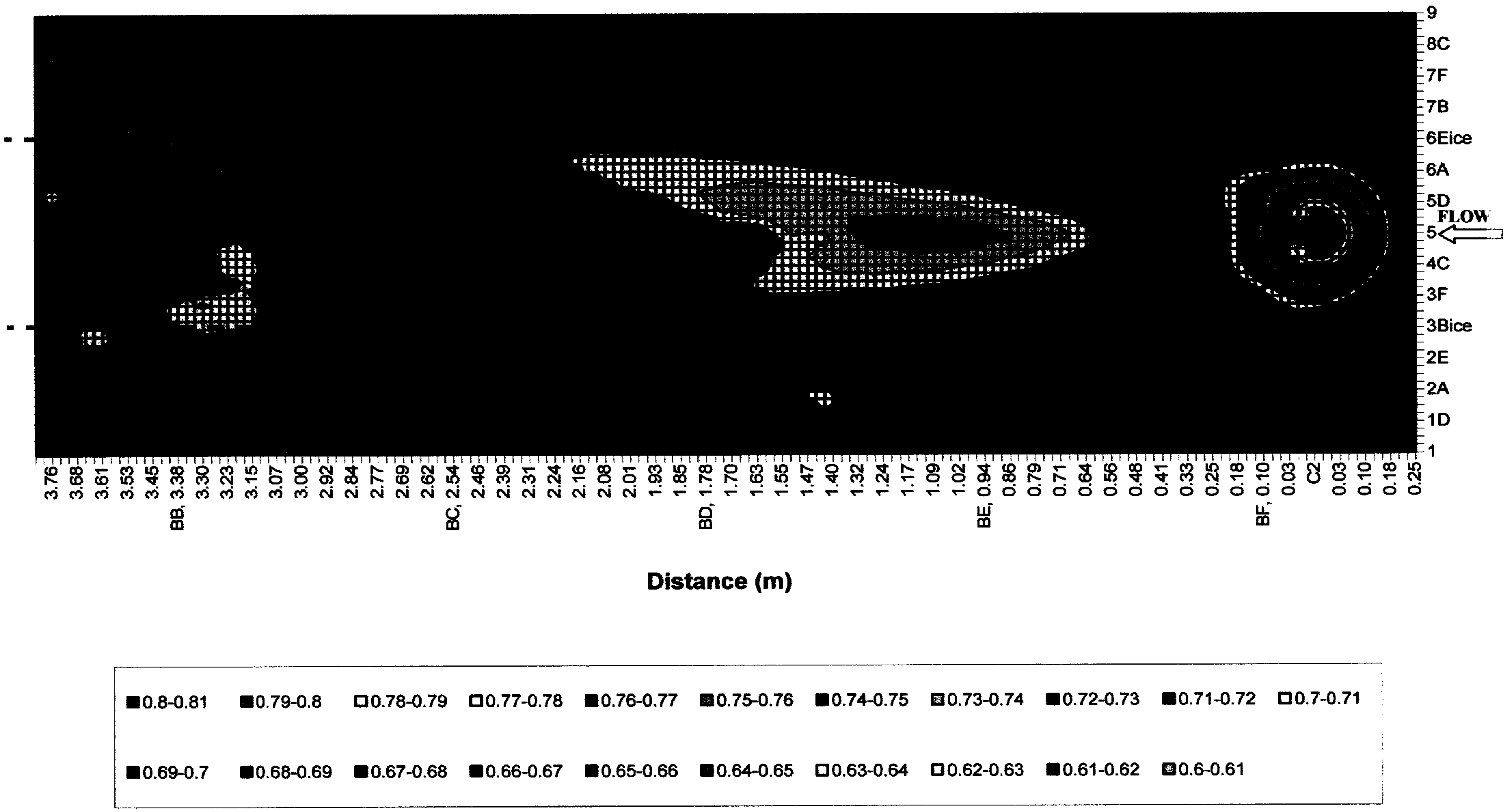

APPENDIX A17

Scour depths and erosion/deposition profiles (3 D representation)

OBS: the following images present a vertical distortion of 27%

Scour depth around cylindrical bridge pier and erosion/deposition features downstream

(ExpBP#1/FS)

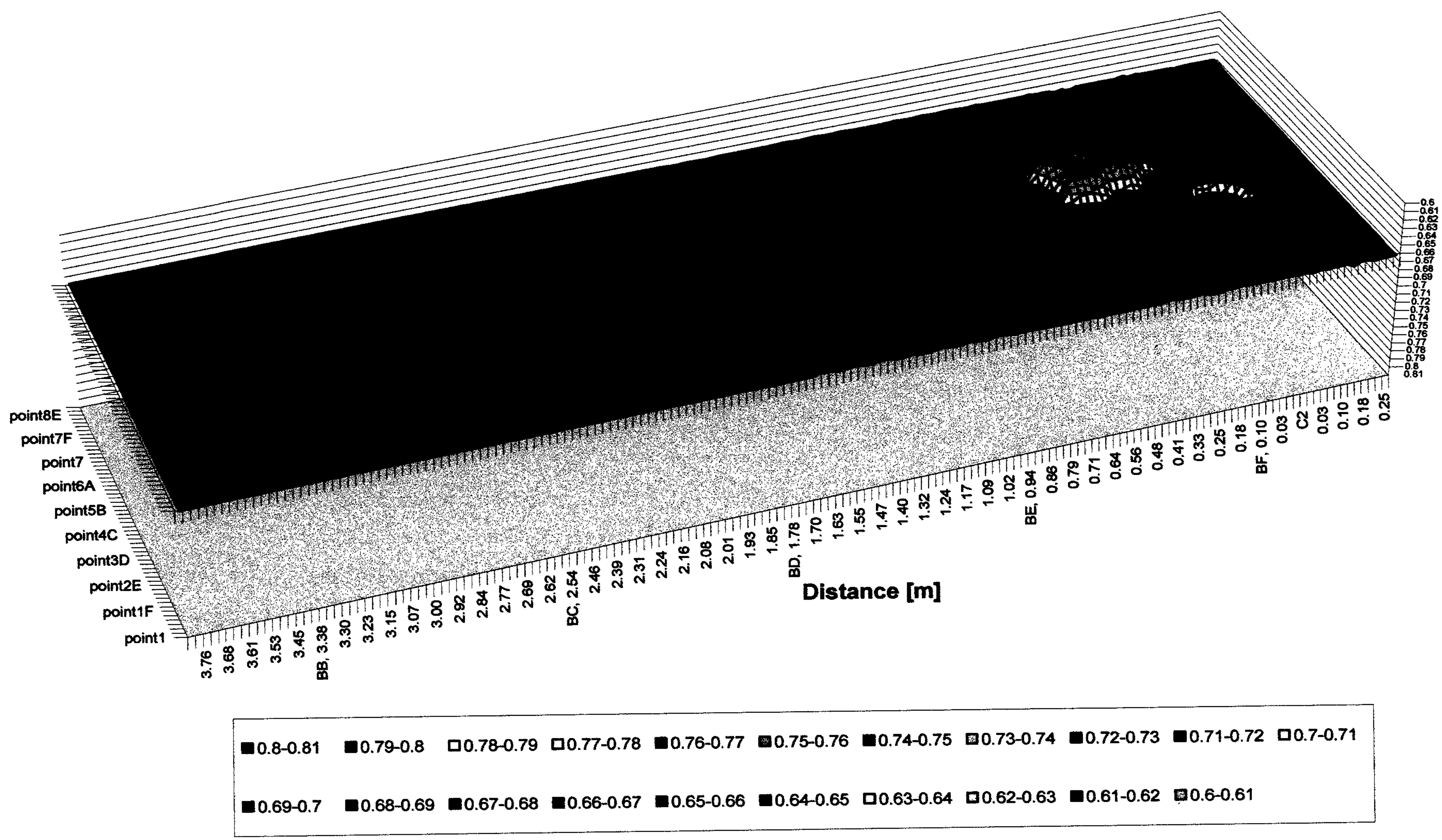

Scour depth around cylindrical bridge pier and erosion/deposition features downstream
(ExpBP#2/2PIC)

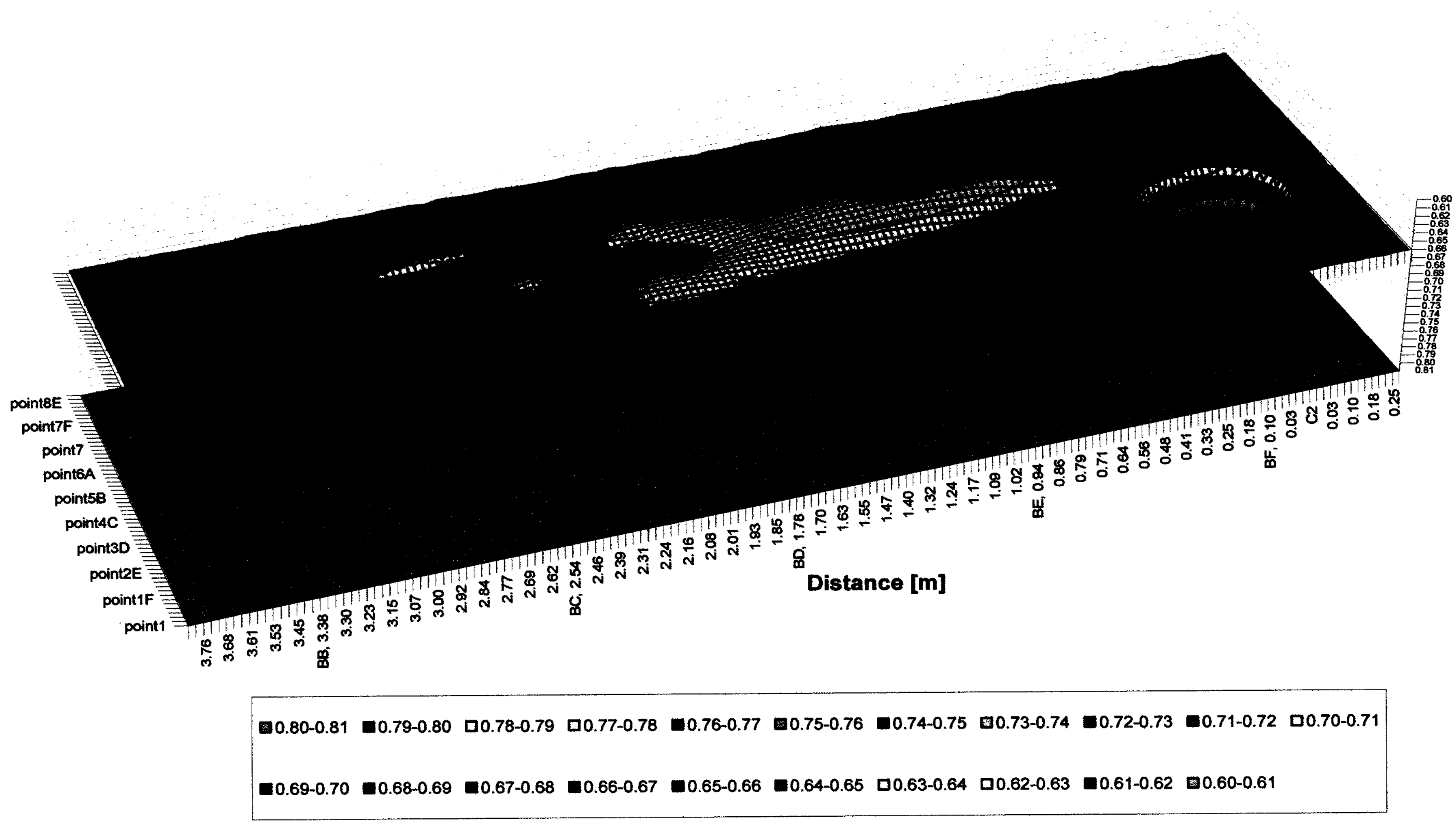

Scour depth around cylindrical bridge pier and erosion/deposition features downstream

(ExpBP#3/2PIC)

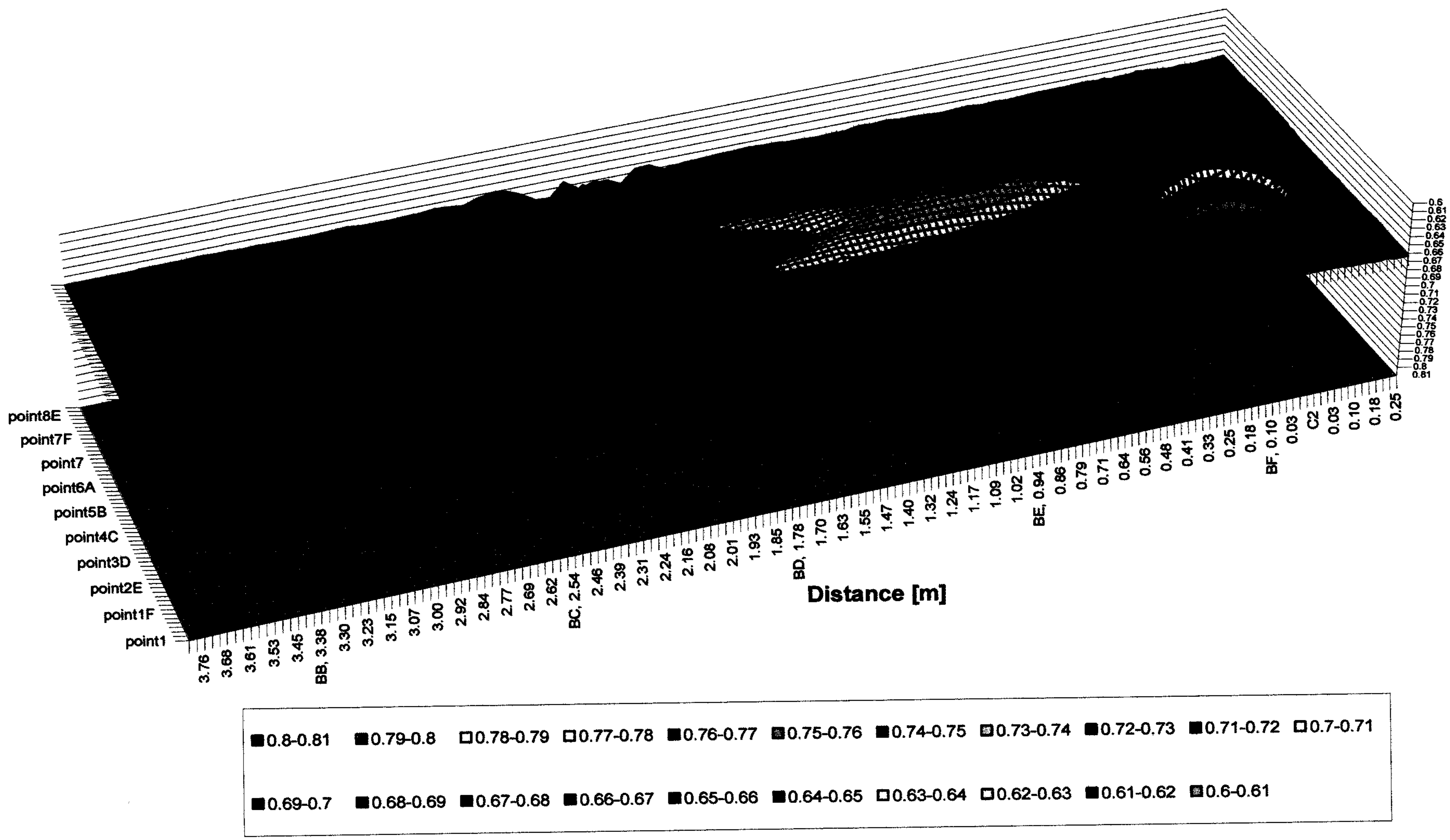

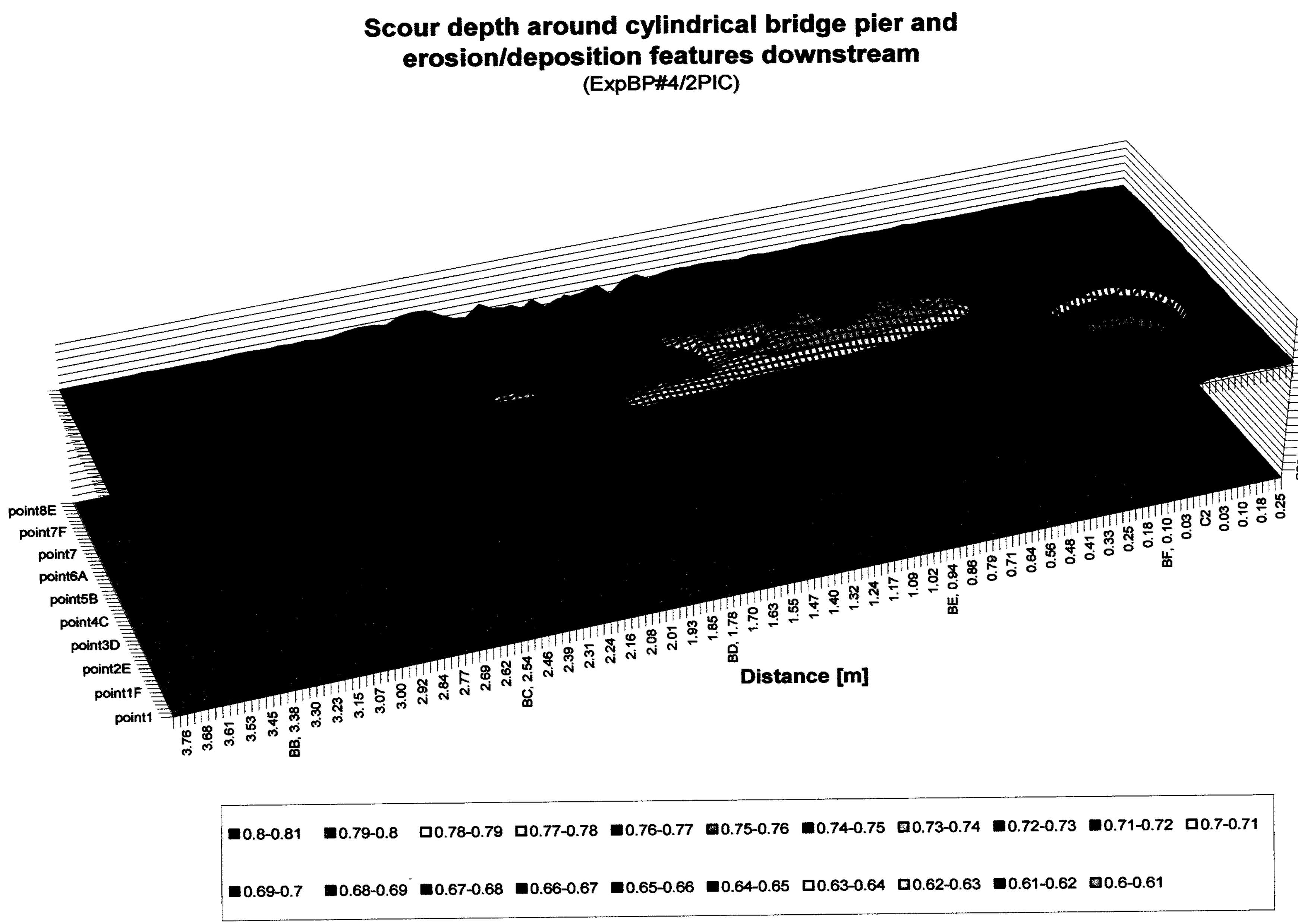
Scour depth around cylindrical bridge pier and
erosion/deposition features downstream
(ExpBP#4/2PIC)
Distance [m]
point8E
point7F
point7
point6A
point5B
point4C
point3D
point2E
point1F
point1
3.76 3.68 3.61 3.53 3.45 BB, 3.38 3.30 3.23 3.15 3.07 3.00 2.92 2.84 2.77 2.69 2.62 BC, 2.54 2.46 2.39 2.31 2.24 2.16 2.08 2.01 1.93 1.85 BD, 1.78 1.70 1.63 1.55 1.47 1.40 1.32 1.24 1.17 1.09 1.02 BE, 0.94 0.86 0.79 0.71 0.64 0.56 0.48 0.41 0.33 0.25 0.18 BF, 0.10 0.03 C2 0.03 0.10 0.18 0.25
0.6 0.61 0.62 0.63 0.64 0.65 0.66 0.67 0.68 0.69 0.7 0.71 0.72 0.73 0.74 0.75 0.76 0.77 0.78 0.79 0.8 0.81
0.8-0.81 0.79-0.8 0.78-0.79 0.77-0.78 0.76-0.77 0.75-0.76 0.74-0.75 0.73-0.74 0.72-0.73 0.71-0.72 0.7-0.71
0.69-0.7 0.68-0.69 0.67-0.68 0.66-0.67 0.65-0.66 0.64-0.65 0.63-0.64 0.62-0.63 0.61-0.62 0.6-0.61

Scour depth around cylindrical bridge pier and erosion/deposition features downstream

(ExpBP#5/FS)